

## NASA Contractor Report 159136

(NASA-CR-159136) EXPLORATORY STUDIES OF THE  
CRUISE PERFORMANCE OF UPPER SURFACE BLOWN  
CONFIGURATIONS: PROGRAM ANALYSIS AND  
CONCLUSIONS (Lockheed-Georgia Co.,  
Marietta.) 349 p HC A15/MF A01

N80-15072

Unclas  
46620

CSCL 01C G3/05

# Exploratory Studies of the Cruise Performance of Upper Surface Blown Configurations

---

## Program Analysis and Conclusions

J. A. Braden, J. P. Hancock,  
J. E. Hackett, and V. Lyman

LOCKHEED-GEORGIA COMPANY  
Marietta, Georgia 30063

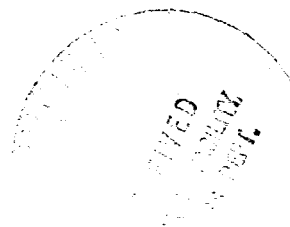
NASA Contract NAS1-13871  
OCTOBER 1979

**NASA**

National Aeronautics and  
Space Administration

Langley Research Center

Hampton, Virginia  
22061-2199



## FOREWORD

This document is submitted in accordance with the requirements of NASA Contract NAS1-13871, Exploratory Studies of the Cruise Performance of Upper Surface Blown Configurations. W. C. Sleeman, Jr. is the NASA-Langley Contract Monitor and J. A. Braden is the Lockheed-Georgia Project Manager.

The technical results under this contract are presented in five reports. For convenience, the overall program documentation is summarized below:

## DOCUMENTATION SUMMARY

<u>CR Number</u>	<u>Title</u>
CR-3193	Summary Report
CR-3192	Experimental Program - Test Facilities, Model Design, Instrumentation, and Low-Speed, High-Lift Tests
CR-159134	Experimental Program - High-Speed Force Tests
CR-159135	Experimental Program - High-Speed Pressure Tests
CR-159136	Program Analysis and Conclusions

## TABLE OF CONTENTS

	<u>Page</u>
FOREWORD . . . . .	ii
LIST OF FIGURES . . . . .	v
SUMMARY . . . . .	xvii
1.0 INTRODUCTION . . . . .	1
2.0 SYMBOLS . . . . .	3
3.0 EXPERIMENTAL DATA ANALYSIS - TASK II TRANSONIC CRUISE . . . .	7
3.1 ANALYSIS PROCEDURES . . . . .	8
3.1.1 Corrections/Validations . . . . .	8
3.1.1.1 Wall-Interference and Blockage . . . . .	8
3.1.1.2 CFF Data Corrections . . . . .	16
3.1.2 Performance Bookkeeping . . . . .	18
3.1.2.1 Sign Convention . . . . .	20
3.1.2.2 Axes . . . . .	20
3.1.2.3 Thrust and Drag Components . . . . .	20
3.1.2.4 Lift Components . . . . .	29
3.1.3 Data Reduction . . . . .	30
3.1.4 Data Formats . . . . .	33
3.2 DISCUSSION OF RESULTS . . . . .	34
3.2.1 Basic Wing-Body Performance . . . . .	39
3.2.1.1 Two-Dimensional Pressure Tests . . . . .	39
3.2.1.2 Wing-Body Force Tests . . . . .	44
3.2.2 USB Nacelle Installations - Pressure Tests . . . . .	52
3.2.2.1 Static Performance . . . . .	55
3.2.2.2 Wind-On Performance . . . . .	60
3.2.2.3 Aerodynamic/Geometric Effects . . . . .	65
3.2.3 USB Installations — Force Tests . . . . .	112
3.2.3.1 Static Performance-Force Tests . . . . .	112
3.2.3.2 General Wind-On Performance . . . . .	114
3.2.3.3 Aerodynamic and Geometric Effects . . . . .	197
4.0 USB THEORETICAL MODEL . . . . .	215
4.1 INTRODUCTION . . . . .	215
4.2 POWER EFFECTS MODELING: GENERAL PRINCIPLES . . . . .	216

## TABLE OF CONTENTS (CONTINUED)

	<u>Page</u>
4.3 WING SECTIONAL AERODYNAMICS . . . . .	224
4.3.1 Pressure Distribution . . . . .	224
4.3.2 Sectional Forces . . . . .	230
4.4 FINITE-WING AERODYNAMICS . . . . .	230
4.5 SURFACE PRESSURES ON THE FLOW-THROUGH NACELLE . . . . .	233
4.5.1 Nacelle Representation . . . . .	233
4.5.2 Nacelle Surface Pressures . . . . .	236
4.6 SURFACE PRESSURES FOR POWERED CASES . . . . .	238
4.6.1 Predicted Effects of Angle-of-Attack and Pressure Ratio . . . . .	241
4.6.2 Comparisons with Measured Surface Pressures . . . .	248
4.7 DRAG ANALYSIS AND CORRELATION: FLOW-THROUGH CASES . . .	253
4.7.1 Analysis of Drag Distribution . . . . .	253
4.7.2 Correlation with Experiment . . . . .	257
4.8 DRAG ANALYSIS AND CORRELATION: POWER EFFECTS . . . . .	260
4.8.1 Analysis of Power Effects on the Wing . . . . .	260
4.9 LIFT ANALYSIS AND CORRELATION . . . . .	275
4.9.1 Vortex Lattice Results . . . . .	275
4.9.2 Simplified Jet Flap Theory . . . . .	276
4.9.3 Correlation by Simplified Jet-Flap Theory . . . . .	278
4.9.4 Correlation by Lifting Line Theory . . . . .	286
5.0 CONCLUSIONS - TASK II . . . . .	291
5.1 EXPERIMENTAL PROGRAM . . . . .	291
5.2 THEORETICAL PROGRAM . . . . .	293
5.2.1 Vortex Lattice Studies . . . . .	294
5.2.2 Applications of Jet Flap Theory . . . . .	295
6.0 COMPATABILITY STUDIES — TASK III . . . . .	297
7.0 REFERENCES . . . . .	298



## LIST OF FIGURES

<u>Number</u>	<u>Title</u>	<u>Page</u>
1	CFF test-section instrumentation for wall-interference study.	10
2	Effect of Mach number on wall static pressures in empty tunnel at $Re_c = 7 \times 10^6/\text{ft}$ .	11
3	Effect of Reynolds number on wall static pressures in empty tunnel at $M_\infty = .8$ .	12
4	Effect of traversing wake rake installation on wall static pressures.	13
5	Effect of nacelle installation on wall static pressures at $M_\infty = .6$ .	14
6	Effect of power on wall static pressures at $M_\infty = .6$ .	15
7	Comparison of static installed thrust ratio and CFF-corrected drag increments. (a) Static installed thrust (b) Nacelle drag increments	19
8	Wind axes system.	21
9	Gross thrust losses.	23
10	Configuration drag.	24
11	Identifiable installation and aerodynamic penalty components.	27
12	Variation of nozzle gross thrust with Mach no. and pressure ratio, nozzle $N_{3E}$ .	31
13	Variation of nozzle gross thrust with Mach no. and pressure ratio, nozzle $N_{g^2}$ .	32
14	(a) Data analysis formats. (b) Data analysis formats. (c) Data analysis formats. (d) Data analysis formats.	35 36 37 38
15	Comparison of airfoils LG3-316 and LG7-516.	40

<u>Number</u>	<u>Title</u>	<u>Page</u>
16	Pressure distribution comparison of original and modified airfoils, $M_\infty = 0.73$ , $\alpha = 3^\circ$ .	41
17	Pressure distribution comparison of original and modified airfoils, $M_\infty = 0.72$ , $\alpha = 3^\circ$ .	42
18	Operating envelopes for original and modified airfoil sections.	43
19	Comparison of swept wing pressures as modified by simple sweep theory to straight wing pressures.	45
20	Variation of lift coefficient with Mach number, straight wing. $R_{NC} = 3.5 \times 10^6$	46
21	Variation of drag coefficient with Mach number, straight wing. $R_{NC} = 3.5 \times 10^6$	47
22	Variation of pitching-moment coefficient with Mach number, straight wing. $R_{NC} = 3.5 \times 10^6$	48
23	Variation of lift coefficient with Mach number, swept wing. $R_{NC} = 3.5 \times 10^6$	49
24	Variation of drag coefficient with Mach number, swept wing. $R_{NC} = 3.5 \times 10^6$	50
25	Variation of pitching-moment coefficient with Mach number, swept wing. $R_{NC} = 3.5 \times 10^6$	51
26	Derivation of equivalent expression for jet-turning loads.	54
27	Jet centerline surface pressures, static tests, $\alpha = 0^\circ$ .	
	(a) $H_j/p_\infty = 1.44$	57
	(b) $H_j/p_\infty = 2.66$	57
	(c) $H_j/p_\infty = 3.3$	58
28	Effects of nozzle size on jet-centerline pressures, static, $\alpha \approx 2^\circ$ , $H_j/p_\infty = 2.7$ .	59
29	Comparison of force and pressure-derived wing loads at static conditions.	61
30	Jet centerline pressure distributions, "D-Duct" noz ( $N_6$ ) $H_j/p_\infty = 2.6$ , $\alpha = 2.6^\circ$ .	62

<u>Number</u>	<u>Title</u>	<u>Page</u>
31	Comparison of static and wind-on jet isobars one chord length behind straight wing, $H_j/p_\infty = 2.2$ , $\alpha = 2.6^\circ$ .	64
32	Effect of Mach no. on jet core location at rake, "D-Duct" noz ( $N_3$ ) $\alpha = 3^\circ$ .	66
33	Effect of Mach no. on jet centerline pressures, $H_j/p_\infty = 2.2$ , $\alpha = 2^\circ$ .	67
34	Jet centerline pressure distributions at constant $q_j/q_\infty = 2.3$ , $\alpha = 2^\circ$ .	69
35	Jet dynamic pressure ratio, fully expanded jet - incompressible.	70
36	Effect of Mach no. on pressure - integrated drag, $\alpha \approx 2^\circ$ , $H_j/p_\infty \approx 2.4$ .	72
37	Effect of Mach no. on lift developed in scrubbed area, $\alpha = 2^\circ$ , $H_j/p_\infty = 2.2$ .	73
38	Effect of nozzle pressure ratio on jet centerline pressures, $\alpha \approx 3^\circ$ , $M_\infty = 0.70$ .	73
39	Effect of nozzle pressure ratio on jet centerline pressures, $\alpha \approx 3^\circ$ , $M_\infty = 0.68$ .	76
40	Variation of scrubbed area pressure drag with pressure ratio, $\alpha \approx 2^\circ$ , $M_\infty = 0.68$ .	77
41	Variation of scrubbed area pressure drag with pressure ratio, $\alpha \approx 2^\circ$ , $M_\infty = 0.68$ .	78
42	Comparison of pressure drag developed in scrubbed area.	79
43	Lift developed in scrubbed area with blowing, $\alpha = 2^\circ$ , $M_\infty = 0.70$ .	80
44	Lift developed in scrubbed area with blowing, $\alpha = 2^\circ$ , $M_\infty = 0.70$ .	81
45	Variation of pressure drag with Mach no. and pressure ratio, $\alpha \approx 2^\circ$ .	84
46	Variation of pressure drag in scrubbed area with Mach no. and pressure ratio, $\alpha \approx 2^\circ$ .	85

<u>Number</u>	<u>Title</u>	<u>Page</u>
47	Variation of lift increment developed in scrubbed area with Mach no. and pressure ratio, $\alpha = 2^\circ$ .	87
48	Lift increase in scrubbed area due to blowing, $\alpha \approx 2^\circ$ - $3^\circ$ .	88
49	Variation of excess pressure drag due to nacelle installation and blowing within scrubbed area, $\alpha = 2^\circ$ .	89
50	Variation of incremental lift due to nacelle installation and blowing within the scrubbed area, $\alpha = 2^\circ$ .	90
51	Comparison of USB and jet-flap pressure drag.	92
52	Effect of nozzle exit shape on jet centerline pressures, $\alpha \approx 2^\circ$ , $M_\infty = 0.60$ , $H_j/p_\infty = 1.4$ .	93
53	Effect of nozzle exit aspect ratio on pressure drag, $\alpha = 3^\circ$ , $M_\infty = 0.68$ , $H_j/p_\infty = 2.6$ .	95
54	Effect of nozzle aspect ratio on lift developed in scrubbed area, $M_\infty = 0.68$ , $\alpha \approx 2^\circ$ , $H_j/p_\infty = 2.6$ .	96
55	(a) Effect of nozzle size on jet centerline pressures, $M_\infty = 0.68$ , $\alpha = 2^\circ$ , $H_j/p_\infty \approx 1.4$ .	99
	(b) Concluded. $H_j/p_\infty \approx 3.0$ .	100
56	Spanwise influence of jet, "D-Duct" nozzle ( $N_3$ ), $\alpha = 3^\circ$ , $M_\infty = 0.68$ , $h_j/p_\infty = 2.0$ .	102
57	Spanwise influence of jet, "D-Duct" nozzle ( $N_3$ ), $\alpha = 3^\circ$ , $M_\infty = 0.68$ , $H_j/p_\infty = 3.57$ .	103
58	Spanwise influence of jet, noz $N_5$ , $AR = 6$ , $\alpha = 3^\circ$ , $M_\infty = 0.68$ , $H_j/p_\infty = 2.0$ .	105
59	Spanwise influence of jet, noz $N_5$ , $AR = 6$ , $\alpha = 3^\circ$ , $M_\infty = 0.68$ , $H_j/p_\infty = 2.75$ .	106
60	Spanwise influence of jet on swept wing, noz $N_8$ , $AR = 2.5$ , $\alpha = 3^\circ$ , $M_\infty = 0.68$ .	107
61	Spanwise influence of jet on swept wing, noz $N_{13}$ , $AR = 6$ , $\alpha = 3^\circ$ , $M_\infty = 0.68$ , $H_j/p_\infty = 1.96$ .	108
62	Swept-wing pressure distribution along median line of twin-jet configuration, "D-Duct" noz ( $N_8$ ), $\alpha = 3^\circ$ , $M_\infty = .60$ , $H_j/p_\infty = 2.6$ .	110

<u>Number</u>	<u>Title</u>	<u>Page</u>
63	Swept wing pressure distribution along median line of twin-jet configuration, "D-Duct" noz ( $N_8$ ), $\alpha = 3^\circ$ , $M_\infty = 0.73$ , $H_j/p_\infty = 2.6$ .	111
64	Tabulation of $\eta_{TS}$ ( $\delta_{js}$ ) for test nozzles; static data.	113
65	Incremental nacelle drag and component build-up noz $N_{3E}$ , $AR = 2.5$ , $M_\infty = 0.68$ , $C_{LM} = 0.40$ .	115
66	Incremental nacelle drag and component build-up noz $N_{3E}$ , $AR = 2.5$ , $M_\infty = 0.60$ , $C_{LM} = 0.40$ ..	117
67	Incremental nacelle drag and component build-up noz $N_{3E}$ , $AR = 2.5$ , $M_\infty = 0.72$ , $C_{LM} = 0.40$ .	118
68	Incremental nacelle drag and component build-up noz $N_2$ , circular, $M_\infty = 0.60$ , $C_{LM} = 0.40$ .	119
69	Incremental nacelle drag and component build-up noz $N_2$ , circular, $M_\infty = 0.68$ , $C_{LM} = 0.40$ .	120
70	Incremental nacelle drag and component build-up noz $N_2$ , circular, $M_\infty = 0.72$ , $C_{LM} = 0.40$ .	121
71	Incremental nacelle drag and component build-up noz $N_{2E}$ , circular, $M_\infty = 0.60$ , $C_{LM} = 0.40$ .	122
72	Incremental nacelle drag and component build-up noz $N_{2E}$ , circular, $M_\infty = 0.68$ , $C_{LM} = 0.40$ .	123
73	Incremental nacelle drag and component build-up noz $N_{2E}$ , circular, $M_\infty = 0.72$ , $C_{LM} = 0.40$ .	124
74	Incremental nacelle drag and component build-up noz $N_{3B}$ , $AR = 2.5$ , $M_\infty = 0.60$ , $C_{LM} = 0.40$ .	125
75	Incremental nacelle drag and component build-up noz $N_{3B}$ , $AR = 2.5$ , $M_\infty = 0.68$ , $C_{LM} = 0.40$ .	126
76	Incremental nacelle drag and component build-up noz $N_{3B}$ , $AR = 2.5$ , $M_\infty = 0.72$ , $C_{LM} = 0.40$ .	127
77	Incremental nacelle drag and component build-up noz $N_4$ , $AR = 4$ , $M_\infty = 0.60$ , $C_{LM} = 0.40$ .	128
78	Incremental nacelle drag and component build-up noz $N_4$ , $AR = 4$ , $M_\infty = 0.68$ , $C_{LM} = 0.40$ .	129
79	Incremental nacelle drag and component build-up noz $N_4$ , $AR = 4$ , $M_\infty = 0.72$ , $C_{LM} = 0.40$ .	130

<u>Number</u>	<u>Title</u>	<u>Page</u>
80	Incremental nacelle drag and component build-up noz $N_{4E}$ , $AR = 4$ , $M_\infty = 0.60$ , $C_{LM} = 0.40$ .	131
81	Incremental nacelle drag and component build-up noz $N_{4E}$ , $AR = 4$ , $M_\infty = 0.68$ , $C_{LM} = 0.40$ .	132
82	Incremental nacelle drag and component build-up noz $N_{4E}$ , $AR = 4$ , $M_\infty = 0.72$ , $C_{LM} = 0.40$ .	133
83	Incremental nacelle drag and component build-up noz $N_5$ , $AR = 6$ , $M_\infty = 0.60$ , $C_{LM} = 0.40$ .	134
84	Incremental nacelle drag and component build-up noz $N_5$ , $AR = 6$ , $M_\infty = 0.68$ , $C_{LM} = 0.40$ .	135
85	Incremental nacelle drag and component build-up noz $N_5$ , $AR = 6$ , $M_\infty = 0.72$ , $C_{LM} = 0.40$ .	136
86	Incremental nacelle drag and component build-up noz $N_6$ , $AR = 2.5$ , $M_\infty = 0.60$ , $C_{LM} = 0.40$ .	137
87	Incremental nacelle drag and component build-up noz $N_6$ , $AR = 2.5$ , $M_\infty = 0.68$ , $C_{LM} = 0.40$ .	138
88	Incremental nacelle drag and component build-up noz $N_6$ , $AR = 2.5$ , $M_\infty = 0.72$ , $C_{LM} = 0.40$ .	139
89	Incremental nacelle drag and component build-up noz $N_8^2$ , $AR = 2.5$ , $M_\infty = 0.60$ , $C_{LM} = 0.40$ .	140
90	Incremental nacelle drag and component build-up noz $N_8^2$ , $AR = 2.5$ , $M_\infty = 0.68$ , $C_{LM} = 0.40$ .	141
91	Incremental nacelle drag and component build-up noz $N_8^2$ , $AR = 2.5$ , $M_\infty = 0.73$ , $C_{LM} = 0.40$ .	142
92	Incremental nacelle drag and component build-up noz $N_{11}$ , circular, $M_\infty = 0.60$ , $C_{LM} = 0.40$ .	143
93	Incremental nacelle drag and component build-up noz $N_{11}$ , circular, $M_\infty = 0.68$ , $C_{LM} = 0.40$ .	144
94	Incremental nacelle drag and component build-up noz $N_{11}$ , circular, $M_\infty = 0.73$ , $C_{LM} = 0.40$ .	145
95	Incremental nacelle drag and component build-up noz $N_{12}$ , $AR = 4.0$ , $M_\infty = 0.60$ , $C_{LM} = 0.40$ .	146
96	Incremental nacelle drag and component build-up noz $N_{12}$ , $AR = 4.0$ , $M_\infty = 0.68$ , $C_{LM} = 0.40$ .	147

<u>Number</u>	<u>Title</u>	<u>Page</u>
97	Incremental nacelle drag and component build-up noz N <sub>12</sub> , AR = 4, M <sub>∞</sub> = 0.73, C <sub>LM</sub> = 0.40.	148
98	Incremental nacelle drag and component build-up noz N <sub>13</sub> , AR = 6, M <sub>∞</sub> = 0.60, C <sub>LM</sub> = 0.40.	149
99	Incremental nacelle drag and component build-up noz N <sub>13</sub> , AR = 6, M <sub>∞</sub> = 0.68, C <sub>LM</sub> = 0.40.	150
100	Incremental nacelle drag and component build-up noz N <sub>13</sub> , AR = 6, M <sub>∞</sub> = 0.73, C <sub>LM</sub> = 0.40.	151
101	Incremental nacelle drag and component build-up nozs N <sub>8</sub> <sup>1</sup> + N <sub>8</sub> <sup>2</sup> (dual), AR = 2.5, M <sub>∞</sub> = 0.69, C <sub>LM</sub> = 0.40.	152
102	Incremental nacelle drag and component build-up nozs N <sub>8</sub> <sup>1</sup> + N <sub>8</sub> <sup>2</sup> , dual, AR = 2.5, M <sub>∞</sub> = 0.68, C <sub>LM</sub> = 0.40.	153
103	Incremental nacelle drag and component build-up nozs N <sub>8</sub> <sup>1</sup> and N <sub>8</sub> <sup>2</sup> , dual, AR = 2.5, M = 0.73, C <sub>LM</sub> = 0.40.	154
104	Tabulation of estimated skin friction drag of test nacelles.	156
105	Variation of effective drag-due-to-lift parameter with thrust and Mach no., nozzle N <sub>2</sub> , circular.	158
106	Variation of effective drag-due-to-lift parameter with thrust and Mach no., nozzle N <sub>2E</sub> , circular.	159
107	Variation of effective drag-due-to-lift parameter with thrust and Mach no., nozzle N <sub>3B</sub> , AR = 2.5.	160
108	Variation of effective drag-due-to-lift parameter with thrust and Mach no., nozzle N <sub>3E</sub> , AR = 2.5.	161
109	Variation of effective drag-due-to-lift parameter with thrust and Mach no., nozzle N <sub>4</sub> , AR = 4.	162
110	Variation of effective drag-due-to-lift parameter with thrust and Mach no., nozzle N <sub>4E</sub> , AR = 4.	163
111	Variation of effective drag-due-to-lift parameter with thrust and Mach no., nozzle N <sub>5</sub> , AR = 6.	164
112	Variation of effective drag-due-to-lift parameter with thrust and Mach no., nozzle N <sub>6</sub> , AR = 2.5.	165
113	Variation of effective drag-due-to-lift parameter with thrust and Mach no., nozzle N <sub>11</sub> , circular.	166

<u>Number</u>	<u>Title</u>	<u>Page</u>
114	Variation of effective drag-due-to-lift parameter with thrust and Mach no., nozzle $N_8^2$ , AR = 2.5.	167
115	Variation of effective drag-due-to-lift parameter with thrust and Mach no., nozzle $N_{12}$ , AR = 4.	168
116	Variation of effective drag-due-to-lift parameter with thrust and Mach no., nozzle $N_{13}$ , AR = 6.	169
117	Variation of effective drag-due-to-lift parameter with thrust and Mach no., nozzle $N_8^2 + N_8^2$ , dual, AR = 2.5.	170
118	Oil-flow photograph of high-boattail nozzle ( $N_{4E}$ ), $\beta = 36^\circ$ , $M_\infty = 0.70$ , $\alpha = 2.6^\circ$ .	174
119	The effect of nozzle pressure ratio on total lift, noz $N_2$ , circular, $M_\infty = 0.68$ .	178
120	The effect of nozzle pressure ratio on total lift, noz $N_{3E}$ , AR = 2.5, $M_\infty = 0.68$ .	179
121	Effect of nozzle pressure ratio on total lift, noz $N_5$ , AR = 6.0, $M_\infty = 0.68$ .	180
122	Variation of lift and moment increments due to blowing, noz $N_2$ , circular.	182
123	Variation of lift increments due to blowing, noz $N_{2E}$ , circular.	183
124	Variation of lift increment due to blowing, noz $N_{3B}$ , AR = 2.5.	184
125	Variation of lift and moment increments due to blowing, noz $N_{3E}$ , AR = 2.5.	185
126	Variation of lift and moment increments due to blowing, noz $N_4$ , AR = 4.	186
127	Variation of lift and moment increments due to blowing, noz $N_{4E}$ , AR = 4.	187
128	Variation of lift and moment increments due to blowing, noz $N_5$ , AR = 6.	188
129	Variation of lift and moment increments due to blowing, noz $N_6$ , AR = 2.5.	189



<u>Number</u>	<u>Title</u>	<u>Page</u>
130	Variation of lift increment due to blowing, noz N <sub>11</sub> , circular.	190
131	Variation of lift increment due to blowing, noz N <sub>12</sub> , AR = 4.	191
132	Variation of lift increment due to blowing, noz N <sub>13</sub> , AR = 6.	192
133	Effect of nozzle pressure ratio on pitching-moment, noz N <sub>2</sub> , circular, M <sub>∞</sub> = 0.68.	194
134	Effect of nozzle pressure ratio on pitching-moment, noz N <sub>3E</sub> , AR = 2.5, M <sub>∞</sub> = 0.68.	195
135	Effect of nozzle pressure ratio on pitching-moment, noz N <sub>5</sub> , AR = 6, M <sub>∞</sub> = 0.68.	196
136	Effect of nozzle aspect ratio on nacelle drag.	198
137	Effect of nozzle boattail angle on nacelle drag.	200
138	Effect of Mach number on drag for faired-over vs flow-through forebodies, straight wing with circular noz N <sub>2</sub> .	201
139	Comparison of "long" and "short" faired forebodies, c <sup>2</sup> /A <sub>N</sub> = 24.	203
140	Comparison of lift performance of "short" and "long" forebodies, M <sub>∞</sub> = 0.68, H <sub>j</sub> /p <sub>∞</sub> = flow-through.	204
141	Effect of nacelle installation and blowing on lift α = 3°, M <sub>∞</sub> = 0.68.	206
142	Comparison of streamlined and symmetrical nacelle drag, C <sub>LM</sub> = 0.40.	208
143	Effect of multiple engine installation on drag C <sub>LM</sub> = 0.40, swept wing.	210
144	Comparison of lift-due-to-blowing for 2-eng. and 4-eng. configurations "D-duct" nacelle, swept wing, M <sub>∞</sub> = 0.73.	211
145	Effect of Mach number on drag for pylon-mounted OTW vs. integrated USB nacelle, straight wing with noz N <sub>2</sub> .	213

<u>Figure</u>	<u>Title</u>	<u>Page</u>
146	Stimulation of fan pressure rise.	217
147	Jet simulation methods	220
148	Representation of jet spreading and entrainment by vortex-ring polygons.	223
149	Mathematical model of the USB jet efflux.	225
150	(a) Airfoil sectional characteristics — incidence matched.	227
	(b) Airfoil sectional characteristics — lift coefficient matched.	228
	(c) Airfoil sectional characteristics — leading edge matched.	229
151	Definition of $\Delta C_d$	231
152	Lift curves for the straight wing at $M_\infty = 0.60$ .	232
153	Drag polars for the straight wing at $M_\infty = 0.60$ .	234
154	Panel details for D-Duct nacelle and adjacent wing.	235
155	Calculated chordwise pressure distributions on nacelle surfaces — flow-through condition, $M_\infty = 0.60$ .	237
156	Calculated forward-nacelle surface pressures — flow-through condition, $M_\infty = 0.60$ .	239
157	Calculated blend-region surface pressures — flow-through nacelle, $\alpha = +3^\circ$ , $M_\infty = 0.60$ .	240
158	Predicted clean-wing pressure distributions as a function of $\alpha$ .	242
159	Predicted nacelle spine and wing surface pressure distributions at $H_j/p_\infty = 1.25$ (flow-through).	243
160	Predicted spline and wing surface pressure distributions at $H_j/p_\infty = 1.8$ .	245
161	Predicted nacelle-spline and wing surface pressure distributions as a function of jet pressure ratio, $\alpha = 2^\circ$ , $M_\infty = 0.60$ .	246

<u>Number</u>	<u>Title</u>	<u>Page</u>
162	Predicted incremental surface pressures as a function of jet pressure ratio.	247
163	Predicted and measured surface pressure increments aft of nacelle (Row A).	249
164	Predicted and measured surface pressure increments on wing adjacent to nacelle (Row C).	250
165	Predicted and measured pressures on nacelle-surfaces.	252
166	Computed drag count distribution along nacelle axis (nacelle surfaces only).	254
167	Drag build-up on nacelle surfaces, $M_\infty = 0.60$ , $\alpha = 3.0^\circ$ .	256
168	Wing drag increments in the nacelle overlap region and aft of it.	258
169	Computed drag count distribution along semi-span (all surfaces).	259
170	Drag increments due to unpowered nacelle.	261
171	Typical $C_p$ plots for drag integration (a) Row E (b) Rows C and A	263
172	Power-induced changes in wing pressure coefficients.	265
173	Location of drag-producing and thrust-producing regions due to application of power.	267
174	Predicted drag increments due to addition of powered $N_{3E}$ nacelle, $M_\infty = 0.60$ .	268
175	Comparison between predicted and measured drag increments for nacelle $N_{3E}$ at $M_\infty = 0.60$ . (a) $H_j/p_\infty = 1.40$ (b) $H_j/p_\infty = 1.60$ (c) $H_j/p_\infty = 1.80$ (d) $H_j/p_\infty = 2.00$ (e) $H_j/p_\infty = 2.20$	260 270 271 272 273

<u>Number</u>	<u>Title</u>	<u>Page</u>
176	Residual difference between experimental and predicted drag increments for nacelle N <sub>3E</sub> at $M_\infty = 0.60$ .	274
177	Comparison of USB-test results with modified jet-flap theory, noz N <sub>2E</sub> , circular, $M_\infty = 0.68$ .	279
178	Comparison of USB-test results with modified jet-flap theory, noz N <sub>3E</sub> , AR = 2.5, $M_\infty = 0.68$ .	280
179	Comparison of USB-test results with modified jet-flap theory, noz N <sub>4E</sub> , AR = 4, $M_\infty = 0.68$ .	281
180	Comparison of USB-test results with modified jet-flap theory, noz N <sub>5</sub> , AR = 6, $M_\infty = 0.68$ .	282
181	Comparison of USB-test results with modified jet-flap theory, noz N <sub>3E</sub> , AR = 2.5, $M_\infty = 0.68$ .	283
182	Comparison of USB-test results with modified jet-flap theory, noz N <sub>4E</sub> , AR = 4, $M_\infty = 0.68$ .	284
183	Comparison of USB test results with three-dimensional lifting line theory, nozzle N <sub>3E</sub> , AR = 2.5, $M_\infty = 0.68$ .	287
184	Comparison of USB test results with three-dimensional lifting line theory, noz N <sub>4E</sub> , AR = 4, $M_\infty = 0.68$ .	288
185	Comparison of USB test results with three-dimensional lifting line theory, noz N <sub>5</sub> , AR = 6, $M_\infty = 0.68$ .	289

## SUMMARY

The purpose and scope of the USB-Cruise Program (NAS1-13871) are briefly reviewed in Section 1.0 of this document. A major objective under Task II of the overall contractual work has been the experimental investigation of a comprehensive matrix of upper-surface nacelle installations across a wide range of nozzle blowing pressure ratios ( $1.0 \leq H_j/p_\infty \leq 3.0$ ) and cruise Mach numbers ( $0.60 \leq M_\infty \leq 0.80$ ). The present report provides an analysis of the experimental data encompassing surface pressure measurements, force-measurements and wake surveys, at both static and wind-on test conditions. As fundamental to the analysis, cruise performance trends are evaluated as reflecting nacelle geometric variations and nozzle operating conditions. A supporting study in the Task II work has been the theoretical modeling of the USB-system via a vortex-lattice method. Simulated power, or thrust, effects are an integral part of the theoretical model. The present document presents details of the modeling process and provides an over-view of the design and analysis capabilities provided. As an outgrowth of the Task II experimental/analytical effort, a candidate nacelle is selected for a more detailed, systems-oriented study. The selection and evaluation of the candidate propulsive system, as applied to a large transport aircraft, represents the major objective of Task III in the basic program. This phase of the overall study, that is, Task III - Computability Studies, has been performed in concert with a similar, acoustics-oriented contractual effort (NAS1-13870, Noise Characteristics of Upper Surface Blown Configurations). Documentation of the Task III studies and conclusions are contained herein as an appendix.

## 1.0 INTRODUCTION

In early 1975, the NASA awarded a contract (NAS1-13871) to the Lockheed-Georgia Company for the acquisition of a high-speed, experimental data base for aircraft configurations featuring nacelles mounted on the upper wing surface. This design concept, known as USB (upper-surface blowing), had received earlier, experimental endorsements as a viable means of achieving moderate-to-good powered lift performance along with beneficial noise reduction in the STOL environment. In the interest of further development of the USB-system, the contractual work performed by the Lockheed-Georgia Company emphasized the transonic cruise characteristics of USB-designs on an exploratory basis. The overall program is comprised of extensive experimental tests of USB-configurations in a transonic wind-tunnel with support provided by an analytical modeling of the system. Testing was planned around a matrix of nozzle configurations suitable for evaluating the effects of key USB-design variables. The primary intent of the USB-Cruise Program has been the development of a compendium of experimental and theoretical information from which refined upper-surface-blowing (USB) nacelle installations can evolve. The present report documents an analysis of the basic experimental and theoretical results obtained under Task II (Cruise Performance Data Base) and Task III (Compatability Studies).

The objective of the experimental phase of the program has been to isolate characteristic aero/propulsive phenomena representing variations in wing/nacelle geometric parameters. For this purpose, the model component matrix was selected on the basis of geometric arrangements which could be of

foreseeable interest. A high degree of refinement in model component design was not appropriate to the exploratory nature of the program, nor to the extensive array of model hardware employed in a "build-up" fashion. Therefore, the emphasis of the experimental program lies more in the interpretation of incremental aero/propulsive "effects" rather than absolute levels of magnitude. As will be noted, however, reasonable care has been exercised, in both model design and specialized testing, to minimize effects which could tend to obscure incremental aero/propulsive phenomena.

## 2.0 SYMBOLS

Dimensional data are presented herein in both the International System of Units (SI) and the U.S. Customary Units. The measurements and calculations were made in the U.S. Customary Units.

A	area, cross-sectional, $\text{cm}^2$ (in. <sup>2</sup> )
AR	aspect ratio
b	model span, cm (in.)
c	local wing chord, cm (in.)
$\bar{c}$	mean aerodynamic chord, cm (in.)
$C_d$	section drag coefficient $D/q_\infty S_W$
$C_D$	model drag coefficient, $D/q_\infty S_W$
$C_{D_i}$	induced drag coefficient for complete model, $D_i/q_\infty S_W$
$C_{D_M}$	measured drag coefficient, $D_M/q_\infty S_W$
$C_{D_O}$	profile drag coefficient for model without nacelles, $D_O/q_\infty S_W$
$C_{D_P}$	pressure drag coefficient, $D_P/q_\infty S_W$
$C_l$	section lift coefficient, $l/q_\infty c$
$C_L$	model lift coefficient, $L/q_\infty S_W$
$C_m$	section pitching moment coefficient about quarter chord, $M_Y/q_\infty c^2$
$C_M$	model pitching moment coefficient about quarter chord, $M_Y/q_\infty S_W c$
$C_p$	pressure coefficient, $(p_1 - p_\infty)/q_\infty$ , based on freestream
$C_{p_j}$	pressure coefficient, $(p_1 - p_\infty)/q_j$ , based on jet
$C_T$	nozzle gross thrust coefficient, $F/q_\infty S_W$
$C_X$	coefficient of total force on model in thrust direction, $= -C_{D_M}$



$d_N$	diameter of nozzle, cm (in.)
$D$	drag force, N(lb)
$D_i$	induced drag, N(lb)
$D_o$	profile drag, N(lb)
$D_p$	pressure drag, N(lb)
$e$	wing efficiency factor
$F$	force, N(lb)
$F_A$	axial force, N(lb)
$F_N$	normal force, N(lb)
$g$	acceleration due to gravity, $Nm^2/kg^2(ft-lbf/lbm \text{ sec}^2)$
$h$	jet or nozzle height above surface at jet centerline, cm (in.)
$h_w$	height above wing reference plane, cm (in.)
$H$	total pressure, $N/m^2(lb/in.^2)$
$L$	model lift, N(lb)
$M$	Mach number
$M_Y$	pitching moment about quarter chord, $m-N(in.-lb)$
$p$	static pressure, $N/m^2(lb/in.^2)$
$q$	dynamic pressure, $N/m^2(lb/in.^2)$
$R$	radius of curvature, cm (in.)
$R_N$	Reynolds number per foot
$R_{NC}$	Reynolds number based on streamwise chord
s.m.	statute mile
$S_w$	semispan wing area, $cm^2 (in^2)$
$t$	thickness, cm (in.)
$T$	thrust N(lb)
$V$	velocity, m/s (ft/sec)
$w$	width of nozzle at wing surface, cm (in.)

W	airflow, Kg/s (lb m/sec)
x	ordinate along airfoil chord line measured from leading edge, cm (in.)
y,Y	ordinate along wing span measured from model centerline, cm (in.)
z	ordinate measured normal to wing shord plane, cm (in.)
$\alpha$	geometric angle of attack of airfoil chord line, degrees
$\beta$	boattail angle, degrees
$\delta$	deflection angle, degrees
n	percent semispan
$\eta_T$	jet turning efficiency, $\frac{\sqrt{F_N + F_A}}{F}$
$\gamma$	circulation strength
$\rho$	mass density, Kg/m (slugs/ft)
$\theta$	angular displacement at radius vector, ring cylinder

Subscripts:

A	aerodynamic
E	exit
INST	installed
INTERF	interference
ISOL	isolated
j	jet
jv	jet velocity
M	measured
MAX	maximum
MISC	miscellaneous
N	nacelle
NF	nacelle friction

R	ring cylinder maximum radius
S	static condition
SV	scrubbing and vectoring
TOT	total
V	vectoring
WB	wing body
$\infty$	freestream conditions
$H_j/p_\infty$	at pressure-ratio
CLEAN	clean wing value

### 3.0 EXPERIMENTAL DATA ANALYSIS - TASK II TRANSONIC CRUISE

The overall experimental program encompassed a wide variety of tests inclusive of force measurements, surface-pressure measurements and wake surveys at both static and wind-on conditions. Certain preliminary investigations were also undertaken early in the experimental phase to assure compatibility between the powered models and the relatively small, variable-porosity blowdown tunnel.

The general order in which the more significant investigations were conducted is:

- o Nozzle Calibrations
- o Wall-Interference/Blockage Tests
- o Surface-Pressure Measurements
- o Wake Surveys
- o Force Testing (CFF-blowdown)
- o Force Testing (4' x 4' blowdown)

The complete run schedules for all of these tests are provided in Volume IIA. Volume IIB provides basic data plots for all force testing inclusive of that obtained in Lockheed Compressible Flow (CFF) and 4' x 4' test facilities. Details of the nozzle calibrations are also contained in Volume IIB. All basic data pertinent to surface pressure measurements and wake-surveys are given in Volume IIC.

The initial static calibrations of the isolated USB-nozzles were conducted in the Lockheed V/STOL test facility with checks made at various points in

the test program against the several other balance systems used in the high-speed investigations (CFF and 4' x 4' balance systems). With the nozzle calibrations available, the experimental phase proceeded to the study of wall-interference and blockage corrections. This was followed by the measurement of surface pressures on a variety of wing/nacelle combinations along with wake survey measurements in the jet efflux. Force testing, the final phase of the experimental work, was conducted in several steps with most of the data derived from the Lockheed Compressible Flow Facility (CFF).

In the paragraphs which follow, the specialized tests, preliminary to the main body of the basic force and pressure investigations, are discussed with appropriate conclusions drawn. Also in this section, details of the aero/propulsive bookkeeping process and data formats necessary to force and pressure data analysis are provided.

### 3.1 ANALYSIS PROCEDURES

#### 3.1.1 Corrections/Validations

3.1.1.1 Wall-Interference and Blockage - The USB test program included peripheral experimental studies designed to study the effects of a relatively high blockage, powered model in a small, variable porosity test facility. While tests of a similar nature had been successfully conducted in this facility, the approximately 5 percent physical blockage due to the model plus the additional momentum introduced by the blowing nacelle

created a need for these additional studies. Specifically, these tests investigated the effects of the powered and unpowered model on test-section wall interference for a range of test Reynolds numbers. For this, static pressure taps were installed along the tunnel side wall 10.7 cm (4.2 in.) above the tunnel centerline as shown in Figure 1.

A plot of measured wall pressures with the model removed is shown in Figure 2 which indicates an essentially constant Mach number in the region of the model over a wide range of freestream Mach conditions. Similar data are given in Figure 3 for three test conditions corresponding to Reynolds numbers of 3.5, 7.0 and  $11 \times 10^6$  based on the 17.8 cm (7.0 in.) chord of the test wing. These data also indicate no appreciable effect of Reynolds number on the Mach number distribution in the free tunnel.

Introduction of the traversing wake-rake and supporting rods into the tunnel produced a slight blockage effect in that the flow tends to slow down in the region of the model as shown in Figure 4. A correction for this relatively small effect, in terms of a Mach-dependent  $\Delta C_p$ , was developed and applied accordingly whenever the traversing wake-rake was installed.

Addition of the nacelle to the wing produced a conventional blockage increment as evidenced in Figure 5; this effect was considered via a standard blockage correction when setting the desired freestream condition. Adding power (thrust) to the nacelle produced the data shown in Figure 6. The effect of the added momentum of the jet in the test section appeared to be quite small.

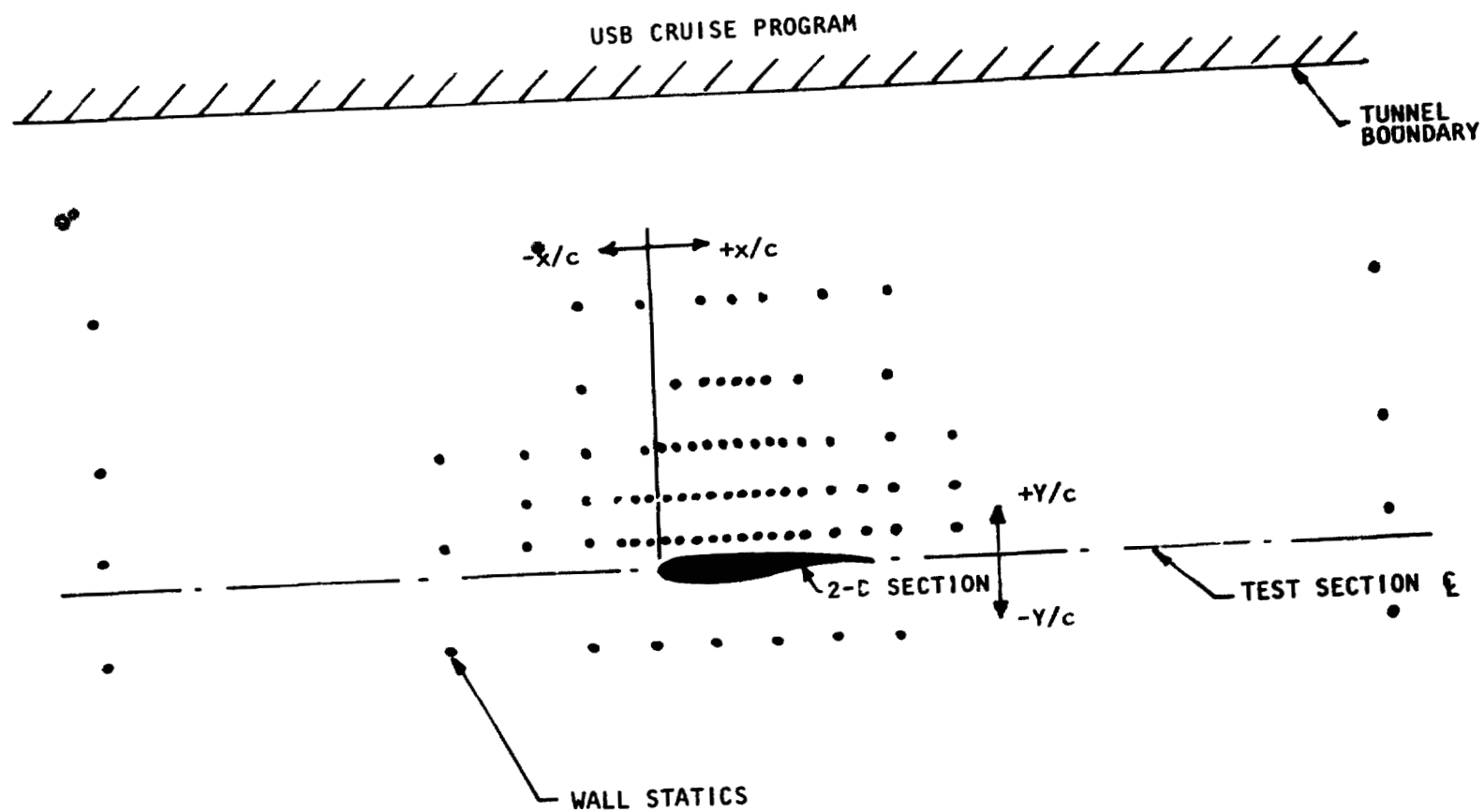


Figure 1 . CFF test-section instrumentation for wall-interference study.

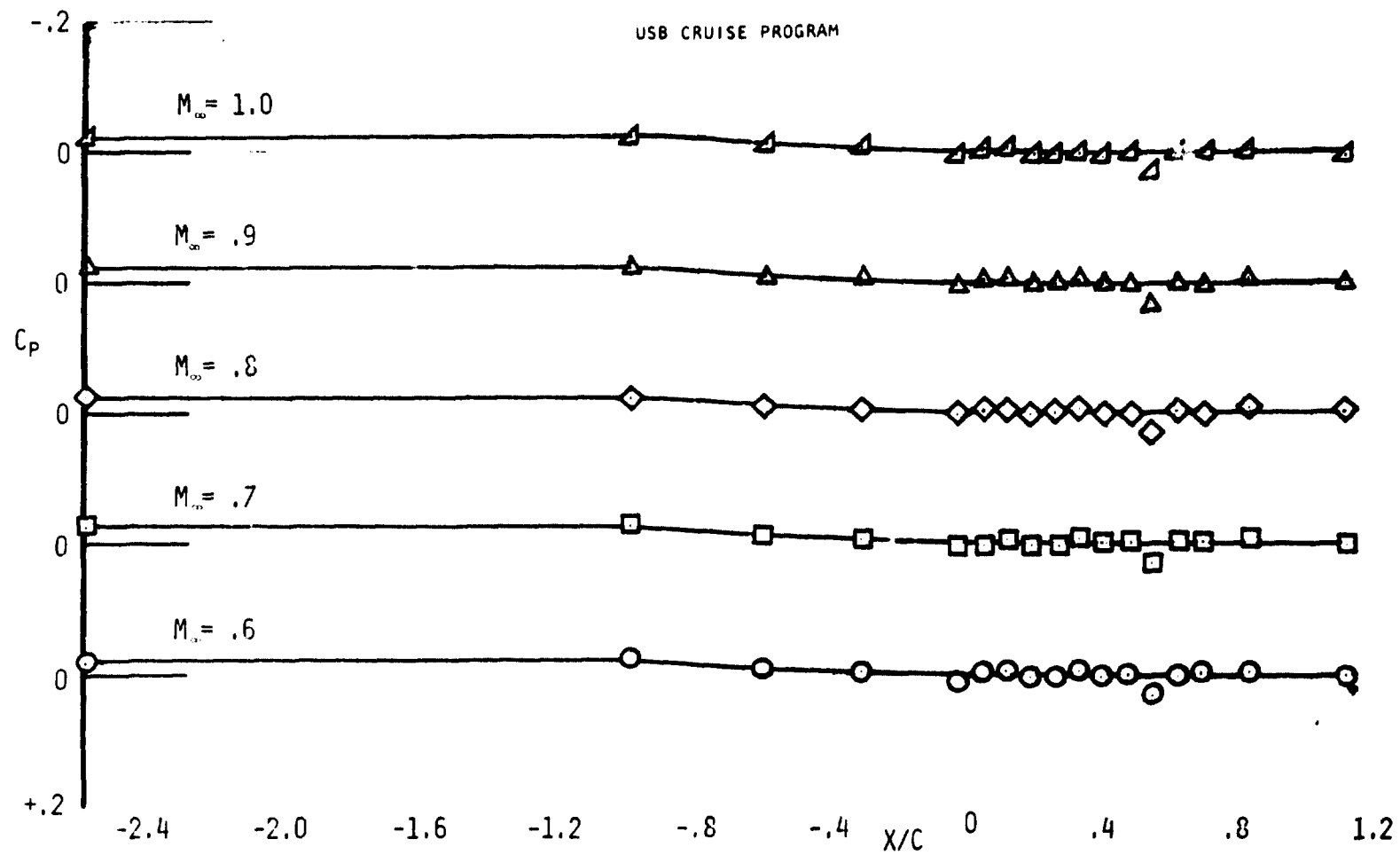


Figure 2. Effect of Mach number on wall static pressures in empty tunnel at  $Re_C = 7 \times 10^6$



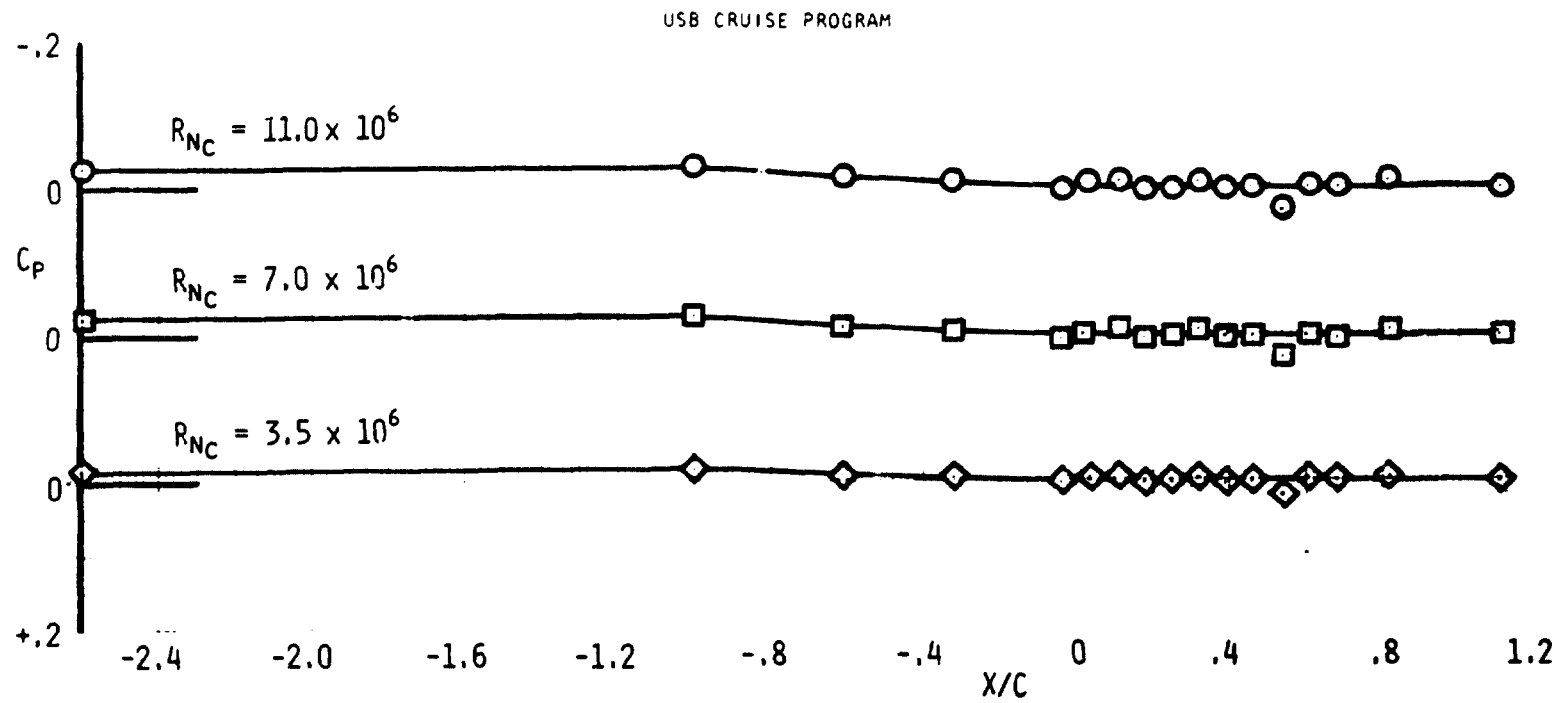


Figure 3. Effect of Reynolds number on wall static pressures in empty tunnel at  $M_\infty = .8$

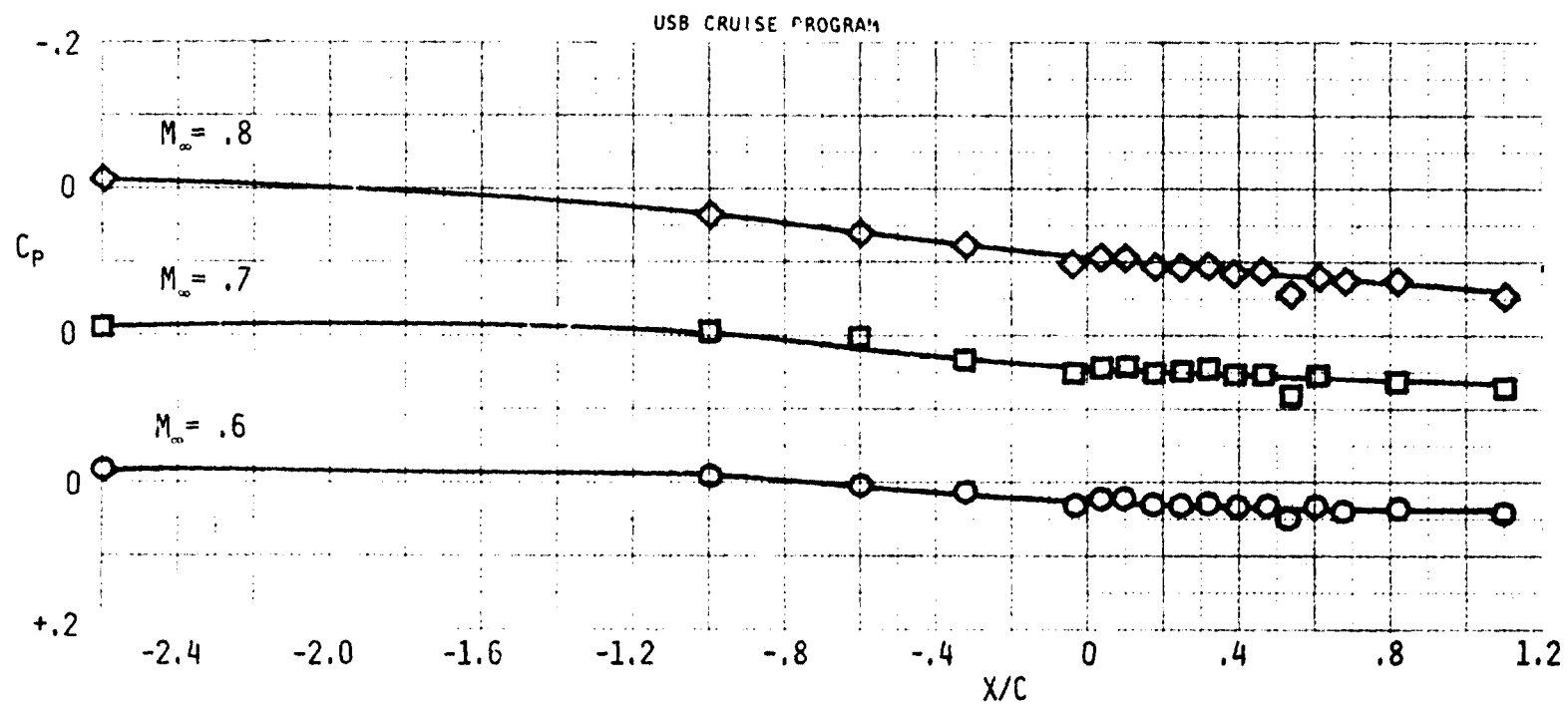
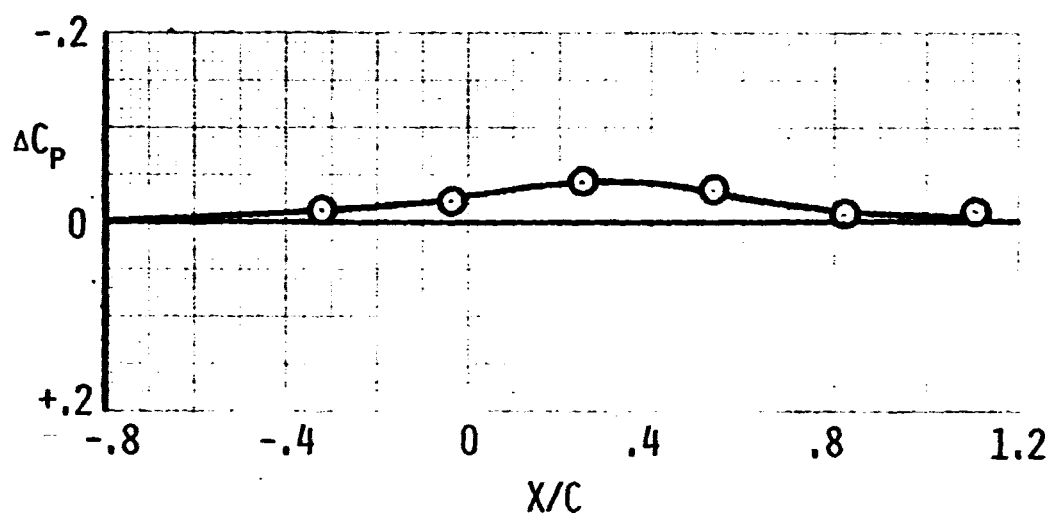


Figure 4. Effect of traversing wake rake installation on wall static pressures.

USB CRUISE PROGRAM

$$\Delta C_p = C_{p_{\text{WING} + \text{NACELLE}}} - C_{p_{\text{WING ALONE}}}$$



ORIGINAL PAGE IS  
OF POOR QUALITY

Figure 5. Effect of nacelle installation on wall static pressures at  $M_\infty = .6$ .

USB CRUISE PROGRAM

$$\Delta C_P = C_{P|_{H_j/p_\infty = 2.6}} - C_{P|_{H_j/p_\infty = 1.0}}$$

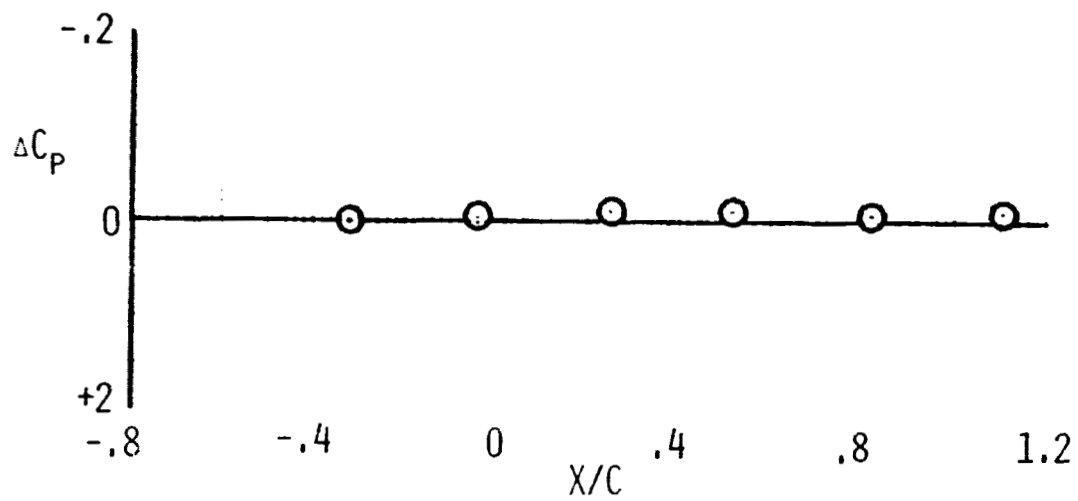


Figure 6. Effect of power on wall static pressures at  $M_\infty = .6$ .

To study the effects of wake blockage, a method described in Reference 1 was used. Wind tunnel sidewall pressures were installed 53.3 cm (21 in.) forward and 53.3 cm (21 in.) aft of the model for this investigation. Changes in local velocity were calculated as caused by the addition of the circular ( $N_{2E}$ ) nacelle and due to the application of power up to a pressure ratio of 2.6. At the aft measuring station, local tunnel surface velocities under datum conditions were found to be approximately 10% higher than those further forward due to the presence of the wake rake. Positive wake blockage (drag) would tend to increase this value, negative wake blockage (jet-ejector effect) would reduce it. Addition of the unpowered nacelle caused about one-half percent increase in aft velocities and the addition of power caused a further one-half percent. Using the referenced theory, the total effect of adding the powered nacelle was shown to be equivalent to slightly more than a one-percent increase in dynamic pressure at the model in a severe case. In view of the magnitude of these changes, together with those mentioned in the previous paragraph, no additional, systematic corrections were made for wake blockage effects.

3.1.1.2 CFF Data Corrections - In the latter stages of the USB force-test program, the exceptionally high cruise drag penalties evidenced in the test data created a concern for the basic validity of the results. As an outgrowth of this concern, an investigation was undertaken of the wall-balance system utilized in the Compressible Flow Facility for USB-force testing. This investigation included "piggy-back" tests of the wall-balance with blowing model installed and mated to the pyramidal-balance system of the Lockheed V/STOL tunnel, flow and pressure-tare studies, temperature and

humidity effects and multiple-loading checks. The primary results of these investigations indicated that the CFF wall-balance was consistently reading axial force (i.e., thrust or drag) too low by a factor of from 5-10 percent when under powered (blowing) conditions. Other wall-balance axes (normal force or lift) appeared to be essentially unaffected with the anticipated level of accuracy for these forces corroborated in the "piggy-back" tests. While the basic inaccuracies in the wall-balance appeared to be a systematic variation (i.e., always offset in one direction) and thereby offering some hope of a corresponding systematic data correction, it was nevertheless deemed necessary that additional, corroborative tests be performed. Accordingly, a test program involving selected wing-nacelle combinations was performed at the Lockheed 4' x 4' blowdown test facility under the same test conditions (i.e., Reynolds number, Mach number) as utilized for the CFF. In this test program, a similar wall-balance, bridged by an opposing bellows arrangement, was employed. The model hardware was the same as that tested in the CFF. The test program included checks on the thrust levels of the isolated nacelles, static installed thrust levels and wind-on lift, drag and pitching-moment measurements for the selected nacelle configurations.

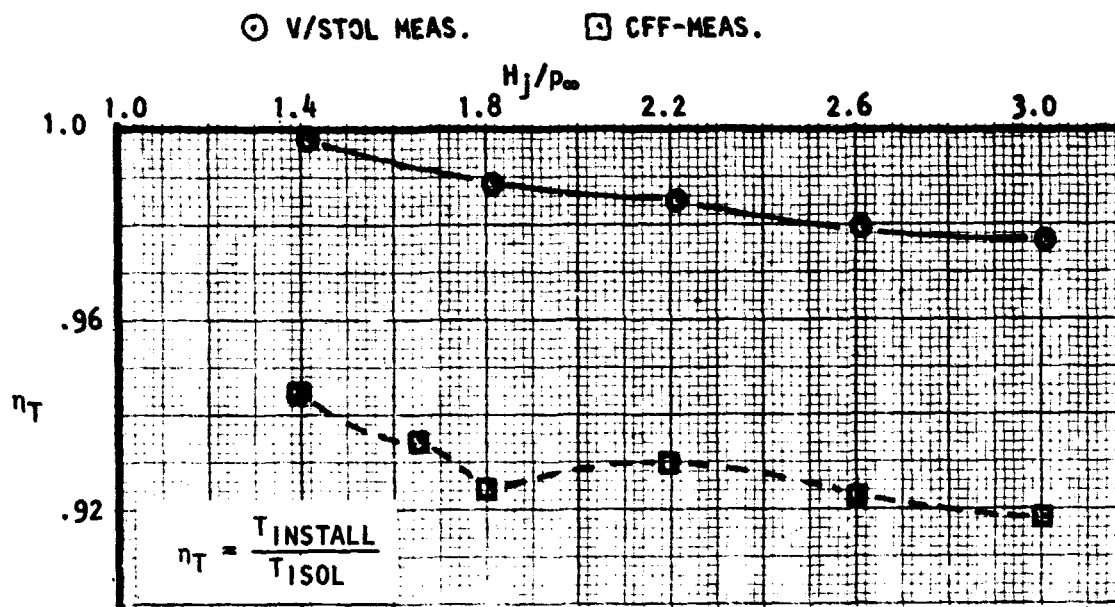
Results from the 4' x 4' tunnel tests corroborated the earlier findings of the CFF wall-balance investigation in that the normal forces were accurately portrayed by the CFF balance system, but that the measured thrust (or drag), under powered conditions, was too low by about 5-10 percent. The isolated nacelle thrust levels and static-installed thrust levels obtained in the 4' x 4' facility essentially checked the corresponding data obtained in the V/STOL tunnel. Additionally, the difference in static-installed thrust levels

between CFF and 4' x 4' (or V/STOL) appeared to accurately reflect the major discrepancies in the CFF - balance system. Figure 7(a) compares the static installed thrust as obtained in the 4' x 4' tunnel with that obtained in the CFF-balance for a "D-Duct" nacelle (N<sub>3</sub>E); the data is in terms of the ratio  $\left[\frac{T_{\text{installed}}}{T_{\text{isolated}}}\right]$ , where  $T_{\text{isolated}}$  represents the more accurate thrust measurements in the 4' x 4' or V/STOL tunnels. The difference in this ratio multiplied by the appropriate thrust coefficient should therefore represent an incremental correction to the CFF data. Figure 7(b) compares the incremental drag of the same "D-Duct" nacelle as obtained in the 4' x 4' tunnel, with that derived from the original CFF test data and as corrected by the foregoing procedures. As noted, the corrected data falls within  $\partial(\Delta C_{D_N}) \approx .0010-.0012$  of the 4' x 4' results. This difference is typical of the agreement obtained across the spectrum of nozzle configurations, lift coefficient and Mach number. It is believed that for a powered configuration of the type used in the present studies tested at transonic speeds, an accuracy level of about  $\partial(\Delta C_D) \approx .0010-.0012$  should be anticipated. Therefore, the drag data from all CFF configurations not re-tested in the 4' x 4' tunnel were corrected in the prescribed manner. In the basic data, presented in Volume IIB, the 4' x 4' test results are identified as Test S-345-11; all other basic data plots represent CFF-corrected results.

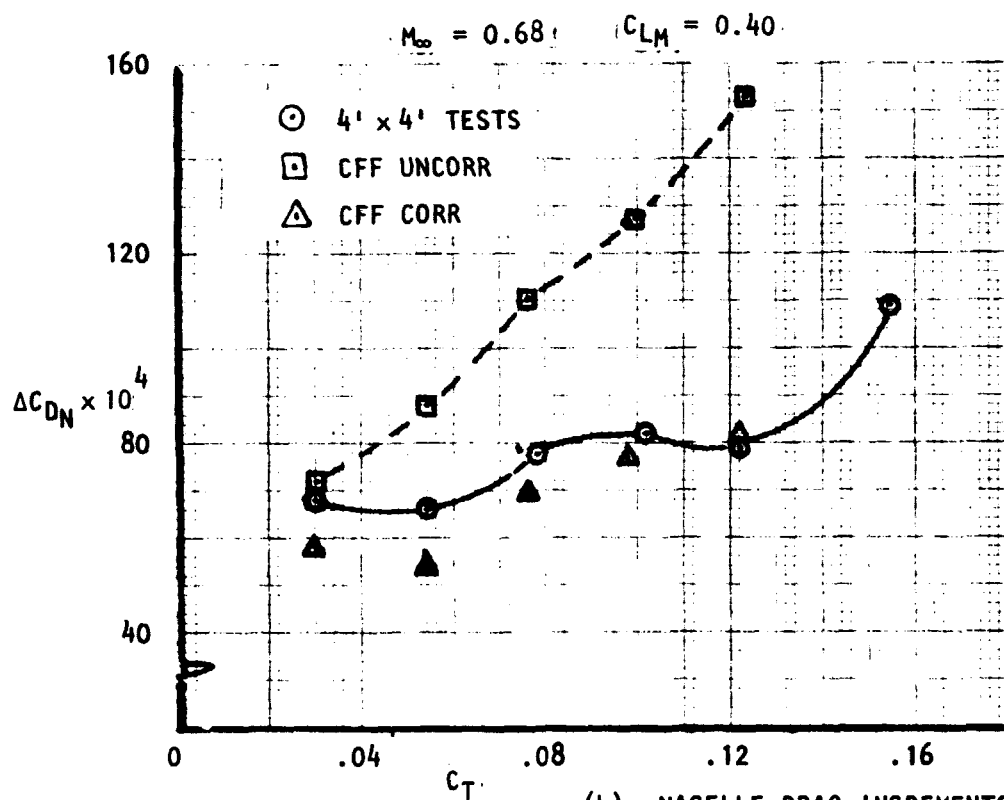
### 3.1.2 Performance Bookkeeping

In the USB-Cruise Program, several basic rules for data accountability were believed to be mandatory:

- (1) Basic equations must be sufficiently general such that applicability



(a) STATIC INSTALLED THRUST



(b) NACELLE DRAG INCREMENTS

Figure 7. Comparison of static installed thrust ratio and CFF-corrected drag increments.  
Nozzle N<sub>3E</sub>, Straight Wing



to any powered configuration can be demonstrated; the USB-configuration is a special case derived from this generality.

- (2) The thrust of the isolated nacelle, calibrated according to accepted procedures, represents the true (gross) thrust input to the system.
- (3) The differences between the force (thrust) generated by the isolated nacelle and those forces measured by a balance metric with the combined configuration (wind-on), represents the total penalty of the wing-body plus the nacelle installation. One of the basic objectives of the data accountability process is the breakdown of this difference into logical, identifiable components.

3.1.2.1 Sign Convention – The sign convention used for data processing is shown in Figure 8. As noted, forces in the drag direction are positive (+) in sense with measured accelerating forces (thrust minus drag) denoted as negative (-). This convention is used for convenience, since identification of drag components received primary emphasis in the data reduction.

3.1.2.2 Axes – The axes system utilized is basically the wind axes as indicated in Figure 8. Lift, drag (or thrust) and pitching moment are the three primary balance-measured variables in the test program.

3.1.2.3 Thrust and Drag Components – All thrust and drag components are developed around the fundamental equation:

USB CRUISE PROGRAM

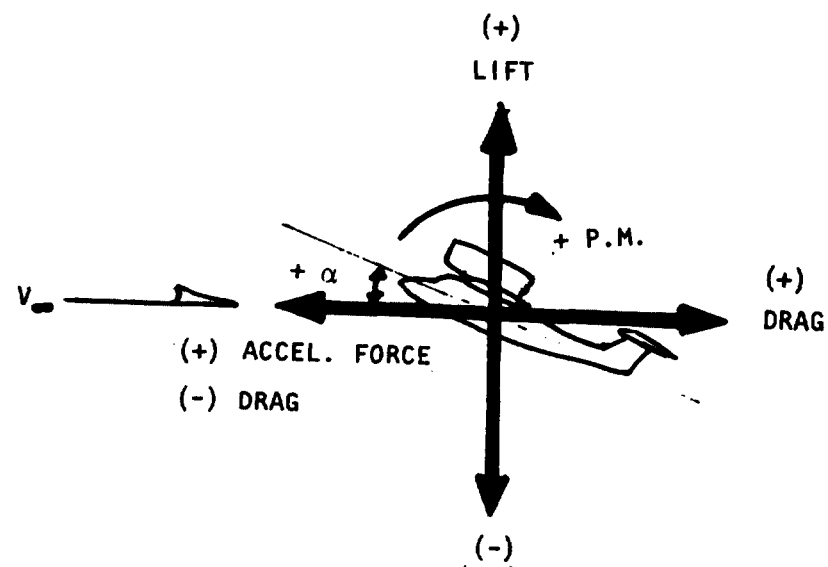


FIGURE 8. WIND AXES SYSTEM

$$\begin{aligned} \text{POSITIVE ACCEL. FORCE} &= -(\text{NET DRAG}) = \\ &= -(\text{TOTAL DRAG} - \text{ISOLATED NAC THRUST} \times \cos \alpha) \end{aligned} \quad (1)$$

Under the small angle assumption (i.e.  $\cos \alpha \approx 1.0$ ), the isolated thrust vector is aligned with the relative wind. "Total Drag" represents all system losses in terms of aerodynamic drag, thrust losses or any other loss which reduces the resultant, accelerating force of the system when the isolated nacelle thrust is introduced. To differentiate between thrust and aerodynamic losses, Equation (1) may be written as:

$$\begin{aligned} \text{ACCEL. FORCE} &= \text{THRUST INSTALL. LOSSES} \\ &+ \text{CONFIG. DPAGS} - \text{ISOLATED NAC THRUST} \end{aligned} \quad (2)$$

Equations (1) and (2) are completely general and are applicable to either conventional under-wing propulsion systems or, in the present case, upper-surface blown configurations. Taking the first two of the above three components of the balance-measured accelerating force in turn:

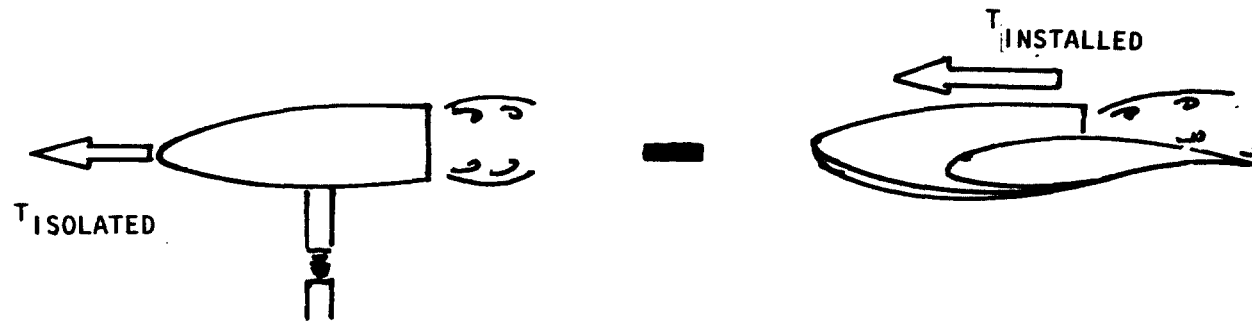
$$\text{THRUST INSTALL. LOSSES} = \frac{T_{\text{ISOL}}}{q_{\infty} S_W} - \frac{T_{\text{INST}}}{q_{\infty} S_W} = C_T [1 - \eta_T] \quad (3)$$

(See Figure 9)

The installed thrust,  $T_{\text{INST}}$ , is determined from static tests of the blowing nacelle installed on the wing. Balance-measured forces are vectorially summed to determine the effective, installed thrust of the wing-nacelle system relative to that of the isolated nacelle,  $T_{\text{ISOL}}$ . The thrust installation losses, represented by  $C_T (1 - \eta_T)$ , are generally assumed to represent jet-scrubbing and jet mixing losses.

$$\text{CONFIGURATION DRAG} = C_{D_{WB}} + \Delta C_{D_N} \quad (\text{See Figure 10}) \quad (4)$$

# USB CRUISE PROGRAM



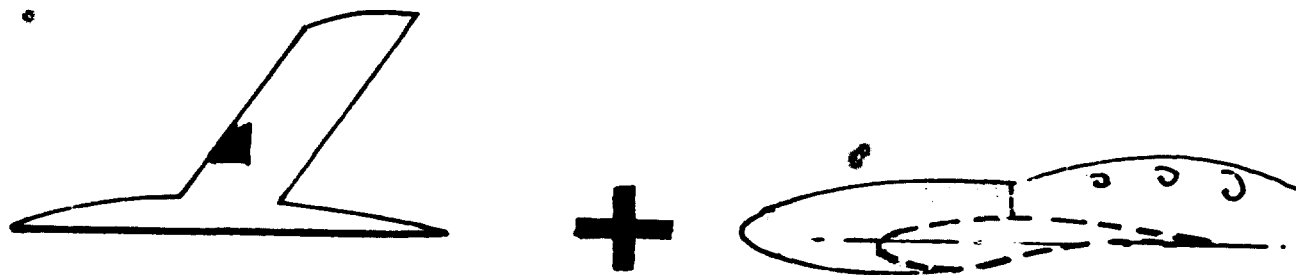
$$\text{THRUST LOSSES} = T_{\text{ISOLATED}} - T_{\text{INSTALLED}}$$

$$\Delta C_{D_n} = C_{\mu} [1 - \eta_T]$$

$$\eta_T = \frac{T_{\text{INSTALLED}}}{T_{\text{ISOLATED}}}$$

FIGURE 9. GROSS THRUST LOSSES

## USB CRUISE PROGRAM



CONFIG. DRAG = DRAG OF WING/BODY +  $\Delta C_{DNAC}$  DRAG

$$C_{DA} = C_{DWB} + \Delta C_{DNAC}$$

$$= C_{DWB} + [\Delta C_{DNF} + \Delta C_{Di} + \sum \Delta C_{Dp}]$$

$$= C_{DWB} + \left\{ \Delta C_{DNF} + \Delta C_{Di} + [\Delta C_{DB} + \Delta C_{DV} + \Delta C_{DMISC.}] \right\}$$

FIGURE 10. CONFIGURATION DRAG

where  $C_{D_{WB}}$  = drag of clean wing plus fuselage  
less interfacing footprints

and  $\Delta C_{D_N}$  = incremental nacelle drag

$$\Delta C_{D_N} = \Delta C_{D_{NF}} + \Delta C_{D_i} + \sum \Delta C_{D_P} \quad (4a)$$

$\Delta C_{D_{NF}}$  = incremental nacelle friction drag

$\Delta C_{D_i}$  = incremental induced drag (or effective  
drag-due-to-lift) due to the nacelle/  
jet/wing interactions

$\sum \Delta C_{D_P}$  = summation of all incremental pressure  
drags due to aerodynamic interferences,  
separation, jet vectoring, etc.

$$\sum \Delta C_{D_P} = \Delta C_{D_\beta} + \Delta C_{D_{MISC}} + \Delta C_{D_j} \quad (4b)$$

where  $\Delta C_{D_\beta}$  = incremental pressure drag due to boattail  
separation

$\Delta C_{D_{MISC}}$  = unidentified miscellaneous pressure drags  
(shock losses, etc.)

$$\Delta C_{D_j} = \text{incremental wind-on pressure drag due to the jet-induced load on the wing}$$

Substituting equations (3) and (4) into equation (2) gives:

$$\begin{aligned} \text{ACCEL FORCE} = C_{D_M} = C_T (1 - \eta_T) + C_{D_{WB}} + \Delta C_{D_{NF}} + \Delta C_{D_i} \\ + \Delta C_{D_e} + \Delta C_{D_{MISC}} + \Delta C_{D_j} - C_T \end{aligned} \quad (5)$$

These relationships are summarized schematically in Figure 11.

The incremental jet-induced pressure drag,  $\Delta C_{D_j}$  requires special attention since this parameter is a partially identifiable drag term where surface pressures within the jet scrubbing area are available. Integration of such pressures (in the drag direction) can normally quantify this term which can then be weighed against an ideal value. To this end, it may be shown from a simple momentum balance that the theoretical jet-induced pressure drag (due to vectoring) on the wing may be written as:

$$\Delta C_{D_j} = \eta_T C_T [1 - \cos(\alpha + \delta_j)] \quad (6)$$

where  $\delta_j$  = effective turning angle of the jet

It is noted that for interactive powered-lift applications, the turning angle,  $\delta_j$ , is conventionally determined from static tests of the installed nacelles,

# USB CRUISE PROGRAM

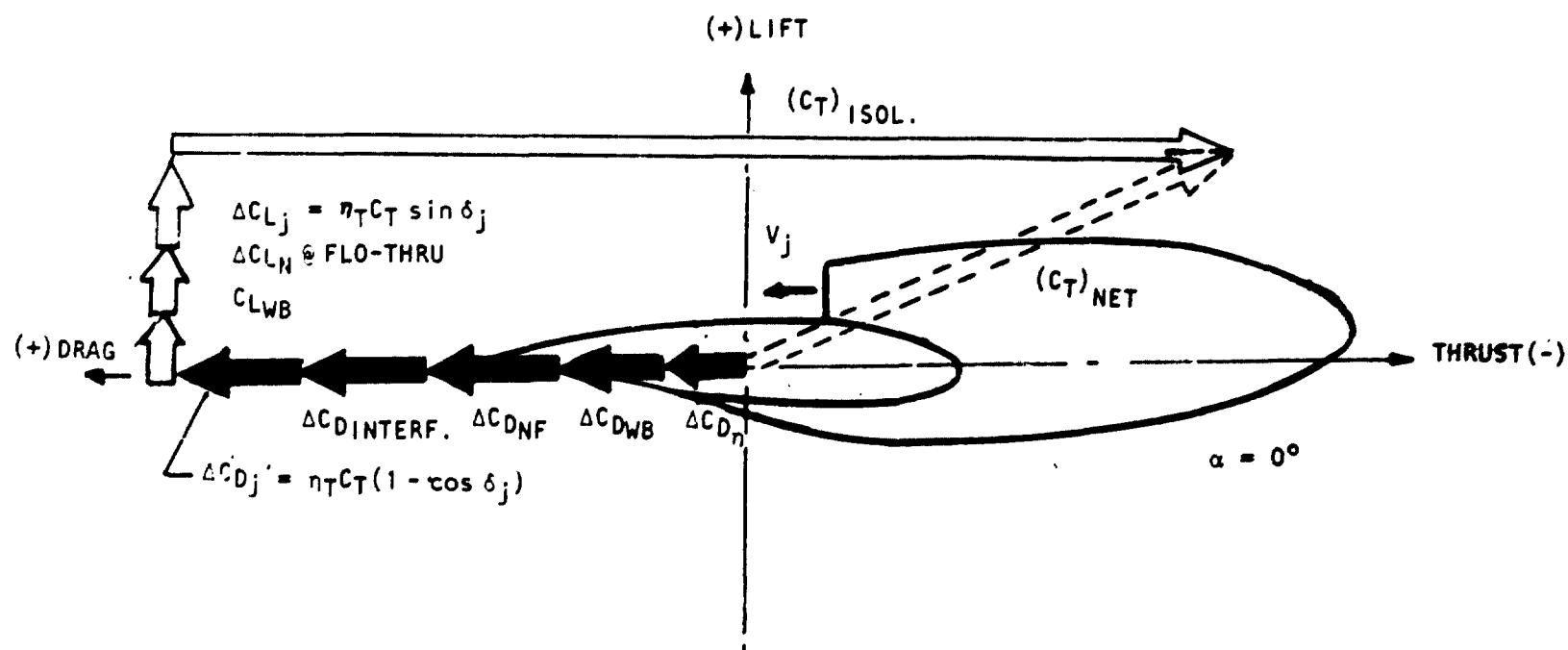


Figure 11. Identifiable installation and aerodynamic penalty components.



along with the parameter,  $\eta_T$ , and the assumption made that both  $\eta_T$ , and  $(\delta_j)_s$  remain invariant at wind-on conditions. However, the wing pressure load can change from that determined statically due to a response of the jet to alpha and Mach number effects on the wing pressure field.

The thrust and drag relationships shown in Figure 11 also indicate why the wing pressure load must be accounted for when the thrust of the isolated nacelle is used as a basis for drag accountability in lieu of the system net thrust vector  $(C_{T_{net}})$ . Introducing equation (6) into equation (5) and simplifying gives:

$$\begin{aligned} \text{ACCEL FORCE} = C_{D_H} = & - \eta_T C_T \cos (\alpha + \delta_j) + C_{D_{WB}} + \Delta C_{D_i} \\ & + \Delta C_{D_{NF}} + \Delta C_{D_{\beta}} + \Delta C_{D_{MISC}} \end{aligned} \quad (7)$$

where  $\eta_T C_T \cos (\alpha + \delta_j)$  is the drag-wise component of  $(C_T)_{net}$ . Equation (7) is the conventional form of the accelerating force expression relating a system net thrust vector to the more common aerodynamic drag penalties. In the analyses of the experimental results, emphasis is on the identification of the various drag components indicated in equation (5). As an aid

to such identification, both force and pressure test-results need to be utilized.

The pressure data are instrumental in making approximations to  $\Delta C_{D_j}$ ,  $\Delta C_{D_\beta}$  and  $\Delta C_{D_{MISC}}$ , while the force results may be used for defining  $C_{D_{WB}}$ , and  $\Delta C_{D_i}$ ; the parameter  $\Delta C_{D_{NF}}$  is estimated. Static installed test results may be compared to isolated (calibrated) thrust to determine  $\Delta C_{D_\eta}$ . In order to maintain perspective on the relative magnitudes of all drag and thrust losses, a progressive buildup can be performed for each nozzle configuration such that the fundamental equation (i.e. Equation (1)) is validated; that is, when total system losses are combined with the isolated nacelle gross thrust, the balance-measured accelerating force is reproduced.

3.1.2.4 Lift Components - The total lift of the system may be summarized by (see Figure 11):

$$C_{L_{TOT}} = C_{L_N} = C_{L_{WB}} + \Delta C_{L_N} + \Delta C_{L_j} \quad , \quad (8)$$

where  $C_{L_{WB}}$  = lift of the wing-body combination

$\Delta C_{L_N}$  = lift increment (or decrement) due to the installed nacelle at a flow-through pressure ratio

$\Delta C_{L_j}$  = lift increment induced by jet-vectoring at  $\alpha$  at  $H_j/p_\infty >$  flow-through inclusive of direct thrust in lift direction

### 3.1.3 Data Reduction

All balance-measured forces and moments in the wind-on condition were reduced to coefficient form using standard formats. They were:

$$C_{L_M} = \frac{\text{measured total lift}}{q_\infty S_W}$$

$$C_{D_M} = \frac{\text{measured accelerating (or drag) force}}{q_\infty S_W}$$

$$C_{M_M} = \frac{\text{measured pitching moment about wing quarter chord point}}{q_\infty S_W \bar{c}}$$

For static, nacelle-installed force testing, the balance-measured normal and axial forces were vectorially summed to provide an installed thrust, which, when ratioed to the calibrated thrust of the nacelle, provided the static efficiency factor  $\eta_T$ .

The thrust produced by the various isolated nozzles was reduced to the coefficient form  $C_T = (T/q_\infty S_W)$ ; examples of these data are shown in Figures 12 and 13 across the appropriate ranges of nozzle pressure ratio and Mach number. For nacelles of a specified size, the thrust variations with nacelle shape are relatively small, as was noted in the nozzle calibrations.

Surface pressure measurements on wing and nacelle surfaces were reduced to standard pressure coefficient form with which lift or drag-wise integrations

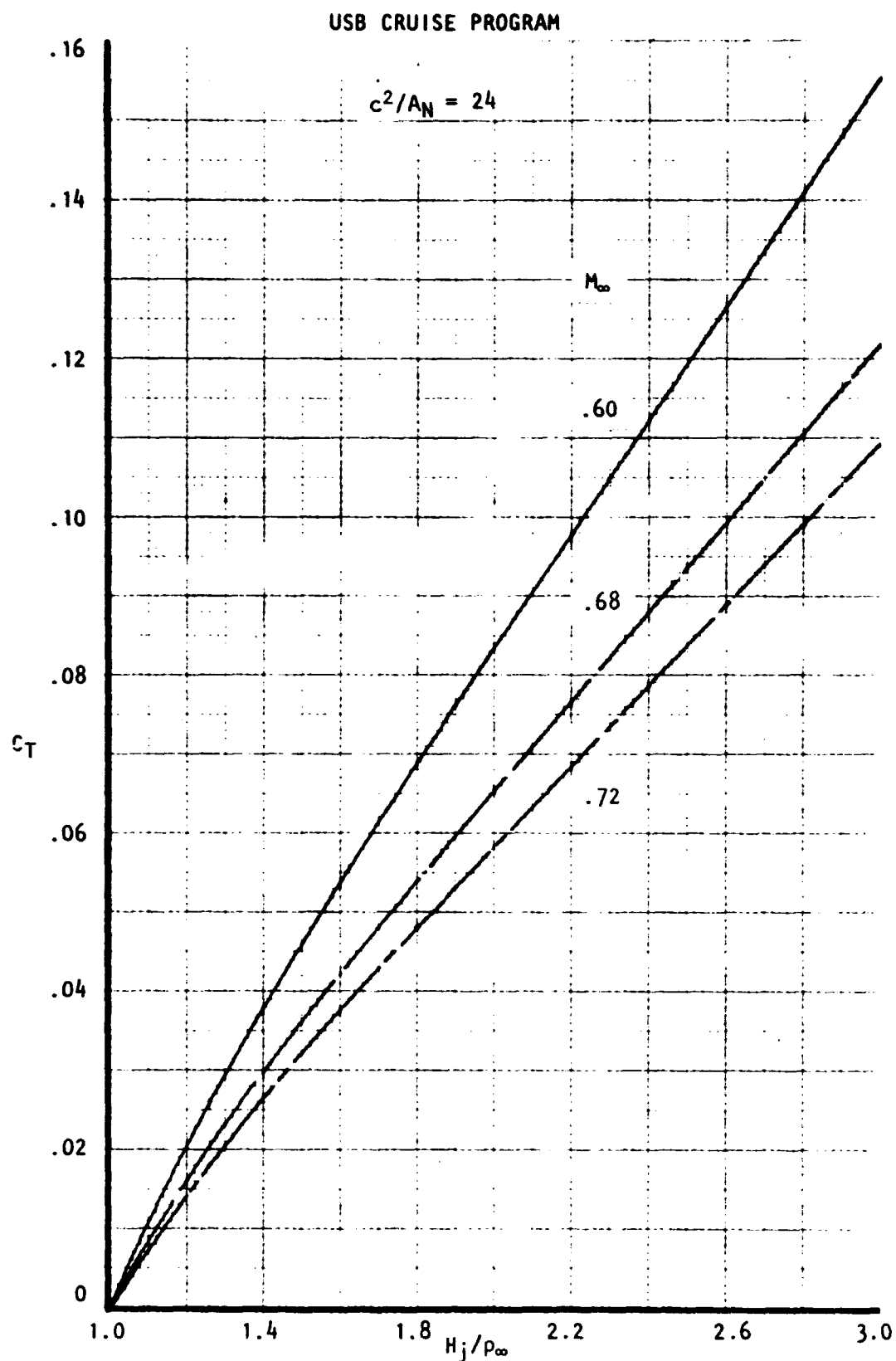


Figure 12. Variation of nozzle gross thrust with Mach No. and pressure ratio, nozzle  $N_{3E}$ .

ORIGINAL PAGE IN  
OF POOR QUALITY

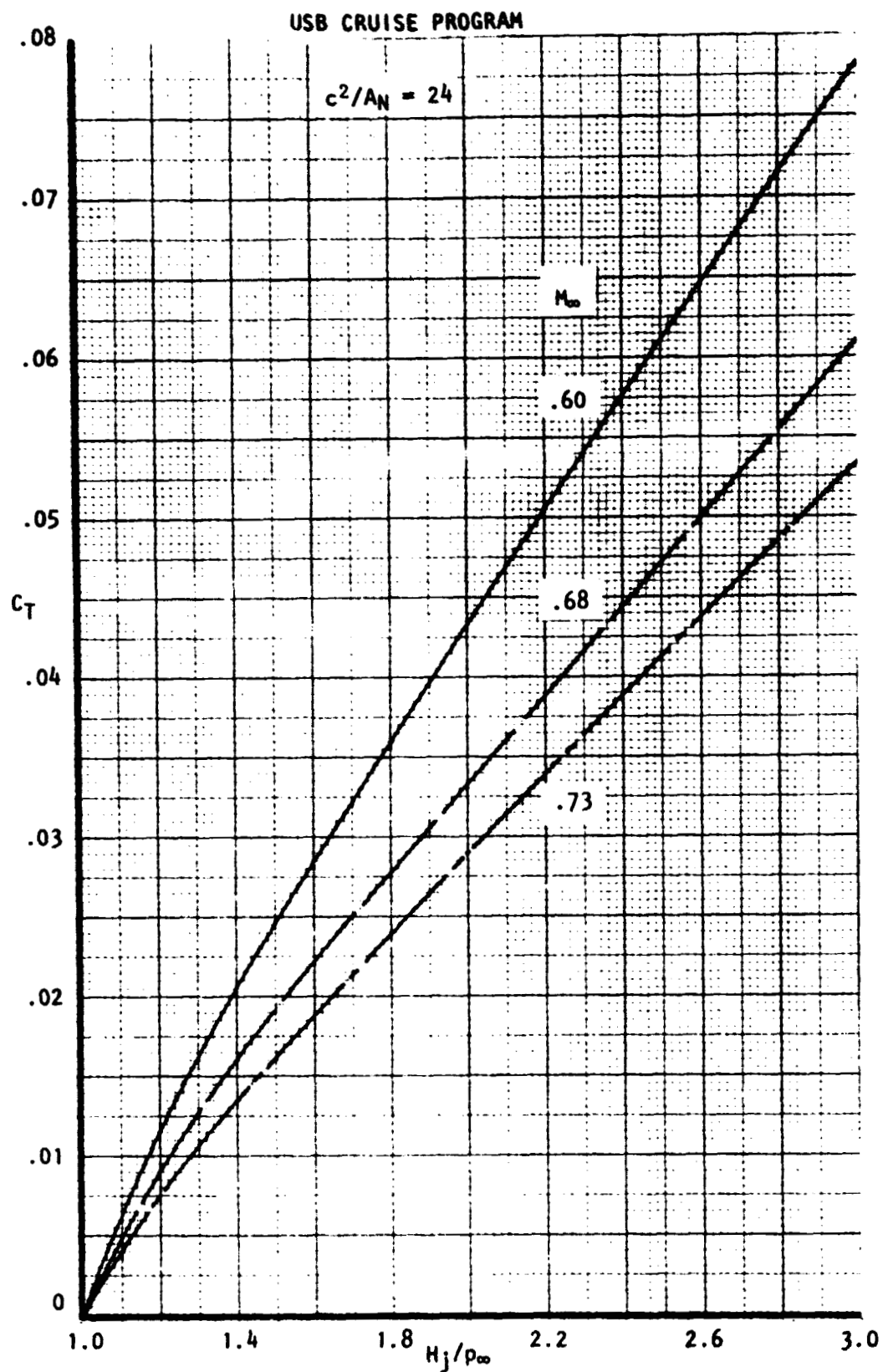


Figure 13 . Variation of nozzle gross thrust with Mach No. and pressure ratio, nozzle  $N_8^2$ .

could be performed. Wake rake measurements, in terms of local total pressure, were reduced to the ratio form,  $\Delta H/p_\infty$ , and plotted as a function of wing semi-span station.

#### 3.1.4 Data Formats

The nacelle matrix described in Volume IIA was tested in the low transonic speed range at the following approximate conditions:

Straight Wing Configurations	$0.60 \leq M_\infty \leq 0.72$
Swept Wing Configurations	$0.60 \leq M_\infty \leq 0.80$
Both Wings	$1^\circ \leq \alpha \leq 5^\circ$
Both Wings	$1.0 \leq H_j/p_\infty \leq 3.0^+$
Both Wings	$R_{NC} \approx 3.5 \times 10^6$

Additional detail as to model geometries, test conditions and test facilities are provided in CR-3192.

Because of losses in the wing supply duct, nozzle pressure ratios were limited to about 2.5 at  $M_\infty = 0.60$ , where tunnel static pressure was high. The full range specified above was usually available at Mach numbers higher than 0.68. The general method for acquiring both force and pressure measurements in the test facility was to hold constant values of nozzle pressure ratio across a spectrum of angle of attack and Mach number. However, since the test facility was of the blow-down type, it was necessary to pre-set nozzle pressure ratio prior to each data acquisition blow. Slight variations in predicted test section conditions could therefore change the pre-set

nozzle pressure ratio by a small amount. To maintain constant levels of nozzle pressure ratio for the purpose of analysis, the force and moment measurements were first cross-plotted against nozzle pressure ratio as shown in the typical data of Figure 14(a) and 14 (b). The maps of measured lift and drag, as shown in Figure 14(c), could then be constructed using both measured and cross-plotted results. An identical procedure (cross-plotted test conditions) has been used where small variations in pre-set angle of attack have occurred across a matrix of Mach number and nozzle pressure ratios. A typical example is provided in Figure 14(d). Due to the dynamic nature of powered testing in general, and due to the highly interactive nature of the subject tests in particular, some data scatter was observed across a matrix of pressure ratios and angles of attack at a fixed Mach number. Most of this scatter appeared to be associated with abrupt detachment or reattachment of the jet. As an analysis aid, ten cross-plots of the measured and reduced data were made to establish basic trends. Volume IIB presents detailed results of this process. In these forms, the data could be further reduced, incremented, or processed in keeping with the bookkeeping procedure outlined in Section 3.1.2.

### 3.2 DISCUSSION OF RESULTS

To present an analysis of the experimental data obtained in the USB-Cruise Program, the general format for discussion is to first consider results from the pressure tests followed by an analysis of the force-measurements. In the sections which follow, a brief analysis of the basic wing-body performance is first given (Section 3.2.1); this is followed by an analysis of USB-nacelle installations (Section 3.2.2).

1517 MAY 11 1976

USB CRUISE PROGRAM

LFL 5-345-11

CALAC 4-FT TUNNEL

USB CRUISE PROGRAM

EFFECT OF NOZZLE PRESSURE RATIO ON  
MEASURED LIFT & PITCHING MOMENT COEFFICIENTS

$M_\infty = .66$

$R_{nc} = 3.6 \times 10^6$

CONFIGURATION : F, W, P, C, N<sub>0</sub>

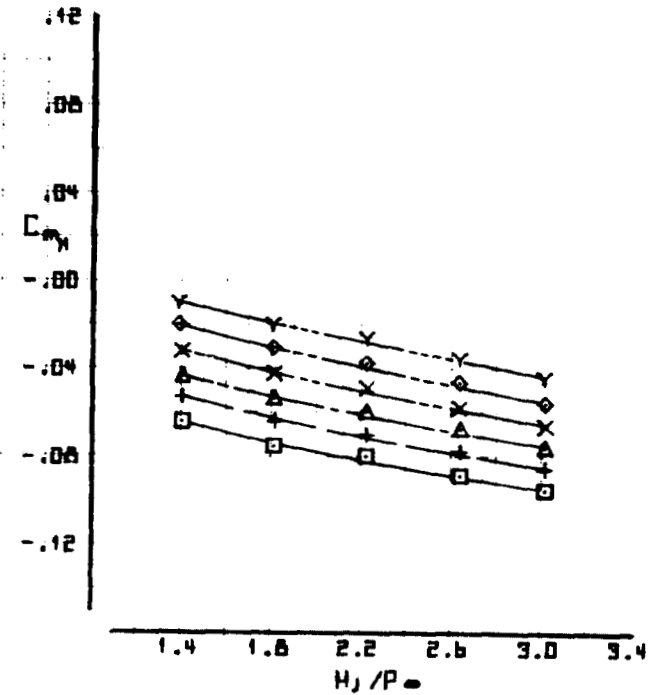
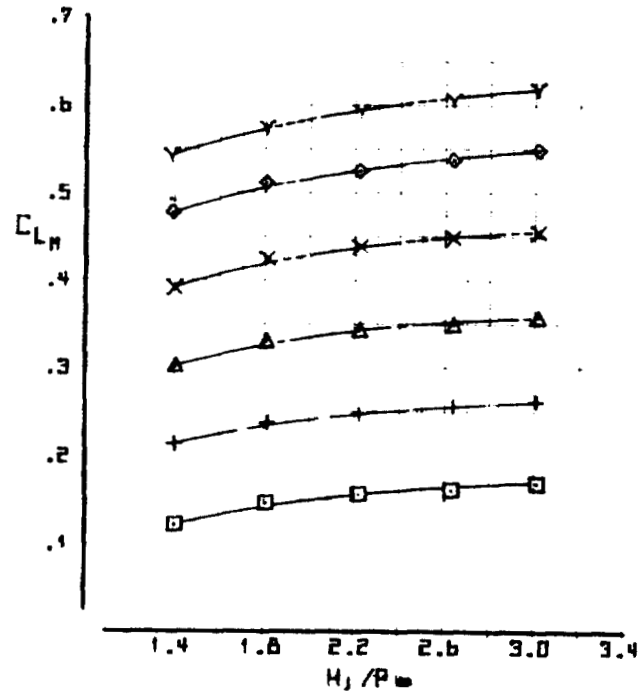


Figure 14(a), Data analysis formats.



# USB CRUISE PROGRAM

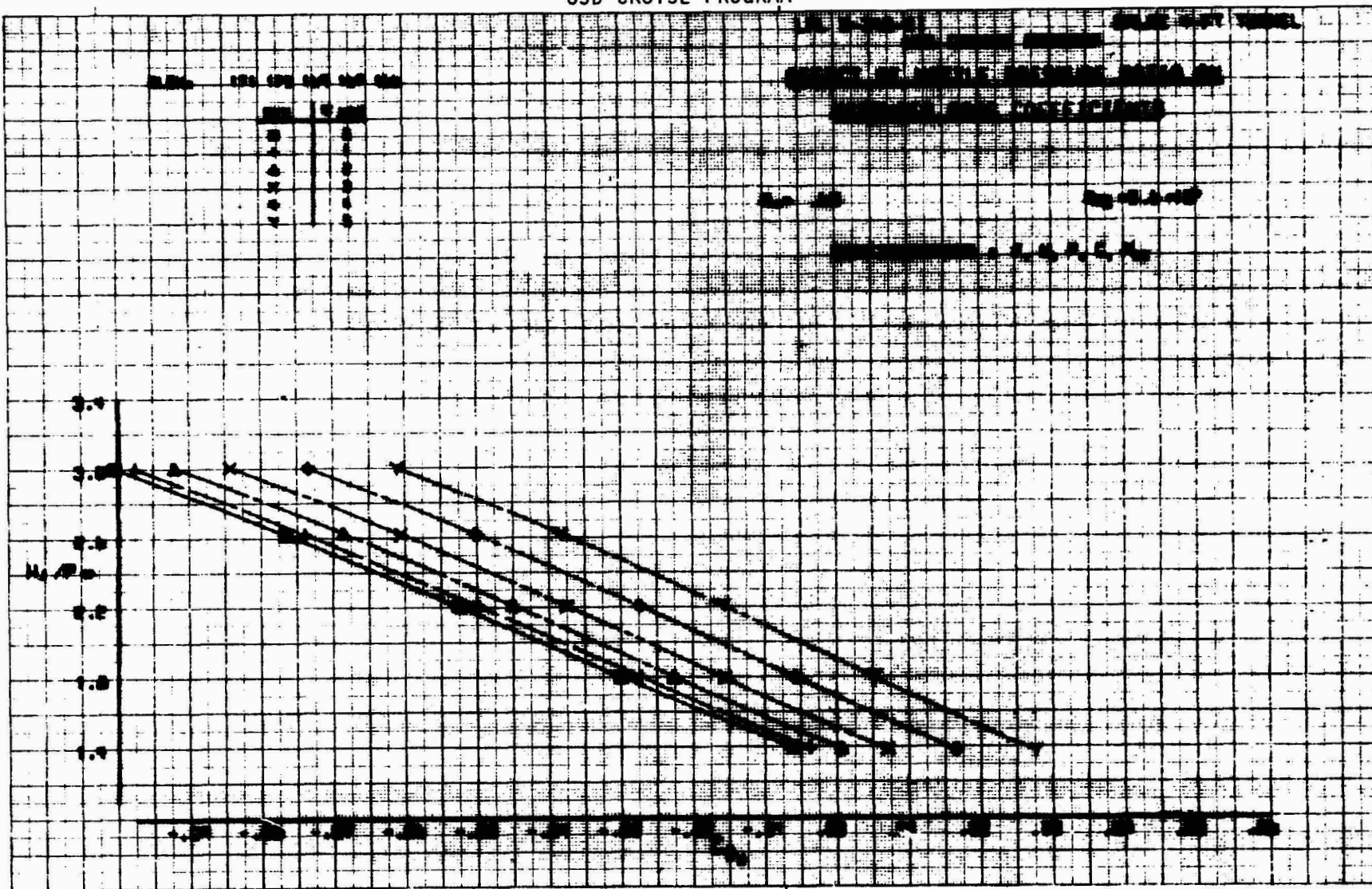


Figure 14(b), Data analysis formats.

# USB CRUISE PROGRAM

LFL 9-345-11 CALAC 4-FT TUNNEL

USB CRUISE PROGRAM

MEASURED DRAG POLARS

FOR SEVERAL NOZZLE PRESSURE RATIOS

$P_{no} = .50$

$Re = 3.0 \times 10^5$

COORDINATION: F, M, E, C, N<sub>no</sub>

BLOW: 171 172 184 182 184

NO	110 / P <sub>no</sub> = 1000
0	FLIGHT
1	1.0
2	2.0
3	3.0

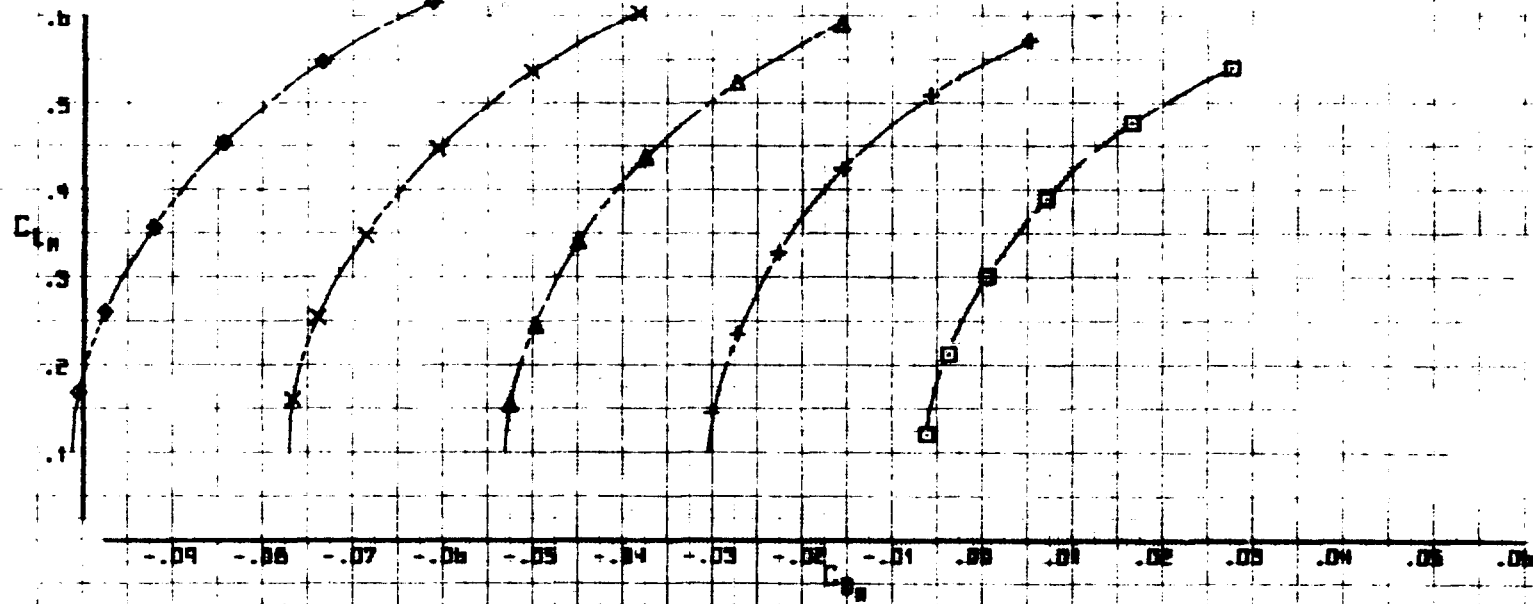


Figure 14(c). Data analysis formats.

# USB CRUISE PROGRAM

LFL 5-345-11

CALAC 4-F

USB CRUISE PROGRAM

BLDN 17. 178 1b9 1b7 1b6

SYM	1H/P-10M
□	FLOW-THERM
+	1.2
△	2.2
x	2.6
◆	3.0

## MEASURED LIFT & PITCHING MOMENT COEFFICIENTS FOR SEVERAL NOZZLE PRESSURE RATIOS

$M_\infty = .66$

$Re_c = 3.6 \times 10^6$

CONFIGURATION : F, U, P, C, N

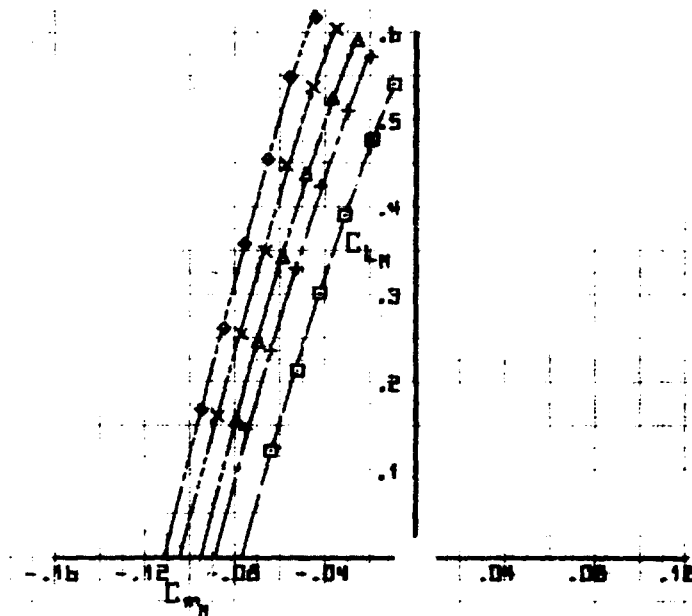
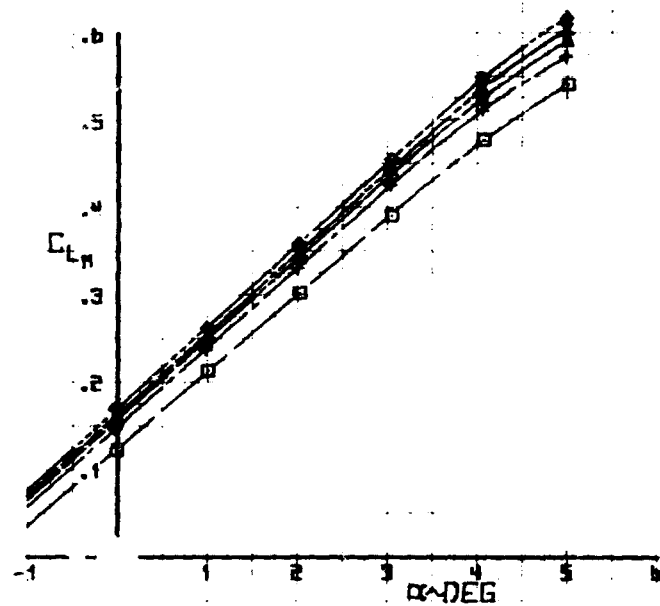


Figure 14(d). Data analysis formats.

15:10 MAY 11, '78

### 3.2.1 Basic Wing-Body Performance

3.2.1.1 Two-Dimensional Pressure Tests - The airfoil used in the present experimental program is a supercritical type designed for application to STOL aircraft. In particular, the airfoil differs from a conventional supercritical airfoil by reduction in the aft loading normally carried by that type section. A sketch of this airfoil, designated LG 3-316, is shown in Figure 15. Basic criteria for the design reflected (typically) a  $C_{L_i} = 0.3$  at a cruise Mach number of 0.70. Since aircraft parametric optimization studies have indicated that USB aircraft configurations of interest would operate at somewhat higher lift coefficients (0.35 to 0.50), this airfoil was modified to increase the design lift coefficient by removing material from the lower surface. The modified airfoil, designated LG 7-516, is also shown in Figure 15. A comparison of experimental pressure distributions for the two airfoils at  $M_\infty = 0.6$  and  $\alpha = 3^\circ$  is shown in Figure 16. The two airfoils have identically the same upper surface, but the increased aft loading makes the modified airfoil operate at a higher lift coefficient for a given angle of attack. A similar comparison in Figure 17 at a supercritical Mach number of 0.72 shows that the more negative pressures on the upper surface of the modified airfoil cause the shock to move further aft. The effect of increasing the airfoil aft loading on drag-rise Mach number is shown in Figure 18. This loading change serves to shift the drag-rise Mach number boundary to a higher lift coefficient range.

The swept wing airfoil used for these tests was obtained by using the LG 7-516 airfoil normal to the leading edge of the swept wing. As a check on

## USB CRUISE PROGRAM

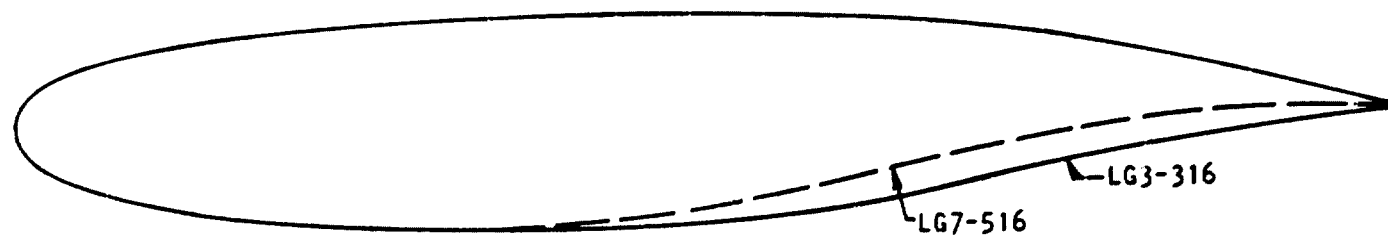


Figure 15. Comparison of airfoils LG3-316 and LG7-516.

USB CRUISE PROGRAM

○ LG7-516, MODIFIED,  $C_L = 0.45$

□ LG3-316, ORIGINAL,  $C_L = 0.30$

$R_{NC} = 3.5 \times 10^6$

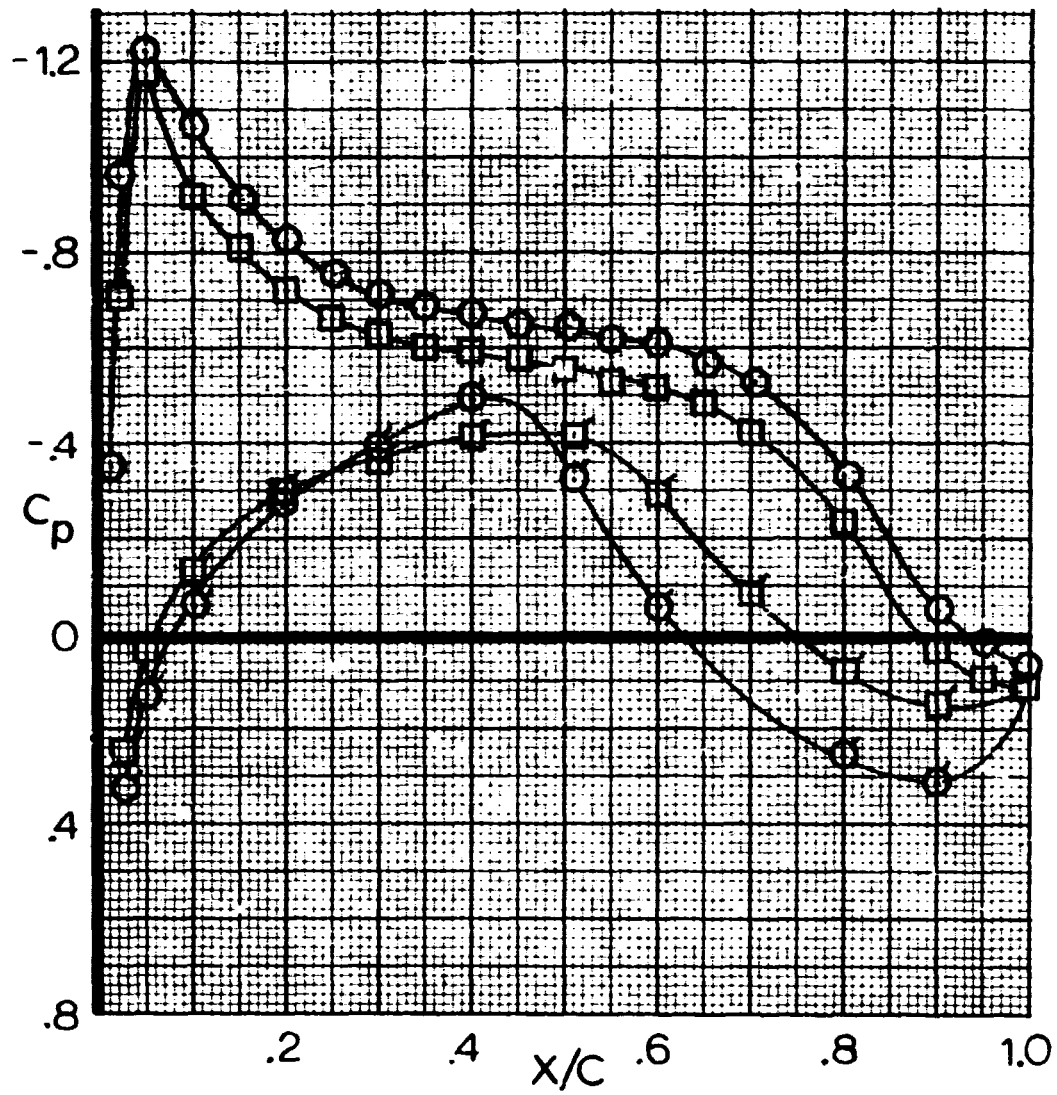


Figure 16. Pressure distribution comparison of original and modified airfoils,  $M_\infty = 0.73$ ,  $\alpha = 2.6^\circ$

# USB CRUISE PROGRAM

⊙ LG7-516 MODIFIED  $C_L = 0.56$   
 □ LG3-316 ORIGINAL  $C_L = 0.38$   
 $R_{NC} = 3.5 \times 10^6$

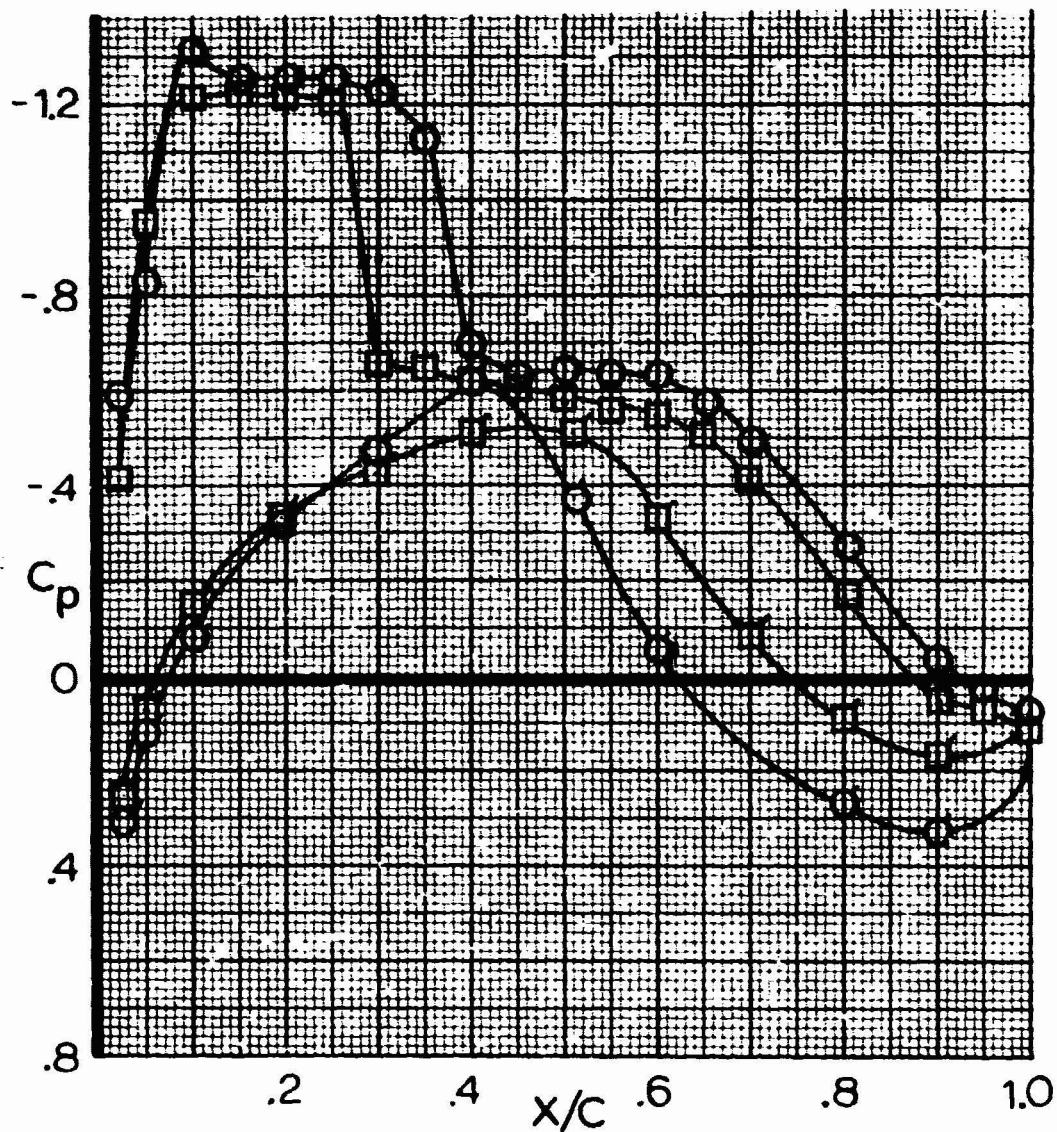


Figure 17. Pressure distribution comparison of original and modified airfoils,  $M_\infty = 0.72$ ,  $\alpha = 3^\circ$ .

USB CRUISE PROGRAM

⊙ LG7-516, MODIFIED

□ LG3-316, ORIGINAL

$$R_{NC} = 3.5 \times 10^6$$

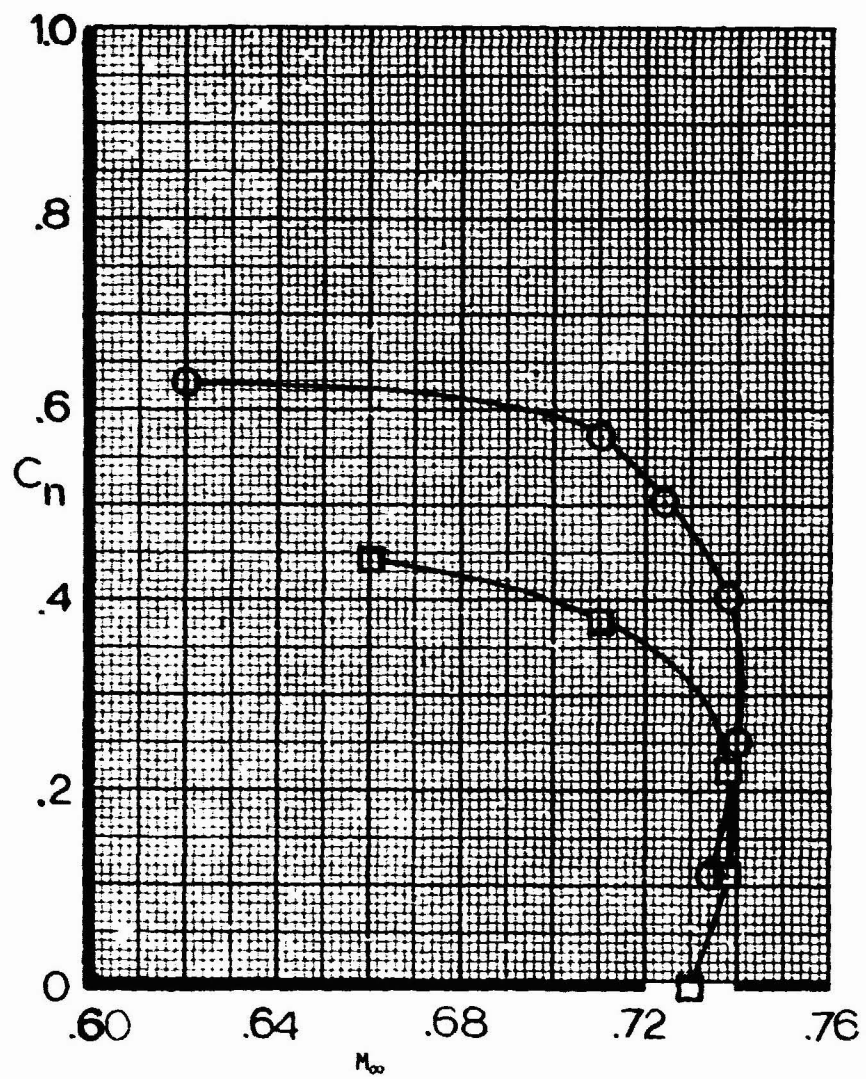


Figure 18. Operating envelopes for original and modified airfoil sections.



the simple sweep theory, the pressure distribution from the swept wing factored by the cosine<sup>-2</sup> 25° is compared with the unswept wing in Figure 19.

Experimental results (2-D) on both the swept and unswept sections indicated satisfactory agreement with the design objectives. Indications were that incorporation of these sections into the three-dimensional straight and swept finite wings could provide a reasonable range of cruise parameters before strong compressibility or other high-speed effects would be encountered.

3.2.1.2 Wing-Body Force Tests - Transonic tests of both the straight and 25 degree swept wing and fuselage combinations were performed in both the CFF and 4' x 4' blowdown tunnels. With these unpowered configurations, good agreement between facilities was obtained on both lift and drag. Data showing the lift, drag and pitching-moment variations for the straight wing are provided in Figures 20 through 22. Figures 23 through 25 show similar data for the swept wing/fuselage configuration. The performance of both wing-bodies were about as anticipated from the earlier two-dimensional pressure tests of the two sections. The drag-rise Mach number for the straight wing at  $C_L = 0.4$  is  $M_{\infty} = 0.70$  and  $M_{\infty} = 0.75$  for the swept configuration at the same condition. An analysis of oil-flow photographs (see Volume 116) for both wings showed no extraneous effects occurring on either wing at subcritical Mach numbers.

USB CRUISE PROGRAM

⊙ STRAIGHT WING,  $\eta = 0.39$ ,  $M_\infty = 0.60$

□ SWEPT WING,  $\eta = 0.42$ ,  $M_\infty = 0.68$

$R_{NC} = 3.5 \times 10^6$

$\alpha = 2^\circ$

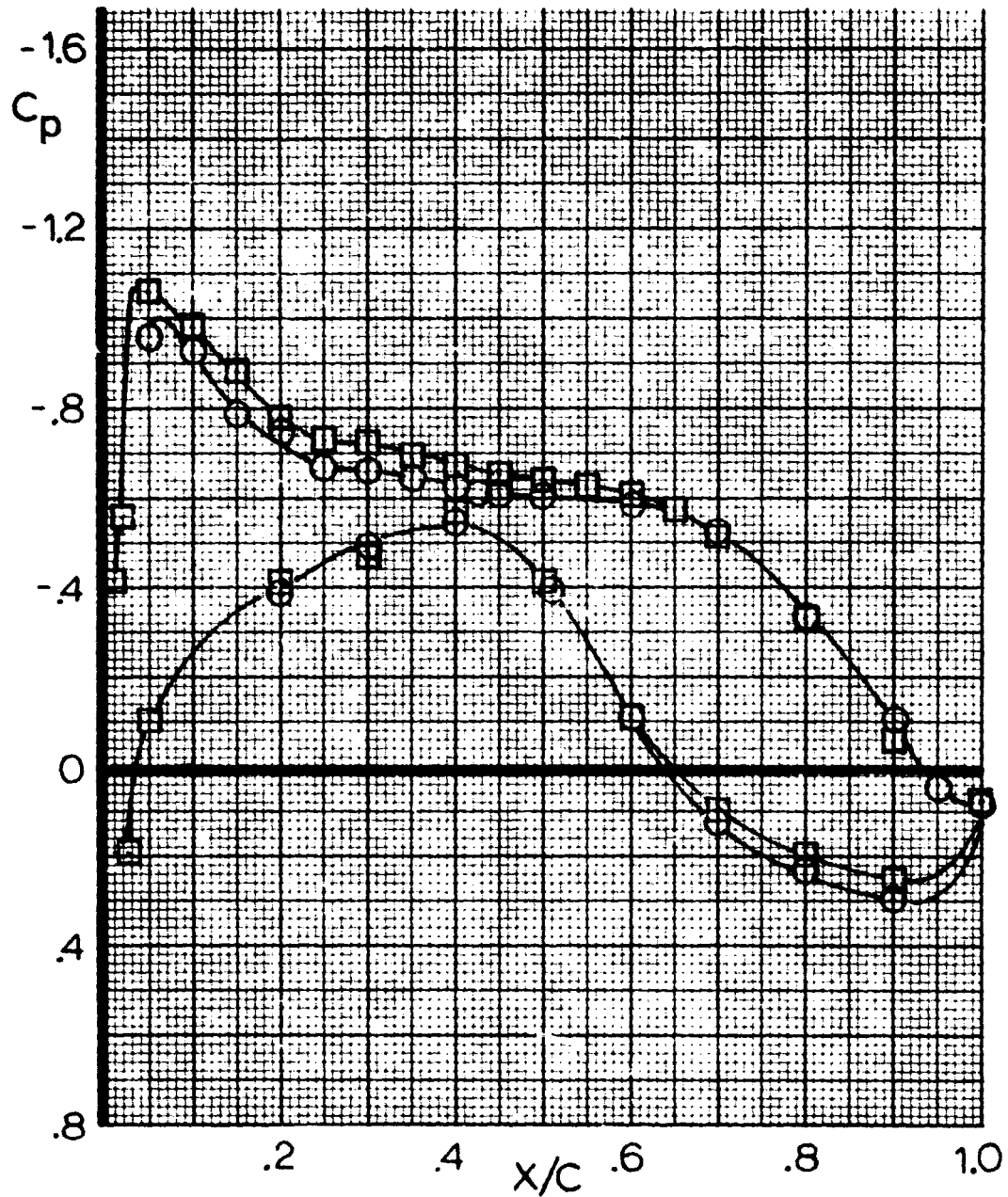


Figure 19. Comparison of swept wing pressures as modified by simple sweep theory to straight wing pressures.

USB CRUISE PROGRAM  
 CONFIGURATION F<sub>1</sub>W<sub>1</sub>  
 CLEAN WING-BODY  
 4' x 4' TEST S-345-11

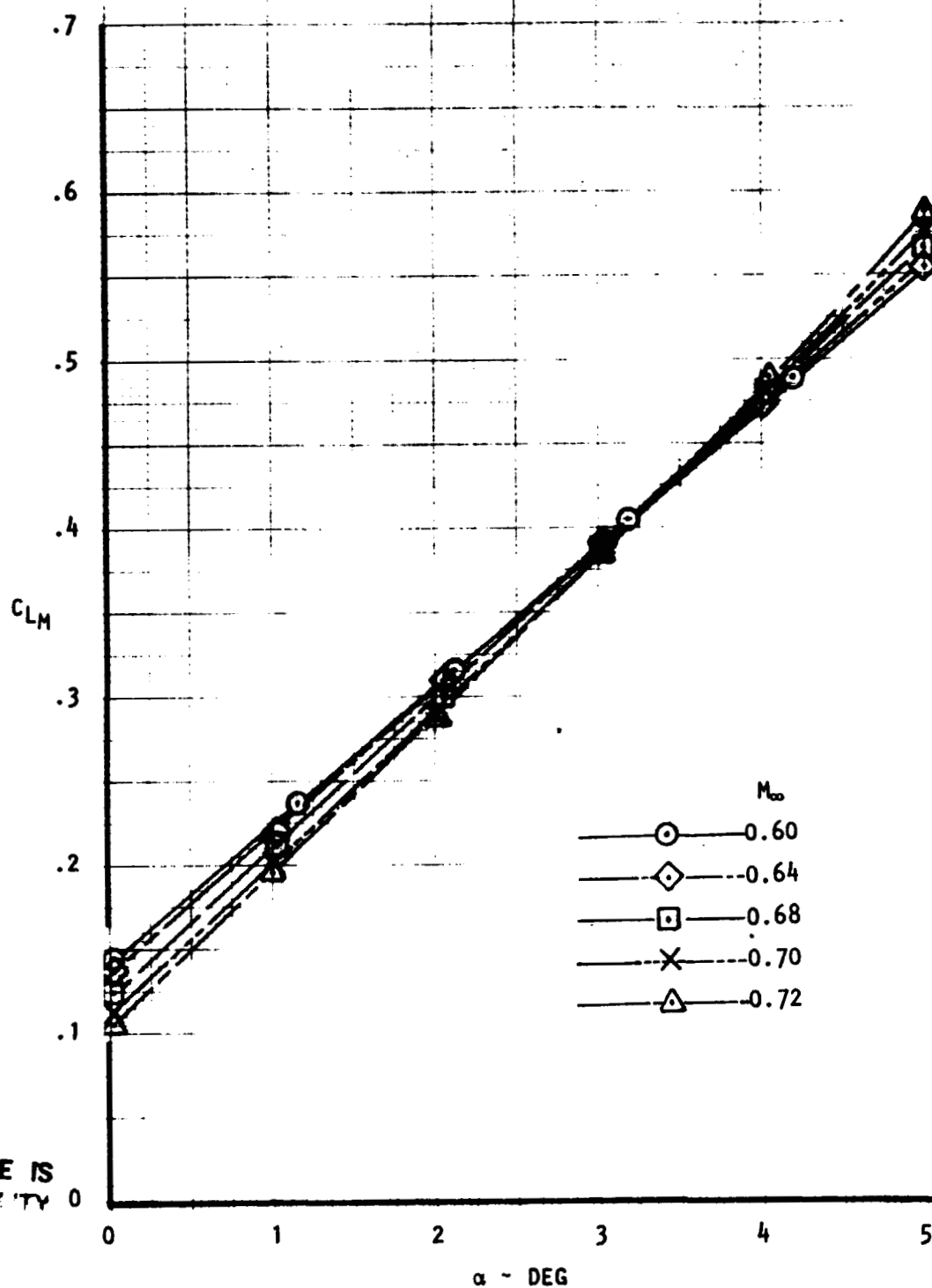


Figure 20. Variation of lift coefficient with Mach number, straight wing.  $R_{NC} = 3.5 \times 10^6$

ORIGINAL PAGE IS  
 OF POOR QUALITY 0

# USB CRUISE PROGRAM

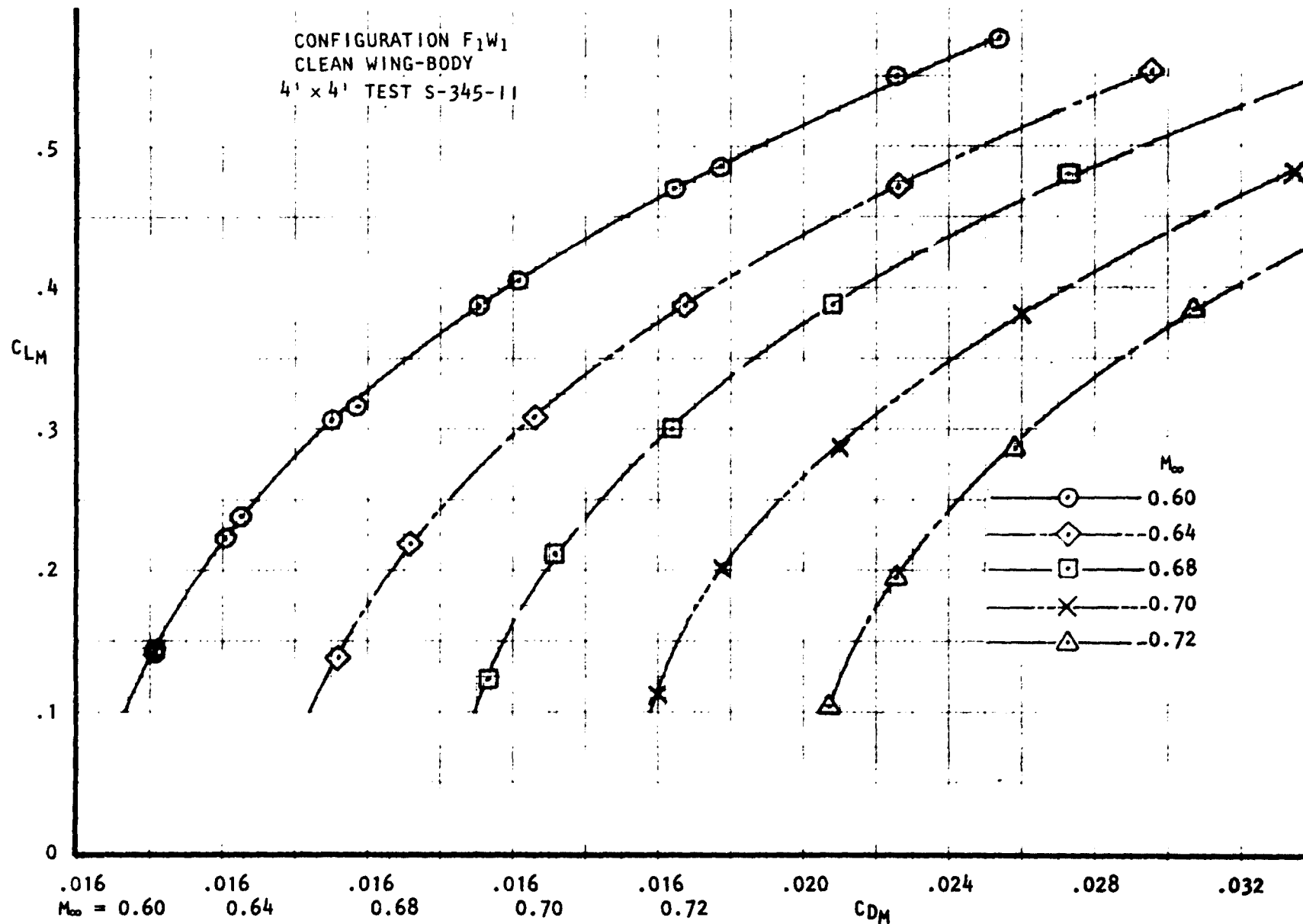


Figure 21. Variation of drag coefficient with Mach number, straight wing.  $R_{NC} = 3.5 \times 10^6$

## USB CRUISE PROGRAM

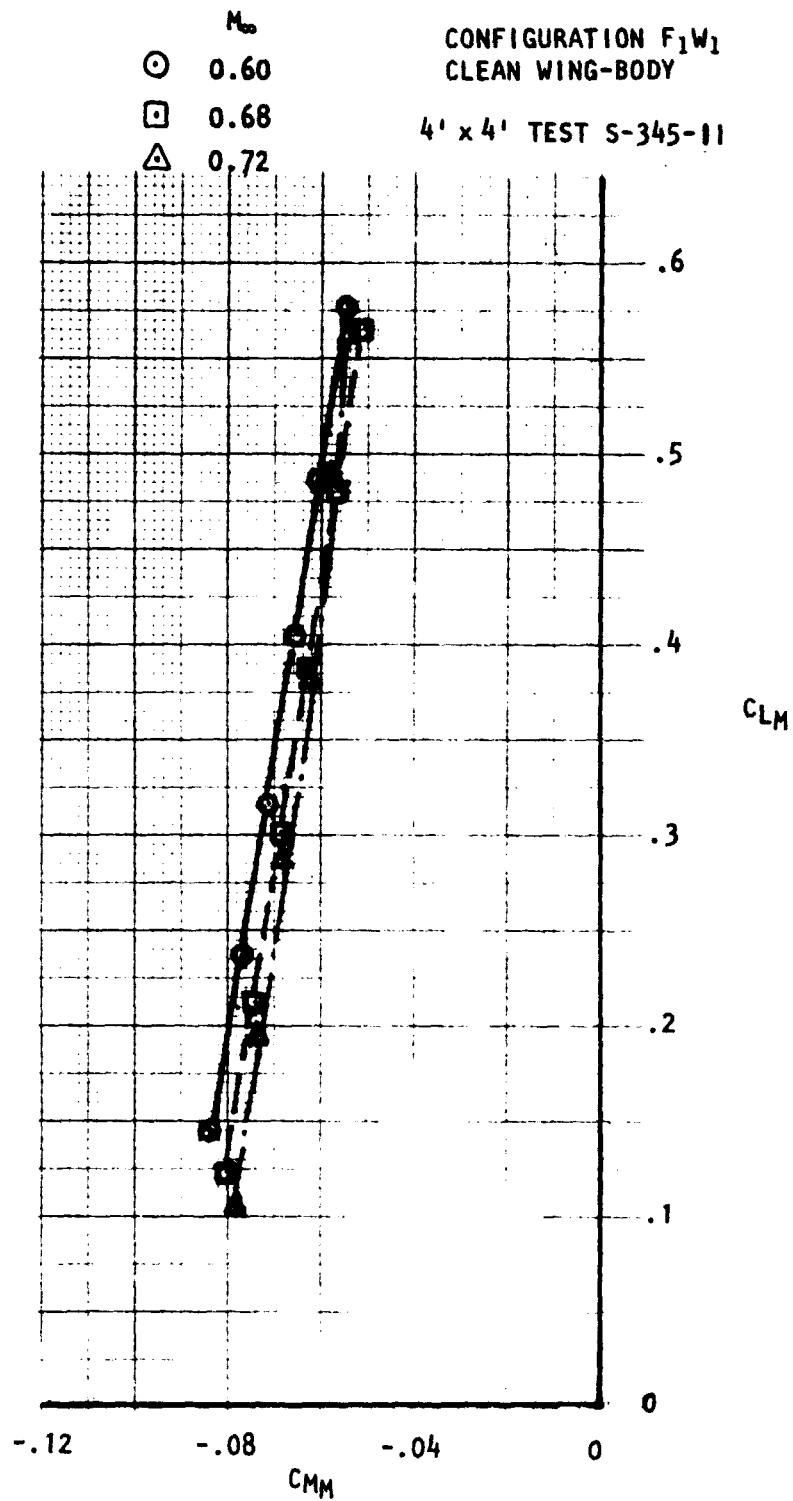


Figure 22. Variation of pitching-moment coefficient with Mach number, straight wing.  $R_{NC} = 3.5 \times 10^6$

USB CRUISE PROGRAM

CONFIGURATION F<sub>2</sub>W<sub>2</sub>  
CLEAN WING-BODY

4' x 4' TEST S-345-11

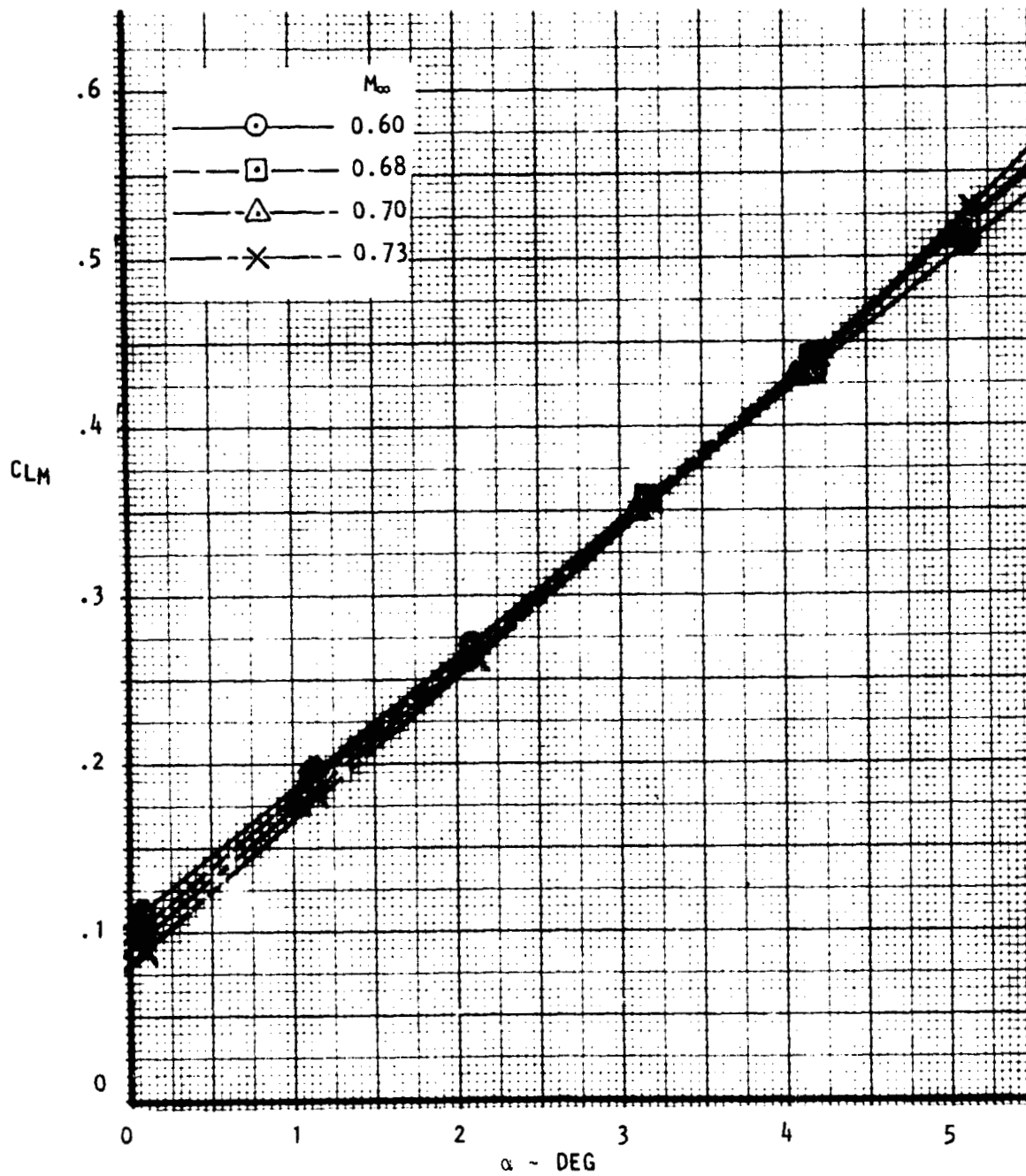


Figure 23 . Variation of lift coefficient with Mach number, swept wing.  $R_{NC} = 3.5 \times 10^6$

# USB CRUISE PROGRAM

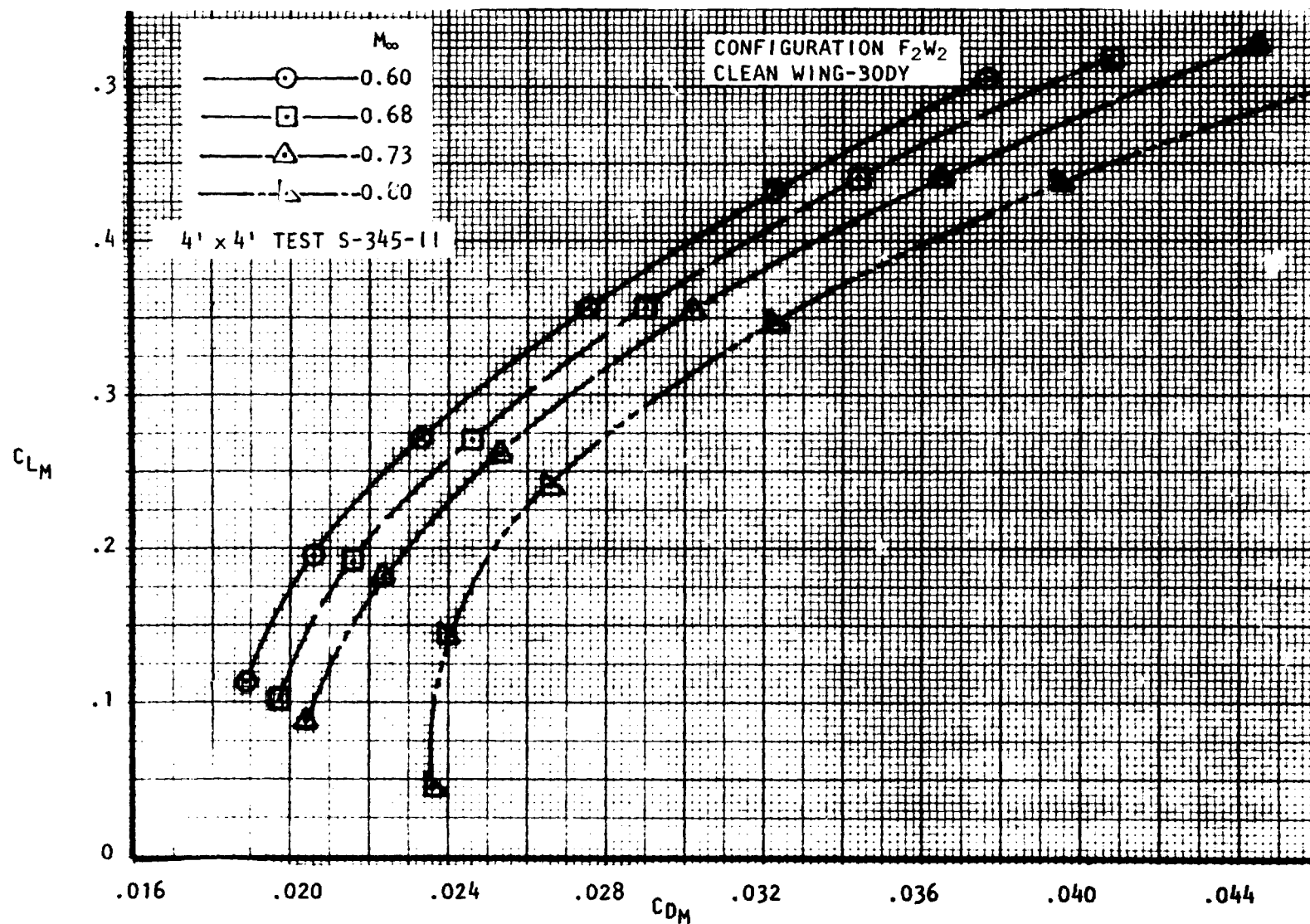


Figure 24. Variation of drag coefficient with Mach number, swept wing.  
 $R_{NC} = 3.5 \times 10^6$

# USB CRUISE PROGRAM

$M_{\infty}$   
 $\odot$  0.60       $\triangle$  0.70  
 $\square$  0.68       $\times$  0.73

CONFIGURATION F<sub>2</sub>W<sub>2</sub>  
 CLEAN WING-BODY

4' x 4' TEST S-345-11

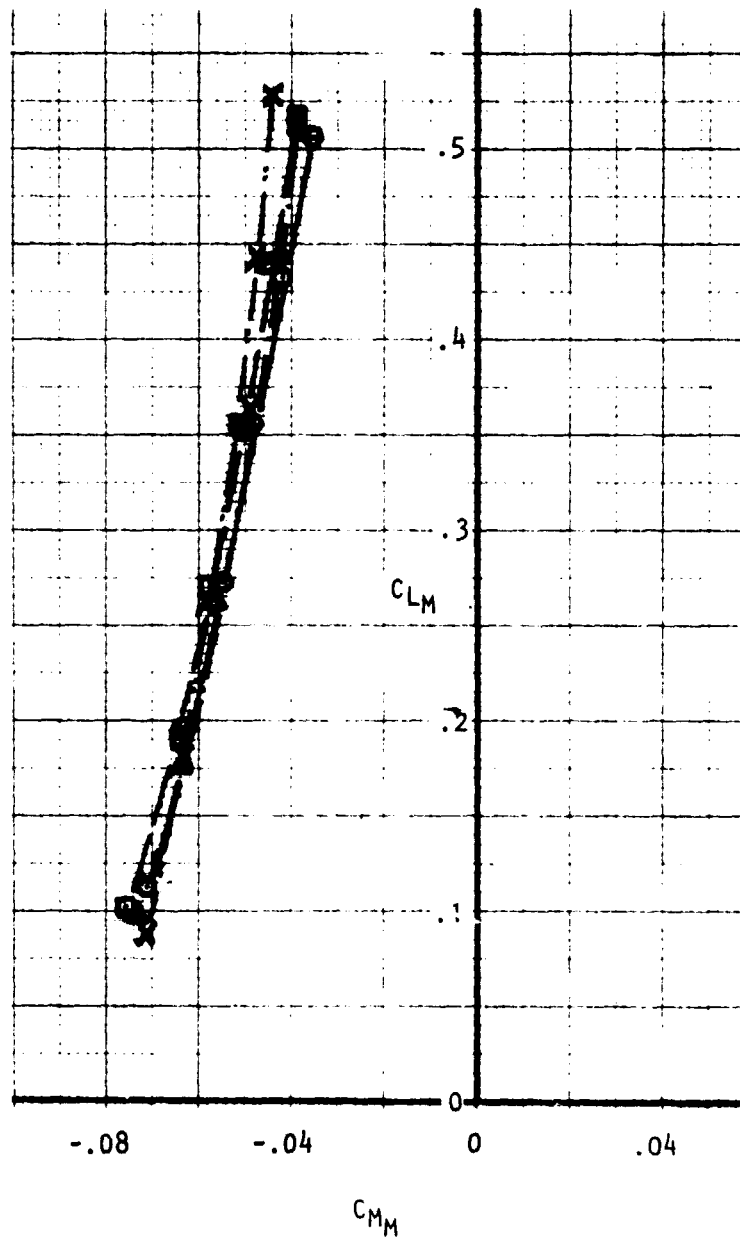


Figure 25. - Variation of pitching-moment coefficient with Mach number, swept wing.

$$R_{NC} = 3.5 \times 10^6$$



### 3.2.2 USB Nacelle Installations - Pressure Tests

Pressure tests of the two-dimensional wing with selected nacelles installed were conducted to provide supportive detail to the conclusions to be drawn from the force measurements. Such tests included both surface static pressures and wake-rake traverses of the jet one chord length downstream of the wing trailing-edge. In the analysis of the pressure data which follows, use is made of several equations for correlation purposes. For convenience, these will be discussed below:

As noted in Section 3.1.3, the momentum equations relation to the generation of lift and drag forces on the wing alone by a vectoring jet are:

$$\Delta C_L = \eta_t C_T \sin (\alpha + \delta_j) \quad (9a)$$

$$\Delta C_D = \eta_t C_T [1 - \cos (\alpha + \delta_j)] \quad (9b)$$

These forces are, of course, manifested on the constant radius turning surface,  $R_w$ , as a pressure field which, for thin, attached jets, may be approximated by:

$$C_{P_j} = \frac{-\Delta p}{q_j} = \frac{-2h}{R_w} \quad (10)$$

In Reference 2, documenting results of static tests involving Coanda phenomena, it is noted that the peak negative pressures on the deflection surface are approximated by those derived by equation (10). Where shock conditions are present, the referenced results indicate that the calculated

value represents an approximate mean level of pressure about which the experimental values fluctuate. That equation (10) is essentially an equivalent of equations (9) when the pressure load is integrated over an increment of wing chord ( $\Delta c$ ) and effective nozzle width ( $\Delta w$ ) is shown in Figure 26. The corresponding lift and drag increments are:

$$\Delta C_{Lj} = \frac{2h}{R_W} \frac{q_j}{q_\infty} \frac{\Delta c \Delta w}{S_W} \quad (11a)$$

$$\Delta C_{Dj} = \frac{2h}{R_W} \frac{q_j}{q_\infty} \frac{\Delta t \Delta w}{S_W} \quad (11b)$$

In this form, these may be further incremented relative to the flow-through nozzle condition as:

$$\Delta C_{Lj} = \frac{2h}{R_W} \left( \frac{q_j}{q_\infty} - 1 \right) \frac{\Delta c \Delta w}{S_W} \quad (12a)$$

$$\Delta C_{Dj} = \frac{2h}{R_W} \left( \frac{q_j}{q_\infty} - 1 \right) \frac{\Delta t \Delta w}{S_W} \quad (12b)$$

or similarly:

$$\Delta C_{Lj} = \eta_T \Delta C_T \sin (\alpha + \delta_j) \quad (13a)$$

$$\Delta C_{Dj} = \eta_T \Delta C_T [1 - \cos (\alpha + \delta_j)] \quad (13b)$$

where

$$\Delta C_T = (C_T)_{H_j/p_\infty} - (C_T)_{H_j=H_\infty}$$

$$\Delta C_{Dj} = C_T (1 - \cos \delta_j)$$

$$C_T = \frac{\rho_j A_j V_j^2}{q_\infty S_{REF}} = \frac{\rho_j h \Delta W_e V_j^2}{\frac{\rho_\infty V_\infty^2 S_{REF}}{2}}$$

$$\cos \delta_j = \frac{R_w - \Delta t}{R_w}$$

$$\Delta C_{Dj} = \frac{\rho_j h \Delta W_e V_j^2}{\frac{\rho_\infty V_\infty^2 S_{REF}}{2}} \left[ 1 - \frac{(R_w - \Delta t)}{R_w} \right]$$

$$\Delta C_{Dj} = 2 \left[ \frac{(\rho_j V_j^2)}{\rho_\infty V_\infty^2} \right] \left[ \frac{(h \Delta W_e)}{S_{REF}} \right] \left[ \frac{(-\Delta t)}{R_w} \right]$$

$$\Delta C_{Dj} = - \left[ \frac{2h}{R_w} \right] \left[ \frac{q_j}{q_\infty} \right] \left[ \frac{\Delta W_e \Delta t}{S_{REF}} \right]$$

NOTE: BY SIMILAR DERIVATION:

$$\Delta C_{Lj} = C_T \sin \delta_j = \left| \frac{2h}{R_w} \right| \left| \frac{q_j}{q_\infty} \right| \left| \frac{\Delta W_e \Delta c}{S_{REF}} \right|$$

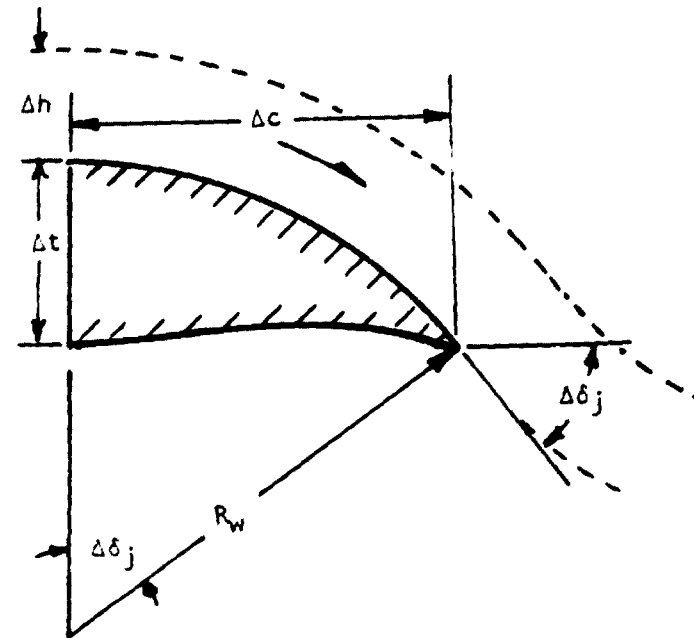


Figure 26 . Derivation of equivalent expression for jet-turning loads.

In the use of equations (11) or (12) for correlation purposes, the assumption is made that the jet height,  $h$ , is the nozzle centerline height which requires that an effective width,  $\Delta w$ , be employed to account for the non-rectangular shape and specified area of the nozzle exit. Additionally, the radius of curvature,  $R_w$ , is taken to be that of the aft airfoil upper surface which, for the test wings (straight and swept), is approximated by a constant radius of 4.72 cm (12-inches) from  $x/c = 0.50$  to  $x/c = 1.0$ . It should also be noted from the geometry of Figure 26, that by specifying the ratio  $\frac{\Delta c}{R_w}$ , the angle through which the jet is turned is also specified, which would equal the trailing-edge angle of the aft-wing upper surface when the foregoing geometric values are introduced; this angle is 17 degrees and 16 degrees for the straight and swept wings, respectively. In the discussions which follow, equations (12) and (13) are used interchangeably as appropriate to the subject matter.

In the pressure analyses, pressure integrations are frequently used to quantify relative magnitudes and trends of lift and drag increments usually within the jet-scrubbed area of the nozzle. Carry-over effects can obviously influence the pressures beyond the wing-stations considered and, therefore, the pressure results can qualitatively support but not replace the force measurements.

3.2.2.1 Static Performance - It was noted in Section 3.1.3 that the observed pressure load on the wing alone bears a relationship to the jet deflection angle obtained from force measurements. Additionally, the jet-vectoring load can be portrayed as a part of the total installation penalty of the

wing/body/nacelle system (i.e., isolated thrust vector deleted) under static conditions. Thus, a study of the static pressure distributions are of value in verifying the equations and assumptions employed in the bookkeeping process.

Typical chordwise pressure distributions along the jet centerline are provided in Figure 27 for a small, "D-duct" nozzle ( $N_6$ ) statically tested on the straight wing. The nozzle pressure ratio varies from about 1.4 to 3.3 and the plotted pressure coefficient has been normalized on jet-dynamic pressure,  $q_j$ . It may be noted from these data that the pressure load on the wing increases rapidly with blowing rate and that, in the higher range, the compression/expansion waves within the jet cause abrupt variations in the pressure distribution. It may also be noted that the peak pressure coefficients generated on the wing tend toward more positive values as the trailing-edge is approached. Such a trend would be in keeping with an assumption of jet detachment just ahead of the trailing edge resulting in jet-deflection angles somewhat less than that of the wing upper surface ( $17^\circ$ ).

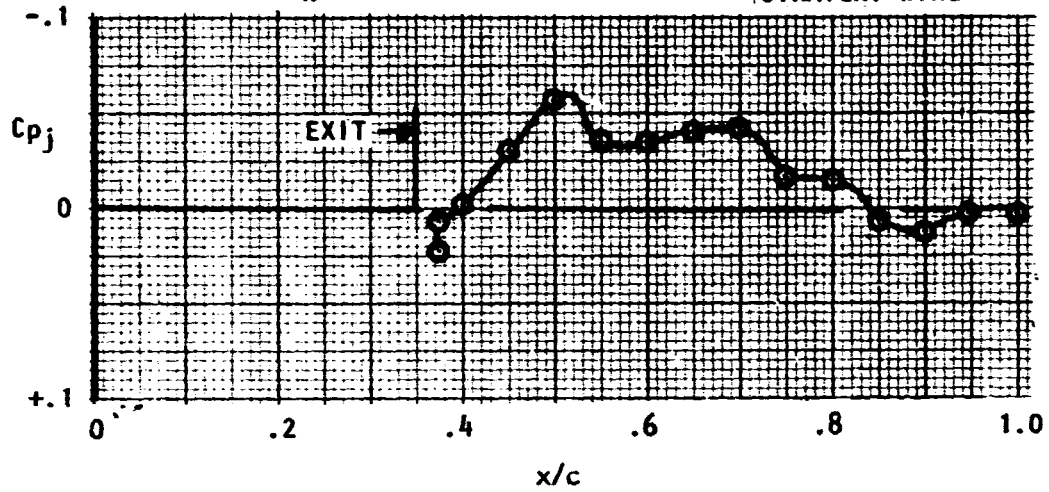
Also shown on Figure 27 are the values of  $C_{p_j}$  calculated by equation (10). As the nozzle pressure ratio is raised, the calculated pressure level tends to represent a mean of the experimental pressures and, as such, suggests that the nozzle geometry plays a role in establishing the pressure level as in equation (12). Further evidence that centerline pressure may be governed by geometric nozzle height is provided in Figure 28. Several sizes of semi-circular nozzles are represented by the size parameter,  $c^2/A_N$  varying

# USB CRUISE PROGRAM

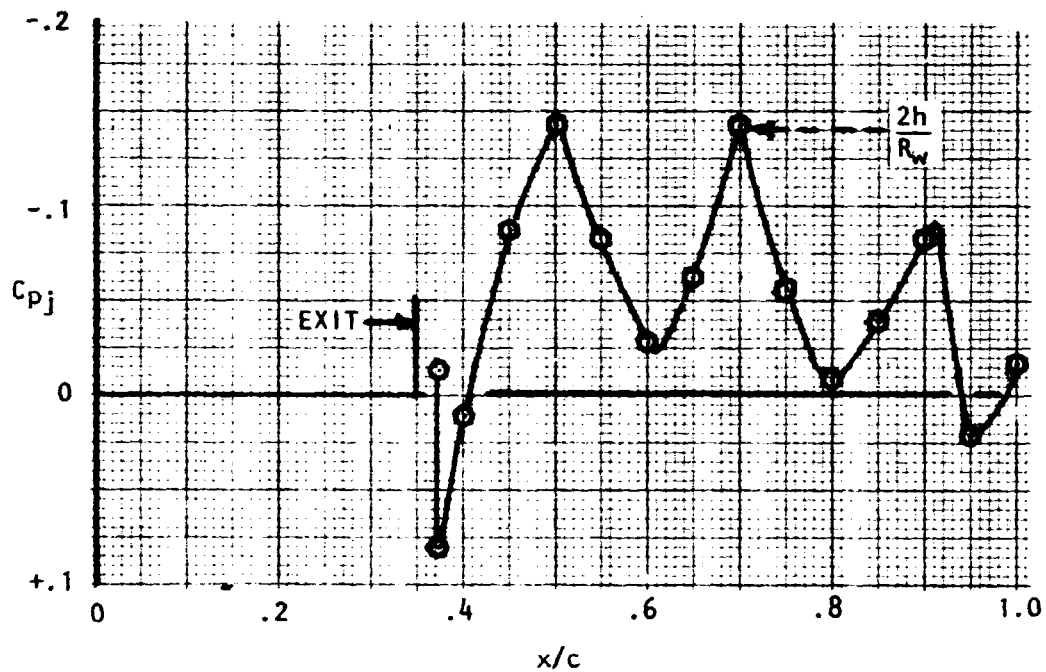
D-DUCT NOZZLE ( $N_6$ )

$$\frac{c^2}{A_N} = 48$$

STRAIGHT WING



(a)  $H_j/\rho_\infty = 1.44$



(b)  $H_j/\rho_\infty = 2.66$

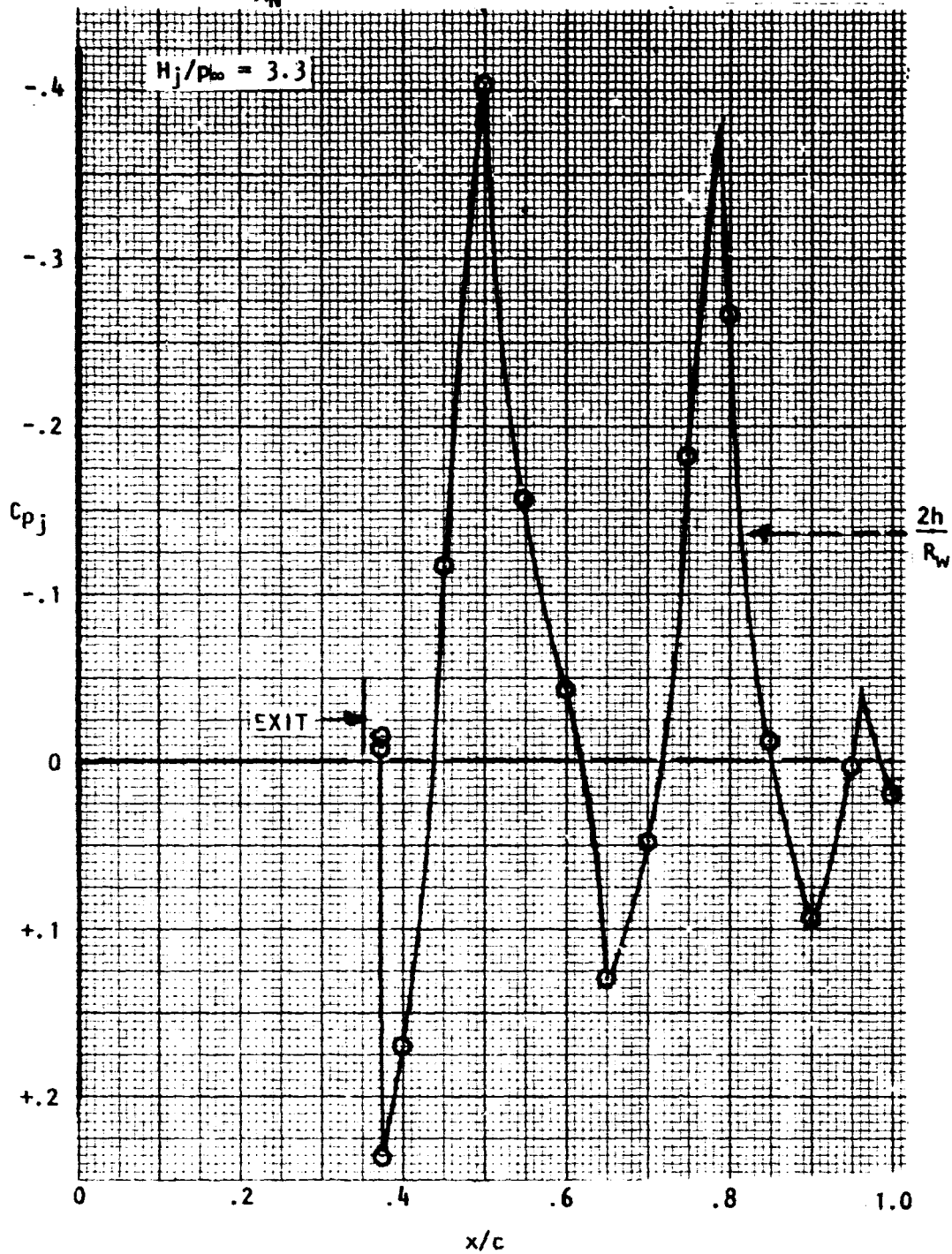
Figure 27 . Jet centerline surface pressures, static tests,  $\alpha = 0^\circ$ .

# USB CRUISE PROGRAM

D-DUCT NOZZLE ( $N_6$ )

$$\frac{c^2}{A_N} = 48$$

STRAIGHT WING



(c)  $H_j/p_{\infty} = 3.3$

Figure 27 . Continued.

# USB CRUISE PROGRAM

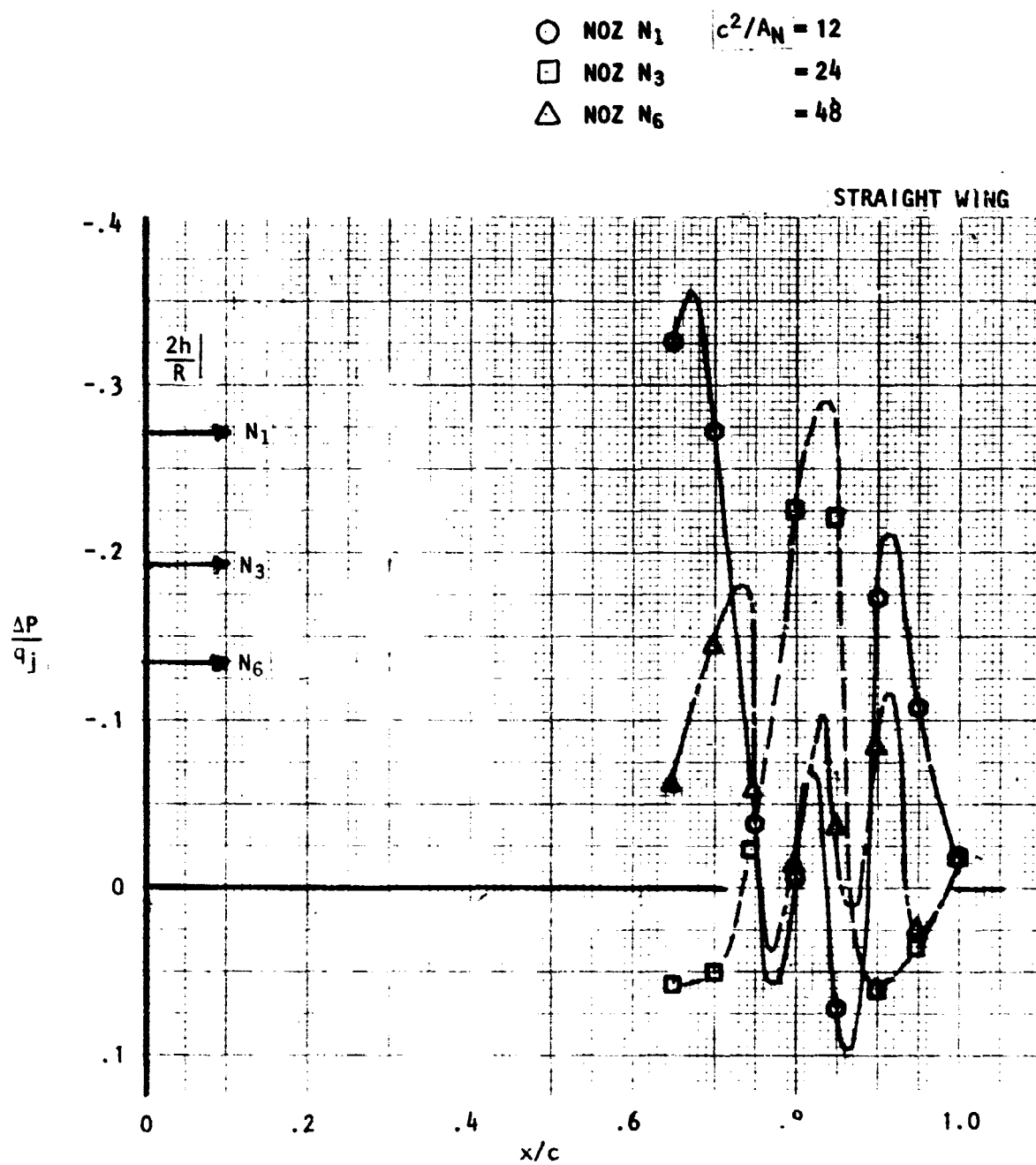


Figure 28. - Effect of nozzle size on jet-centerline pressures, static,  $\alpha \approx 2^\circ$ ,  $H_j/p_\infty = 2.7$ .



in magnitude from 12 to 48. For the pressure ratio represented (2.7), the parameter,  $\frac{2h}{R_w}$ , correctly predicts the increase in peak pressure within the scrubbed area as the jet height increases. Thus, over part of the downstream wing surface, at least, the pressures indicate an attached jet turning with the wing upper surface.

Pressure data similar to the foregoing have been integrated in a lift and drag direction, assuming that centerline pressures act over the nozzle width, for a semi-circular nozzle ( $N_3$ ). The results, shown in Figure 29 in terms of  $\frac{\Delta L}{T_{ISOL}}$  and  $\frac{\Delta D}{T_{ISOL}}$ , show good agreement with force test measurements; it should be noted here, that at high pressure ratios, shock-induced pressure fluctuations create some difficulty with the pressure integrations. However, the basic agreement between force and pressure measurements, as shown in Figure 29, verifies the expected consistency between the static wing loads and the Coanda expressions as used in the bookkeeping process.

3.2.2.2 Wind-On Performance - Before considering basic wind-on test results, a comparison between static and wind-on pressures offers considerable insight into USB aerodynamic phenomena. The wing pressure load due to the deflecting jet appears to be substantially changed at wind-on conditions as opposed to the static observations. Figure 30 compares upper-surface pressure coefficients generated along the jet centerline under both static and wind-on conditions ( $M_\infty = 0.68$ ) for the small, D-duct nozzle ( $N_6$ ); the pressure coefficient under either condition is based on jet dynamic pressure,  $q_j$ , and the nozzle pressure ratio is constant at about 2.6. Clean wing pressure

# USB CRUISE PROGRAM

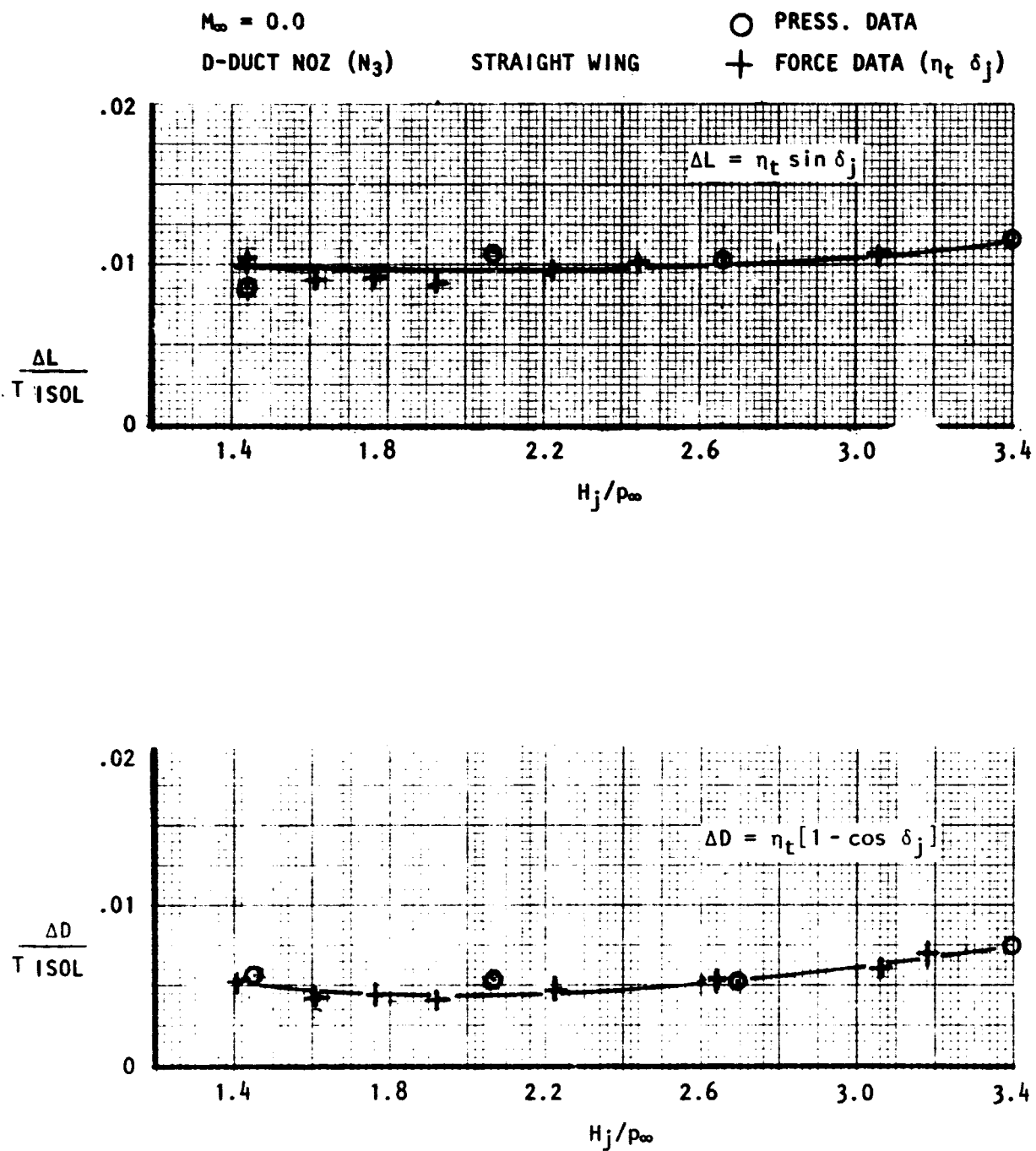
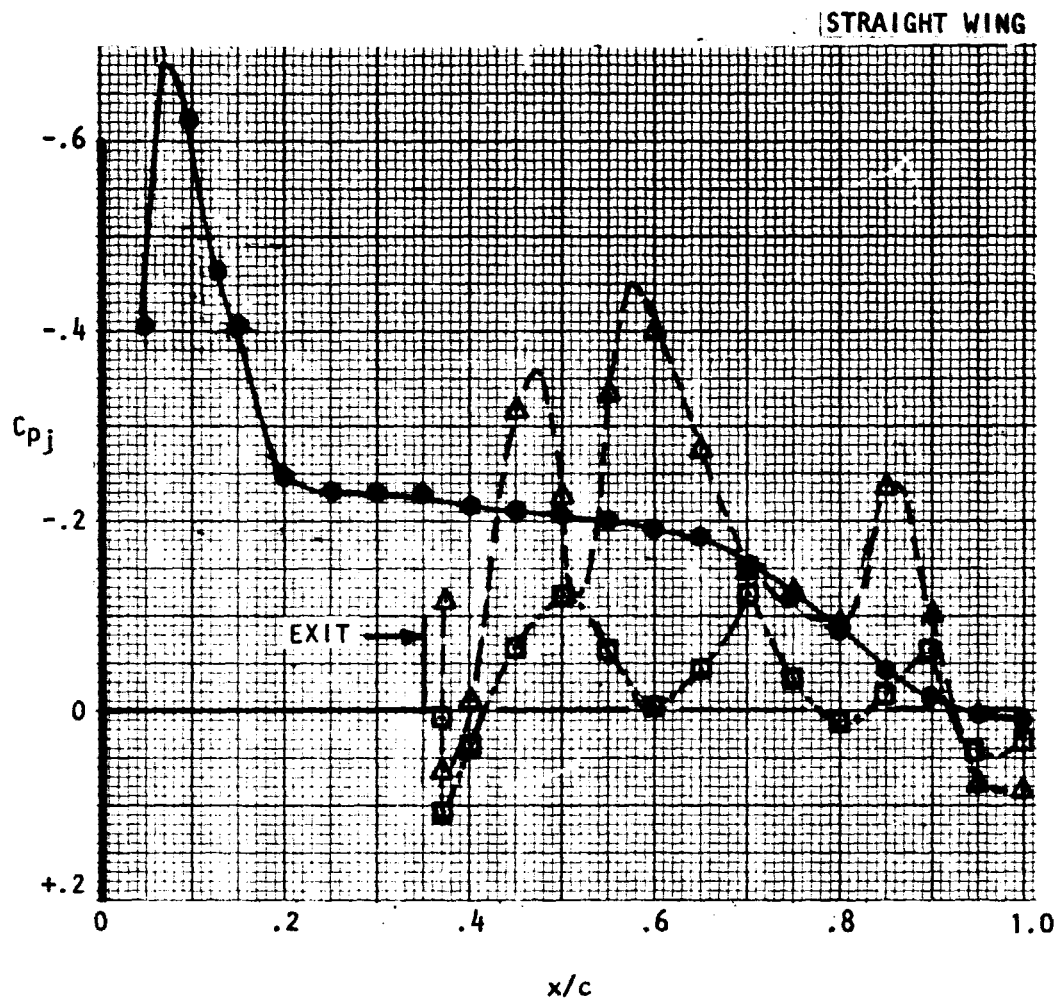


Figure 29. Comparison of force and pressure-derived wing loads at static conditions.

# USB CRUISE PROGRAM

- CLEAN WING
- WING + NAC - STATIC
- △ WING + NAC -  $M_\infty = 0.68$



ORIGINAL PAGE IS  
POOR QUALITY

Figure 30 . Jet centerline pressure distributions,  
"D-Duct" noz ( $N_6$ )  $H_j/p_\infty = 2.6$ ,  $\alpha = 2.6^\circ$ .

data are also shown for reference. It is apparent from the results that, with nacelle installed, an increase in the scrubbing area pressure load (positive lift and drag) occurs at wind-on conditions relative to the static case. A general observation would be that the total, wind-on pressure load on the wing aft-surface is more closely approximated by some combination of the wing-alone and jet-induced pressures rather than just the static pressure load. In this case a basic difference in the loading could reflect a change in the cross-product terms of a pressure coefficient as derived by  $(\Delta V_j)^2$  statically and  $(V_1 + \Delta V_j)^2$  at wind-on conditions. Further, the presence of the jet can introduce a local cambering effect by suppression of the aft boundary-layer build-up on the clean wing thus providing an increased pressure load as the section approaches local potential-flow performance. Therefore, through such mechanisms, the vectoring jet at wind-on conditions can produce lift and drag increments which exceed the simple superposition of wing alone and static vectoring loads on the aft surface.

Additional evidence that the wind-on behavior of the jet varies considerably from that found statically is shown in Figure 31 where jet profiles obtained from the traversing wake rake are compared. Statically, the jet appears to be more diffused and does not penetrate the wake to the same extent as indicated for the wind-on case. Also, the wind-on jet core appears to follow the wing surface more closely indicating a higher turning angle ( $\delta_j$ ) at Mach number than was obtained statically. While an exact determination of the parameter,  $\delta_j$ , from the wake profiles may be questionable due to rapid changes in jet curvature between the wing trailing edge and rake, an attempt was made to quantify the static versus wind-on changes in  $\delta_j$ ; the results

USB CRUISE PROGRAM

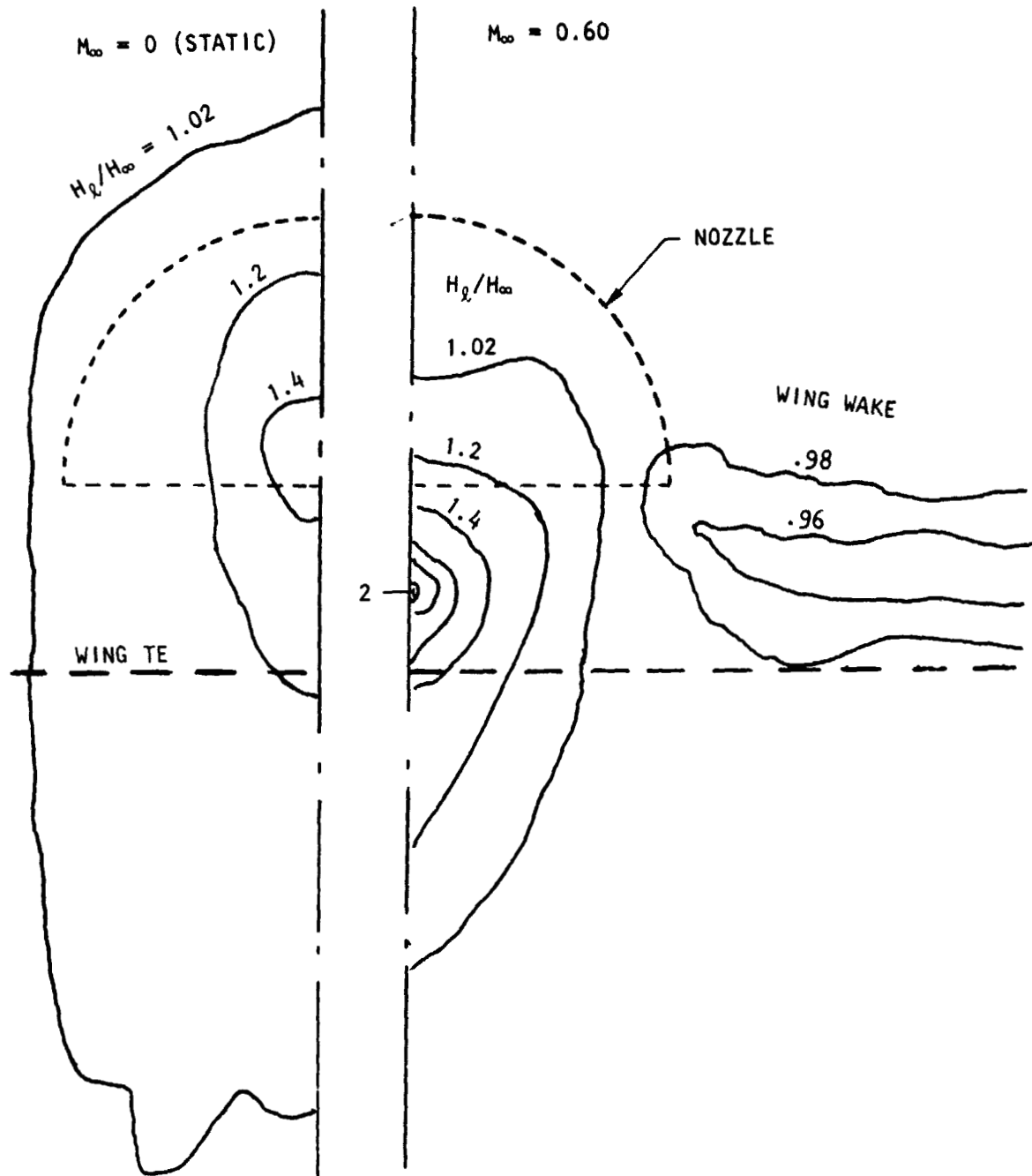


Figure 31 . Comparison of static and wind-on jet isobars one chord length behind straight wing,  $H_j/\rho_\infty = 2.2$ ,  $\alpha = 2.6^\circ$ .

are shown in Figure 32. The rake data provided were obtained behind an aspect ratio 2.53 "D-duct" nozzle ( $N_3$ ) designed with a low boattail angle ( $\beta \approx 9^\circ$ ) to suppress jet attachment. The upper half of Figure 32 shows the location of the jet core as obtained from the wake traverses, both statically and wind-on. The increment in jet deflection,  $\Delta\delta_j$ , shown at the bottom of the figure was obtained from full-scale geometric lay-outs of the wing and wake profile. In the lower figure, the jet deflection angle as resolved from static force measurements is shown along with the added increment as evaluated from the wake traverse. About 3 degrees of increase in angle at the wind-on state is indicated from these measurements. At the typical cruise angle-of-attack of approximately 3 degrees, the pressure drag on the wing would be increased by this additional vectoring as would also the reaction thrust in the lift direction. Later discussions concerning the drag increment associated with this nozzle configuration (see Section 3.2.3.3) will show that in the high pressure-ratio range, the jet pressure drag corresponds to  $\delta_j \approx 10^\circ - 12^\circ$  or a slightly higher effective angle than that deduced from the foregoing wake traverse.

3.2.2.3 Aerodynamic/Geometric Effects - Wind-on aerodynamic effects are discussed below in terms of the operating environment of the wing/nacelle/jet combination at simulated cruise conditions. These discussions are then followed by similar discussions of the geometric effects of the nozzle shape and size on local pressure distributions.

- o Effect of Mach number - Typical effects of Mach number on jet centerline pressures are shown in Figure 33 at a constant nozzle pressure ratio of 2.2 for a D-duct nozzle. The major differences occurring with Mach

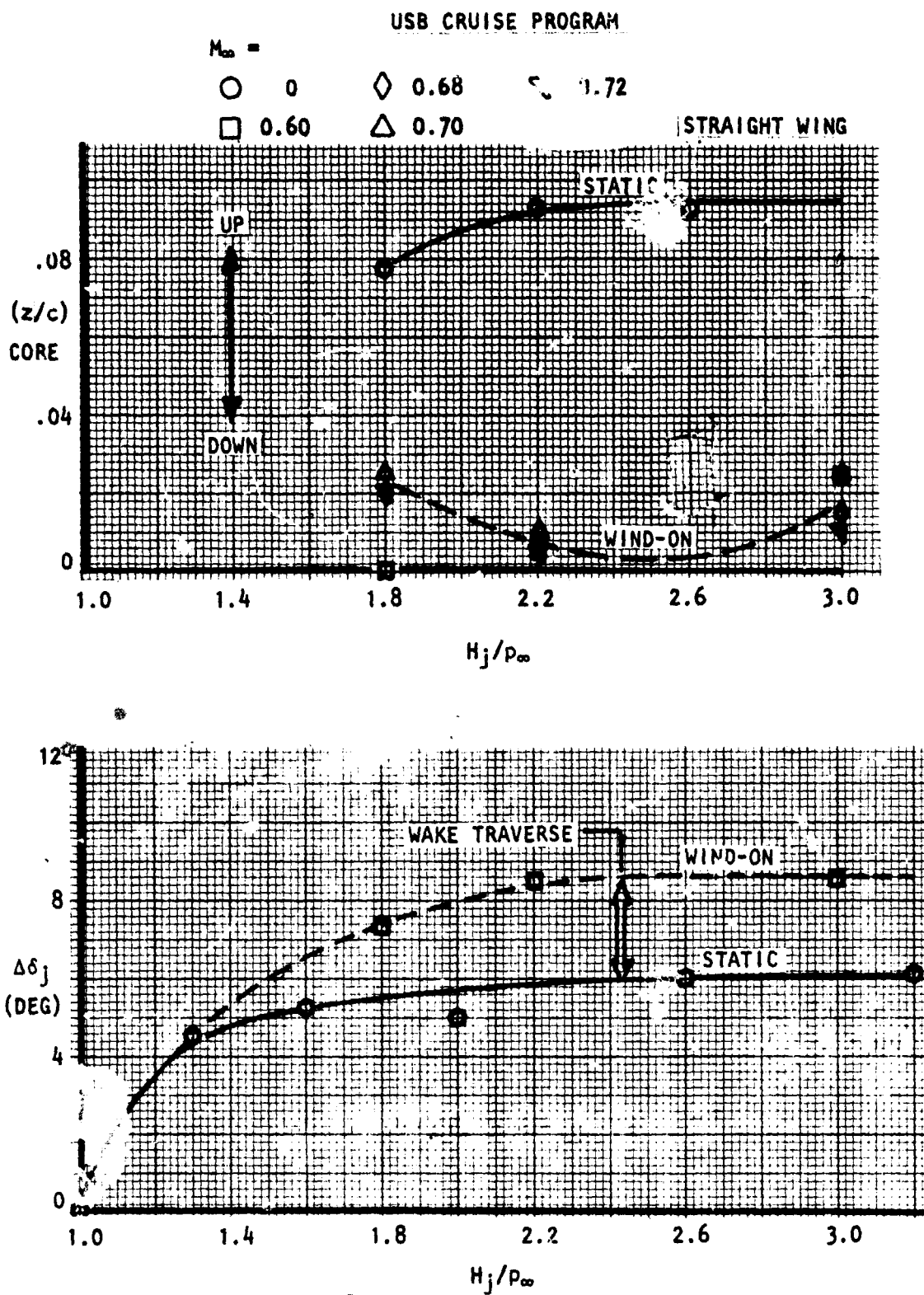


Figure 32 . Effect of Mach No. on jet core location at rake, "D-Duct" noz ( $N_3$ )  $\alpha = 3^\circ$ .

# USB CRUISE PRG. 'AM'

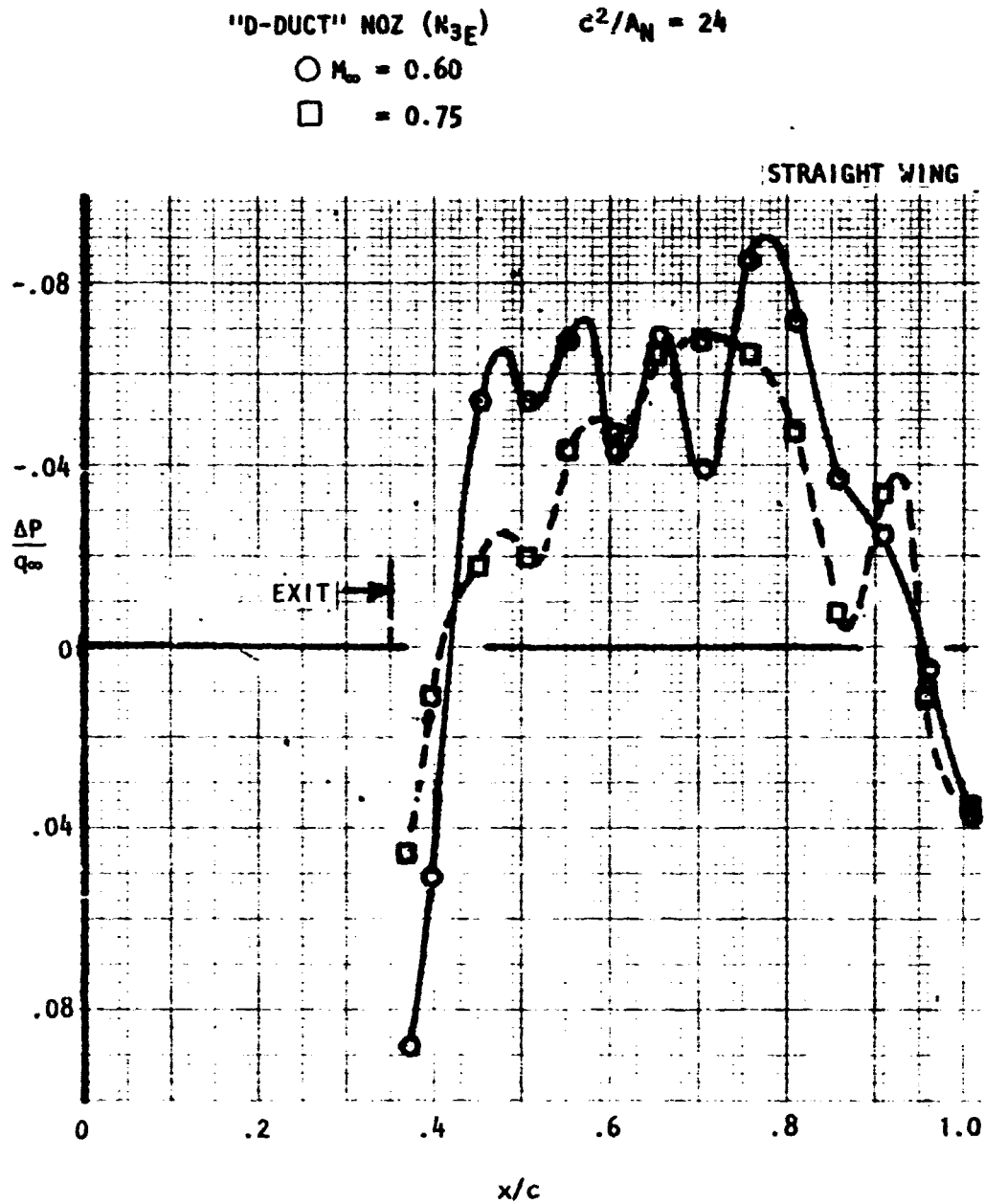


Figure 33 . Effect of Mach No. on jet centerline pressures,  $H_j/p_\infty = 2.2$ ,  $\alpha = 2^\circ$ .



number are those associated with the changes in jet shock structure and the indication of higher negative pressures within the scrubbed area at the lower Mach number. Inasmuch as Equation (11) suggests that the centerline pressures should be dependent upon the parameter,  $\frac{q_j}{q_\infty}$ , similar pressure distributions have been plotted in Figure 34 at a constant value of  $q_j/q_\infty$  for two Mach numbers. Except for the presence of the shock structure at the higher pressure ratio (2.25), the centerline pressures are reasonably equal for the two widely different free-stream speed conditions. These, and similar test results, indicate that freestream Mach number has little effect on pressures within the jet scrubbed area and that the primary controlling factor is the jet dynamic pressure,  $q_j$ , or the jet velocity ratio,  $(\frac{V_j}{V_\infty})$ . This would imply that at constant levels of  $q_j/q_\infty$ , the jet-induced lift and drag increments should be approximately constant when considering only the jet-induced pressures within the scrubbed area.

For reference, the variation of the jet dynamic pressure ratio with Mach number and nozzle pressure ratio is provided in Figure 35. As shown, and as used herein, the data represent a fully-expanded jet. At a specified level of nozzle pressure ratio, it may be also noted that the ratio  $q_j/q_\infty$  varies inversely with Mach number. Therefore, from these as well as the foregoing considerations, pressure changes due to the jet should vary inversely with Mach number when the pressure ratio is held constant.

In keeping with the foregoing conclusions, centerline pressures have been integrated from a nozzle exit to the wing trailing-edge and the

# USB CRUISE PROGRAM

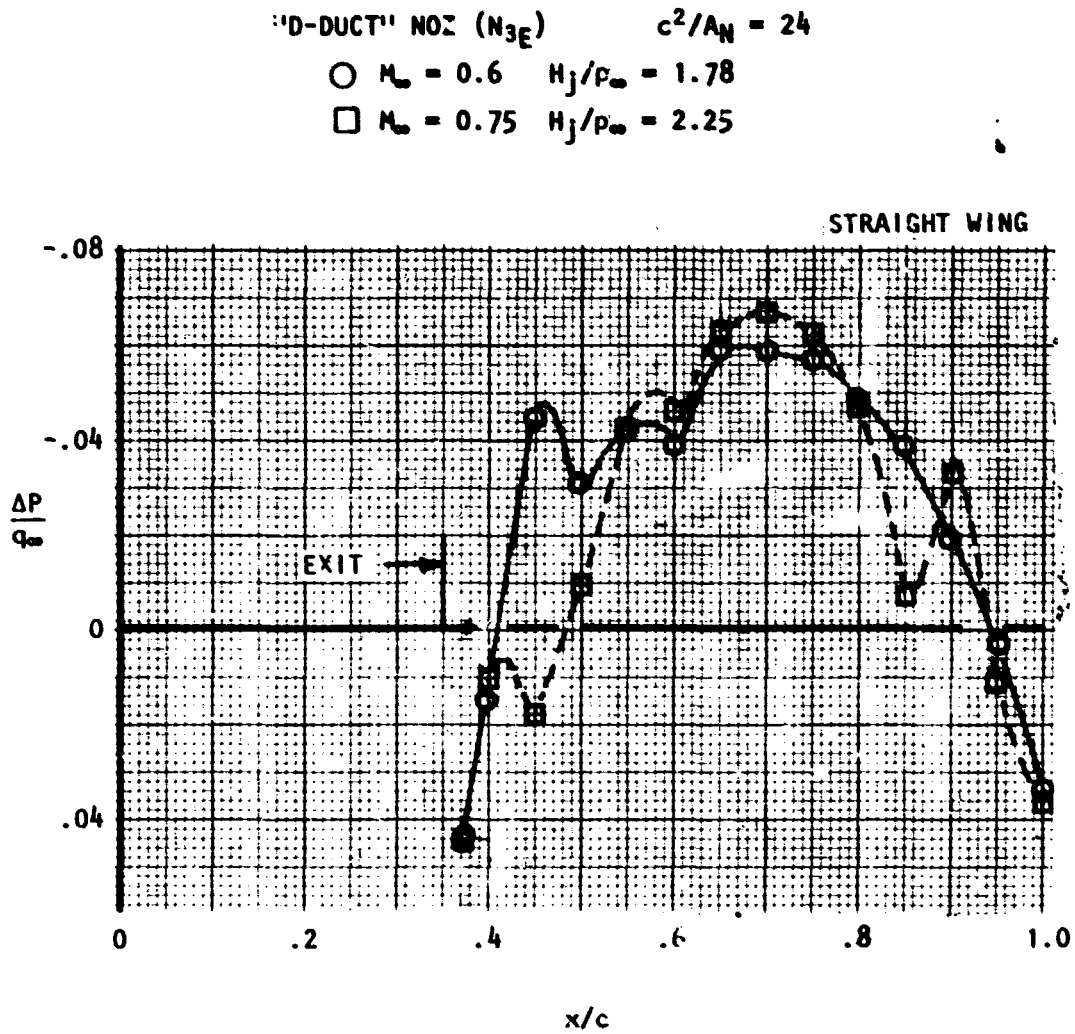


Figure 34 . Jet centerline pressure distributions at constant  $q_j/q_\infty = 2.3$ ,  $\alpha = 2^\circ$ .

# USB CRUISE PROGRAM

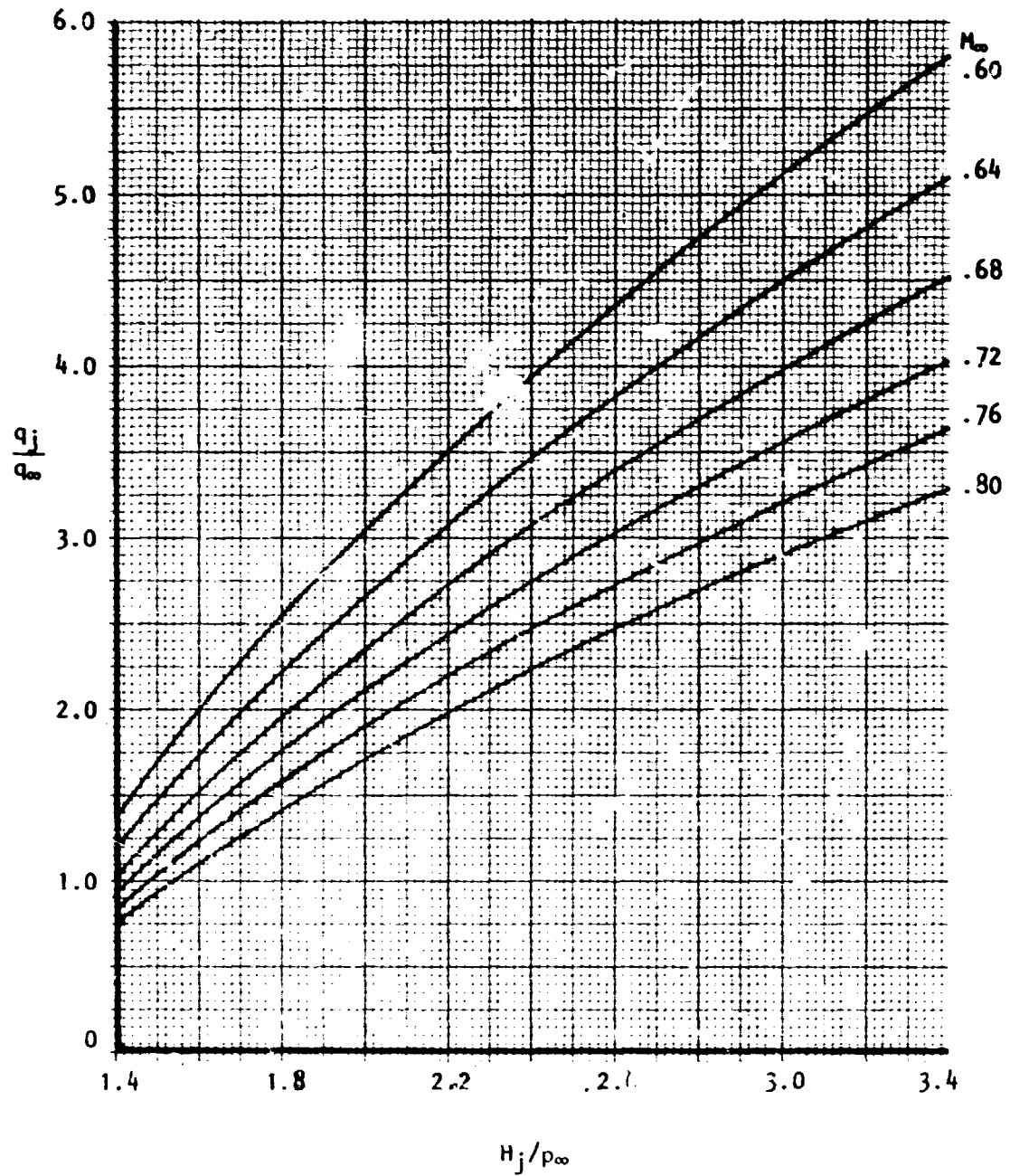


Figure 35 . Jet dynamic pressure ratio,  
fully expanded jet - incompressible

assumption made that the centerline pressure levels are sustained across the nozzle width. The results are shown in Figures 36 and 37. In Figure 36 the data are presented as the ratio of the drag increase due to blowing relative to that found at the flow-through ( $H_j = H_\infty$ ) condition. The trends confirm the earlier conclusion as to the anticipated effect of Mach number. Included on Figure 36 are data determined in a like manner for a similar test configuration and reported on in Reference 3. For the referenced tests, the nozzle is essentially rectangular in shape ( $AR = 3.3$ ) with air supplied from upstream of the test section via an air-supply pipe. Also shown on Figure 36 is a calculated trend of pressure drag with Mach number, based on Equation (12), which can be reduced to:

$$\frac{\Delta C_D}{\Delta C_{D_{H_j=H_\infty}}} = K \left[ \frac{q_j}{q_\infty} - 1 \right] \quad (14)$$

The function is matched to the referenced results (via K) at  $M_\infty = 0.70$  inasmuch as the details of the wing/nacelle geometrics are largely unknown. Both sets of experimental data as well as the calculation indicate that the effects of Mach number on pressure drag are manifested primarily through the jet dynamic pressure ratio,  $\frac{q_j}{q_\infty}$ . Figure (37) shows the lift increment as integrated within the jet scrubbing area as a function of Mach number for a range of nozzle shapes and based on the foregoing assumptions. Again, a calculated trend, similar to equation (14), is shown with the calculation matched to the wide nozzle ( $AR = 4$ ) data at  $M_\infty = 0.72$ . For the wide nozzle, the experimental trend of lift

# USB CRUISE PROGRAM

D-DUCT NOZZLE ( $N_{3E}$ ) AR = 2.5

STRAIGHT WING

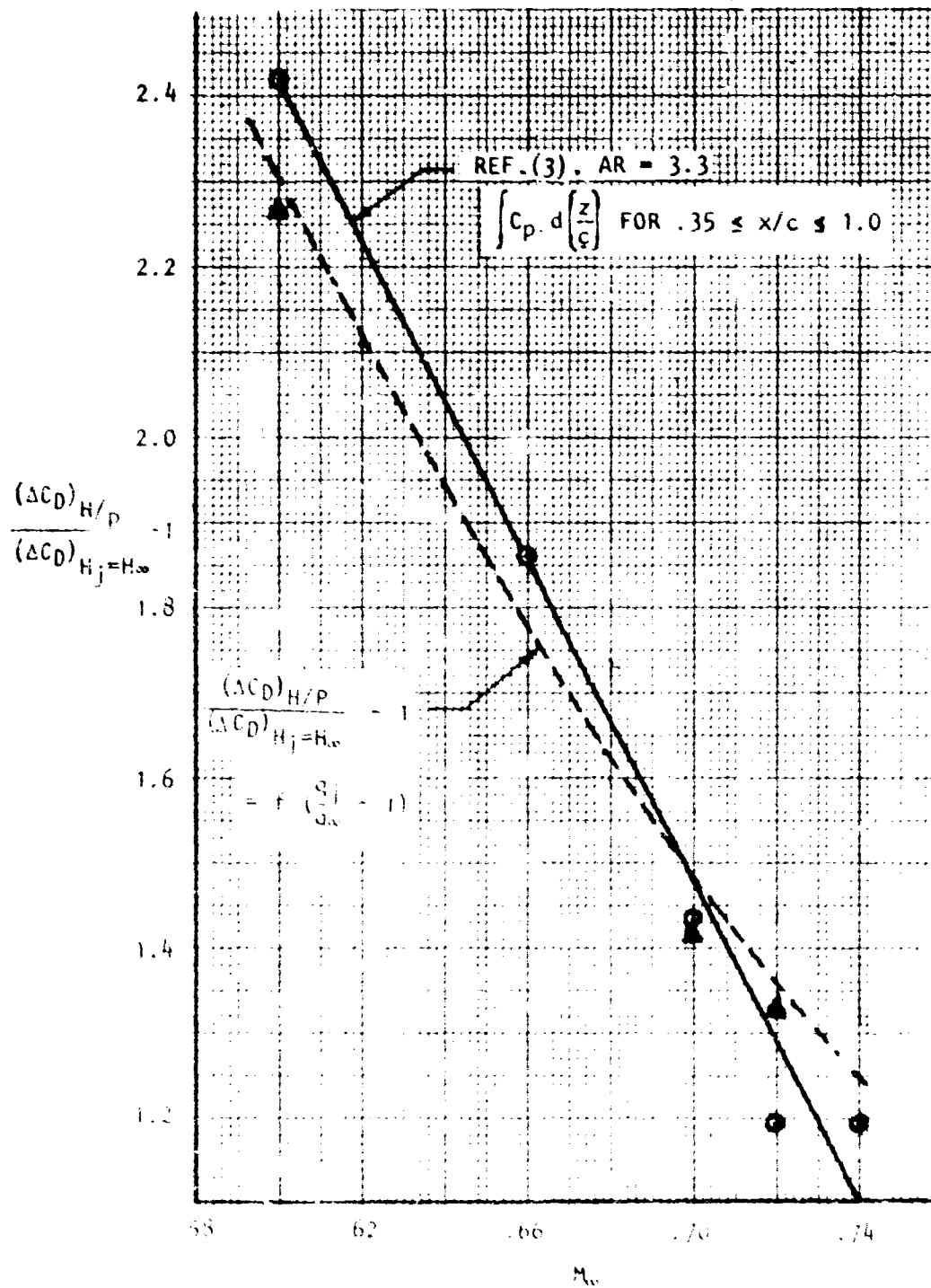


Figure 46 Effect of Mach No. on pressure - integrated drag,  $\alpha = 2^\circ$ ,  $H_j/p_\infty = 2.4$ .

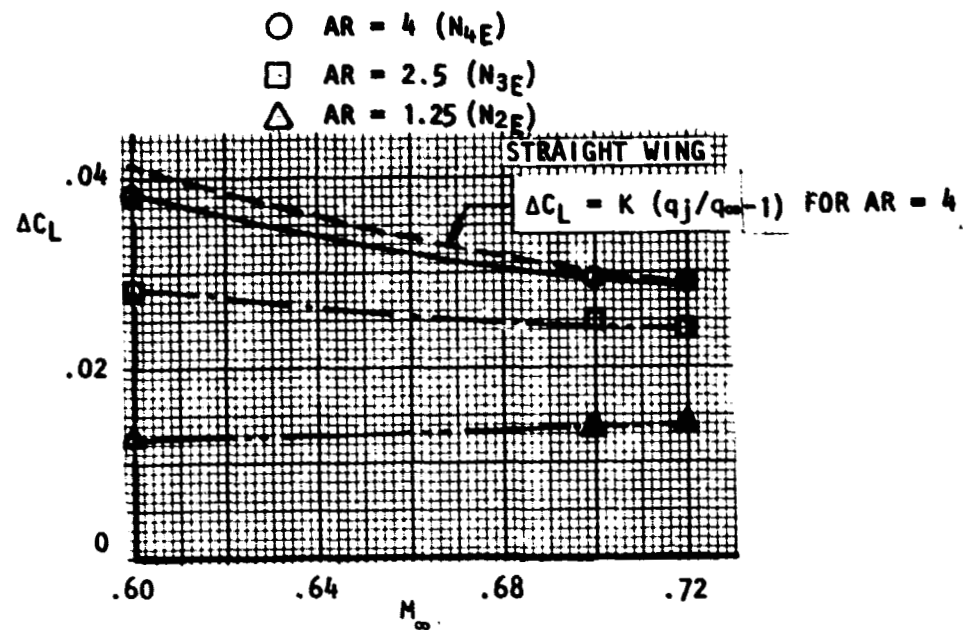


Figure 37 . - Effect of Mach No. on lift developed in scrubbed area,  $\alpha = 2^\circ$ ,  $H_j/p_\infty = 2.2$ .

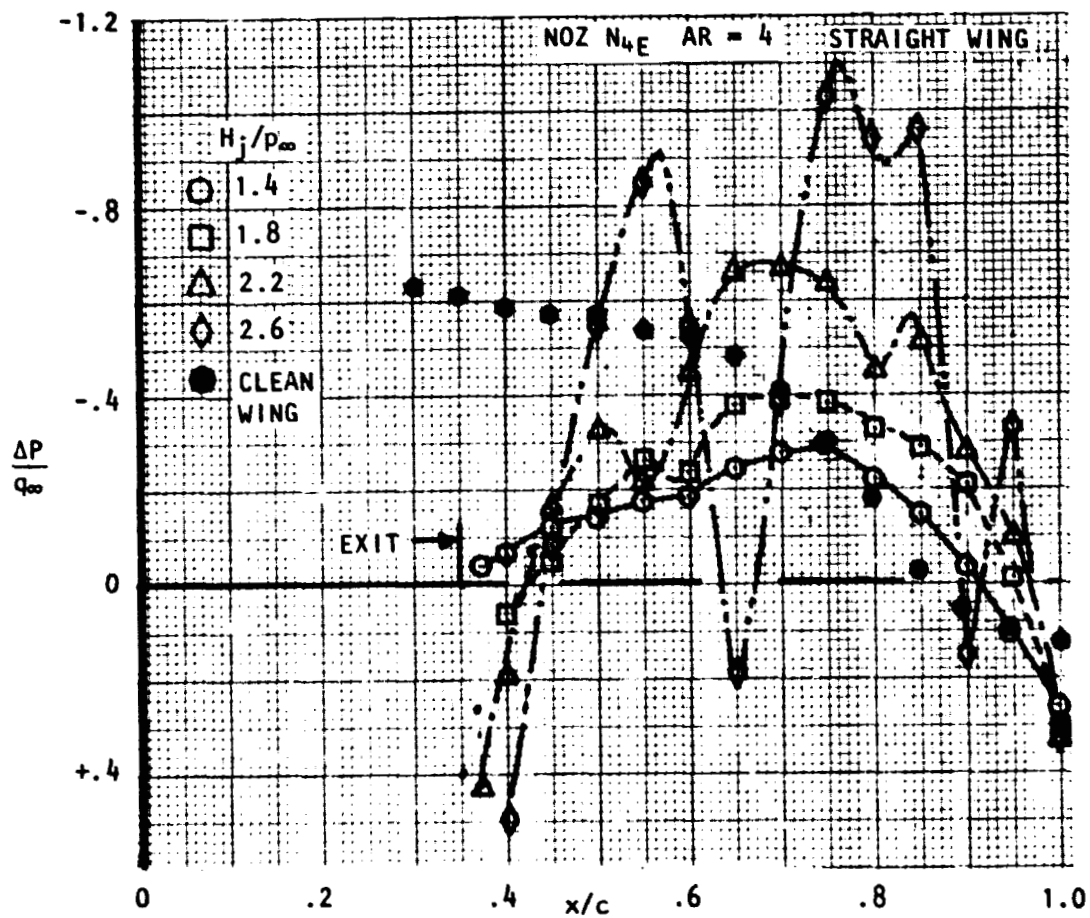


Figure 38 . Effect of nozzle pressure ratio on jet centerline pressures,  $\alpha \approx 3^\circ$ ,  $M_\infty = 0.70$ .

increment with Mach number is seen to match reasonably well with the calculation, again indicating that the jet-induced lift is controlled primarily by jet dynamic pressure. As the three-dimensionality of the jet increases, however, the data show that the anticipated increase in lift with decreasing Mach number is suppressed due to the inability of the thickening jet to remain fully attached to the wing surface as the ratio  $q_j/q_\infty$  grows in magnitude. The circular nozzle ( $N_{2E}$ ) is shown to produce an almost constant lift increment regardless of Mach number.

- o Effects of Pressure Ratio - The effects of nozzle pressure ratio are shown in Figure 38 for  $M_\infty = .68$ ,  $\alpha = 2^\circ$ . The nozzle ( $N_{4E}$ ) is an aspect ratio 4 configuration mounted on the straight wing; the clean wing pressure distribution is also shown. With this type of configuration, the major effect of pressure ratio is a gradual reduction in centerline static pressure as the nozzle pressure ratio increases. Near the nozzle exit ( $x/c = .35$ ), a high-pressure region which grows with pressure ratio is also evident. This latter region arises as a result of the relatively high boattail angle of the nozzle ( $36^\circ$ ) and, in effect, tends to suppress the lift increment carried by the scrubbed area. It would be expected from such distributions that, at the flow-through condition, the lift increment due to the jet would be less than that sustained by the clean wing over the same area and, as the pressure ratio is advanced, such losses would tend to be recovered. It would also be anticipated that the exit high-pressure region would have only negligible effects on the pressure drag, since the test wing has little curvature between  $x/c = 0.35$  and  $x/c = .65$ . Downstream of  $x/c = 0.65$ , the aft-facing thickness of the

wing grows rapidly and it is in this region that the effects of pressure ratio on centerline pressures become pronounced.

The data of Figure 38 have been replotted in Figure 39 with the pressure coefficient normalized on  $q_j$  rather than  $q_\infty$ . As noted earlier in the discussion of Mach effects, the centerline pressures tend toward a common level aft of  $x/c \approx 0.70$ , again illustrating the predominant influence of the jet dynamic pressure as the nozzle pressure ratio is varied.

To evaluate the relative magnitudes of the lift and drag increments generated within the scrubbed area, pressure distributions for a series of nozzles have been integrated over a range of nozzle pressure ratios. Typical results are provided in Figures 40 through Figure 44 as the variation of the integrated force increment with nozzle pressure ratio at a specified cruise Mach number. Figure 40 shows the pressure drag generated by several wide (aspect ratios 4 and 6) nozzles within the jet scrubbed area. Also shown are the clean wing increments (integrated over the same area) as well as a predicted trend based on equations (12) or (13). As noted, the experimentally-derived trends confirm those predicted indicating the pressure-drag equivalent of fully-attached jets closely following the wing contour and turning through an angle approaching that of the wing trailing-edge, ( $17^\circ$ ). The increase in pressure drag over that obtained by a simple superposition of the statically-derived turning angle to the wing alone can be evaluated by adding the expression:

$$\Delta C_{D_j} = \eta_{T_s} \Delta C_T [1 - \cos(\alpha + \delta_{j_s})] \quad (15)$$



# USB CRUISE PROGRAM

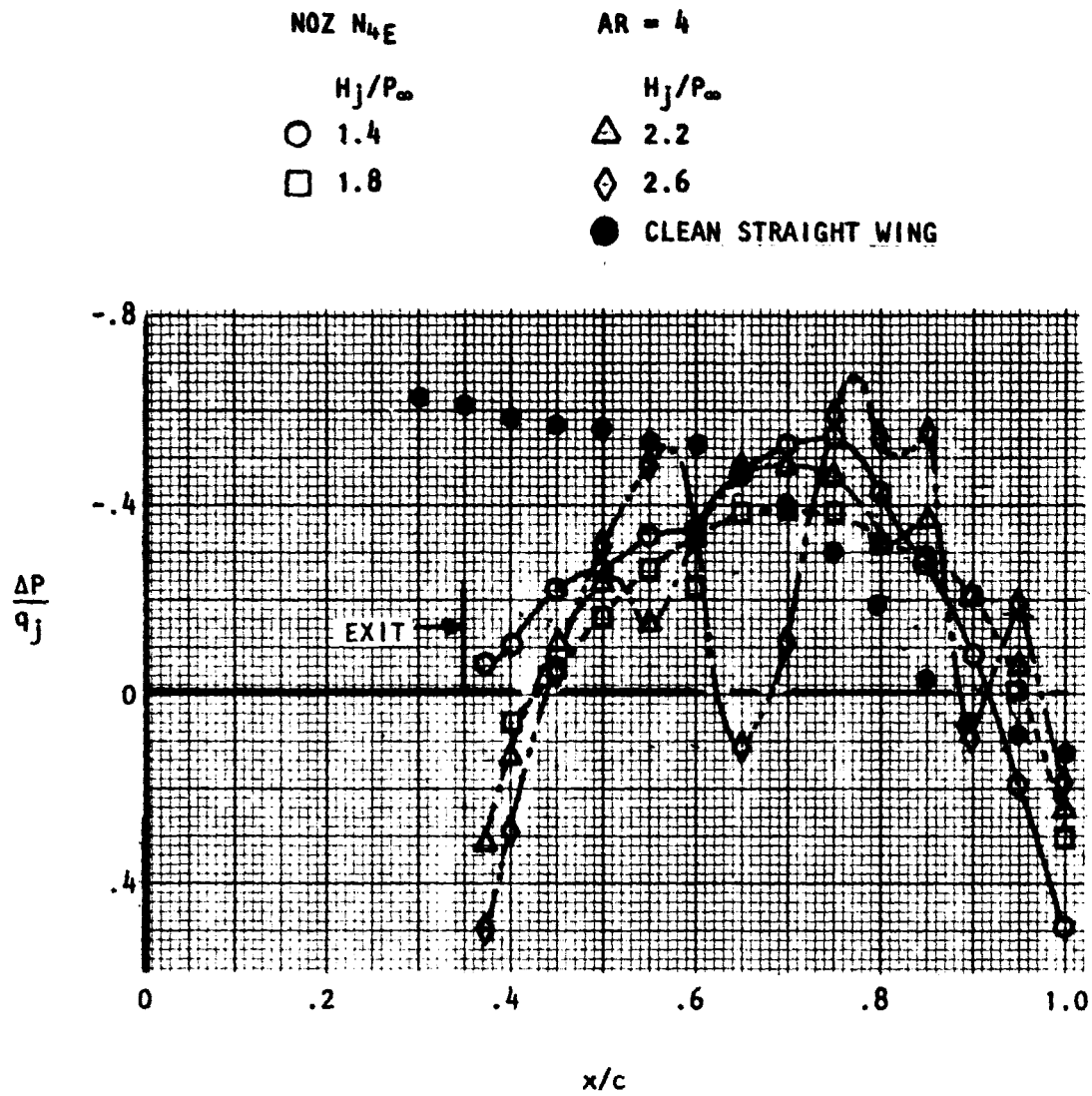


Figure 39 . Effect of nozzle pressure ratio on jet centerline pressures,  $\alpha \approx 3^\circ$ ,  $M_\infty = 0.68$ .

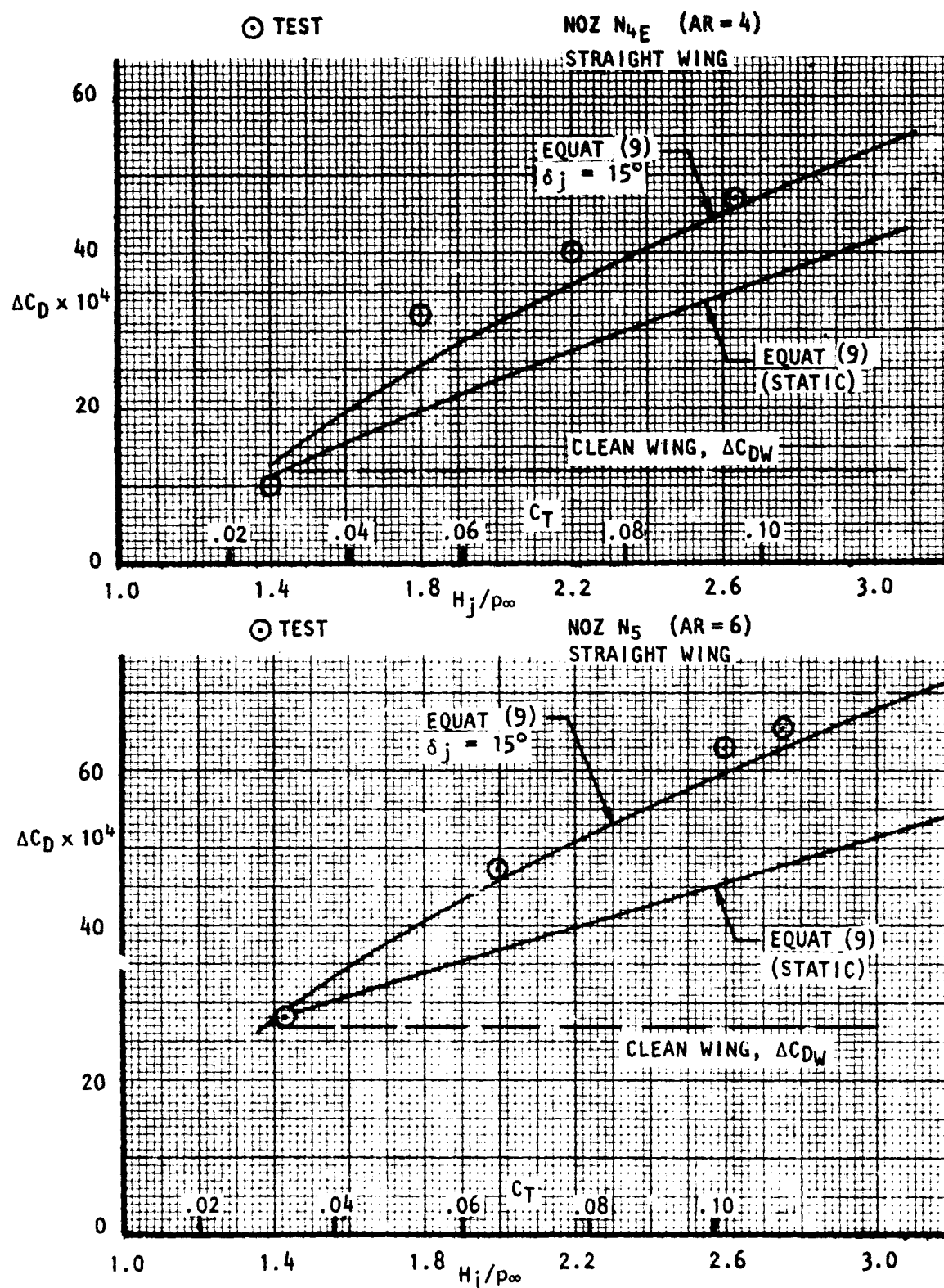


Figure 40 . Variation of scrubbed area pressure drag with pressure ratio,  $\alpha \approx 2^\circ$ ,  $M_\infty = 0.68$ .

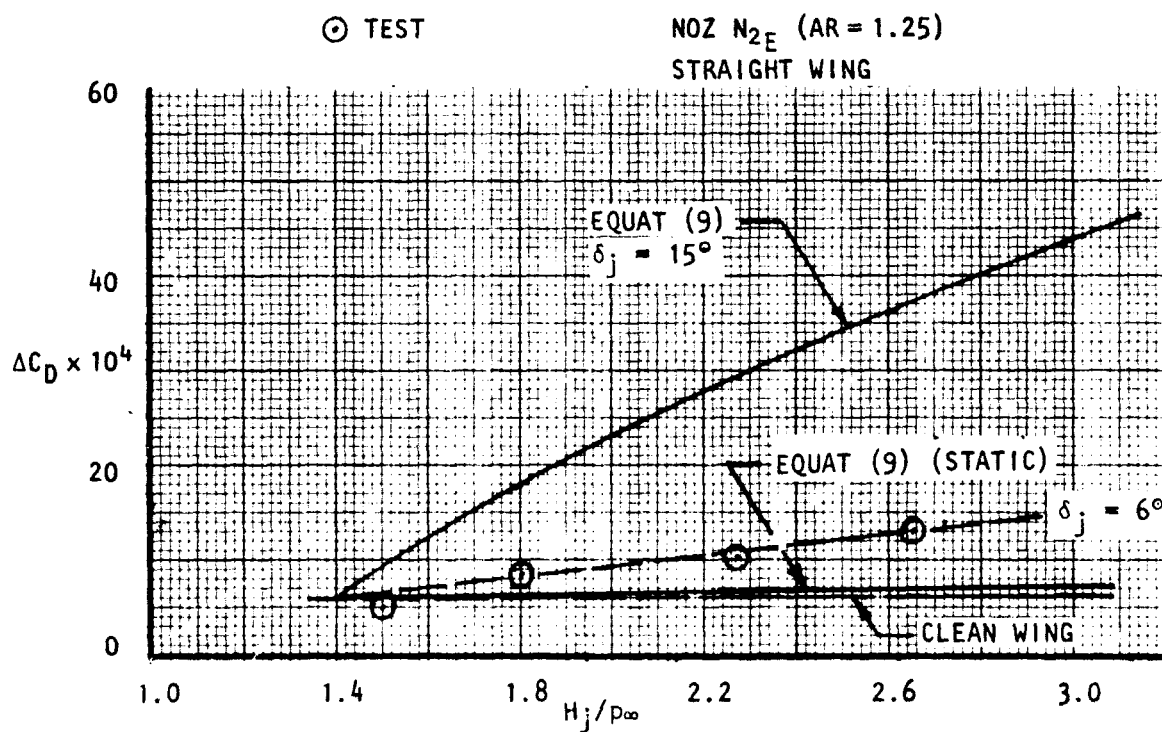
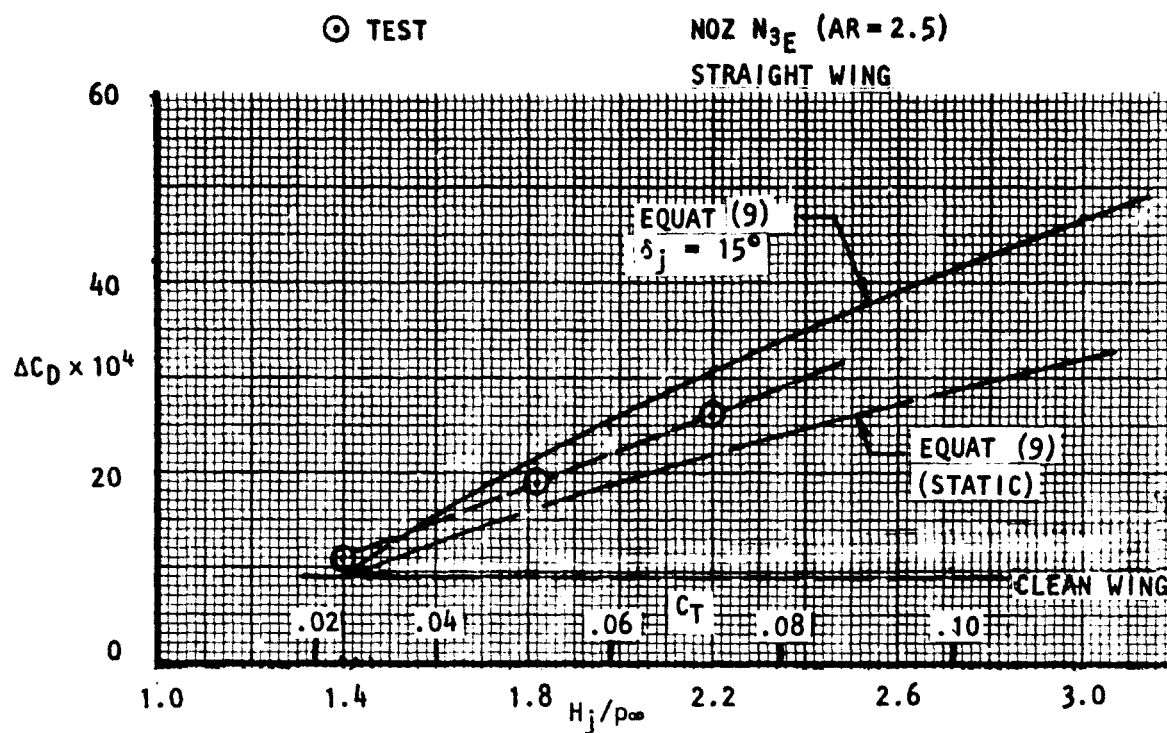


Figure 41 Variation of scrubbed area pressure drag with pressure ratio,  $\alpha \approx 2^\circ$ ,  $M_\infty = 0.68$ .

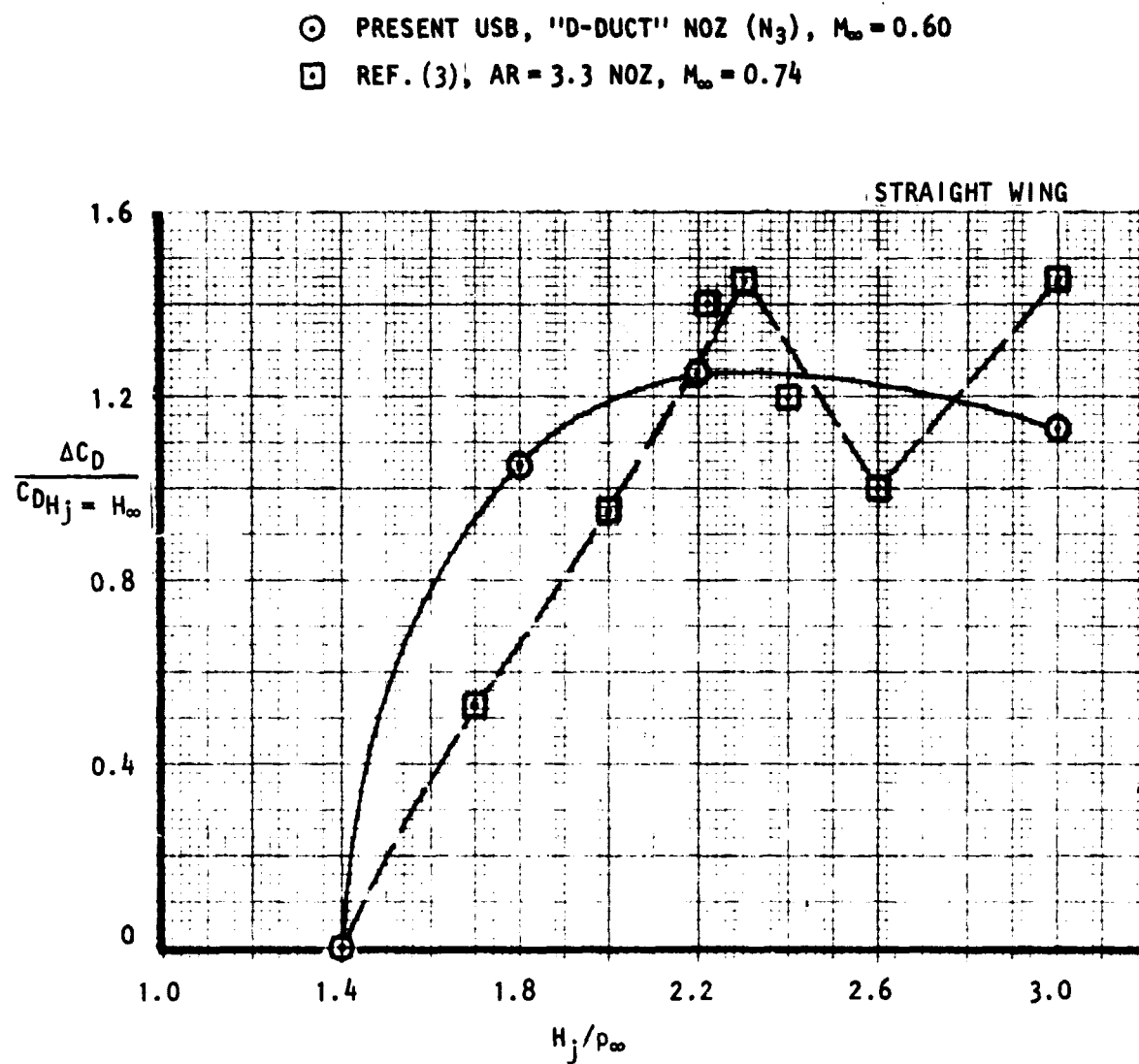


Figure 42 . Comparison of pressure drag developed in scrubbed area.

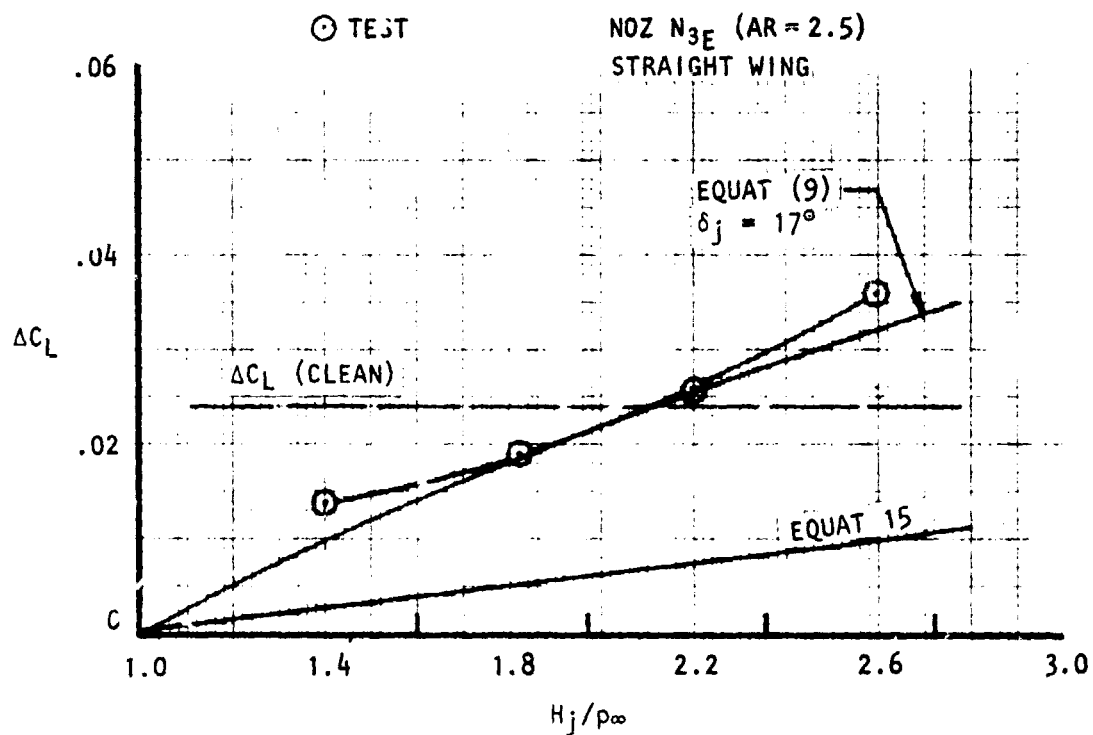
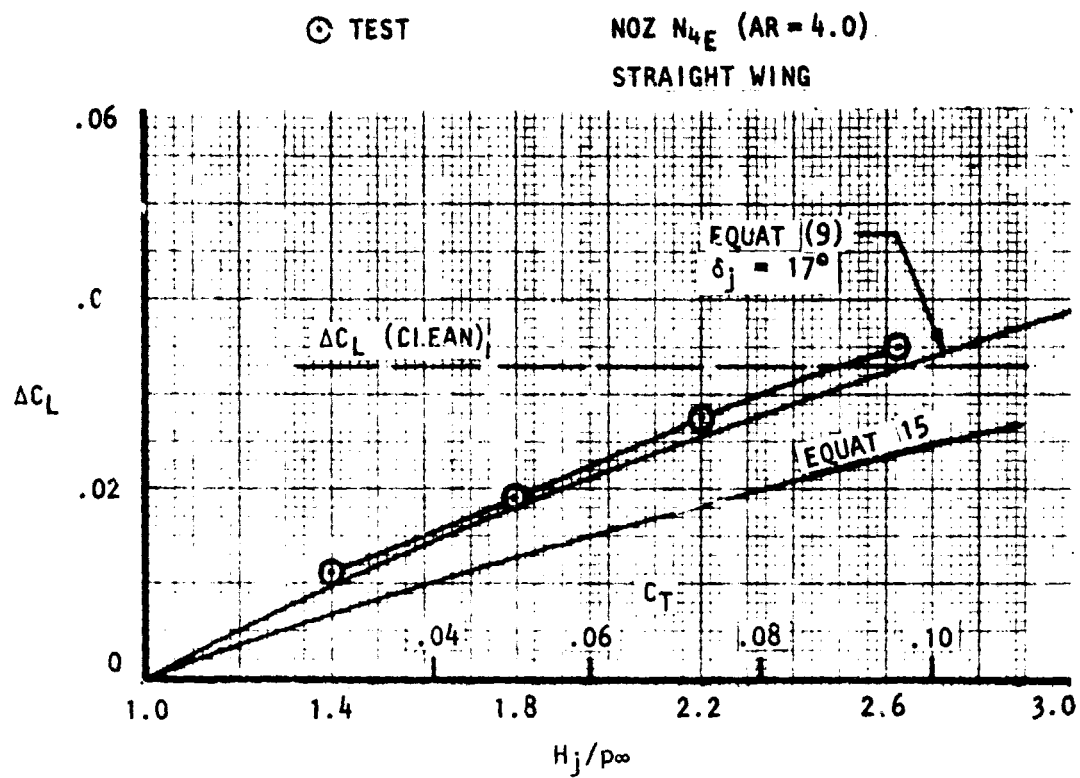


Figure 43 . Lift developed in scrubbed area with blowing, α = 2°, M<sub>∞</sub> = 0.70.

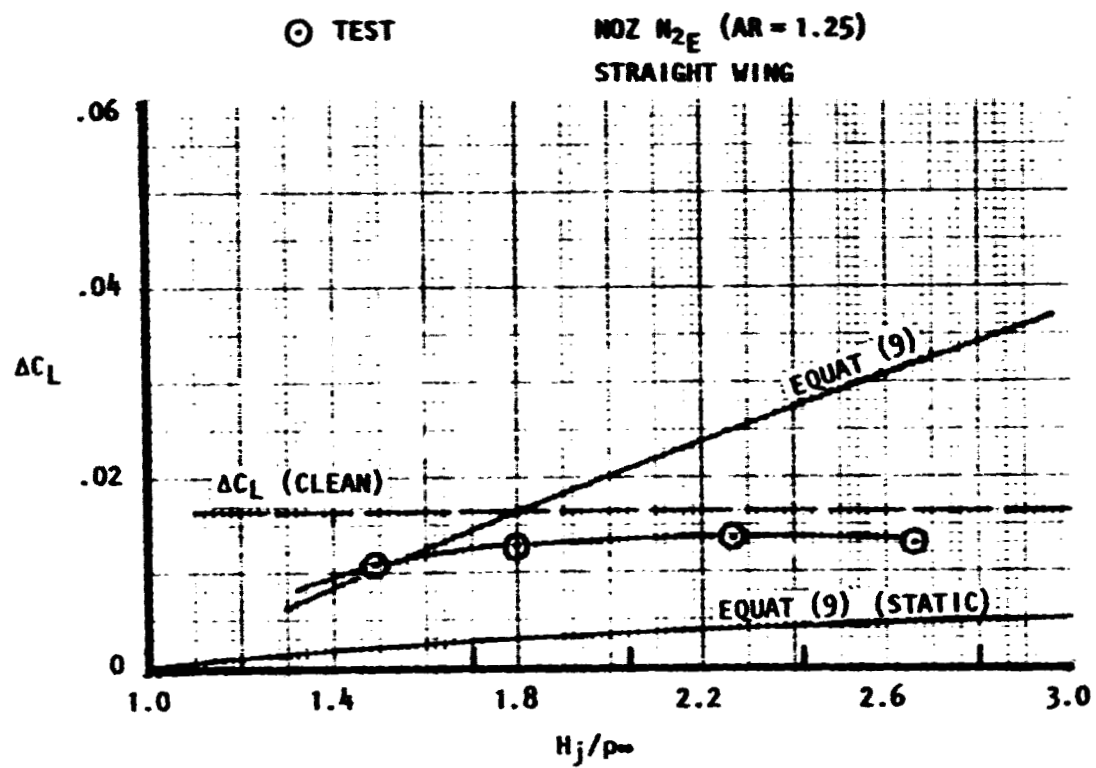


Figure 44 . Lift developed in scrubbed area with blowing,  $\alpha = 2^\circ$ ,  $M_\infty = 0.70$ .

to the clean wing drag increment,  $\Delta C_{DW_j}$ , the  $\eta_{T_s}$  and  $\delta_{j_s}$  parameters reflect the static test values. An evaluation by this procedure is shown in Figure 40. A comparison of the drag coefficient level obtained by simple superposition with those representating the experimental values show the latter to be higher by about  $\Delta C_D = .0010$  to  $.0013$ . In the bookkeeping process, the higher drag would be manifested as an aerodynamic loss over and above the static installation loss.

Additional drag integrations over the scrubbed area, as generated by increasingly three-dimensional nozzle shapes, are shown in Figure 41. These data show that the integrated pressure drag falls below the fully-attached jet level as nozzle aspect ratio is reduced toward the circular shape. Even the circular nozzle, however, shows some increase in pressure drag over that which would be predicted by superposition of static turning loads onto the clean wing. That other investigators have found a similar effect from USB-type configurations is shown in Figure 42. In this figure, integrated pressure drags from the present study are compared to data taken from Reference 3; the reference nozzle has an exit aspect ratio of about 3.3.

When only pressure results, such as these, are considered, a logical question arises concerning the clean wing drag increment shown on Figure 40 or 41. This drag increment in the wing-alone configuration (2-D) is normally offset by a leading-edge suction force such that under pre-drag-rise conditions, the net drag is primarily that due to skin friction. With a three-dimensional closed forebody present to suppress this suction

force over the width of the nozzle, the total drag penalty could well include that shown as representing the clean wing level in addition to the aforementioned increase. Pressure surveys in the tests were insufficient to formulate a definite conclusion in this regard and recourse must be made to the force tests results.

Treating the lift generated in the jet-scrubbed area in the same fashion, integrated lift results are shown in Figures 43 and 44 for nozzle aspect ratios of 4, 2.5 and 1.25 (circular). As concluded earlier, the lift increment within the scrubbed area falls below that of the wing alone at the flow-through pressure ratio. For the two wider nozzle shapes, this initial lift loss is essentially recovered by blowing at a pressure ratio of about 2.0 or higher. The circular jet, on the other hand, never recovers the initial lift loss within the scrubbed area due to the nacelle installation. Relative to the flow-through case, the increase in lift with blowing is seen to be also generally higher than would be predicted by a superposition of statically-derived wing loads to the lift level present on the wing at flow-through conditions.

In the foregoing discussions, it has been observed that the parameter  $q_j/q_\infty$  represents a major influence on pressure distributions as well as jet-induced lift and drag increments. Figures 45 and 46 utilize this ratio as a correlating parameter to collapse the integrated drag increments to a common curve regardless of pressure ratio or Mach number. The calculated trend is shown for reference along with the clean wing pressure drag increment. As indicated, the jet dynamic pressure ratio serves the



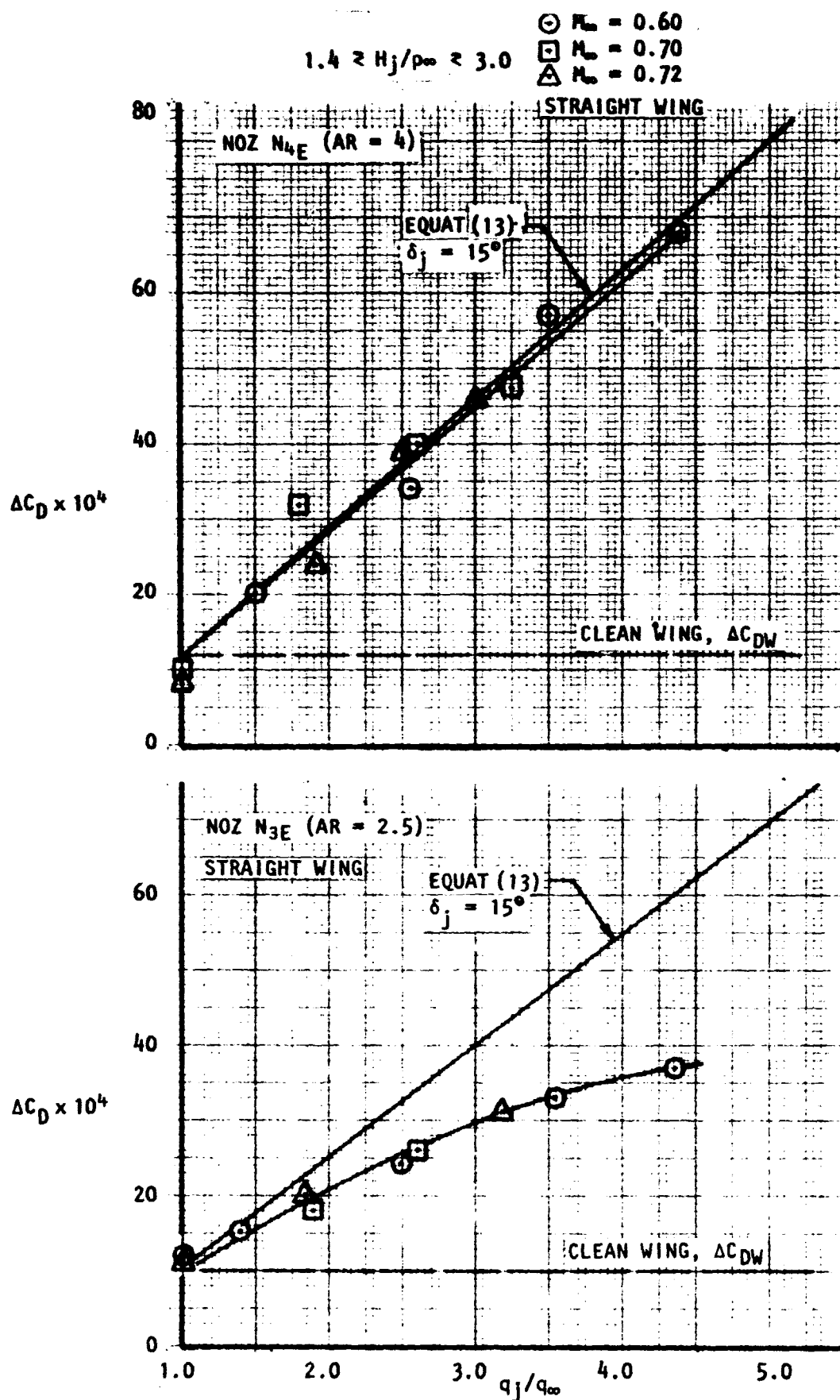


Figure 45 . Variation of pressure drag with Mach No. and pressure ratio,  $\alpha \approx 2^\circ$ .

ORIGINAL PAGE IS  
OF POOR QUALITY

# USB CRUISE PROGRAM

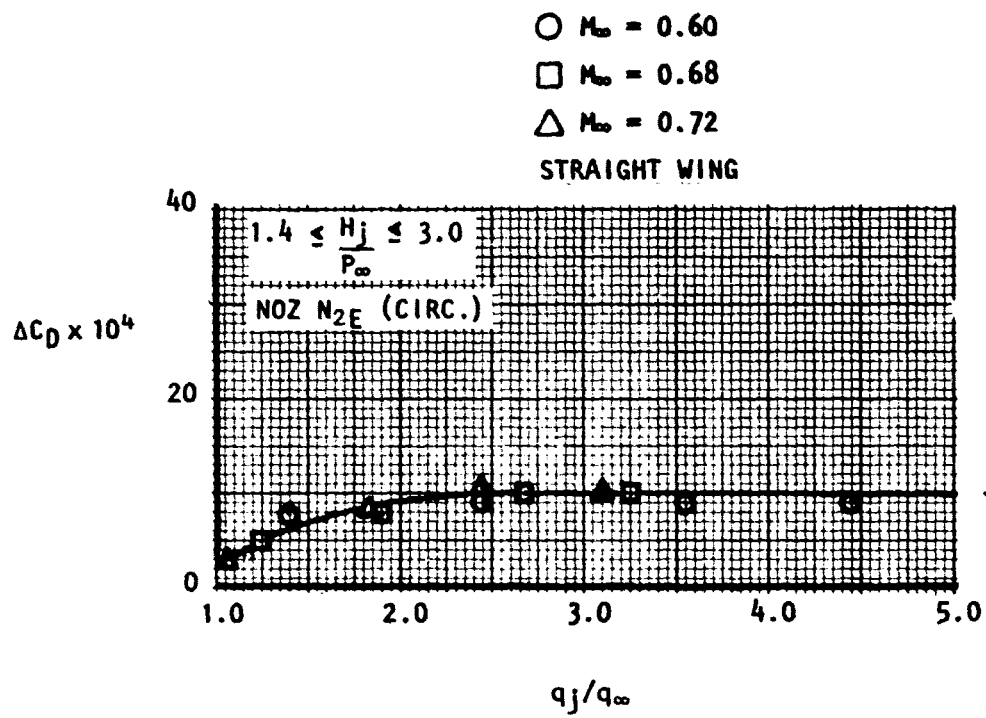


Figure 46 . Variation of pressure drag in scrubbed area with Mach No. and pressure ratio,  $\alpha \approx 2^\circ$ .

intended purpose for the three nozzle shapes. A similar correlation of the integrated lift increments is provided in Figure 47, which again shows the value of  $q_j/q_\infty$  as an effective correlating parameter. In an effort to assess the influence of the aforementioned high pressure near the nozzle exit, a re-integration of the centerline-pressures was performed deleting this region from the integration; the open symbols on Figure 47 represent the results. At a high pressure ratio, the relative loss in lift due to the impingement and re-direction of the high-pressure air at the exit is seen to be appreciable. The data of Figure 47 has been utilized to prepare Figure 48. In this figure, lift increase due to thrust (relative to flow-through) is shown as a function of jet dynamic pressure ratio and a comparison is made with the data provided in Reference 3. The referenced results, reflecting tests of an aspect ratio 3.3 nozzle, compare favorably with the present results from an aspect ratio 2.53 nozzle (D-duct).

The variation of the drag and lift penalty with blowing is portrayed in Figures 49 and 50 respectively, by normalizing the increments to that representing the clean wing. Figure 49 indicates that the excess pressure drag behind an aspect ratio 4 nozzle can be as much as 4 times that present on the clean wing and that the D-duct nozzle can reach a level of about 2.5 times the latter. Although marginally attached, the circular jet can generate an excess pressure drag about equal in magnitude to that of the same area on the clean wing. A similar presentation for the lift increments is shown in Figure 50. A larger, initial lift loss is sustained at flow-through conditions by a wide nozzle ( $AR = 4$ ), but this loss is

SYMB.-TEST  $0.6 \leq M_\infty \leq 0.72$   
 $1.4 \leq H_j/p_\infty \leq 3.0$   
 STRAIGHT WING

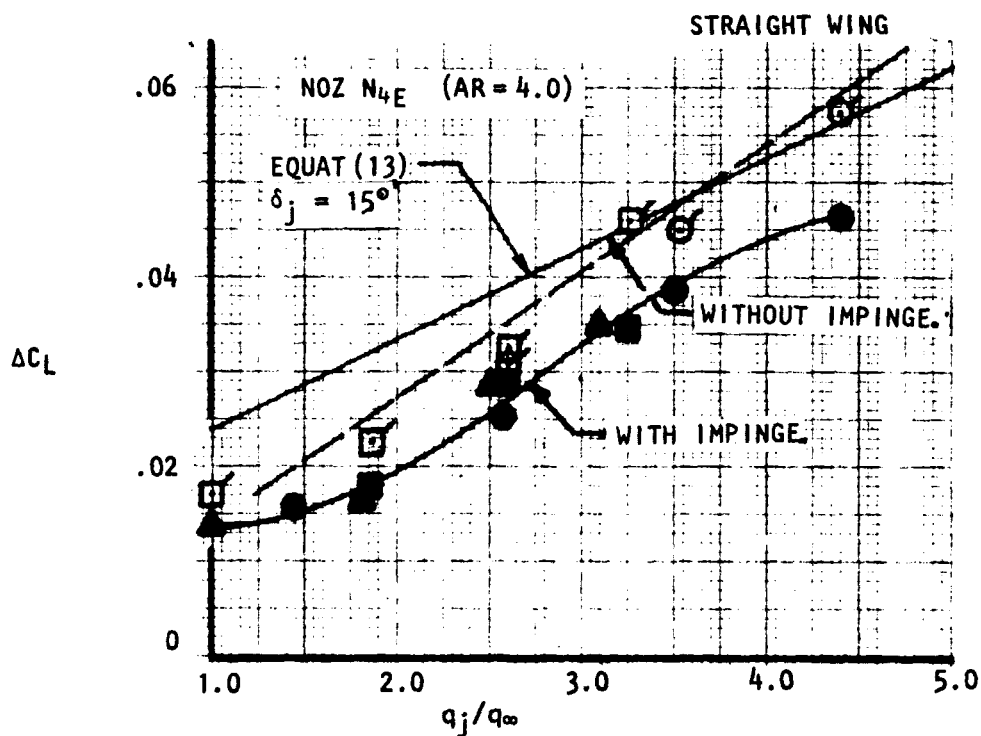
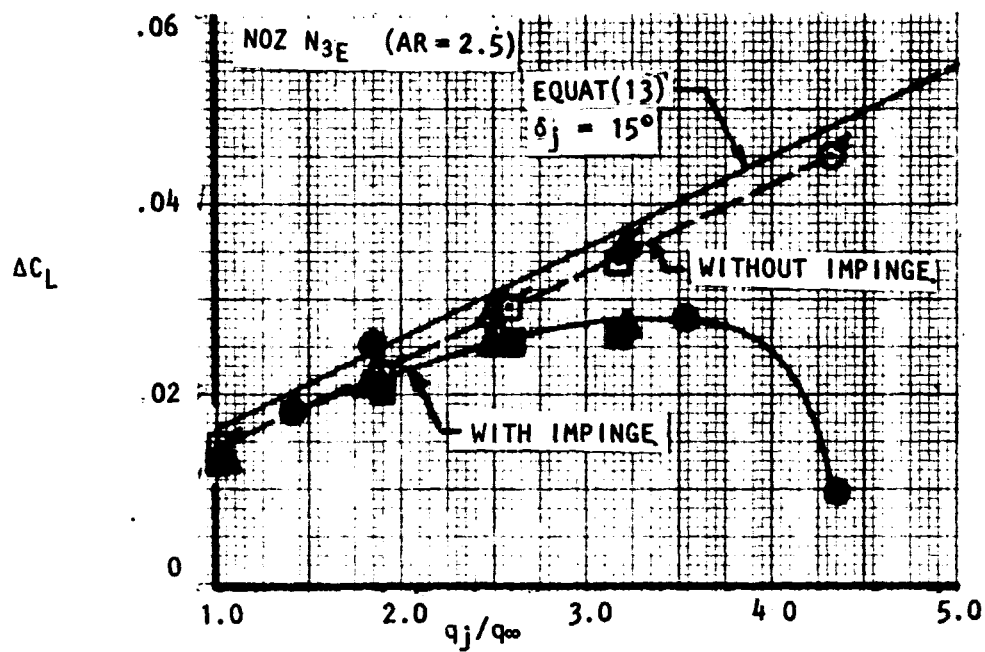


Figure 47 . Variation of lift increment developed in scrubbed area with Mach No. and pressure ratio,  $\alpha = 2^\circ$ .

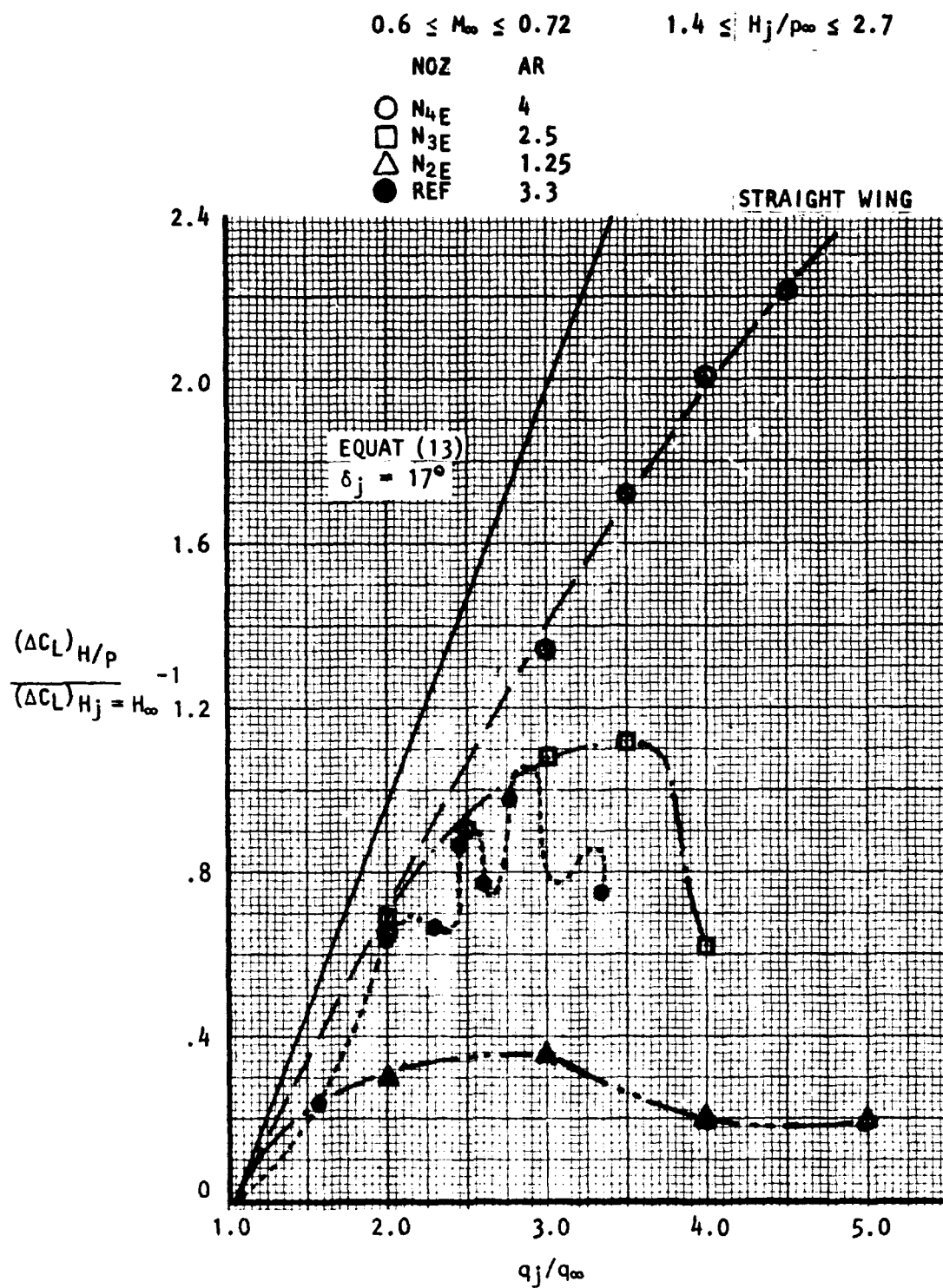


Figure 48 . Lift increase in scrubbed area due to blowing,  $\alpha \approx 2^\circ$ - $3^\circ$ .

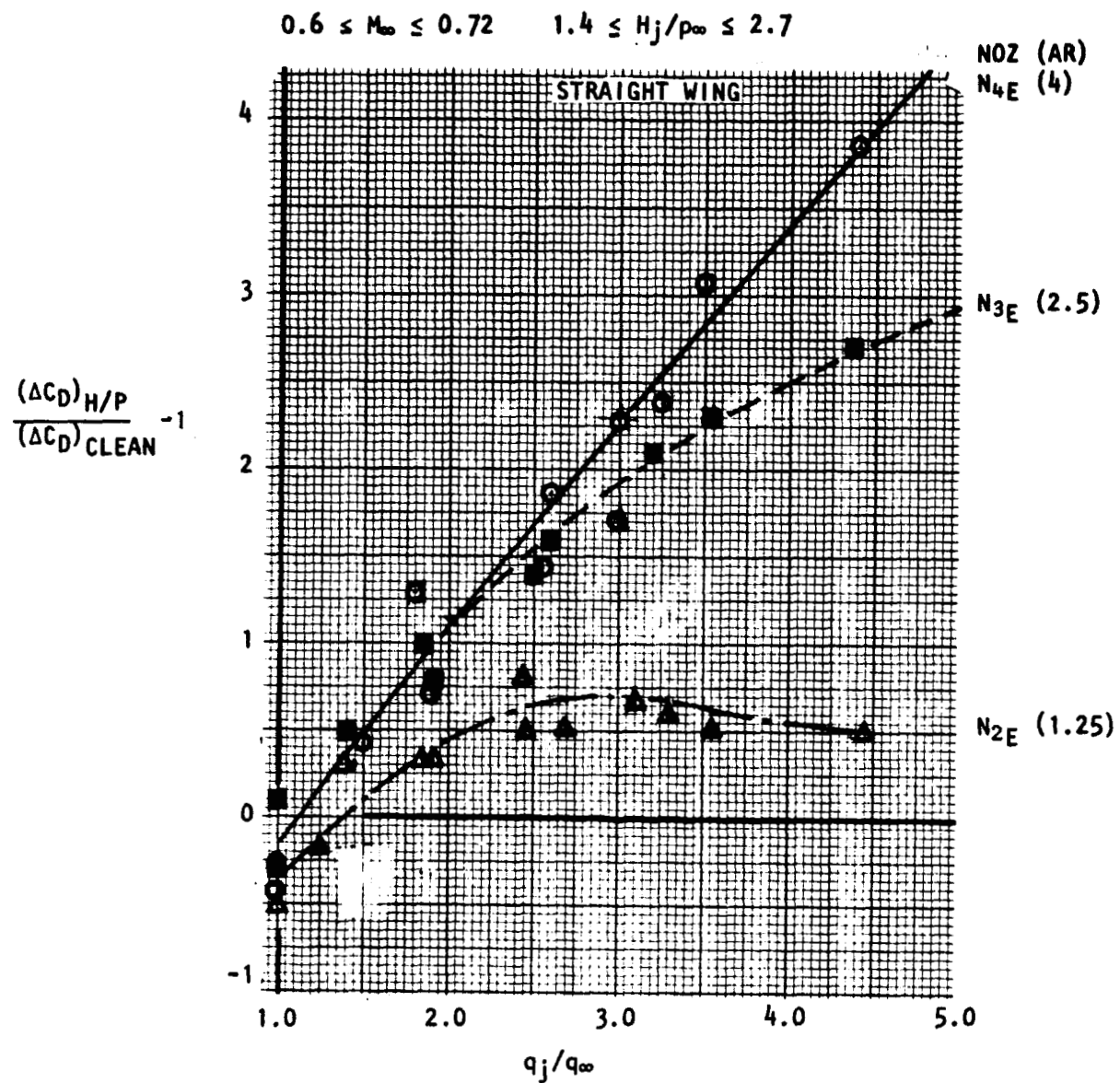


Figure 49 . Variation of excess pressure drag due to nacelle installation and blowing within scrubbed area,  $\alpha = 2^\circ$ .

# USB CRUISE PROGRAM

$$0.6 \leq M_\infty \leq 0.72 \quad 1.4 \leq H_j/p_\infty \leq 2.7$$

NOZ	AR
○ N <sub>4</sub> E	4
□ N <sub>3</sub> E	2.5
△ N <sub>2</sub> E	1.25

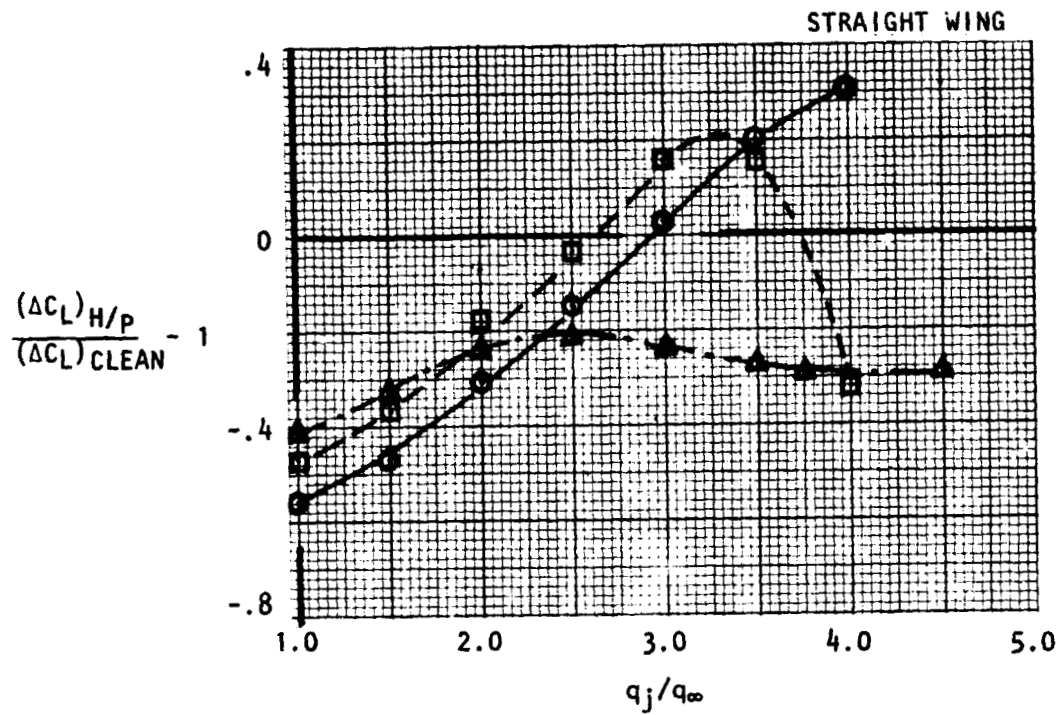


Figure 50 . Variation of incremental lift due to nacelle installation and blowing within the scrubbed area,  $\alpha = 2^\circ$ .

more than recovered with a small excess lift benefit indicated at high blowing rates. The "D-duct" nozzle shows some instability at high blowing rates and may, depending upon pressure ratio, recover the initial lift loss or essentially separate from the wing surface, as in the case of the circular nozzle.

It is of some interest to note that jet-induced pressure drags similar to those of the USB-configuration have been observed in tests of jet flaps. Reference 4 refers to this pressure drag component as "jet-drag", where the source of the drag is an induced effect due to flow entrainment near the wing trailing-edge. The data shown in Figure 51 have been excerpted from the referenced document and compared to USB-data taken from Figure 40 (aspect ratio 4 nozzle). The referenced material represents several tests of a jet-flap force model with some scatter in the measured results; this is shown as a band in Figure 51. As indicated, the USB results, representing a more three-dimensional nozzle shape relative to the 2-D jet-flap, produce a pressure drag increase with  $C_T$  very similar to that observed in the jet-flap study.

- o Effects of Nozzle Shape (Aspect Ratio) — The variation of jet centerline pressures are shown in Figure 52 for three different nozzle shapes at  $H_j/p_\infty = 1.4$ . The relatively low pressure ratio (approximately flow-through) is employed to minimize the extraneous effects of the shock structure on the distributions. As noted, the pressures immediately aft of the airfoil crest ( $x/c \approx 0.45$ ) vary essentially with nozzle height except in the case of the circular nozzle which characterizes a marginal or unattached jet.



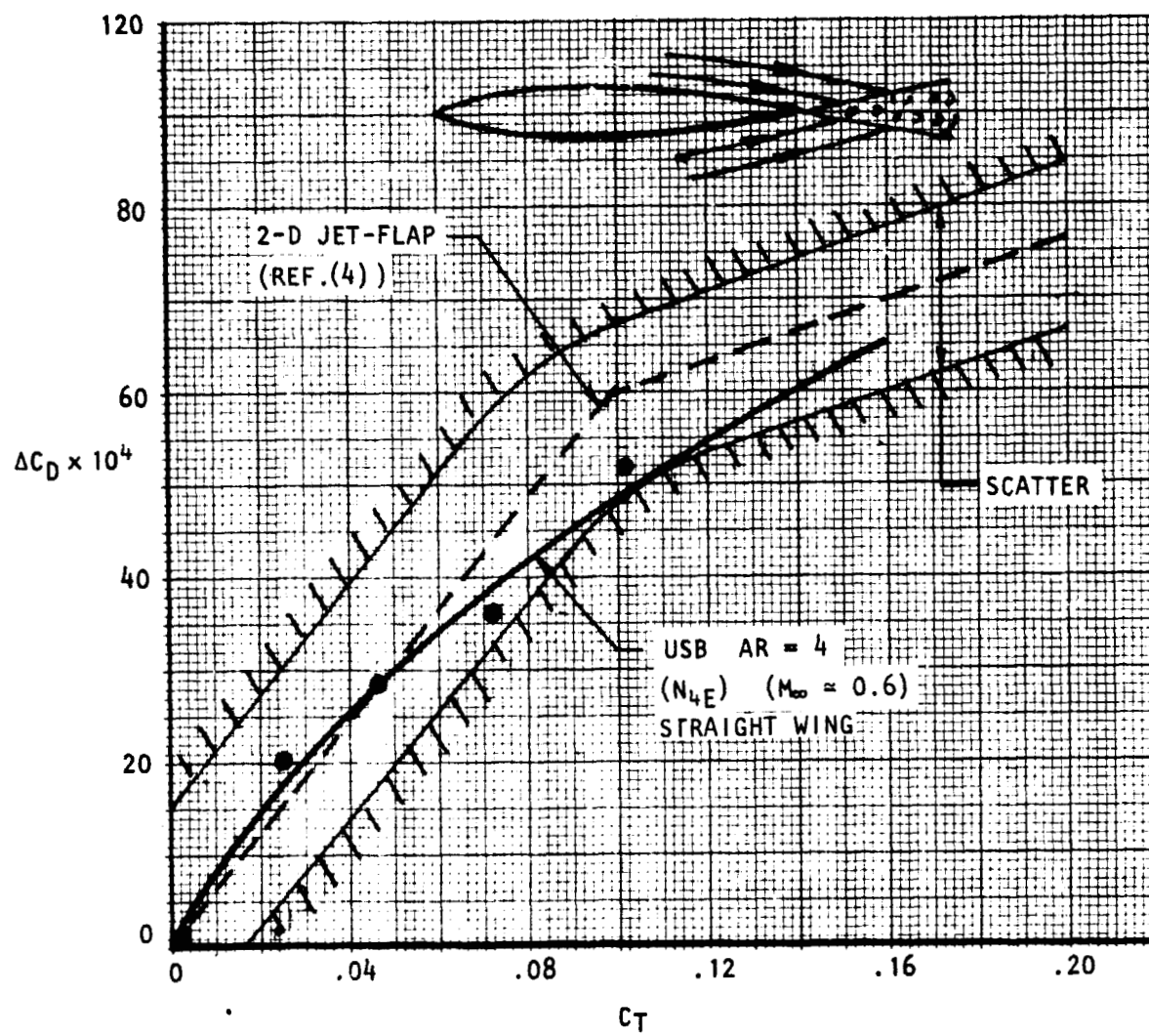


Figure 51 . Comparison of USB and jet-flap pressure drag.

NOZ	AR	$\frac{c^2}{AN} = 24$
○ N <sub>2</sub> E	1.25	
□ N <sub>3</sub> E	2.5	
△ N <sub>4</sub> E	4	
●	CLEAN STRAIGHT WING	

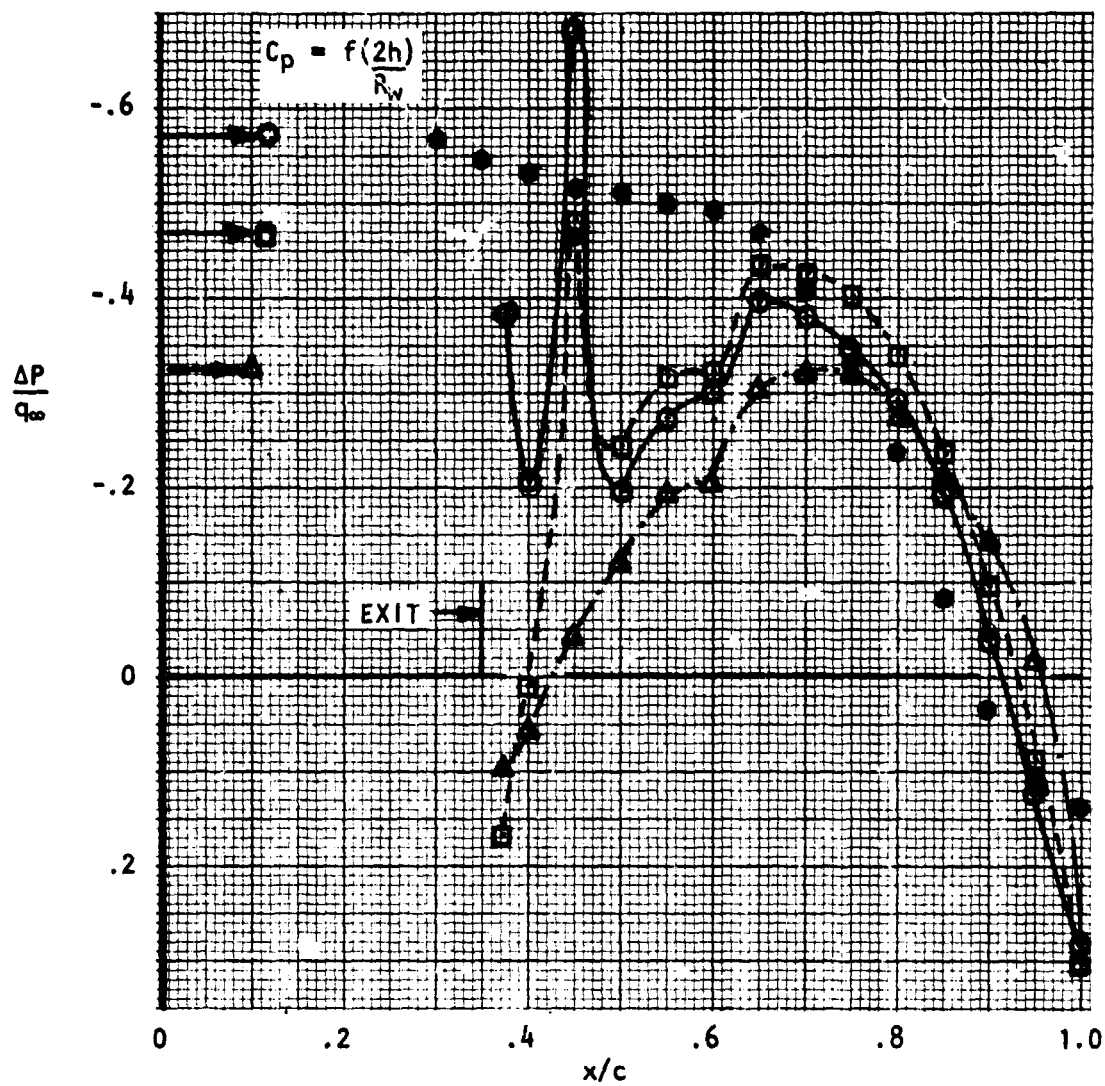


Figure 52 . Effect of nozzle exit shape on jet centerline pressures,  $\alpha \approx 2^\circ$ ,  $M_\infty = 0.60$ ,  $H_j/p_\infty = 1.4$ .

Predicted incremental pressure levels based on:

$$C_{p_j} = \frac{-2h}{R} \left[ q_j / q_\infty \right] \quad (16)$$

are shown to correctly evaluate the change in pressure coefficient for the two wider nozzles while the poorly attached circular jet does not attain the predicted level.

The data presented in the earlier discussions have been utilized to prepare Figures 53 and 54 for illustrating typical drag and lift variations in the jet scrubbing area with nozzle aspect ratio. Figure 53 considers the pressure drag variation at a nozzle pressure ratio of 2.6 at  $M_\infty = 0.68$ .

The trends show that the circular nozzle efflux represents an unattached jet with the pressure drag increment close to that which would be predicted from static test observations. As the aspect ratio increases, the jet becomes marginally attached, which, combined with a greater nozzle width, produces a higher pressure drag. At an aspect ratio of about 4 and higher, the pressure drag increments correspond to that of a fully-attached jet turning through essentially the full angle range of the aft wing surface. As before, the wind-on pressure drag exceeds that which would be predicted by a simple superposition of the static pressure load onto the clean wing pressure level.

A similar presentation for incremental lift coefficients developed in the scrubbed area by the jet operating at  $H_j/p_\infty \approx 2.6$  is shown in Figure 54. Also shown are the clean wing lift increments over the appropriate

# USB CRUISE PROGRAM

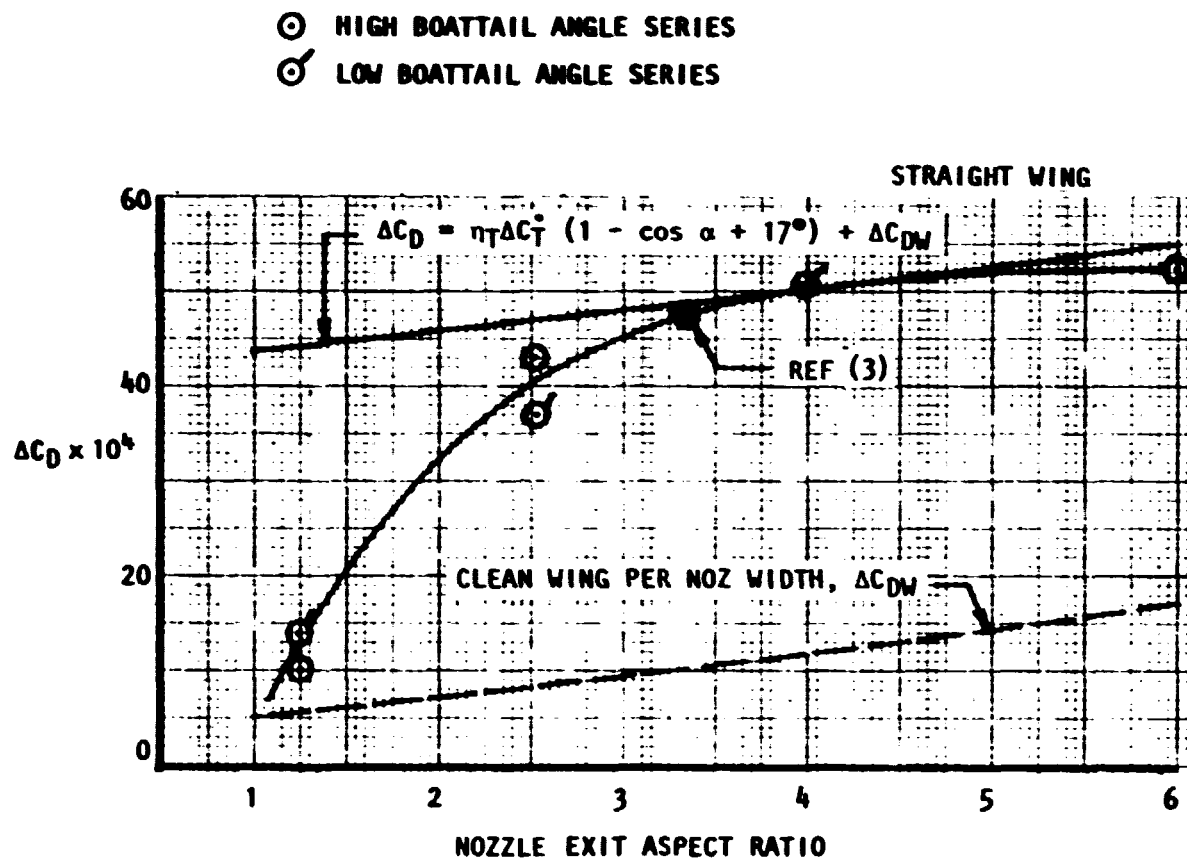


Figure 53 . Effect of nozzle exit aspect ratio on pressure drag,  $\alpha = 3^\circ$ ,  $M_\infty = 0.68$ ,  $H_j/p_\infty = 2.6$ .

# USB CRUISE PROGRAM

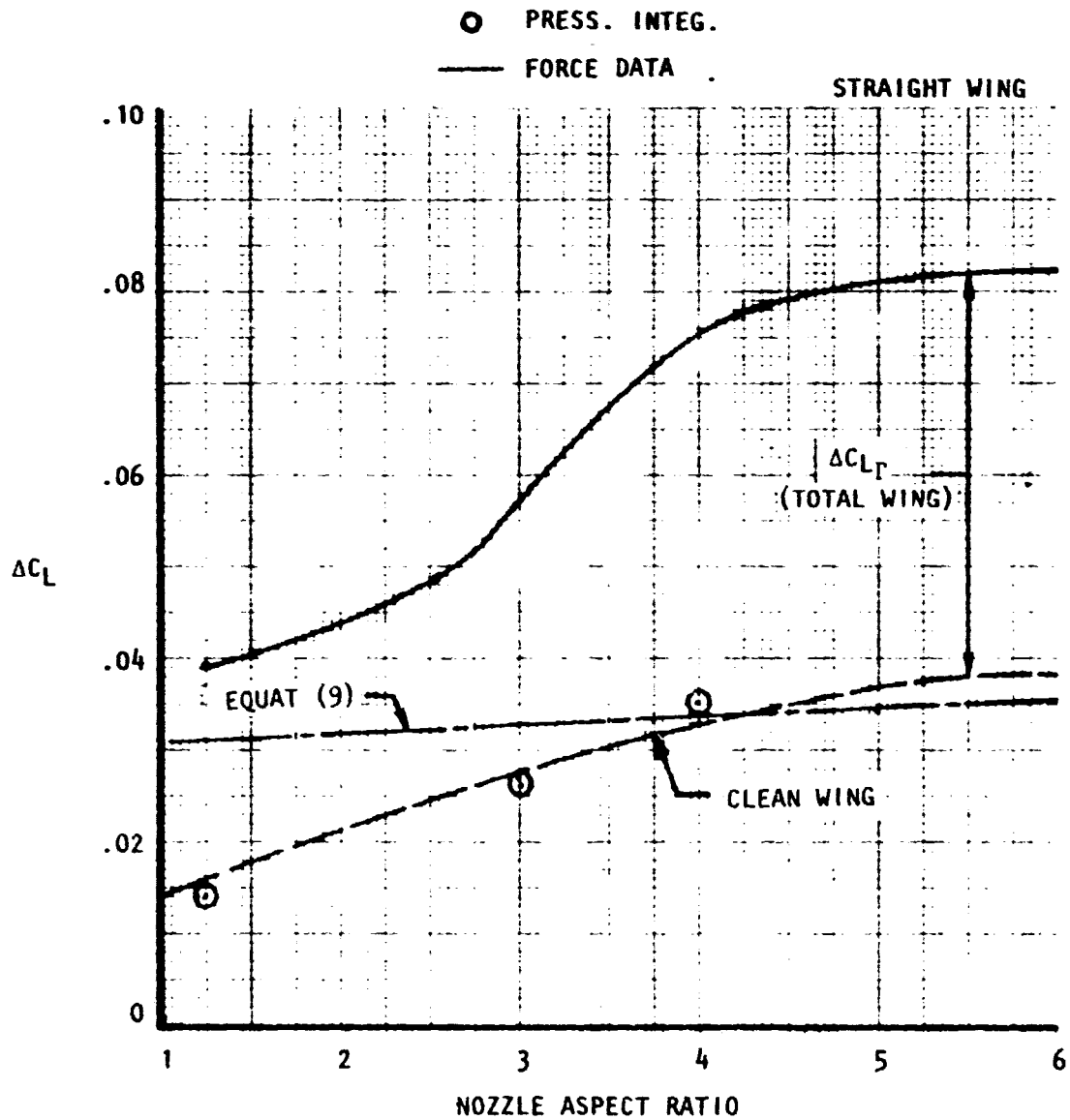


Figure 54 . Effect of nozzle aspect ratio on lift developed in scrubbed area,  $M_\infty = 0.68$ ,  $\alpha = 2^\circ$ ,  $H_j/p_\infty = 2.6$ .

nozzle widths and the lift increment as calculated by:

$$\Delta C_{L_j} = \eta_T C_T \sin (\alpha + 17^\circ) \quad (17)$$

This latter increment is almost a constant at a specified pressure ratio except for slight variations in  $\eta_T$  and  $C_T$ . At the pressure ratio selected, the integrated pressure indicates that between the nozzle exit and wing trailing-edge, the lift increments essentially correspond to a level very little different that developed by the clean wing over the same footprint area, at least in the lower nozzle aspect ratio range. Data obtained from Reference 4, shown on the figure, corroborates this trend. Force data, discussed later, will show that the total lift developed by the entire wing with blowing jet installed is greater than that of the clean wing (at the same  $\alpha$ ) by about  $\Delta C_L = .04 - .05$  (typically). Shown on Figure 54 is an incremental circulation lift calculated from force data by;

$$\Delta C_{L_T} = C_{L_M} \frac{H_j}{p_\infty} - \eta_T C_T \sin (\alpha + \delta_j) - C_{L_M \text{ CLEAN}} \quad (18)$$

where,  $\delta_j \approx 15^\circ$  is used in the calculations. This increment represents the circulation lift increase due to installing the nacelle and blowing at  $H_j/p_\infty = 2.6$ . Since the pressure test results suggest that very little of this lift benefit is carried by the area scrubbed by the jet itself, then  $\Delta C_{L_T}$  must represent lift induced on adjacent sections of the wing, the lower surface of the wing or the nacelle forebody. For the most part,

the spanwise influence of the jet on adjacent wing sections, as discussed later, appears to be the major mechanism accounting for this difference.

- o Effect of Nozzle Size — In the discussions of the pressure model results at static conditions, it was noted that peak negative pressures generated along the jet centerline varied roughly in proportion to jet height. It was likewise shown in Figure 52 that for wind-on conditions, centerline pressures varied similarly when nozzle size (and  $C_T$ ) was specified and jet height changed with nozzle exit aspect ratio. The variation of centerline pressures when nozzle shape is specified and jet height is allowed to vary with nozzle size is considered in Figure 55(a). For these data, three "D-duct"-shaped nozzles are represented with exit areas varying from  $c^2/A_N = 48$ , ( $N_6$ ) to  $c^2/A_N = 12$  ( $N_1$ ). A low, constant nozzle pressure ratio ( $H_j/p_\infty = 1.4$ ) is used for the comparison to suppress the rapid fluctuations in the distributions due to shock formations. As noted, the three nozzles, although varying significantly in jet (or nozzle) height, show about the same level of centerline pressures as the clean wing over the aft-portion of the airfoil; little or no variation with nozzle height is indicated. This implies that the centerline surface flows are turning through similar angles for the three nozzles. As provided in Figure 55(b) wherein similar data are plotted for  $H_j/p_\infty = 3.0$ , centerline pressures for the large jet ( $N_1$ ) indicate a separated jet aft of  $x/c = 0.65$ . While all three jet sizes show indications of separation or marginal attachment at this pressure ratio, the smaller, ( $N_6$ ), generates more negative pressures as, would generally be expected. As will be discussed later in terms of force measurements, pressure drag due to

USB CRUISE PROGRAM

"D-DUCT" NOZ

- $N_1 \quad c^2/A_N = 12$
- $N_3 \quad c^2/A_N = 24$
- △  $N_6 \quad c^2/A_N = 48$
- CLEAN STRAIGHT WING

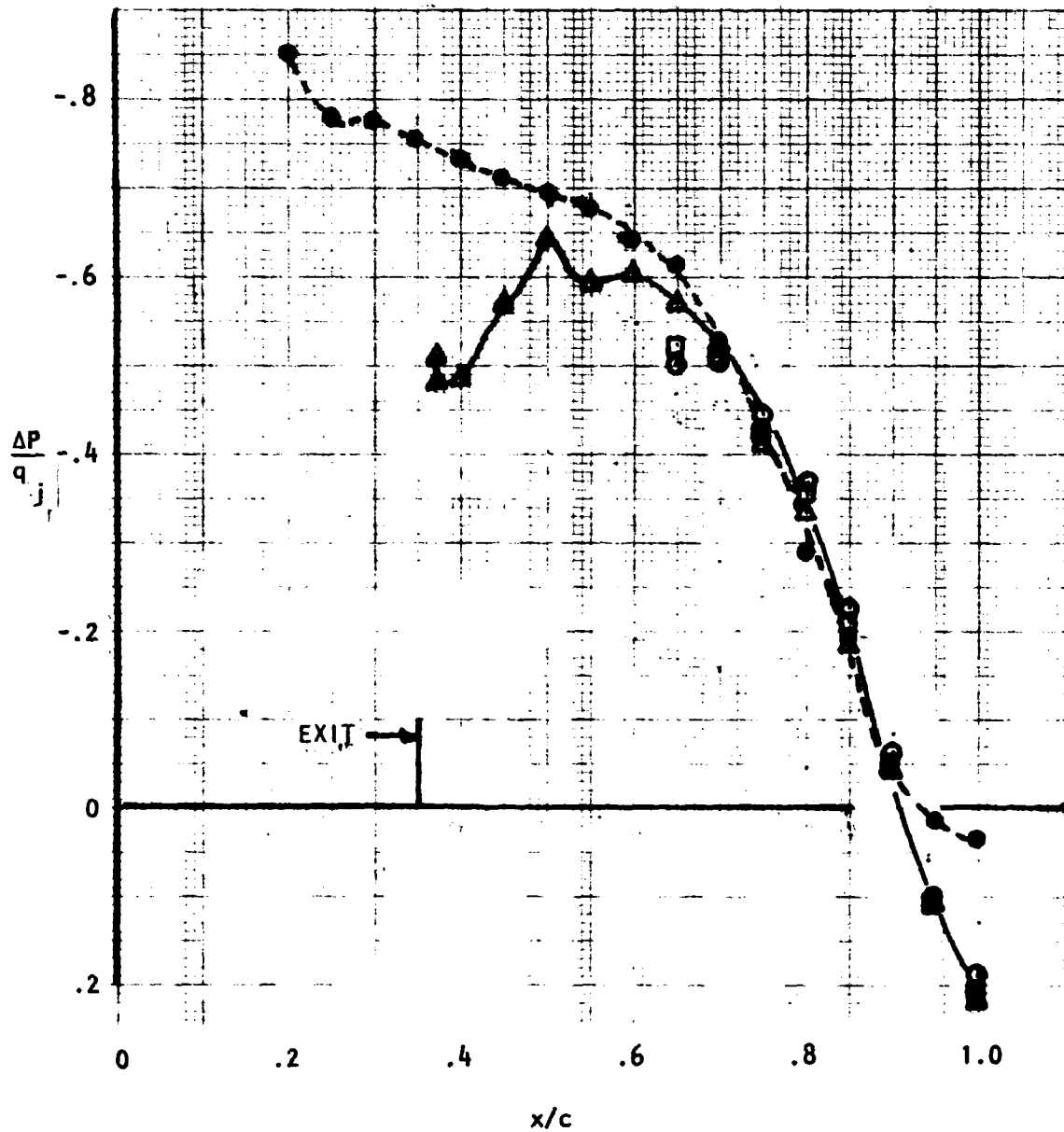


Figure 55(a). Effect of nozzle size on jet centerline pressures  
 $M_\infty = 0.68$ ,  $\alpha = 2^\circ$ ,  $H_j/p_\infty = 1.4$ .



# USB CRUISE PROGRAM

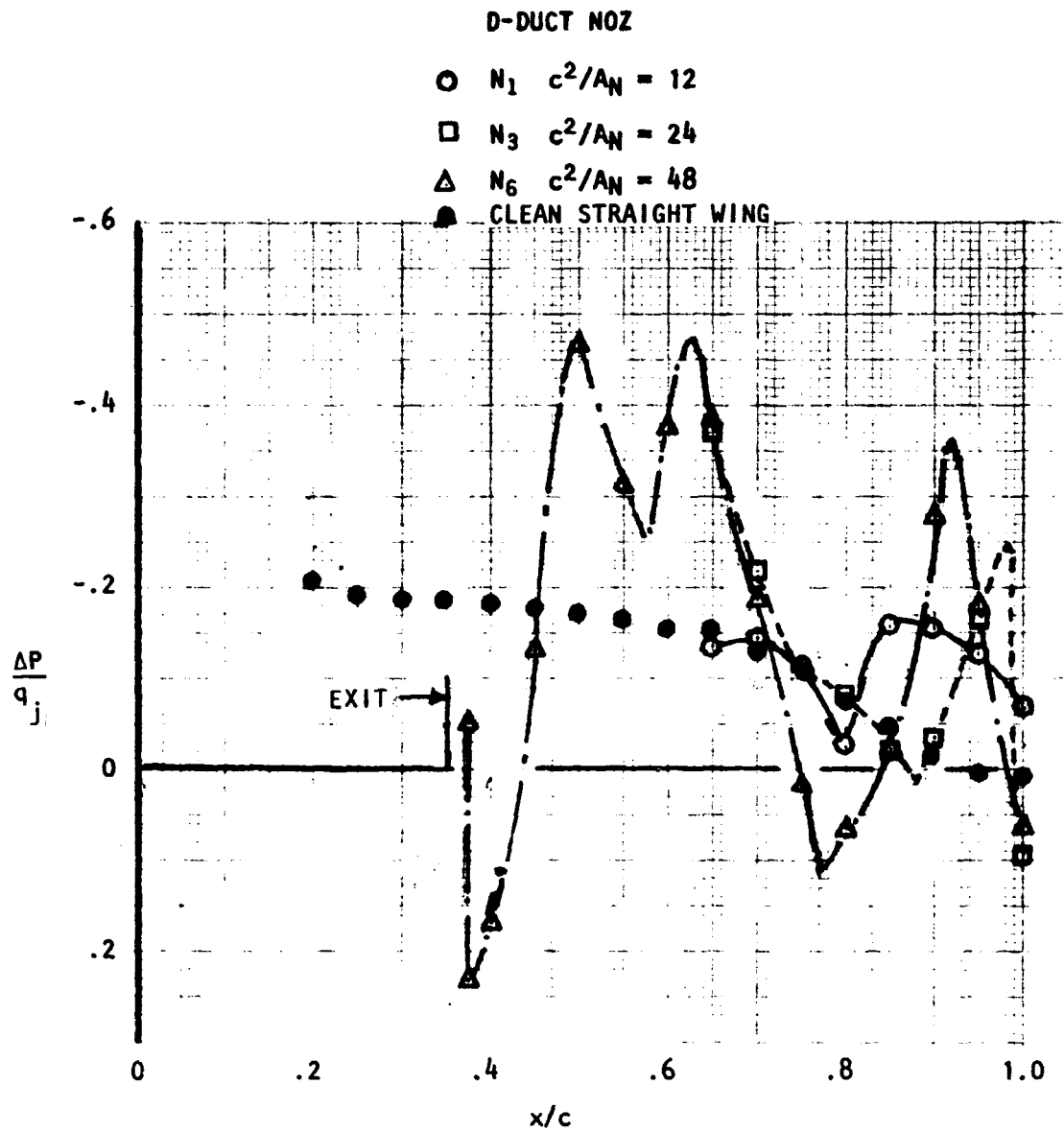


Figure 55(b). Concluded.  $H_j/p_\infty \approx 3.0$ .

blowing tends to be reduced at pressure ratios of this magnitude. As shown in Figure 55(b), it would be improbable that even the smallest jet is well attached aft of  $x/c = 0.80$  due to the presence of the strong compression wave existing at that point.

- o Spanwise Effect of Nacelle Installation — In a spanwise direction the major effects of the jet appear to be localized to the immediate vicinity of the nozzle. Figure 56 compares chordwise pressure distributions at several spanwise stations close to a "D-duct" nacelle,  $N_3$ , at  $M_\infty = 0.68$ ,  $H/p_\infty = 2.0$ . The spanwise location in this figure, as well as those figures immediately following, is given in terms of nozzle half-widths ( $\Delta Y/\frac{W}{2}$ ). As shown in Figure 56, the major effect of the jet is to produce a high-pressure region near the nozzle exit ( $x/c = 0.35$ ), which propagates outward for a distance of at least several nozzle half-widths; this spanwise influence has essentially damped out at a distance of four nozzle half-widths. At those measuring stations under the strong influence of this high-pressure region, a saddle-shaped chordwise distribution of pressures is noted. At the selected Mach number, this type of distribution effectively fixes the position of the leading-edge wing shock well forward of the nozzle exit. At more remote stations, the shock can move further aft with a greater chordwise extent of induced, supersonic over-velocity near the leading-edge. Pressures on the lower surface of the wing indicate very little spanwise influence of the jet. Effects similar to those noted above are shown for the same nozzle operating at a much higher nozzle pressure ratio ( $H/p_\infty = 3.57$ ) in Figure 57.

# USB CRUISE PROGRAM

$\Delta Y/w$  FROM  $\xi$

2

○ 1.39

□ 1.91

△ 4.0

● CLEAN STRAIGHT WING, FLAGGED SYMB, LOW. SURF.

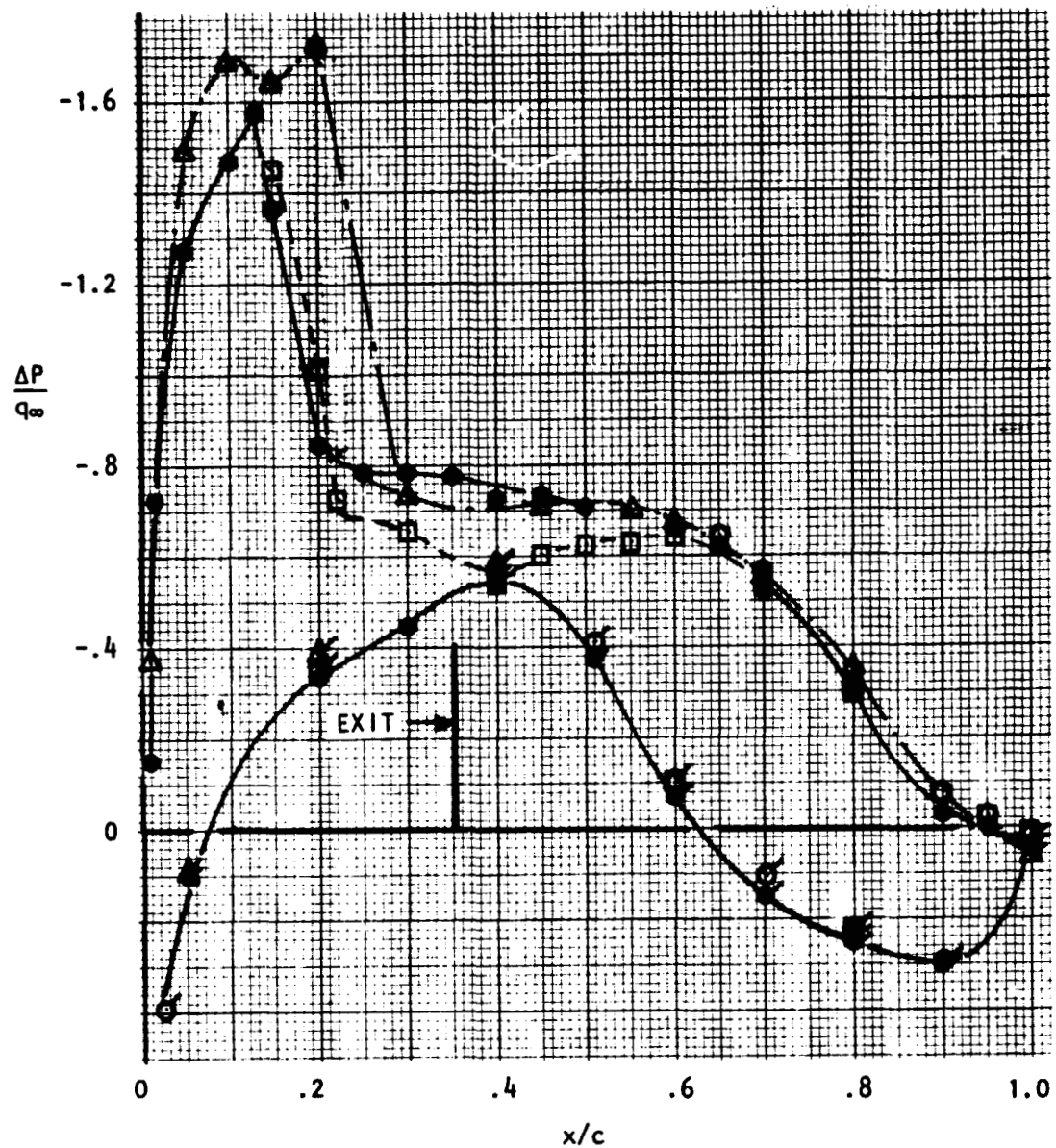


Figure 56 . Spanwise influence of jet, "D-Duct" nozzle ( $N_3$ ),  $\alpha = 3^\circ$ ,  $M_\infty = 0.68$ ,  $H_j/p_\infty = 2.0$ .

# USB CRUISE PROGRAM

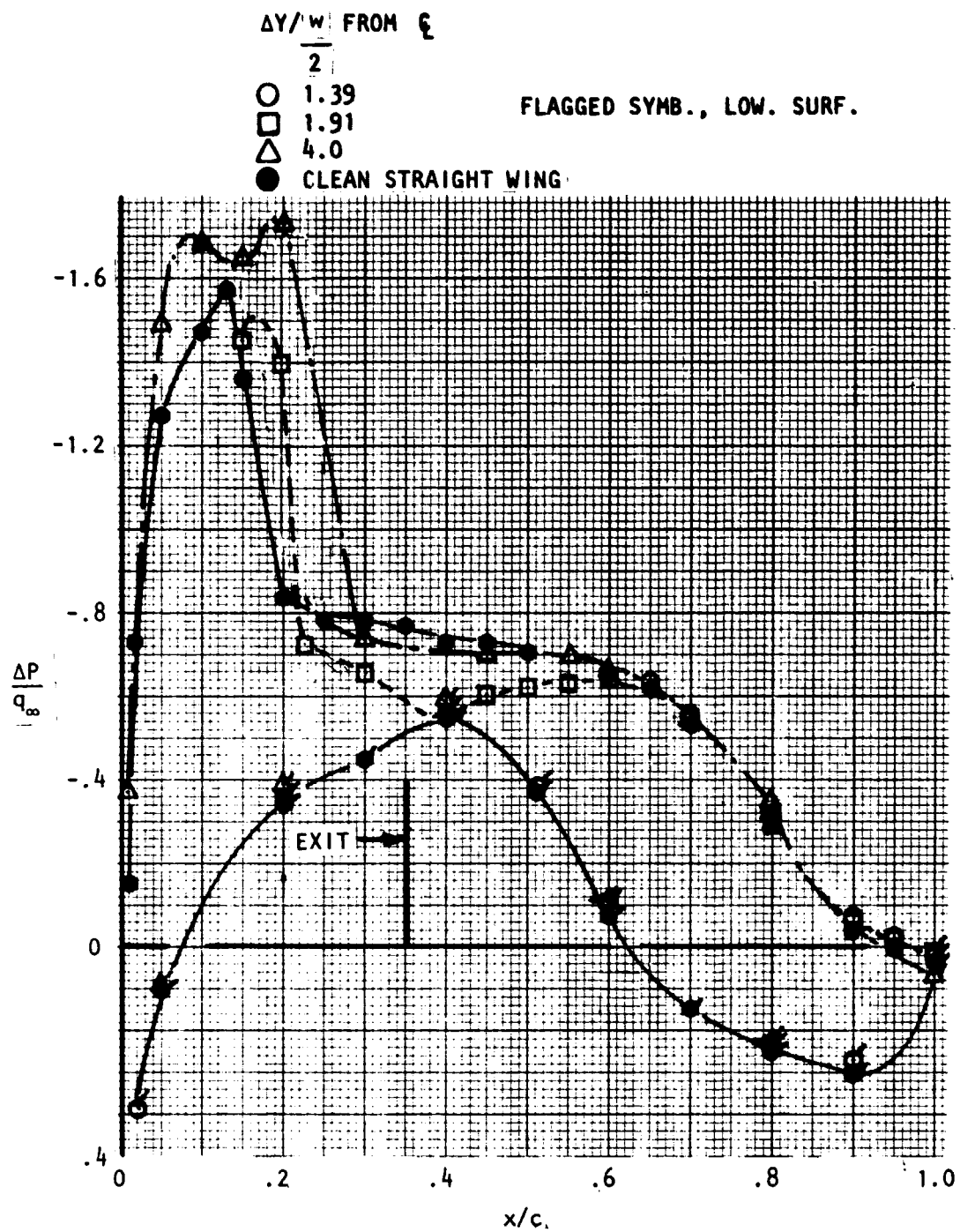


Figure 57 . Spanwise influence of jet, "D-Duct" nozzle ( $N_3$ ),  $\alpha = 3^\circ$ ,  $M_\infty = 0.68$ ,  $H_j/p_\infty = 3.57$ .

The same type of data are given in Figures 58 ( $H/p_\infty = 3.0$ ) and 59 ( $H/p_\infty = 2.75$ ) for the wide (aspect ratio 6) nozzle tested on the straight wing. Increased interference velocities, or super-velocities, are noted near the wing leading-edge close to the jet ( $\Delta Y/\frac{w}{2} = 1.16$ ); these are generated by the expanding shape of the wide, flat nozzle at the wing/nacelle juncture. The pressures at  $\Delta Y/\frac{w}{2} = 0.84$  fall within the jet scrubbed area and therefore are under the direct influence of the jet and associated shock structure. These data also show that the influence of the jet has essentially disappeared at approximately 2.5 nozzle half-widths from the jet centerline.

Data similar to the foregoing, but for representative small nacelles installed on the swept wing are provided in Figures 60 and 61. Figure 60 shows pressure distributions at two spanwise stations inboard of the P duct nacelle ( $\Delta Y/\frac{w}{2} = -2.7$  and  $-7.9$ ) and one station outboard of the nozzle ( $\Delta Y/\frac{w}{2} = +2.21$ ) at Mach = 0.68 and  $H_j/p_\infty = 2.0$ . The results show the inboard side of the nacelle to be more sensitive to jet-induced interference than the outboard side (compare  $\Delta Y/\frac{w}{2} = -2.7$  and  $+2.2$ ); in fact, some slight changes from clean wing pressures are noted at an inboard station 7.9 nozzle half-widths away. Pressure data obtained from tests of the wide nozzle ( $N_{13}$ ,  $AR = 6$ ), as tested on the swept wing and shown in Figure 61, also indicate a sensitivity of the inboard flow-field to jet-induced interference. Some effect is noted at five nozzle half-widths inboard of the centerline. The data of both Figures 60 and 61 show relatively high supervelocities generated on the inboard side of the nacelle at the leading-edge. While the fillets used with these models were of some

# USB CRUISE PROGRAM

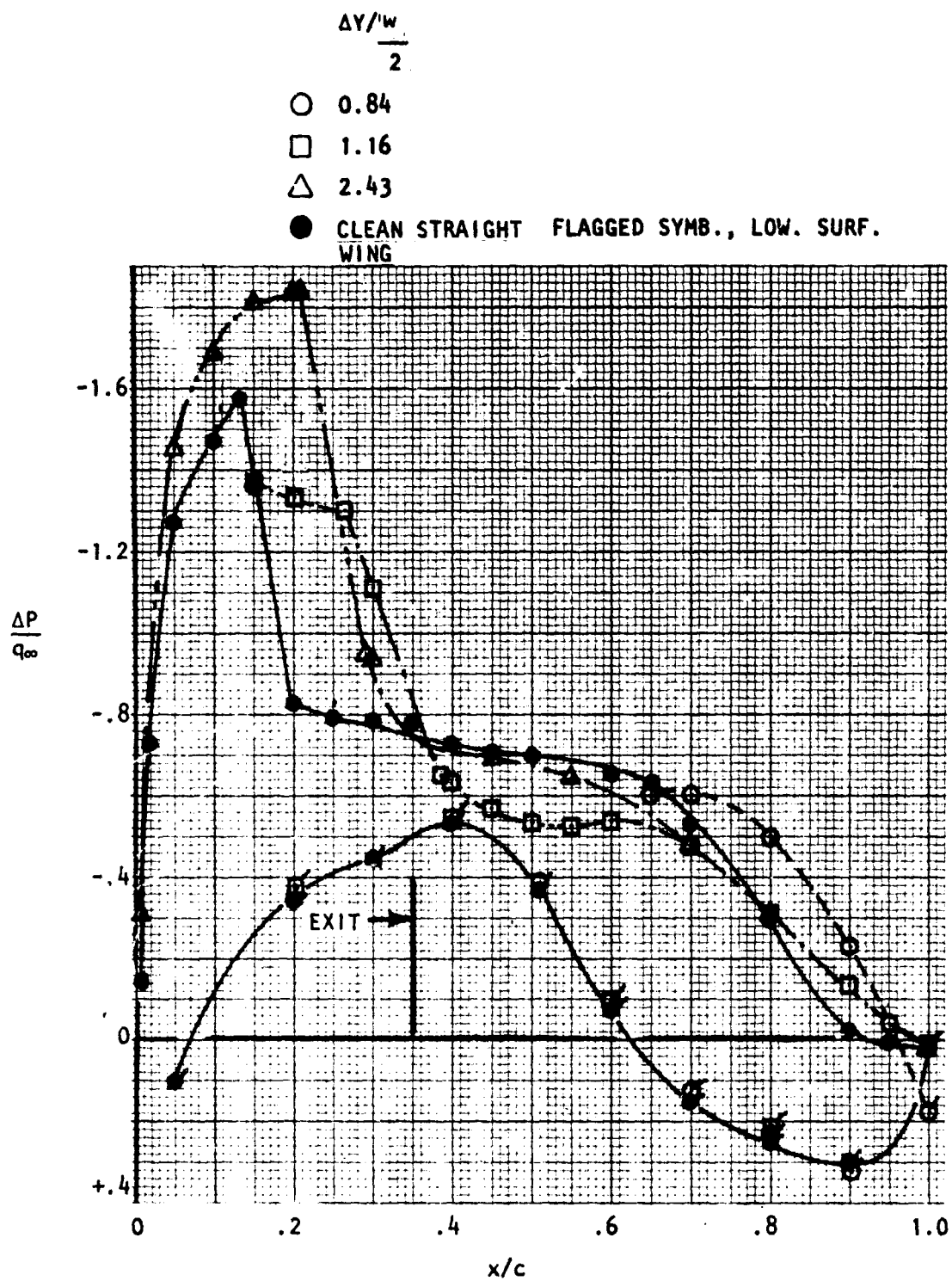


Figure 58 . Spanwise influence of jet, noz. N<sub>5</sub>  
AR = 6,  $\alpha = 3^\circ$ ,  $M_{\infty} = 0.68$ ,  $H_j/p_{\infty} = 3.0$

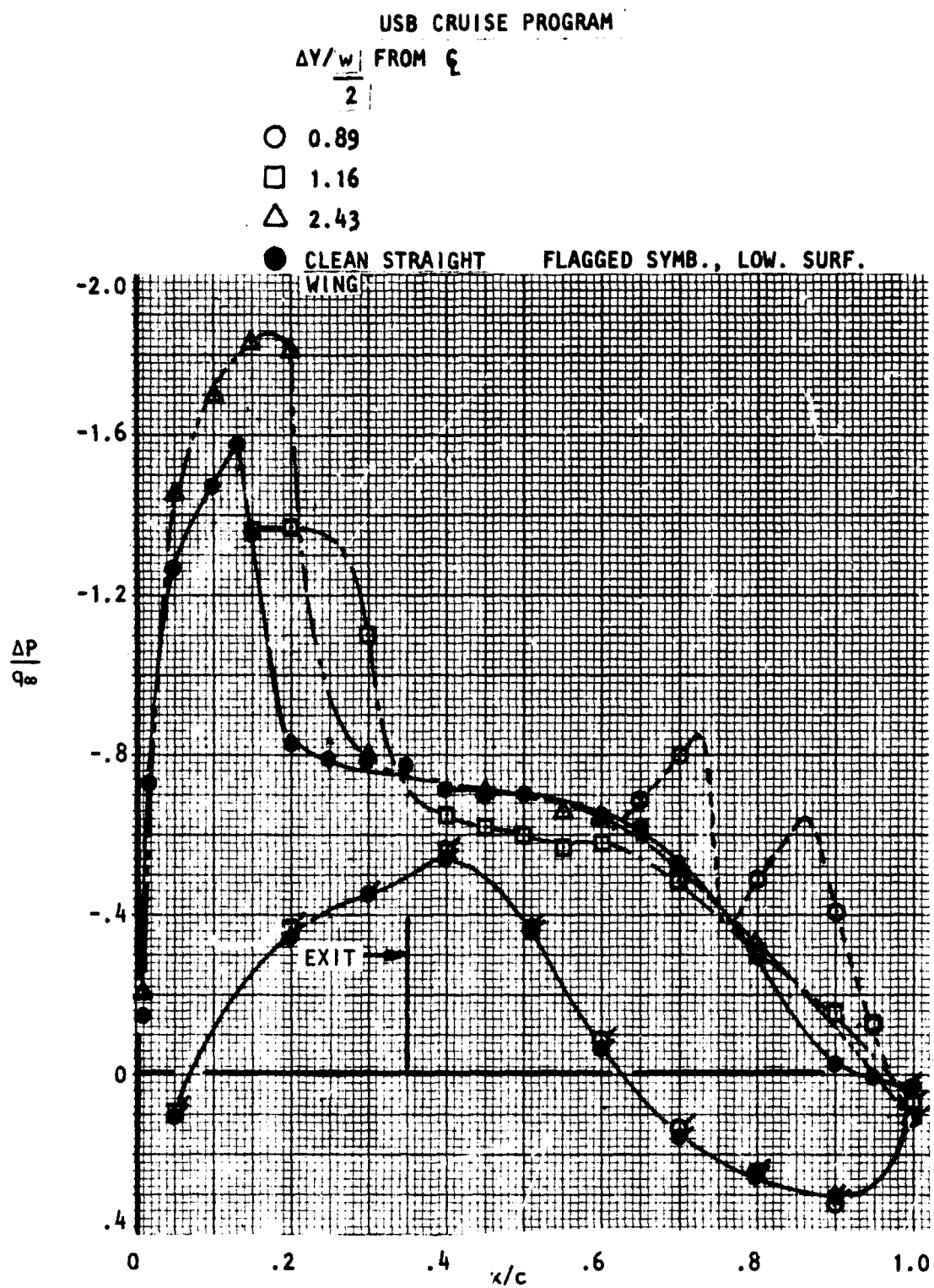


Figure 59 . Spanwise influence of jet, noz N<sub>5</sub>,  
 AR = 6,  $\alpha = 3^\circ$ ,  $M_\infty = 0.68$ ,  $H_j/p_\infty = 2.75$ .

# USB CRUISE PROGRAM

$\frac{\Delta Y/w}{2}$  FROM  $\xi$

○ -2.7 (INB'D OF  $\xi$ )

□ -7.9 (INB'D OF  $\xi$ )

△ +2.21

● CLEAN SWEEP WING

FLAGGED SYMB., LOW. SURF.

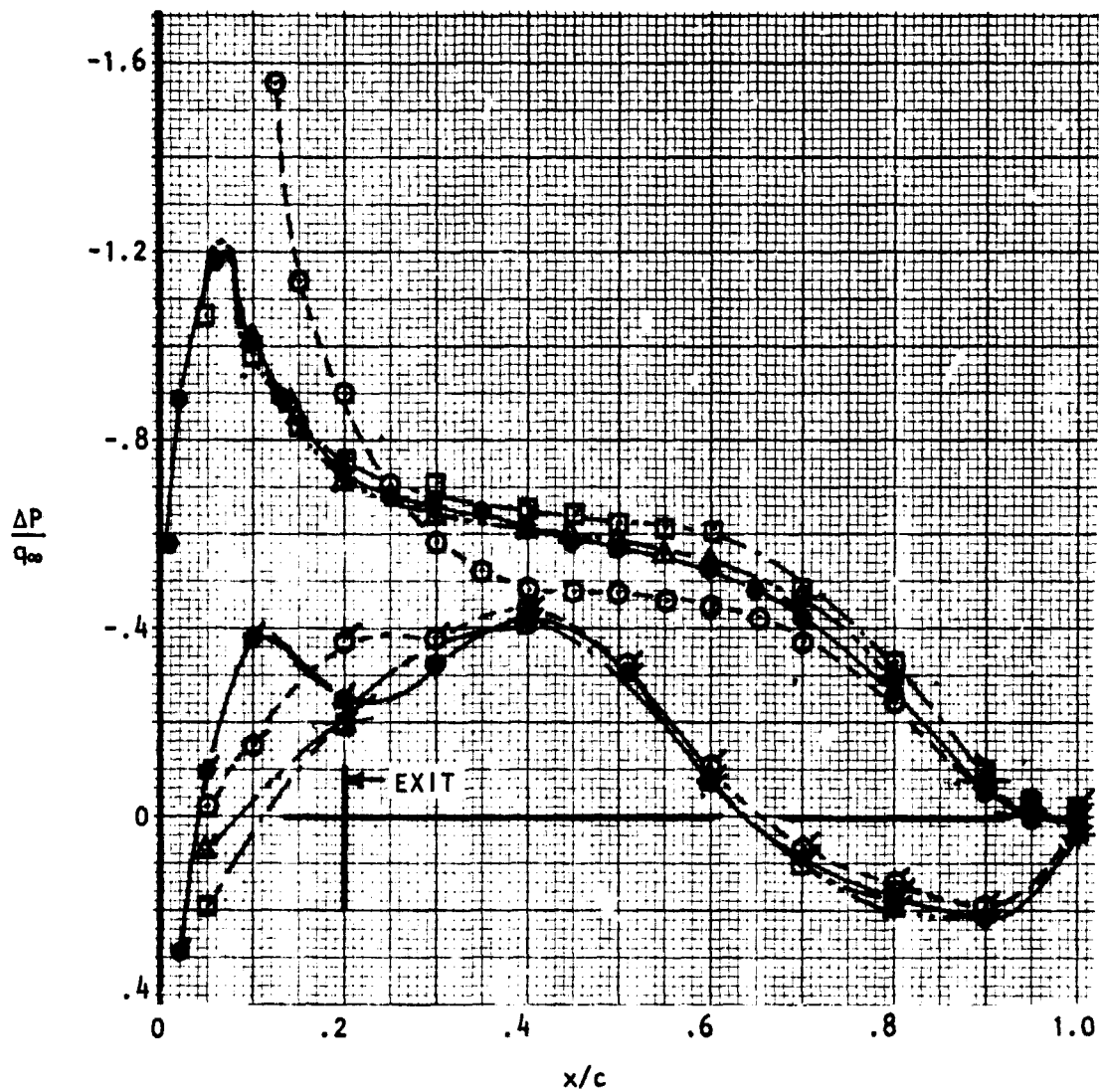


Figure 60 . Spanwise influence of jet on swept wing, noz N<sub>8</sub>, AR=2.5,  $\alpha = 3^\circ$ ,  $M_\infty = 0.68$ .



# USB CRUISE PROGRAM

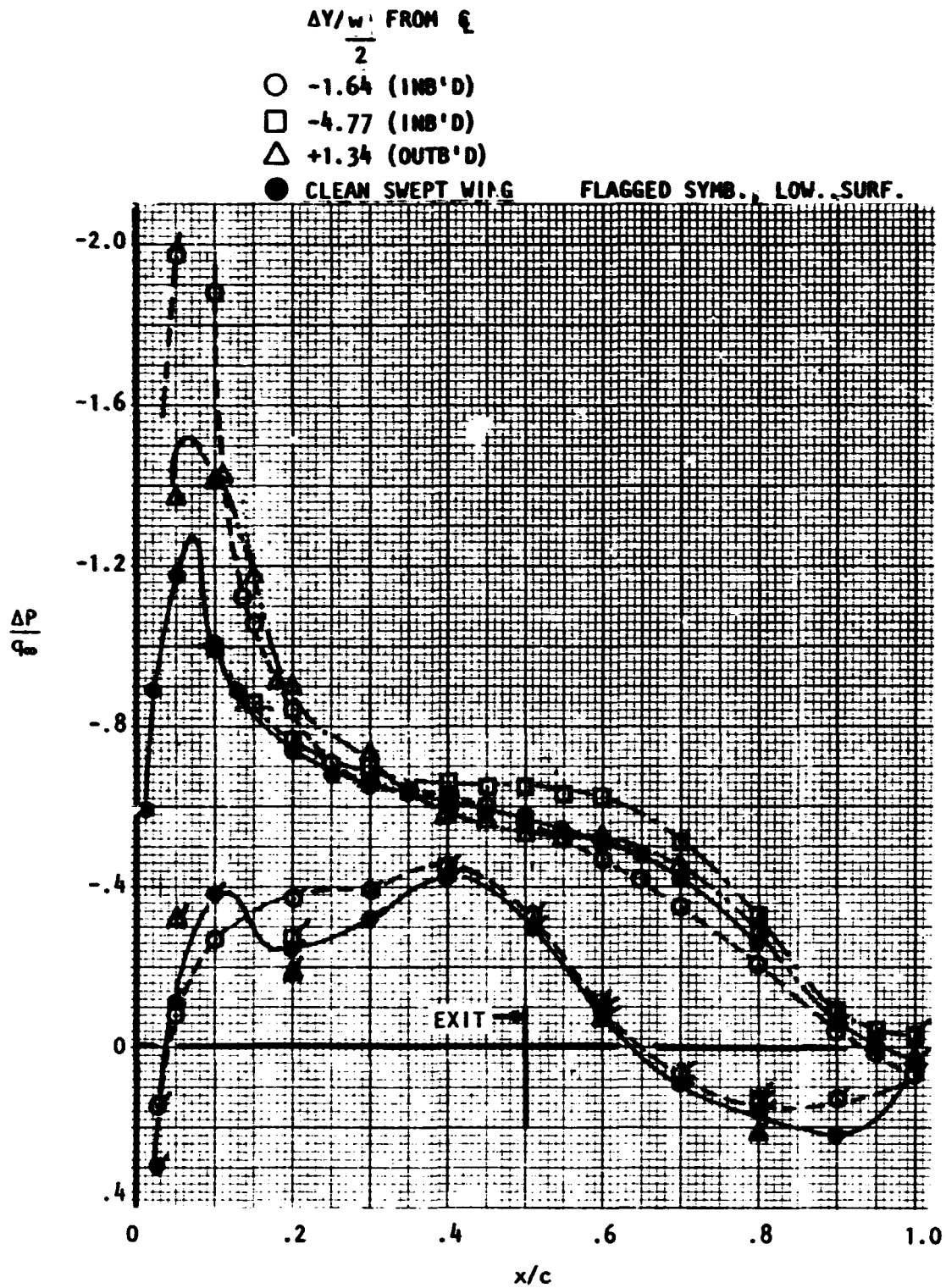


Figure 61 . Spanwise influence of jet on swept wing, noz N<sub>13</sub>, AR = 6,  $\alpha = 3^\circ$ ,  $M_\infty = 0.68$ ,  $H_j/p_\infty = 1.96$ .

benefit in suppressing such supervelocities, the need for a more effective method, such as area-ruling or streamlining, is indicated by the available data.

It is concluded from the foregoing and other data that lift induced by the jet is generally confined to the immediate spanwise vicinity of the nozzle. While lift increases are noted on the adjacent wing sections, these appear to be associated with nacelle and nozzle planform shapes as much as with the jet-induced effects. The general trend appears to be an increase in adjacent section lift as the nozzle width increases, which probably accounts for the lift changes noted in the discussions of pressure data (Figure 54).

- o Effects of Multiple Jets – Pressure tests of a four-engine configuration using small ( $c^2/A_N = 48$ ) "D-duct" nacelles spaced 1.6 nacelle diameters apart (surface-to-surface) are represented in the data of Figures 62 and 63. These data compare clean wing chordwise pressure distributions with those obtained at a chordwise station mid-way between the two jets ( $\Delta Y/\frac{W}{2} = \pm 2.6$ ). In Figure 62, the major effect appears to be in the region of the leading-edge where rather extensive filleting had been used to prevent excessive shock losses. At  $M_\infty = 0.60$ , Figure 62, the high-velocity region appears to recover to the clean wing trailing-edge pressure level without separating. At  $M_\infty = 0.73$ , Figure 63, the forward high-velocity region is moved aft relative to that of the clean wing with the predominant effect being the high-pressure region near the nacelle exit positions. The aft pressure gradient resulting from the saddle-

# USB CRUISE PROGRAM

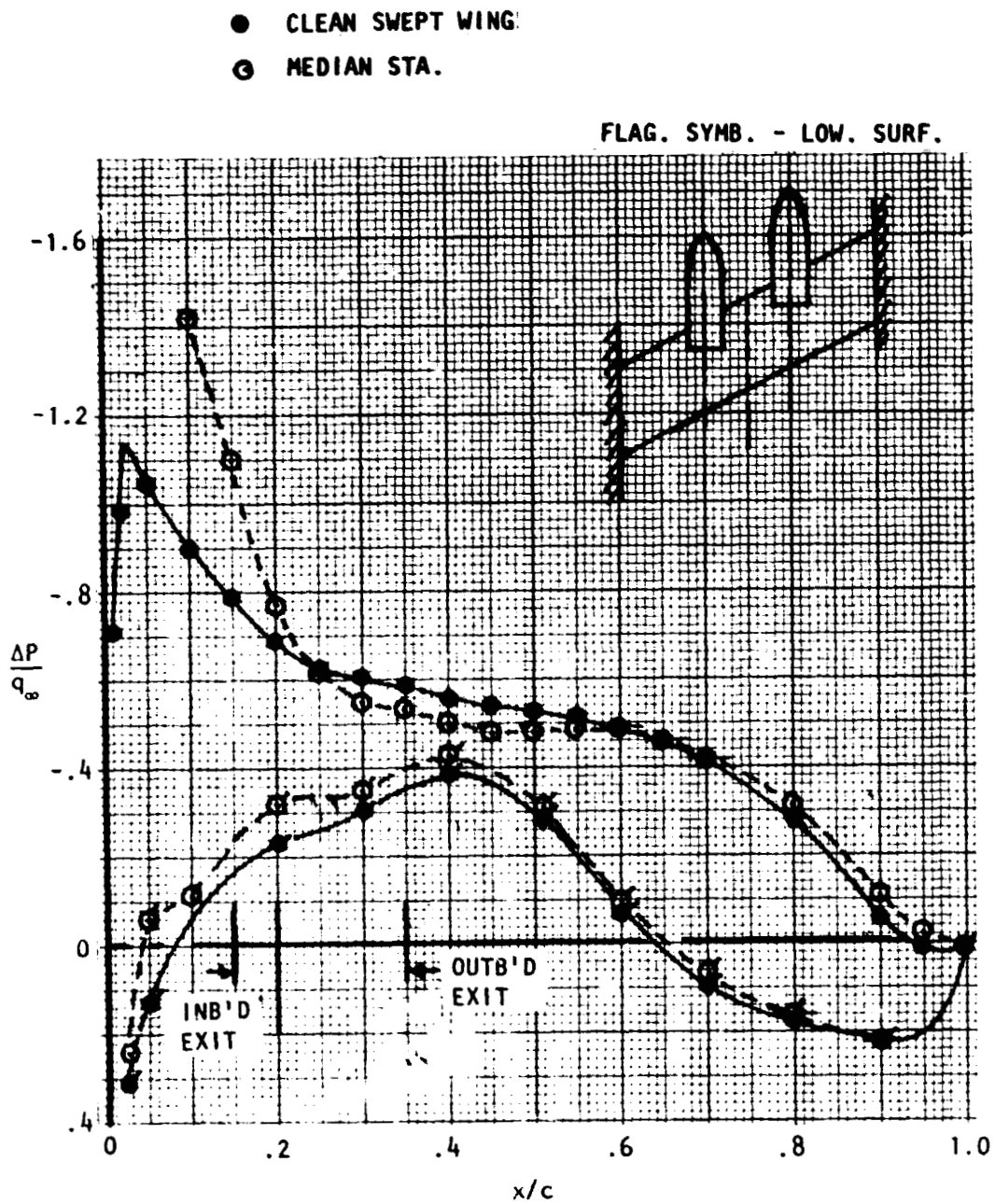


Figure 62 . Swept-wing pressure distribution along median line of twin-jet configuration, "D-Duct" Noz ( $N_8$ ),  $\alpha = 3^\circ$ ,  $M_\infty = .60$ ,  $H_j/p_\infty = 2.6$ .

# USB CRUISE PROGRAM

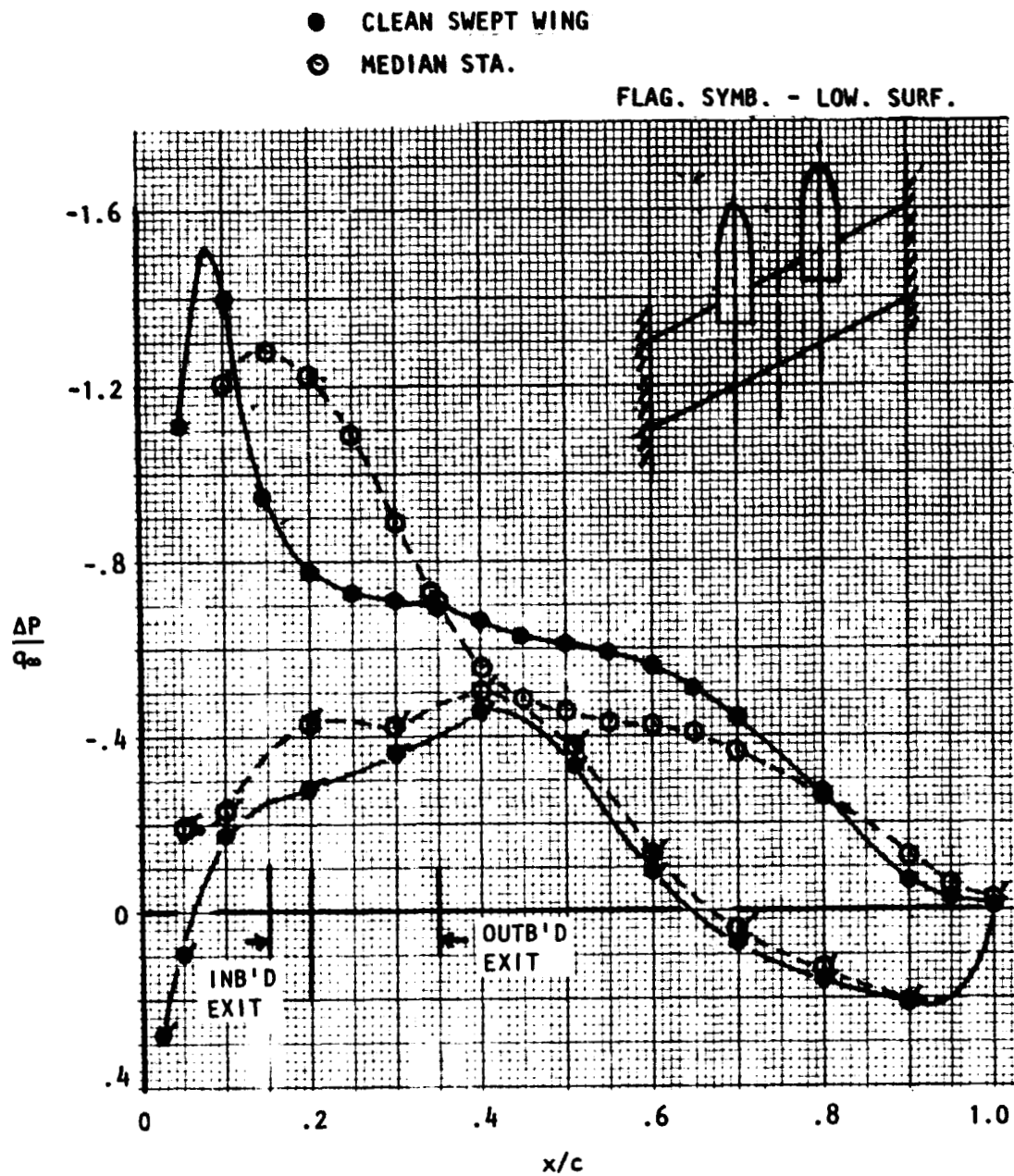


Figure 63 . Swept wing pressure distribution along median line of twin-jet configuration, "D-Duct" noz ( $N_8$ ),  $\alpha = 3^\circ$ ,  $M_\infty = 0.73$ ,  $H_j/p_\infty = 2.6$ .

shaped distribution, along with flow-entrainment into the jets, would tend to suppress boundary-layer build-up or separation at this median position. Again, the trailing-edge pressure level essentially matches that of the clean wing. From these data, no severe flow problems suggesting a high interference drag penalty are noted at the median position; this would not be surprising in view of the relatively large spacing between nacelles. Wake traverses behind the multi-jet configuration, Figures 193 and 194 of Volume IIC, indicate a substantial loss in total head immediately downstream of the median station, which tends to conflict with the foregoing conclusion. As will be shown in Section 3.2.3.2, force test results indicate very little drag penalty identifiable as an interference type of drag for this configuration.

### 3.2.3 USB Installations – Force Tests

Discussion of the force-test results follows the same format as used for the analyses of the pressure-tests. The following sections consider first the static performance of the USB-system along with the balance-measured parameter derived. These discussions are followed by the wind-on force-test results.

#### 3.2.3.1 Static Performance-Force Tests – Static, installed force tests

were conducted on all test nozzles to evaluate the two parameters:  $\eta_{T_s}$  (static efficiency) and  $\delta_{j_s}$  (static turning angle). Figure 64 provides a summary of static installed thrust efficiencies ( $\eta_{T_s}$ ) and the effective static jet deflection angle, ( $\delta_{j_s}$ ) for each test nozzle as a function of

# USB CRUISE PROGRAM

NOZZLE	$H_j/p_\infty = 1.6$	2.0	12.6	3.2
N <sub>2</sub>	1.0 (1.0)	1.0 (0)	1.0 (.6)	1.0 (1.3)
N <sub>2E</sub>	.990 (1.2)	.984 (1.0)	.989 (1.0)	.989 (1.0)
N <sub>3</sub>	1.0 (5.2)	1.0 (5.0)	.994 (6)	.990 (6.1)
N <sub>3E</sub>	.993 (4.5)	.988 (3.2)	.978 (3.0)	.975 (4.0)
N <sub>4</sub>	.933 (8.6)	.966 (9.2)	.968 (9.8)	.970 (10)
N <sub>4E</sub>	.964 (13)	.975 (13)	.969 (13)	.975 (13)
N <sub>5</sub>	.971 (12)	.993 (12)	.977 (12.5)	.985 (11)
N <sub>6</sub>	.946 (2)	.972 (2.0)	.982 (2.8)	.978 (3.3)
N <sub>8</sub>	.946 (2)	.972 (2.0)	.982 (2.8)	.978 (3.3)
N <sub>11</sub>	1.0 (2.3)	1.0 (2.8)	1.0 (2.5)	1.0 (2.0)
N <sub>12</sub>	.966 (0.5)	.968 (2.5)	.972 (4.7)	.964 (4.8)
N <sub>13</sub>	1.0 (7)	.962 (7.5)	.963 (7.3)	.966 (7)
N <sub>8</sub> <sup>1</sup> + N <sub>8</sub> <sup>2</sup> (DUAL)	.941 (1.5)	.967 (1.5)	.977 (2.1)	.973 (2.4)

NOTE:  $\eta_{TS} = \frac{\text{INSTALL. THRUST}}{\text{ISOLAT. THRUST}}$

$\delta_{js}$  IN DEG.

Figure 64 . - Tabulation of  $\eta_{TS} (\delta_{js})$  for test nozzles; static data.

nozzle pressure ratio. Inasmuch as an accurate determination of these parameters can involve very low force loadings (normal force with a marginally attached jet, for instance), a separate check was made on several more sensitive balance systems; Section 3.1.1 provides additional discussion of these supplementary tests. For each of the several balance systems utilized under the Task II effort, it was necessary to obtain the isolated thrust as well as the static installed thrust to derive the several static parameters. The values of the static parameters shown in Figure 64 are based on the more accurate balance measurements.

3.2.3.2 General Wind-On Performance — The wind-on aerodynamics of the wing/nacelle combinations are discussed in the following paragraphs in terms of incremental effects on cruise drag, lift and pitching moment. Where possible, these force and moment increments are further broken down in an effort to identify the sources of the aerodynamic changes induced by the installation of the blowing nacelle and for corroborating trends developed from the pressure test results. These discussions will be followed by data pertaining to geometric effects.

- o Total Cruise Drag Penalty — Figure 65 shows a typical trend of the total nacelle drag penalty ( $\Delta C_{D_N}$ ) as a function of the nozzle gross thrust coefficient,  $C_T$ ; the Mach number of 0.68 is at the drag-rise of the straight wing/nacelle combination and the nozzle has a "D-duct" shape and size of  $c^2/A_N = 24$ . The experimentally-derived increments illustrated are obtained from:

# USB CRUISE PROGRAM

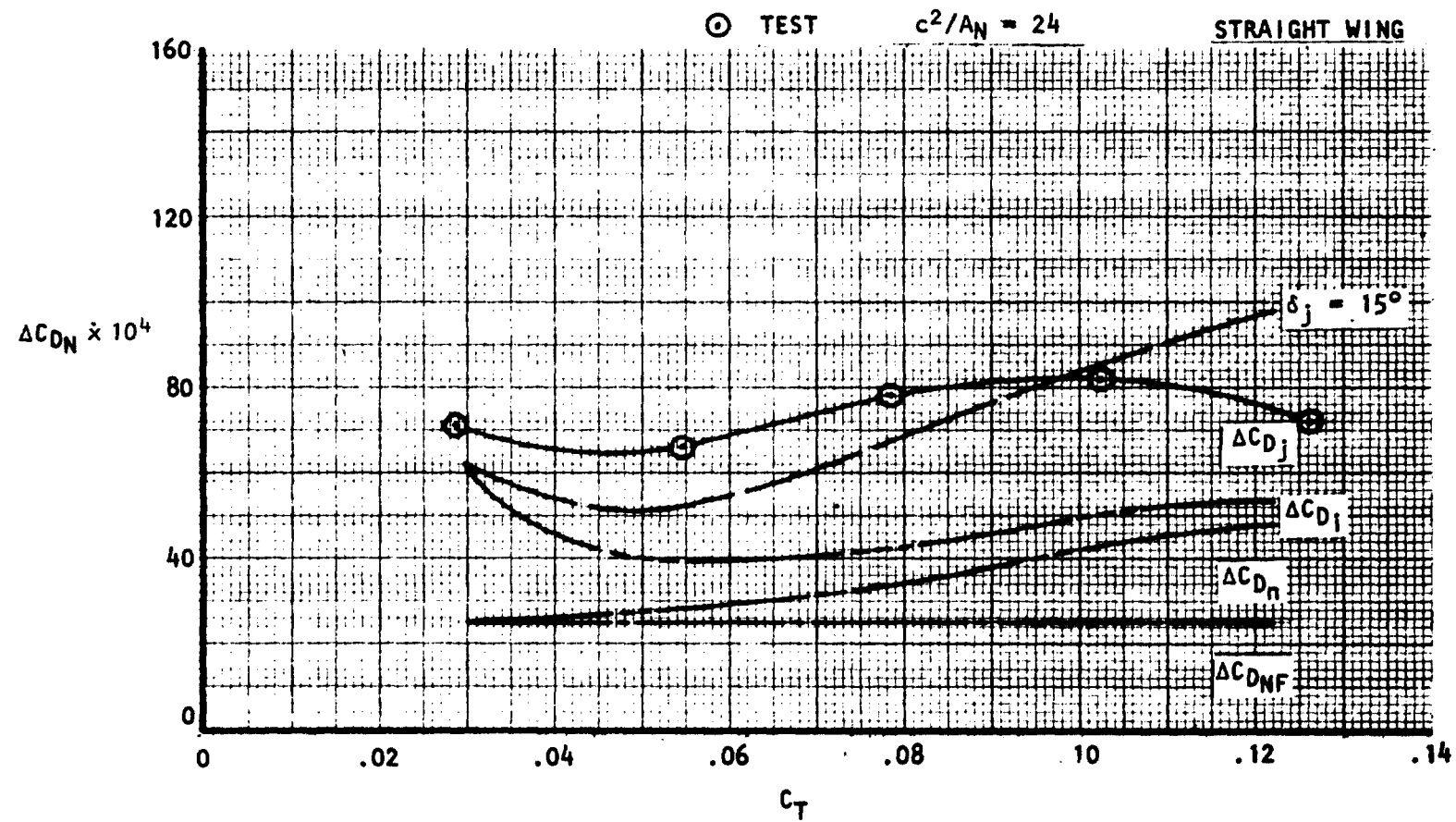


Figure 65. Incremental nacelle drag and component build-up  
noz N<sub>3E</sub>, AR=2.5,  $M_\infty=0.68$ ,  $C_{LH}=0.40$ .



$$\Delta C_{D_N} = C_{D_M} + (C_T)_{ISOL} - C_{D_{WB}} \quad (19)$$

at a constant (total) lift coefficient of 0.40. The data points shown have been obtained at fixed nozzle pressure ratios of 1.4, 1.8, 2.2, 2.6 and 3.0. Starting with the flow-through nozzle pressure ratio ( $H_j/p_\infty = 1.40$ ), there is a gradual reduction in the drag increment as the thrust coefficient is increased to about .06 followed by a more rapid increase between  $C_T$  - values of .06 and 0.10. Above  $C_T = 0.10$ , the initial trends appear to be repeated with a gradual increase in the overall drag penalty.

It will be shown that this trend is reasonably typical for the wider (higher aspect ratio) nacelles with the perturbations in basic drag level created by a changing trade-off between the scrubbing losses,  $\Delta C_{D_\eta}$ , the drag-due-to-lift,  $\Delta C_{D_i}$ , and the pressure drag induced by the deflecting jet,  $\Delta C_{D_j}$ .

Duplicating the foregoing format, the total cruise drag penalties of all of the straight wing nozzles are given in Figures 65 through 88 at fixed Mach numbers of 0.60, 0.68 and 0.72. Corresponding swept wing nozzle configurations are similarly presented in Figures 89 through 103 at fixed Mach numbers of 0.60, 0.68 and 0.73; the drag-rise (or cruise) condition for the swept wing configurations is Mach 0.73,  $C_L = 0.40$ . For the single-nacelle installations, the swept wing drag penalties are shown to be approximately one-half that of the straight wing installations, inasmuch as the nacelle sizes on the swept wing are normally one-half those of the straight-wing ( $c^2/A_N = 48$ , swept). In addition to

# USB CRUISE PROGRAM

EST. DRAG  
COMPONENTS

⊙ TEST

$c^2/A_N = 24$

STRAIGHT WING

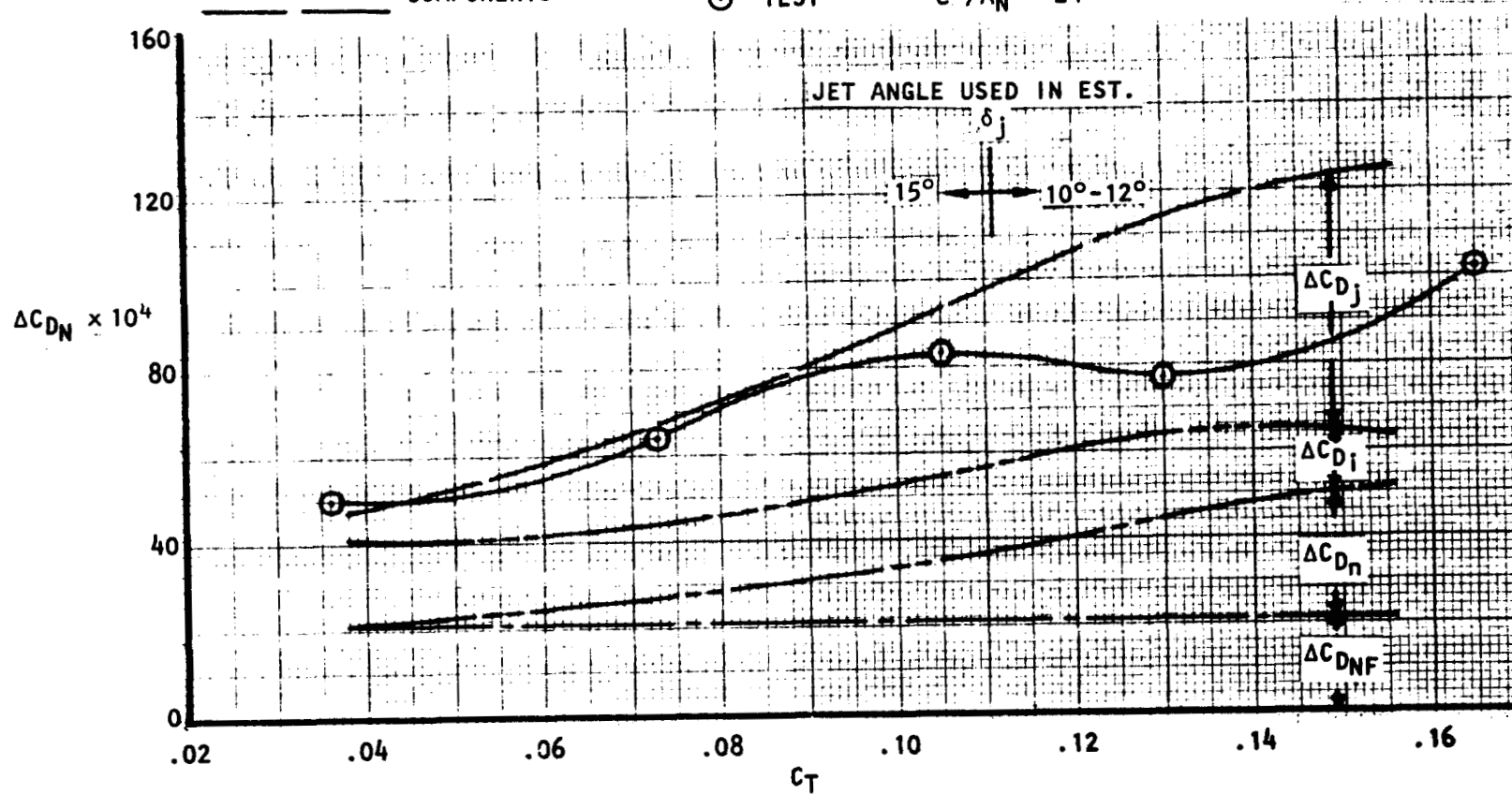


Figure 66. Incremental nacelle drag and component build-up  
noz N<sub>3E</sub>, AR = 2.5, M<sub>∞</sub> = 0.60, CL<sub>M</sub> = 0.40

ORIGINAL PAGE IS  
OF POOR QUALITY

# USB CRUISE PROGRAM

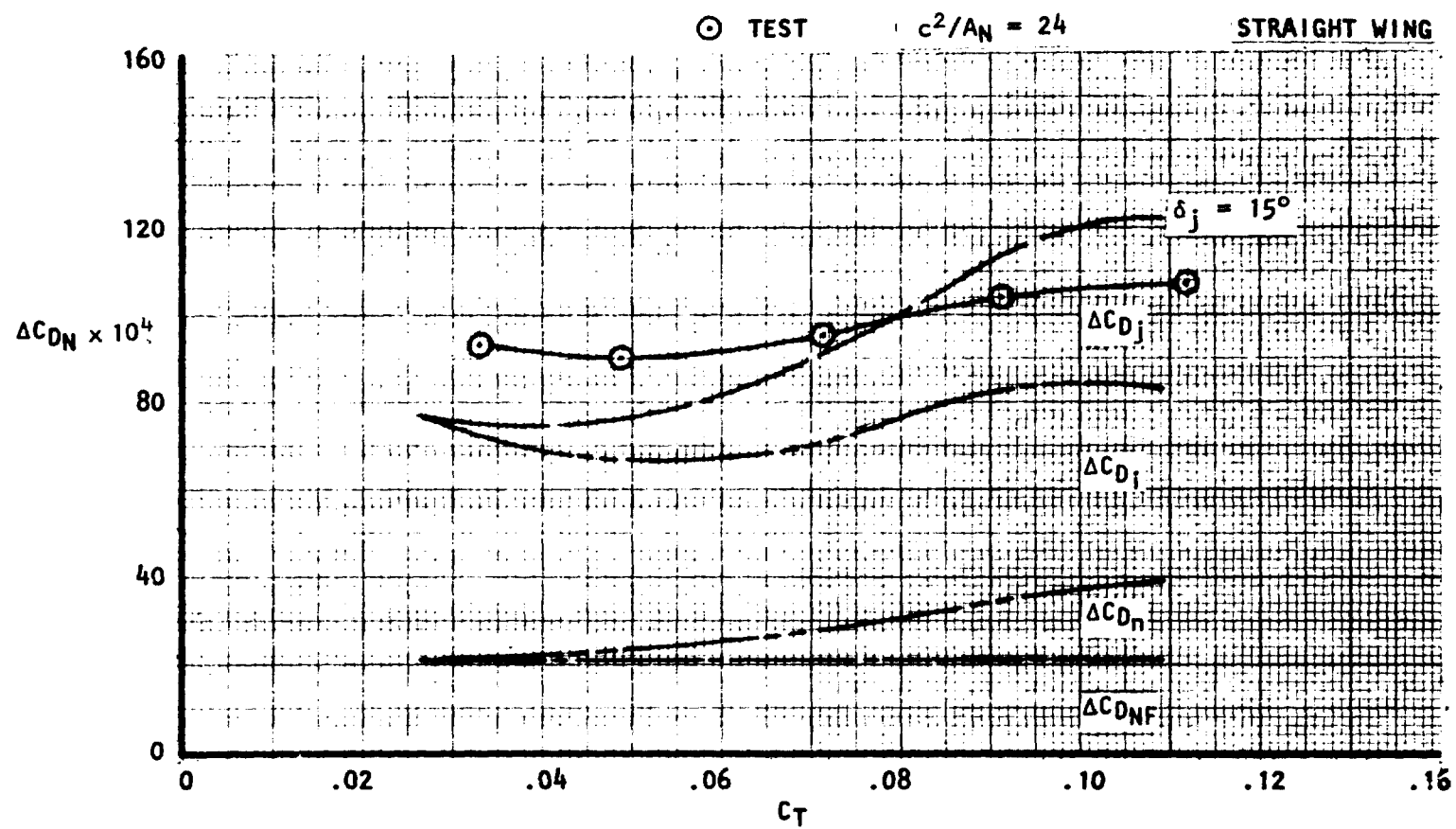


Figure 67. Incremental nacelle drag and component build-up  
noz  $N_{3E}$ ,  $AR = 2.5$ ,  $M_\infty = 0.72$ ,  $C_{LM} = 0.40$ .

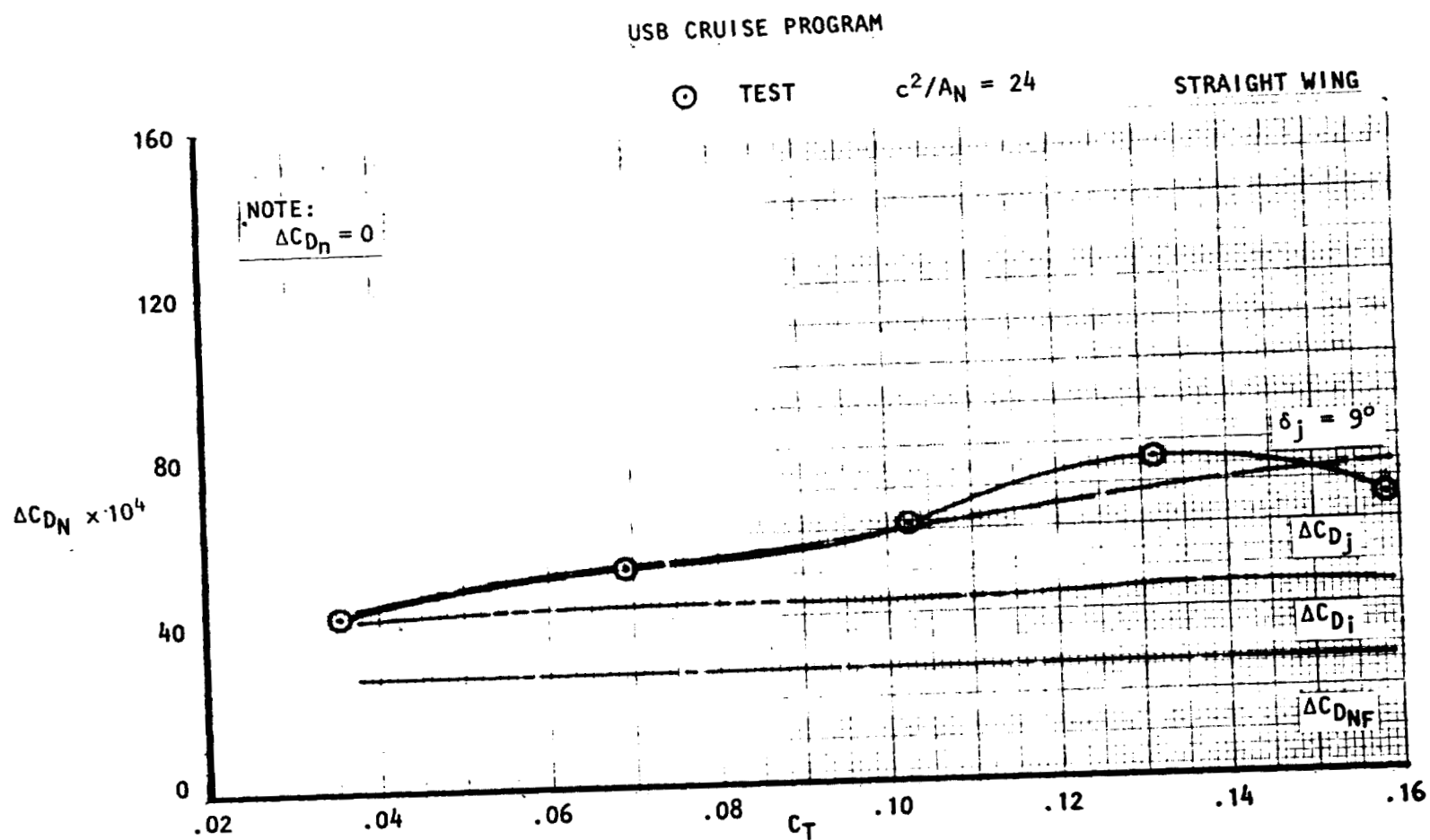


Figure 68 . Incremental nacelle drag and component build-up  
noz,  $N_2$ , circular,  $M_\infty = 0.60$ ,  $C_{LM} = 0.40$

## USB CRUISE PROGRAM

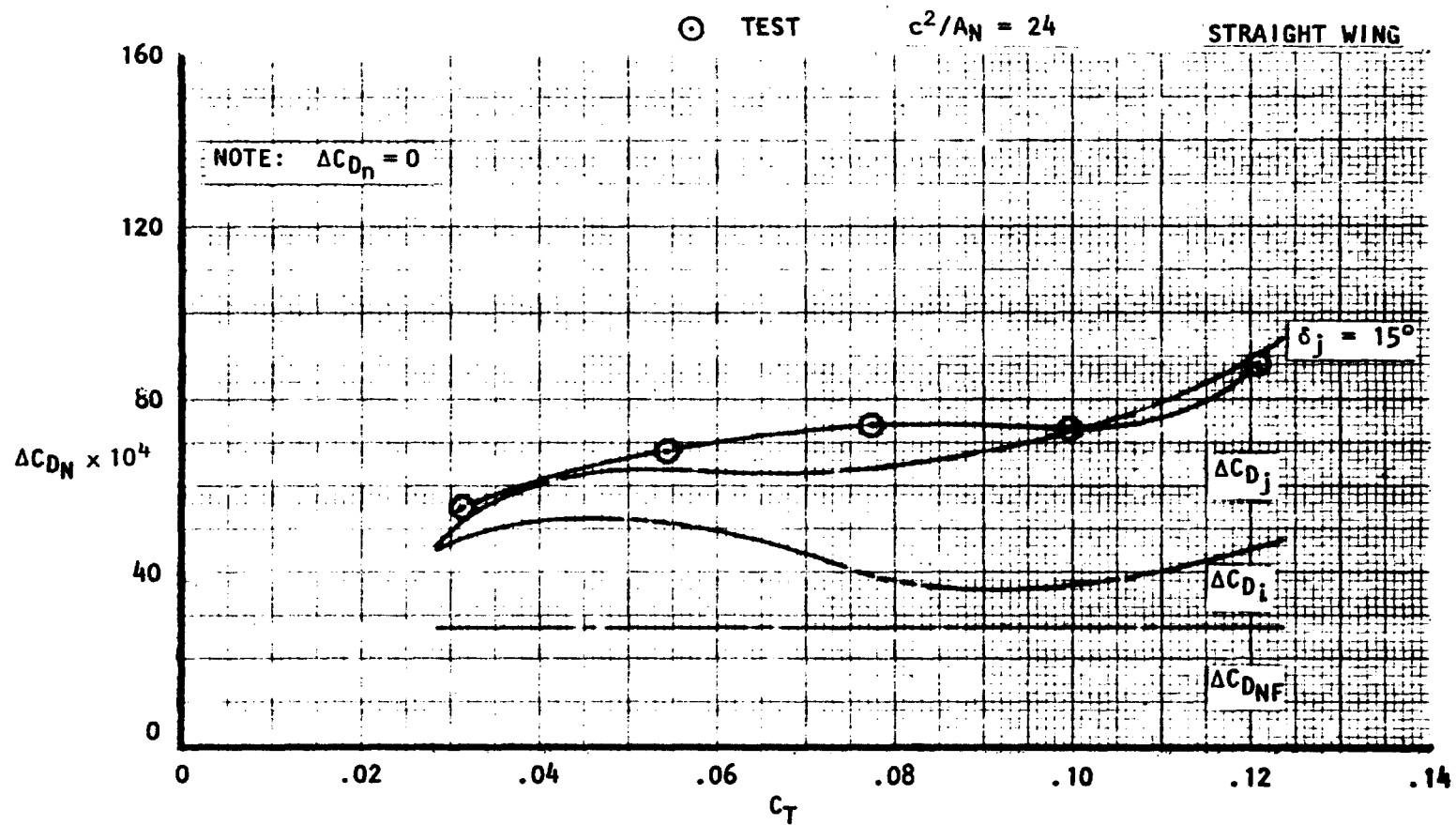


Figure 69. Incremental nacelle drag and component build-up  
noz N<sub>2</sub>, circular,  $M_\infty = 0.68$ ,  $C_{LM} = 0.40$ .

# USB CRUISE PROGRAM

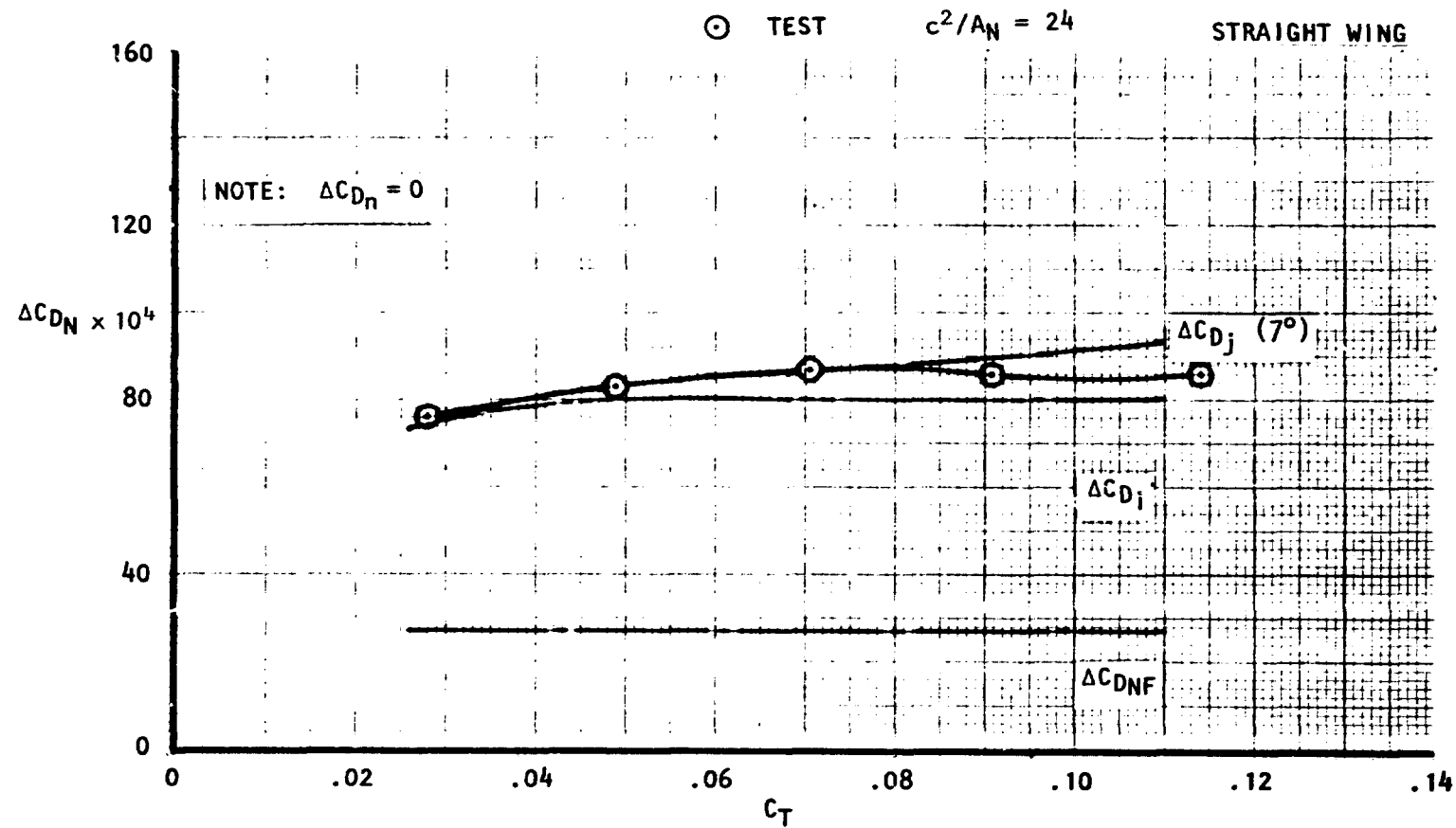


Figure 70. Incremental nacelle drag and component build-up  
noz N<sub>2</sub>, circular,  $M_\infty = 0.72$ ,  $C_{LM} = 0.40$ .

# USB CRUISE PROGRAM

STRAIGHT WING

⊙ TEST  $c^2/A_N = 24$

ORIGINAL PAGE IS  
OF POOR QUALITY

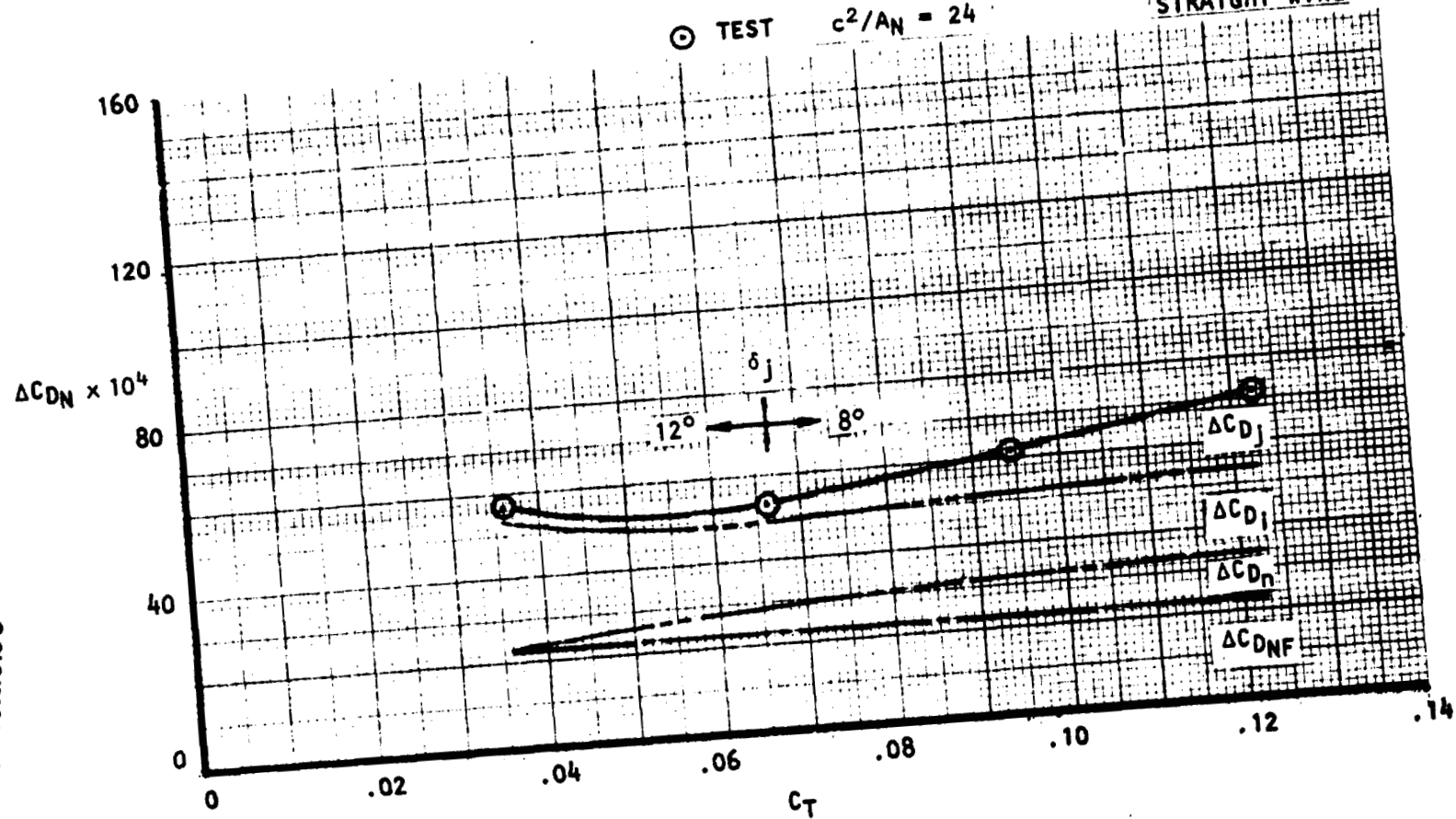


Figure 71. Incremental nacelle drag and component build-up  
noz N2E, circular,  $M_\infty = 0.60$ ,  $C_{LM} = 0.40$ .

# USB CRUISE PROGRAM

⊙ TEST

$c^2/A_N = 24$

STRAIGHT WING

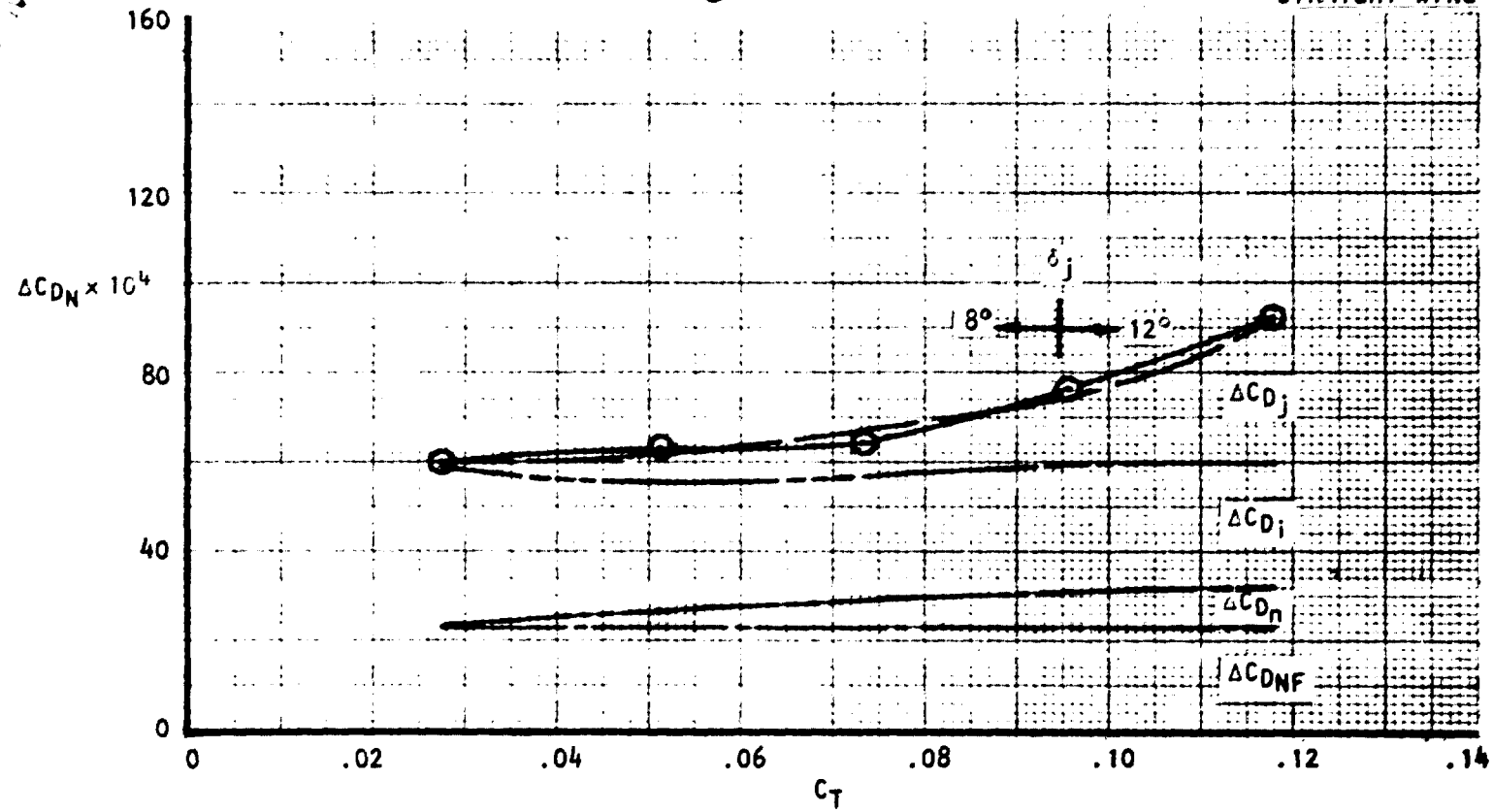


Figure 72. Incremental nacelle drag and component build-up  
noz  $N_{2E}$ , circular,  $M_\infty = 0.68$ ,  $C_{LM} = 0.40$ .



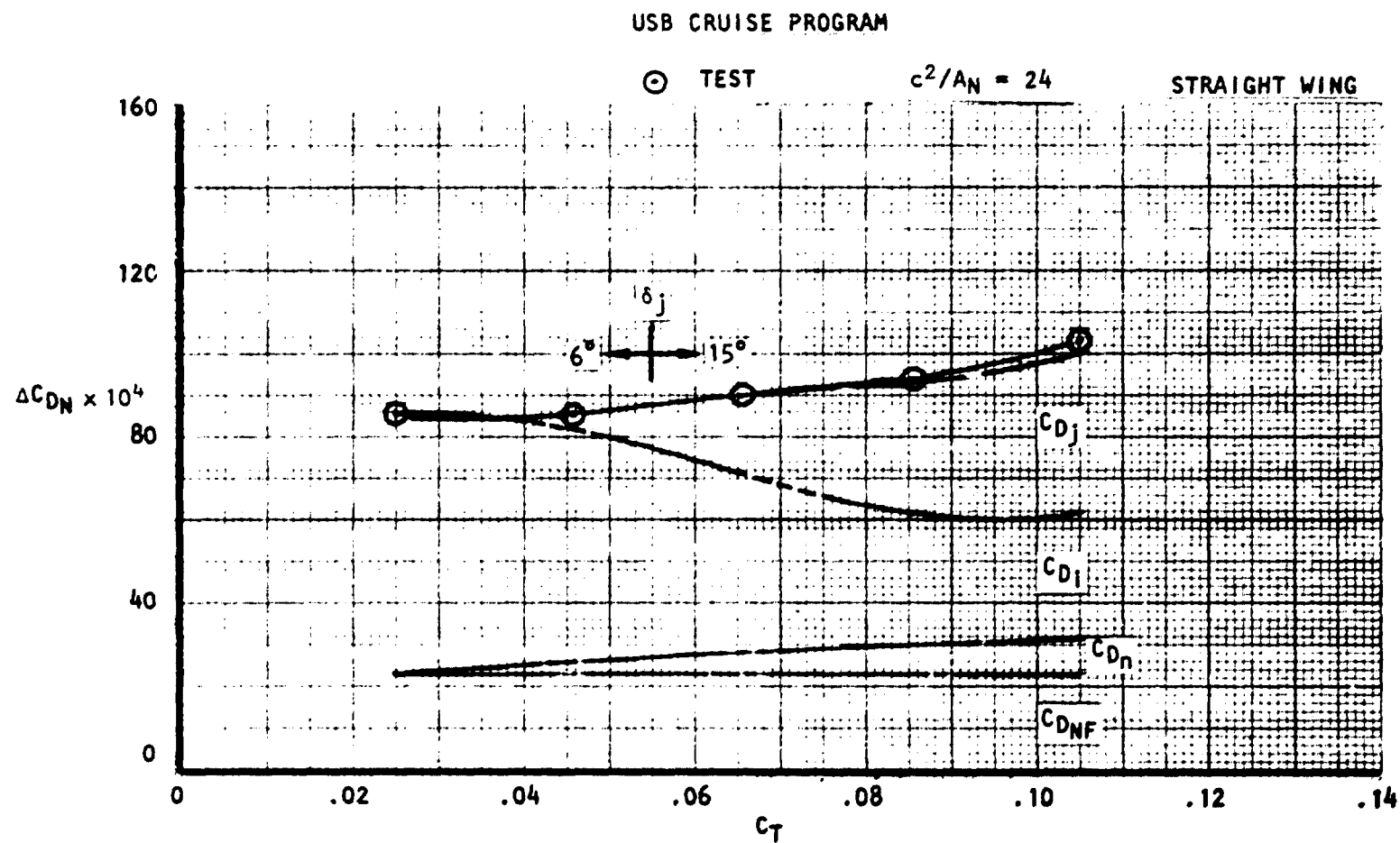


Figure 73. Incremental nacelle drag and component build-up  
 noz N<sub>2E</sub>, circular,  $M_\infty = 0.72$ ,  $C_{LM} = 0.40$ .

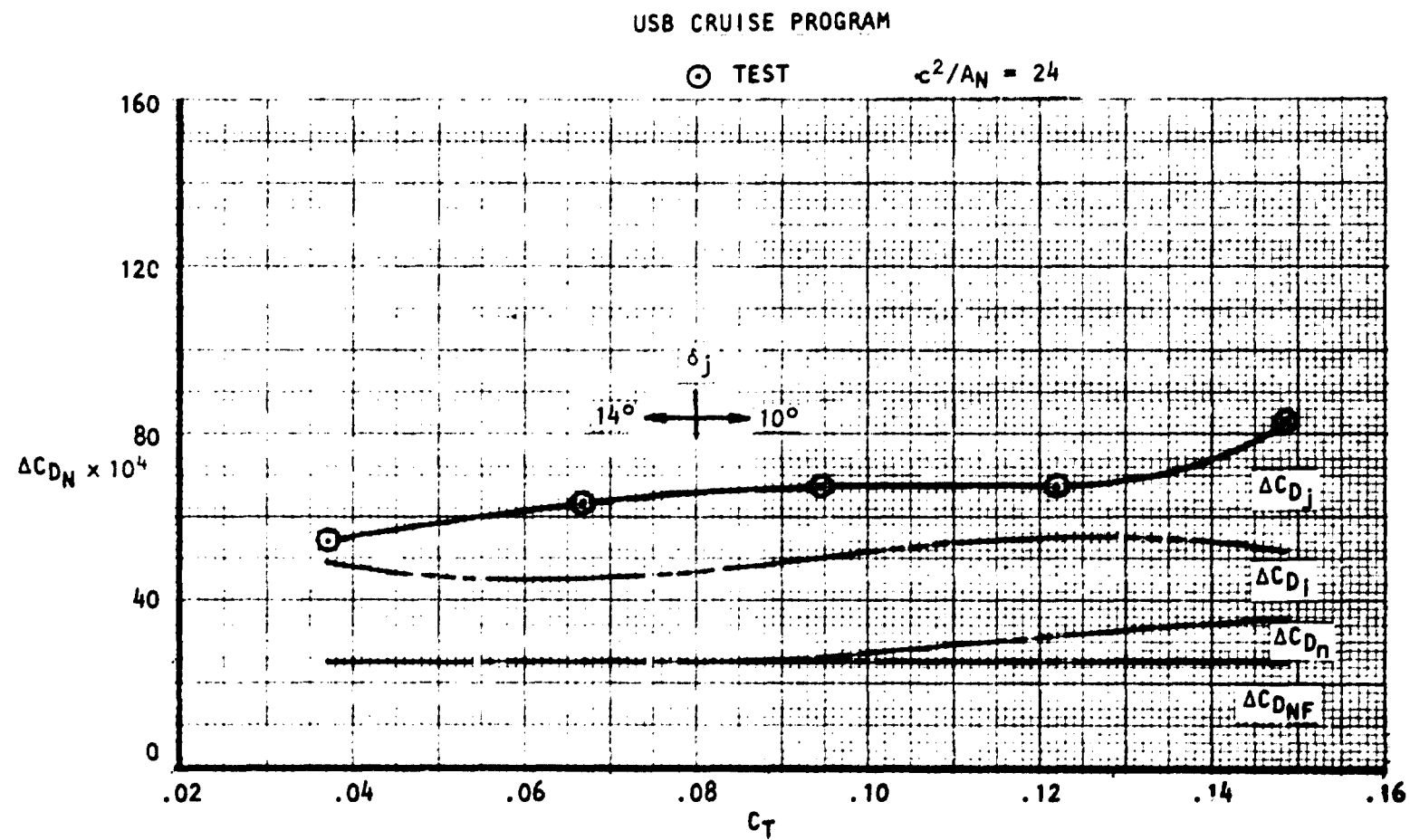


Figure 74. Incremental nacelle drag and component build-up  
 noz N<sub>3B</sub>, AR = 2.5,  $M_\infty = 0.60$ ,  $C_{LM} = 0.40$ .

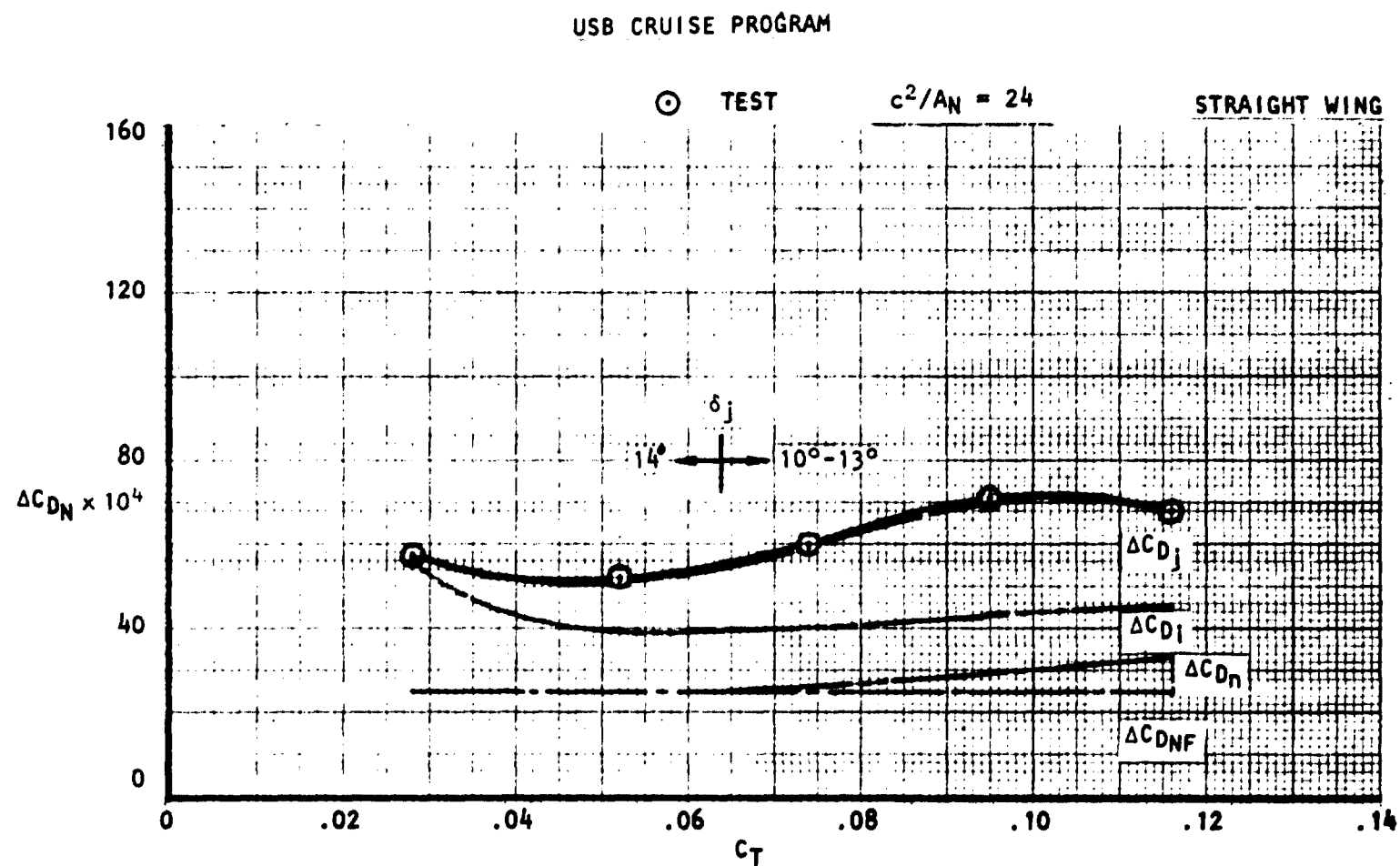


Figure 75. Incremental nacelle drag and component build-up  
 noz N<sub>3B</sub>, AR=2.5,  $M_\infty=0.68$ ,  $C_{LM}=0.40$ .

# USB CRUISE PROGRAM

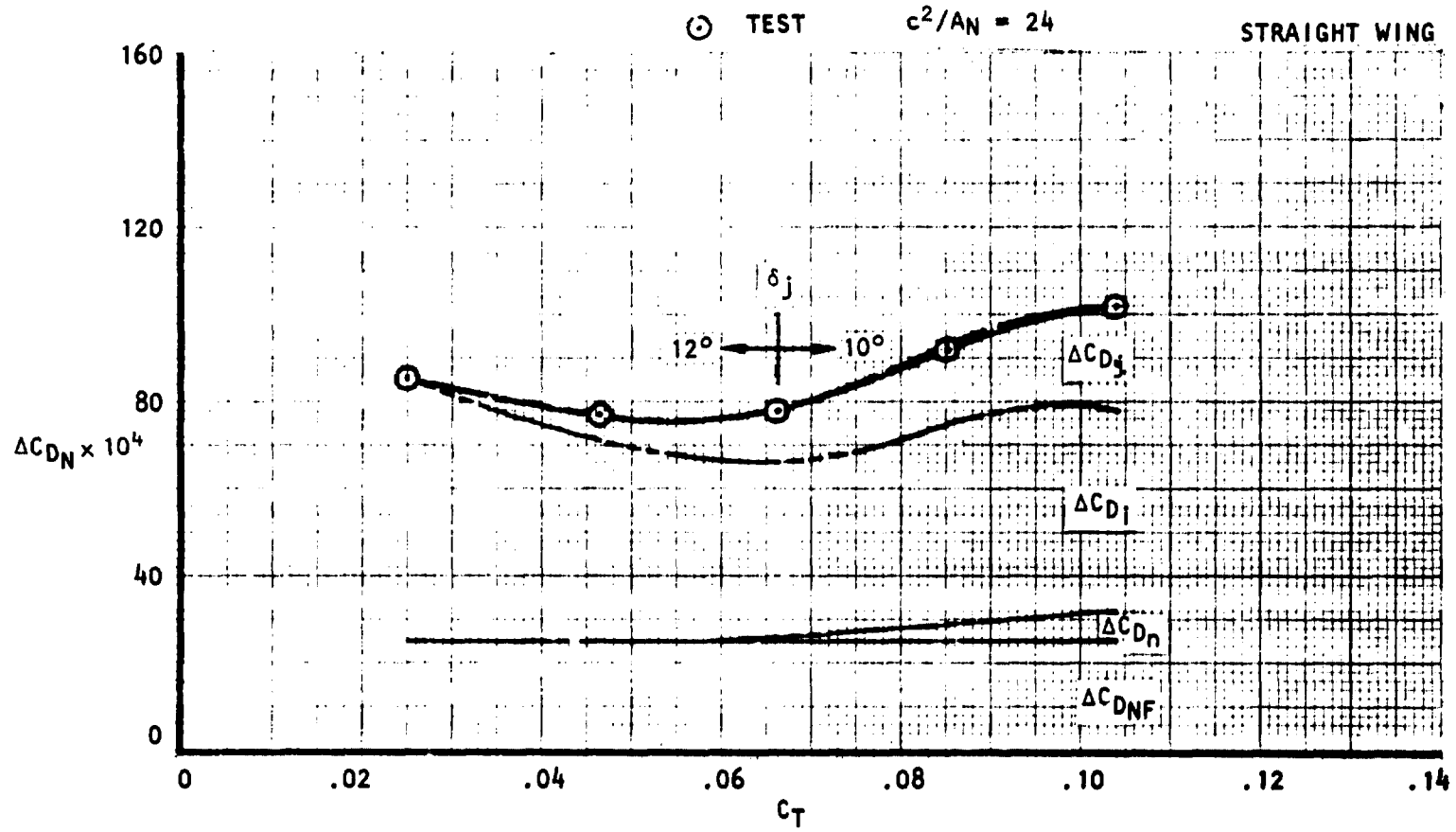


Figure 76. Incremental nacelle drag and component build-up  
 noz N<sub>3B</sub>, AR = 2.5,  $M_\infty = 0.72$ ,  $C_{LM} = 0.40$ .

ORIGINAL PAGE IS  
 OF POOR QUALITY

## USB CRUISE PROGRAM

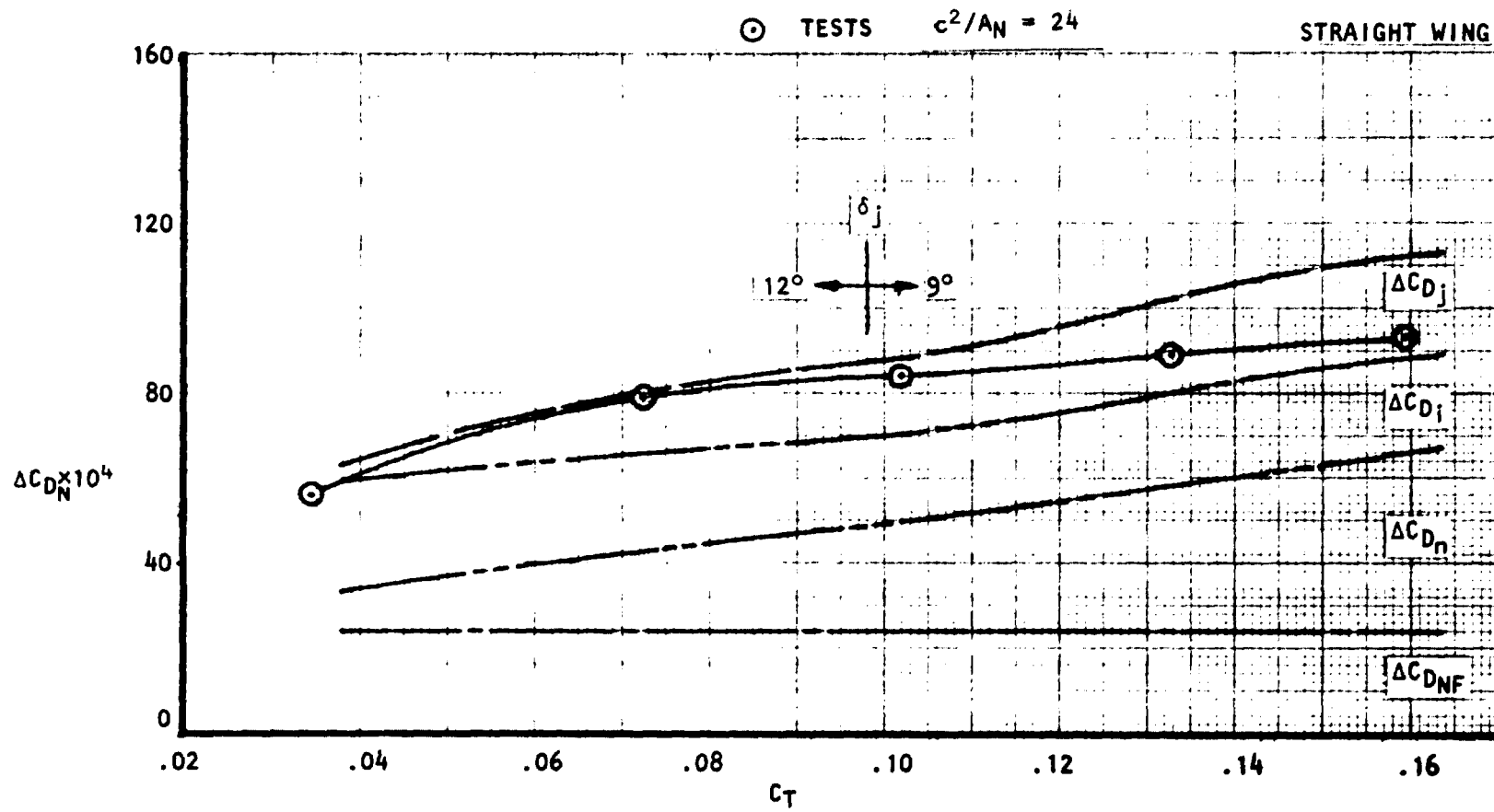


Figure 77. Incremental nacelle drag and component build-up  
noz  $N_4$ ,  $AR = 4$ ,  $M_\infty = 0.60$ ,  $C_{LM} = 0.40$ .

# USB CRUISE PROGRAM

⊙ TEST

$c^2/A_N = 24$

STRAIGHT WING

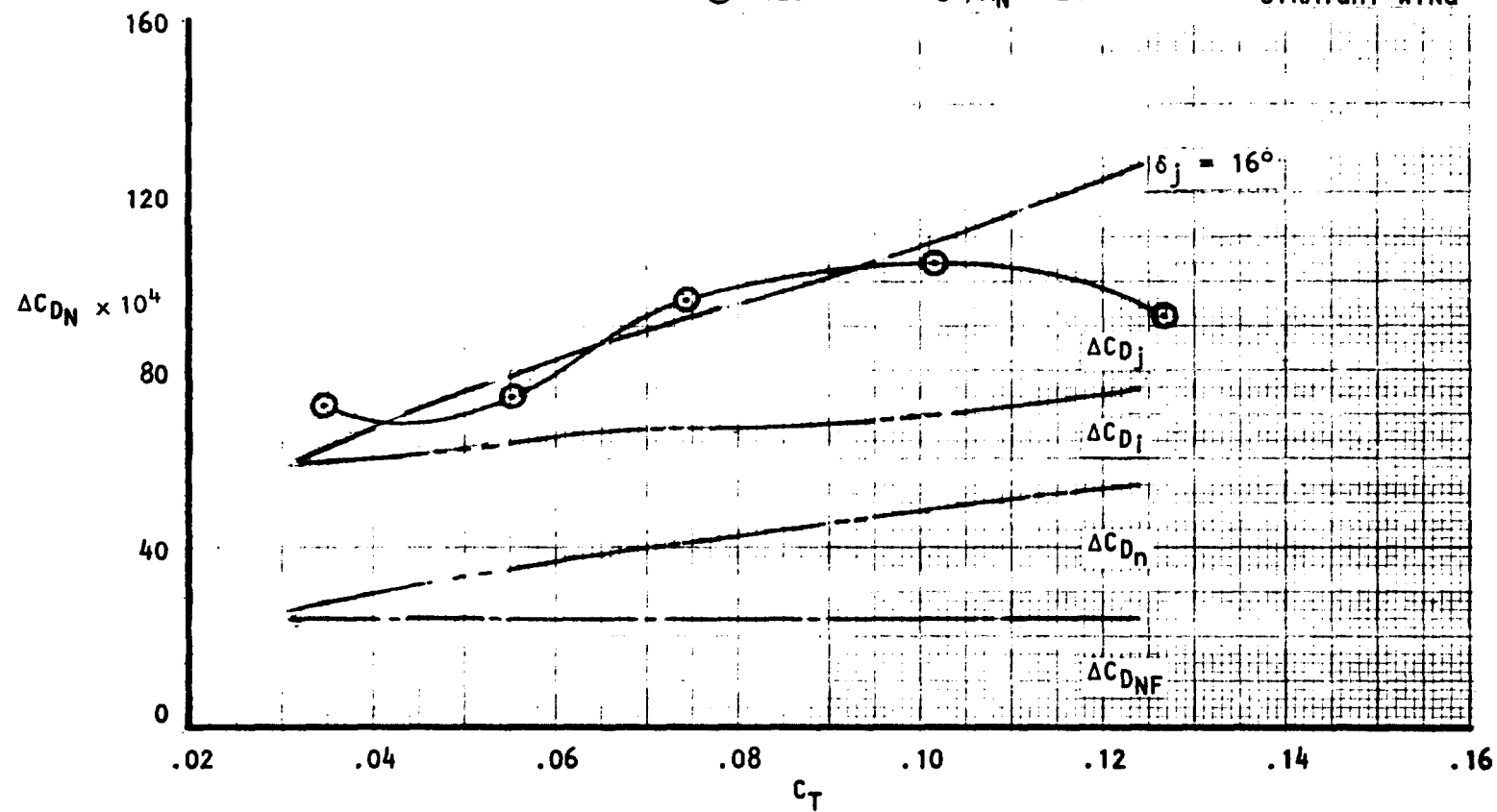


Figure 78. Incremental nacelle drag and component build-up  
noz  $N_4$ ,  $AR=4$ ,  $M_\infty=0.68$ ,  $C_{LM}=0.40$

ORIGINAL PAGE IS  
OF 1400 PAGES

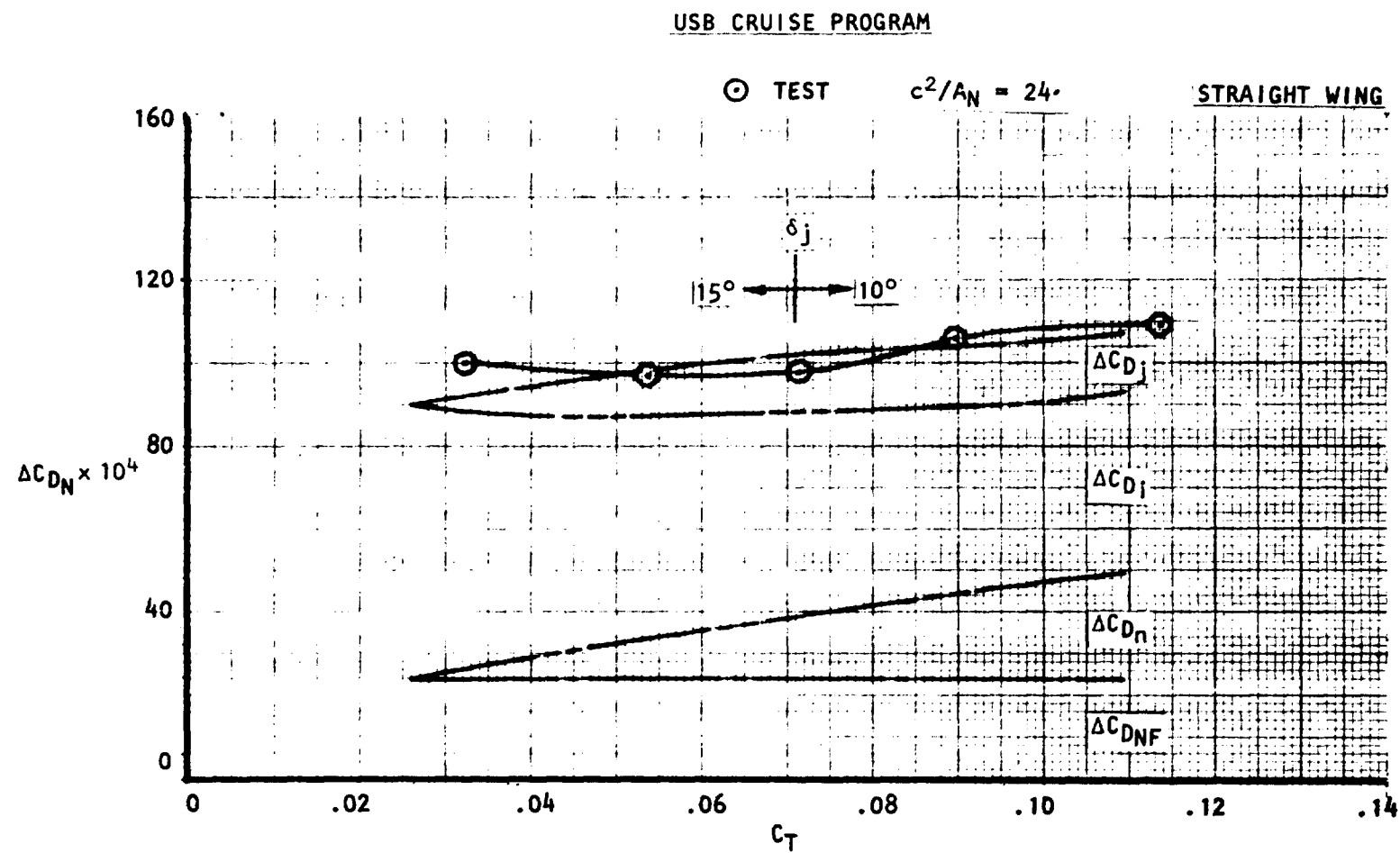


Figure 79 . Incremental nacelle drag and component build-up.  
noz  $N_4$ ,  $AR = 4$ ,  $M_\infty = 0.72$ ,  $C_{LM} = 0.40$

# USB CRUISE PROGRAM

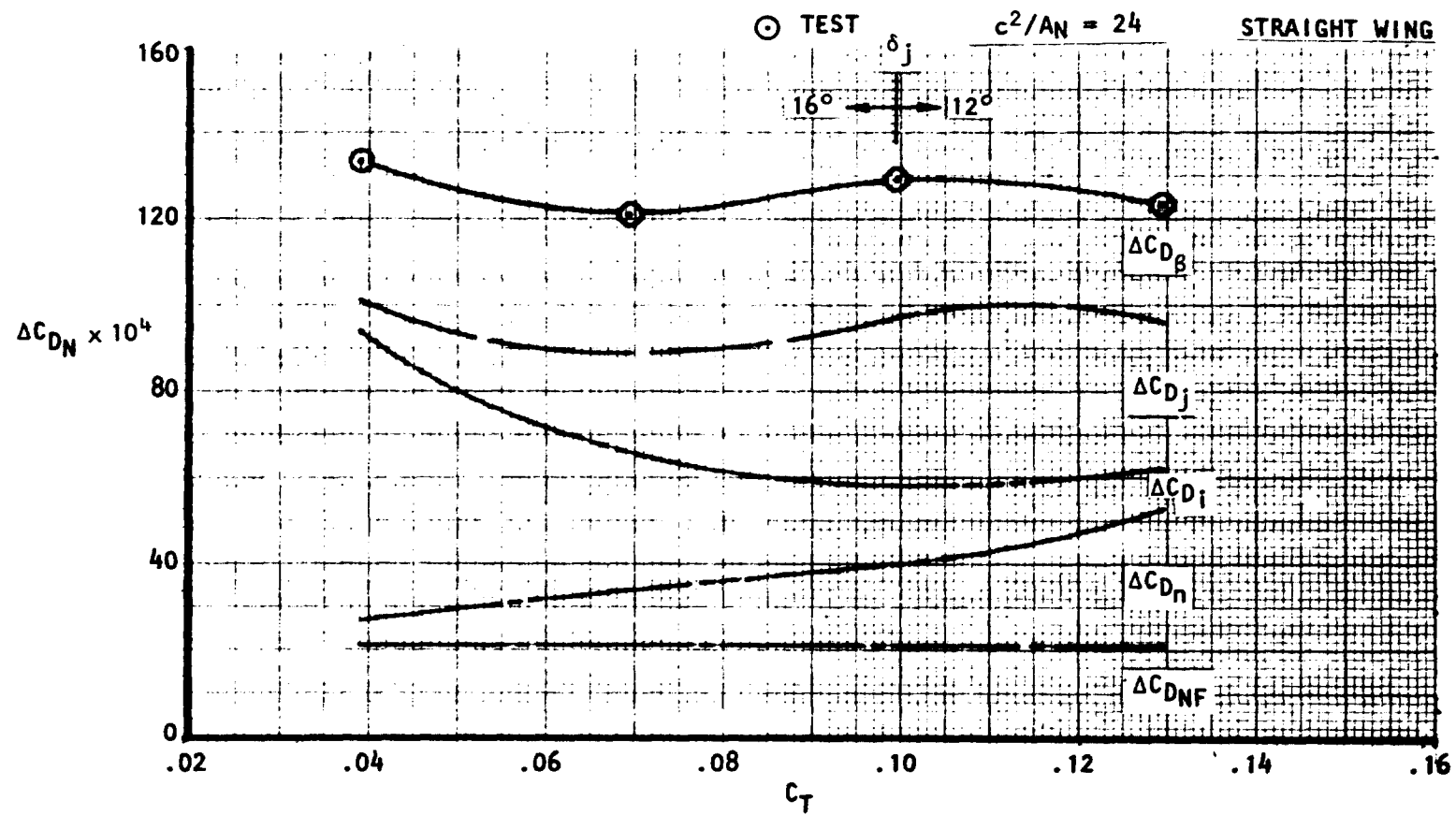


Figure 80 . Incremental nacelle drag and component build-up  
noz  $N_{4E}$ ,  $AR = 4$ ,  $M_\infty = 0.60$ ,  $C_{LM} = 0.40$ .



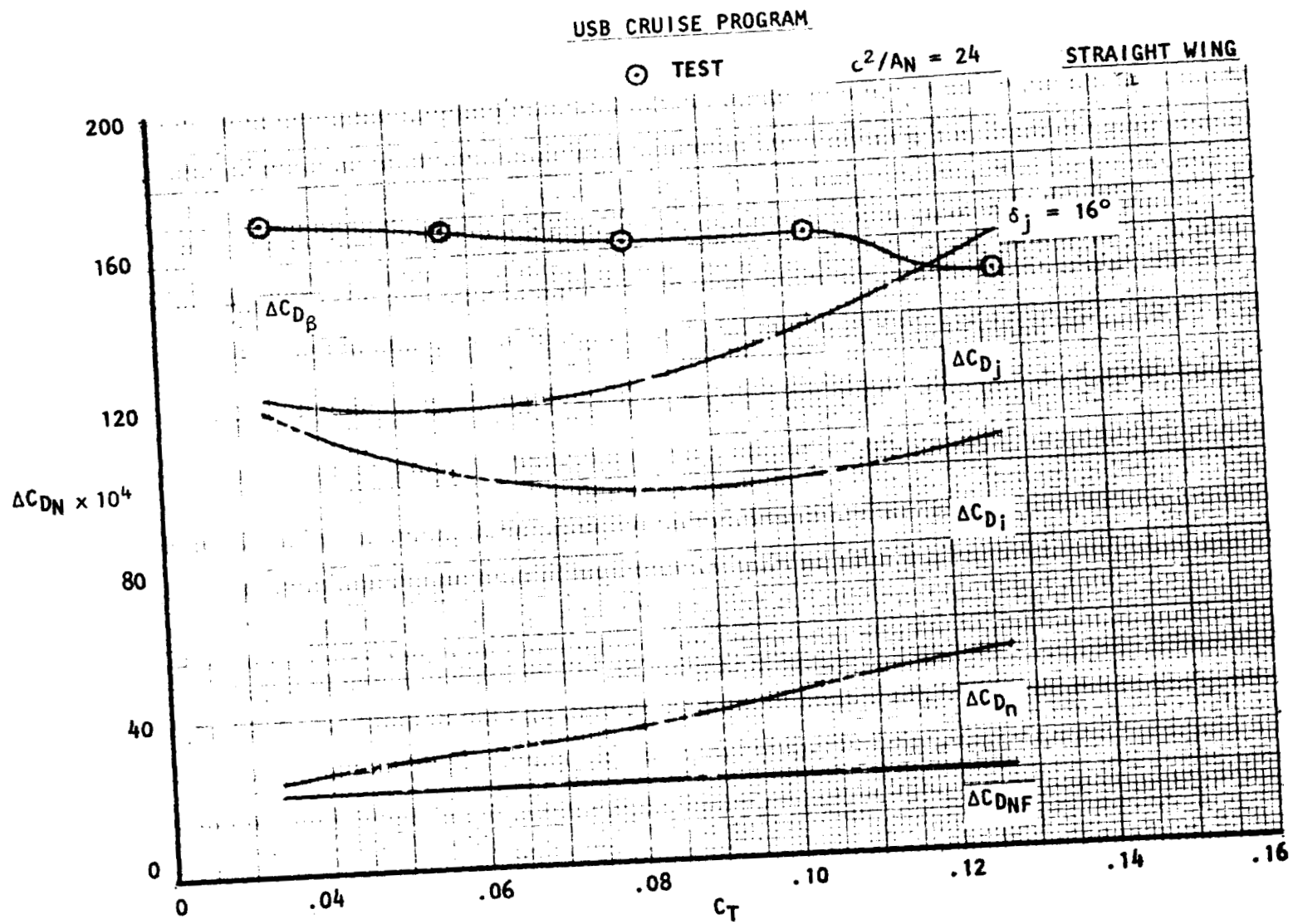


Figure 81. Incremental nacelle drag and component build-up  
noz N<sub>4E</sub>, AR = 4,  $M_\infty = 0.68$ ,  $C_{LM} = 0.40$ .

# USB CRUISE PROGRAM

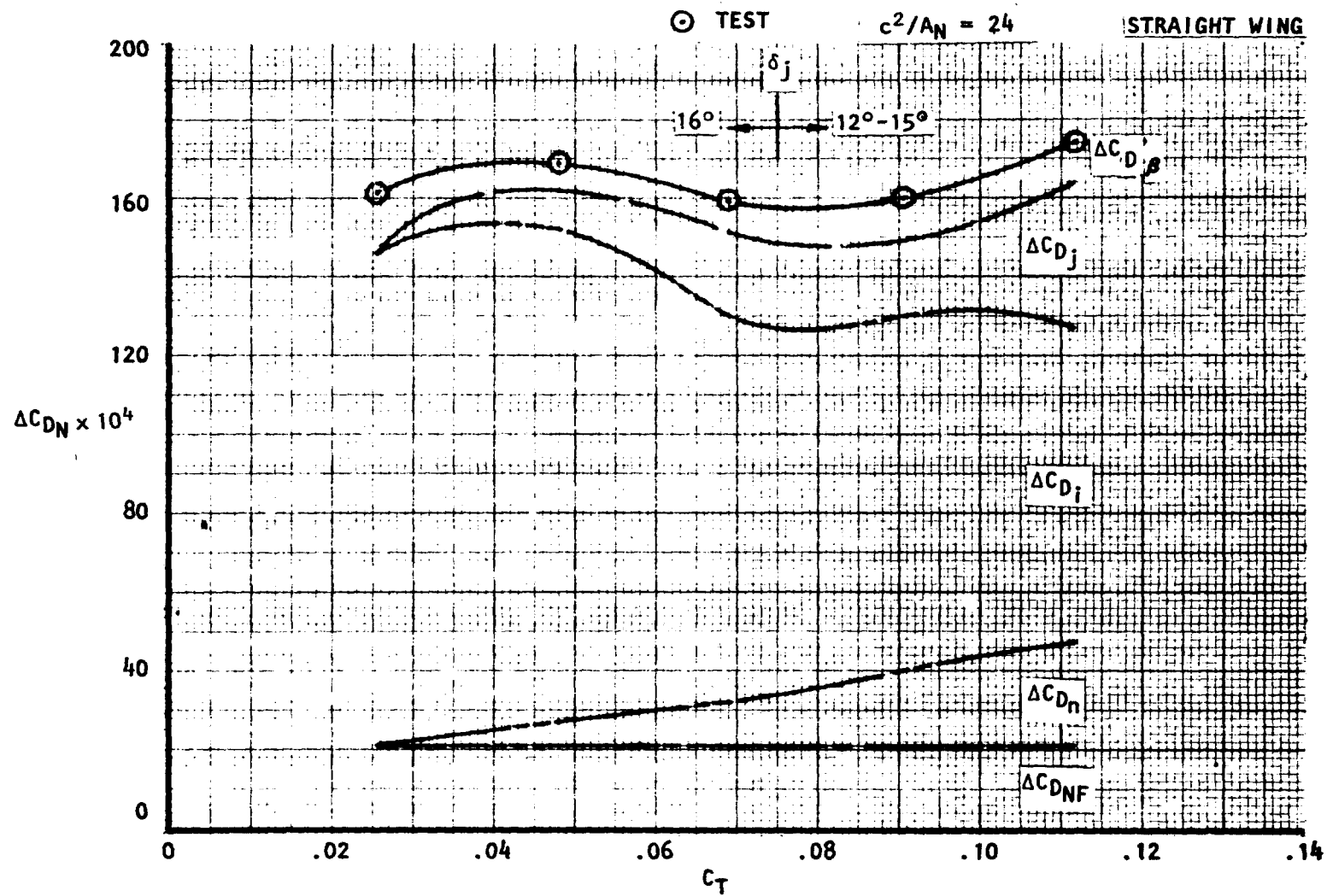


Figure 82 . Incremental nacelle drag and component build-up  
noz  $N_{4E}$ ,  $AR=4$ ,  $M_\infty=0.72$ ,  $C_{LM}=0.40$ .

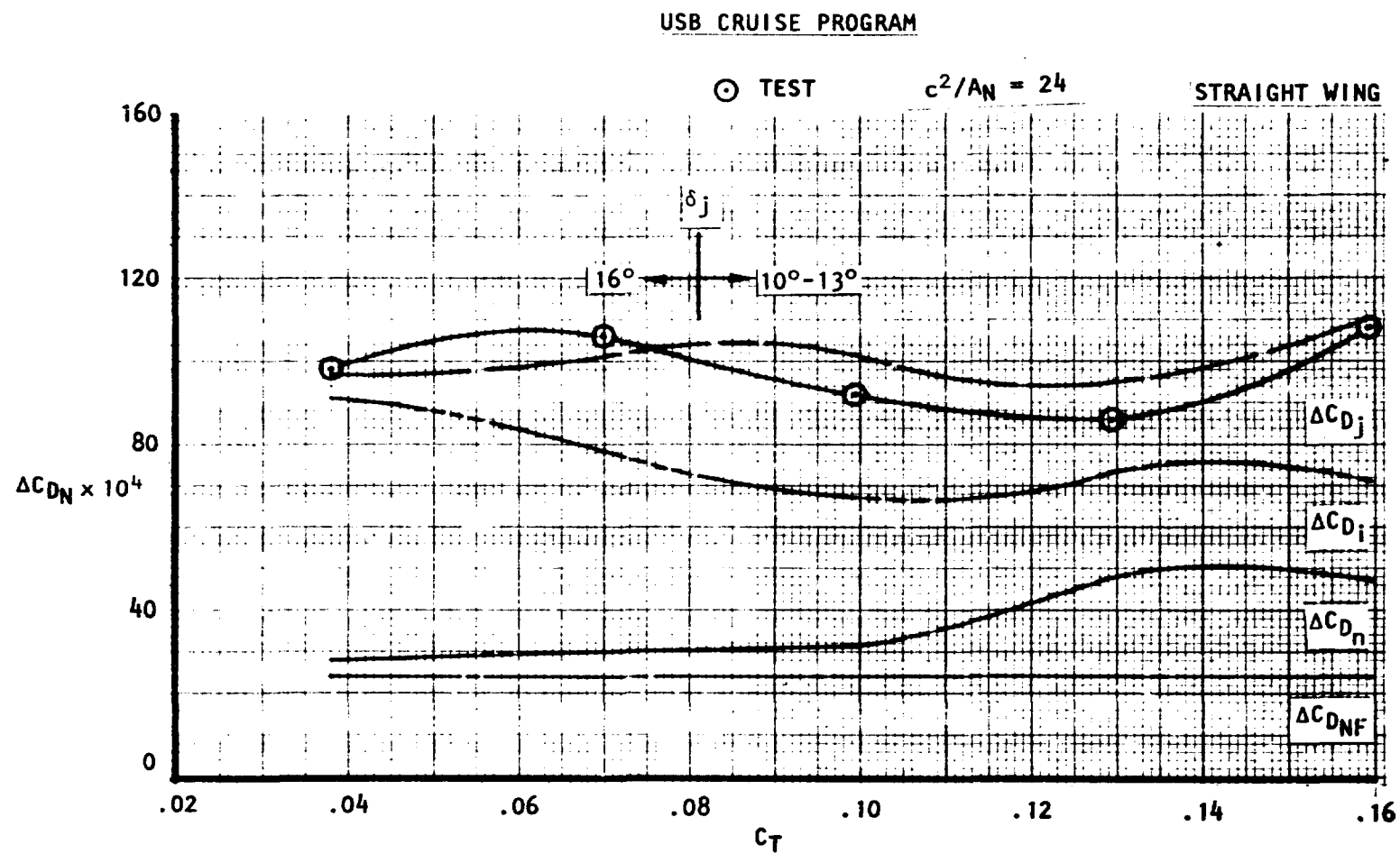


Figure 83. Incremental nacelle drag and component build-up  
noz  $N_5$ ,  $AR = 6$ ,  $M_\infty = 0.60$ ,  $C_{LM} = 0.40$ .

# USB CRUISE PROGRAM

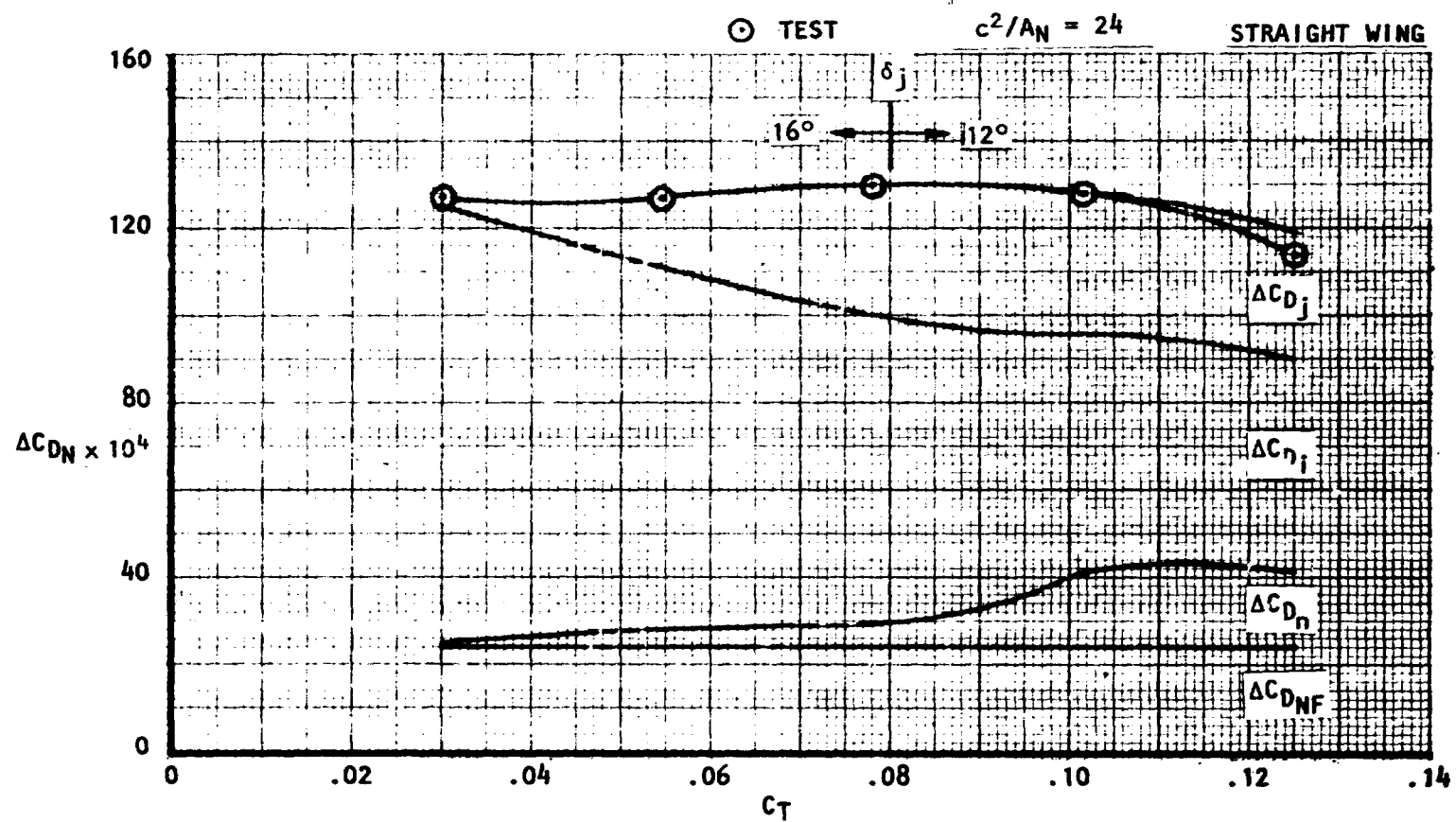


Figure 84. Incremental nacelle drag and component build-up  
noz N<sub>5</sub>, AR = 6,  $V_\infty = 0.68$ ,  $C_{LM} = 0.40$

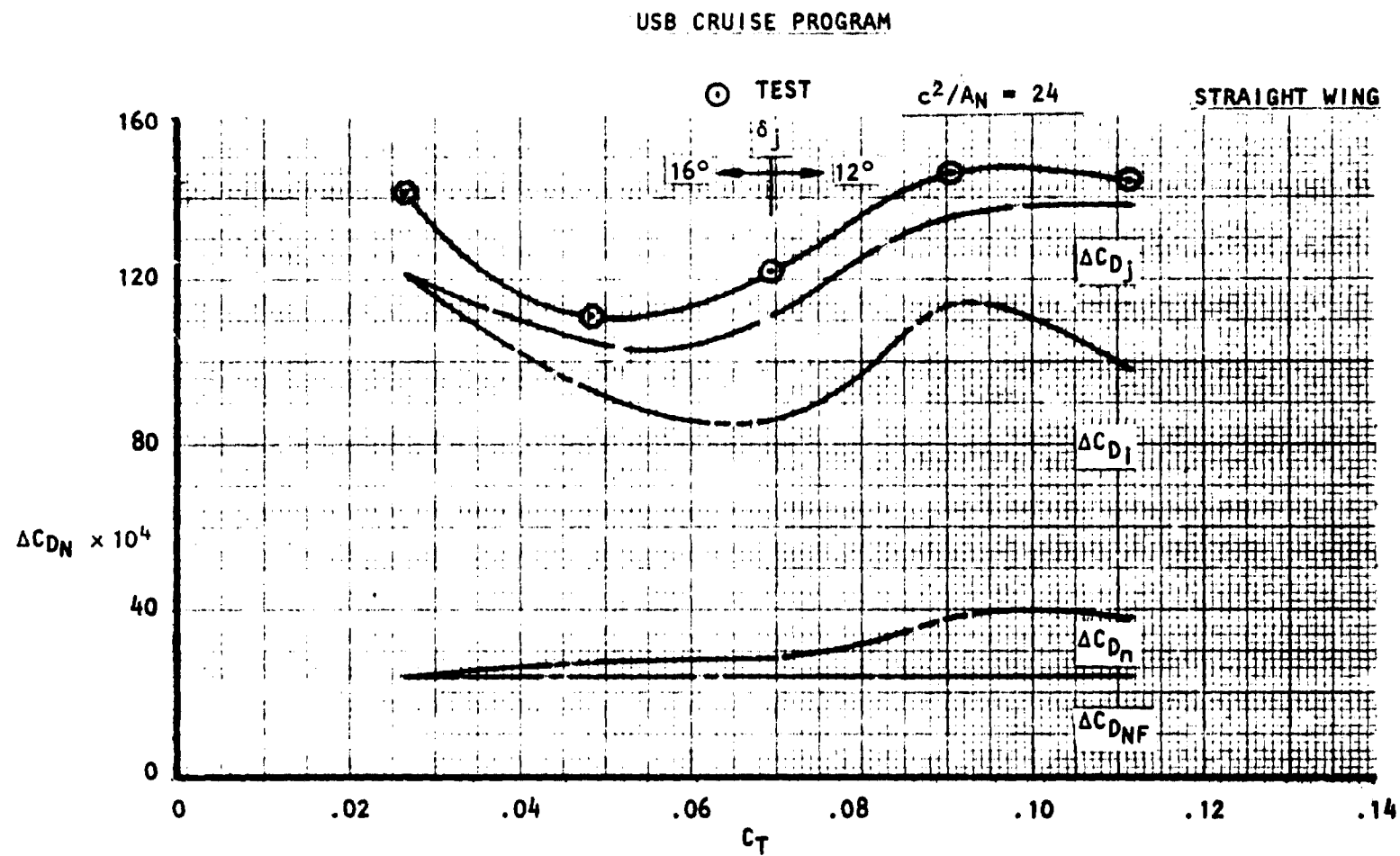


Figure 85. Incremental nacelle drag and component build-up  
noz N<sub>5</sub>, AR = 6,  $M_\infty = 0.72$ ,  $C_{LM} = 0.40$ .

# USB CRUISE PROGRAM

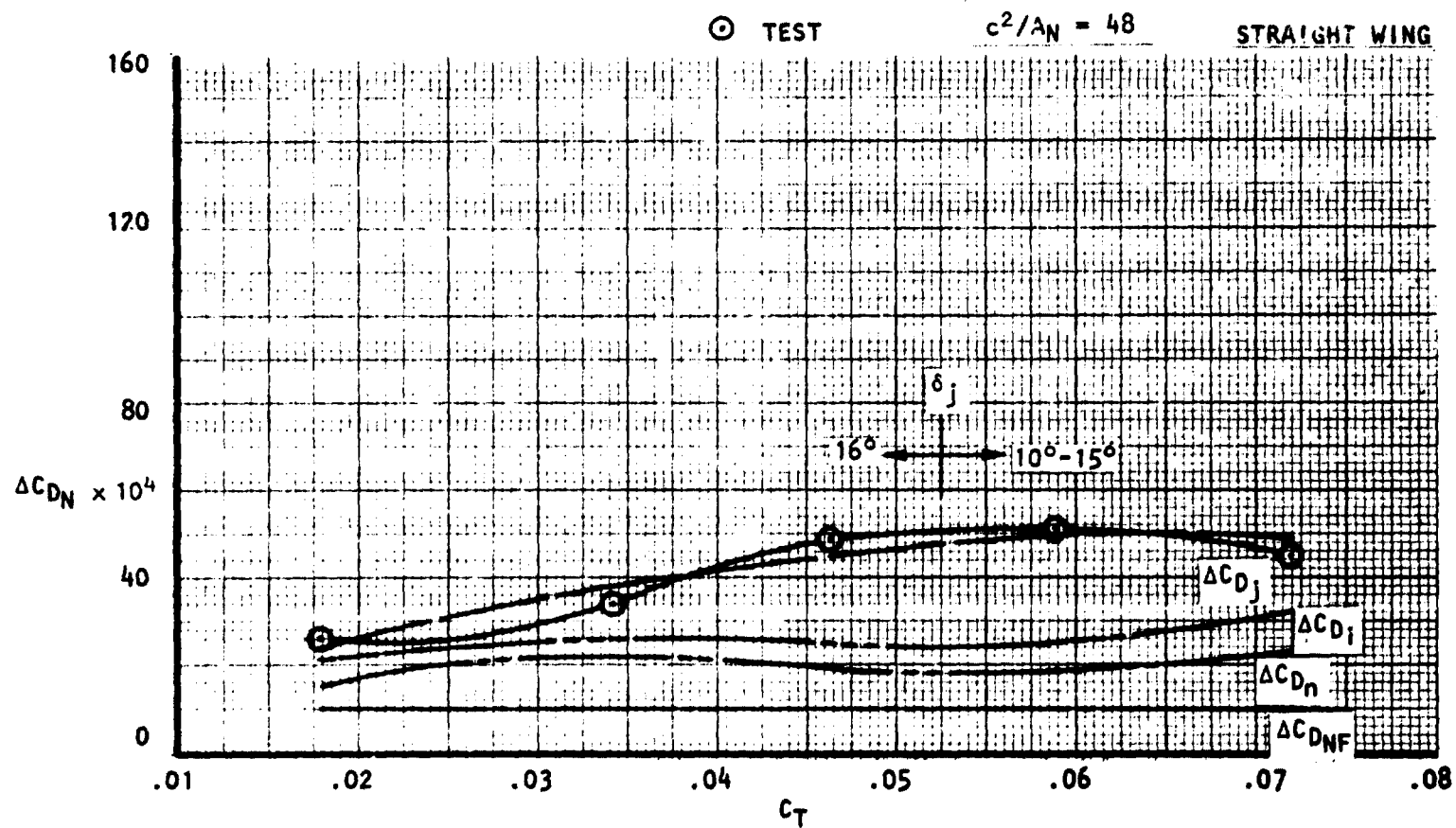


Figure 86. Incremental nacelle drag and component build-up  
noz  $N_6$ ,  $AR = 2.5$ ,  $M_\infty = 0.60$ ,  $C_{LM} = 0.40$ .

ORIGINAL PAGE IS  
OF POOR QUALITY

## USB CRUISE PROGRAM

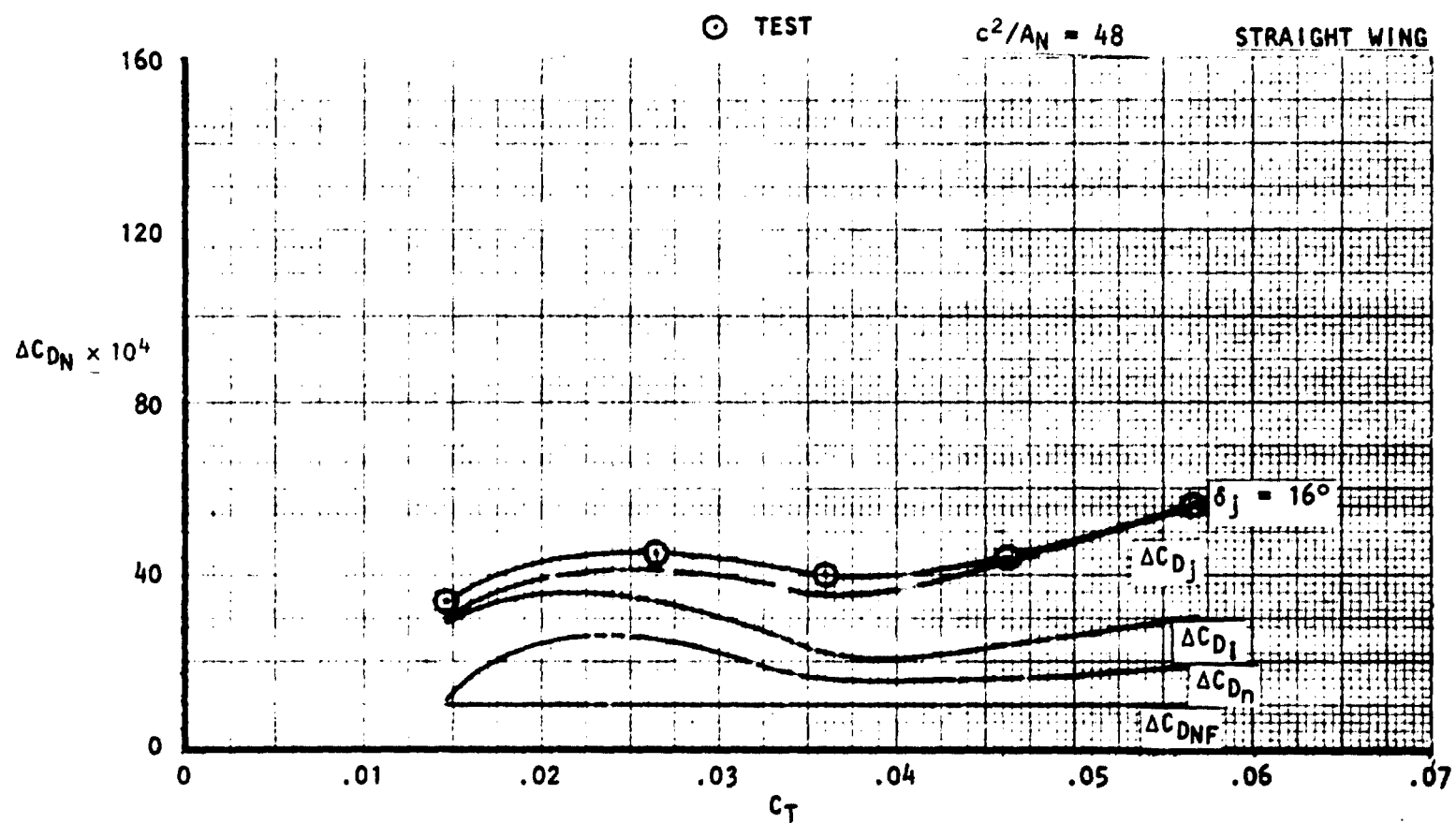


Figure 87 . Incremental nacelle drag and component build-up,  
noz N<sub>6</sub>, AR = 2.5,  $M_\infty = 0.68$ ,  $CL_M = 0.40$ .

# USB CRUISE PROGRAM

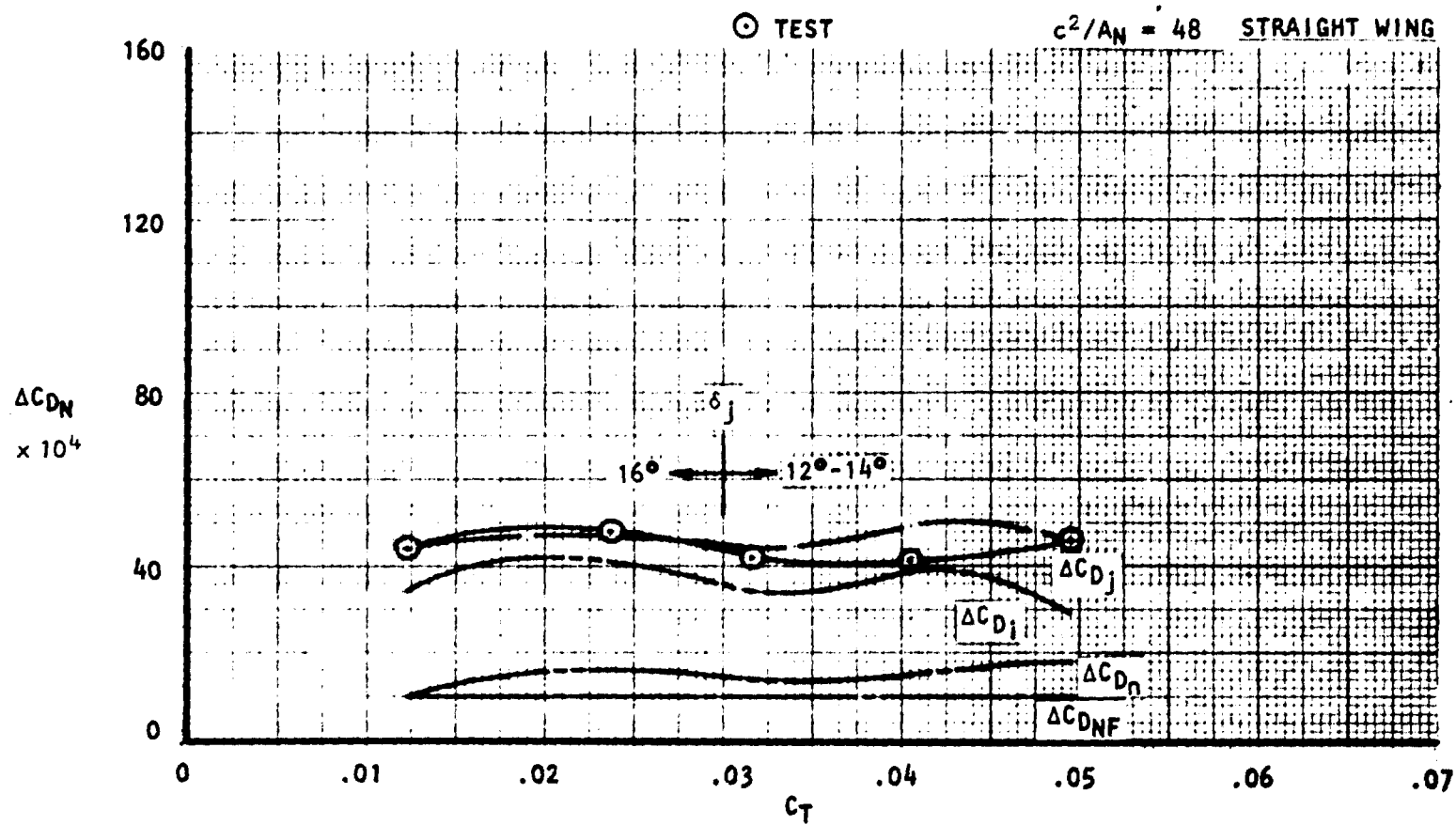


Figure 88 . Incremental nacelle drag and component build-up, noz  $N_6$ ,  $AR = 2.5$ ,  $M_\infty = 0.72$ ,  $CL_M = 0.40$ .



## USB CRUISE PROGRAM

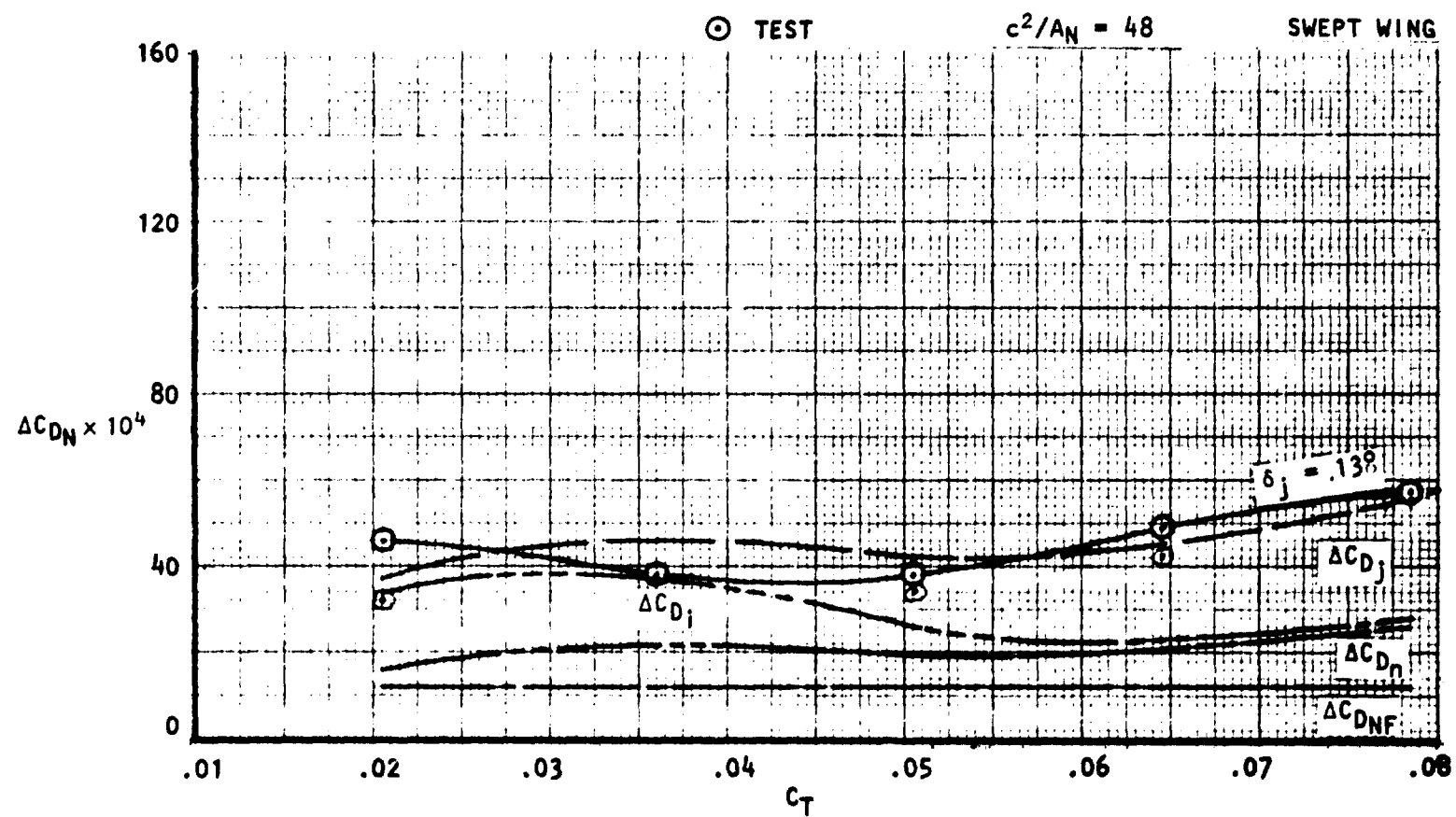


Figure 89 . Incremental nacelle drag and component build-up,  
 noz  $N_g^2$ ,  $AR = 2.5$ ,  $M_\infty = 0.60$ ,  $C_{LM} = 0.40$ .

# USB CRUISE PROGRAM

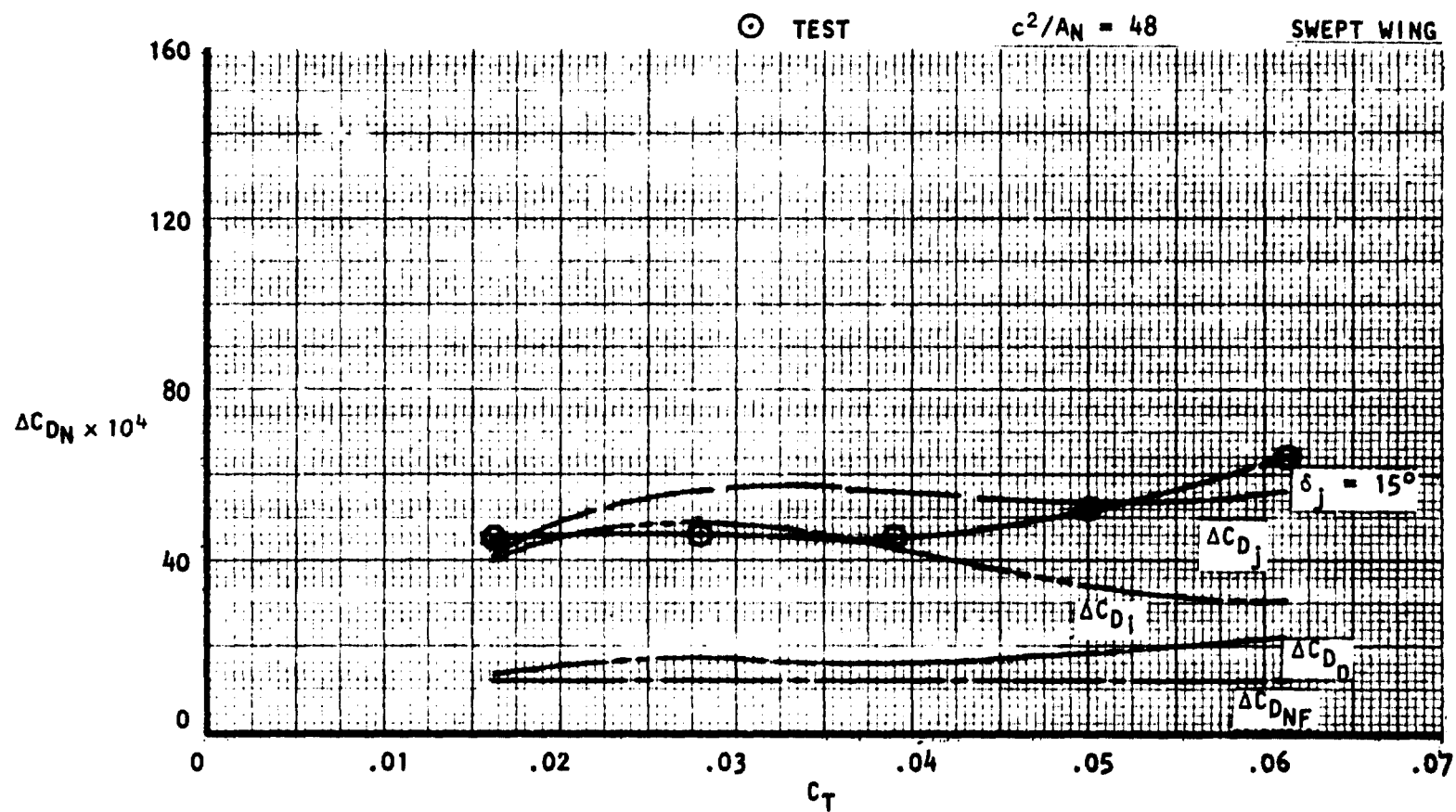


Figure 90 . Incremental nacelle drag and component build-up, noz  $N_8^2$ ,  $AR = 2.5$ ,  $M_\infty = 0.68$ ,  $C_{LM} = 0.40$ .

## USB CRUISE PROGRAM

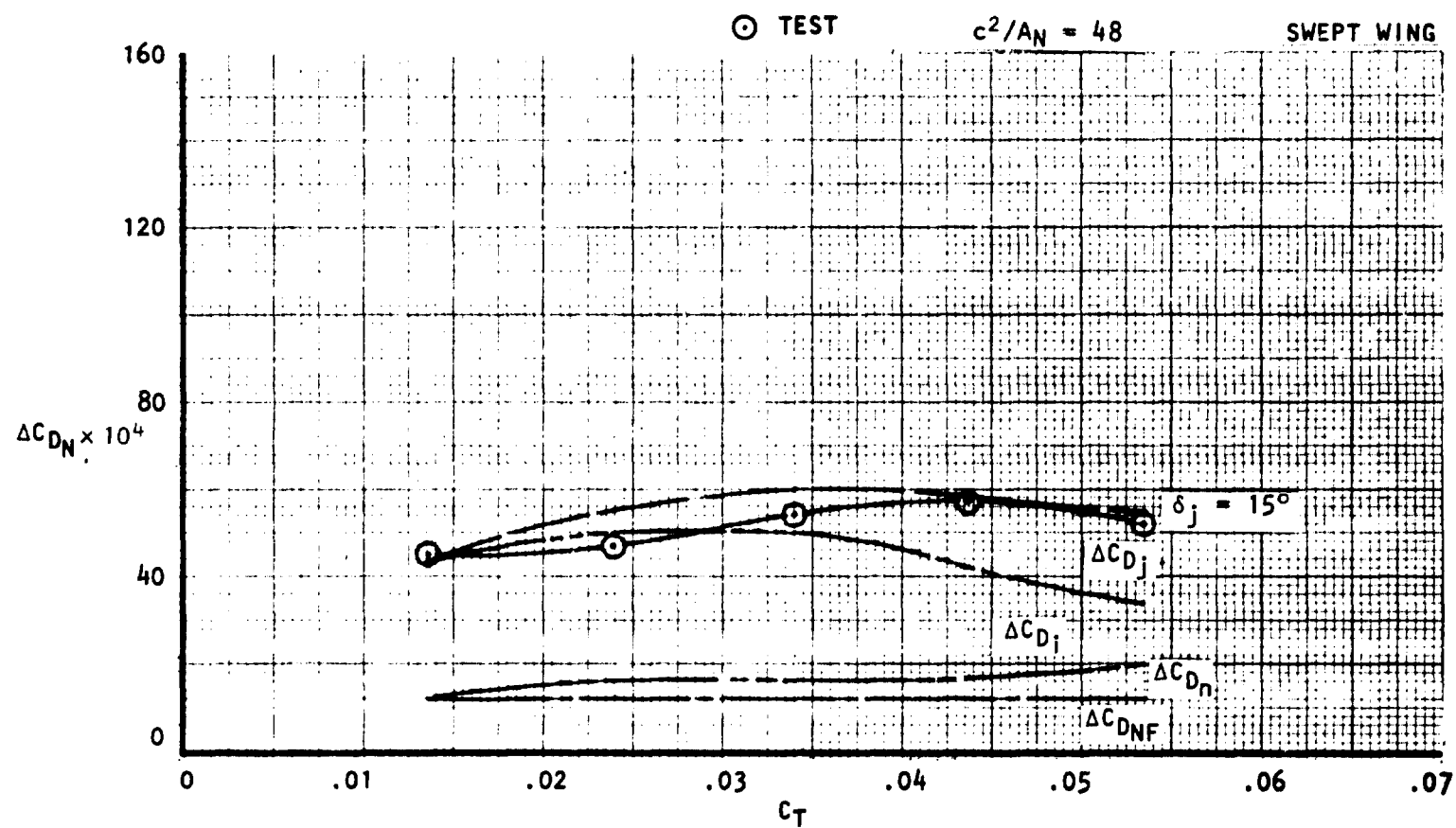


Figure 91 . Incremental nacelle drag and component build-up,  
noz  $N_8^2$ ,  $AR = 2.5$ ,  $M_\infty = 0.73$ ,  $CL_M = 0.40$ .

# USB CRUISE PROGRAM

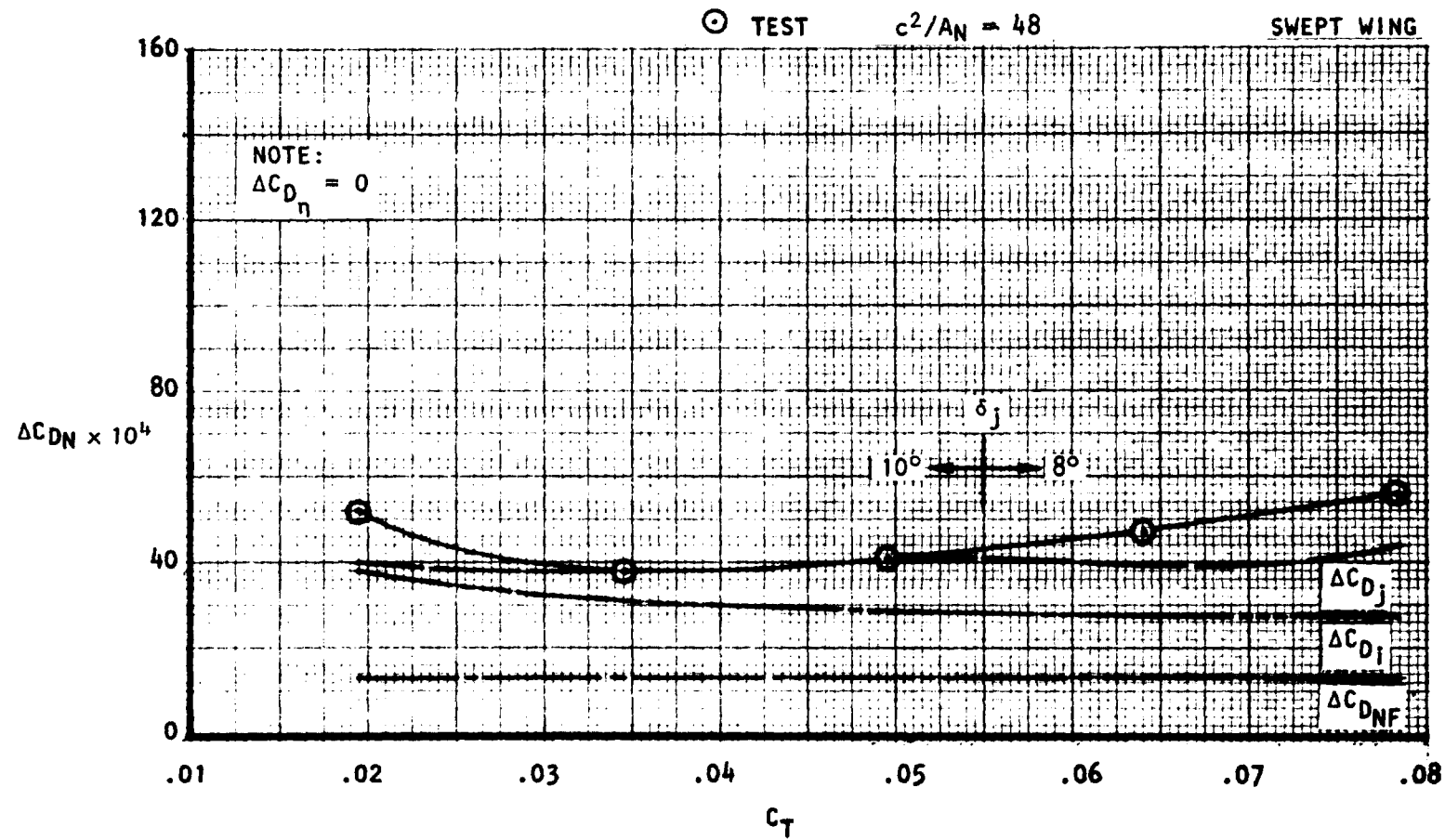


Figure 92 . Incremental nacelle drag and component build-up, noz N<sub>11</sub>, circular,  $M_\infty = 0.60$ ,  $C_{LM} = 0.40$ .

## USB CRUISE PROGRAM

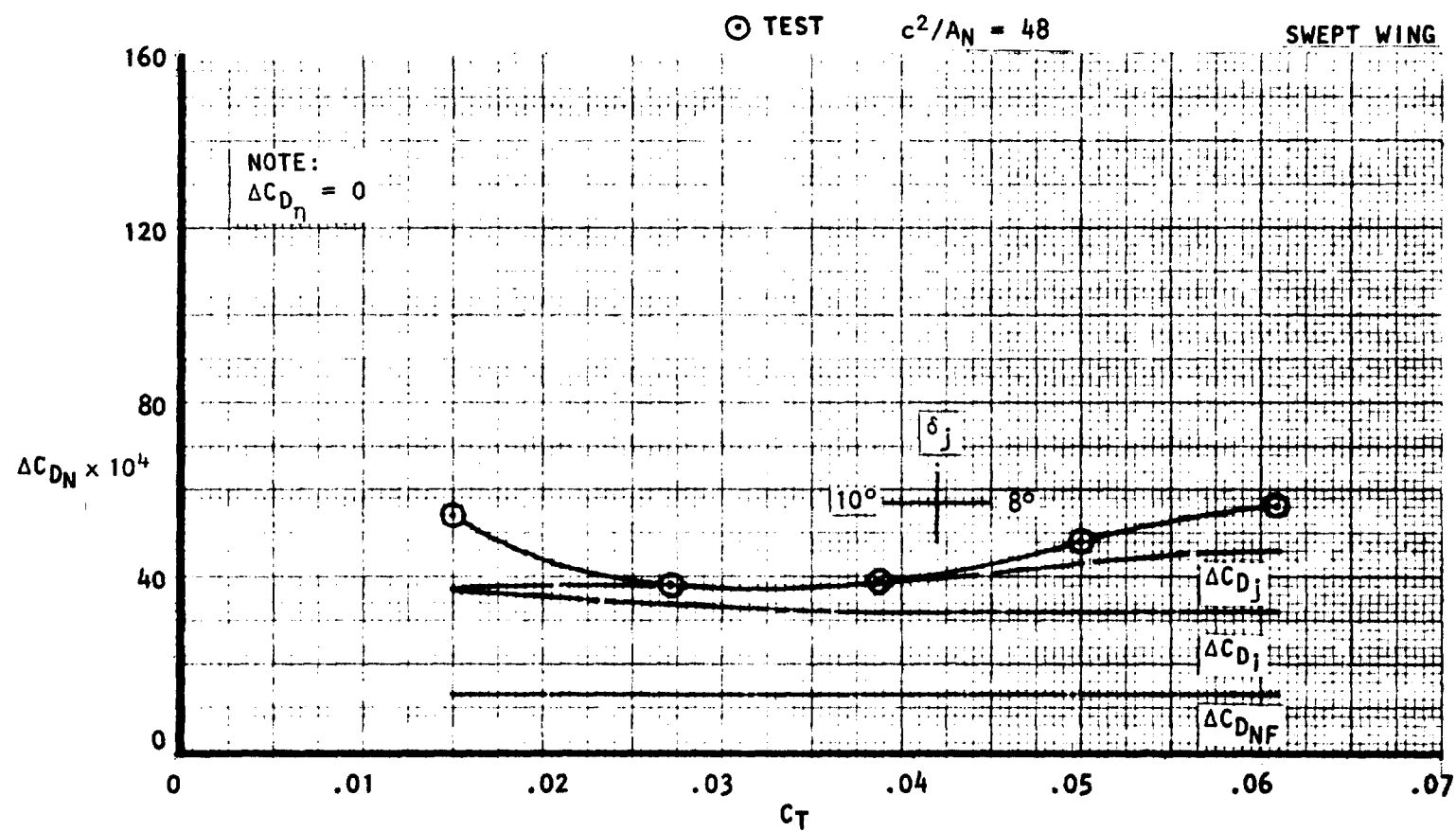


Figure 93 . Incremental nacelle drag and component build-up,  
noz N<sub>11</sub>, circular,  $M_\infty = 0.68$ ,  $C_{LM} = 0.40$ .

# USB CRUISE PROGRAM

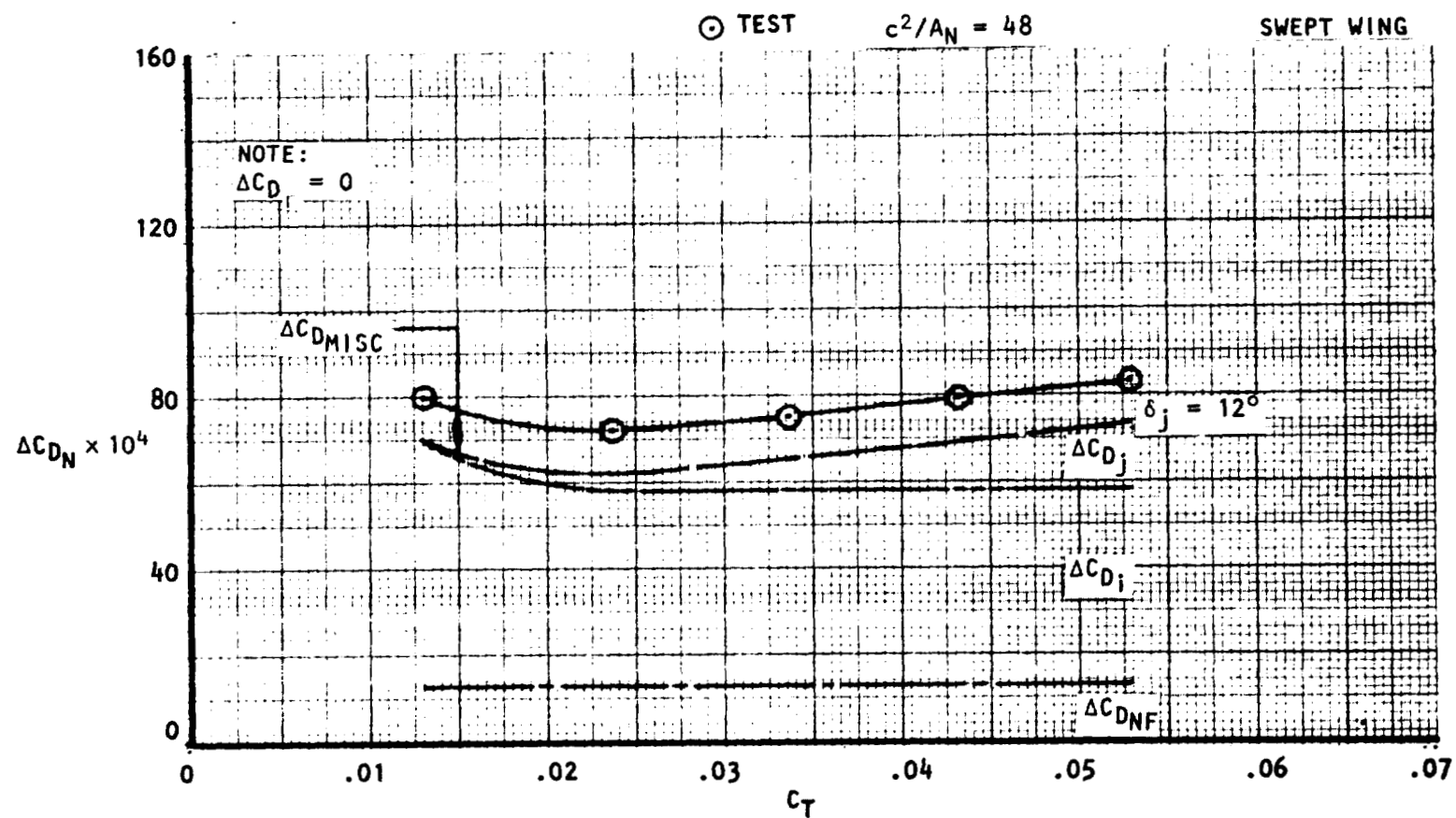


Figure 94 . Incremental nacelle drag and component build-up, noz N<sub>11</sub>, circular,  $M_\infty = 0.73$ ,  $C_{LM} = 0.40$ .

## USB CRUISE PROGRAM

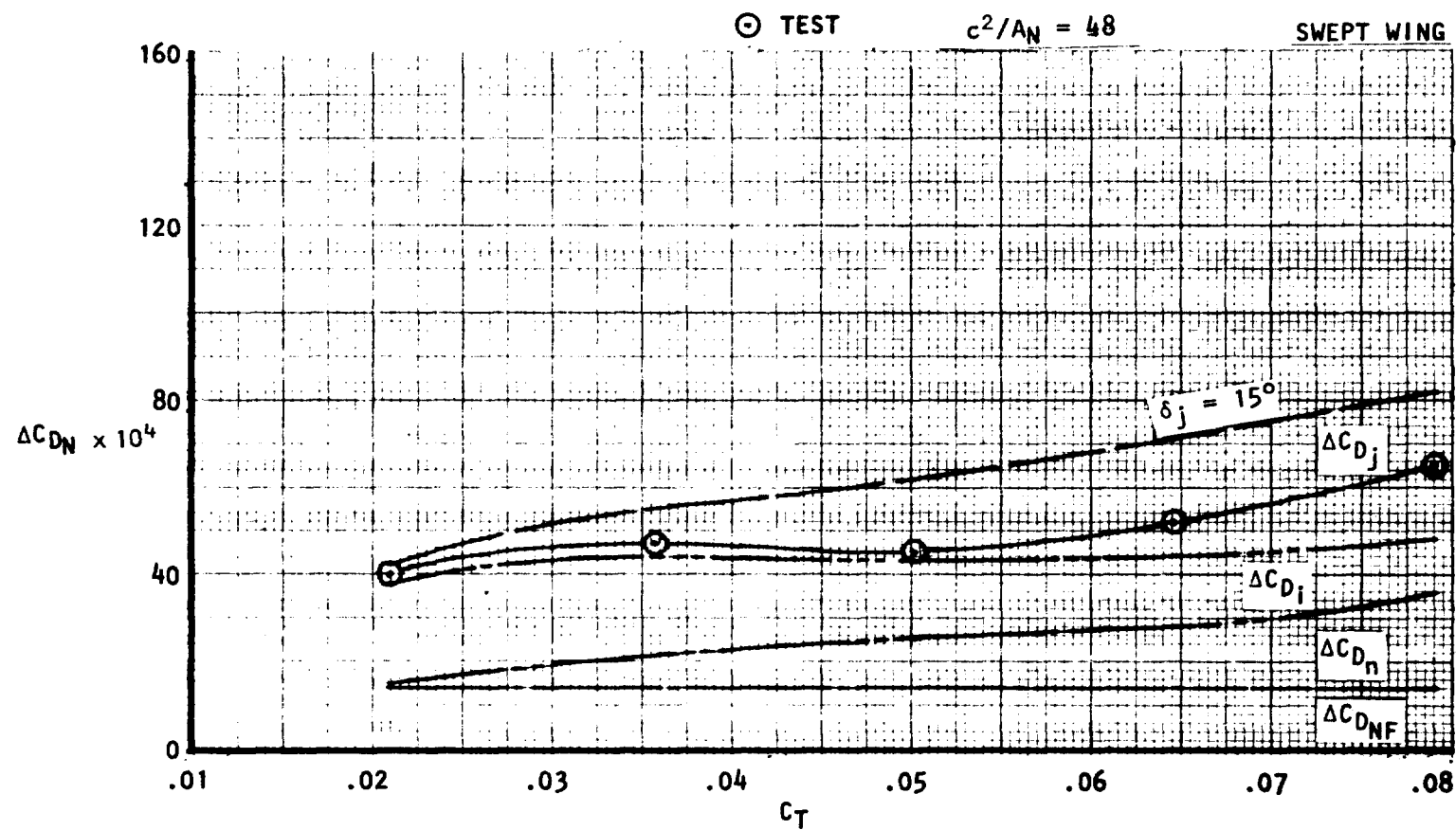


Figure 95 . Incremental nacelle drag and component build-up,  
noz N<sub>12</sub>, AR = 4.0,  $M_\infty = 0.60$ ,  $C_{LM} = 0.40$ .

# USB CRUISE PROGRAM

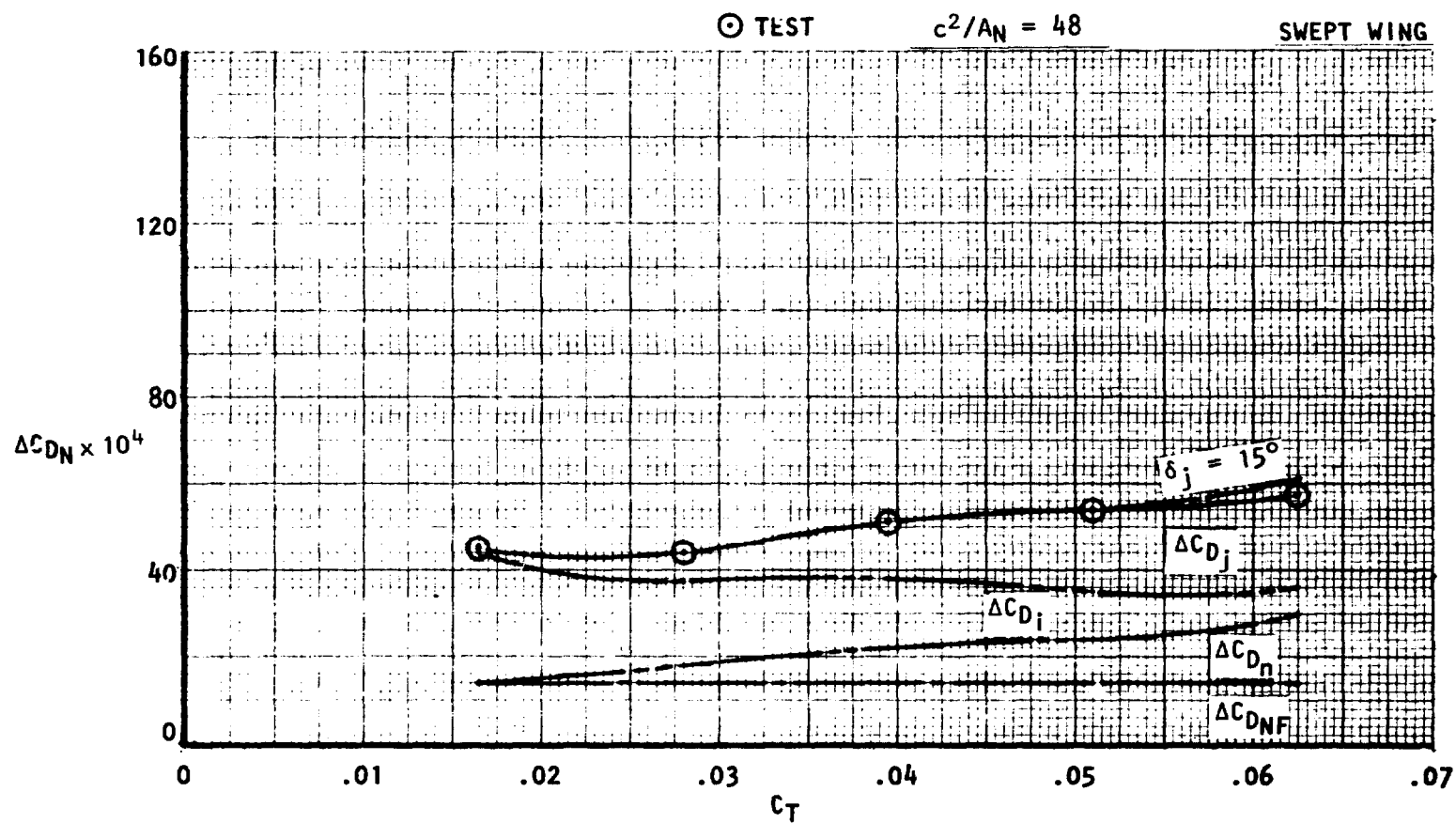


Figure 96 . Incremental nacelle drag and component build-up, noz N12, AR = 4.0,  $M_\infty = 0.68$ ,  $C_{LM} = 0.40$ .



## USB CRUISE PROGRAM

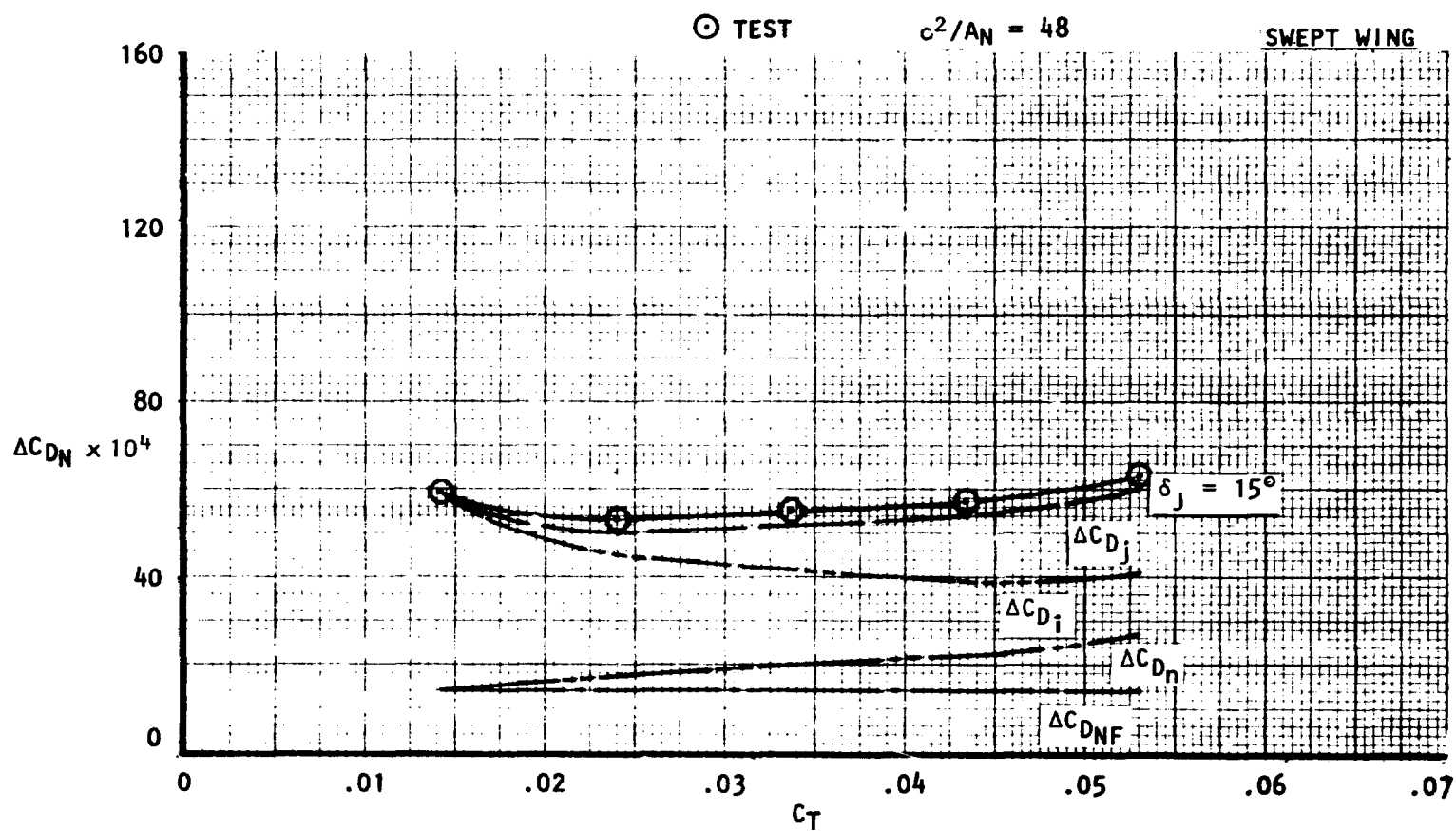


Figure 97 Incremental nacelle drag and component build-up,  
noz  $N_{12}$ ,  $AR = 4$ ,  $M_\infty = 0.73$ ,  $C_{LM} = 0.40$ .

# USB CRUISE PROGRAM

⊙ TEST

$c^2/A_N = 48$

SWEPT WING

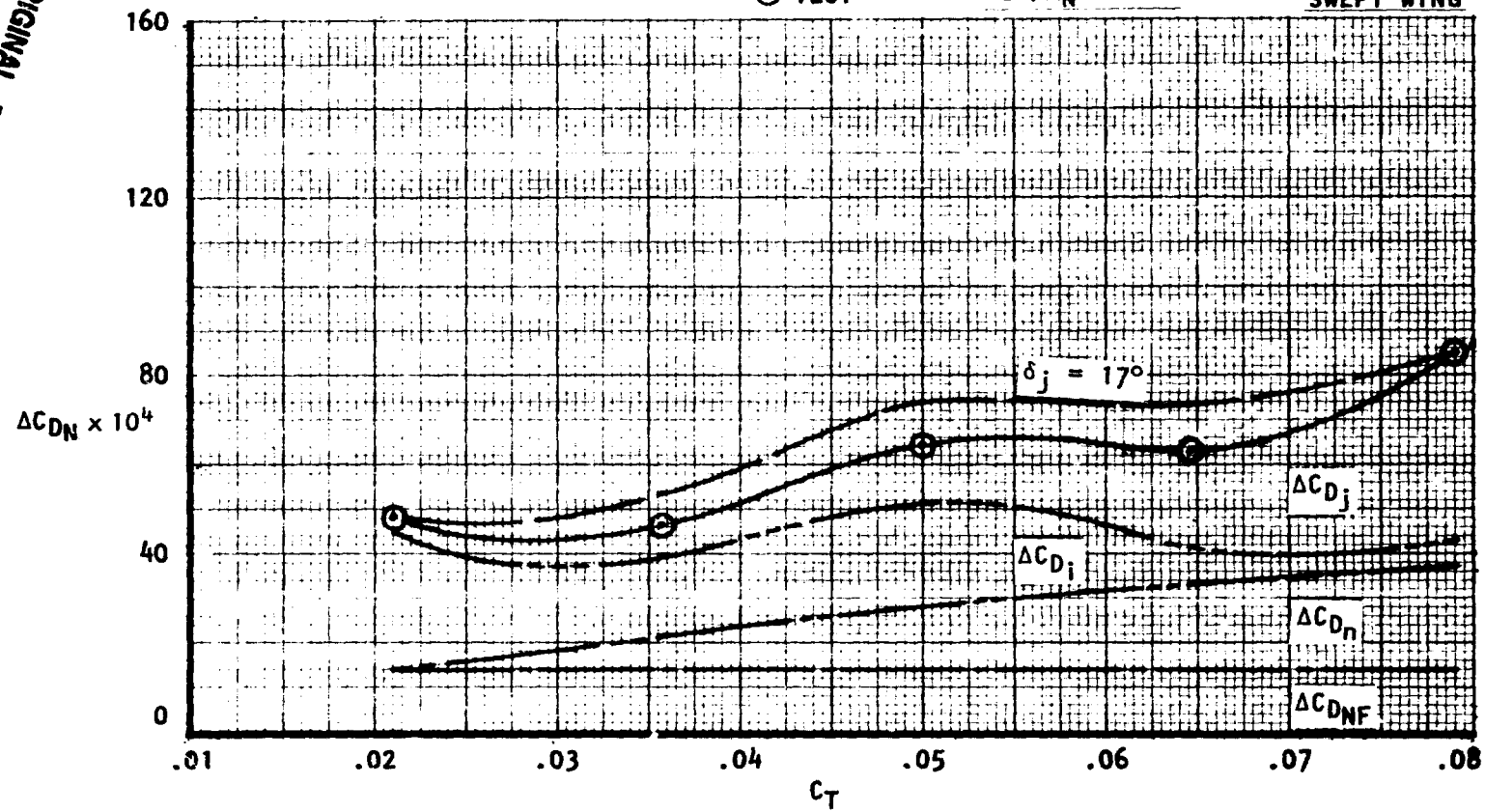


Figure 98 . Incremental nacelle drag and component build-up, noz N<sub>13</sub>, AR = 6,  $M_\infty = 0.60$ ,  $C_{LM} = 0.40$ .

## USB CRUISE PROGRAM

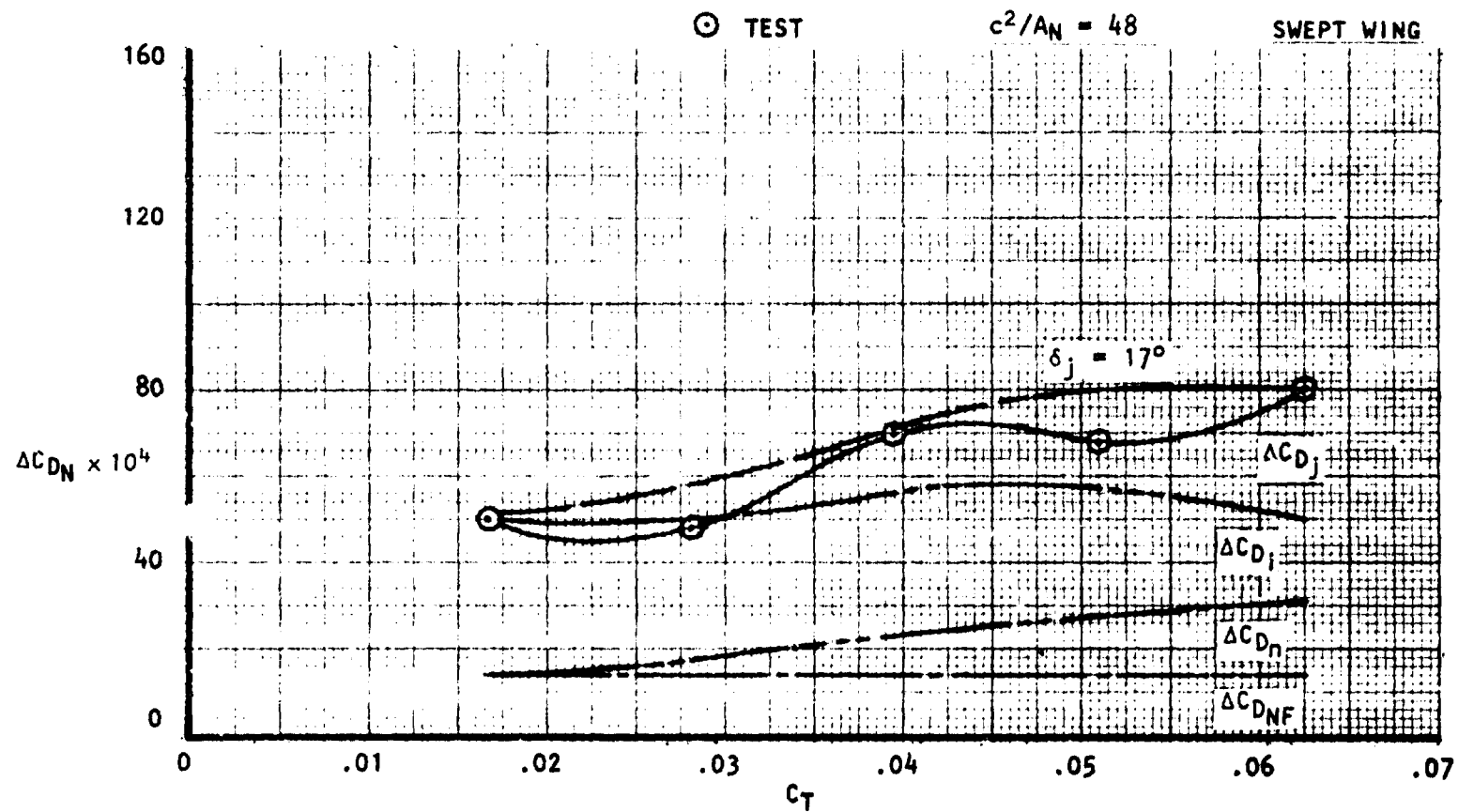


Figure 99 . Incremental nacelle drag and component build-up,  
noz  $N_{13}$ ,  $AR = 6$ ,  $M_\infty = 0.68$ ,  $C_{LM} = 0.40$ .

# USB CRUISE PROGRAM

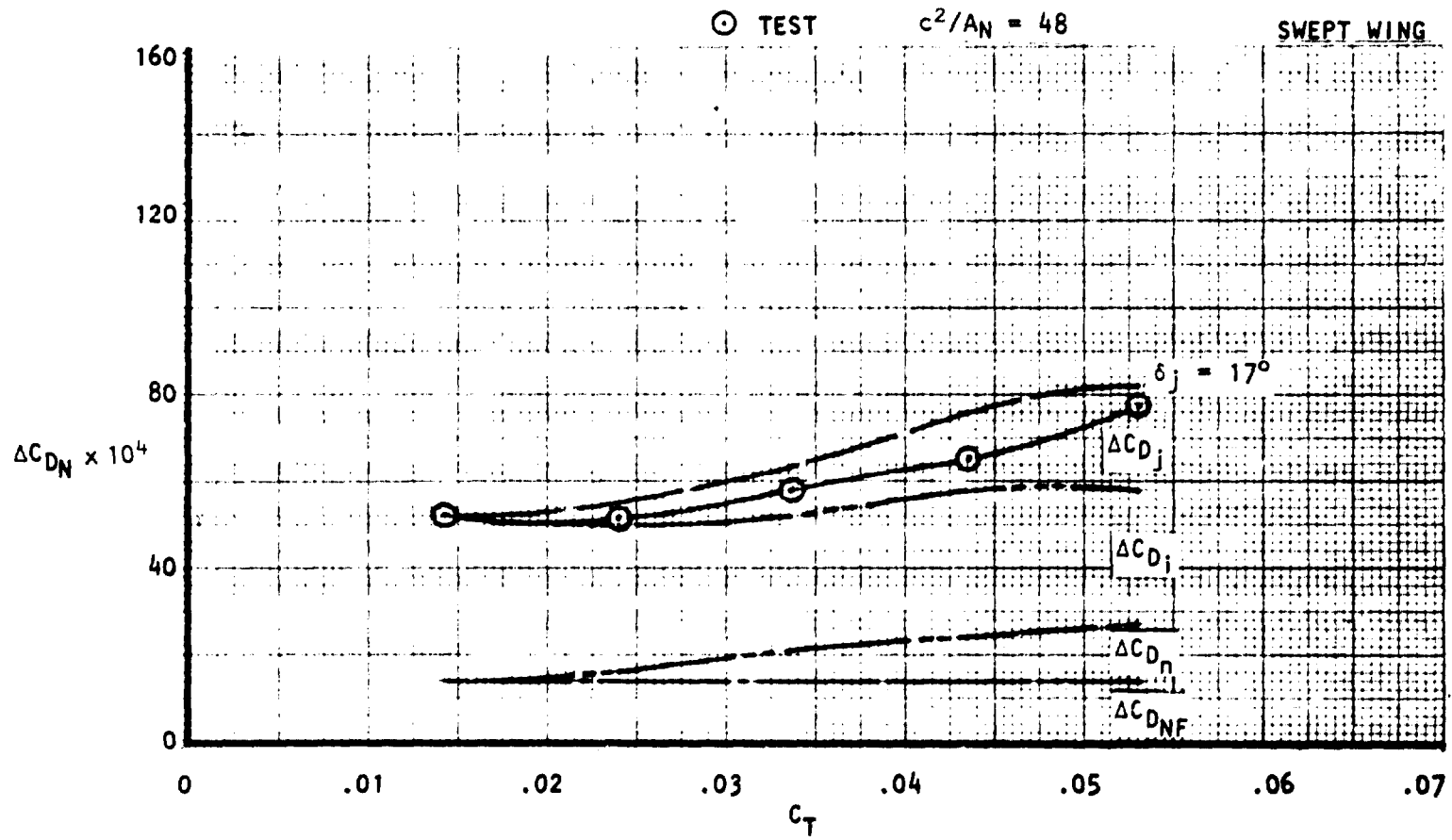


Figure 100 . Incremental nacelle drag and component build-up,  
noz N<sub>13</sub>, AR = 6,  $M_\infty = 0.73$ ,  $C_{LM} = 0.40$ .

## USB CRUISE PROGRAM

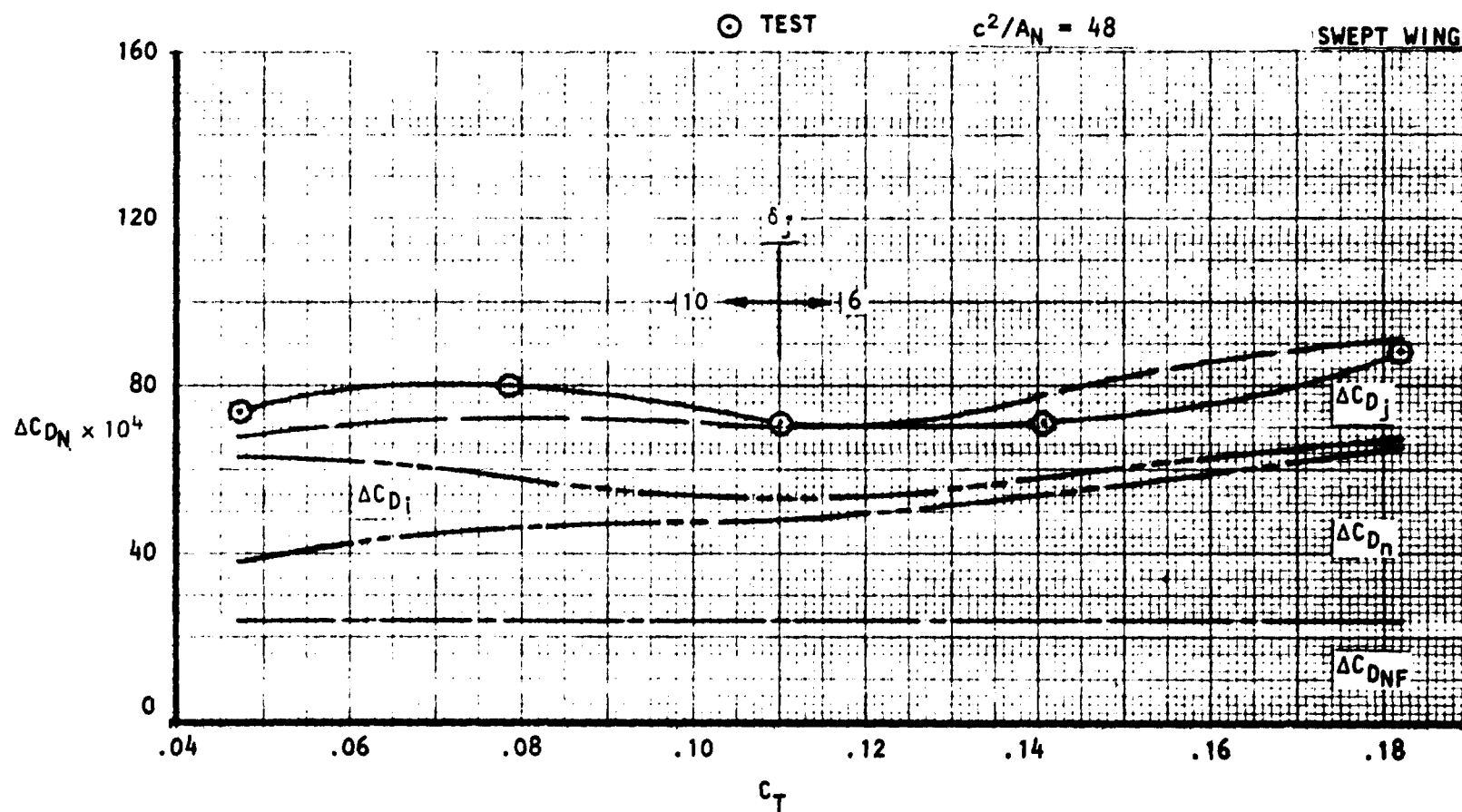


Figure 101 . Incremental nacelle drag and component build-up,  
nozs  $N_8^1 + N_8^2$  (dual),  $AR = 2.5$ ,  $M_\infty = 0.60$ ,  $C_{LM} = 0.40$ .

# USB CRUISE PROGRAM

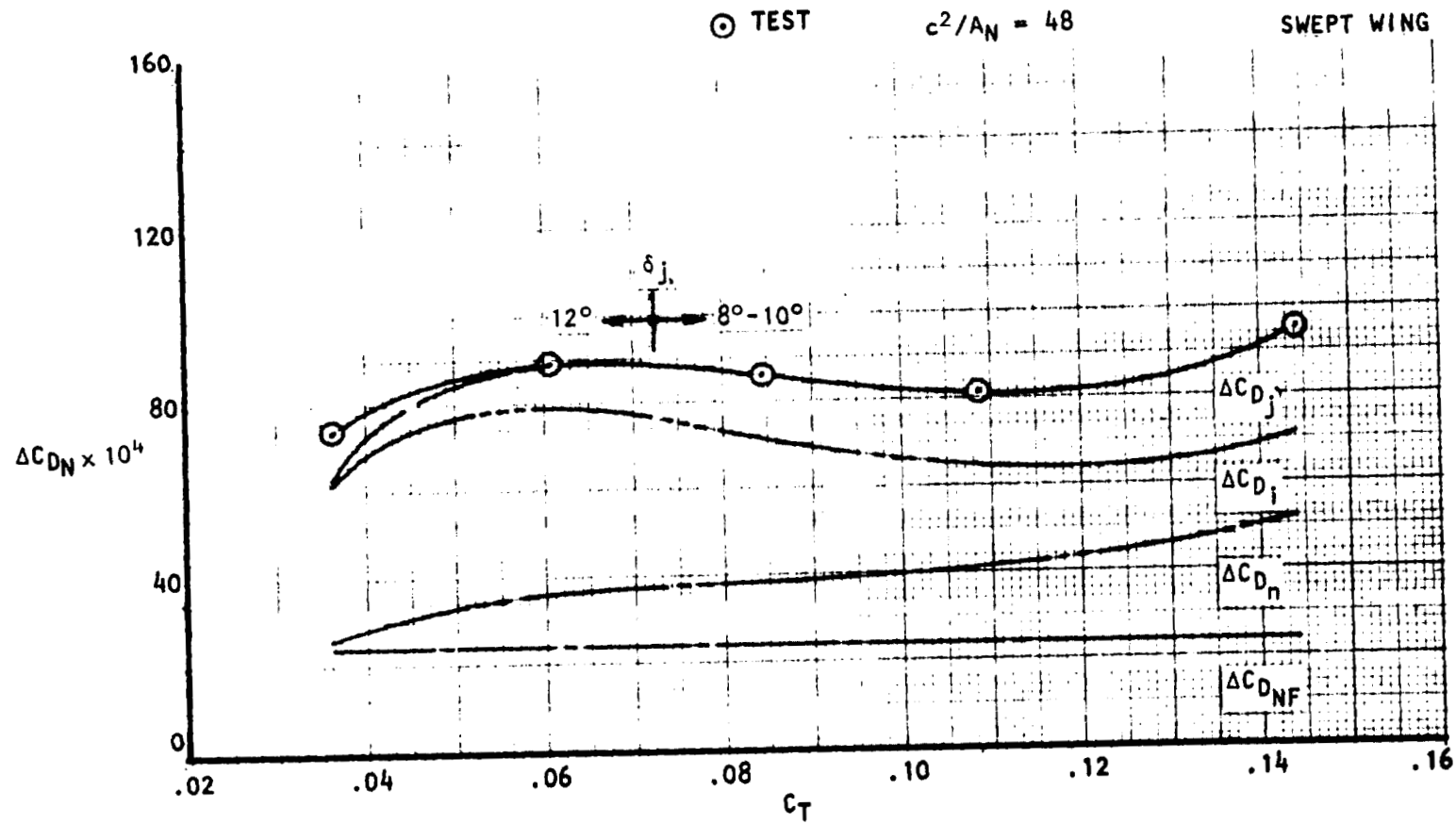


Figure 102 . Incremental nacelle drag and component build-up, noz  $N_8^1 + N_8^2$ , dual,  $AR = 2.5$ ,  $M_\infty = 0.68$ ,  $C_{LM} = 0.40$ .

ORIGINAL PAGE IS  
OF POOR QUALITY

## USB CRUISE PROGRAM

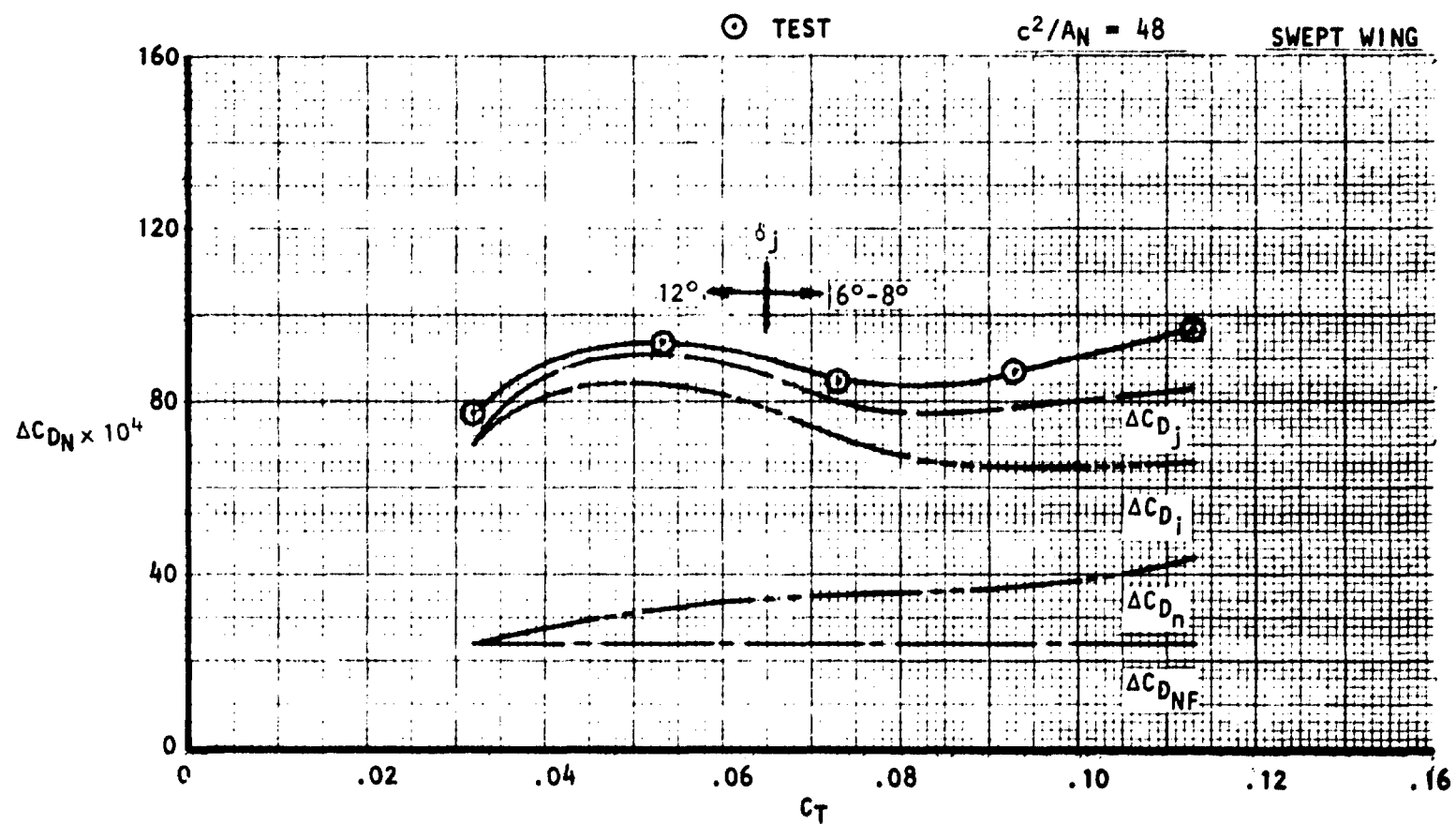


Figure 103 . Incremental nacelle drag and component build-up  
 noz  $N_8^1$ , and  $N_8^2$ , dual,  $AR = 2.5$ ,  $M_\infty = 0.73$ ,  $C_{LM} = 0.40$ .

illustrating the range of incremental drag penalties found for varying nozzle and wing geometries, nozzle pressure ratio and Mach number, the foregoing data (i.e., Figures 65 through 103) form the basis of the geometric effects studies provided in Section 3.2.3.2. Shown on the figures representing the cruise drag penalties of the various nacelles are curves reflecting the estimated component drag penalties as progressively summed for comparison to the measured total drag penalty. The sources and assumptions made in the generation of the component curves are explained in the following discussions.

- o Nacelle Friction Drag ( $\Delta C_{D_{NF}}$ ) – This component is the skin friction drag coefficient of the nacelle  $_{NF}$  installation inclusive of lower surface pylons, ducting, forebodies and nozzles. These have been estimated by standard aerodynamic procedures and have been modified to account for interfacing footprint areas between nacelle and wing such that the tested values of the drag of the basic wing/body combination can be applied. Figure 104 provides the estimated values of  $\Delta C_{D_{NF}}$  used in the drag build-up process.
  
- o Scrubbing-drag Coefficient, ( $\Delta C_{D_{\eta}}$ ) – Evaluation of the scrubbing drag component makes the assumption that the value of the statically-derived installed thrust ratio ( $\eta_T = \frac{T_{\text{installed}}}{T_{\text{isolated}}}$ ) remains invariant in the wind-on condition. Therefore, the scrubbing drag loss is represented by:

$$\Delta C_{D_{\eta}} = \Delta C_T (1 - \eta_T) \quad (20)$$



# USB CRUISE PROGRAM

<u>NOZZLE</u>	<u>WING INSTALL.</u>	<u><math>\Delta C_{DNF}</math></u>	
N <sub>2</sub>	STRAIGHT WING ↓	0.0022	
N <sub>2E</sub>		0.0023	
N <sub>3</sub>		0.0025	
N <sub>3E</sub>		0.0021	
N <sub>4</sub>		0.0024	
N <sub>4E</sub>		0.0020	
N <sub>5</sub>		0.0024	
N <sub>6</sub>	↓	0.0010	
N <sub>2</sub> + OTW PYLON		0.0023	(FLOW-THROUGH FOREBODY)
N <sub>8</sub>	25° SWEPT WING ↓	0.0012	
N <sub>11</sub>		0.0013	
N <sub>12</sub>		0.0014	
N <sub>13</sub>		0.0013	
N <sub>8</sub> <sup>1</sup> + N <sub>8</sub> <sup>2</sup> (DUAL)	↓	0.0024	

Figure 104 . Tabulation of estimated skin friction drag of test nacelles.

where  $\Delta C_T = (C_T)_{H_j/p_\infty} - (C_T)_{\text{FLOW-THROUGH}}$

Variations of  $\eta_T$  with nozzle pressure ratio are provided in Figure 64, Section 3.2.3.1 for all of the test nozzles. Values of  $C_T$  at the flow-through pressure ratio can be obtained from the  $C_T$  vs  $H_j/p_\infty$  curves in Volume II(B).

- o Drag-Due-To-Lift ( $\Delta C_{Di}$ ) — Assessment of the drag-due-to-lift penalty combines all lift - (or  $\alpha$ -) related drag penalties under one coefficient. Thus, this component is comprised of true potential-flow induced drag changes due to the nacelle-plus blowing jet, profile drag variations with lift as well as any variations in the shock/boundary-layer interaction with  $\alpha$ . The derivation of this component penalty has made use of plots of  $C_{LTOT}^2$  vs  $C_{DTOT}$  for each of the fixed nozzle pressure ratio (i.e.,  $1.4 \leq H_j/p_\infty \leq 3.0$ ). Utilizing the shapes of these curves in a conventional manner results in an "effective" induced drag factor,  $e$ , which can then be compared to a similar factor derived for the basic wing/body combination. The results of these calculations are presented in Figures 105 through 117 in the form of  $\Delta e/e_w$  across the blowing- and Mach-ranges or:

$$\frac{\Delta e}{e_w} = \frac{("e'')_{H_j/p_\infty} - "e''_w}{"e''_w} \quad (21)$$

In taking the slopes of the lift-drag curves, emphasis was placed on the lift range  $0.3 \leq C_{LTOT} \leq 0.5$  inasmuch as such curves are generally not entirely linear over the lift range of interest. Typical variations of

## USB CRUISE PROGRAM

SYM  $M_\infty$ 

⊙ 0.60

□ 0.68

△ 0.72

$$c^2/A_N = 24$$

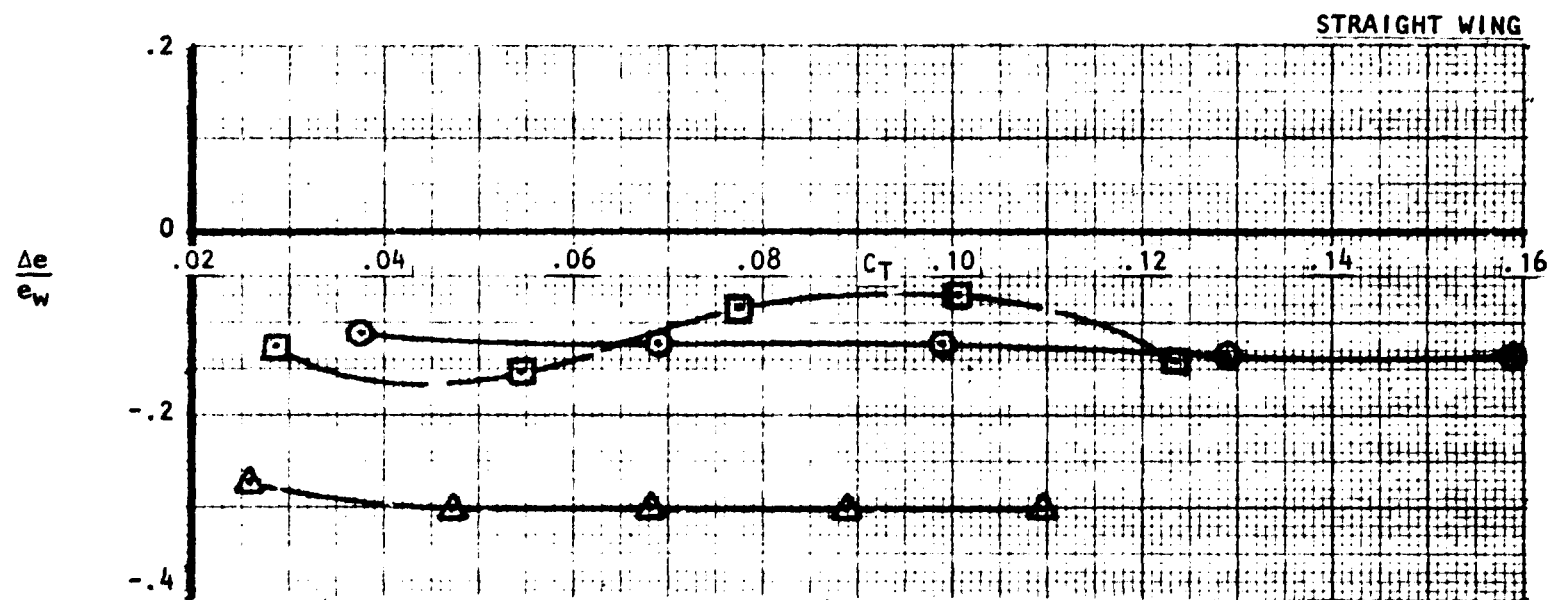


Figure 105. Variation of effective drag-due-to-lift parameter with thrust and Mach no., nozzle  $N_2$ , circular.

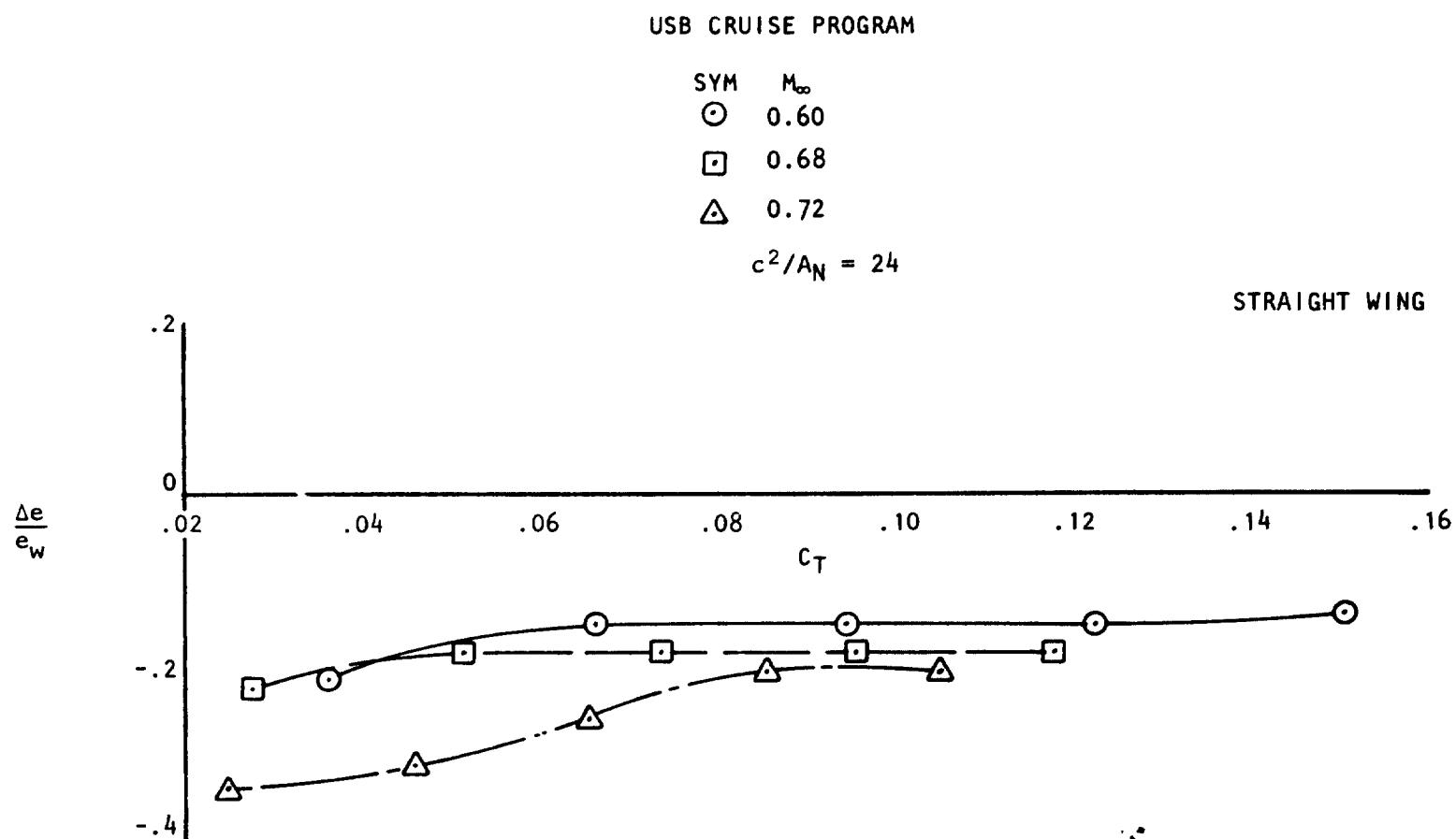


Figure 106 . Variation of effective drag-due-to-lift parameter with thrust and Mach no., nozzle  $N_{2E}$ , circular.

## USB CRUISE PROGRAM

SYM     $M_\infty$   
 ○    0.60  
 □    0.68  
 △    0.72  
 $c^2/A_N = 24$

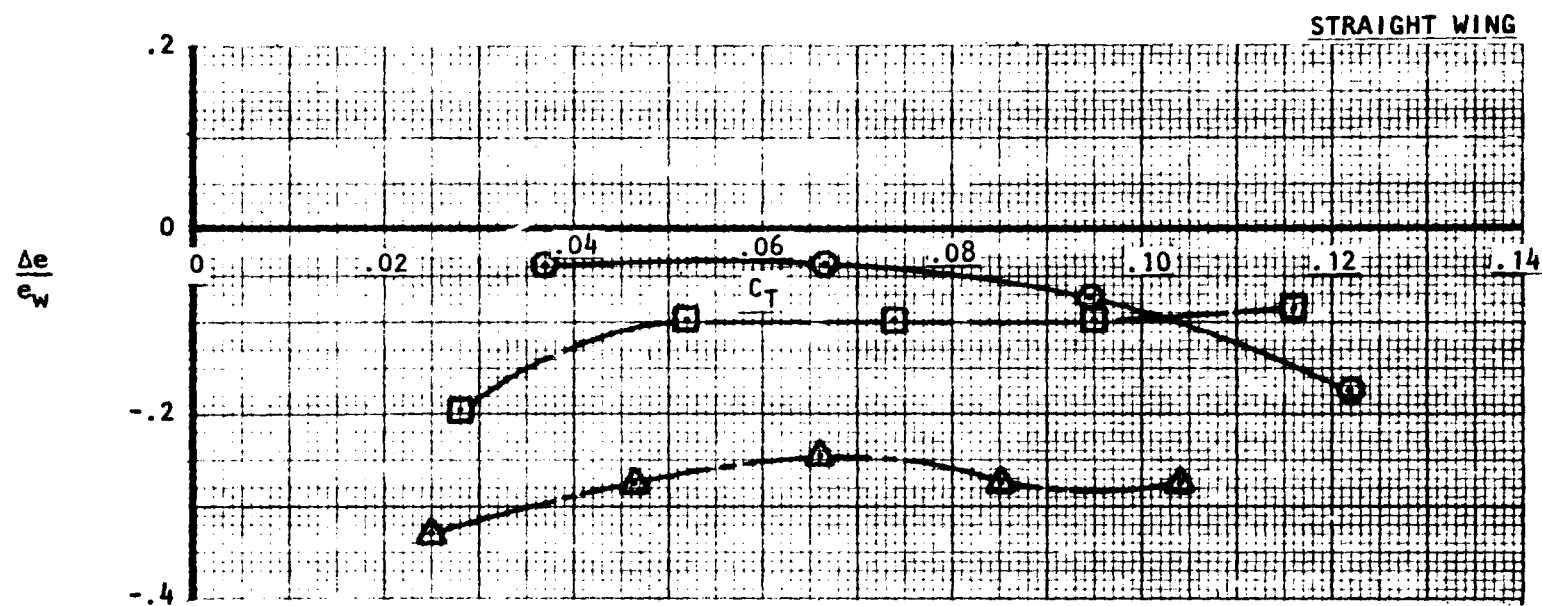


Figure 107 . Variation of effective drag-due-to-lift parameter with thrust and Mach no., nozzle  $N_{3B}$ ,  $AR = 2.5$ .

# USB CRUISE PROGRAM

SYM	$M_\infty$
⊙	0.60
□	0.68
△	0.72
$c^2/A_N = 24$	

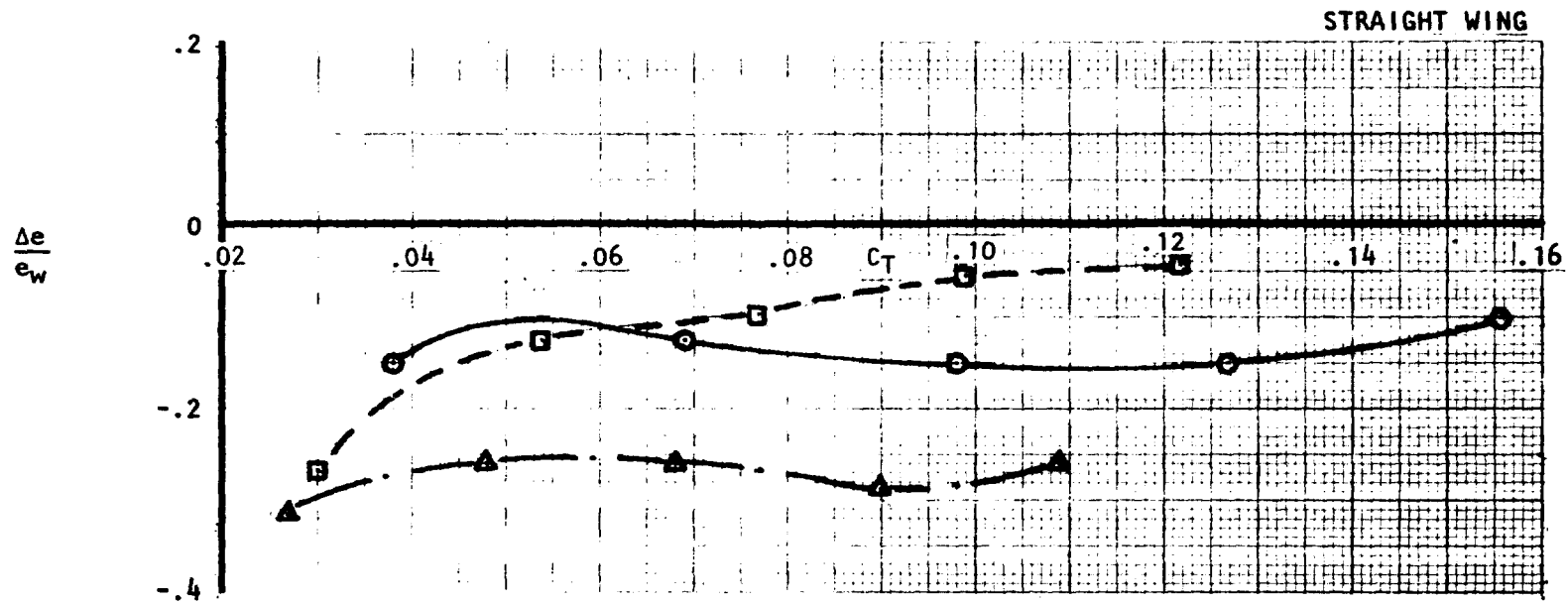


Figure 108 . Variation of effective drag-due-to-lift parameter with thrust and Mach no., nozzle  $N_{3E}$ ,  $AR = 2.5$ .

## USB CRUISE PROGRAM

SYM     $M_\infty$   
 ○      0.60  
 □      0.68  
 △      0.72  
 $c^2/A_N = 24$

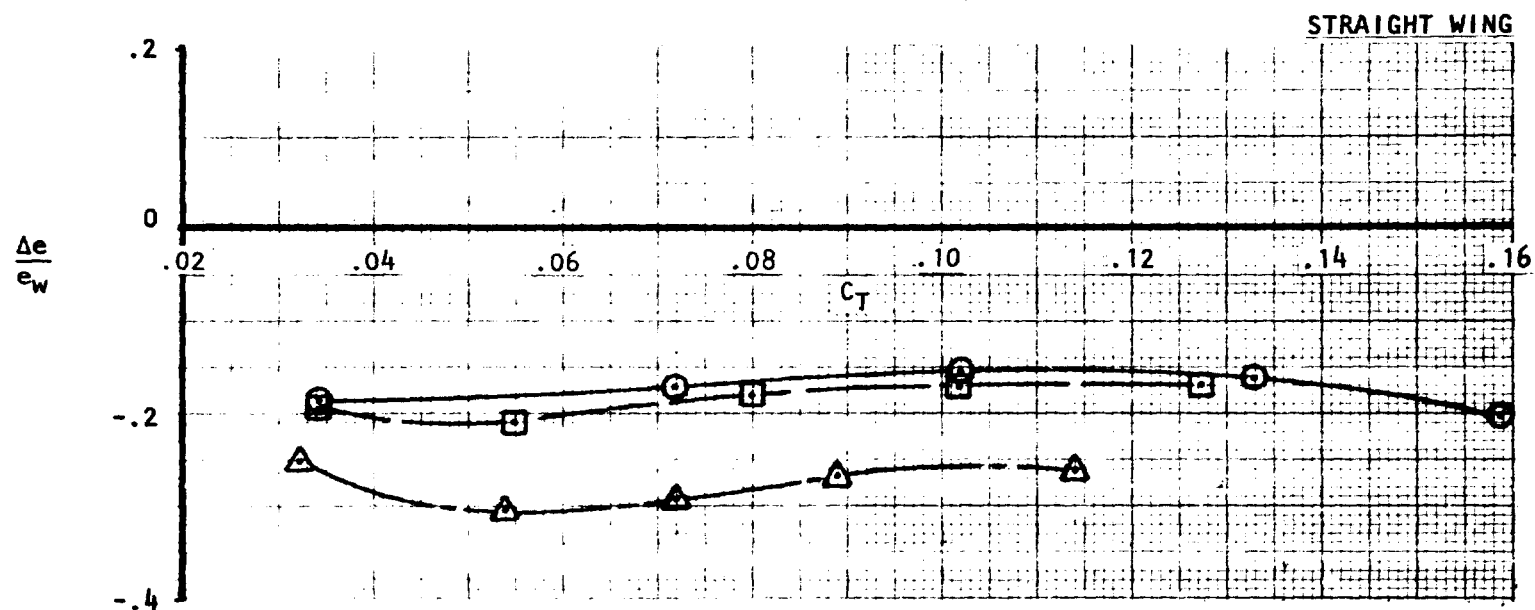


Figure 109 . Variation of effective drag-due-to-lift parameter with thrust and Mach no., nozzle  $N_4$ ,  $AR = 4$ .

ORIGINAL PAGE IS  
OF POOR QUALITY

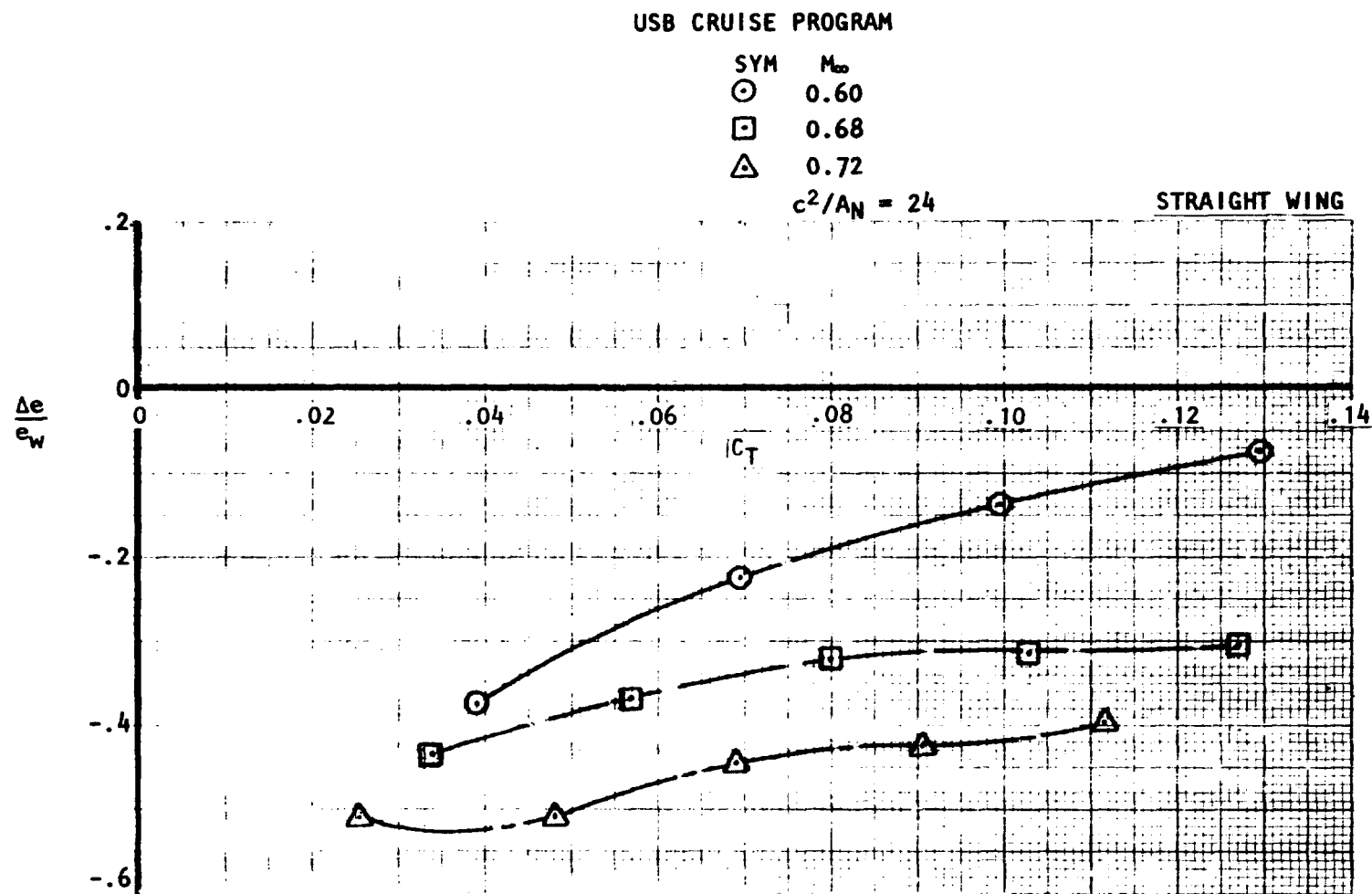


Figure 110 . Variation of effective drag-due-to-lift parameter with thrust and Mach no., nozzle  $N_{4E}$ ,  $AR = 4$ .



# USB CRUISE PROGRAM

SYM	$M_\infty$
○	0.60
□	0.68
△	0.72

$$c^2/A_N = 24$$

STRAIGHT WING

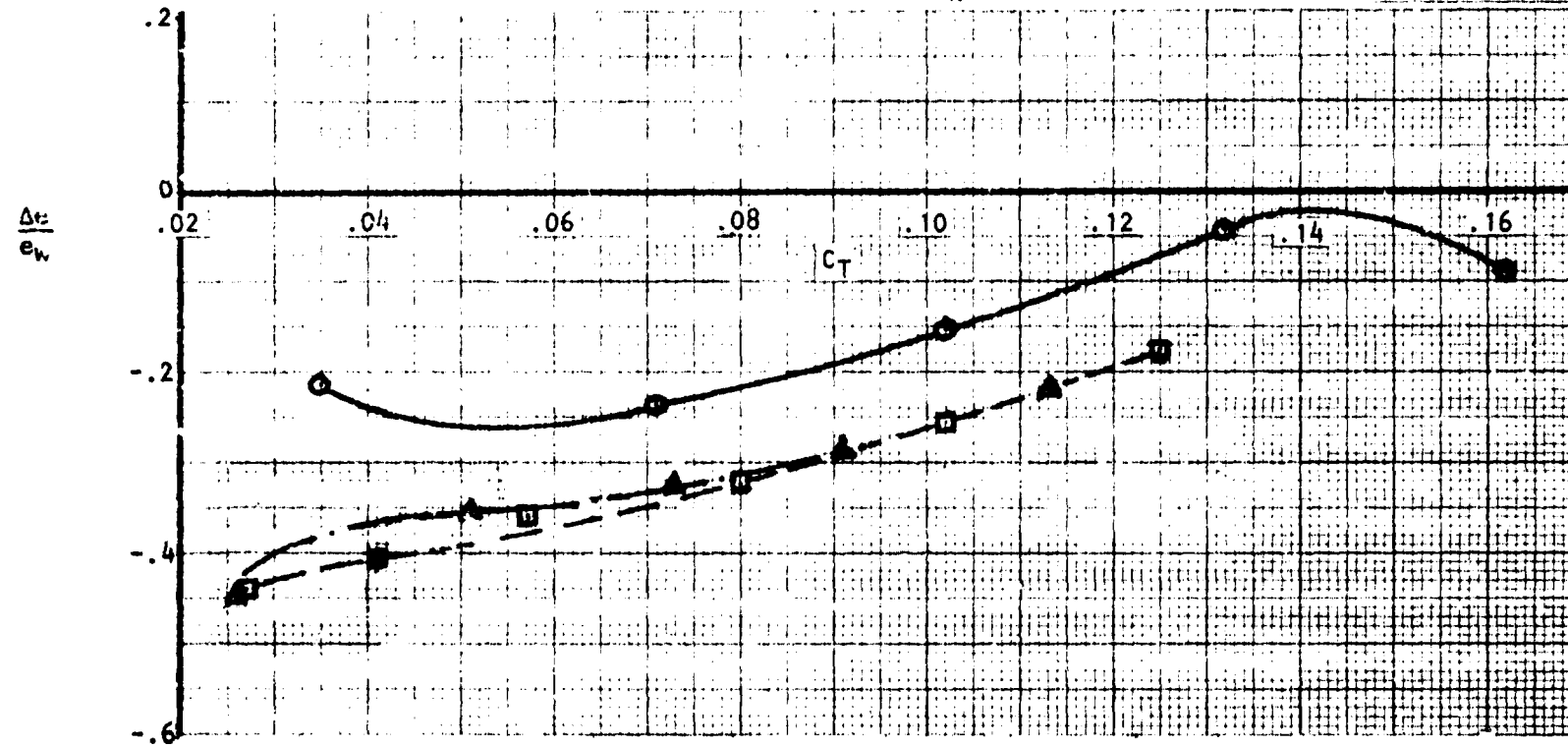


Figure 111 . Variation of effective drag-due-to-lift parameter with thrust and Mach no., nozzle  $N_5$ ,  $AR = 6$ .

# USB CRUISE PARAMETER

SYM  $M_\infty$   
 $\odot$  0.60  
 $\square$  0.68  
 $\triangle$  0.72

$$c^2/A_N = 48$$

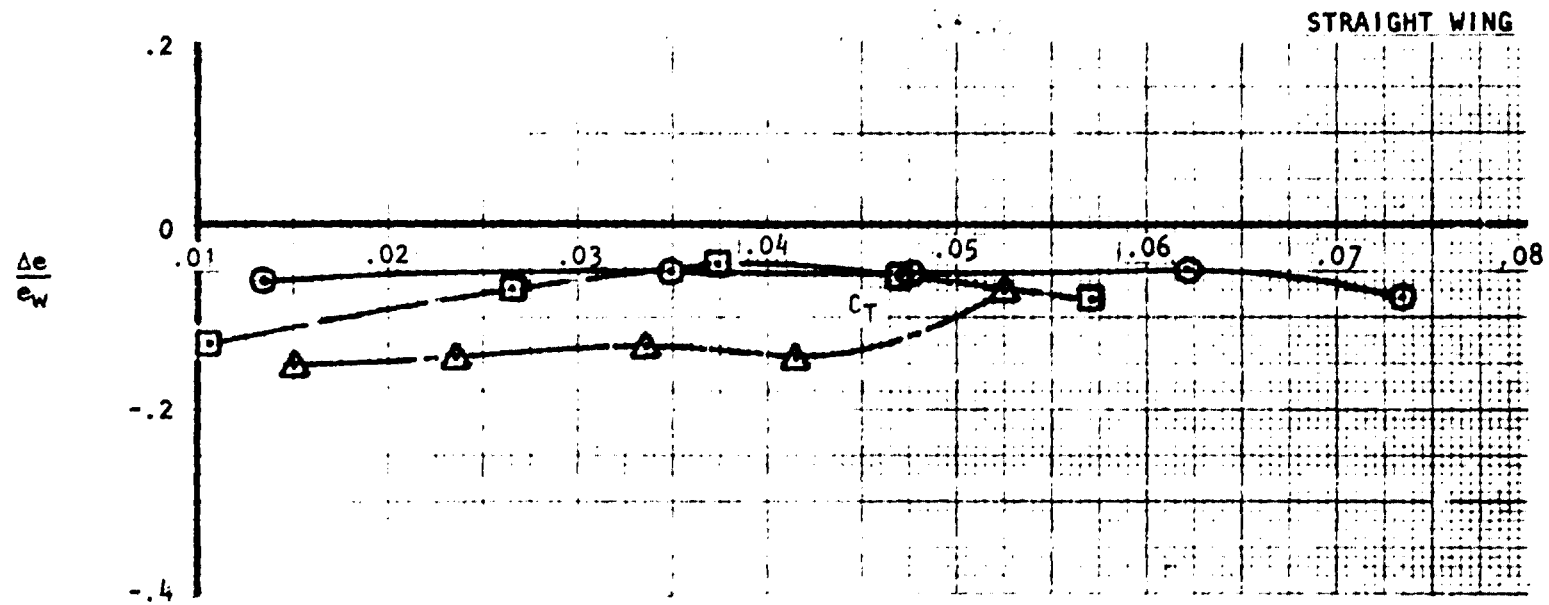


Figure 112 . Variation of effective drag-due-to-lift parameter with thrust and Mach no., nozzle  $N_6$ ,  $AR = 2.5$ .

## USB CRUISE PROGRAM

SYM     $M_\infty$   
 ○    0.60  
 □    0.68  
 △    0.73  
 $c^2/A_N = 48$

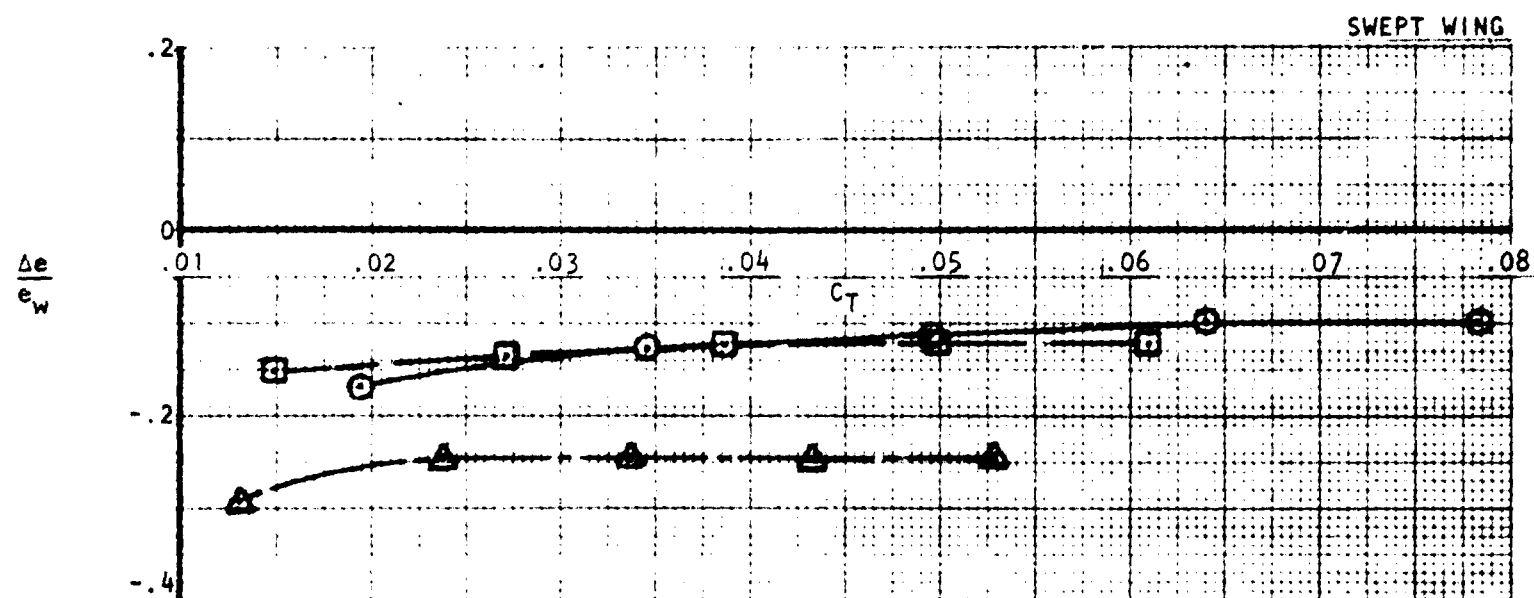


Figure 113 . Variation of effective drag-due-to-lift parameter with thrust and Mach no., nozzle  $N_{11}$ , circular.

# USB CRUISE PROGRAM

SYM      $M_\infty$   
 ○     0.60  
 □     0.68  
 △     0.73  
 $c^2/A_N = 48$

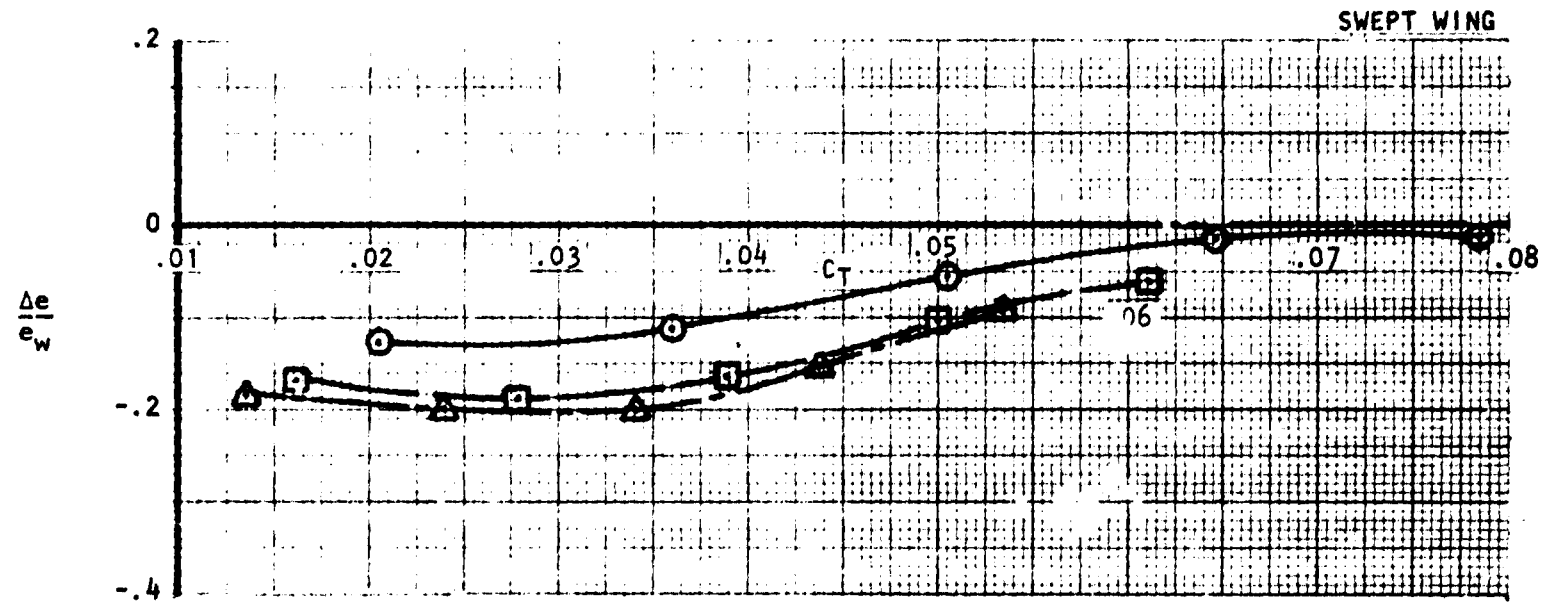


Figure 114 . Variation of effective drag-due-to-lift parameter with thrust and Mach no., nozzle  $N_0^2$ ,  $AR = 2.5$ .

# USB CRUISE PROGRAM

SYM  $M_\infty$   
 ○ 0.60  
 □ 0.68  
 △ 0.73  
 $c^2/A_N = 48$

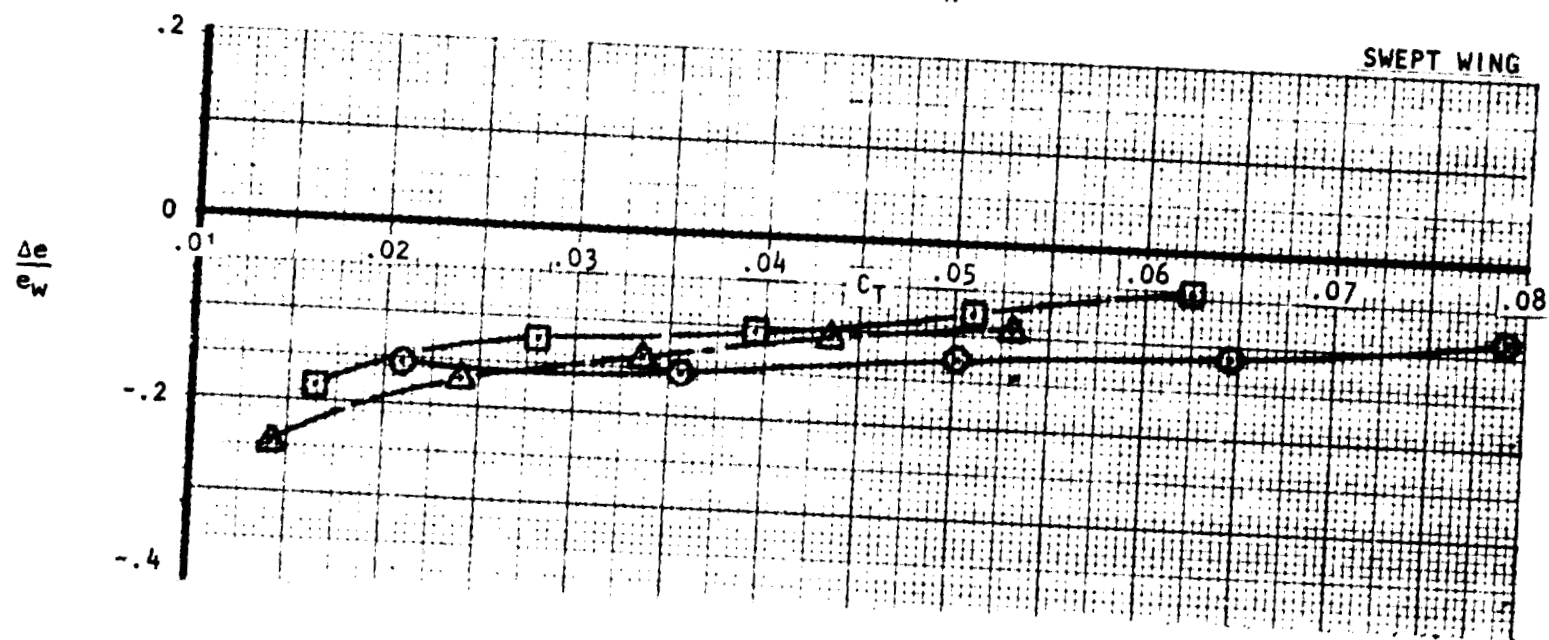


Figure 115. Variation of effective drag-due-to-lift parameter with thrust and Mach no., nozzle  $N_{12}$ ,  $AR = 4$ .

# USB CRUISE PROGRAM

SYM	$M_{\infty}$
⊙	0.60
□	0.68
△	0.72

$c^2/A_N = 48$

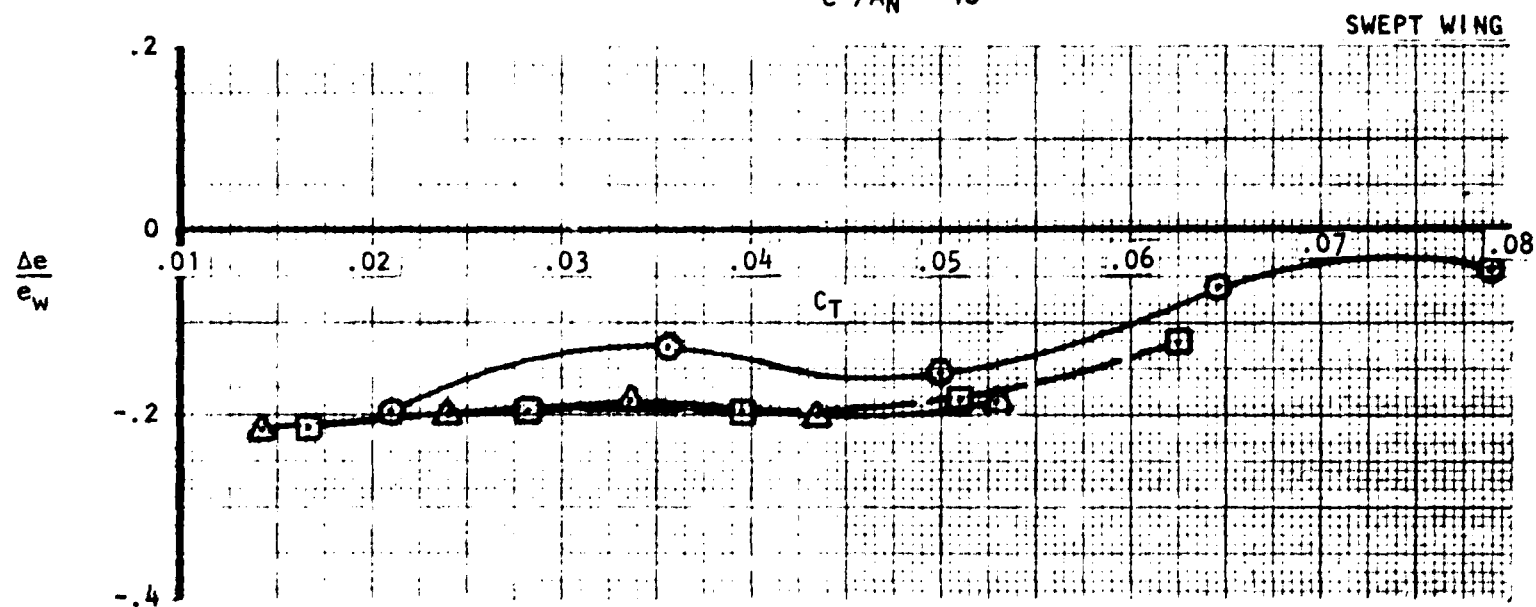


Figure 116 . Variation of effective drag-due-to-lift parameter with thrust and Mach no., nozzle  $N_{13}$ ,  $AR = 6$ .

## USB CRUISE PROGRAM

SYM     $M_\infty$   
 ⊙    0.60  
 □    0.68  
 △    0.73  
 $c^2/A_N = 48$

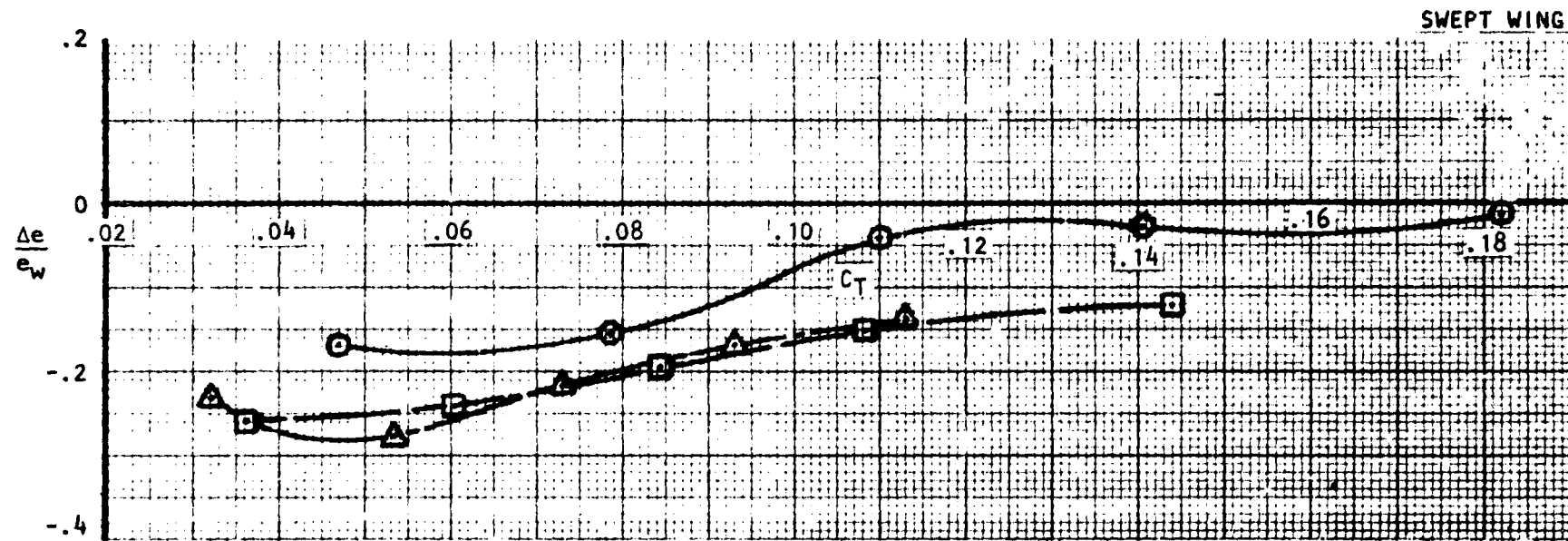


Figure 117 . Variation of effective drag-due-to-lift parameter with thrust and Mach no., nozzle  $N_8^1 + N_8^2$ , dual,  $AR = 2.5$ .

the  $\Delta e/e_w$  curves with blowing coefficient show a large drag penalty at the flow-through condition ( $C_T = .025$ ) with a gradual improvement as the blowing rate increases. It is believed that such an improvement, more notable with the wider nozzles, reflects a flow-entrainment process whereby the boundary-layer on the more remote sections of the basic wing are being increasingly controlled (or entrained) into the jet as the blowing rate advances. It is noted that under no condition is the initial loss incurred by the nacelle installation fully recovered by blowing. In fact, at the higher blowing rates where the effective drag-due-to-lift penalty tends toward a minimum, it would be anticipated the true potential flow induced drag should be increasing rapidly and the parameter,  $\frac{\Delta e}{e_w}$ , would become more negative as the thrust is advanced much beyond the limits shown. It may also be noted that for the circular nozzle configurations, Figure 106, for example, the drag-due-to-lift penalty recovers beyond flow-through but to a relatively low level which is almost constant with blowing rate. This trend would tend to support the supposition of an entrainment effect which may be reduced for the circular nozzle due to the marginally attached jet.

- o Jet Pressure Drag ( $\Delta C_{Dj}$ ) — Study of the surface pressure within the jet-scrubbed area (Section 3.2.2) identifies a pressure drag penalty beyond that which would be assessed from purely static measurements of jet deflection. The pressure measurement study suggests that in the wind-on condition, both lift and drag increments due to the jet should represent jet deflection angles more nearly like the trailing-edge angle of the wing upper surface ( $\delta_j \approx 16^\circ\text{-}17^\circ$ ) rather than the considerably lower



deflection angles measured statically (see Figure 64). In keeping with this concept, the jet-pressure drag penalties shown on the figures has been computed from:

$$\Delta C_{Dj} = \eta_T \Delta C_T [1 - \cos(\alpha + \theta_j)] \quad (22)$$

where

$$\Delta C_T = (C_T)_{H_j/p_\infty} - (C_T)_{\text{FLOW-THROUGH}}$$

$$\alpha \approx 2^\circ - 3^\circ \text{ (cruise } C_{L_{TOT}} \approx 0.4)$$

$$\theta_j \approx 17^\circ \text{ (max)}$$

Particularly where thick jets are involved (circular jets being notable examples), lower angles have been used in the calculations to provide insight into the breakdown of test results; the jet angle used in the computation is noted on the figures and in some instances, several angles have been employed.

A progressive summation of the four basic drag components ( $\Delta C_{DNF}$ ,  $\Delta C_{Dn}$ ,  $\Delta C_{Di}$  and  $\Delta C_{Dj}$ ) to a total penalty is identified on Figures 65 through 103 as a long dash line. This summation can then be compared to the measured nacelle drag increment and further drag penalties assessed if the comparison appears to warrant further drag identification. A comparison of the measured drag increments and the componentized build-up shows that, for the most part, the major portion of the total nacelle

drag increment is identified by the summed components. In general, the pressure drag component appears to correspond to a jet deflection of from  $12^\circ$  to  $16^\circ$  at the lower nozzle pressure ratios. Just beyond the theoretical critical pressure ratio, ( $\frac{H_j}{p_\infty} = 1.89$ ), a "hard-choke" condition with accompanying shock formations in the jet create a flow-field and aft wing pressure gradient in which a completely attached jet flow is difficult to maintain. The data provided indicate a resulting jet angle of  $10^\circ$ - $12^\circ$ , whereas for a circular jet, the angle reduces to about  $6^\circ$ . As the blowing rate continues to advance toward  $H_j/p_\infty = 3.0$  and beyond, the downstream movement (and inclination) of the jet compression waves appear to permit some re-attachment of the jet which is accompanied by a higher jet pressure drag loss.

An example, where an additional drag penalty is involved in the total increment is given in Figures 80 through 82 wherein an aspect ratio 4 nozzle ( $N_{4E}$ ) with a high ( $36^\circ$ ) boattail angle is represented. Flow separation on the aft-nozzle is evident from flow-visualization tests, Figure 118 and surface pressure measurements. This drag penalty, identified as  $\Delta C_{Dg}$ , appears to be gradually reduced as  $C_T$  increases. It is believed that this trend, contrasting with the rapid build-up of jet pressure drag ( $\delta_j = 16^\circ$ ), is caused by a suppression of the local separation by a jet-pumping effect. At a  $C_T \approx 0.13$  ( $H_j/p_\infty = 3.0$ ) the boattail separation appears to be entirely suppressed if the assumption of a 16-degree jet angle at the wing trailing-edge is made.

An interesting comparison is offered in the data of Figures 65 and 75. Figure 65 represents a "D-Duct" nozzle with a  $25^\circ$  boattail angle, whereas

USB CRUISE PROGRAM

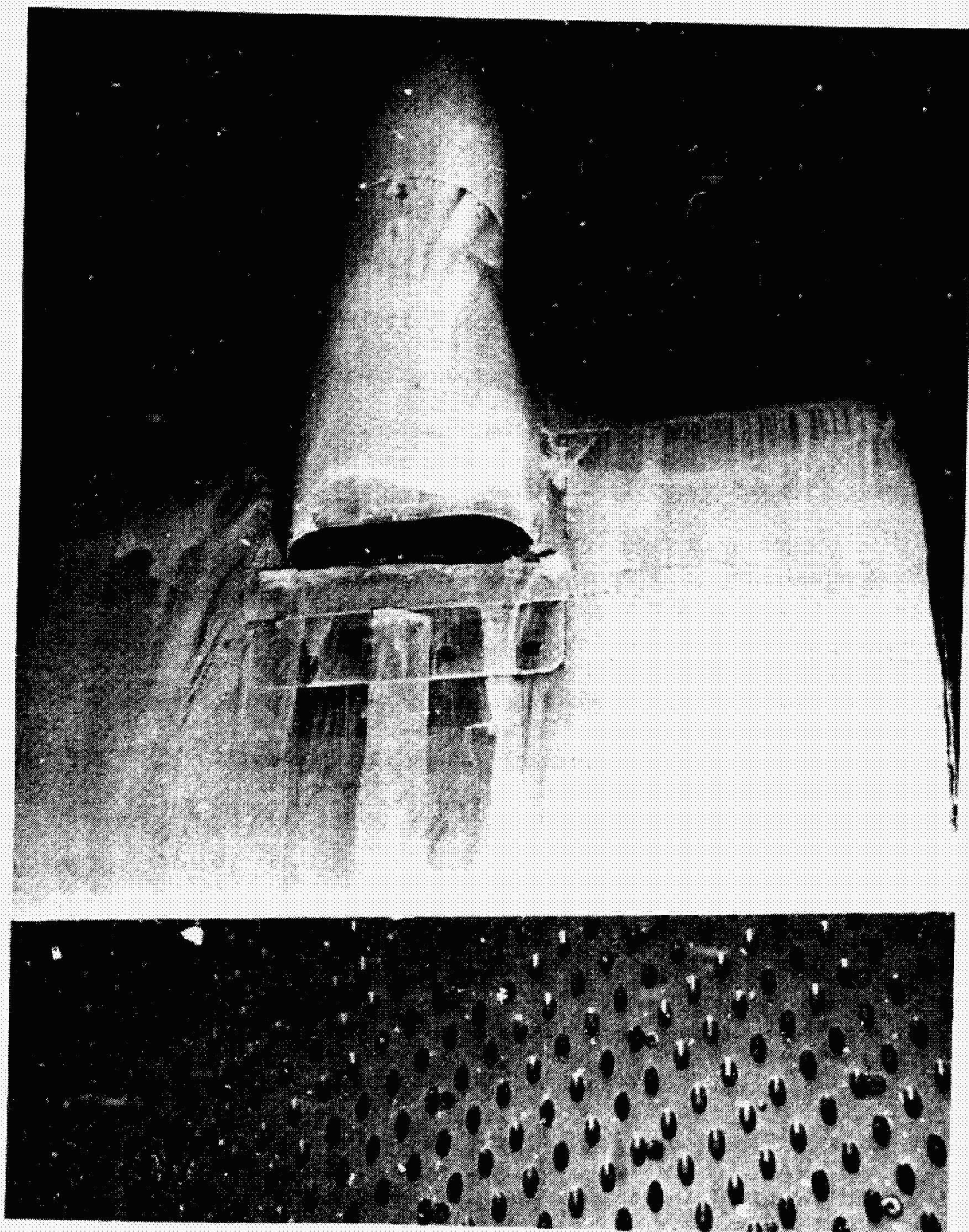


Figure 118 . Oil-flow photograph of high-boattail nozzle ( $N_{uE}$ ),  $\beta = 36^\circ$ ,  $M_\infty = 0.70$ ,  $\alpha = 2.6^\circ$ .

Figure 75 provides drag results from a similar configuration except for the much lower boattail angle of 9 degrees. Based on the component build-up, the 25 degree boattail configuration sustains a higher scrubbing loss (lower  $\eta_T$ ) but a lower drag-due-to-lift penalty than its counterpart. The trailing-edge jet angle appears to be slightly higher for the 25 degree boattail angle configuration, as would be expected for a higher degree of jet attachment. The somewhat higher total drag increment for the case with the high jet-impingement angle appears primarily due to a higher scrubbing loss which is not offset by the improved drag-due-to-lift. Thus, for a given nozzle aspect ratio without significant boattail separation, the basic aerodynamic trade-off in setting boattail (or jet impingement) angle appears to be between the increasing scrubbing losses and pressure drag on one hand versus the improving drag-due-to-lift losses on the other, as pressure ratio advances.

In the foregoing componentized drag increment build-ups, the match with the measured total does not indicate any large, contributing components which remain yet unidentified. In associations with the analysis of the pressure test data, a question was raised regarding the role of a leading-edge suction force on the clean wing which would normally offset the aft-wing pressure drag over an area equivalent to that scrubbed by the jet. The pressure data of Section 3.2.2.2 shows that, at the nozzle flow-through pressure ratio, the aft-wing pressures approach those of the clean wing. With the three-dimensional nacelle forebody spanning that section of the wing, the necessary leading-edge suction force must be carried by the nacelle forebody or, more likely, is accounted for by the

moderate increase in leading-edge negative pressure on adjacent sections. In any event, an identifiable increase in nacelle drag (typically,  $.0010 \leq \Delta C_D \leq .0020$ ) due to a loss in clean wing leading-edge suction force is not apparent in the force measurements.

A second question should be addressed inasmuch as Section 4.0 demonstrates that the USB lift-performance can be represented as a highly-localized jet flap. This question is in regard to the so-called "Thrust Hypothesis" pertinent to jet-flap theory (see Reference 4, for example). It is stated (ideally) in this hypothesis that the total forward thrust will be essentially independent of the jet-deflection angle. This form of thrust recovery, normally referred to in an idealized, two-dimensional situation, has some theoretical justification. However, as in the present case, very little "hard-evidence" of such an effect has been found on three-dimensional wings under experimental conditions. In the USB-program, there are several features of the experimental set-up which tend to mitigate against significant thrust recovery of this type in addition to the three-dimensionality of the jets. In the ideal case, it is suggested that the thrust recovery is manifested by an increase in the leading-edge suction pressures. While some increase in leading-edge pressures are noted on adjacent sections of the wing (Section 3.2.2.2), it is apparent that large increases in suction could not be sustained at the test conditions without the onsets very strong shocks and subsequent flow-separation. Additionally, a significant induction effect over the considerable jet-to-leading-edge chordwise distance with such a highly localized (spanwise) jet is believed to be improbable. It

is therefore concluded that beneficial drag effects, representing the thrust hypothesis, are a highly unlikely contributor to USB cruise performance. The correlation obtained with the build-up process appears to support this view.

- o Lift Due to Blowing — Typical examples of the variation of the total lift coefficient with nozzle pressure ratio are given in Figures 119 through 121 at fixed angles of attack and constant Mach number (0.68). This set of figures covers a range of nozzle exit shapes from circular (Figure 119) to "D-Duct" (Figure 120), to aspect ratio 6 (Figure 121). The wing-body lift coefficient at the same  $\alpha$  is shown for comparison. The general trends of these data show a rapidly increasing lift coefficient in the lower blowing range with a leveling-off as  $H_j/p_\infty \approx 3.0$  is approached. These trends, as well as the comparative greater lift developed by the wider (higher aspect ratio) nozzles, are typical of limited-span jet flap performance; in fact, Section 4.0 shows that excellent agreement can be obtained between the measured USB lift performance and that calculated from simple jet flap theory. While not particularly emphasized in the examples provided, in many cases a slight drop in lift is obtained at or near  $H_j/p_\infty \approx 2.0$  manifesting the onset of a "hard-choke" exit condition of the nozzle. Additionally, a slight drop-off in lift is often noted at the higher blowing level (see Volume II(B)) supporting the speculation of jet detachment under such conditions. While the foregoing drag data show a strong dependence on the extent of jet-attachment, the lift does not appear to be particularly sensitive to moderate changes in the jet angle, since most of the pressure changes with

# USB CRUISE PROGRAM

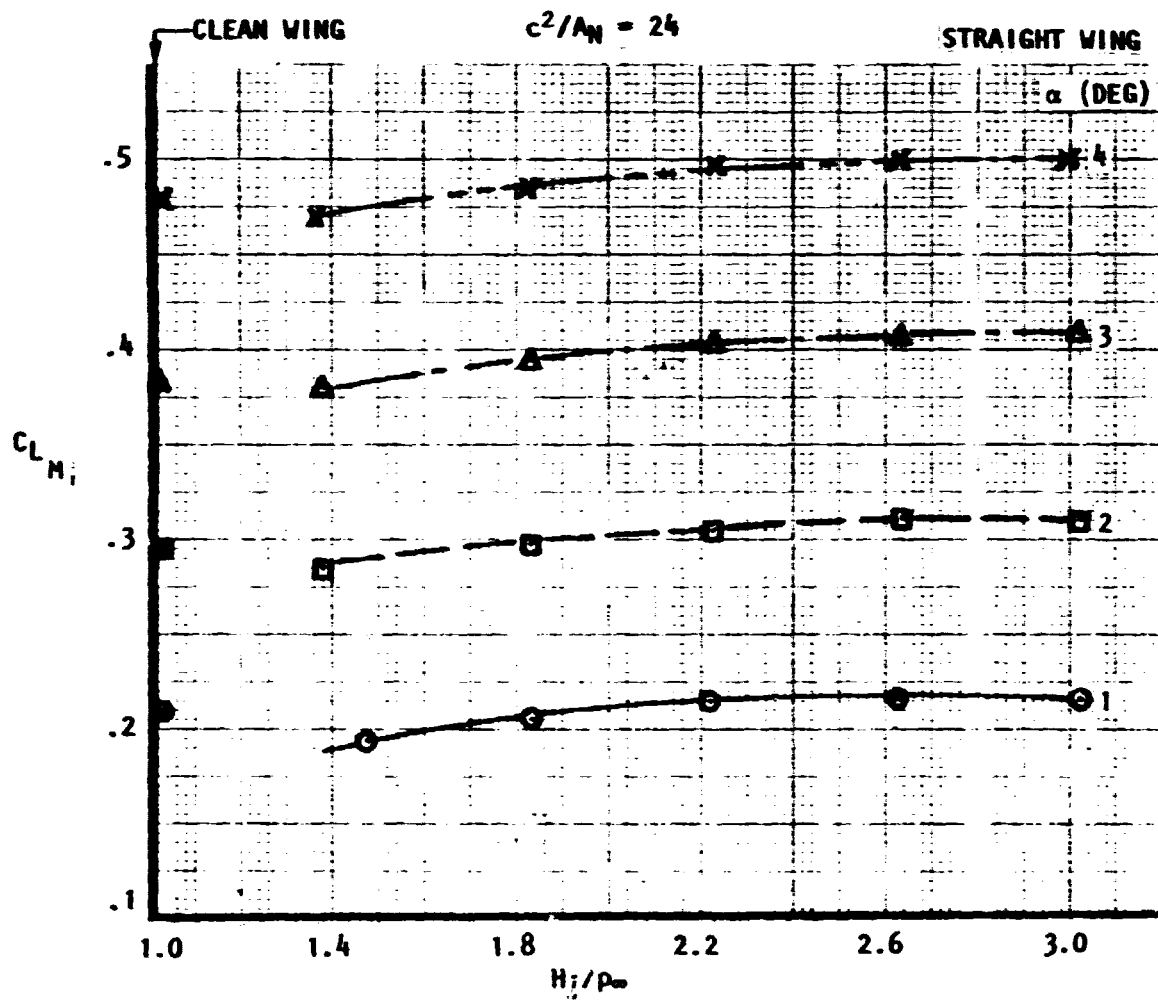


Figure 119 . - The effect of nozzle pressure ratio on total lift, noz  $N_2$ , circular,  $M_\infty = 0.68$ .

# USB CRUISE PROGRAM

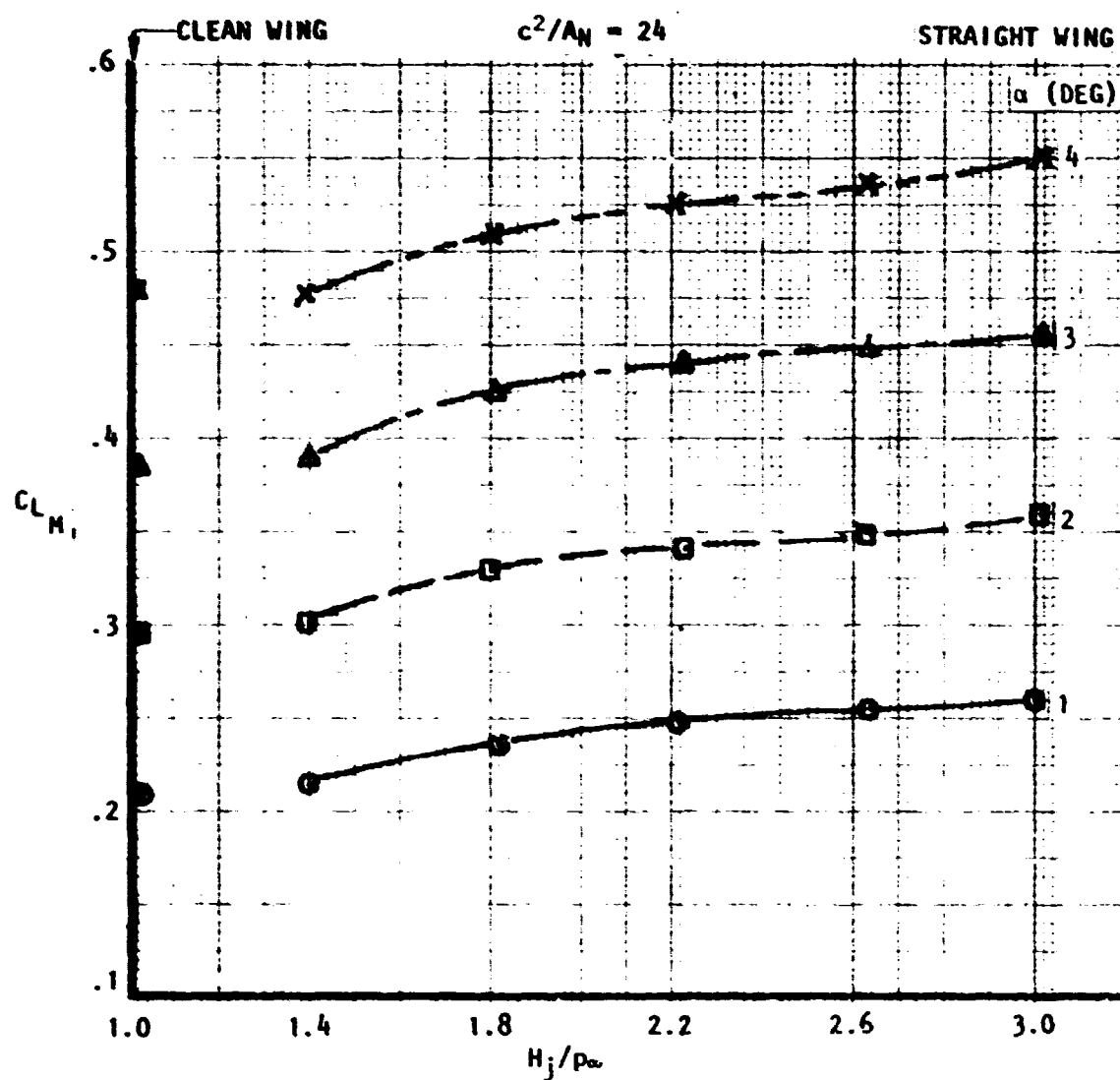


Figure 120 . The effect of nozzle pressure ratio on total lift, noz  $N_{3E}$ ,  $AR = 2.5$ ,  $M_\infty = 0.68$ .



# USB CRUISE PROGRAM

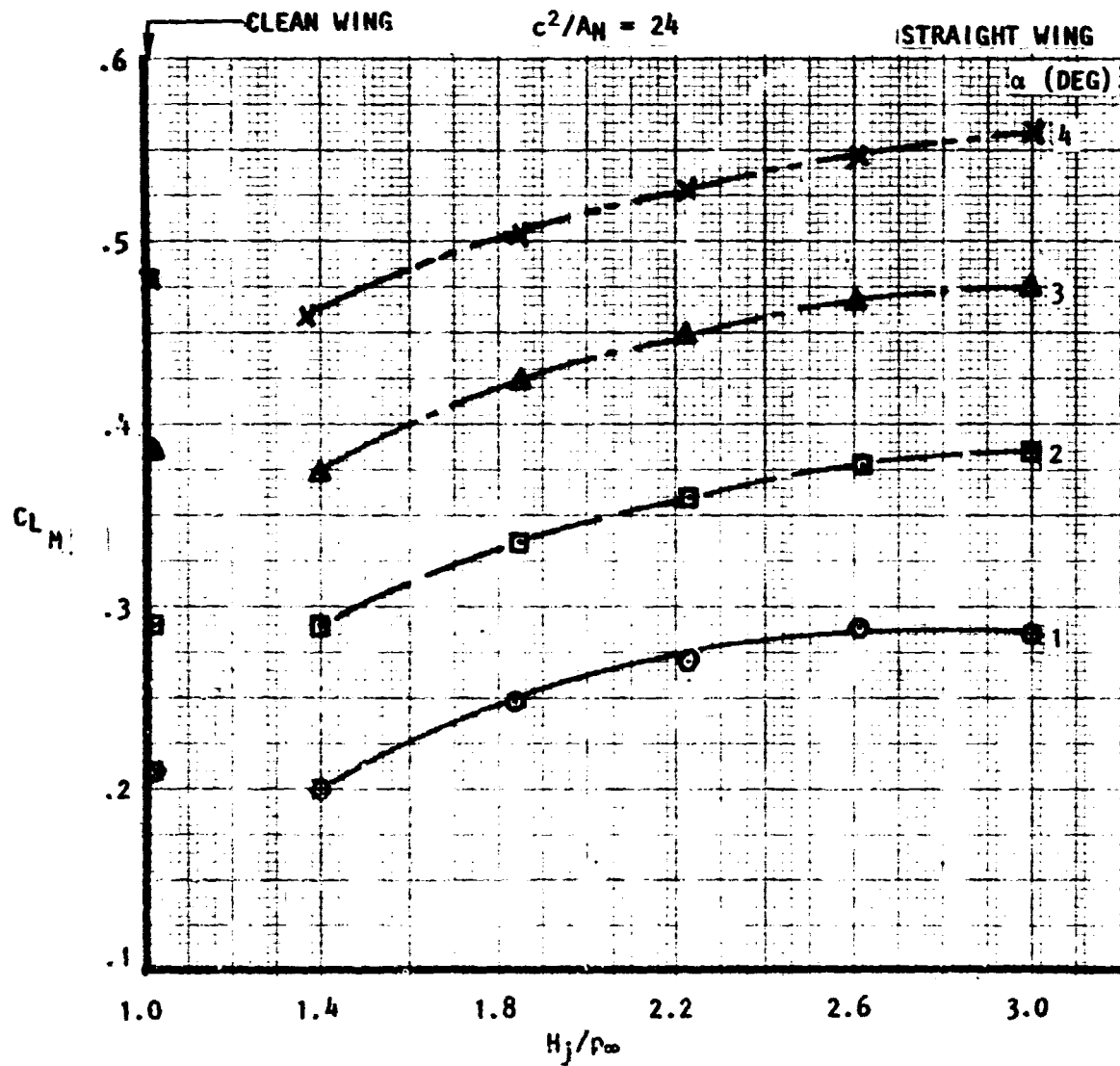


Figure 12i . Effect of nozzle pressure ratio on total lift, noz  $N_5$ ,  $AR = 6.0$ ,  $M_\infty = 0.68$ .

ORIGINAL PAGE IS  
OF POOR QUALITY

jet angle are occurring forward of the wing trailing edge. As will be shown in Section 4.0, reasonable correlation of the USB lift-due-to-blowing with jet-flap theory is obtained only when local jet angles of about the same magnitude as deduced from the drag data are utilized.

As a general trend, the total lift-due-to-blowing improves only slightly with angle-of-attack, as would be anticipated from the above-mentioned similarity to jet-flap performance and considering the limited angle range of interest. However, circular jets tend to show a slightly larger benefit with increases in angle-of-attack indicating that the marginal jet deflection at small  $\alpha$  can be increased as the higher  $\Delta P$  existing across the jet, as the angle-of-attack increases, promotes higher jet deflections.

Lift increments due to blowing have been extracted from the basic data plots discussed in the foregoing, and are shown as a function of  $C_T$  in Figures 122 through 132 for all of the test nacelles. The increment represented is

$$\Delta C_{LN} = (C_{LM})_{H_j/p_\infty} - (C_{LM})_{WB} \quad (23)$$

and therefore contains the lift due to the nacelle installation at flow-through condition as well as the additional lift due to blowing. Inasmuch as for the majority of the nacelles such increments are not strongly  $\alpha$ -dependent, the increments are shown only for  $\alpha \approx 2^\circ$ - $3^\circ$  across the Mach number range.

# USB CRUISE PROGRAM

LINE	$M_\infty$
————	0.60
————	0.68
-----	0.72

## STRAIGHT WING

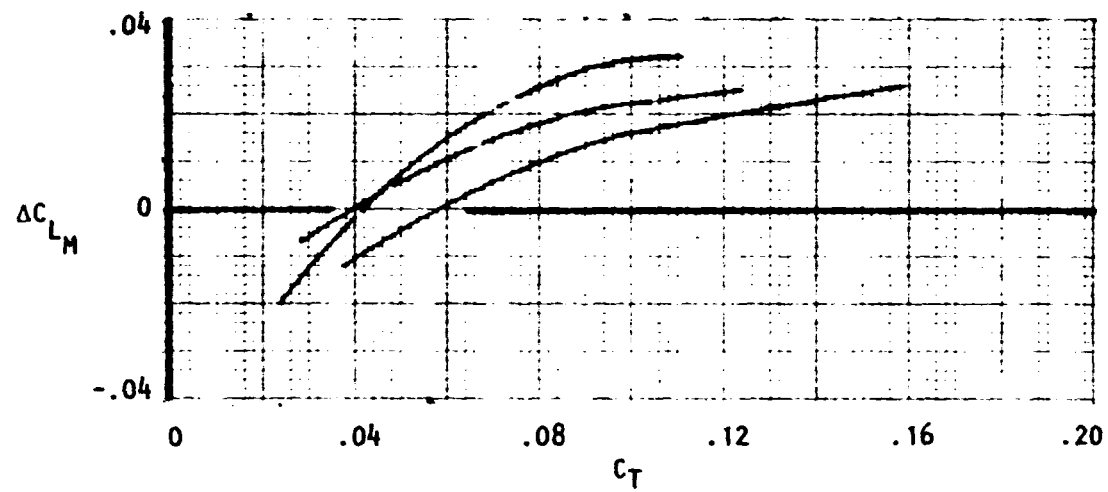
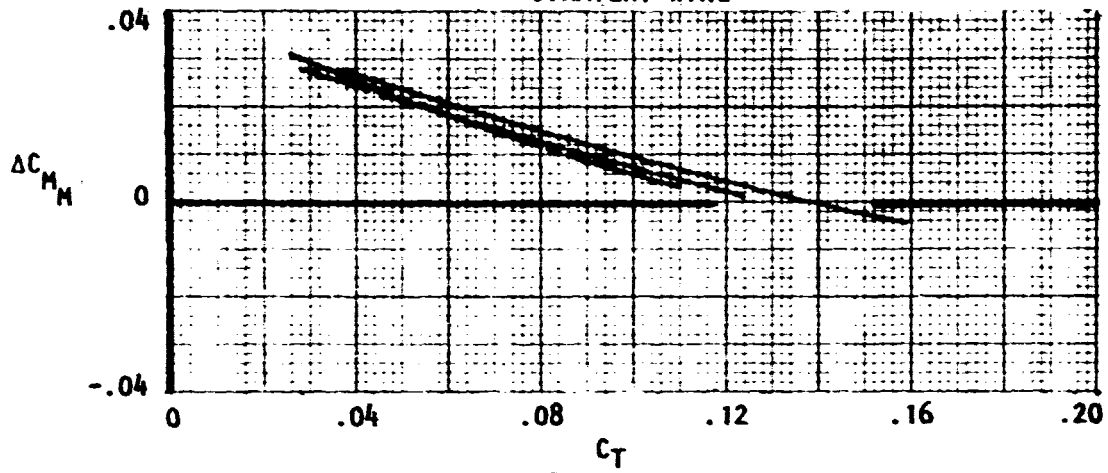


Figure 122 . Variation of lift and moment increments due to blowing, noz  $N_2$ , circular.

# USB CRUISE PROGRAM

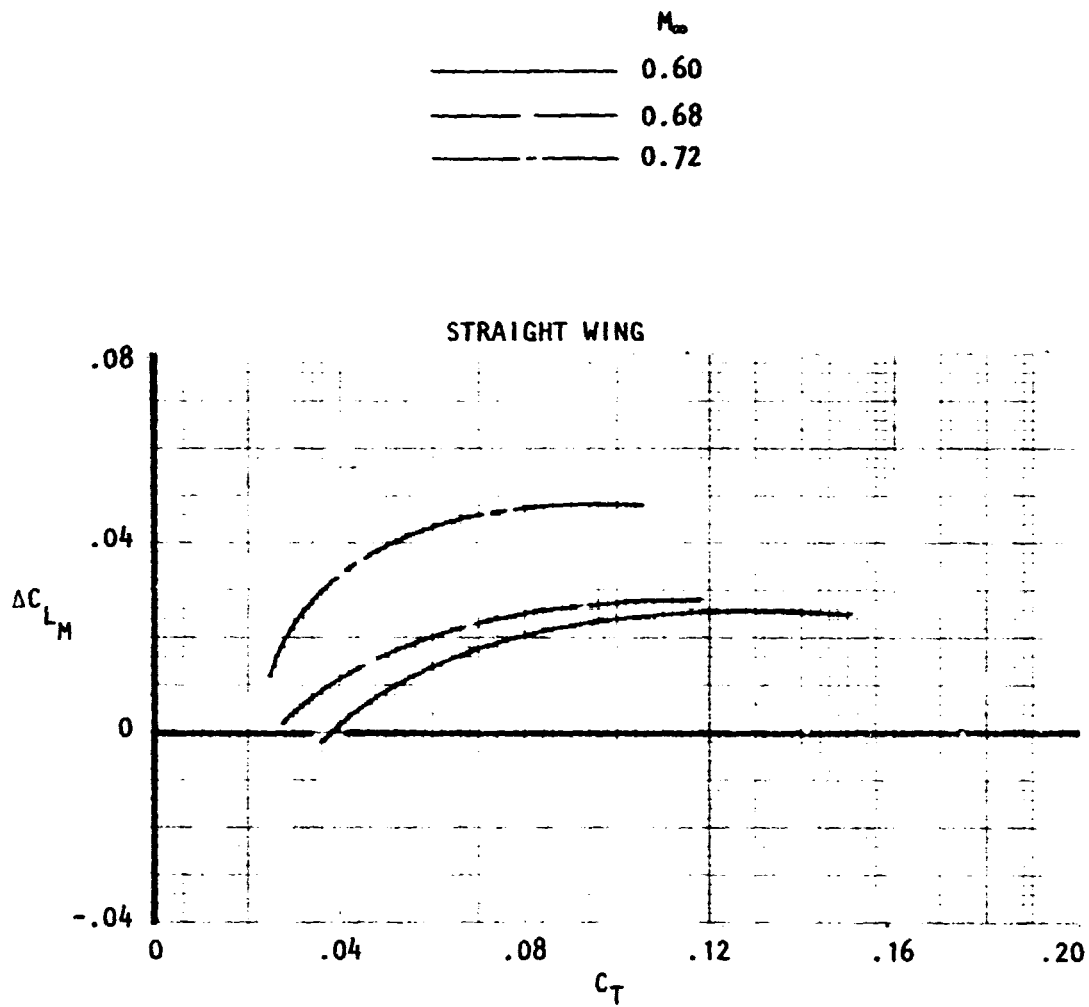


Figure 123 . Variation of lift increments due to blowing, noz  $N_{2E}$ , circular.

ORIGINAL PAGE IS  
OF POOR QUALITY

# USB CRUISE PROGRAM

	$M_\infty$
————	0.60
—— ———	0.68
- - - - -	0.72

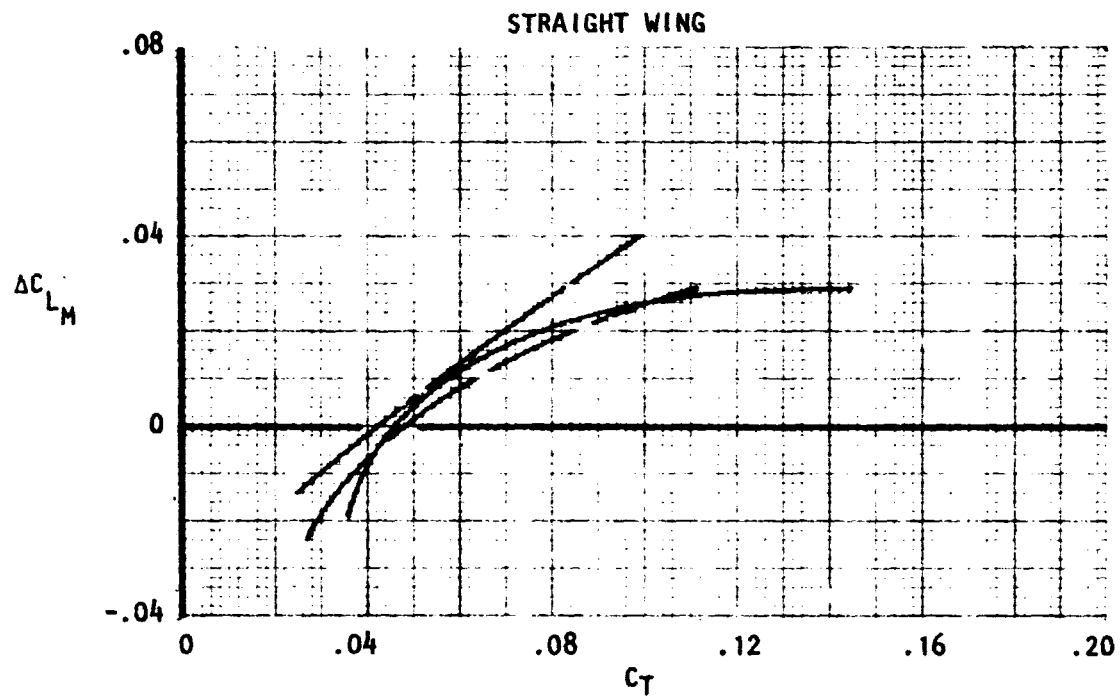


Figure 124 . Variation of lift increment due to blowing,  
noz  $N_{3B}$ ,  $AR = 2.5$ .

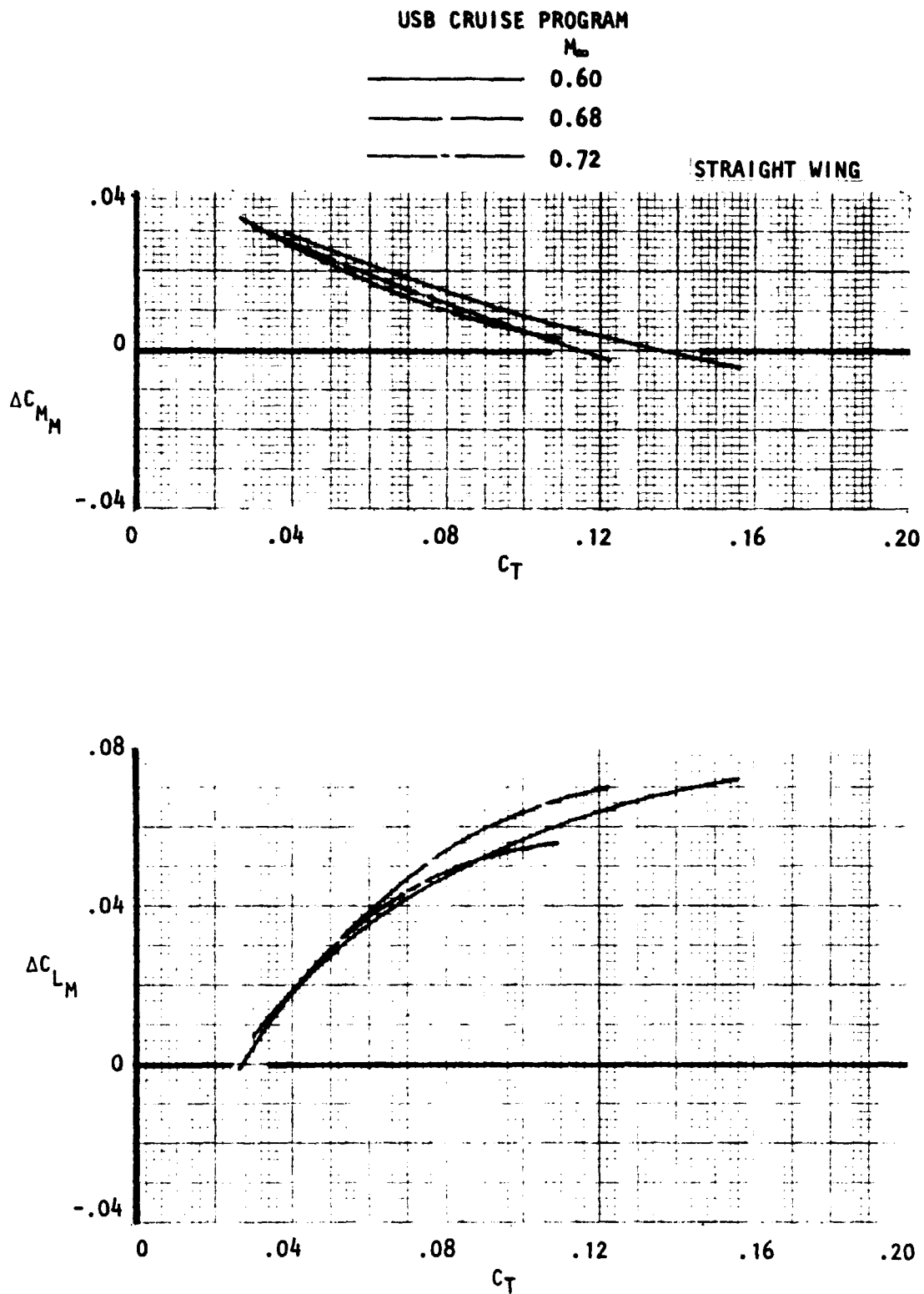


Figure 125 . Variation of lift and moment increments due to blowing, noz  $N_{3E}$ , AR = 2.5.

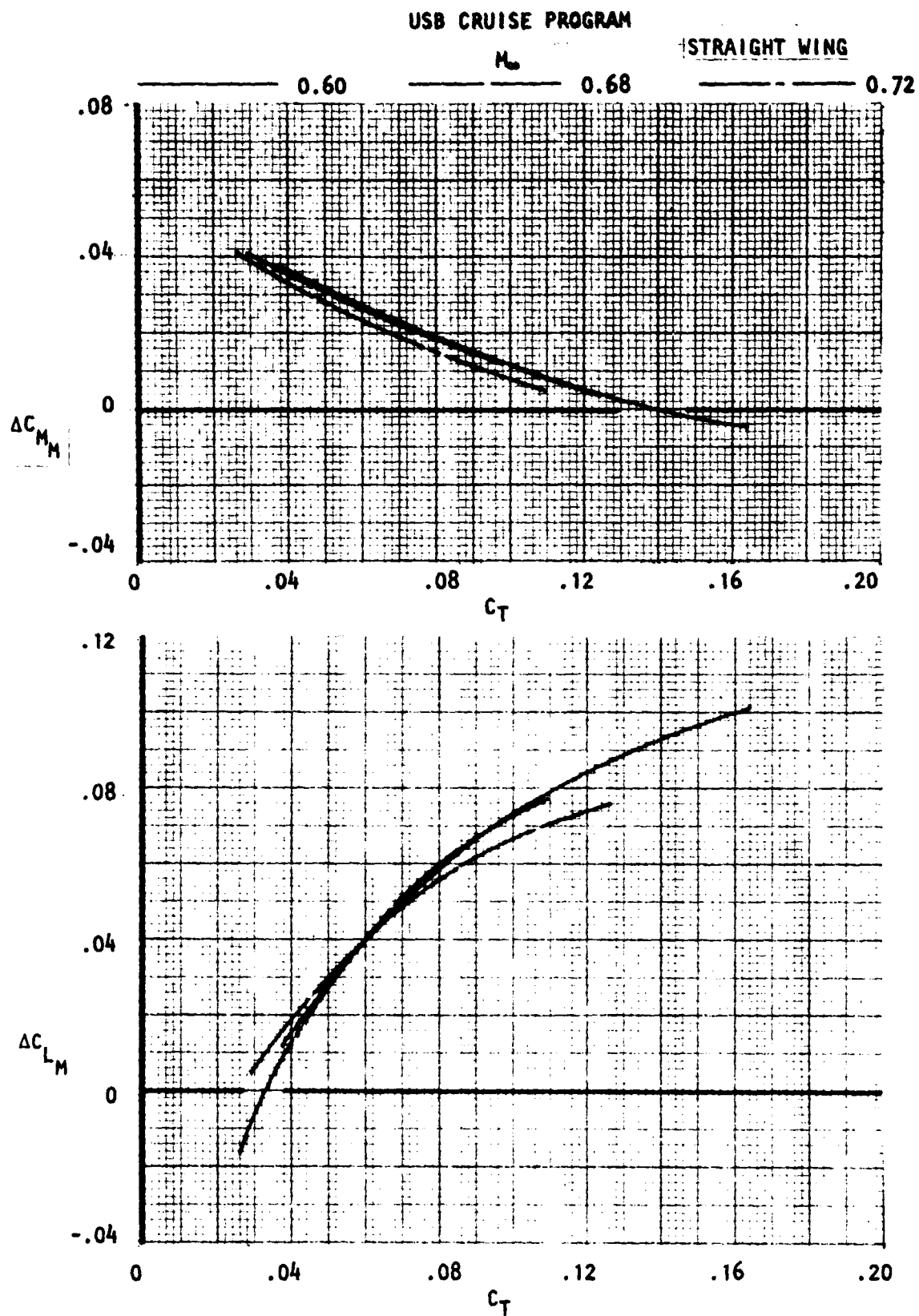


Figure 126 . Variation of lift and moment increments due to blowing, noz  $N_4$ ,  $AR = 4$ .

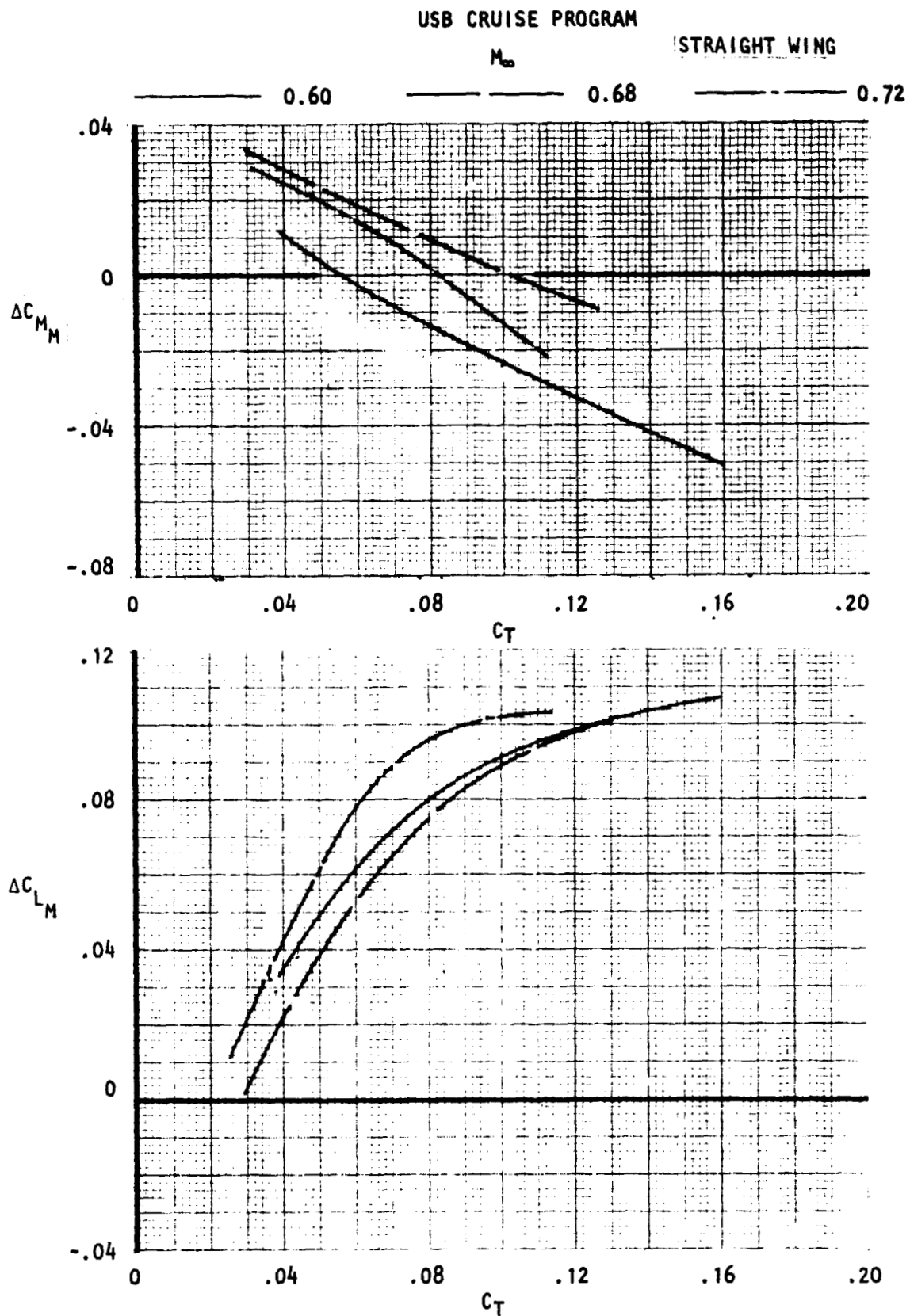


Figure 127 . Variation of lift and moment increments due to blowing, noz  $N_{4E}$ ,  $AR = 4$ .



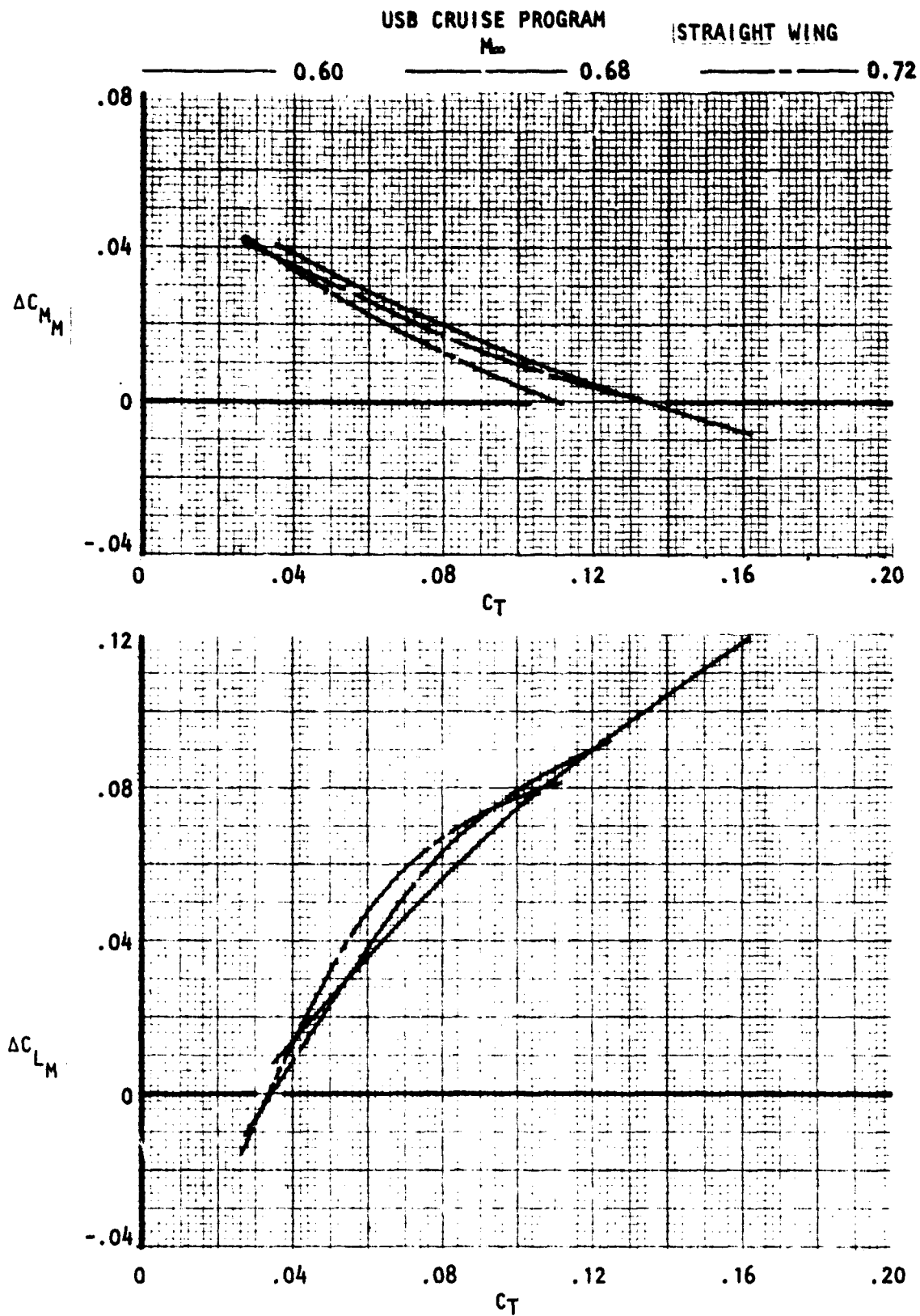


Figure 128 . Variation of lift and moment increments due to blowing, noz  $N_5$ ,  $AR = 6$ .

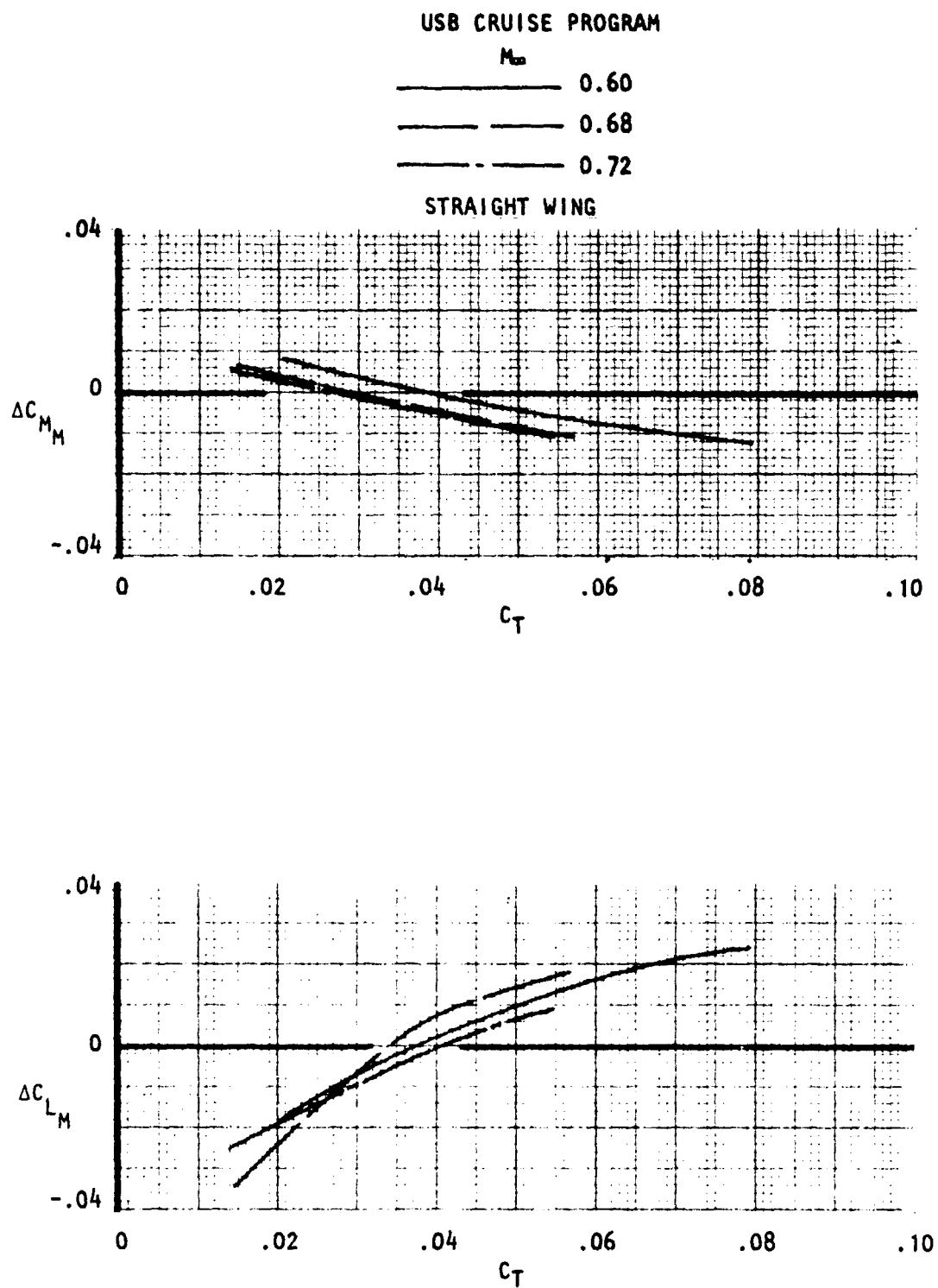


Figure 129. Variation of lift and moment increments due to blowing, noz  $N_6$ ,  $AR = 2.5$ .

# USB CRUISE PROGRAM

$M_{\infty}$

— 0.60  
 - - 0.68  
 - · - 0.73

SWEPT WING

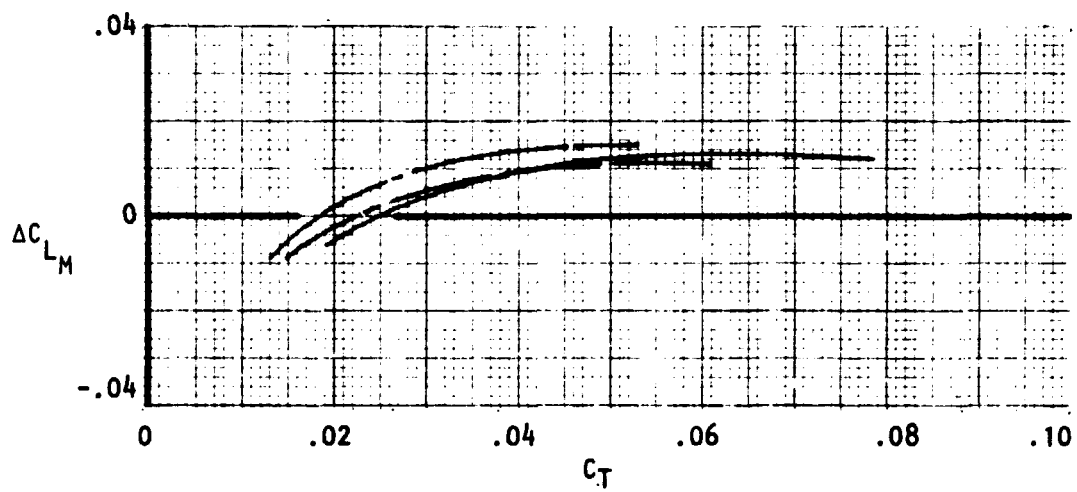


Figure 130 . Variation of lift increment due to blowing, noz  $N_{11}$ , circular.

# USB CRUISE PROGRAM

$M_\infty$

———— 0.60  
 ———— 0.68  
 - - - - 0.73

SWEPT WING

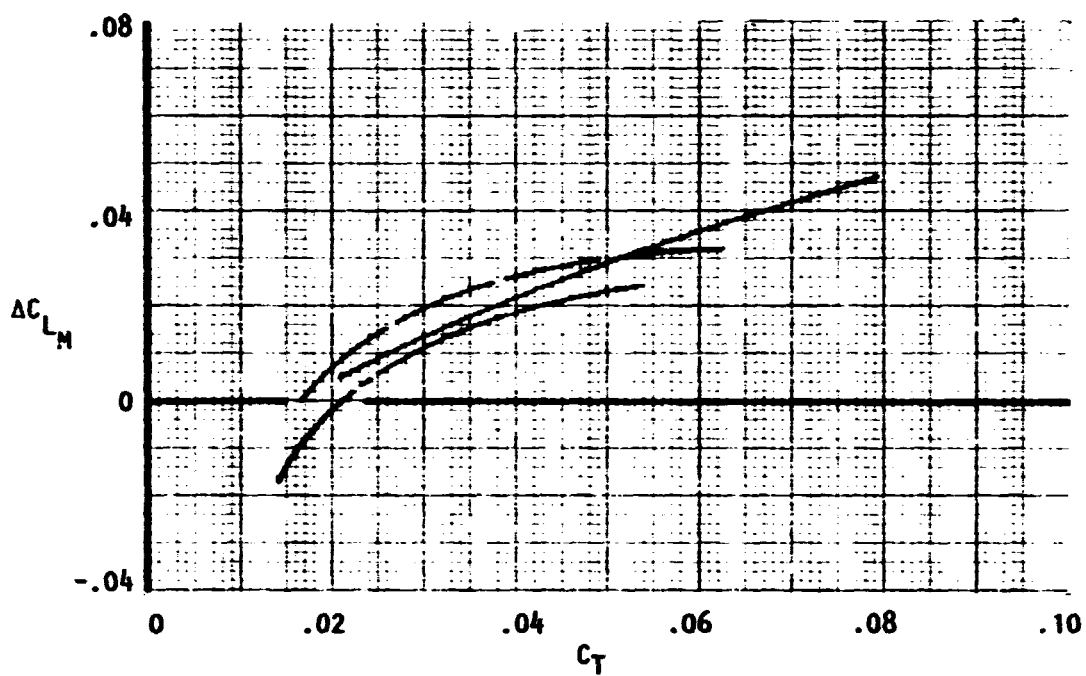


Figure 131 . Variation of lift increment due to blowing,  
 noz  $N_{12}$ ,  $AR = 4$ .

# USB CRUISE PROGRAM

$M_\infty$

———— 0.60

———— 0.68

----- 0.73

SWEPT WING

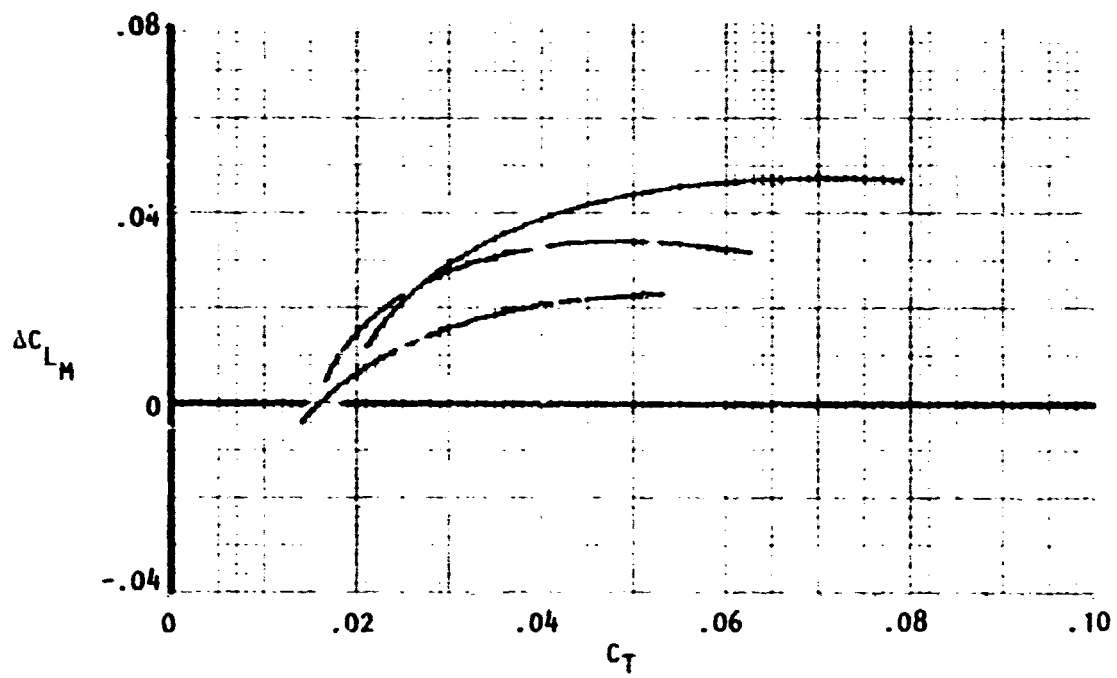


Figure 132 . Variation of lift increment due to blowing, noz  $N_{13}$ ,  $AR = 6$ .

- o Pitching-Moment Due to Blowing — The measured "nacelle-on" pitching-moments are shown as a function of nozzle pressure ratio for typical nozzle exit shapes in Figures 109 through 111. The data are shown at fixed angles-of-attack and for  $M_\infty = 0.68$ . While admittedly, pitching-moment data derived from semi-span models are generally felt to be unreliable, the trends shown with blowing correlate well with theory (as indicated in Section 4.0) and are therefore believed to be a reasonably valid representation of USB-type performance. As noted, the moment variation with  $H_j/p_\infty$  is consistent with the rate-of-change of jet-induced lift over the aft-portion of the wing with a slight trend toward a more nose-up moment as the blowing increases. In the bulk of the data (see Volume 11(B)) slight perturbations in moment are noted near  $H_j/p_\infty \approx 2.0$  as was mentioned in the lift discussions. It is also seen that the increment due to blowing is not strongly dependent on  $\alpha$ . As would be expected, the thick, circular jet produces a lower (less negative) pitching moment (Figure 133) than do the higher aspect ratio nozzles (Figures 134, 135); again, this trend is consistent with both lift and drag evaluations.

The basic data plots shown above have been used to obtain the pitching-moment increments due-to-blowing as a function of thrust coefficient ( $C_T$ ). These data are provided in Figures 125 through 129 for a constant angle-of-attack ( $\alpha \approx 2^\circ$ - $3^\circ$ ) for the various Mach numbers of interest as typical of both straight and swept wing nacelle installations. Further discussions of the pitching-moment data are provided in Section 4.0.

# USB CRUISE PROGRAM

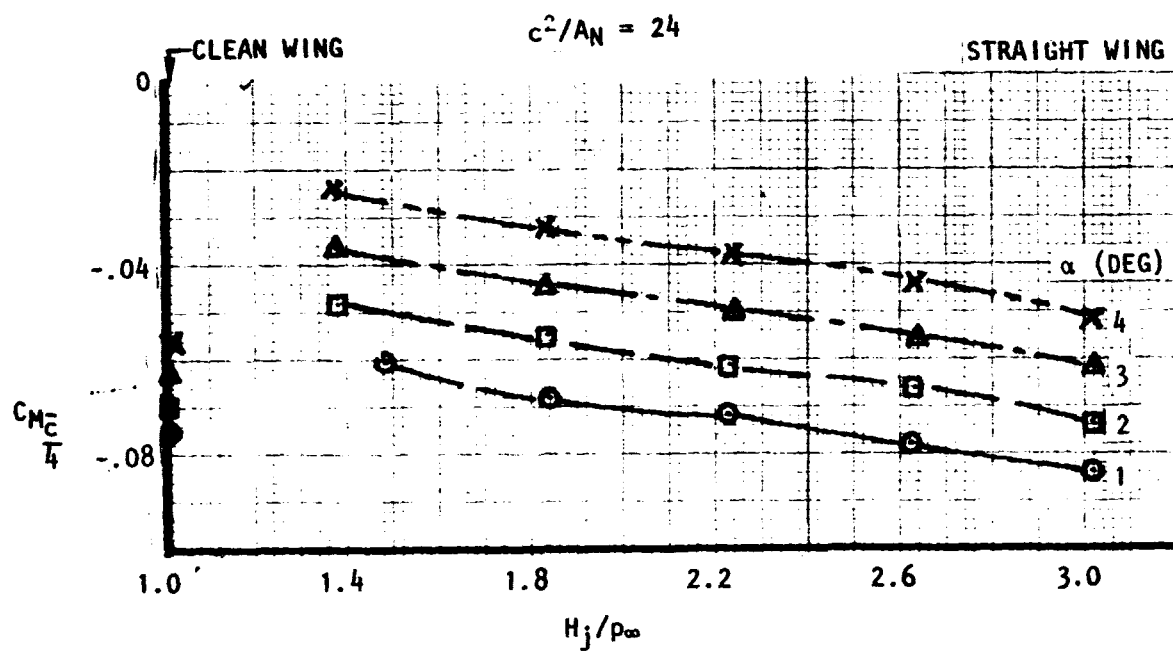


Figure 133 . Effect of nozzle pressure ratio on pitching-moment, noz  $N_2$ , circular,  $M_\infty = 0.68$ .

ORIGINAL PAGE IS  
OF POOR QUALITY

# USB CRUISE PROGRAM

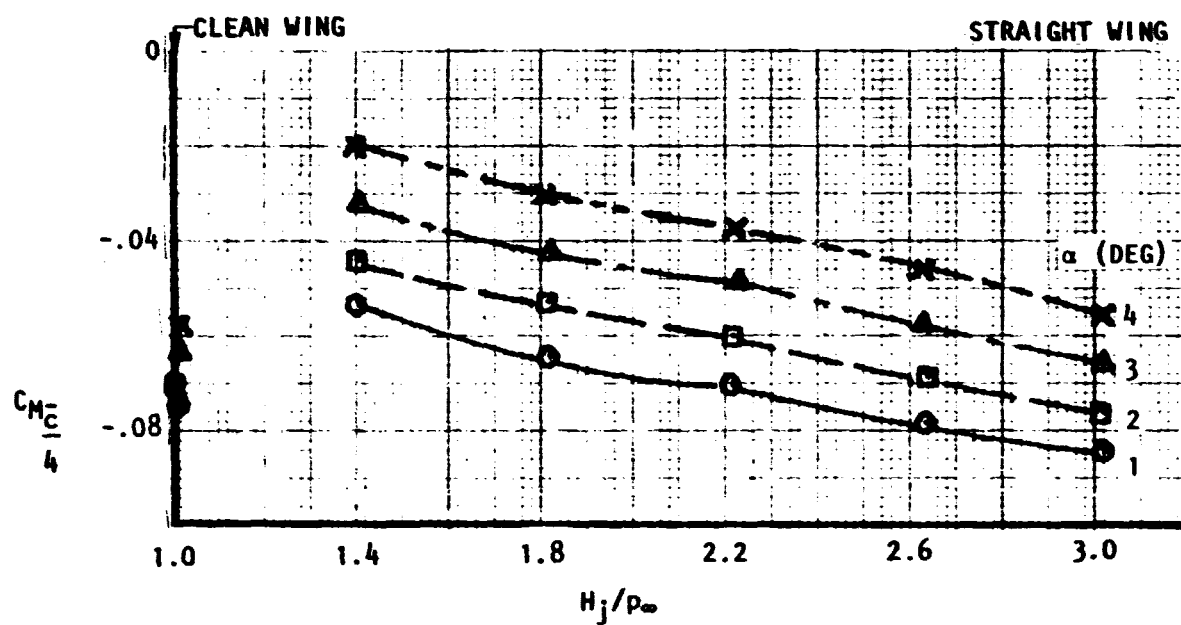


Figure 134 . Effect of nozzle pressure ratio on pitching-moment, noz  $N_{3E}$ ,  $AR = 2.5$ ,  $M_\infty = 0.68$ .



# USB CRUISE PROGRAM

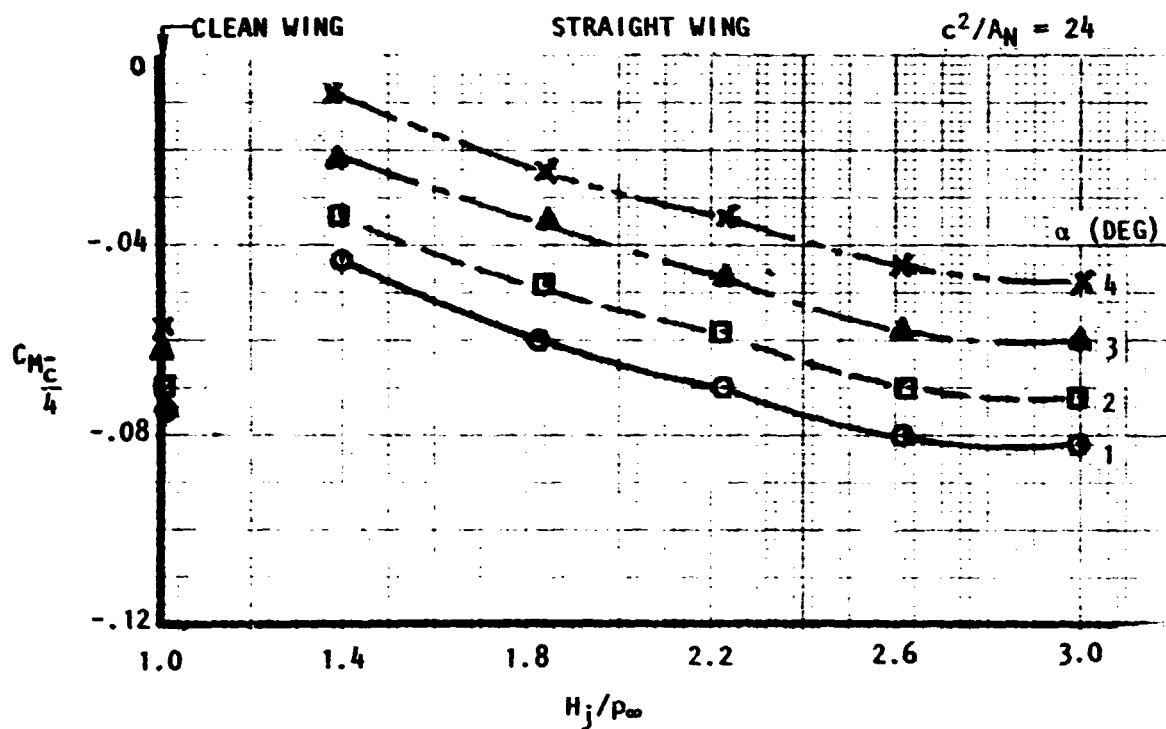
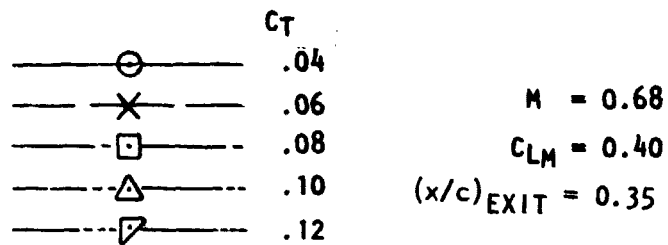


Figure 135 . Effect of nozzle pressure ratio on pitching-moment, noz  $N_5$ , AR = 6,  $M_\infty = 0.68$ .

3.2.3.3 Aerodynamic and Geometric Effects - Based on the incremental data curves presented in the foregoing section, the effects of geometric variations in the nozzles, wing/nacelle combinations and nacelle forebodies can be evaluated. The following sections consider the more significant effects obtained.

- o Effect of Nozzle Exit Aspect Ratio — To show the effect of nozzle exit aspect ratio at or near the wing/nacelle drag-rise ( $M_\infty = .68$ ,  $C_{LM} = 0.40$ ), the data of Figure 136 has been prepared. The drag penalty for each nacelle at various levels of  $C_T$  has been normalized by the drag of the circular nozzle configuration ( $AR = 1.25$ ). This plot indicates that the circular nozzle has the lowest drag of the basic exit shapes considered and that in the exit aspect ratio range 2.5 ("D-Duct") to 4.0, the design thrust coefficient would need to be considered in selecting a minimum-drag configuration. As noted in the discussions and data of Section 3.2.2, the more two-dimensional nozzle configurations suffer from higher scrubbing losses and a high pressure drag induced by a well-attached jet. Although these configurations show a favorable trend in the drag-due-to-lift component as  $C_T$  increases, the improvement is not sufficient to offset the former losses. This would be particularly true at moderate nozzle pressure ratios where the drag-due-to-lift of the wide nozzle shapes has not recovered from an initially large installation loss. For a representative high-by-pass-ratio fan engine, a  $C_T$ -level of about 0.07 would correspond to a nozzle pressure ratio of about 2.0 and a fan pressure ratio of 1.47. From the data of Figure 136, a circular nozzle would be selected from a cruise drag standpoint. However, in the interest of avoiding the need for an extensive variable geometry capability for the

# USB CRUISE PROGRAM



NOTE: DATA BASED ON BOTH  
STRAIGHT & SWEPT  
WING RESULTS.

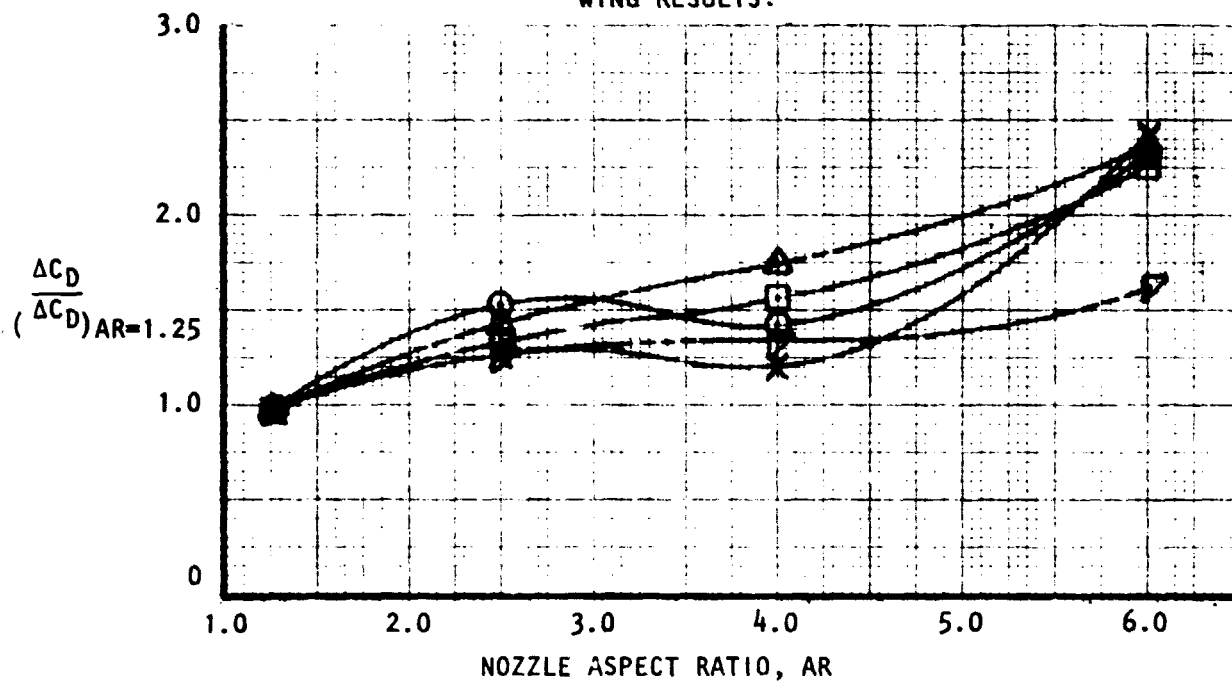


Figure 136 . Effect of nozzle aspect ratio on nacelle drag.

nozzle when operating in the powered high-lift mode, this choice could be compromised without severe cruise penalty by the selection of a higher aspect ratio exit shape. Thus, the "D-Duct" design (aspect ratio 2.5) would represent a reasonable compromise configuration and the Task III Compatibility Study (Section 6.0) reflects this choice.

- o Effect of Nacelle Boattail Angle — The angle between the nacelle center-line upper surface at the exit and the wing chord plane, as used herein, is the boattail angle,  $\beta$ . Across the range of exit shapes tested, this angle varied from about  $6^\circ$  to a maximum of about  $36^\circ$ . In general, the lower angles represented circular nozzle designs with the higher angles required by the wider, high aspect ratio nacelles. For a given nozzle aspect ratio, this angle was also varied by changing the nacelle forebody length. In an attempt to define a limiting angle from a cruise standpoint, the data of Figure 137 has been prepared. Test results are shown in a drag ratio-form with the denominator representing a circular nozzle with  $\beta \approx 6^\circ$ . Below  $\beta \approx 25^\circ$  the trends are not completely uniform due, it is believed, to variations in the effectiveness of the wing/nacelle filleting provided. Above  $25^\circ$ , however, the sharp increase in drag suggests that about  $25^\circ$  represents the maximum value of  $\beta$  if severe boattail separation effects are to be avoided. It is also noted that as  $C_T$  increases, the drag ratio diminishes in value as the jet trends to suppress some of the separation through a pumping effect.
- o Effect of Forebody Fairing — The drag increment associated with an open, or flow-through, type of forebody is compared in Figure 138 to that

# USB CRUISE PROGRAM

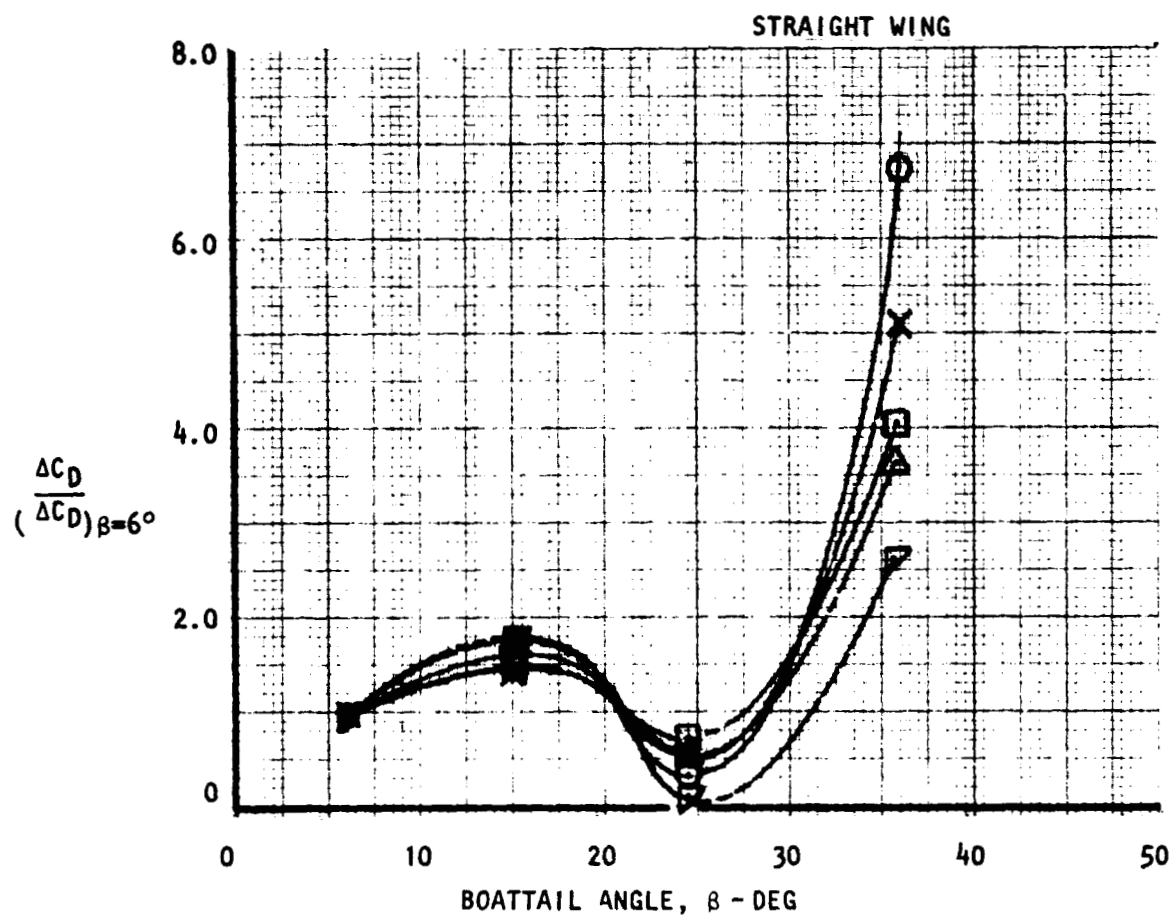
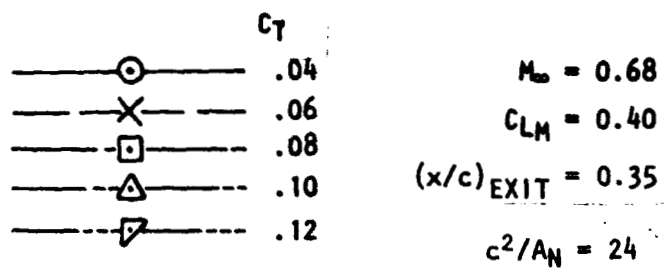


Figure 137 . Effect of nozzle boattail angle on nacelle drag.

# USB CRUISE PROGRAM

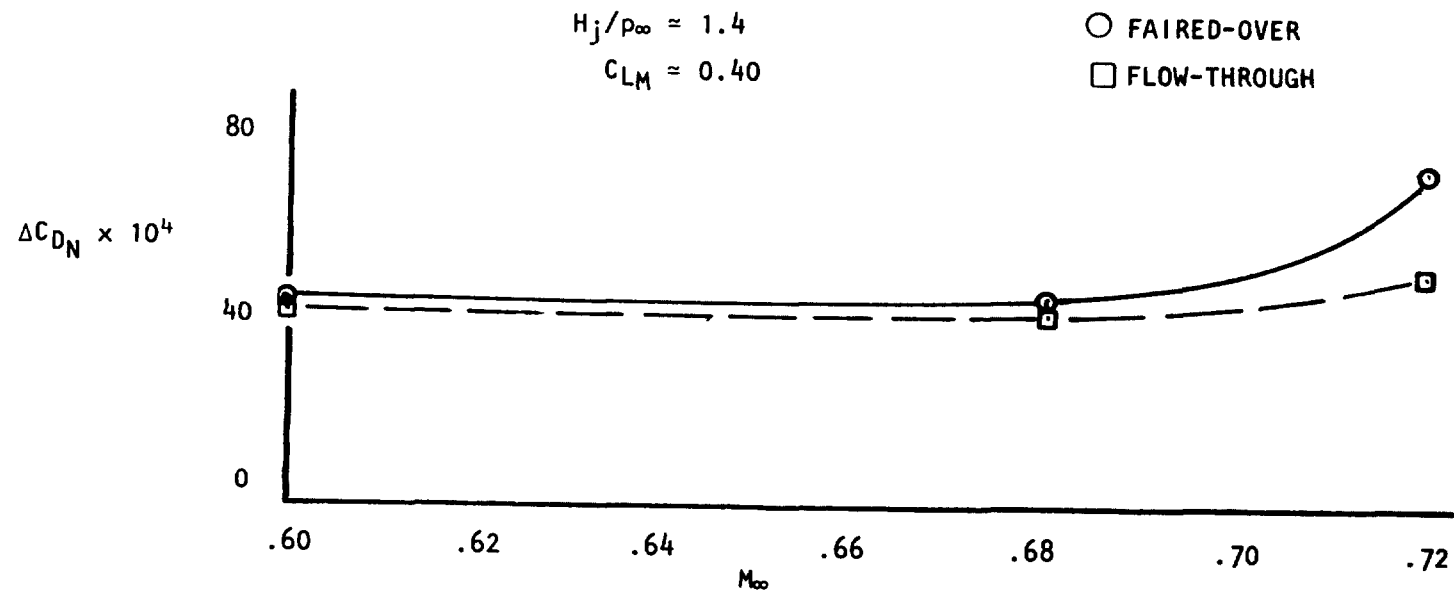


Figure 138 . Effect of Mach number on drag for faired-over vs flow-through forebodies, straight wing with circular noz  $N_2$ .

associated with a faired-over forebody with the latter operating at a flow-through nozzle pressure ratio. The nozzle in both cases is a circular configuration of intermediate size ( $c^2/A_N \approx 24$ ). This study was made to determine if any significant drag differences were incurred when utilizing the two types of testing methods. Note that in this comparison, the internal friction drag of the flow-through nacelle has been subtracted out. The drag difference is only minor at speeds in the sub-critical Mach range. Beyond the drag-rise of the straight-wing/nacelle combination ( $M_\infty \approx 0.68$ ), the faired-forebody yields a substantially high drag penalty probably as a result of a difference in area-ruling effect on the wing-body combination. It is concluded, from this portion of the study that no major drag difference results when using the faired-forebody as a simple means of synthesizing powered nacelles, at least for the lower nozzle pressure ratios and at speeds up to the drag-rise Mach number.

- o Effect of Forebody Length - An interesting sidelight in the study of the faired nacelle forebody indicates that the length of the forebody (Figure 139) does have some effect on the lift performance of the system. Figure 140 compares the total lift variation of the short and long forebodies at a flow-through pressure ratio to that of the basic wing/body; "D-Duct" nozzles ( $N_{3E}$  and  $N_{3B}$ ), are installed as the powered configurations. The longer forebody ( $N_{3B}$ ), designed to minimize boattail angle, apparently causes a shift in the angle-of-zero-lift toward a more positive value such that, for a given  $\alpha$ , a lift penalty of about 0.03 is incurred. In contrast, the short forebody configuration (high boattail angle) produces a  $\Delta C_L \approx +0.01$

USB CRUISE PROGRAM

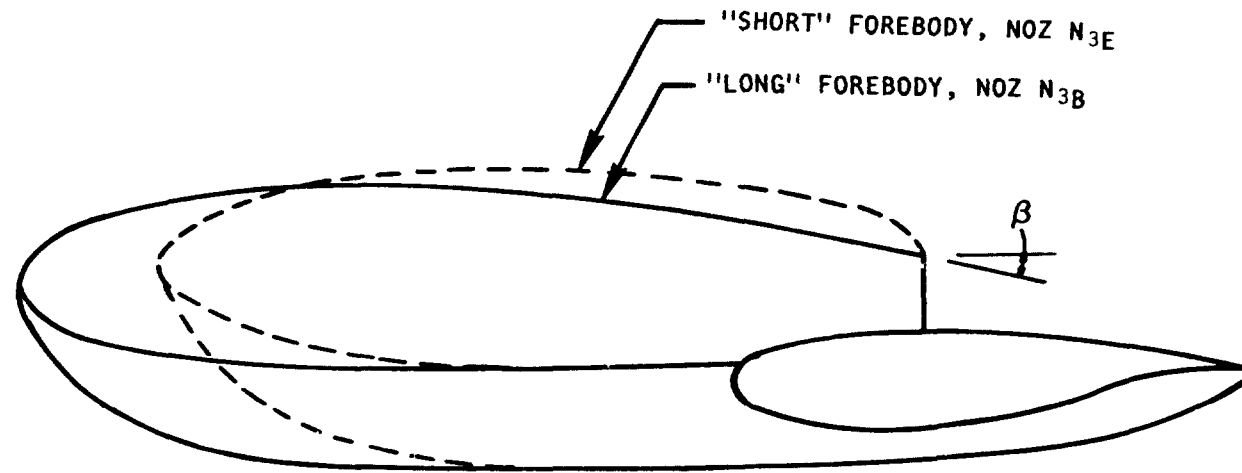


Figure 139 . Comparison of "long" and "short" faired forebodies,  $c^2/A_N = 24$ .



# USB CRUISE PROGRAM

$$c_l^2/A_N$$

○ N<sub>6</sub> 48 (STREAMLINED)

□ N<sub>3E</sub> 24 (SHORT)

△ N<sub>3B</sub> 24 (LONG)

— BASIC STRAIGHT WING

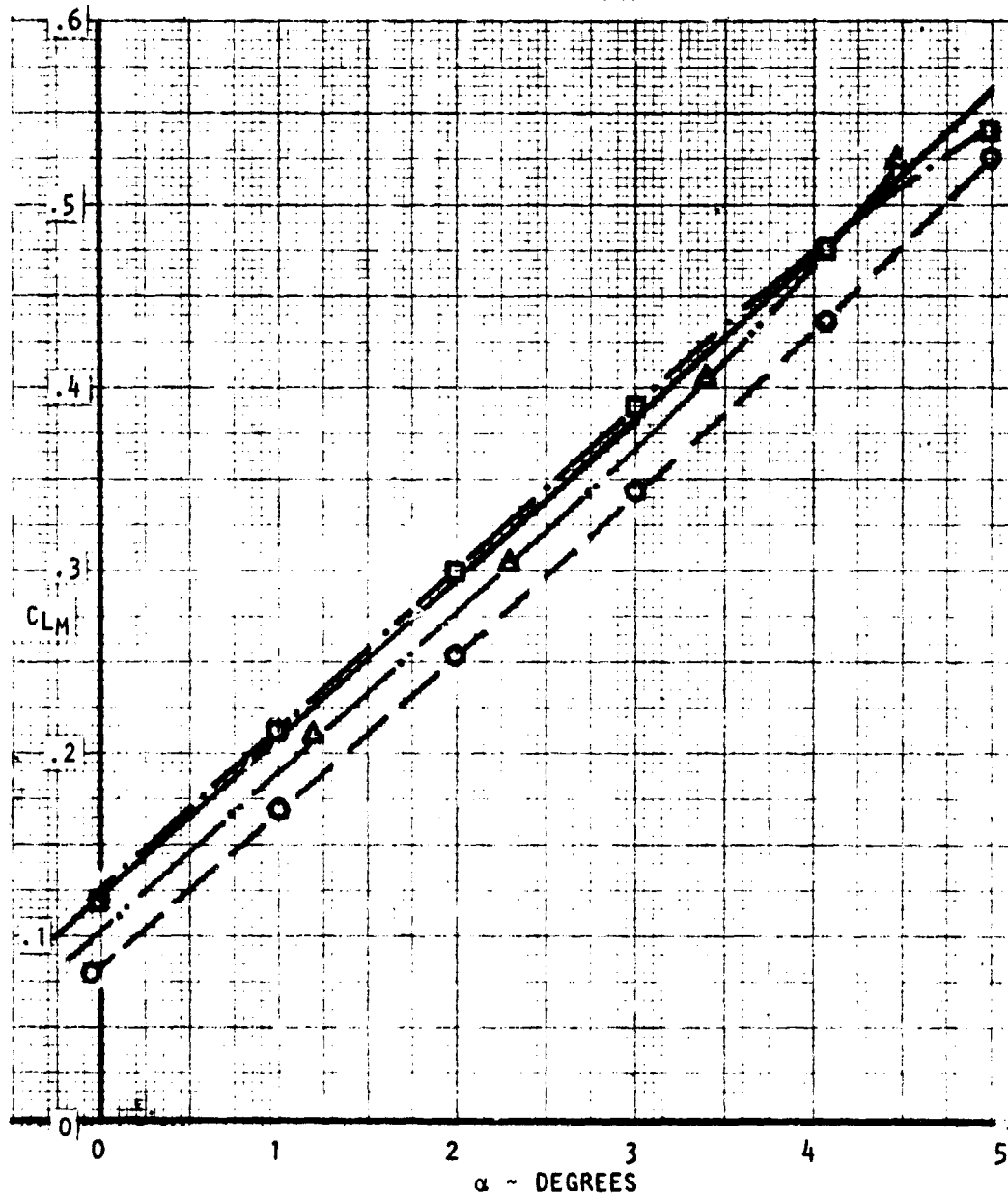


Figure 140 . Comparison of lift performance of "short" and "long" forebodies,  $M_\infty = 0.68$ ,  $H_j/p_\infty = \text{flow-through}$ .

relative to the basic wing. This same trend prevails across the range of nozzle exit aspect ratio as shown in Figure 141. In this figure, the lift increment (or decrement) sustained upon installation of the nacelle on the basic wing at the flow-through condition is denoted by the bottom lines. The top lines indicate the lift increments obtained with blowing at a pressure ratio of 3.0. It is seen that the short-forebody nacelles generally show small positive lift increments upon installation at flow-through pressure ratio, whereas generally negative increments are shown for the longer forebody configurations. Additionally, the lift increment due to blowing is somewhat higher for the former designs which could reflect the higher boattail angles designed into these nozzles. Thus, while the use of the faired forebody does not appear to have a significant effect on drag (at a specified lift), there does appear to be a consistent effect on lift at constant  $\alpha$ .

- o Effect of Nacelle Streamlining — A small "O-Duct" nozzle configuration ( $N_6$ ) was analytically designed (Volume IIA) and tested on the straight wing in an attempt to quantify the merits of streamlining. As noted in Volume IIA, the major difference between the streamline and symmetrical nacelles was a lowering and shaping of the forebody for alignment with the incoming streamlines. While streamlining the plan-view was also performed, the geometric differences from that of the symmetrical nacelles was very slight due to the planform of the unswept wing. A direct drag comparison of the streamlined nacelle versus the symmetrical nacelle is not available in the test data inasmuch as the straight wing nozzles were of generally a larger size ( $c^2/A_N = 24$  vs.  $c^2/A_N = 48$  ( $N_6$ )); the smaller

# USB CRUISE PROGRAM

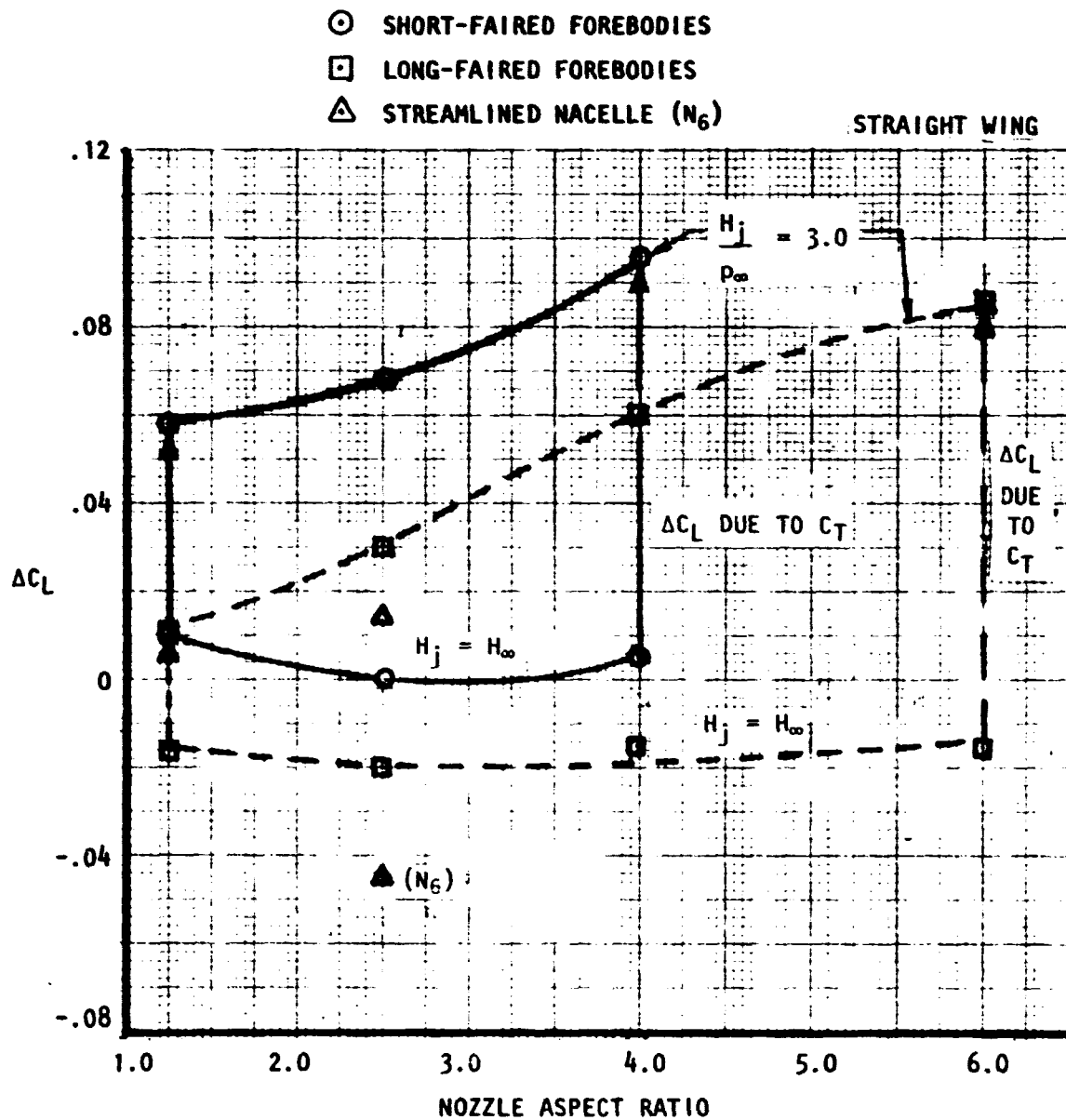


Figure 141. Effect of nacelle installation and blowing on lift  $\alpha = 3^\circ$ ,  $M_\infty = 0.68$ .

nacelle sizes were normally tested on the swept-wing configuration. However, in an attempt to provide such a comparison, Figure 142 shows the drag of the streamlined configuration compared to that of a symmetrical nacelle of the same size, but tested on the swept-wing configuration. On this basis, the effects of sweep and the associated differences, or relative adequacy of the wing-nacelle fillets may play a role in the comparison. As indicated, beneficial drag effects are noted in the lower Mach-range and at the flow-through pressure ratio. This difference is due primarily to the lower drag-due-to-lift penalty of the streamlined configuration which, of course, was a major design objective. At the higher pressure ratio and at cruise Mach numbers, the streamlined nacelle, which was designed with an almost non-existent boattail angle, shows small drag benefits due, in this instance, to a slightly lower pressure drag increment. The lift performance of the streamlined nacelle is compared to that of two-larger "D-Duct" nozzles in Figure 139. Since the streamlined nacelle is designed to carry very little loading on the forebody, the lift penalty upon installation to the basic wing is the highest for any of the nacelles tested. This difference may also be noted on Figure 141, where the streamlined nacelle is represented by a single point ( $AR = 2.5$ ) at flow-through pressure and again at  $H_j/p_\infty = 3.0$ . The beneficial effects of streamlining should become more pronounced as the wing sweep is increased and the present comparison using a straight wing probably should not be generalized. However, from the present results, the design rationale utilized for nacelle streamlining merits some re-examination.

# USB CRUISE PROGRAM

○ STREAMLINED ( $N_6$ ) - STRAIGHT WING

□ SYMM ( $N_8^2$ ) - SWEPT WING

$$c^2/A_N = 48 \quad H_j/p_\infty = 1.4$$

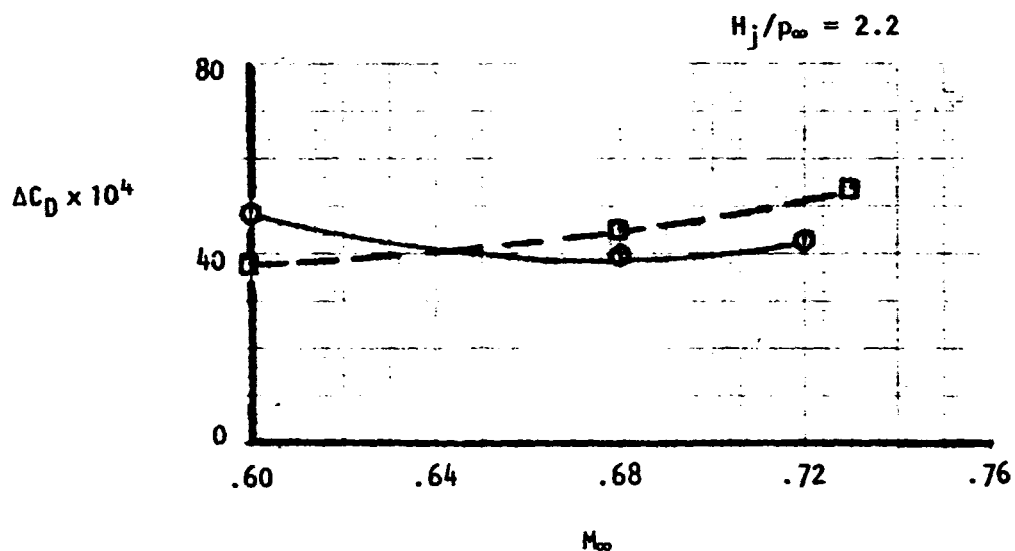
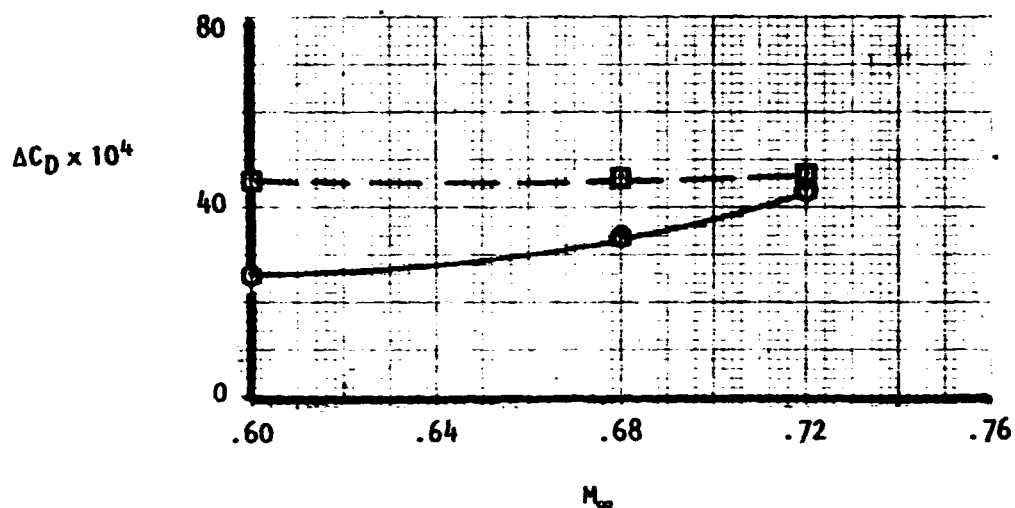


Figure 142. Comparison of streamlined and symmetrical nacelle drag,  $C_{LM} = 0.40$ .

ORIGINAL PAGE IS  
OF POOR QUALITY

- o Effect of Multiple - Nacelles — Figure 143 compares the nacelle drag increment of a 4-engine swept-wing configuration to that of a 2-engine design both with small "D-Duct" nozzles ( $N_8$ ) at several pressure ratios. As presented, the friction drag ( $\Delta C_{D_{NF}}$ ) of the nacelles has been removed from the drag increment. Also shown is a drag level derived by taking one-half of the 4-engine increment for comparison to the 2-engine version. At both of the representative pressure ratios, the data show that the drag does not scale proportionally with the number of engines with the 2-engine configuration showing a higher relative interference drag than does the 4-engine case. In the foregoing drag-due-to-lift data (Figures 114 and 117) it is seen that, while this penalty is larger for the 4-engine version, it is not doubly so, as might be expected. Additionally, the drag build-ups provided in the same section show that, in general, the 4-engine configuration reflects slightly lower turning angles than the 2-engine counterpart thus producing slightly less pressure drag. Further evidence of this difference is shown in Figure 144, where the lift-due-to-blowing is presented for the two cases at  $M_\infty = 0.73$ . Except at the highest pressure ratio, the total lift of the 4-engine configuration is less than that of the 2-engine with the lift trend of the former showing intermittent attachment of the jet in the lower blowing range. Note that in these data, the 4-engine case is producing twice as much thrust as its 2-engine counterpart. Although the jets are widely spaced, it is believed that the two jets, operating in close proximity to each other with exits at a constant  $x/c = 0.20$ , produce a mutual interference which tends to suppress jet attachment. Oil flow photographs are not conclusive in this regard, although they generally show

# USB CRUISE PROGRAM

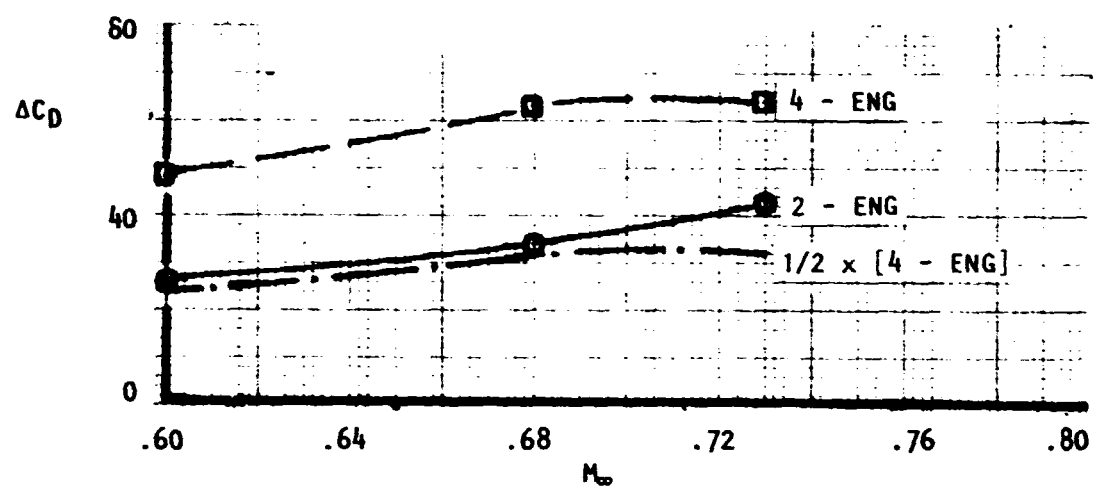
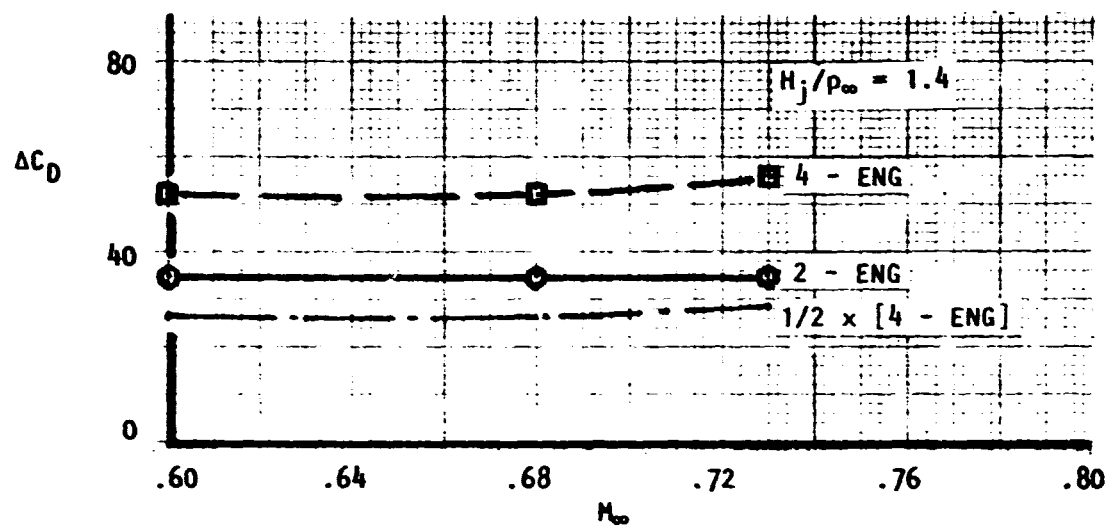


Figure 143 . Effect of multiple engine installation on drag  $C_{LM} = 0.40$ , swept wing.

# USB CRUISE PROGRAM

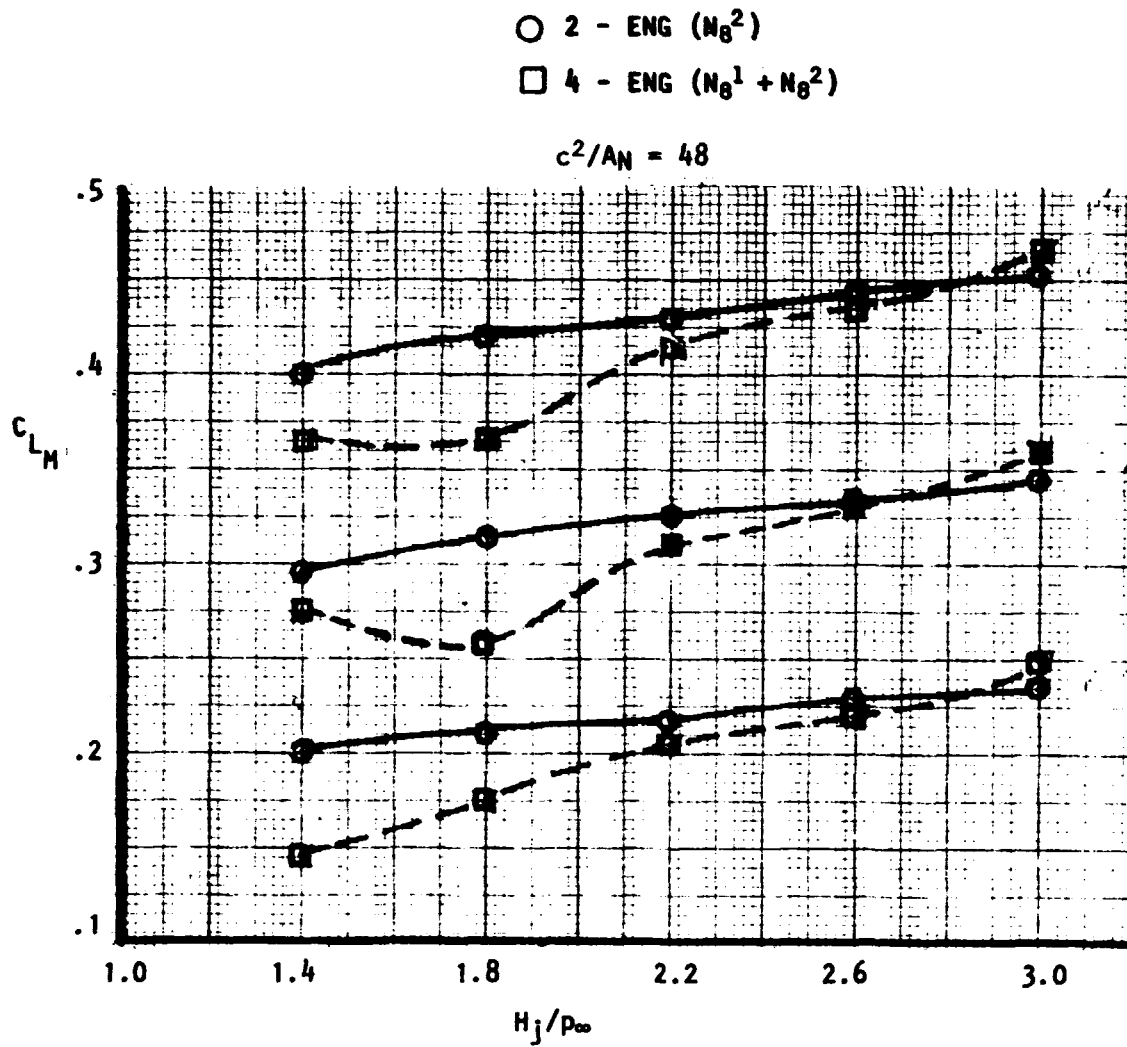


Figure 144 . Comparison of lift-due-to-blowing for 2-eng. and 4-eng. configurations "D-duct" nacelle, swept wing,  $M_{\infty} = 0.73$ .



a slightly larger scrubbing footprint behind the single nacelle than do the photographs of the twin nacelle configuration. A conclusion basic to this study is that the interference drag does not necessarily scale in proportion to the number of USB-type engines and that any effective means of suppressing jet attachment will generally be beneficial to cruise performance drag.

- o Effect of Nozzle Installation Height — In an effort to quantify drag trends as the nacelle is moved vertically from the wing-surface, the circular nacelle was tested in both an integrated (USB) - type model and a pylon-mounted (OTW) configuration. Results are shown in Figure 145 across the test speed range; both pylon and nacelle drags are represented in the data. The short-pylon configuration shows a lower drag coefficient than either the integrated (USB) or the long-pylon OTW configuration, although the drag difference in any case is not large. Since these tests were conducted on the straight wing, camber variations designed into the pylons for minimum load, were very slight. Oil-flow studies of the OTW designs indicated that the pylon intersection near the wing inboard leading-edge generated a vortex-type of flow which should be detrimental to the drag of these configurations. While attempts to modify this flow pattern were made through the use of wax fairings, it appeared that re-design of the pylon in both camber and, particularly, chordwise length, would be required to affect a major improvement in the flow. At the supercritical Mach number of 0.72, both pylon-configurations show a favorable trend in drag reflecting a more moderate drag-rise for the nacelle-on case than for the basic wing-body. The drag differences

ORIGINAL PAGE IS  
OF POOR QUALITY

# USB CRUISE PROGRAM

$$C_{LM} = 0.40 \quad H_j/p_\infty \approx 1.4$$

- SHORT PYLON (NOZ 0.5  $D_N$  ABOVE WING SURF.)
- INTEGRATED (DISCHARGE ON SURF.)
- △ LONG PYLON (NOZ 1.0  $D_N$  ABOVE WING SURF.)

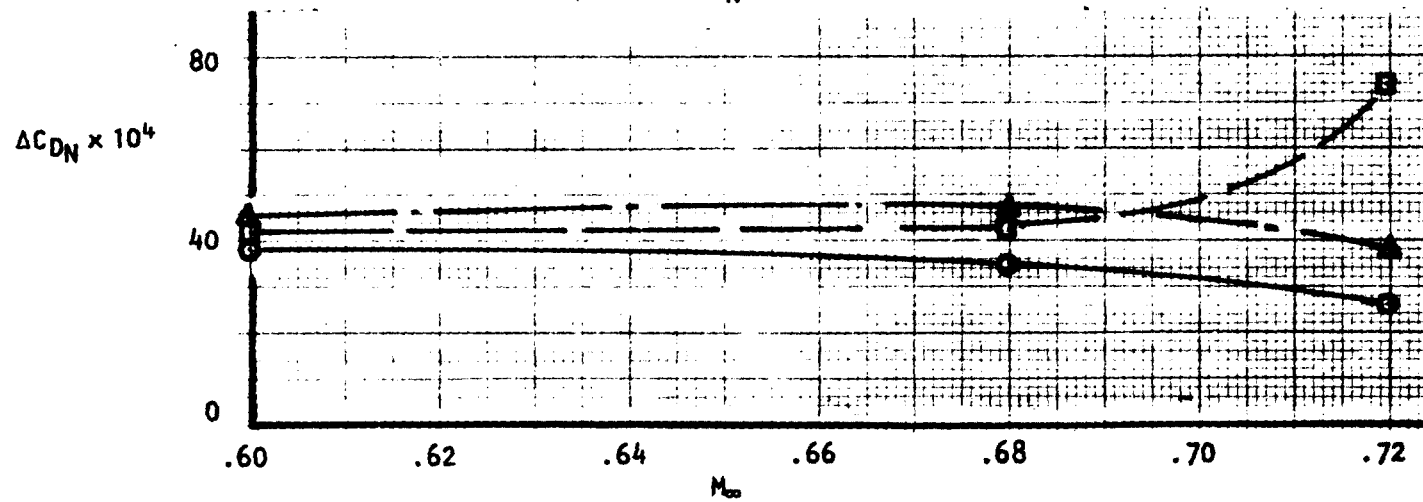


Figure 145 . Effect of Mach number on drag for pylon-mounted OTW vs. integrated USB nacelle, straight wing with noz  $N_2$ .

shown at the lower speeds are due primarily to differences in drag-due-to-lift since scrubbing or jet pressure drag are essentially zero at the flow-through pressure ratio. At realistic nozzle pressure-ratios, these two drag components would need to be offset by a jet-induced improvement to the drag-due-to-lift component if the integrated nacelle is to remain the drag-equivalent of the OTW-design. These factors, together with the analytical and experimental results of References 5 and 6 indicate some merit in additional studies for optimizing the OTW design as a possible cruise configuration.

## 4.0 USB THEORETICAL MODEL

### 4.1 INTRODUCTION

The USB wing/nacelle/propulsive interactions are complex, not only in their viscous aspects, but also with regard to the potential flows involved.

Theoretical studies have heretofore been aimed at improving understanding of potential flows with minimal representation of viscous effects. The overall philosophy has been to implement the simplest realistic method for simulating the nacelle-environment and to embed in this a simplified model of the spreading jet plume. The present studies represent an implementation of methods described in Reference 7 and, in the powered aspects, are somewhat similar to the approach published in Reference 8.

A large degree of realism in the model geometry was enforced by the fact that the present studies support an experimental program embodying thick airfoil sections which, with the exception of a single streamlined design, were fitted with arbitrarily-shaped nacelles. In order to develop proper force trends for such geometries, fairly elaborate panel layouts had to be generated for both the wings and the nacelles.

To place the present work in perspective, the background for power-effects modeling by present methods will be described in Section 4.2. Thick-wing representation and the effects of boundary layer development will then be discussed in Section 4.3 before considering finite-wing and power effects in subsequent sub-sections.

#### 4.2 POWER EFFECTS MODELING: GENERAL PRINCIPLES

The most fundamental aspect of powered-flow modeling concerns the simulation of flows of differing total pressure. Figure 146 illustrates, in vortex-modeling terms, the production of a total pressure jump across a fan situated in a long, constant-area duct, embedded in a 'mainstream' flow of speed,  $V_\infty$ . The fan is situated on plane 'A' and it is assumed that the duct exhausts at the ambient static pressure ( $p_\infty$ ) in a parallel manner. For this to happen, the ring vorticity to the right of 'A' must convect at mainstream velocity plus its self-induced velocity, i.e.,  $(V_\infty + \gamma/2)$ . Conditions downstream of the fan are thereby defined. Upstream of the fan, the absolute pressure is  $(p_\infty - \Delta P)$ , where  $\Delta P (= \Delta H)$  is the pressure rise imparted by the fan. An inward force on the duct wall is also present which can only be generated if the ring vorticity there moves at less than its natural convection speed. This ring vorticity convection speed will now be determined.

If  $V_R$  is the convection speed of the vortex ring vorticity to the left of AA, the velocity of the flow passing over each element is  $(V_\infty + \gamma/2 - V_R)$  and the force,  $dF$ , experienced by an element of axial length  $dz$  is

$$dF = \rho \left( V_\infty + \frac{\gamma}{2} - V_R \right) \gamma \, dz \, R d\theta$$

or

$$\frac{dF}{R d\theta dz} = \rho \left( V_\infty + \frac{\gamma}{2} - V_R \right) \gamma = \Delta p = \Delta H \quad (24)$$

# USB CRUISE PROGRAM

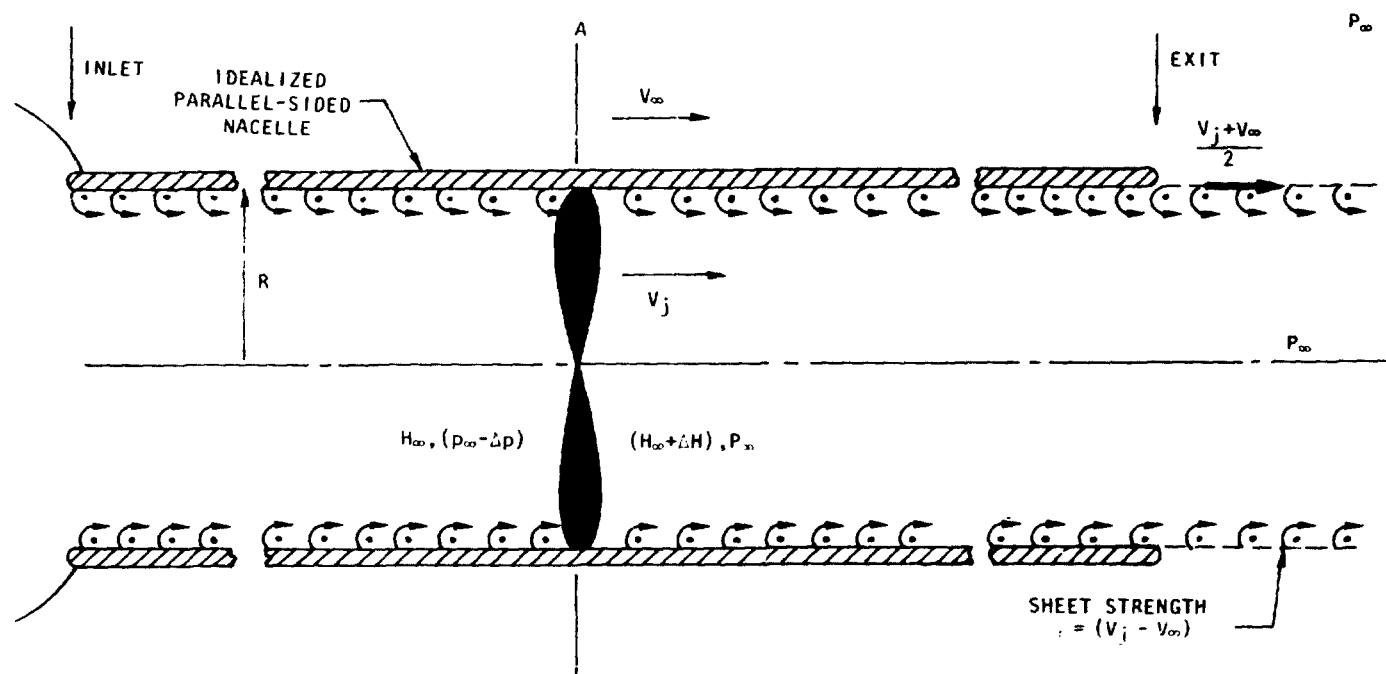


Figure 146. Simulation of fan pressure rise

We note that, if the convection speed  $W_R$  equals the "natural" convection speed  $(V_\infty + \gamma/2)$  there is no radial force. However, for the inlet air

$$H = p_\infty + \frac{1}{2} \rho V_\infty^2$$

while, downstream of the fan,

$$H + \Delta H = p_\infty + \frac{1}{2} \rho V_j^2$$

so that

$$\Delta H = \frac{1}{2} \rho \{V_j^2 - V_\infty^2\} \quad (25)$$

Equating (24) and (25) and substituting for  $\gamma$

$$\rho \left( V_\infty + \frac{1}{2} (V_j - V_\infty) - V_R \right) (V_j - V_\infty) = \frac{1}{2} \rho (V_j + V_\infty) (V_j - V_\infty)$$

which yields

$$V_R = 0. \quad (26)$$

Equation (26) shows that the vortex ring vorticity to the left of "A" is fixed to the nacelle wall. It has been shown that the ring vorticity to the right of AA is moving at a total velocity of  $(V_\infty + \gamma/2)$ , so it follows that fan operation is represented in vortex terms by a continuous injection of ring vorticity from the blade tips. The downstream sheet-strength is the

same as the upstream strength; the instantaneous acceleration of the downstream sheet, at the fan plane, gives rise to the total pressure jump across the fan.

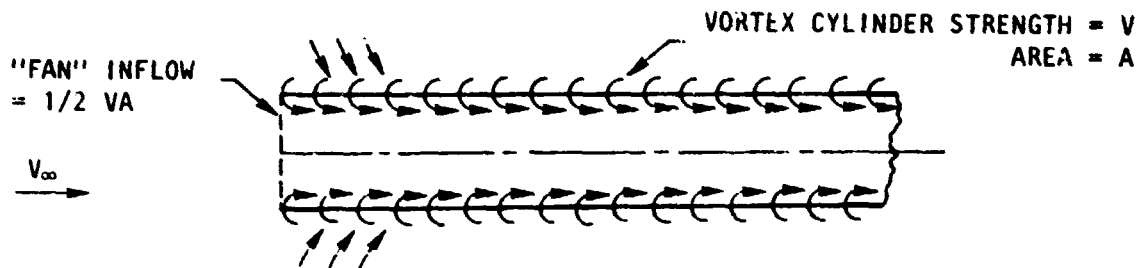
In determining the effect, at some point in the flow, of a combined system of fixed and moving vortex elements, motion of particular elements does not affect the velocities they induce. The flow field just described may be "frozen" at a particular time once jet development reaches equilibrium (see below), and then steady-state conditions may be determined. The ring-vorticity injection plane around the fan tips is not "visible" under such conditions.

Returning to the idealized nacelle of Figure 146, it will be noted that inflow is present through the upstream wall unless additional constraints are applied. Figure 147 shows how a vortex lattice may be used to provide appropriate constraints. Radial velocities, induced at the front of the vortex cylinder, give rise to intake thrust on the vortex lattice.

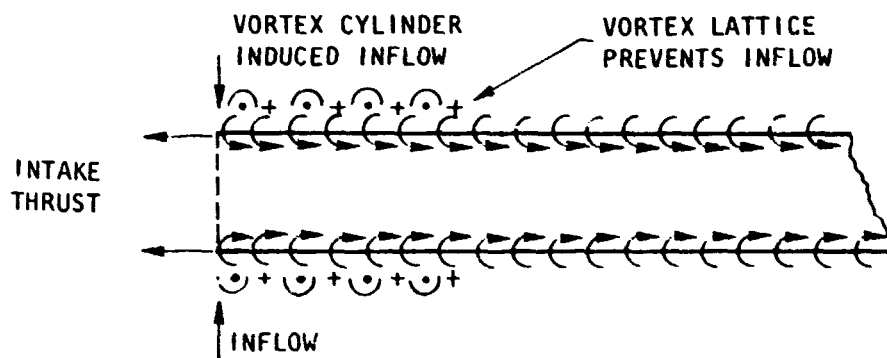
A jet emergent coaxially with a freestream flow spreads and entrains mainstream fluid. A line sink down the jet axis is frequently used for the far-field effects, but this is too crude an approximation for the present study because of the close proximity to the USB wing surface. An acceptable alternative is an expanding, decreasing-strength ring vortex system tailored to conserve axial momentum while entraining mainstream fluid at a rate determined from standard results for axisymmetric jets. An approximate entrainment equation was obtained from results quoted in Reference 9. This



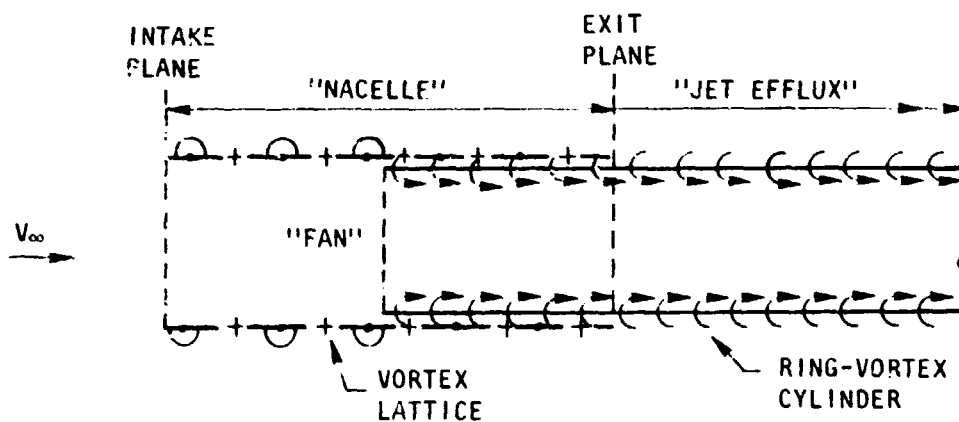
# USB CRUISE PROGRAM



(a) VORTEX CYLINDER ACTING ALONE



(b) VORTEX CYLINDER WITH VORTEX LATTICE CONTROLLED INFLOW



(c) REPRESENTATION OF A POWERED NACELLE

Figure 147. Jet simulation methods.

relates entrainment mass flow rate  $\Delta\dot{m}$  to axial position and vortex sheet strength. Thus,

$$\frac{\Delta\dot{m}}{\dot{m}_E} = 0.115 \frac{(x - x_E)}{R_E} \frac{\gamma_E}{V_E} \quad (27)$$

where subscript E refers to nacelle exit plane values and  $R_E$  is the effective radius at the nacelle exit. If the jet mass flow, area and mean velocity are  $\dot{m}$ , A and V (all functions of x) we may now write

$$\dot{m} = \dot{m}_E \left( 1 + 0.115 \frac{(x - x_E)}{R_E} \frac{\gamma_E}{V_E} \right)$$

or

$$\rho AV = \rho A_E V_E \left( 1 + 0.115 \frac{(x - x_E)}{R_E} \frac{\gamma_E}{V_E} \right) . \quad (28)$$

For conservation of momentum

$$\rho AV^2 = \rho A_E V_E^2 \text{ in a free environment.} \quad (29)$$

Substituting for V in (28) and rearranging yields

$$\frac{A}{A_E} = \frac{V_E^2}{V^2} = \left\{ 1 + 0.115 \frac{(x - x_E)}{R} \frac{\gamma_E}{V_E} \right\}^2 \quad (30)$$

Axial variation of vortex cylinder strength is then obtained from

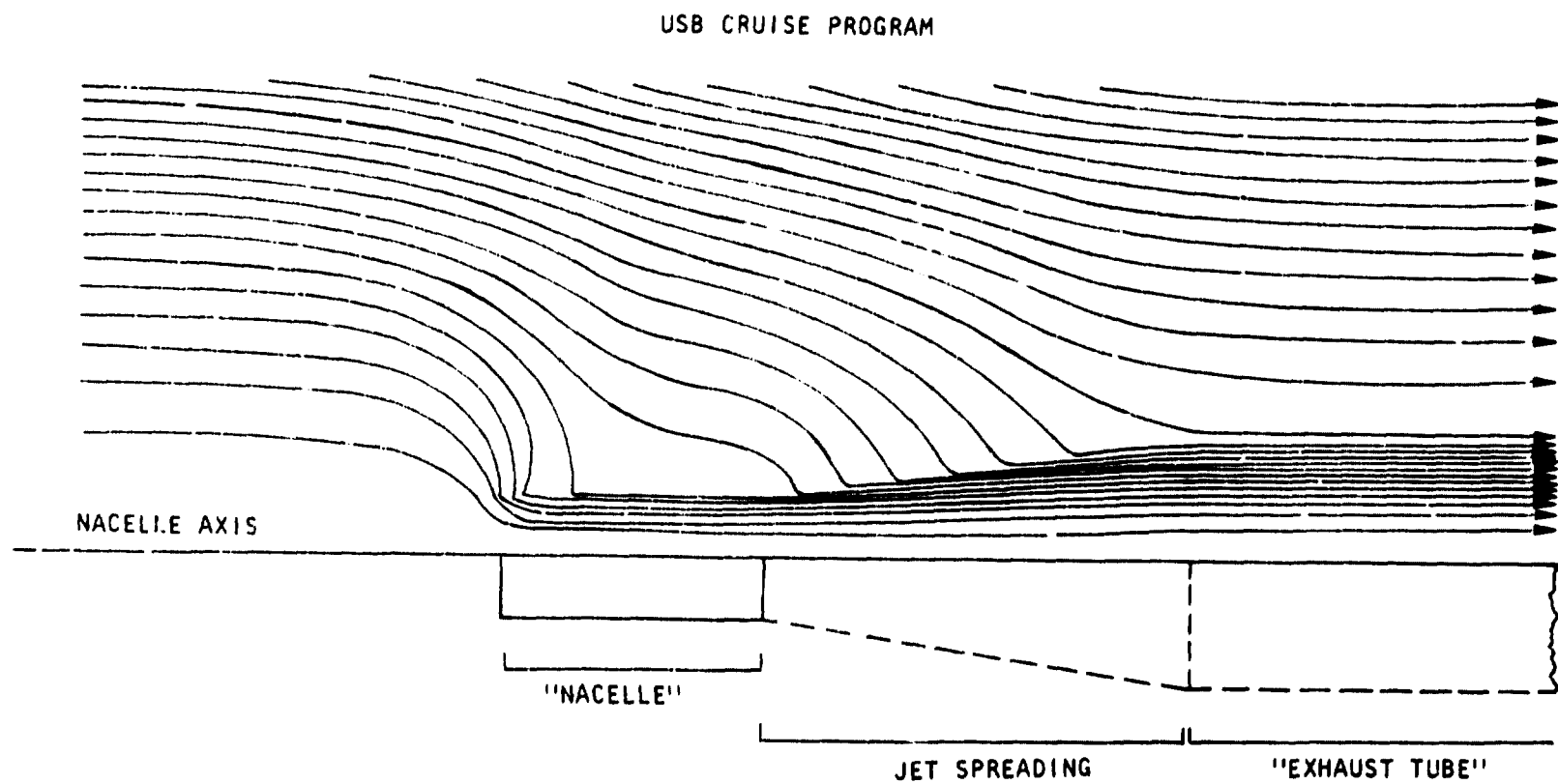
$$\gamma = V - V_{\infty} \quad \text{in free air} \quad (31)$$

$$\text{where } \gamma = V - V_{\text{LOCAL}} \quad \text{in the wing environment.} \quad (32)$$

It will be noticed in Equations (28) and (29) that a constant, ambient-density jet is assumed. This simplification implies that the major features of the flow are dominated by momentum effects and that shock cell patterns, for example, are of secondary importance; this may be questionable.

Figure 148 shows an early example of streamlines generated using the above approach, with no vortex lattice elements present. The entrainment effect along the jet spreading region is very evident. Because continuous vorticity distributions are used to represent the jet surfaces, the numerical problems encountered in discrete-ring solutions (e.g., in Reference 9) do not occur.

For conventionally mounted engines, some nacelle shaping is required to provide proper intake, fan and exit areas; but a good power representation may be obtained essentially as described above. However, for USB configurations, the jet emerges into the wing pressure field and interacts with it. This could be modeled kinematically using a perturbation scheme to calculate the distortion of vortex surfaces emergent from the nacelle exit and as they progress downstream. A similar scheme is applied to a jet-in-crossflow in Reference 9. However, the computer demands are heavy and such detailed modeling of the flow interaction was both inconsistent with several simplifying assumptions made here and is beyond the scope of the present work. Instead,



NOTE: THE VERTICAL SCALE HAS BEEN DOUBLED

Figure 148. Representation of jet spreading and entrainment by vortex-ring polygons.

a simplified fixed geometry was prescribed, based upon the above model, but with geometric transformations applied to represent jet distortion due to impingement and with suitable modifications to jet sheet strength as dictated by the wing flow field. (See Equation (32).)

Figure 149 shows a typical USB jet plume, reshaped to reflect impingement effects. The primary variable involved in this reshaping was the spreading angle in plan view. For the D-duct shown, flow visualization showed this to be approximately 30-degrees. A rectangular sheet at the trailing edge was assumed, with height defined by the above area requirements. In fairing the remainder of the plume, care was taken to accommodate nacelle boattail angles properly and to conform to the mass flow and momentum relationships established above.

### 4.3 WING SECTIONAL AERODYNAMICS

#### 4.3.1 Pressure Distribution

It is clearly very important to provide a good simulation of basic wing aerodynamics before any study of nacelle or power interaction is attempted. Development of the basic model falls into sectional and finite-wing stages. The sectional stages comprises two parts: simulation of airfoil characteristics by accepted, two-dimensional simulation and methods employing continuous vorticity distributions and the adaption of vortex lattice methods to yield an equivalent result, thereby permitting an economical extension to three dimensions.

USB CRUISE PROGRAM

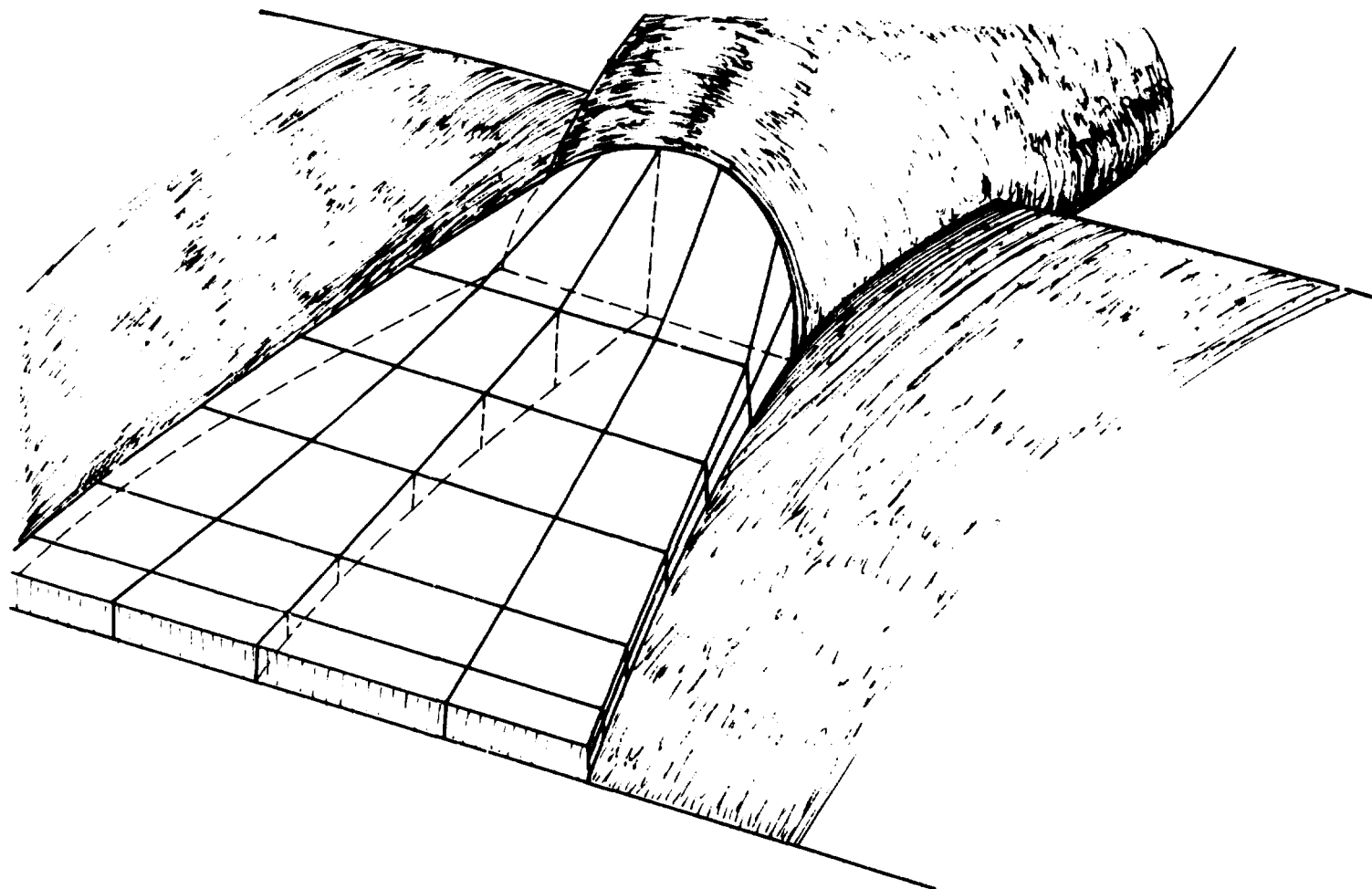


Figure 149. Mathematical model of the USB jet efflux.

ORIGINAL PAGE IS  
OF LOW QUALITY

During a review of experimental data for the basic wing, it became apparent that theoretical prediction of even the sectional pressure distributions is not straightforward. As is usually the case, application of the theory at the nominal incidence [Figure 150(a)] overestimated  $C_L$  — in this case by a large margin. However, reduction in the incidence of the theoretical model to yield the same net  $C_L$  produced a completely unrepresentative pressure distribution [Figure 150(b)]. Contrary to experience with conventional airfoils, the effective aft chamber in the present case was so reduced by boundary layer thickening that a simple shift in incidence, to match  $C_L$ , failed to produce an acceptably-shaped pressure distribution.

Clearly, it would be possible to use an effective aft camber line, with less curvature, to provide a proper match. However, the philosophy was adopted that the theoretical model should remain simple so that real flow effects could be interpreted more readily. Complications to power effects estimation are also avoided if proper sections are maintained.

Since the boundary layers over the front of the airfoil are thin, this region is amenable to matching. This assures that conditions at the nacelle-wing junction, at least, will be proper. Figure 150(c) shows the matched condition for a 2-degree experiment, which requires a 0-degree theoretical setting ( $\Delta\alpha = -2^\circ$ ). A similar exercise, for a 1-degree experiment revealed that an  $\alpha$ -shift of  $1\frac{1}{2}$ -degrees was optimum. Ideally, therefore, the theoretical  $\alpha$ -shift should be made lift-dependent. However, this introduces unwanted (though not insuperable) difficulties in finite-wing calculations so a constant, 2-degree shift was therefore adopted.

# USB CRUISE PROGRAM

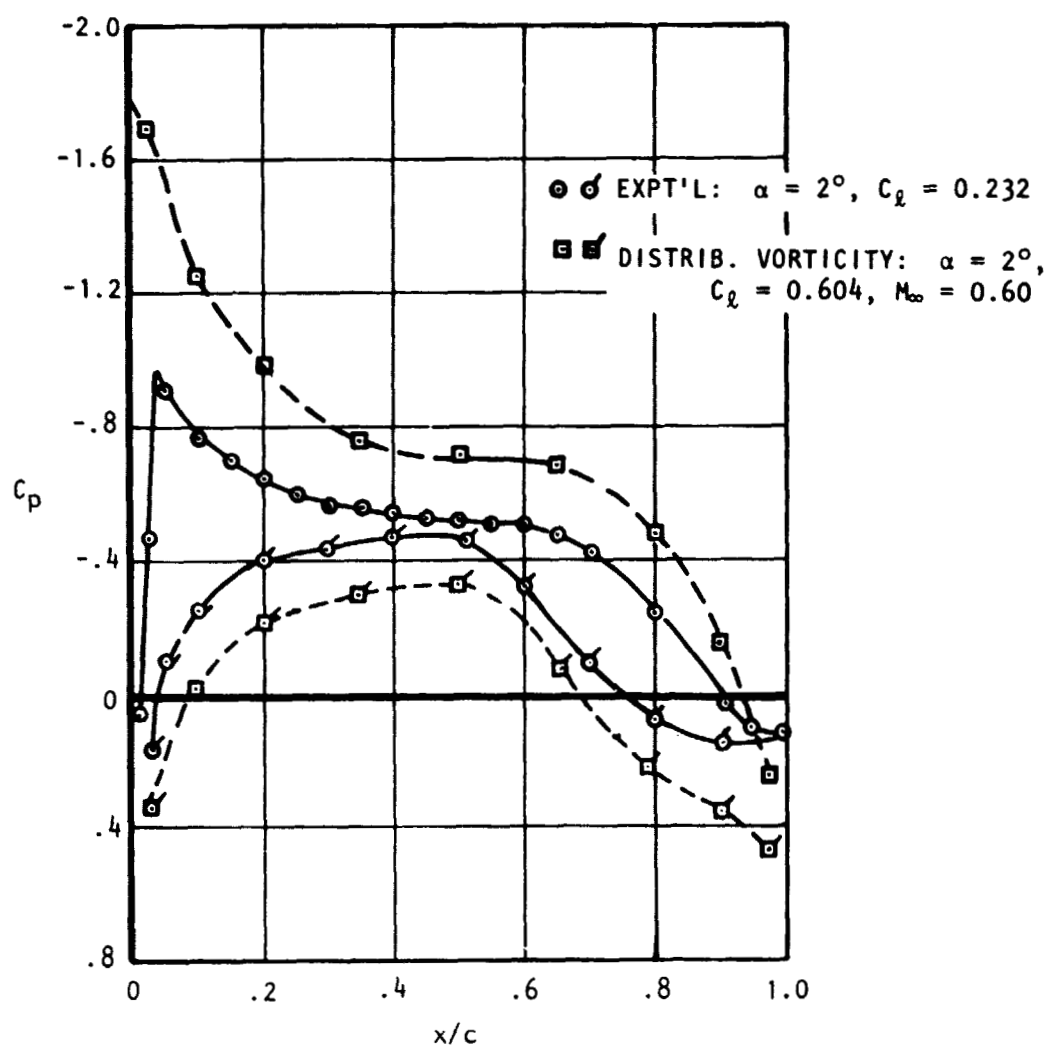


Figure 150(a). Airfoil sectional characteristics  
— incidence matched.



# USB CRUISE PROGRAM

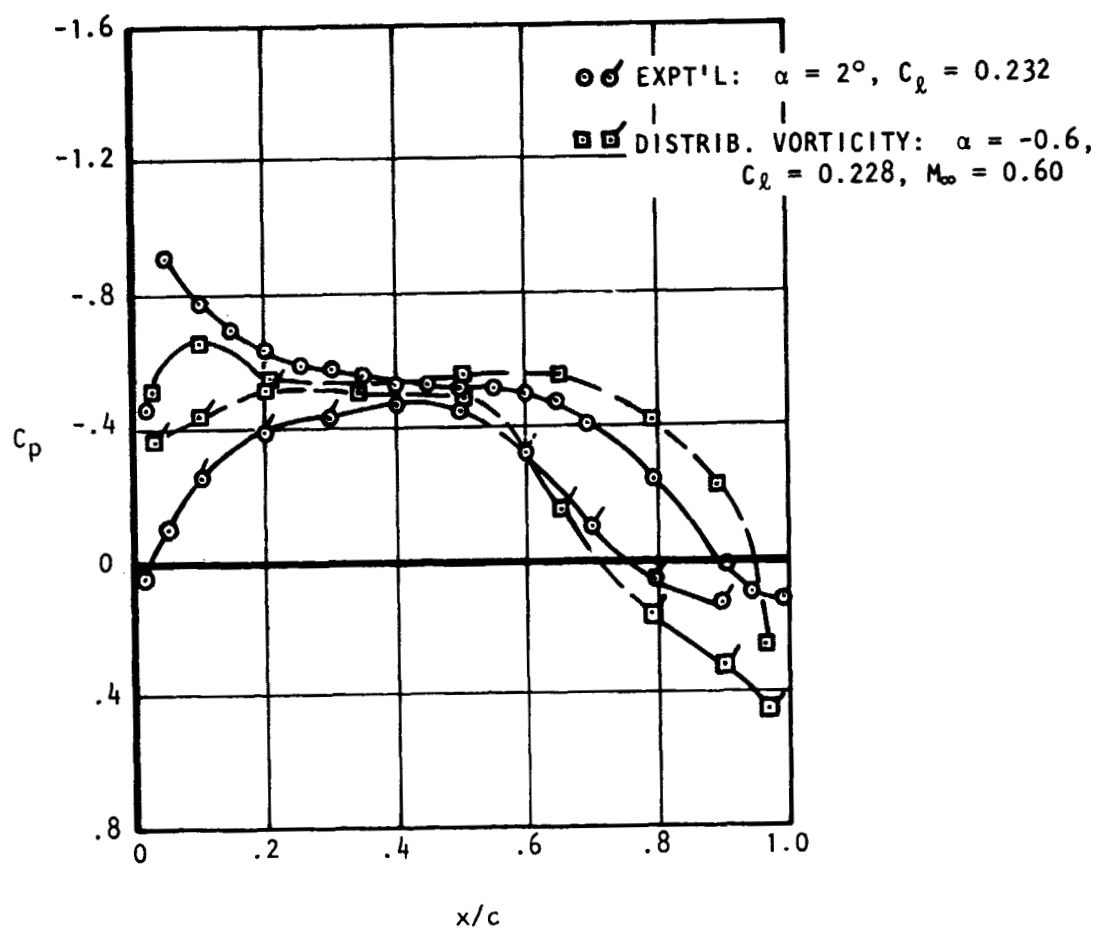


Figure 150(b). Airfoil sectional characteristics  
— lift coefficient matched.

# USB CRUISE PROGRAM

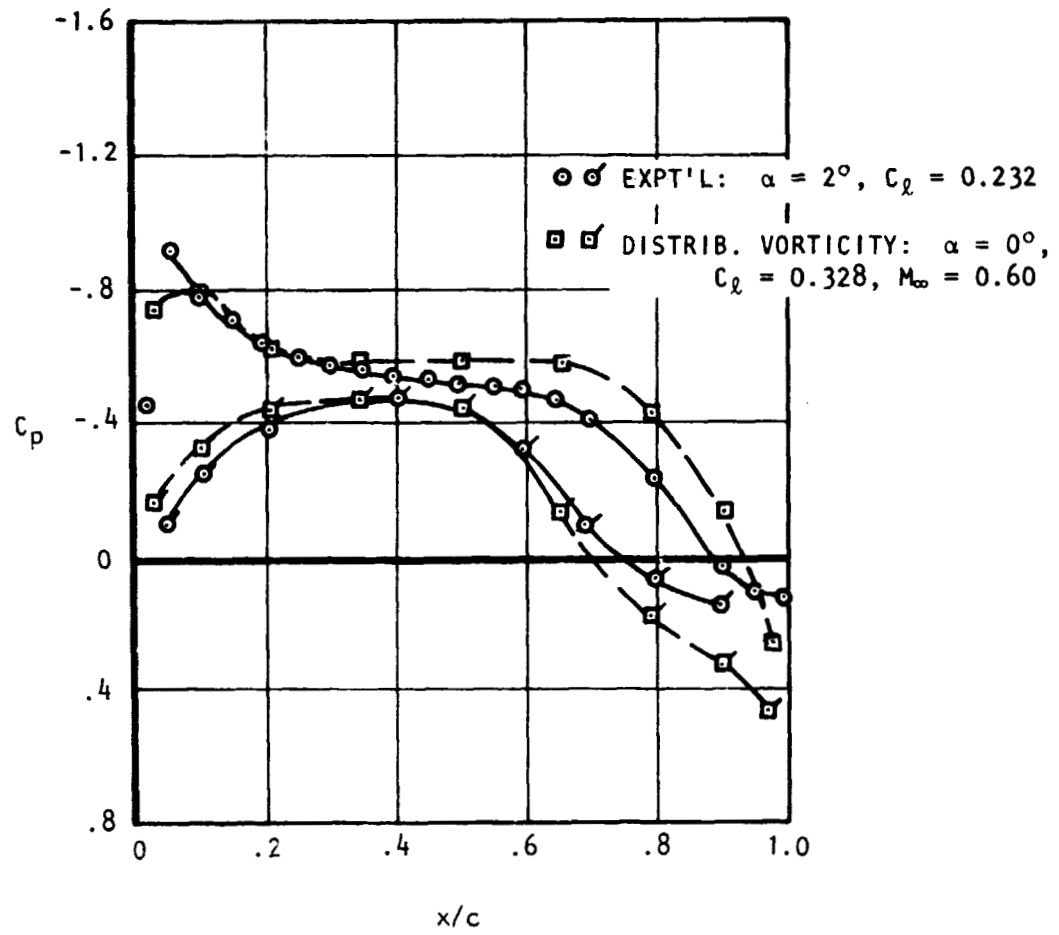


Figure 150(c). Airfoil sectional characteristics  
— leading edge matched.

In order to preserve nacelle orientation to the flow and to avoid misdirecting the jet flow, the above incidence shift was achieved by superimposing an appropriate downwash at each wing panel. This introduces a sectional drag term equal to  $C_{\ell} \cdot \Delta\alpha$ , where  $\Delta\alpha = 2/57.3$  radians.

#### 4.3.2 Sectional Forces

Though the above procedure provides an acceptable match in leading edge pressure distribution over the desired range of  $C_{\ell}$ , such a simple flow model clearly cannot match profile drag over a similar range. Figure 151 shows that the value of  $\Delta\alpha$  used, 2-degrees, results in correct drag representation only at a  $C_L$ -value of 0.36. Elsewhere, simple theory will be used to correct the three-dimensional results and provide the required drag increment, which is  $\Delta C_D = C_{D_0} - C_L \Delta\alpha$ .  $\Delta C_D$  is added to calculated induced drag to give a total which includes allowance for sectional profile drag.

#### 4.4 FINITE-WING AERODYNAMICS

Figure 152 shows the build-up of the straight, finite-wing lift curve using both vortex lattice and compressible aspect-ratio correction methods. The experimental curve is approximated much more closely in slope than conventional predictions might indicate. This is a result of reduced sectional lift curve slope inherent in the present sectional representation. Direct application of conventional aspect ratio corrections plus Gothert corrections for Mach number (which include aspect ratio) to the present two-dimensional lift curve slope yields a three-dimensional slope which agrees quite well with that given by the vortex lattice calculation.

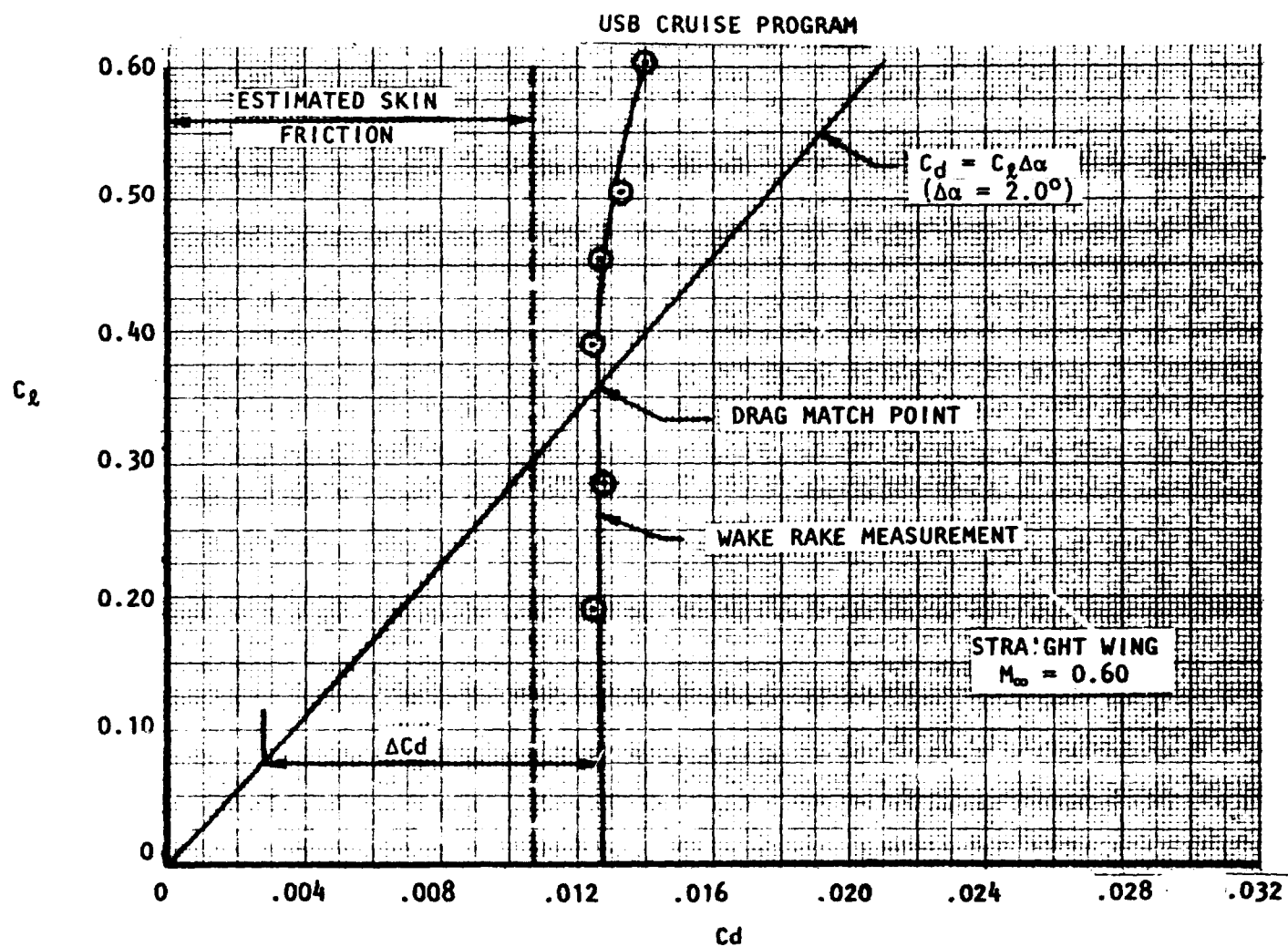


Figure 151. Definition of  $\Delta C_d$ .

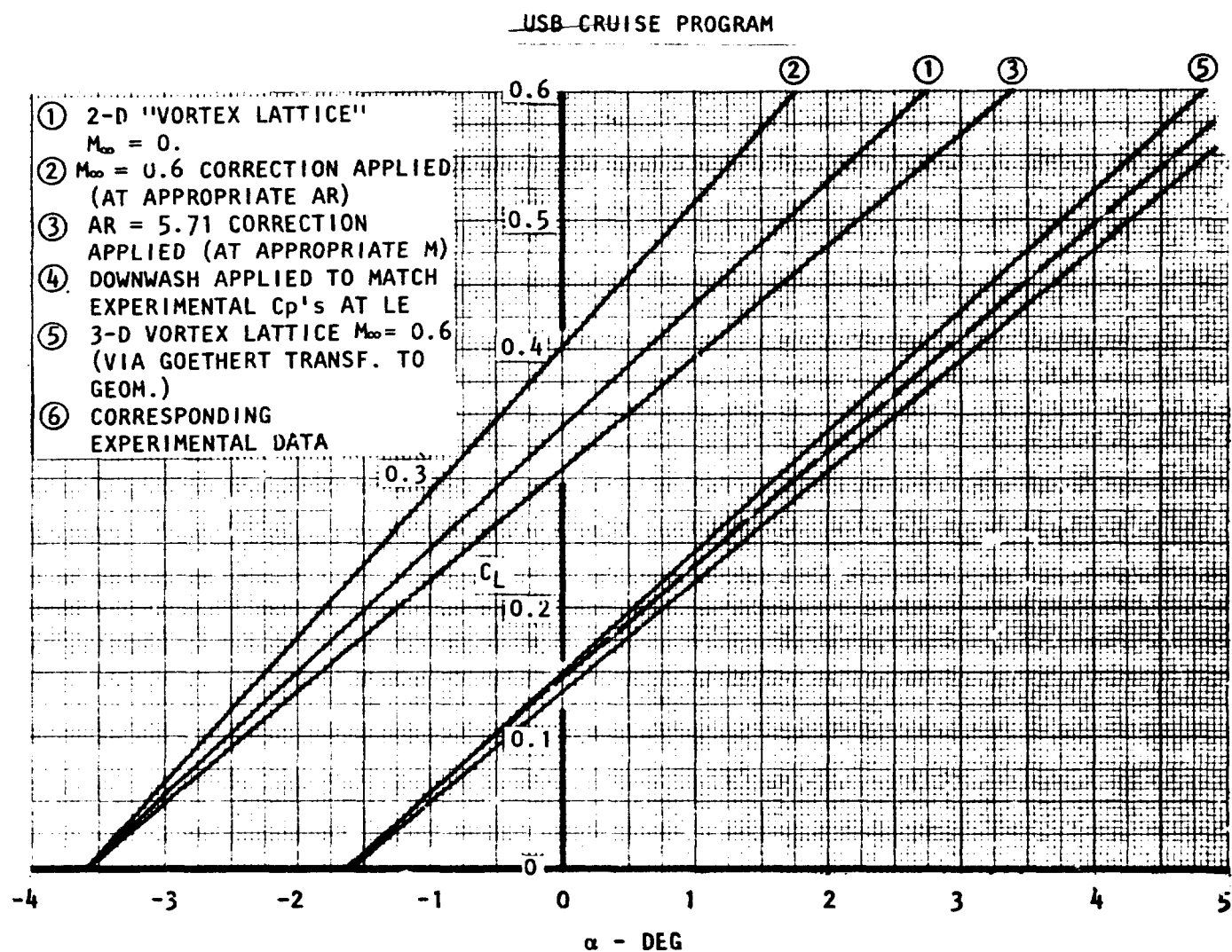


Figure 152. Lift curves for the straight wing at  $M_\infty = 0.60$ .

An illustration of a corresponding drag polar analysis is given in Figure 153. Curve (1) was calculated using a Trefftz-plane drag integration with 2-degrees downwash applied as indicated above. As was mentioned previously, the use of this downwash introduces a drag term directly proportional to  $C_L$ . This is removed by applying the corrections  $\Delta C_d$  (Figure 151) in a stripwise manner. The curvature of the corrected line, on the  $C_L$ -squared plot, indicates some reduction in span efficiency as lift increases.

#### 4.5 SURFACE PRESSURES ON THE FLOW-THROUGH NACELLE

##### 4.5.1 Nacelle Representation

Figure 154 shows the final panel layout adopted for the D-duct nacelle, mounted on the straight, finite wing. Though the paneling is considerably coarser than the ideal, careful attention to detail has made possible a reasonable prediction of interaction effects. Particular care was needed around the leading edge blend and in this region nacelle panels must join the wing surface approximately at right angles.

The joining line used between the wing and nacelle is the intersection of the basic shapes, with no filleting applied. This simple, first-cut approach is intended to highlight the important interactions in the blend region. Detailed 3-D modeling of shaped fillets should be the subject of future studies.

Vortex lattice panels, rather than sources or doublets, were used to represent the nacelle forebody, barrel and contraction regions because it was felt

# USB CRUISE PROGRAM

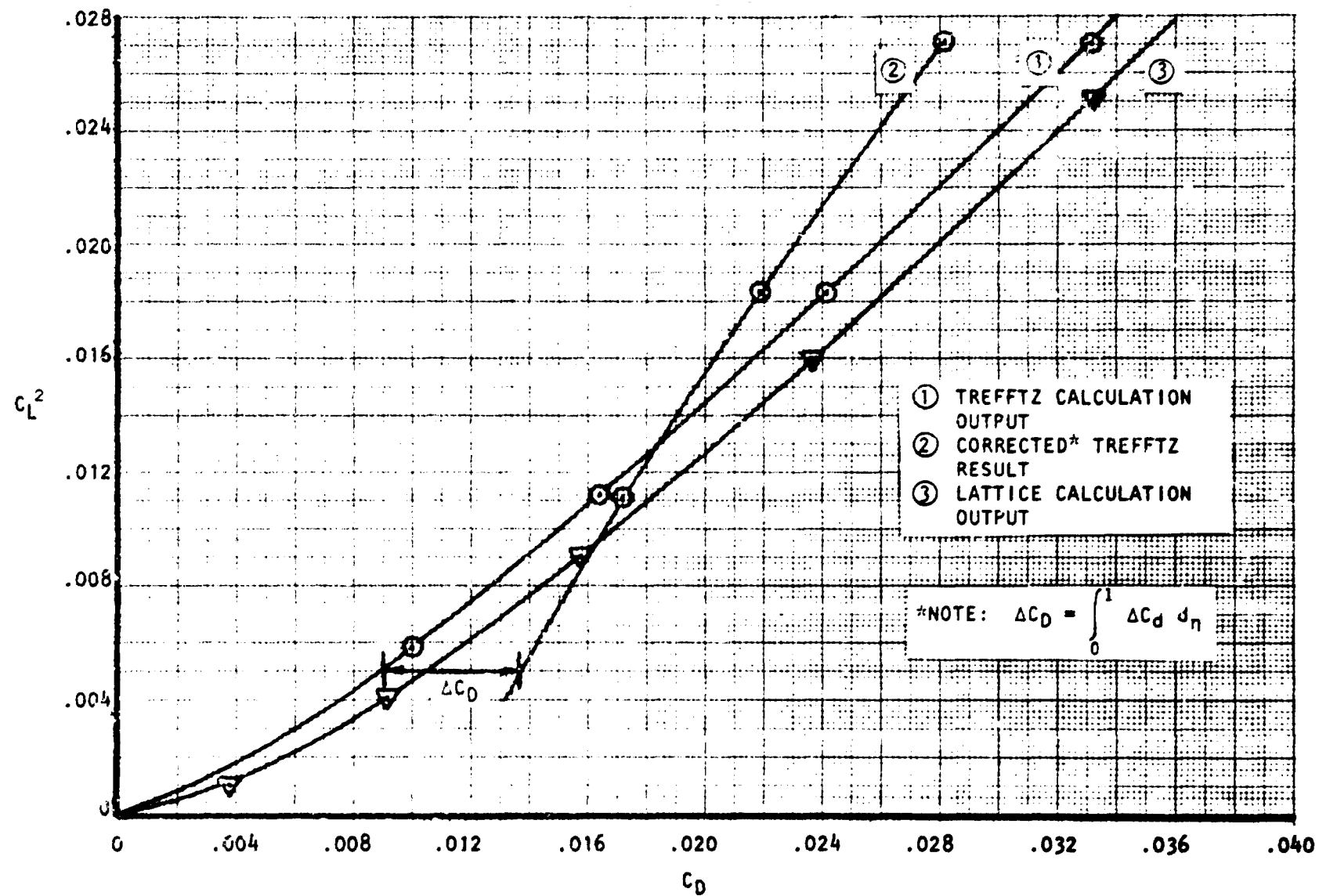


Figure 153. Drag Polars for the straight wing at  $M_\infty = 0.60$ .

USB CRUISE PROGRAM

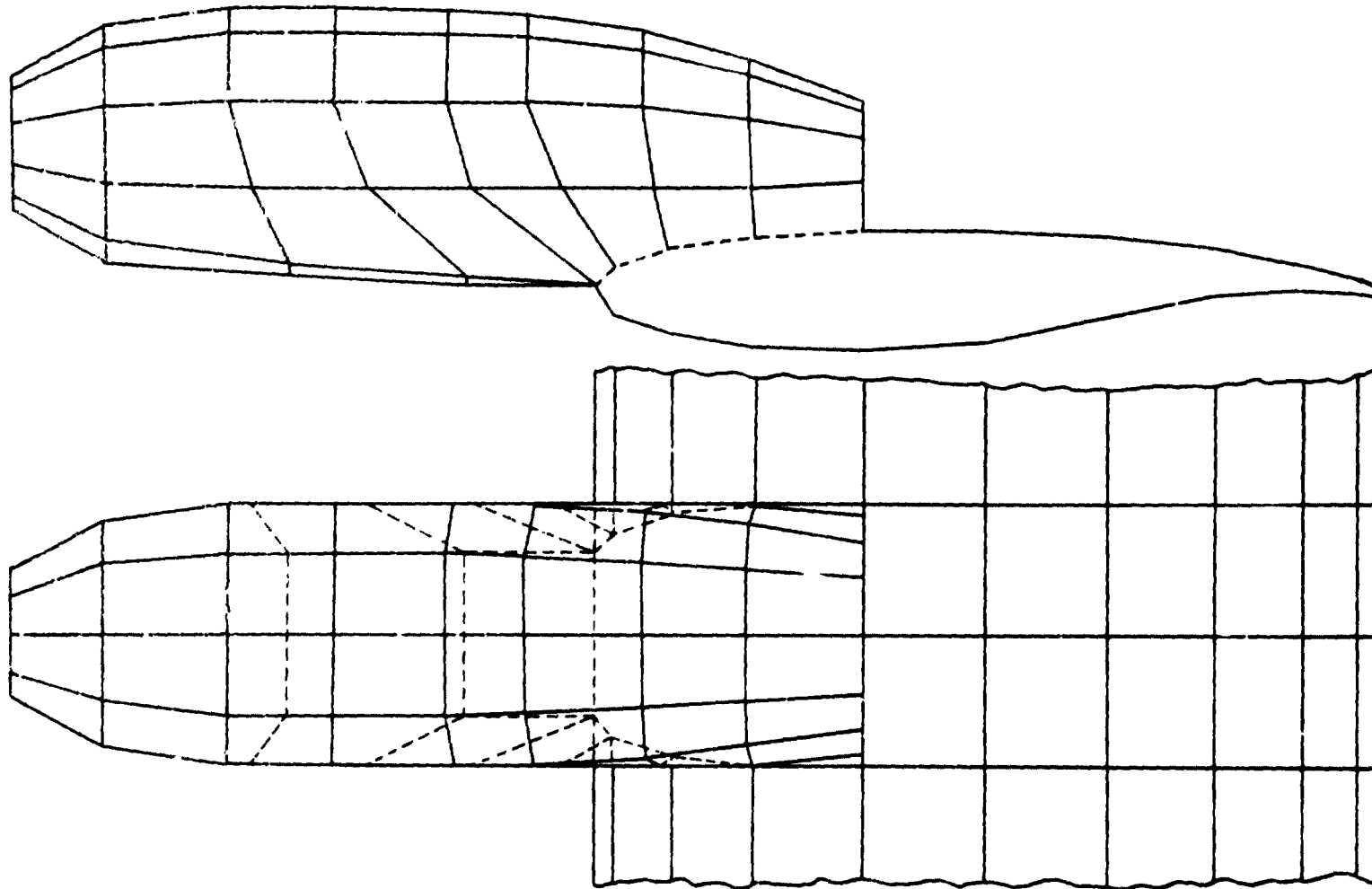


Figure 154. Panel details for D-duct nacelle and adjacent wing.



important to represent forebody lift effects. While it is true that the nacelle lift is itself not large, its creation over a short span generates quite strong trailing vortices, which may have significant lift and drag redistribution effects.

A shortcoming of using only vortex lattice panels in the present application is that the faired-over nose of the experimental nacelles cannot be modeled directly. However, an appropriate retrospective correction is possible which removes unwanted inlet thrust.

A possibly contentious feature of the representation is the removal of the wing upper surface where the nacelle overlaps it. Careful study of the present, single surface representation showed that, for continuity of external surface pressures, wing upper surface bound vortex lines from each side of the nacelle must arch over the nacelle and must not also pass beneath it along wing generators. Early studies with the wing leading edge 'hump' in place produced unacceptable results. Somewhat hesitantly, the hump was removed and a better representation was obtained. It is noteworthy that there were no upper surface pressure anomalies resulting from the free edge at the base of the nacelle exit.

#### 4.5.2 Nacelle Surface Pressures

Due to thickness, outward suction with  $C_p$  in the range -1.0 to -1.5 is generated across the nacelle wall except near the intake and in the wing blend region (see Figure 155). Positive  $C_p$ 's are evident on the first bay; implying external stagnation and a capture area greater than the intake opening.

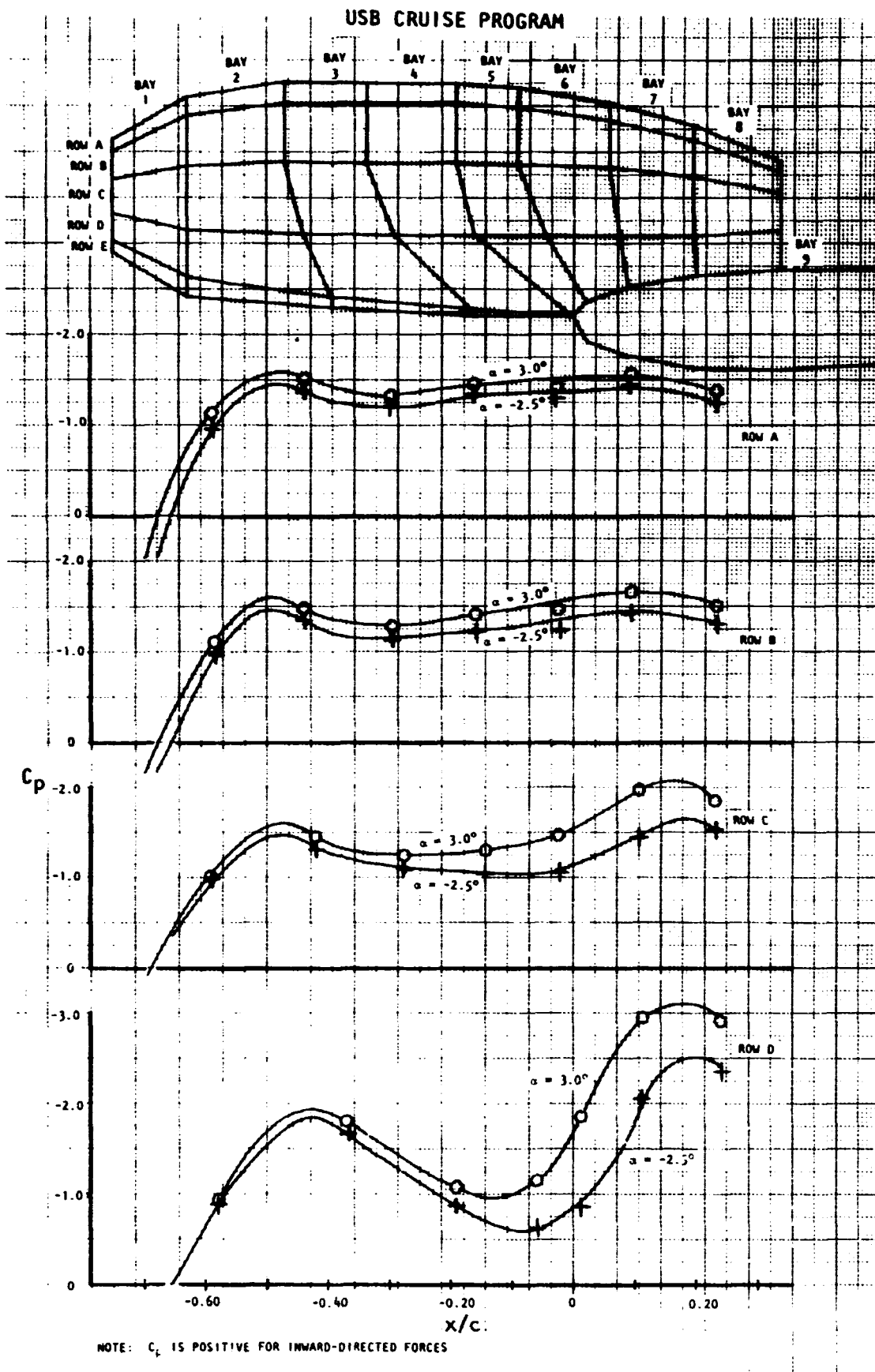


Figure 155. Calculated chordwise pressure distributions on nacelle surfaces — flow-through condition  $M_\infty = 0.60$ .

Along the panels which blend with the wing (Row D), the flow accelerates over the fore-nacelle in a typical manner, but then slows down as the wing leading edge is approached. There is then a reacceleration towards the crest of the wing. The latter effects are amplified near the wing surface because of high curvature in plan view at the unfaired intersection (see Figure 154).

At low angles of attack, the forward nacelle carries very little lift (see Figure 156), but moderate increases occur at higher angles. In the blend region (Figure 157) the nacelle boattail curvature causes lift to develop and the pressure distributions become quite complex. The increments in lift coefficient are not large, but their generation over a short span may lead to significant drag distributional changes which will be discussed later. Aft of the nacelle (Bay 9) surprisingly little change is found from the datum, clean-wing condition.

The lower part of Figure 156 shows that the pressures developed on the inboard and outboard side of the nacelle are virtually identical, even at 3-degrees angle of attack. The nacelle is therefore properly aligned in yaw and develops near-zero net side force.

#### 4.6 SURFACE PRESSURES FOR POWERED CASES

As a prelude to the force-prediction study (Section 4.7), it is appropriate to review the predicted pressure distributions and compare these, where possible, with corresponding measurements. Reliable pressure measurements are relatively few for the medium-sized "D-Duct" (N<sub>3E</sub>), on which most

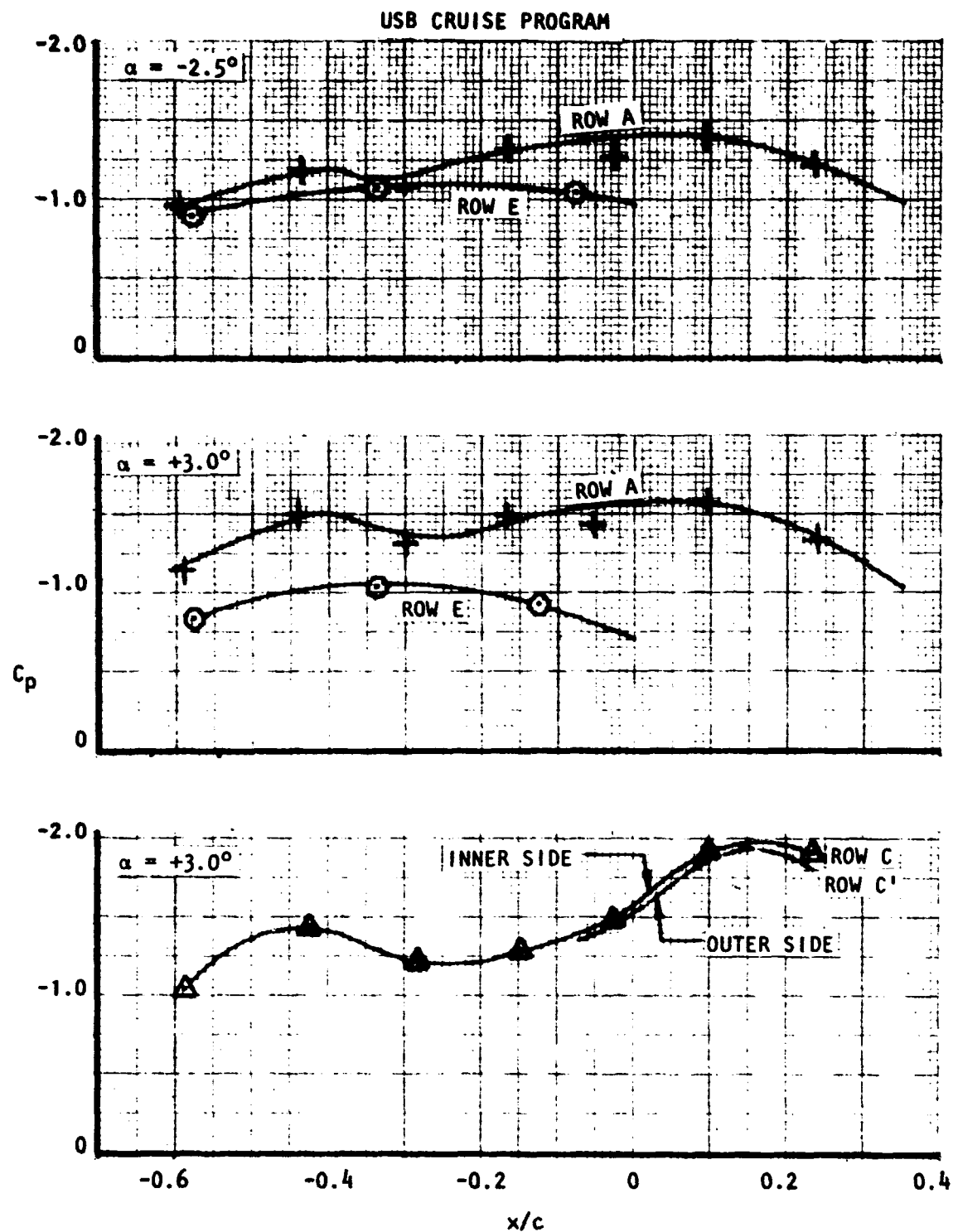


Figure 156. Calculated forward-nacelle surface pressures  
flow through condition,  $M_\infty = 0.60$ .

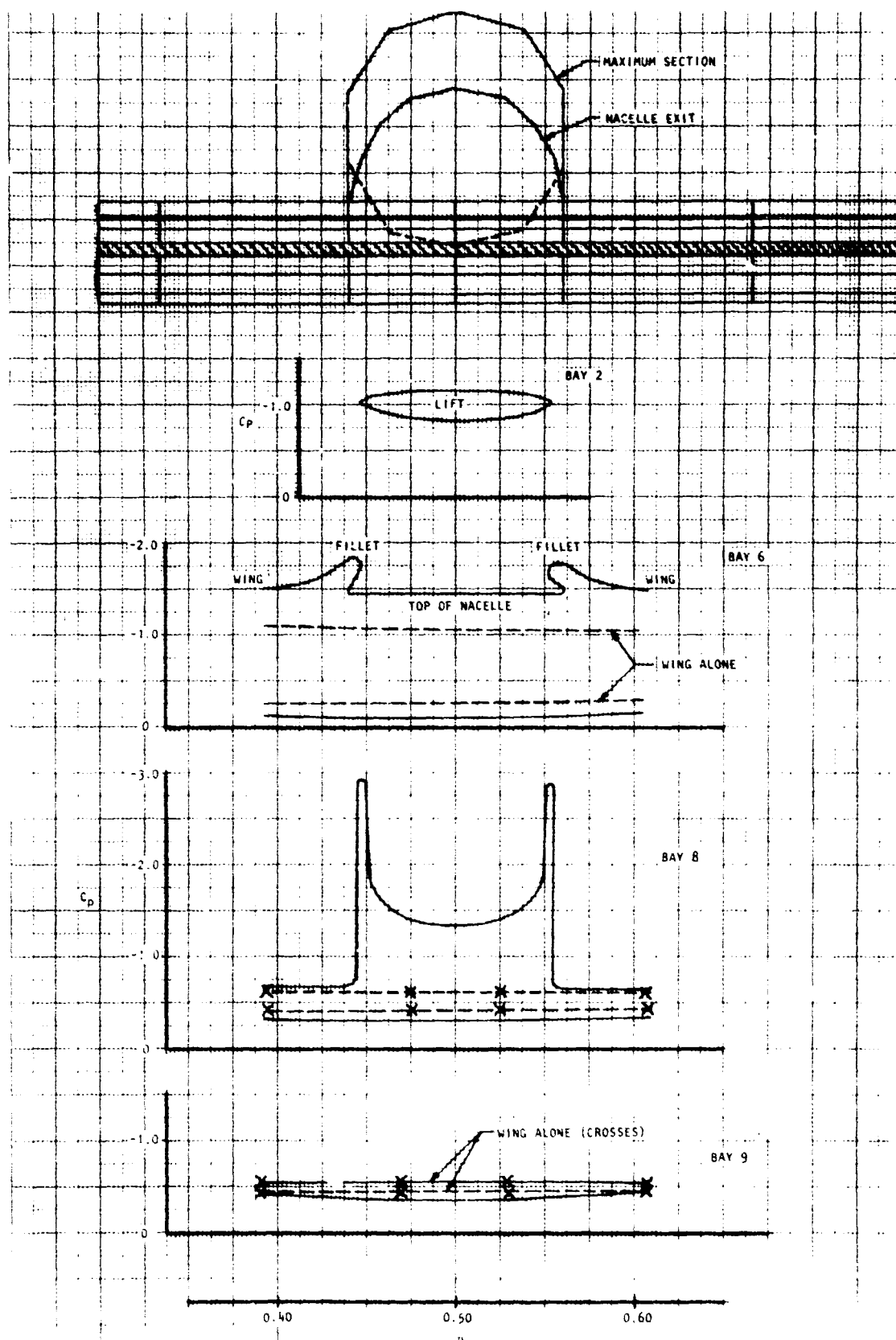


Figure 157. Calculated blend-region surface pressures.  
Flow-through nacelle,  $\alpha = +3^\circ$ ,  $M_\infty = 0.60$ .

ORIGINAL PAGE 13  
OF POOR QUALITY

theoretical study has been carried out, being restricted to one or two angles of attack in the pressure testing. In this test the two-dimensional wing with the unmodified section was used. Pressure measurements are available at three spanwise stations; one row is located on the nacelle center-plane ('A') and two are to the side of the nacelle ('B' and 'C'). On the nacelle itself, pressures are available along the upper centerline only and extend as far forward as the wing leading edge.

To provide a broader view of conditions on the wing and nacelle, theoretical predictions will be reviewed in their own right before comparing them with experimental data.

#### 4.6.1 Predicted Effects of Angle-of-Attack and Pressure Ratio

Figure 158 shows predicted pressure distributions on the clean wing at various angles of attack. The figure is included as a baseline case for comparison with later figures. It is noted that upper and lower surface pressures are approximately equal over the front half of the airfoil at  $\alpha = 1$  degree and the lift then carried in the aft region is a consequence of the camber there.

The pressure distributions on the nacelle center plane, for nacelle N<sub>3E</sub> at the flow-through condition, are shown in Figure 159. Aft of the exit there remains a strong resemblance to clean wing pressure distributions though the lower surface profile is shifted forward somewhat. The nacelle itself experiences apparent suction  $C_p$ 's on its upper and lower surfaces. It will be shown below that these may be attributed largely to positive inner

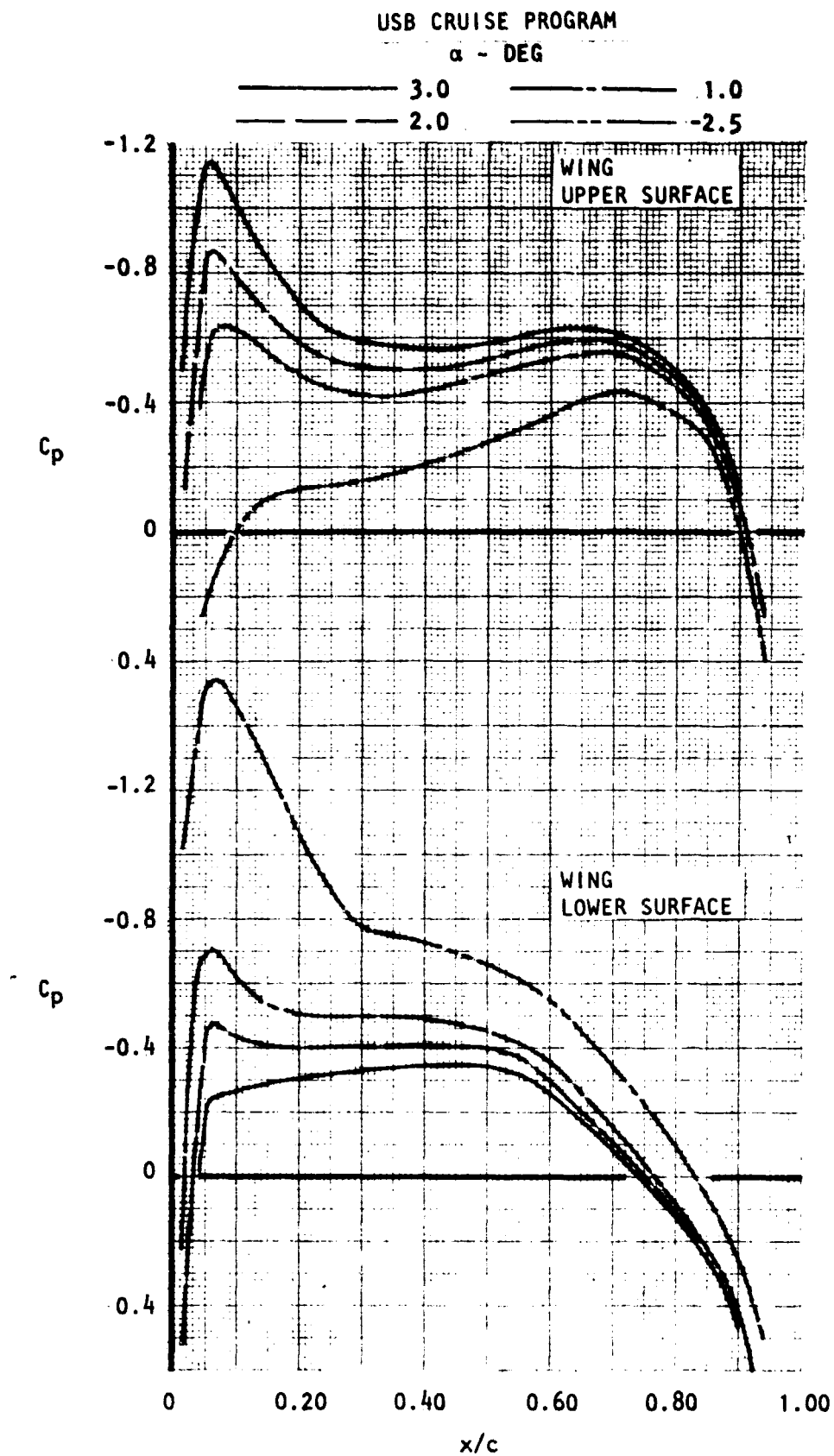


Figure 158. Predicted clean-wing pressure distributions as a function of  $\alpha$ .

# USB CRUISE PROGRAM

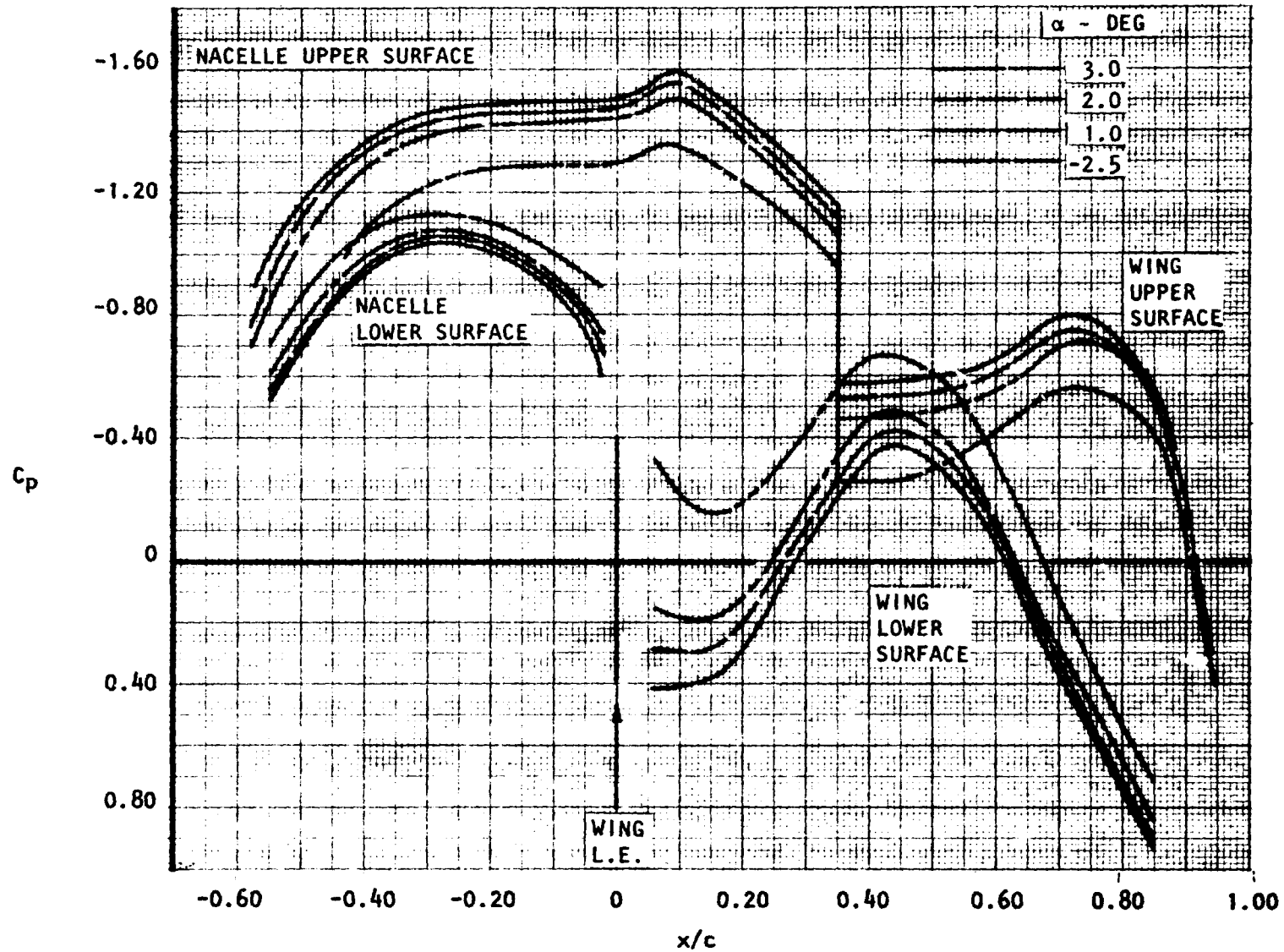


Figure 159. Predicted nacelle spine and wing surface pressure distributions at  $H_j/p_\infty = 1.25$  (flow-through).



surface pressure changes generated by the internal flow. As angle of attack is increased, lift build-up on both nacelle and aft wing is apparent, though the percentage changes are not large.

Figure 160 shows the result of applying power, at a constant, 1.8-pressure ratio, to the previous cases. There is a substantial amplification of the upper surface suction hump towards the rear of the wing, caused by jet turning. Just aft of the nozzle exit, partial impingement of the jet causes a pressure increase. It is noteworthy that angle-of-attack effects are small relative to power effects. Nacelle pressures are affected very little by power.

Figure 161 is similar to the previous figure, but shows the effect of increasing the power setting at constant angle of attack. This brings out the power-dependent increments quite clearly. Of these, the lower surface effects are unexpected and do not seem reasonable. It seems likely that these effects reflect a sparse-lattice which would disappear if panel size was reduced.

Figure 162(a) expresses the previous data in incremental form, using the clean wing as a base. It is interesting that small turning loads appear even at the flow-through pressure ratio; redirection of air flowing through the nacelle has evidently increased the mass flow adjacent to the surface. As a checking exercise, the standard power-unit/wing-vortex cylinder generation procedure was implemented for the flow-through pressure ratio and applied

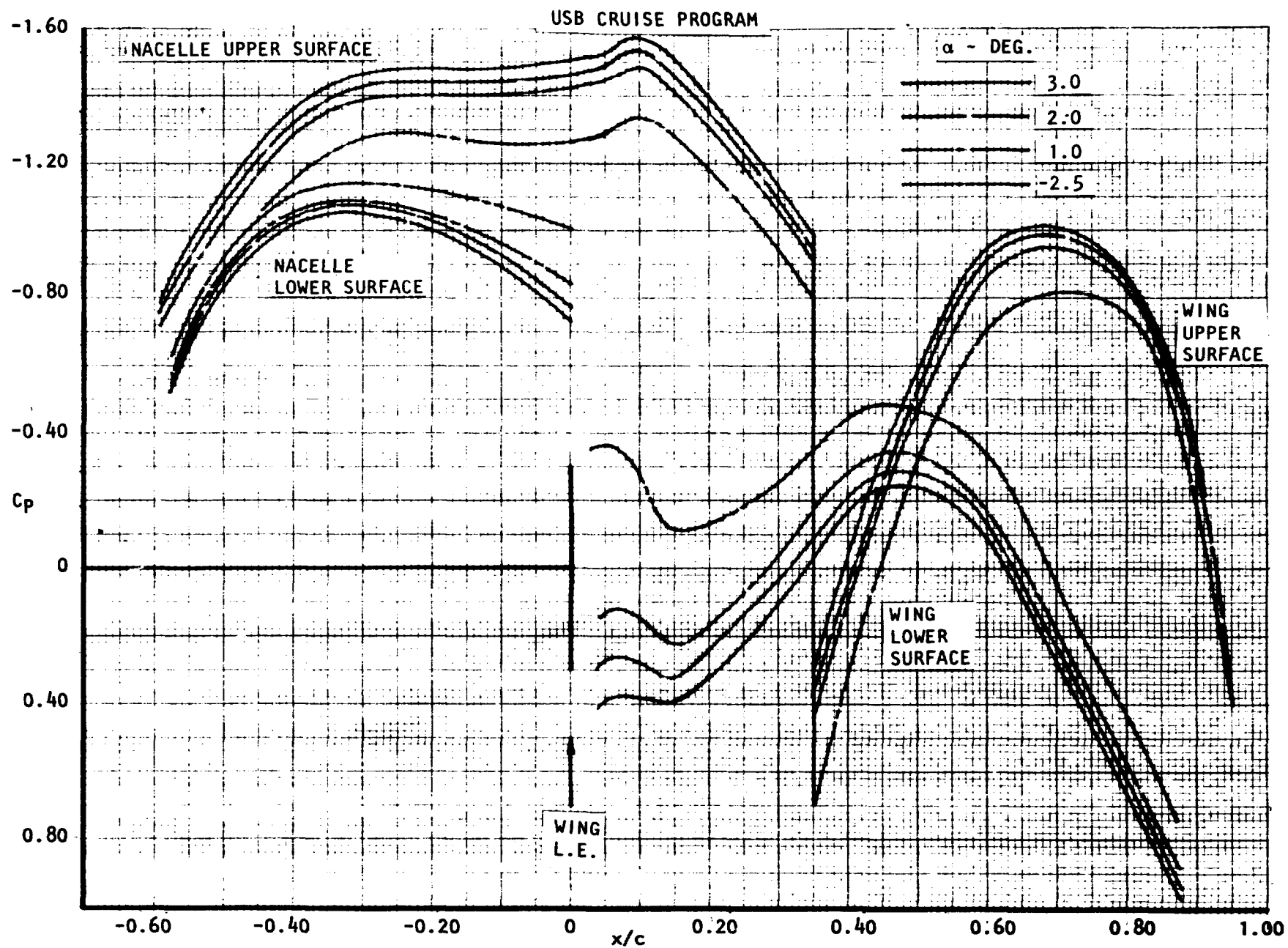


Figure 160. Predicted spline and wing surface pressure distributions at  $H_j/\bar{p}_\infty = 1.8$ .

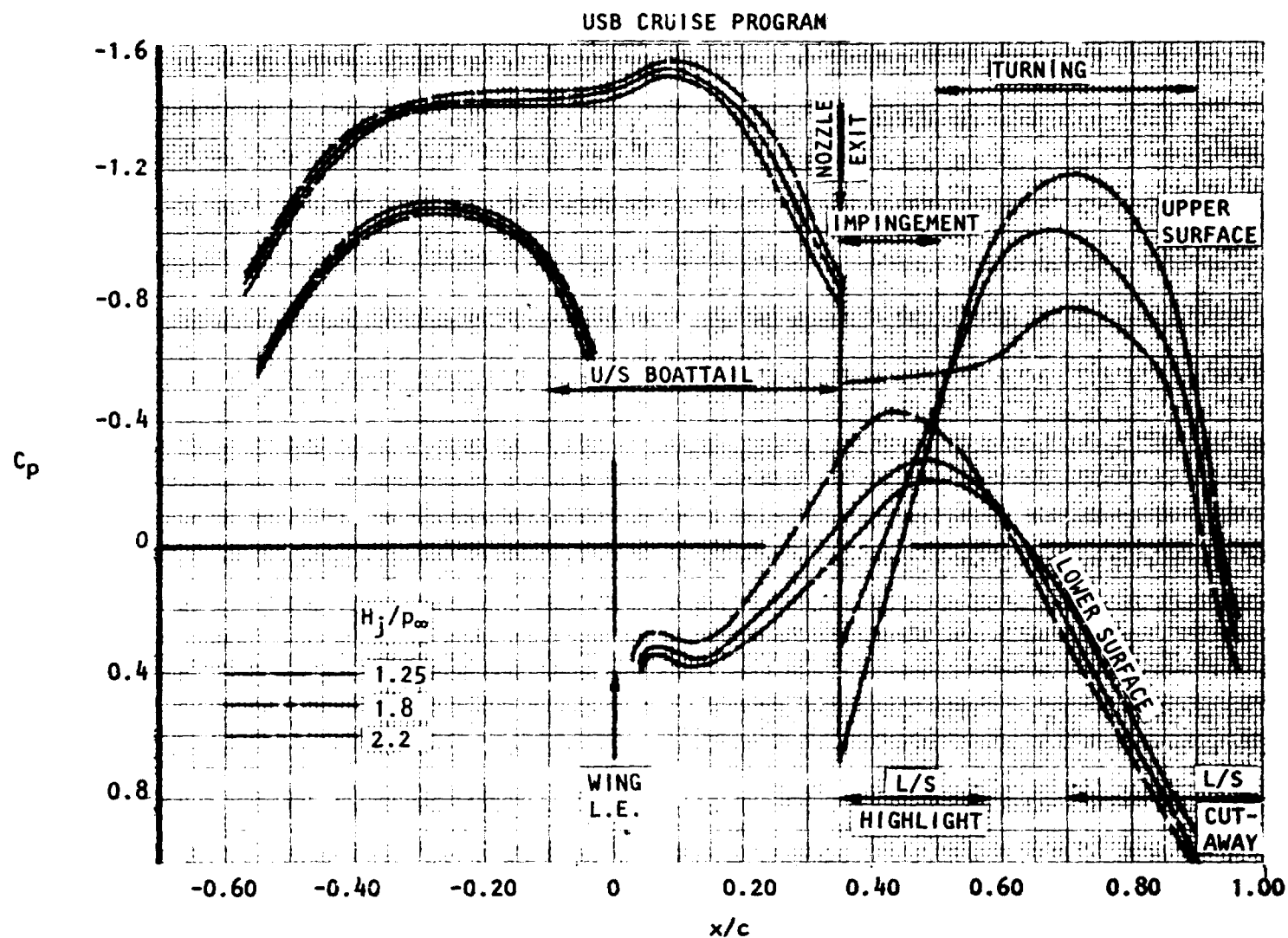


Figure 161. Predicted nacelle-spine and wing surface pressure distributions as a function of jet pressure ratio,  $\alpha = 2^\circ$ ,  $M_\infty = 0.60$ .

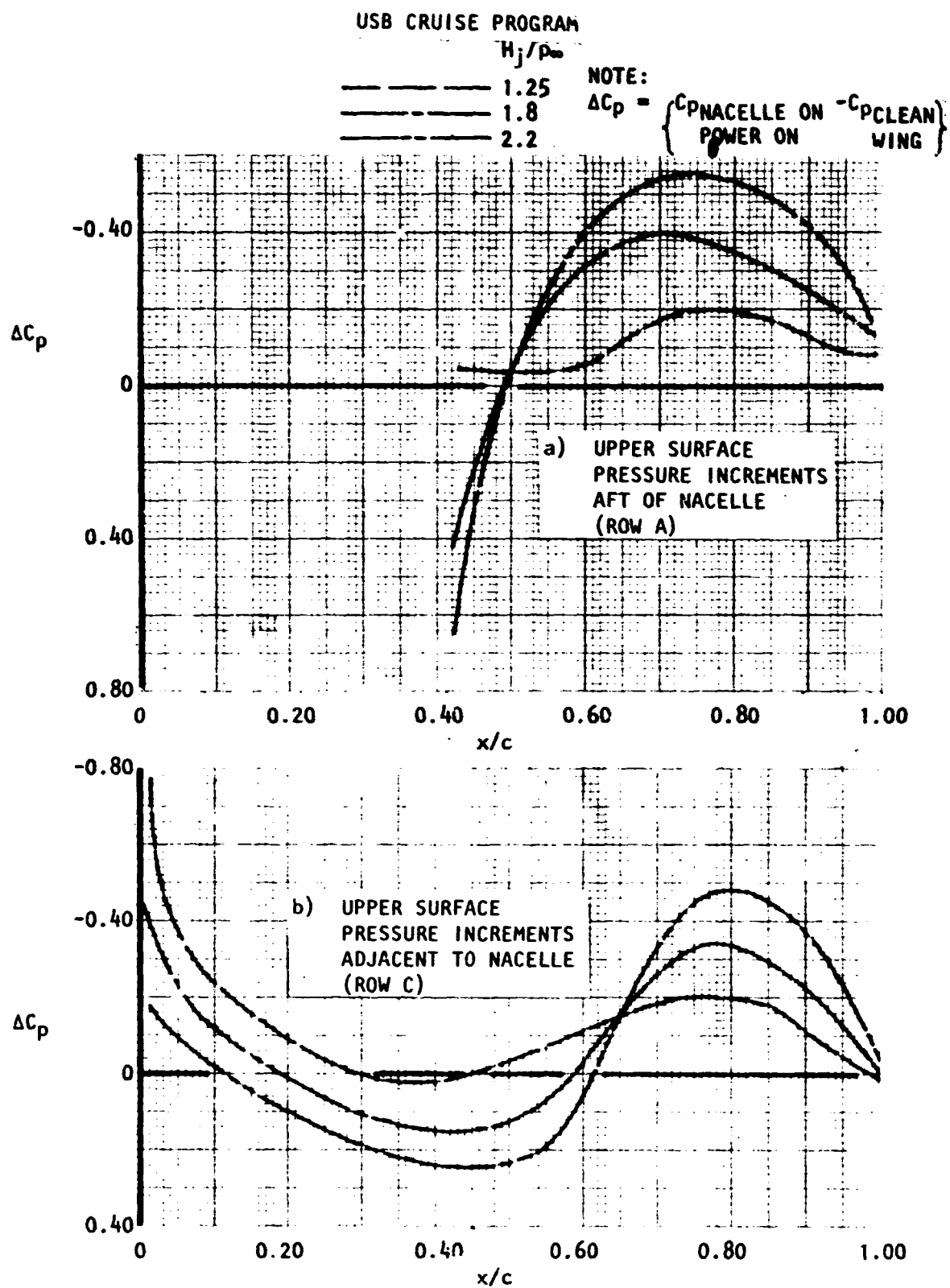


Figure 162. Predicted incremental surface pressures as a function of jet pressure ratio.

to the vortex lattice in the usual way. Though there were small systematic differences from the 1.25 pressure ratio results of Figure 162(a), their magnitudes were not significant. This demonstrated that the power effect modeling techniques were consistent at the flow-through condition. At the position of the row "C" pressure orifices, adjacent to the nacelle, Figure 162(b) reflects an initial speed-up to the flow caused by nacelle displacement effects near the leading edge, followed by a pressure increase towards mid-chord, which is the lateral extension of the impingement region. Towards the trailing edge, suction increments again occur. These reflect not only carry-over from the central suction region, but also some limited direct effects where the spreading simulated jet intersects the row "C" position.

#### 4.6.2 Comparisons with Measured Surface Pressures

Figure 163 shows that the theoretical surface predictions, described above, match the experimental data in the jet efflux region on the nacelle center-line quite well. The partial impingement and turning effects are well reproduced though there is no theoretical counterpart to the shock-cell effects which are evident at the highest pressure ratio.

Predictions of pressures adjacent to the nacelle were less successful (see Figure 164). Towards the front of the section, predicted suction levels were less than those measured, possibly as a result of spurious power-induced flow changes between the upper and lower lattice surfaces. Towards the trailing edge, the addition of the powered nacelle to the clean wing changed the experimental pressure very little. However, the relatively large plan-view spreading angle used in the theoretical model, caused aft

# USB CRUISE PROGRAM

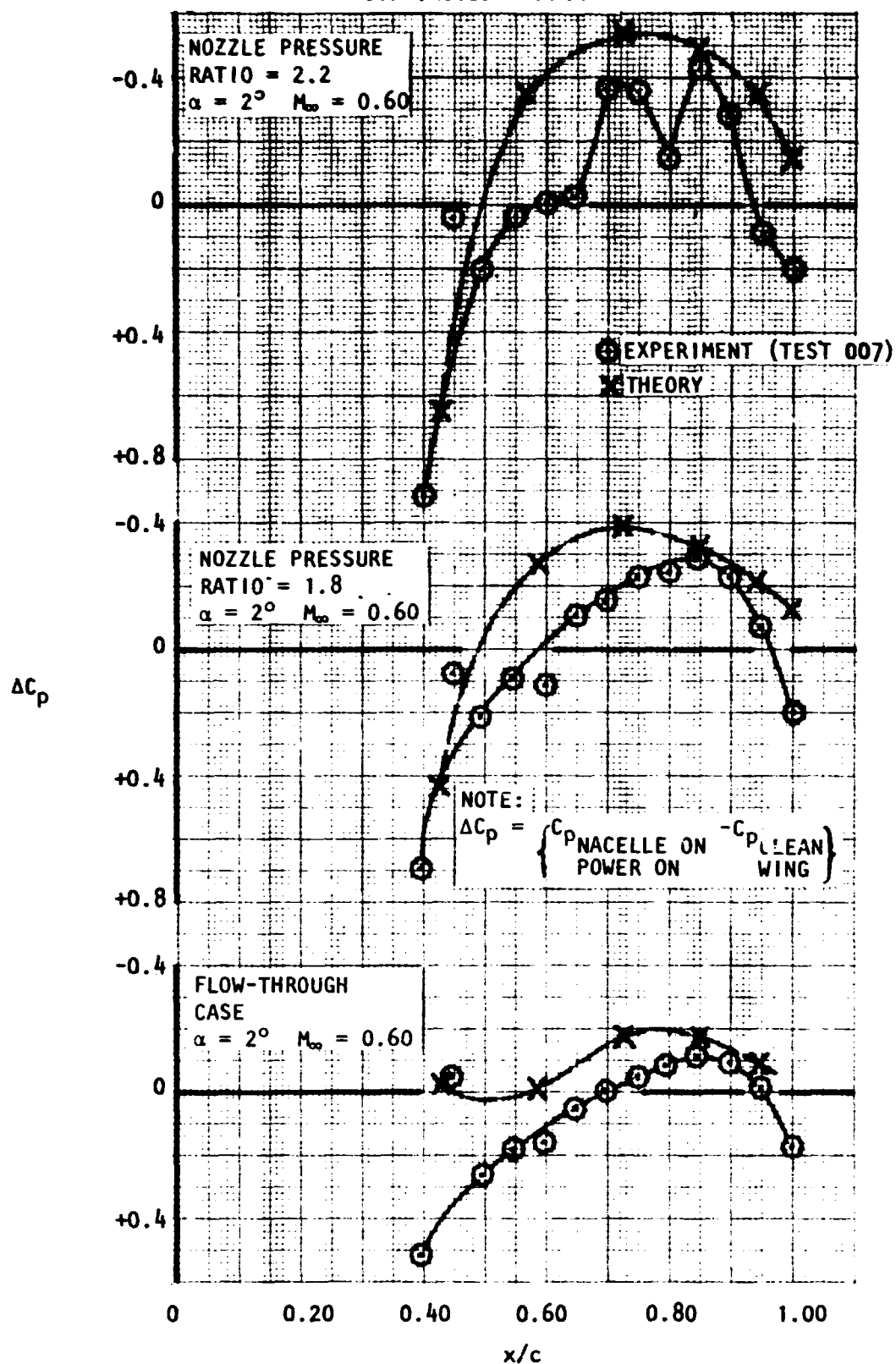


Figure 163. Predicted and measured surface pressure increments aft of nacelle (Row A).

# USB CRUISE PROGRAM

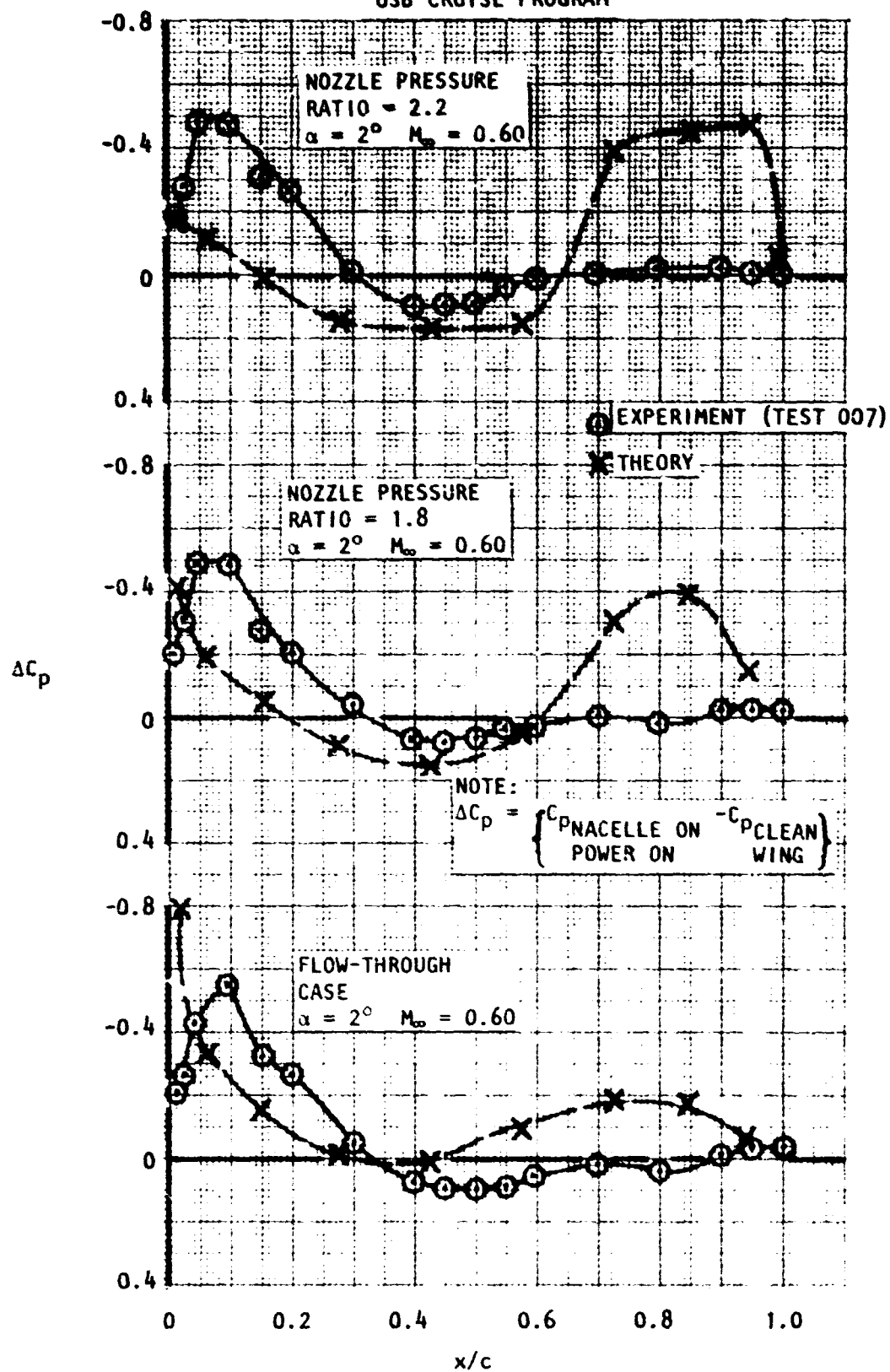


Figure 164. Predicted and measured surface pressure increments on wing adjacent to nacelle (Row C).

suctions which were not found experimentally. With fine tuning, the theoretical model could obviously be adjusted to remove the above deficiencies. However, such arbitrary changes to an already arbitrary model produce results of doubtful generality. It is considered that effort directed towards a system with jet boundaries determined as part of the solution would be more fruitful.

Since the theoretical, thin-lattice representation yields only a pressure difference across the nacelle wall, it is not possible to compare predictions with measured external pressures directly. However, if it is assumed that internal static pressure is constant across the duct, the pressure just inside the nacelle surface may be deduced from velocities at the nacelle centerline, which can be calculated with reasonable accuracy. Figure 165 shows the results of calculations along the upper and lower "spines" of the nacelle upper and lower surface respectively while curve (3) shows the corresponding centerline pressure. On the above one-dimensional internal flow assumption, prediction of upper surface and lower surface pressures are given by (1) minus (3) and (2) minus (3), respectively.

The estimated upper surface external pressure, (1) minus (3), may now be compared with the measured pressure distribution, curve (4). The agreement between these two curves is good at the forward end, but the measured suction are somewhat greater towards the nozzle exit. However, computation of internal pressures in this region is uncertain because of internal flow turning. This provides a static pressure gradient across the internal flow in the correct sense to explain the observed small differences.



# USB CRUISE PROGRAM

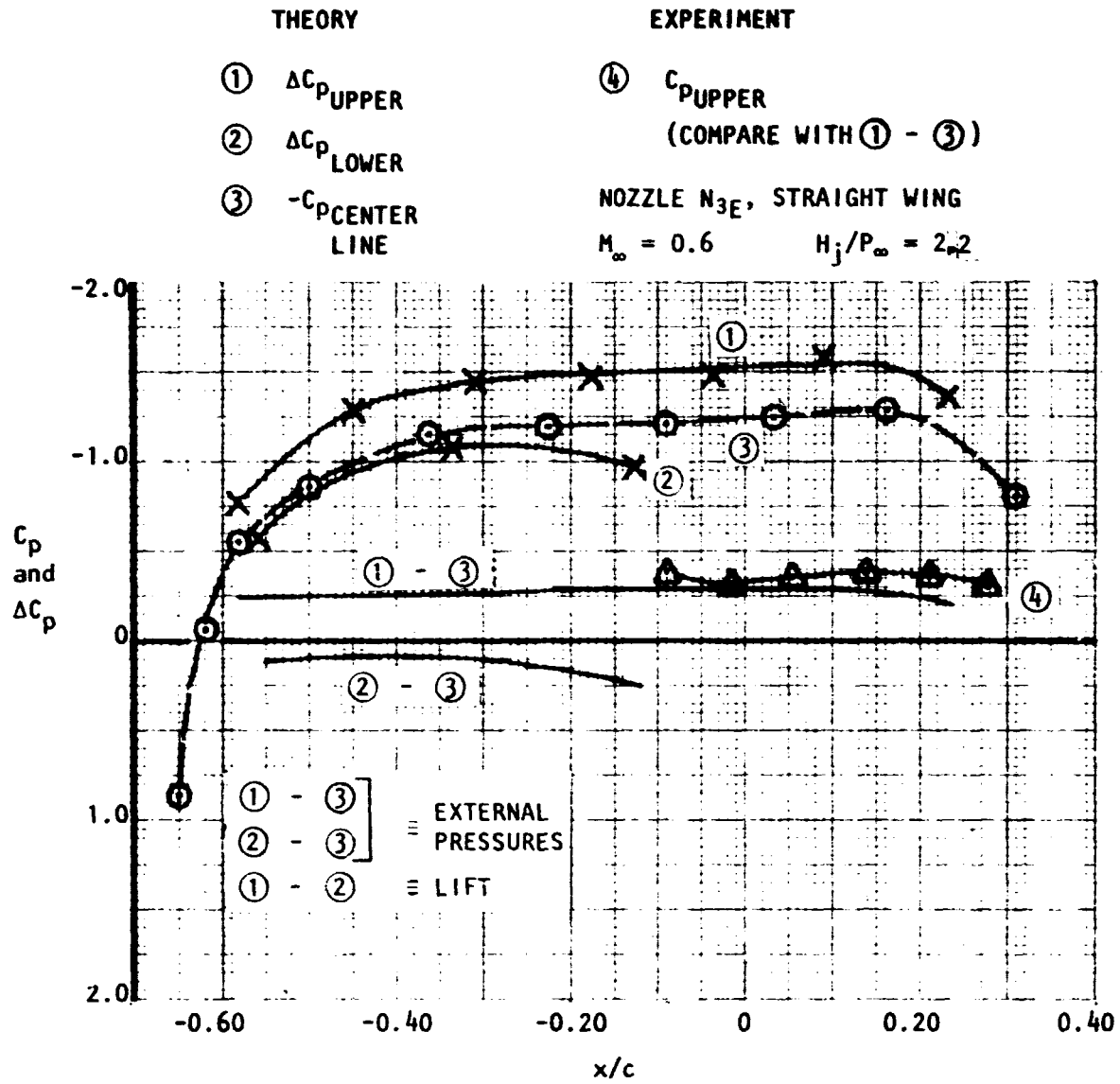


Figure 165. Predicted and measured pressures on nacelle-surfaces.

In summary, it appears that where measurements are available, the theoretical predictions agree quite well with measured pressures. Predictions in the impingement and turning regions and on the aft-nacelle agree particularly well with experiment. However, in its present configuration the jet model spreading angle is somewhat excessive and correlations along each side of the nacelle are affected adversely. "Fine tuning," to remove this effect, is not considered worthwhile.

#### 4.7 DRAG ANALYSIS AND CORRELATION: FLOW-THROUGH CASES

##### 4.7.1 Analysis of Drag Distribution

For unpowered cases, the drag distribution was found using conventional vortex lattice procedures. Figure 166 is a histogram of drag counts calculated at successive bays along the nacelle (see Figure 157). The full line shows the drag distribution, along the nacelle, at a typical cruise angle of attack, with the nacelle carrying noticeable lift. This total drag distribution may be split into nacelle shape-dependent and nacelle lift-dependent parts.

We may define a nacelle shape-dependent drag distribution which occurs at the angle of attack for which the nacelle zero-lift line is aligned with the mainstream. For a particular D-duct nacelle ( $N_{3E}$ ), this is about minus 2.5 degrees. The distribution of shape-dependent drag is shown in Figure 166 by the broken line. There is a strong positive drag region forward, in the forebody stagnation region, followed by an even stronger thrust region as the flow accelerates around the forebody. Up to bay 5, most panels face

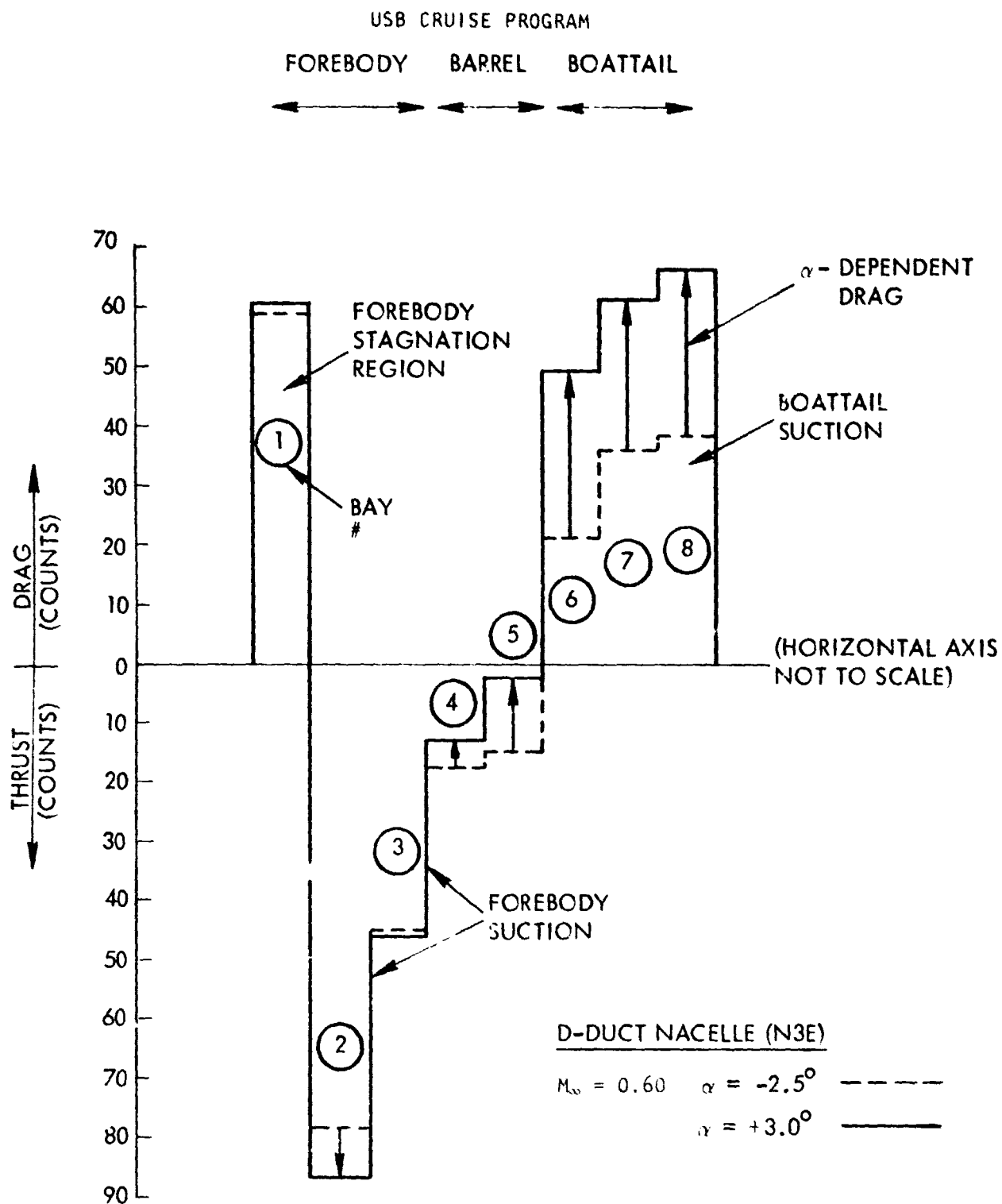


Figure 166. Computed drag count distribution along nacelle axis (Nacelle Surfaces Only).

forward, giving thrust where net suction exists. However, aft of this (bays 6 to 8), boattail drop-away causes the suction on aft-facing panels to give the drag values shown.

In the final analysis, when the large positive and large negative drag increments of the broken line in Figure 166 are combined with appropriate ram drag and exit thrust corrections, it is found that the net drag increment in the zero-nacelle-lift condition is very small — as would be expected for a non-lifting body in potential flow. There is evidently very little net drag due to nacelle-induced effects at this condition.

When the wing angle of attack is increased to a typical cruise value (full line, Figure 166), a detailed study of drag increment distribution (Figure 167) reveals decreased drag on the lower panels D2 to 8 and E2 to 4 (see Figure 157). Many of these panels face forward at  $\alpha = 3^\circ$ . However, on the remaining panels the effects of an increasing downwash field predominate and  $\alpha$ -dependent drag effects are significant, particularly in the boattail region.

The conclusion drawn from this part of the drag analysis is that, although strong opposing thrust and drag forces are generated on the nacelle by thickness effects, they have little if any resultant, and it is nacelle lift which causes significant drag increments. This occurs predominantly in the boattail region.

## USB CRUISE PROGRAM

DRAG LOAD ON NACELLE SURFACES

BAY ROW	FOREBODY		BARREL			CONTRACTION			SUM 3 TO 8
	1	2	3	4	5	6	7	8	
A	+ 1.4	-13.3	- 1.4	+ 8.8	+6.3	+25.7	+29.9	+31.3	100.6
B	+ 4.9	-14.9	- 2.8	+ 6.6	+2.5	+19.4	+25.4	+27.1	78.2
C	+11.3	-16.6	- 5.5	- 2.2	-2.0	+ 6.8	+12.1	+12.4	21.6
D	+18.8	-19.7	- 8.4	- 7.2	-9.3	- 2.8	- 5.8	- 4.2	-37.8
E	+23.9	-21.5	-28.5	-19.0	W I N G				-47.5
SUM	+60.3	-86.0	-46.6	-13.0	-2.5	+49.1	+61.6	+66.5	115.1

-25.7

DRAG "COUNTS" ( $\Delta C_D = 0.0001/\text{CT.}$ )  
 SHOWN FOR LEFT AND RIGHT SIDES  
 COMBINED. REFER TO FIGURE 155.

Figure 167. Drag build-up on nacelle surfaces,  $M_\infty = 0.60$ ,  $\alpha = 3.0^\circ$ .

Figure 168 details the axial forces on the wing in the nacelle overlap region and aft of it. There are large opposing thrust and drag forces, but the net drag increment due to adding the nacelle is quite small. Though the nacelle and aft-wing experience high drag, wing sections each side of the nacelle experience strong thrust increments (see Figure 169). This is caused by upwash generated outboard of the nacelle trailing vortices. Because the spanwise distribution of the panels is sparse, the wing drag data may not be very accurate, but the trends should be correct. It is evident that, at the cruise angle of attack, the flow-through nacelle exerts a strong redistributive influence on drag. Though the generation of a narrowly spaced vortex pair over the nacelle causes large local drag on the boattail and on the wing downstream of it, complementary thrust forces are induced on aft surfaces each side of the nacelle in the upwash regions. It is evident that, in the spanwise summation as well as along the nacelle, the net drag force arises as a small difference between large opposing thrust and drag forces.

#### 4.7.2 Correlation with Experiment

Since the vortex lattice predictions are made using a flow-through nacelle, a correction is necessary to determine closed-forebody results for comparison with experiments. It is possible in principle to do this with a ram-drag correction, but it was found preferable to rely upon the fact that theoretical forebody thickness drag, back to the barrel section, is zero and delete drag increments for the first three bays from the drag summation. This also removes any induced drag on the forebody. However, it was found that forebody contribution to drag is small in comparison with that in the boattail region.

# US3 CRUISE PROGRAM

SECTIONS 3 & 4	CUT OUT	AFT	SUM
UPPER	(ABSENT)	+160.2	160.2
LOWER	-175.2	+ 7.5	-167.7
SUM	-175.2	167.7	- 7.5

WITH  
NACELLE

SECTIONS 3 & 4	CUT OUT	AFT	SUM
UPPER	- 79.1	144.1	+ 65.0
LOWER	-101.9	14.0	- 87.9
SUM	-181.0	158.1	- 22.9

CLEAN  
WING

SECTIONS 3 & 4	CUT OUT	AFT	SUM
UPPER	+ 79.1	+ 16.1	+ 95.2
LOWER	- 73.3	- 6.5	- 79.8
SUM	+ 5.8	+ 9.6	+ 15.4

INCREMENT

Figure 168. Wing drag increments in drag "counts" in the nacelle overlap region and aft of it.

# USB CRUISE PROGRAM

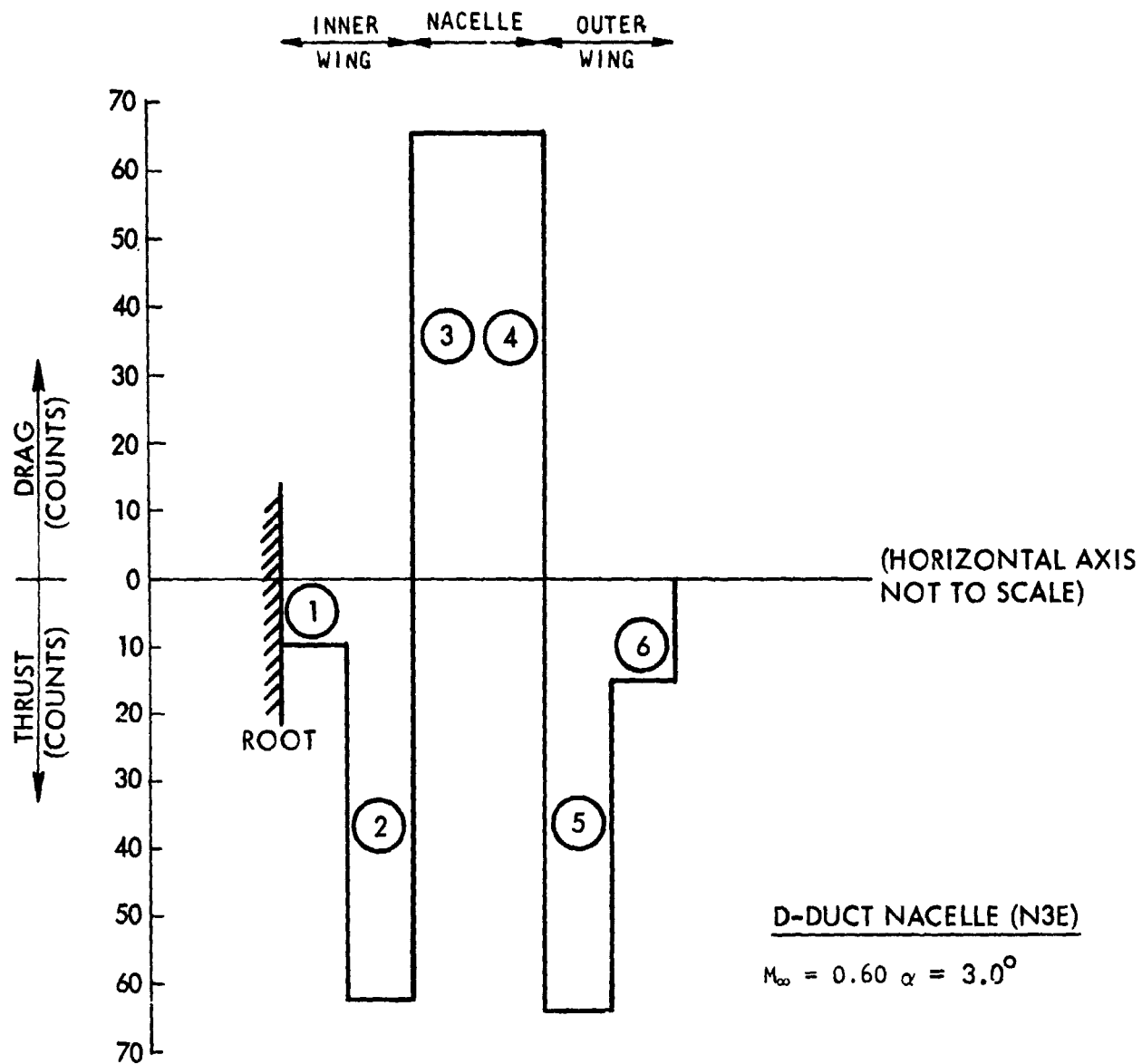


Figure 169. Computed drag count distribution along semi-span (All Surfaces).



Figure 170 shows, in curve (1), the drag increment due to adding flow through nacelle N<sub>3E</sub> to the clean wing. On correcting to the closed-nose condition, curve (2) is obtained, which may be compared with the experimental data of curve (3). Since the theoretical curve, (2), contains no allowance for skin friction, it should underpredict the drag increment. Cross reference to Section 3.3.3.2, in which skin friction estimates are made based upon the change in wetted area, shows that there should be approximately 20 to 23 counts of skin friction for nacelle N<sub>3E</sub>. This agrees very well with the difference between curves (2) and (3) in Figure 170.

#### 4.8 DRAG ANALYSIS AND CORRELATION: POWER EFFECTS

##### 4.8.1 Analysis of Power Effects on the Wing

It was found that a straightforward extension of the previous, conventional vortex lattice methods to drag prediction in powered cases simply did not work. This was not unexpected, since it had already been determined in pressure distribution studies that it was necessary to replace the standard "pVT" approach by a "spread T" method in order to produce acceptable results. One reason for this was that the lattice surface aft of the nacelle exit was fully immersed in the jet efflux and was, therefore, subjected to unrepresentative velocities over the bound vortices. Various approaches were tried using surface velocities typical of the sheet edge, which corresponds to the real flow condition, but without success. The previous "spread T" C<sub>p</sub>'s were therefore used to determine power-dependent drag increments.

Figure 171(a) shows typical  $C_p \sim y/c$  plots. The upper part of the figure, which is for the flow-through case, shows substantial leading edge thrust contributions and some lower surface thrust due to positive pressures just aft of the lower crest. Points corresponding to the upper and lower surface leading edges were joined by a straight line and no attempt was made to locate the front stagnation point. While this procedure will obviously produce incorrect total drag integrals, its consistent use in comparison between powered and unpowered cases should produce acceptable incremental results. A similar rationale was employed at the trailing edge.

Figures 171(a) (lower part) and 171(b) show typical effects of adding power to the flow-through case. One of the more pronounced features is a substantial, but incorrect, loss of leading edge thrust on both upper and lower surfaces. This results from a power-induced decrease in leading edge suction, already noted in the surface pressure correlation study. It appears that power effects have disturbed conditions within the airfoil and have thereby upset the gap tuning process described in Section 4.3. Though it may be possible in principle to overcome this difficulty, it was decided to omit the leading edge region when determining power-induced drag increments.

A review of power-induced effects on the aft lower surface revealed that these are small, both in theoretical predictions and experimentally. Accordingly, attention has been focussed on the aft upper surface and upon the nacelle boattail region.

For greater integration accuracy, data such as those in Figure 171 were replotted as power-induced changes in pressure coefficient. Figure 172

# USB CRUISE PROGRAM

4 x 4 EXPERIMENT

□  $H_j/p_\infty = 1.35$

×  $H_j/p_\infty = 1.25$

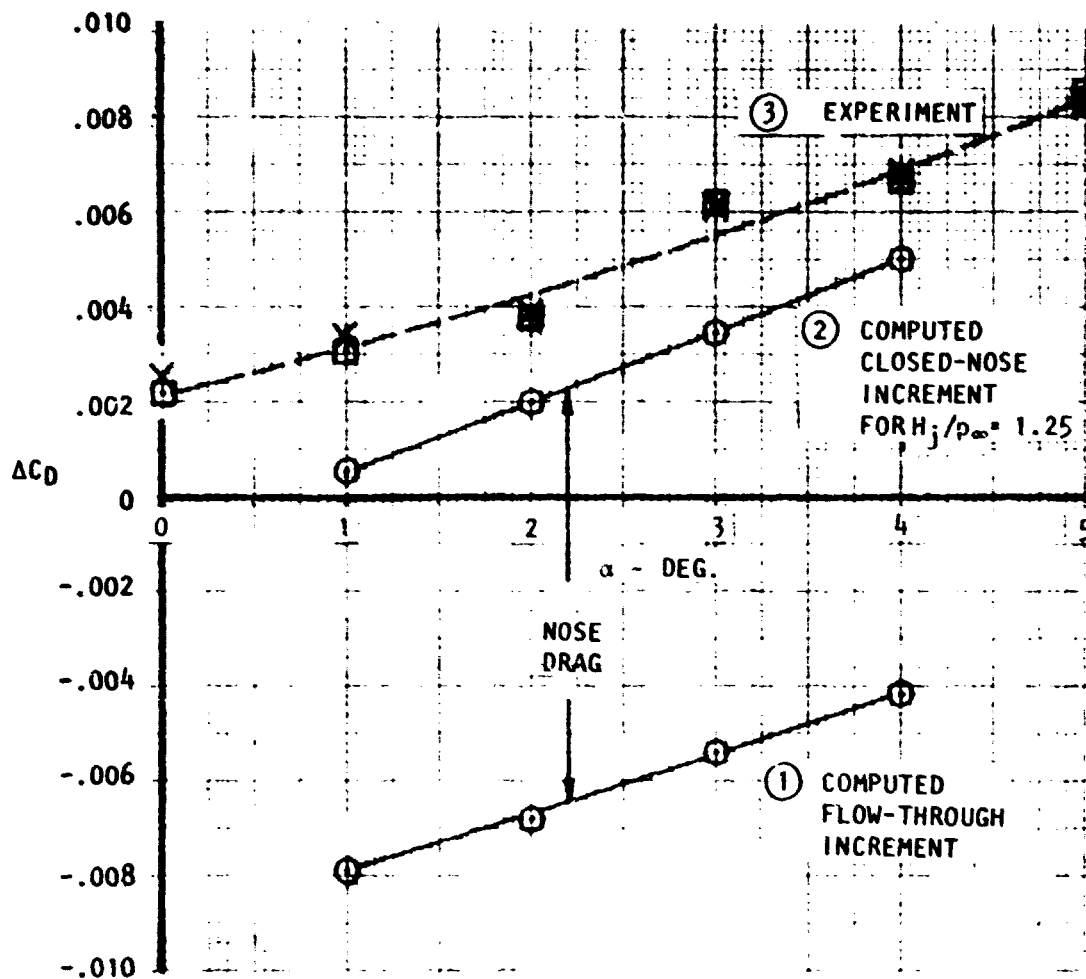


Figure 170. Drag Increments due to unpowered nacelle.

# USB CRUISE PROGRAM

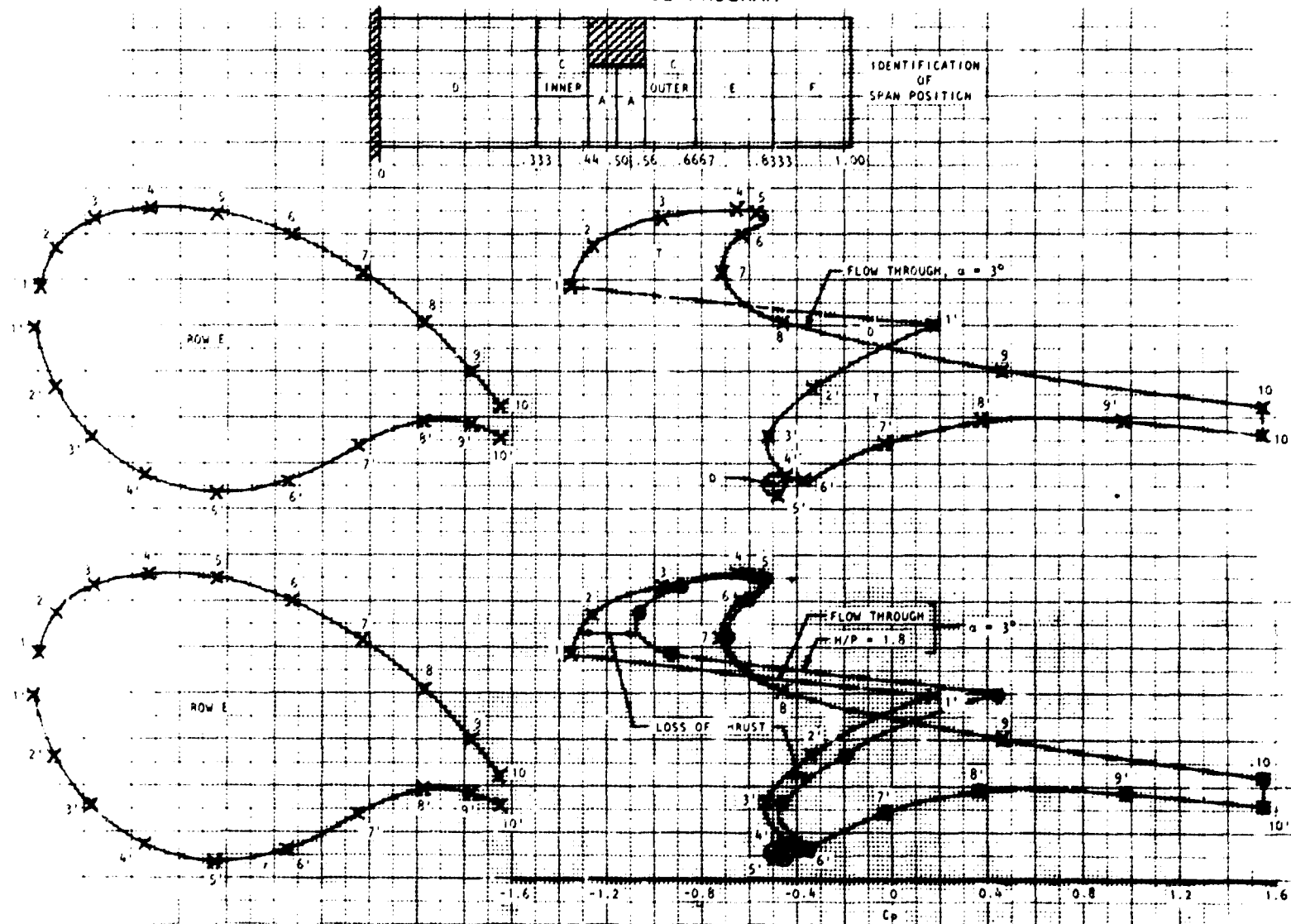
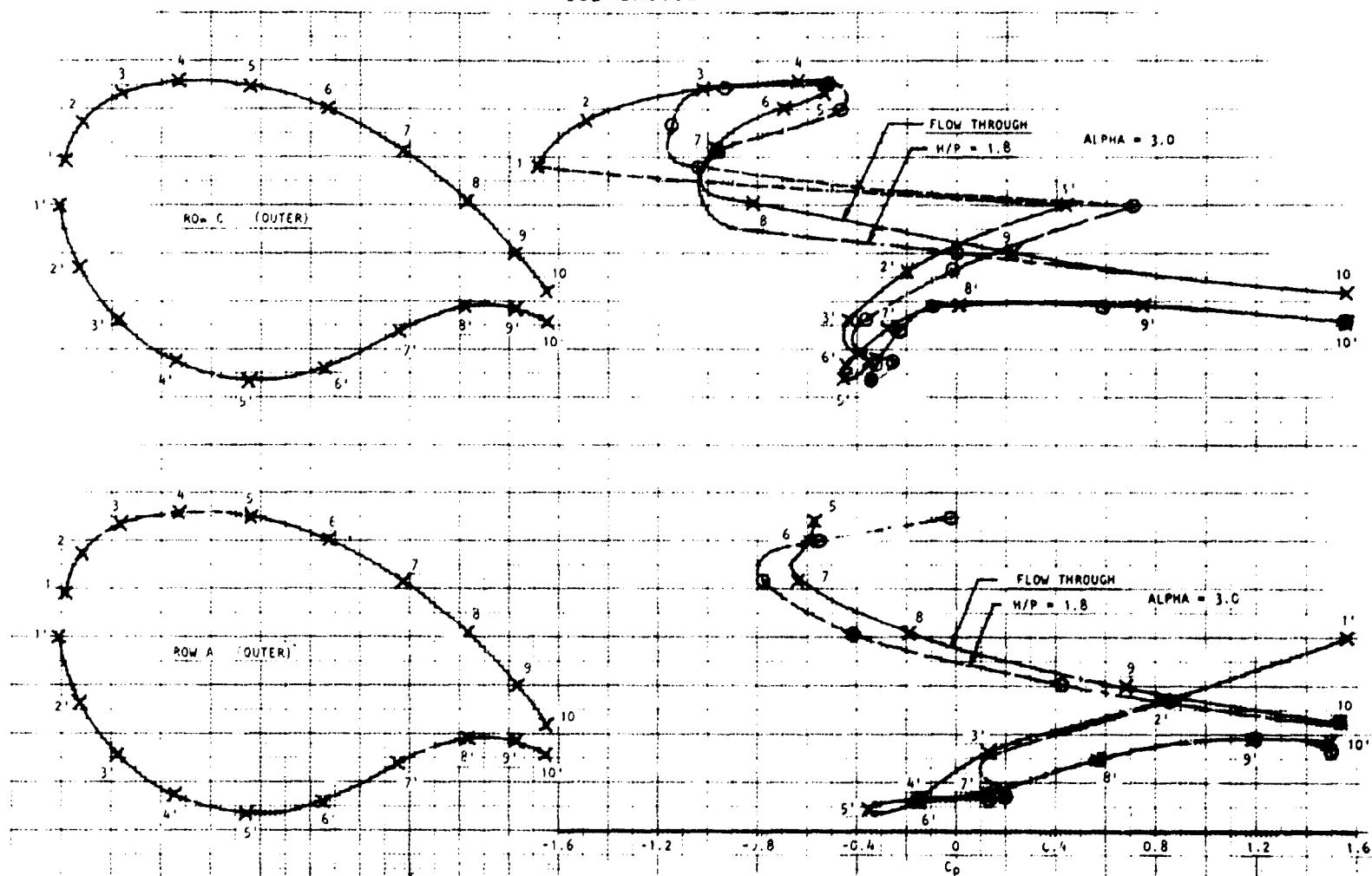


Figure 171(a). Typical  $C_p$  plots for drag integration. (a) ROW E

## USB CRUISE PROGRAM

Figure 171(b). (Continued) Typical  $C_p$  plots for drag integration. (b) ROWS C AND A

# USB CRUISE PROGRAM

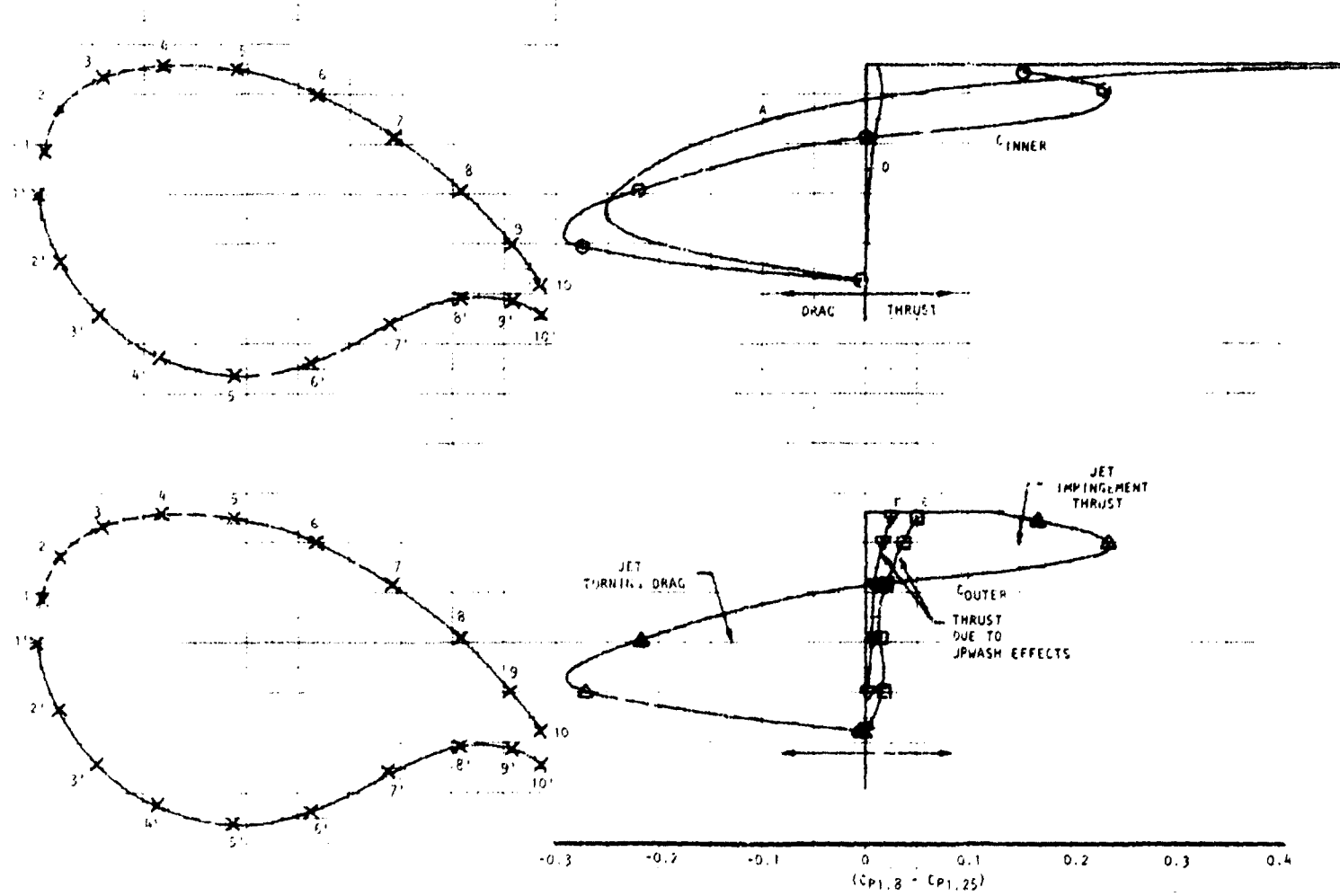


Figure 172. Power-induced changes in wing pressure coefficients.

shows these changes for the aft upper surface at all spanwise stations. Just as for the flow-through cases, the outer stations (D, E and F) experience thrust. Though a thrust component appears at stations A and C, in the aft-facing impingement region, this is overshadowed by turning drag. Figure 173 is derived from Figure 172 and shows that the majority of the wing experiences thrust. However, because of jet turning, the overall effect of power is to increase drag.

Figure 174 shows the resultant wing surface drag increments (full line) relative to the clean wing condition, as a function of blowing pressure ratio at typical angles of attack. As would be expected, drag increments increase with angle-of-attack, due to increase in aft-facing area, and also with pressure ratio, as a consequence of the associated increase in jet-turning loads.

The broken lines show the effect of adding power-induced aft-nacelle loads to the previous curves. Drag is reduced by an increasing amount as power is increased as a result of forward propagation of impingement pressures acting upon the aft-facing boattail surface.

Figures 175(a) through (e) show the variation of drag increments for the powered nacelle, relative to clean wing, with  $\alpha$  for a series of blowing pressure ratios. In all cases the theoretical and experimental curves are almost parallel, being separated by a residual drag increment which varies with  $H_j/p_\infty$  in the manner shown in Figure 176. Near to flow-through pressure ratios, the residual drag can be identified readily with net nacelle skin

USB CRUISE PROGRAM

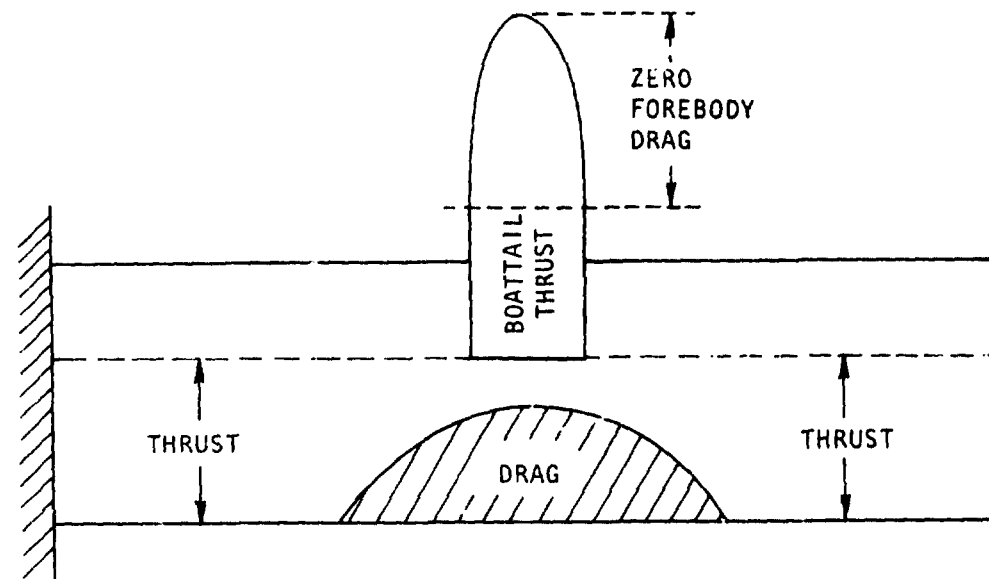


Figure 173. Location of drag-producing and thrust-producing regions due to application of power.



# USB CRUISE PROGRAM

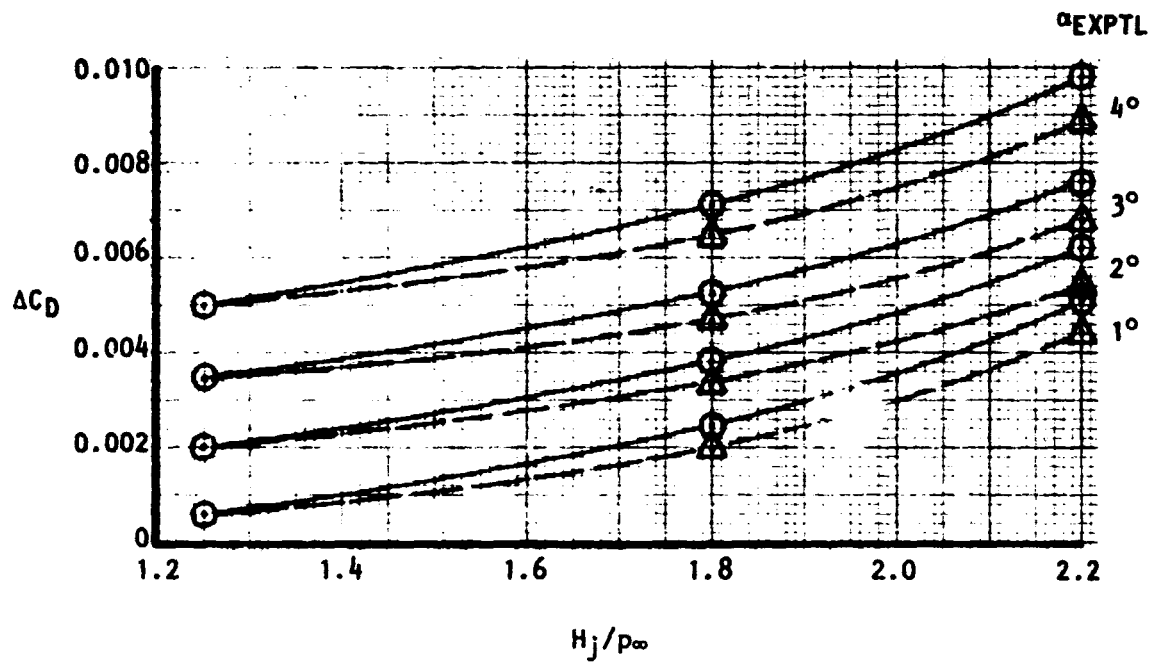


Figure 174. Predicted drag increments due to addition of powered  $N_3E$  nacelle.  $M_\infty = 0.60$ .

# USB CRUISE PROGRAM

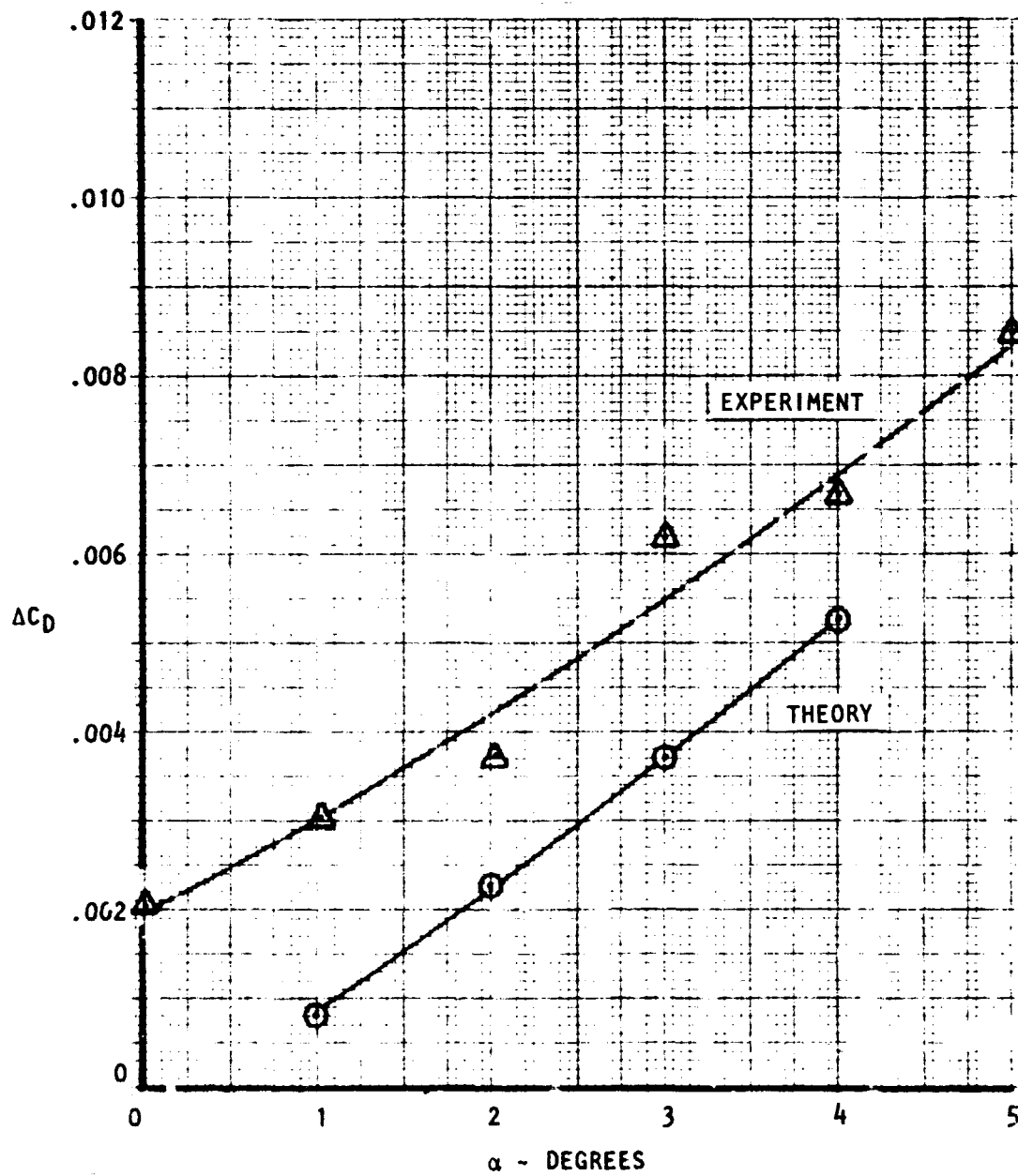


Figure 175. Comparison between predicted and measured drag increments for nacelle N3E at  $M_\infty = 0.60$ .  
(a)  $H_j/p_\infty = 1.40$ .

# USB CRUISE PROGRAM

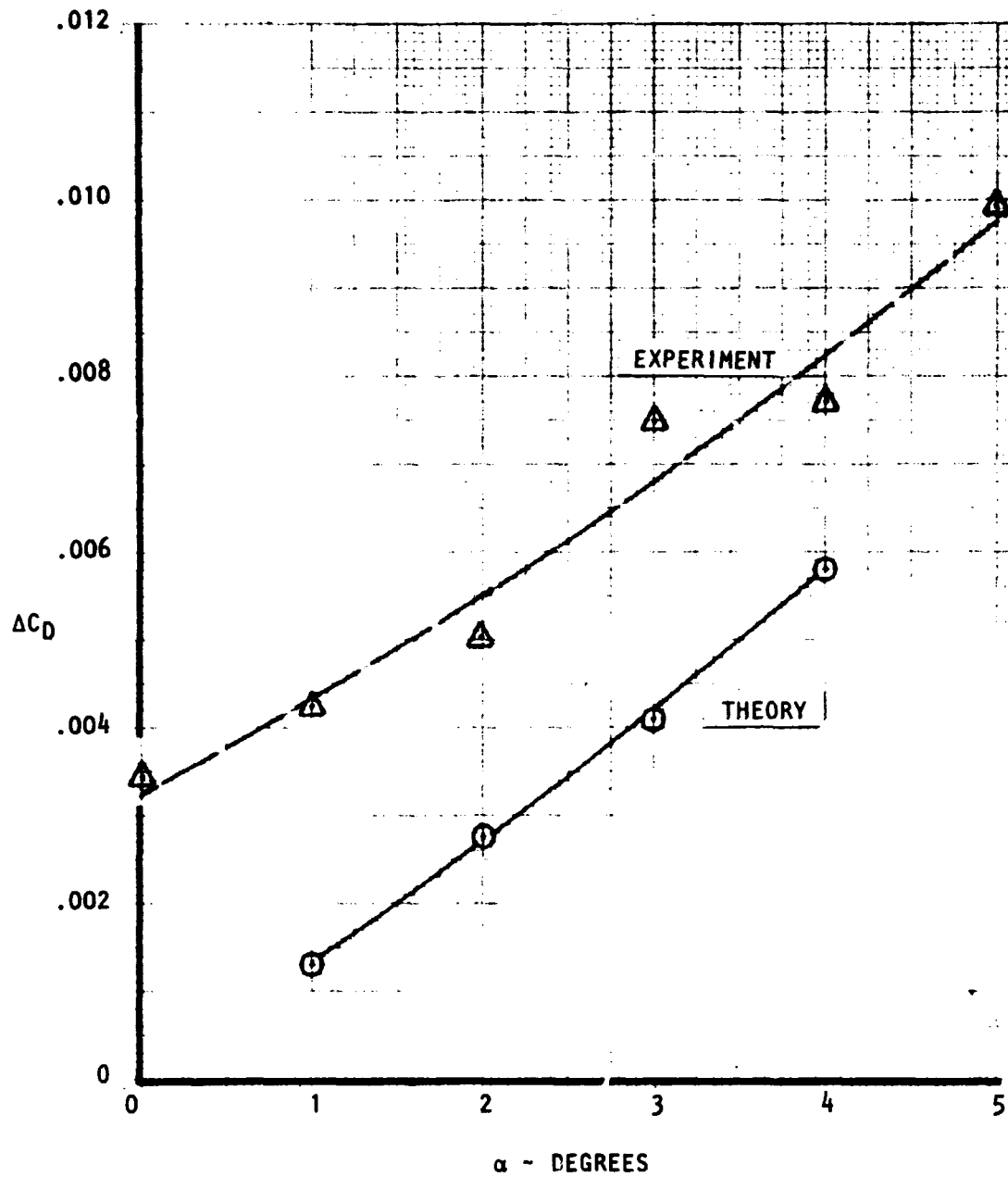


Figure 175. (Continued) Comparison between predicted and measured drag increments for nacelle N<sub>3E</sub> at  $M_\infty = 0.60$ . (b)  $H_j/p_\infty = 1.60$ .

ORIGINAL PAGE IS  
OF POOR QUALITY

# USB CRUISE PROGRAM

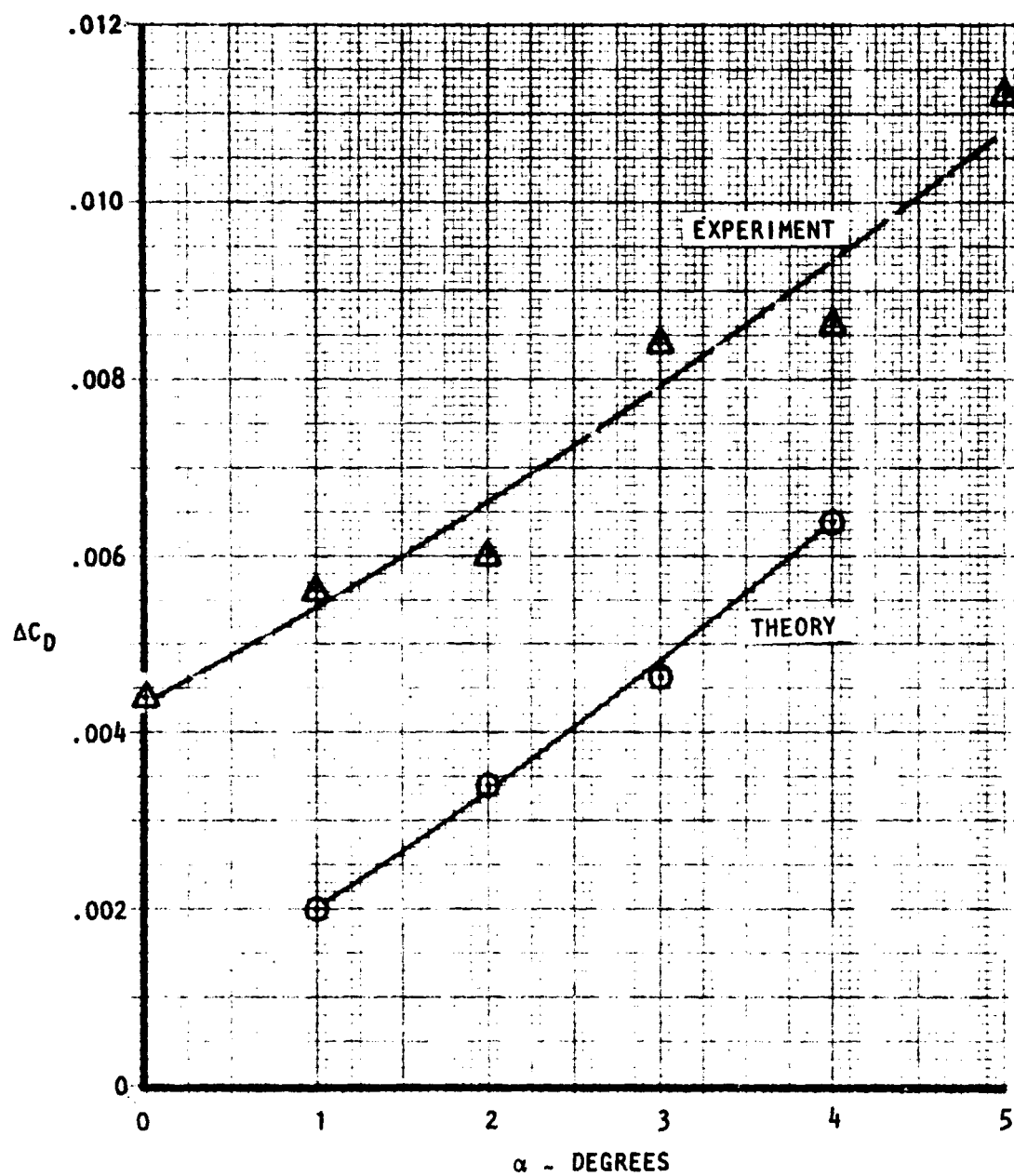


Figure 175. (Continued) Comparison between predicted and measured drag increments for nacelle N<sub>3E</sub> at  $M_\infty = 0.60$ . (c)  $H_j/p_\infty = 1.80$ .

# USB CRUISE PROGRAM

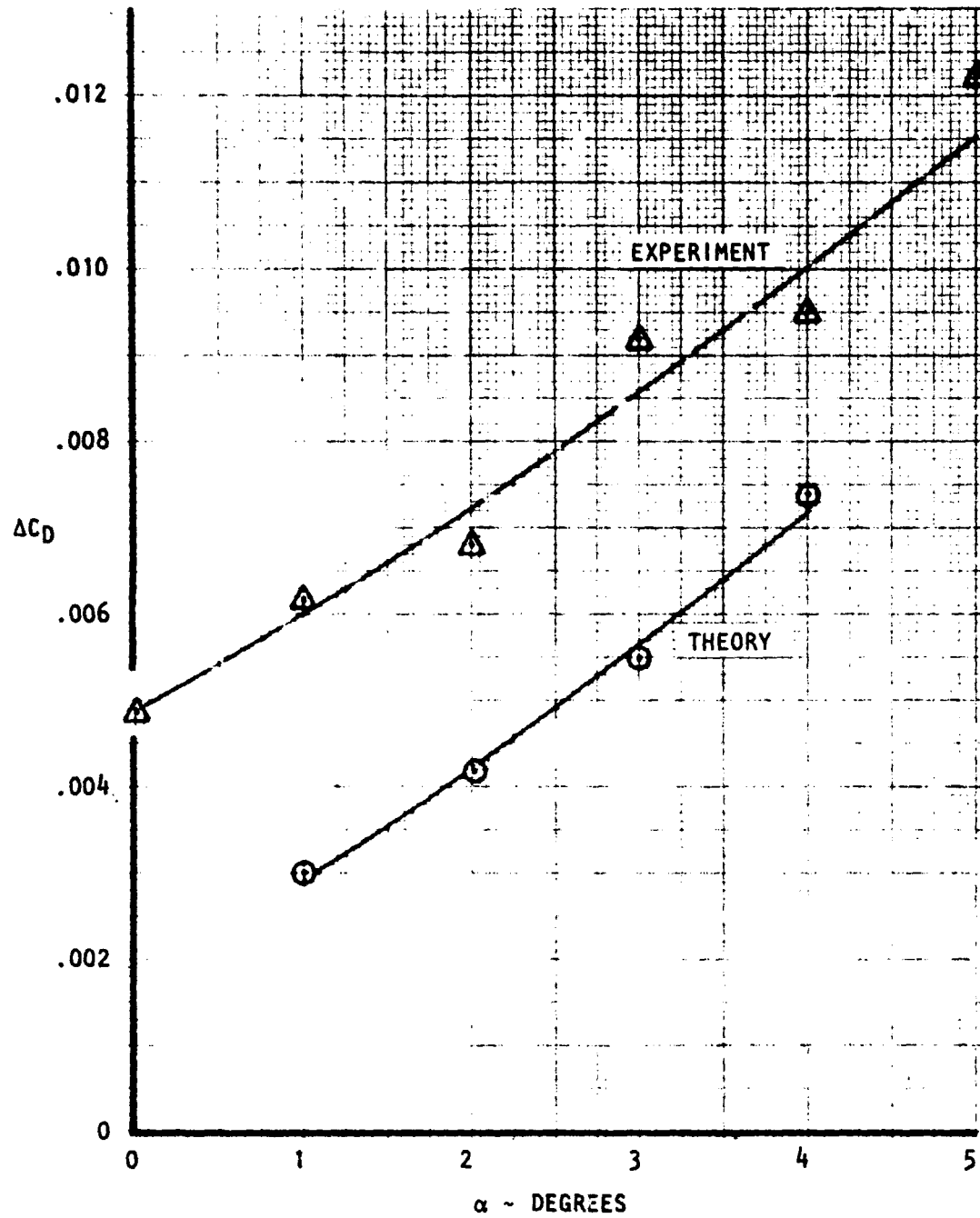


Figure 175. (Continued) Comparison between predicted and measured drag increments for nacelle  $N_{3E}$  at  $M_\infty = 0.60$ . (d)  $H_j/p_\infty = 2.00$ .

# USB CRUISE PROGRAM

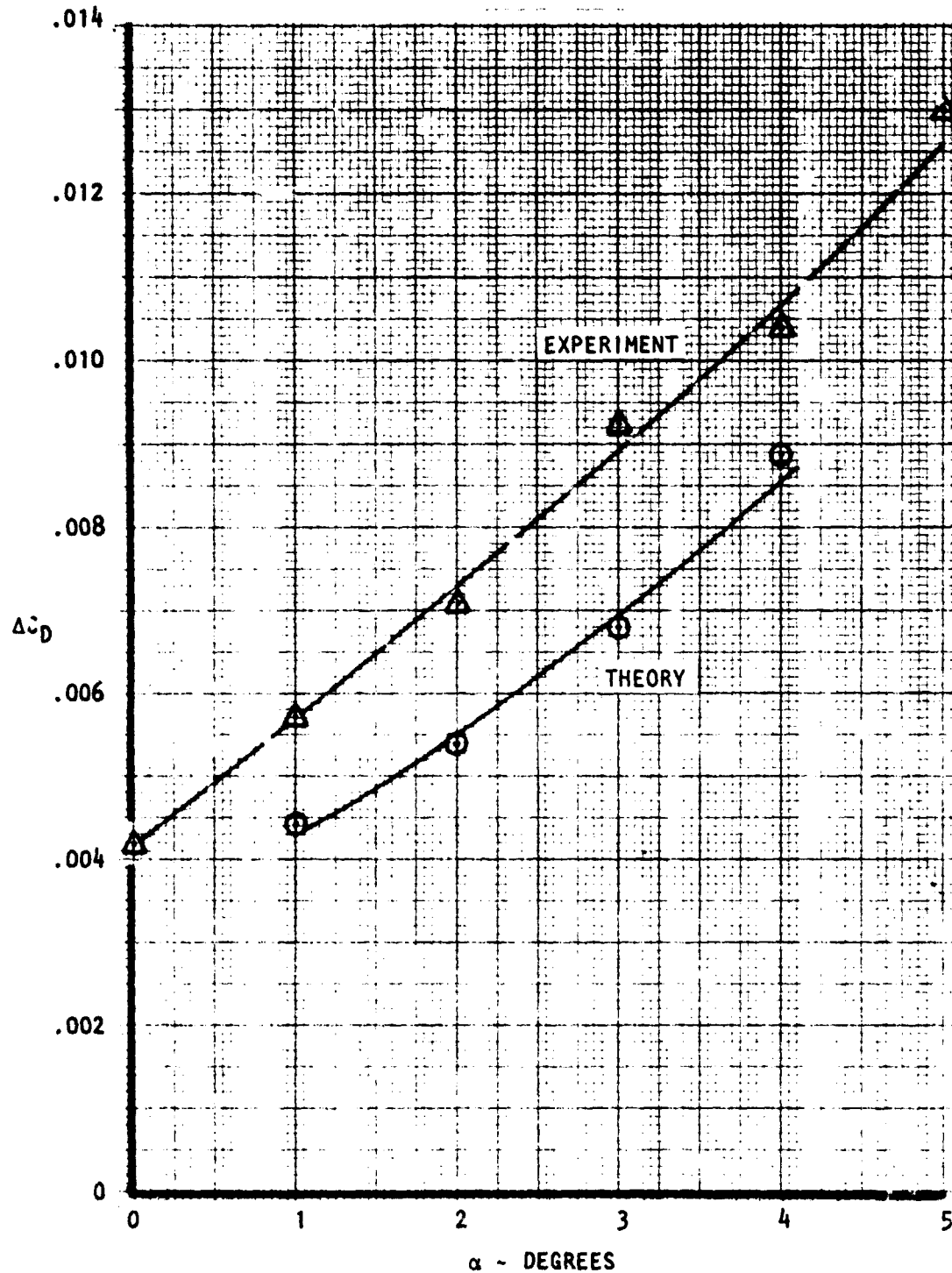


Figure 175. (Concluded) Comparison between predicted and measured drag increments for nacelle N<sub>3E</sub> at  $M_\infty = 0.60$ . (e)  $H_j/P_\infty = 2.20$ .

ORIGINAL PAGE IS  
OF POOR QUALITY

# USB CRUISE PROGRAM

- ① NACELLE SKIN FRICTION
- ② JET SCRUBBING DRAG
- ③ REDUCED TURNING/SCRUBBING  
DRAG AT  $M_{JET} > 1.0$

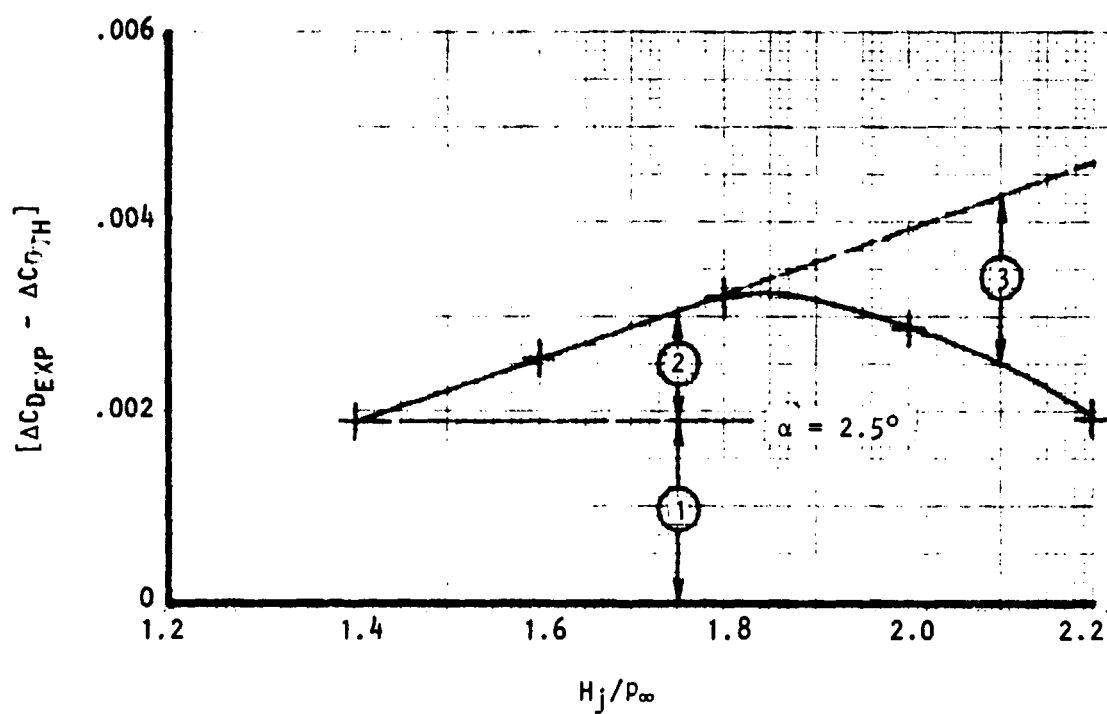


Figure 176. Residual difference between experimental and predicted drag increments for nacelle N3E at  $M_\infty = 0.60$ .

friction (see previous section). As jet pressure ratio is increased, scrubbing drag on the wing surface increases up to the critical pressure ratio. This is reflected in Figure 176 and the increase between  $H_j/p_\infty$ 's of 1.4 and 1.8 appears reasonable in this regard. Beyond  $H_j/p_\infty$  of 1.8, as the nozzle flow goes supercritical, the residual drag increment decreases. Inspection of the relevant pressure plots shows that jet turning is reduced under these conditions, which may be attributable to shock-induced separation of the jet from the wing surface.

It may be concluded that, up to critical jet pressure ratios, the prediction of drag increment is remarkably accurate and suitable additions for nacelle skin friction and for jet scrubbing drag will produce results which correlate well with experiment.

#### 4.9 LIFT ANALYSIS AND CORRELATION

##### 4.9.1 Vortex Lattice Results

Lift increments, due to adding the powered nacelle  $N_{3E}$  to the clean wing, were generally small, with values up to 0.06 at  $H_j/p_\infty = 2.2$ . The net effect again arose as the difference between large positive and negative forces. Positive lift increments arose predominantly in the nacelle boattail region and, with power applied, in the turning region towards the wing trailing edge aft of the nacelle. Download occurred in the impingement region just aft of the nacelle exit plane and to each side of this.

C-4



Comparisons between measured and vortex-lattice-predicted lift increments showed good agreement in trends with angle-of-attack, but the theory was almost totally unresponsive to change in pressure ratio. An almost unique curve of  $\Delta C_L$  versus  $\alpha$  was produced by the theory, corresponding to an experimental pressure ratio of roughly 1.6. Further investigation showed that predicted impingement pressures, which correlated well aft of the jet exit, propagated sideways and produced more download each side of the nacelle position than was indicated by pressure measurements. This excessive download evidently nullified positive lift increments from the boattail and turning regions. Since the anomaly occurred in a region where the wing surface was approximately horizontal, drag predictions were affected very little.

It is evident that, by using a finer spanwise grid in the theory and with some fine tuning of the jet model, better correlation with experimental lift measurements could be obtained. However, a parallel study using jet flap theory produced good lift predictions more readily (see below), though the corresponding drag predictions were unreliable.

#### 4.9.2 Simplified Jet Flap Theory

Basic jet-flap theory, applied to various degrees of sophistication, has generally provided a thread of commonality for the theoretical treatment of most interactive aeropropulsive systems. The theory has been particularly effective for representing powered systems (USB, augmentor wings, EBF, etc.) operating in the low-speed, high-lift mode. The application of the theory to the limited-span interactive powered system, operating in the compressible-flow cruise regime has received only limited attention. In the interest of

developing quick analysis techniques for representing the generalized aeropropulsive system at cruise, correlations have been performed between USB high-speed test results and the two-dimensional jet-flap theory of Spence (Reference 11) modified for finite aspect ratio, part-span blowing, and compressibility effects.

The following terms will be used in addition to the usual terminology:

$C_{LINC}$	incompressible, three-dimensional lift coefficient
$C_{l\delta}$	rate of change of local $C_l$ , with (see Eq. 36)
$C_{l\alpha}$	2-D lift curve slope (see Eq. 38)
$C_T$	airplane thrust coefficient = $T/q S_w$
$C_\mu$	local (2D) momentum coefficient
$F$	finite-wing, aspect-ratio correction function (see Eq. 34)
$S'$	blown area
$\gamma$	part-span factor for $C_{l\delta}$ (see Eq. 37)
$\lambda$	part-span factor for $C_{l\alpha}$ (see Eq. 35)

In Reference 12, it is shown that

$$C_{LINC} = F (1 + t/c) [\lambda C_{l\delta} \Delta\delta + \gamma C_{l\alpha} \Delta\alpha] - t/c C_T (\Delta\delta + \Delta\alpha) \quad (33)$$

where

$$F = \frac{AR + 2 C_\mu / \pi}{AR + 2 + 0.604 C_\mu^{1/2} + 0.876 C_\mu} \quad (34)$$

$$\lambda = \frac{S'}{S_w} \quad (35)$$

$$C_{l\delta} = [4\pi C_\mu (1 + 0.151 C_\mu^{1/2} + 0.139 C_\mu)]^{1/2} \quad (36)$$

$$\gamma = \frac{S'_x C_{l\alpha} - (S_w - S') (C_{l\alpha}) C_\mu}{S_w C_{l\alpha}} = 0 \quad (37)$$

$$C_{l\alpha} = 2\pi (1 + 0.151 C_\mu^{1/2} + 0.219 C_\mu) \quad (38)$$

A further modification is necessary to adapt the calculation to the Mach range of interest ( $0.6 \leq M_\infty \leq 0.8$ ); this subject is dealt with in References 13 and 14. Employing the modification suggested by Reference 13 along with standard Prandtl-Glauert similarity corrections, the compressible lift becomes

$$C_{L_{M_\infty}} = F \left(1 + \frac{t/c}{\beta}\right) \left[\lambda C_{l\delta} \cdot \frac{\Delta\delta}{\beta} + \gamma C_{l\alpha} \cdot \frac{\Delta\alpha}{\beta}\right] - \frac{t/c}{\beta} C_T \left(\frac{\Delta\alpha}{\beta} + \frac{\Delta\delta}{\beta}\right) \quad (39)$$

and  $C_\mu$  and AR in equations (34), (36) and (38) are replaced by  $\beta C_\mu$  and  $\beta$  AR, respectively. A corresponding equation for the compressible flow pitching moment of a system with limited span blowing can be obtained by similar substitutions into the basic equations of Reference 12.

#### 4.9.3 Correlation by Simplified Jet-Flap Theory

Figures 177 through 180 compare the total lift coefficient as calculated by the foregoing expression, to test results obtained for various USB-nozzle shapes, angles-of-attack and nozzle pressure ratios at the drag-rise Mach

# USB CRUISE PROGRAM

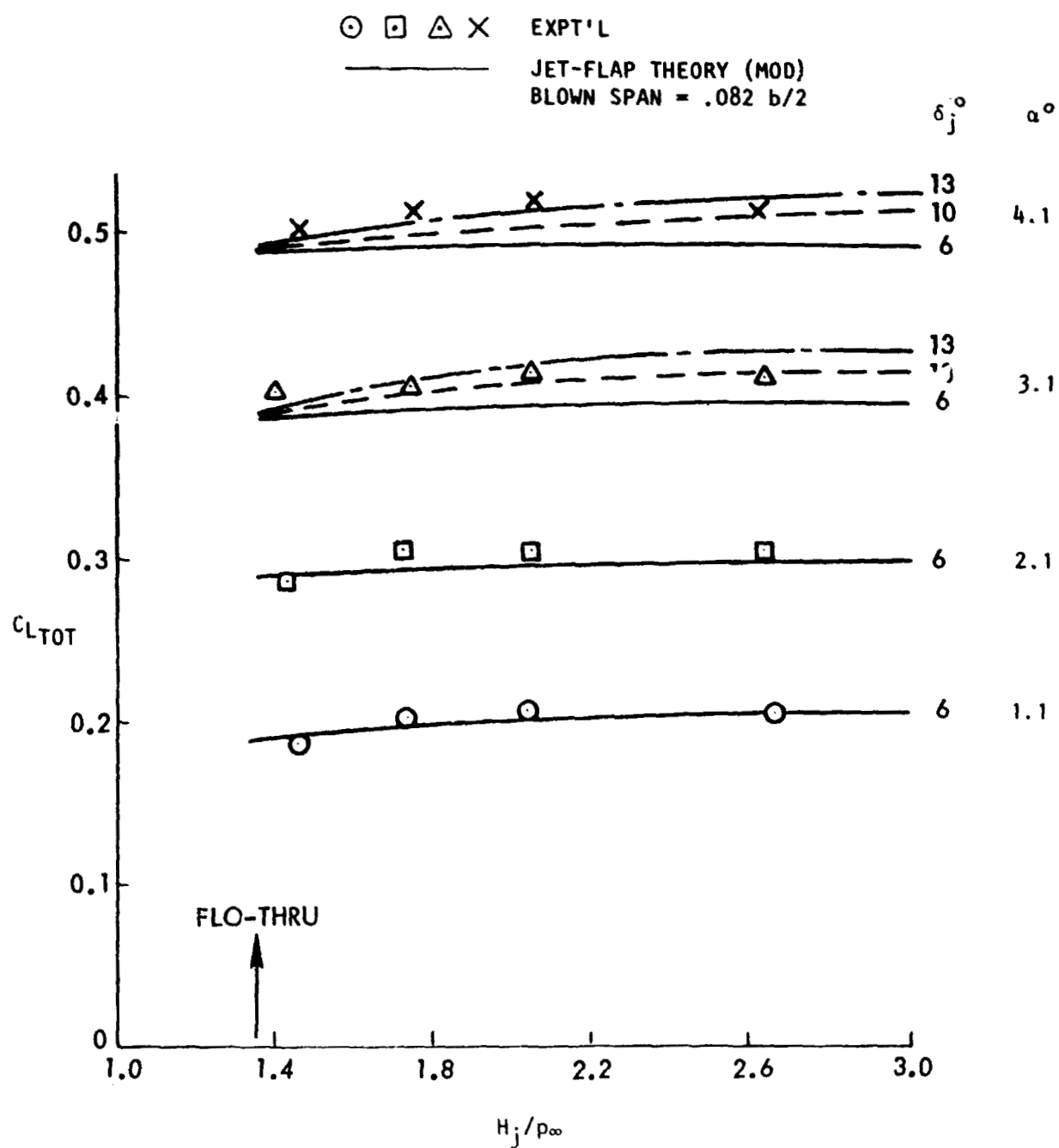


Figure 177. Comparison of USB test results with modified jet-flap theory, noz N<sub>2</sub>E, circular, M<sub>∞</sub> = 0.68.

# USB CRUISE PROGRAM

⊙ □ △ × EXPT'L

— JET-FLAP THEORY (MOD)  
 BLOWN SPAN = .12 b/2  
 $\delta_j = 15^\circ$

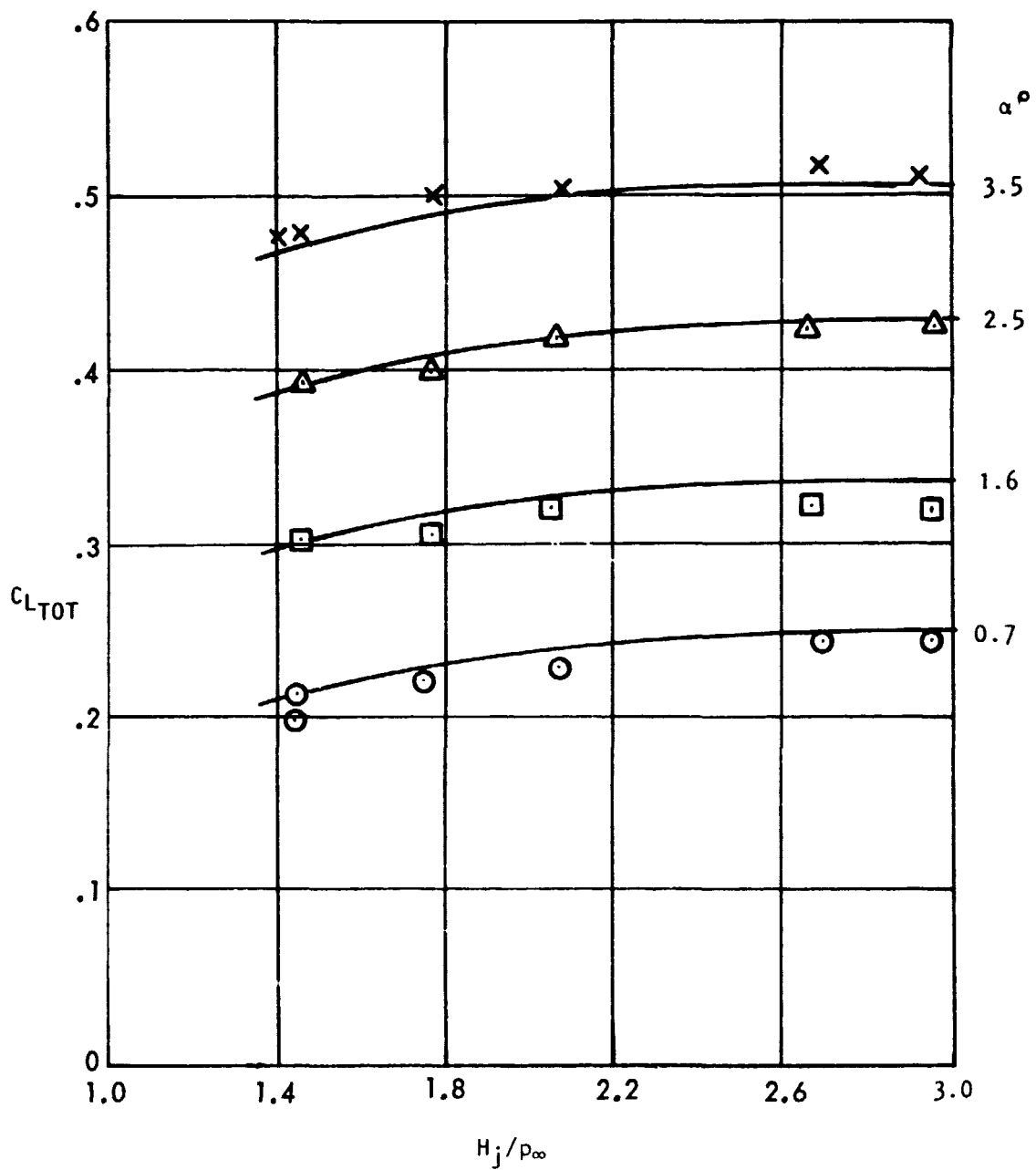


Figure 178. Comparison of USB test results with modified jet-flap theory, noz  $N_{3E}$ ,  $AR = 2.5$ ,  $M_\infty = 0.68$ .

# USB CRUISE PROGRAM

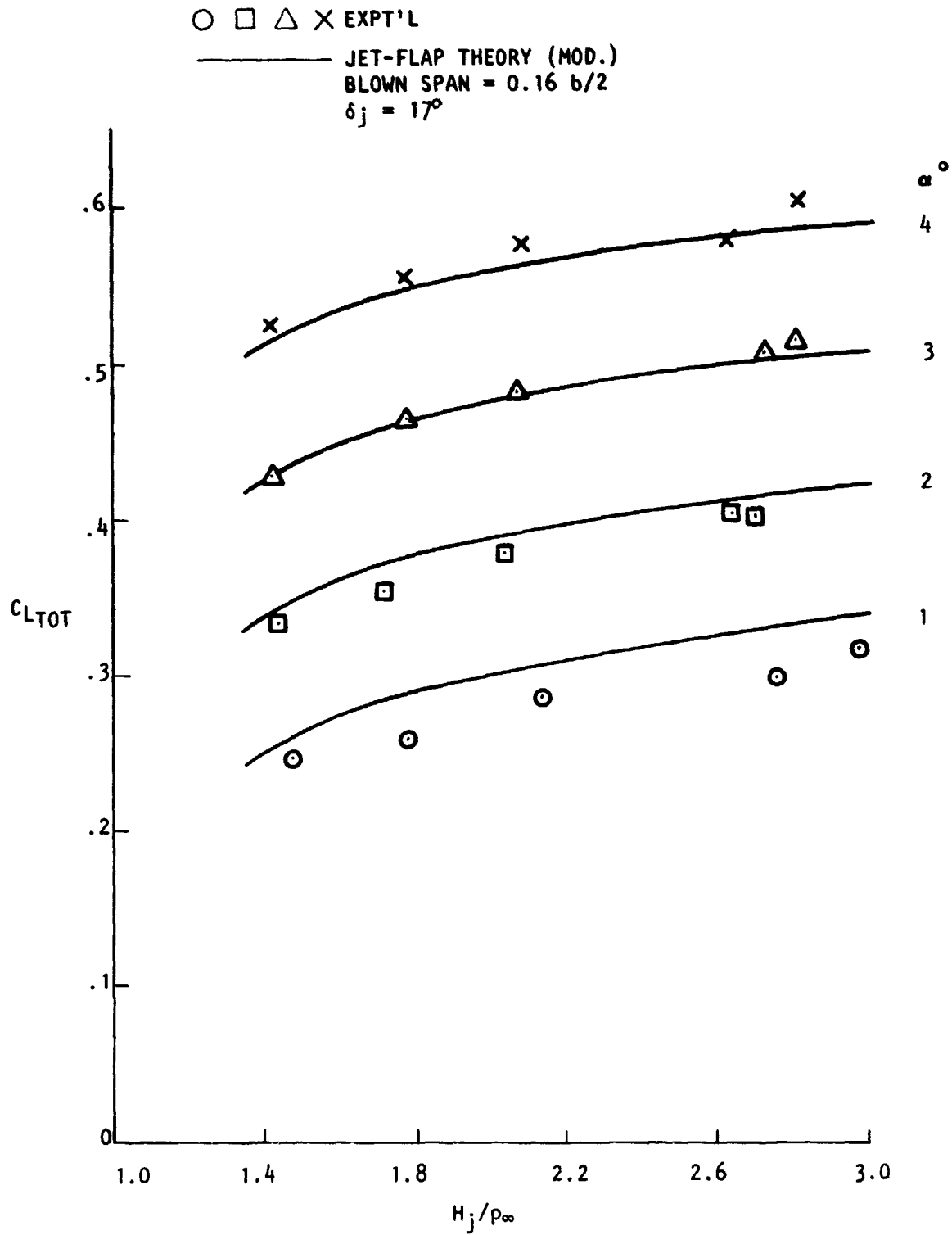


Figure 179. Comparison of USB test results with modified jet flap theory, noz  $N_{4E}$ ,  $AR = 4$ ,  $M_\infty = 0.68$ .

# USB CRUISE PROGRAM

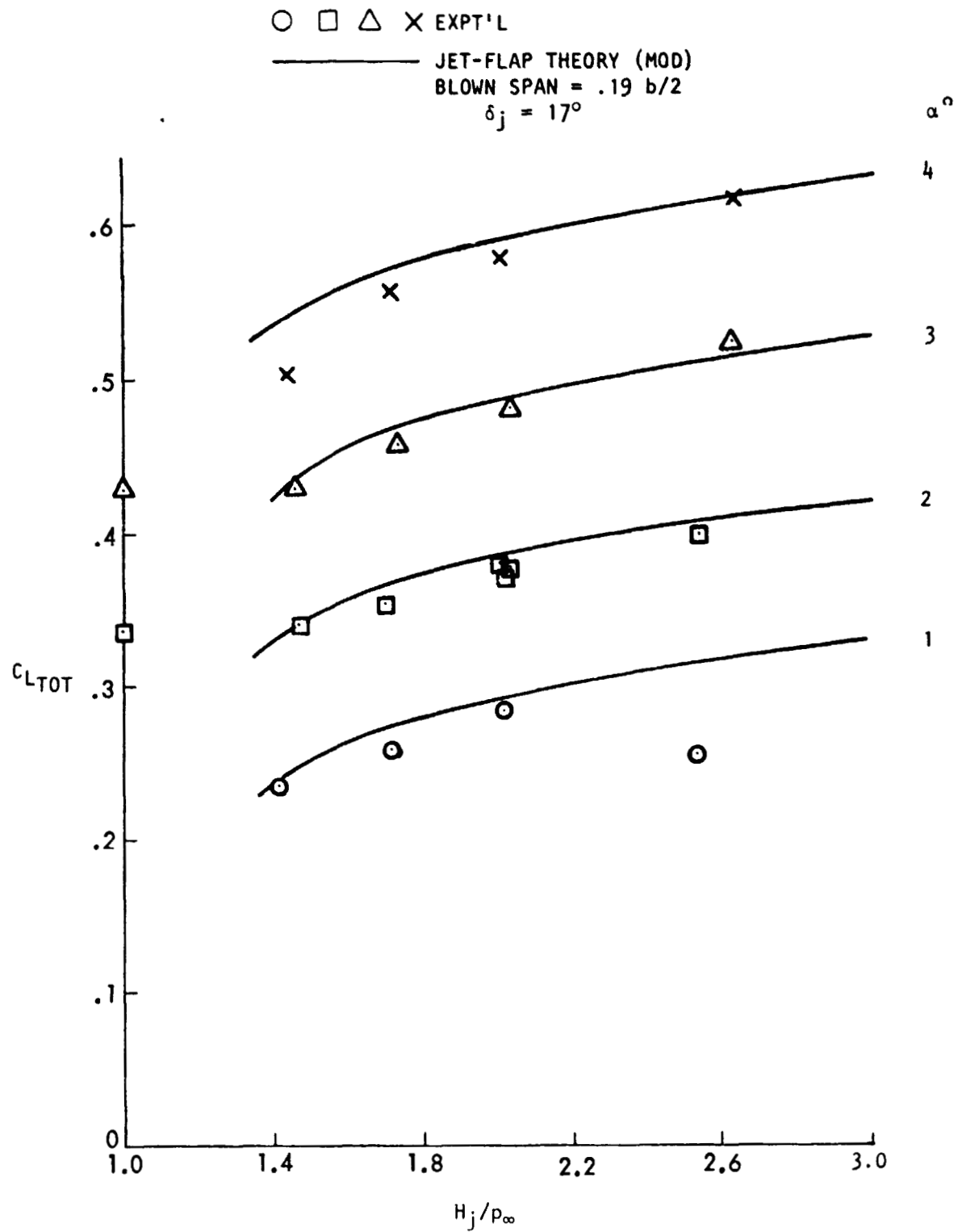


Figure 180. Comparison of USB test results with modified jet-flap theory, noz N<sub>5</sub>, AR = 6,  $M_\infty = 0.68$ .

number ( $M_\infty = 0.68$ ). Figures 181 and 182 show example correlations of the computed pitching-moments with those derived from tests of the semi-span, powered model, also at  $M_\infty = 0.68$ . In both calculations, two-dimensional wing test results at Mach number were used to evaluate the viscous  $C_{l_\alpha}$  (2-D) and  $C_{m_\alpha}$  (2-D) parameters to be used in lieu of the purely potential flow values; this procedure, in effect, establishes the three-dimensional lift and moment coefficients at the nozzle flow-through condition. The comparisons show that the lift and moment increments due to the limited span blowing typifying a USB-installation are accurately predicted by the simplified jet flap theory across the blowing range. While the agreement is gratifying, of more importance are the several facts brought out by the correlation.

An earlier analysis of the USB -pressure test results indicated that jet-induced lift and drag increments (as integrated across the scrubbed area) corresponded to a much higher jet-turning angle at the wind-on condition than had been found from static tests of the system. Typically, the static jet turning angle for a "D-duct nozzle would be about 4 degrees while the wing-on pressure data indicated an increase to 15-16 degrees (i.e., within several degrees of the trailing-edge angle of the airfoil upper surface,  $\delta\tau_E = 17^\circ$ ). The foregoing correlations of lift and pitching moment were obtained only when the assumed jet angle closely approached that of the wing trailing-edge regardless of the shape, this was often contrary to the observed static performance. The thickest jet (i.e., that from the circular nozzle) does show in Figure 177 a tendency to separate from the wing surface at low angles of attack where the pressure change ( $\Delta P$ ) across the jet, due to wing-flow is small. Figure 177 also shows that for  $\alpha = 1.0$  degree, the lift with



# USB CRUISE PROGRAM

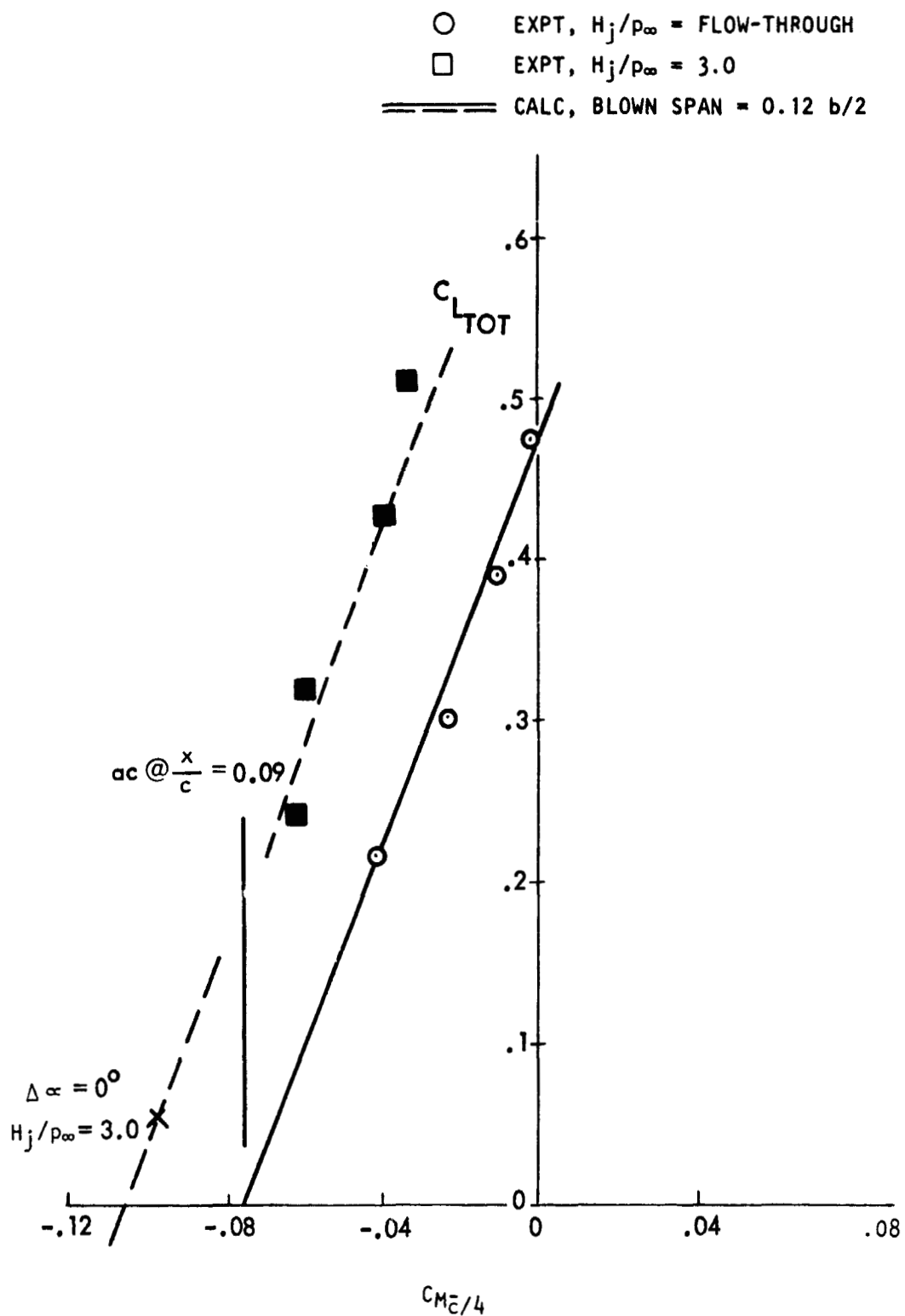


Figure 181. Comparison of USB test results with modified jet-flap theory, noz  $N_{3E}$ ,  $AR = 2.5$ ,  $M_\infty = 0.68$ .

# USB CRUISE PROGRAM

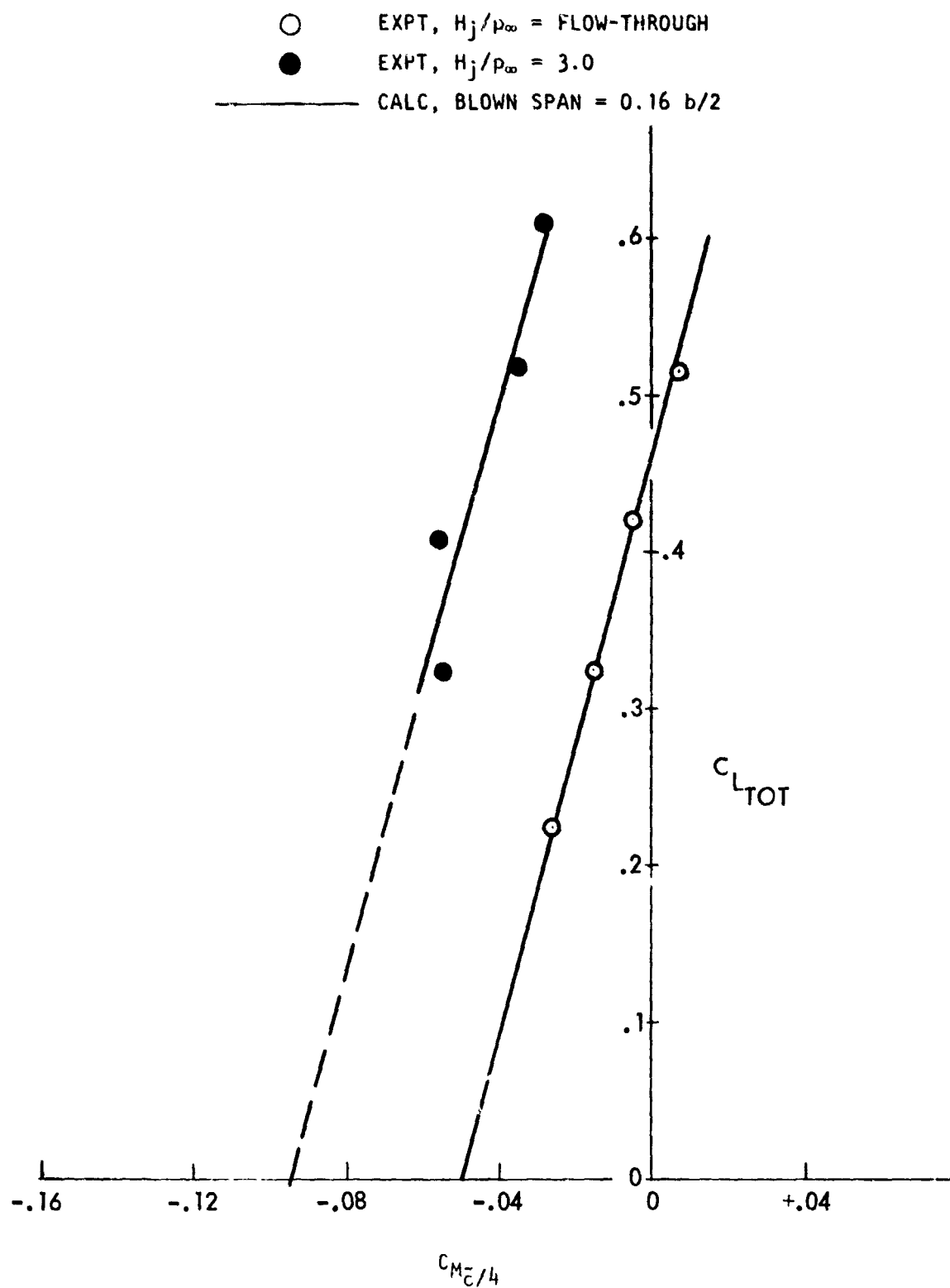


Figure 182. Comparison of USB test results with modified jet-flap theory, noz  $N_{4E}$ ,  $AR = 4$ ,  $M_\infty = 0.68$ .

the circular nozzle correlates best with a jet angle of 6 degrees whereas in the cruise range of  $\alpha = 3^\circ$ - $4^\circ$ , the wing trailing edge angle of  $17^\circ$  is gradually approached by the turning jet. The observed static turning angle with this nozzle (i.e., circular) was essentially zero. It is this apparent change in angle that probably accounts for an observed increase in pressure drag at wind-on conditions (from integrated pressure measurements) for either USB-type configurations or for that matter, a pure-jet-flap system. In the latter case, the wind-on pressure drag results primarily from flow entrainment into the trailing-edge jet, while for the USB, it is effectively an induced turning of the jet by the wing flow-field at the cruise lift coefficient.

#### 4.9.4 Correlation by Lifting Line Theory

The data correlations discussed above have been extended via a computer program developed by Lockheed-Georgia for Aerospace Research Lab (Reference 14). This program, as referenced, utilizes the mechanical flap analogy to predict jet-flap wing/body performance in essentially the incompressible, high-lift mode. The compressible case has, for present purposes, been treated in much the same fashion as the simplified jet-flap calculations above by transforming the input geometry of the configuration by the transonic similarity parameters (i.e.,  $\beta AR$ ,  $\frac{\Delta\alpha}{\beta} \frac{\Delta\delta}{\beta}$ ,  $C_T$ , etc.). Figures 183 through 185 show the excellent correlation achieved by this rather simple program modification to predict USB total lift coefficient at  $M_\infty = 0.68$  as a function of nozzle pressure ratio and exit aspect ratio. As in the modified 2-D approach, the best data match is obtained when the input jet angle

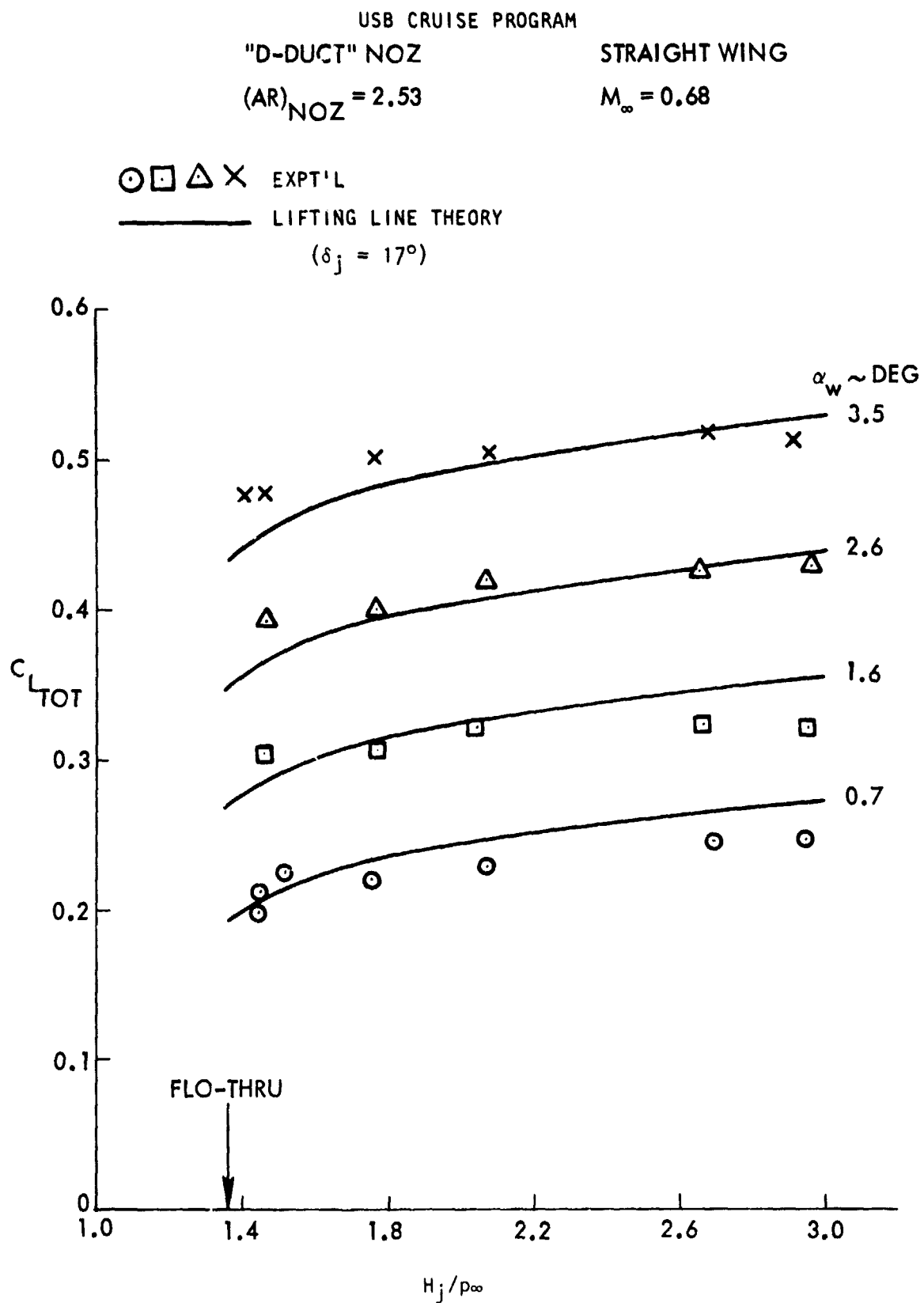


Figure 183. Comparison of USB test results with three-dimensional lifting line theory, nozzle  $N_{3E}$ ,  $AR = 2.5$ ,  $M_\infty = 0.68$ .

# USB CRUISE PROGRAM

○ □ △ × EXPT'L  
 — LIFT LINE THEORY  
 ( $\delta_j \approx 17^\circ$ )

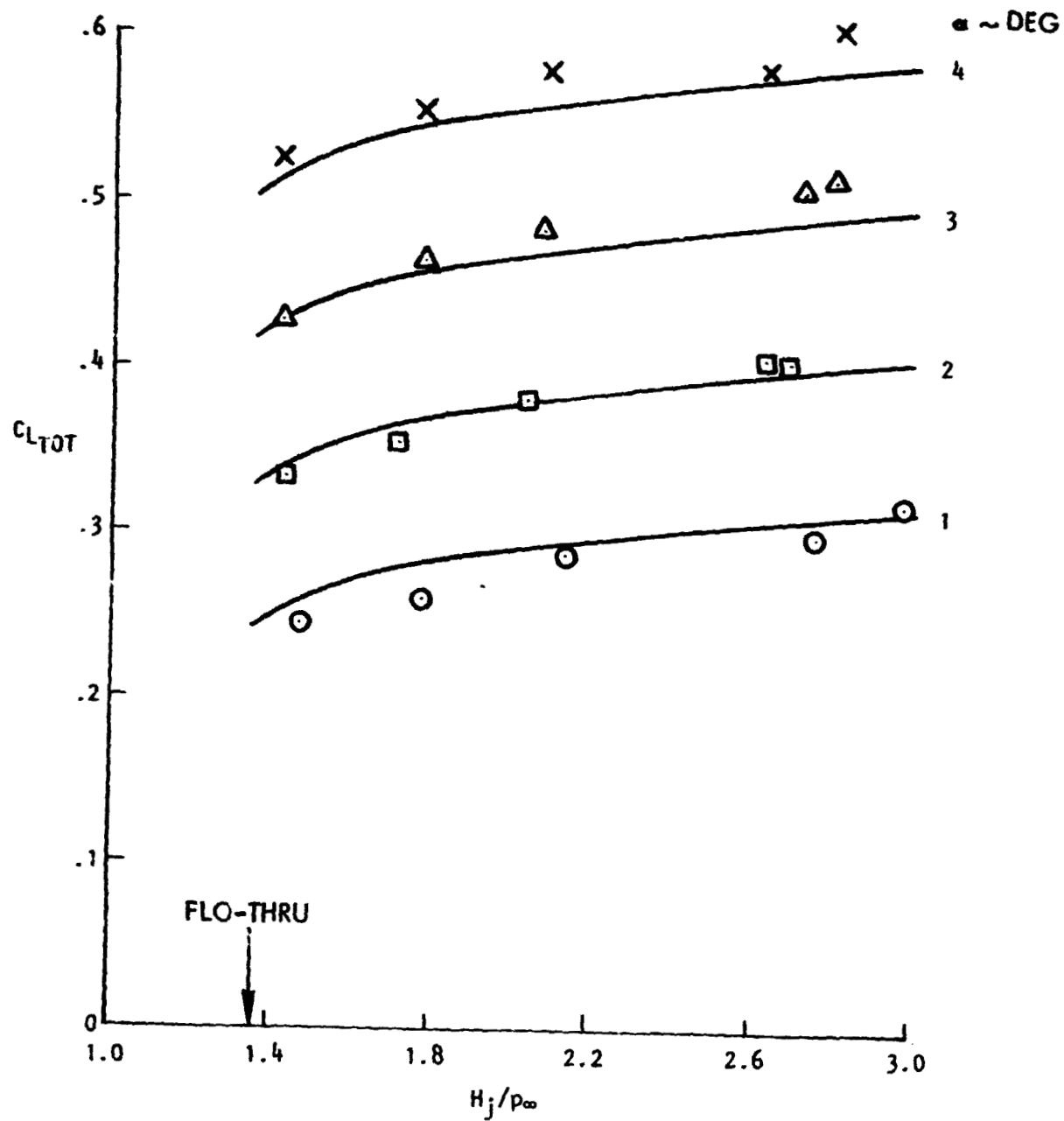


Figure 184. Comparison of USB test results with three-dimensional lifting-line theory, noz  $N_4E$ ,  $AR = 4$ ,  $M_\infty = 0.68$ .

# USB CRUISE PROGRAM

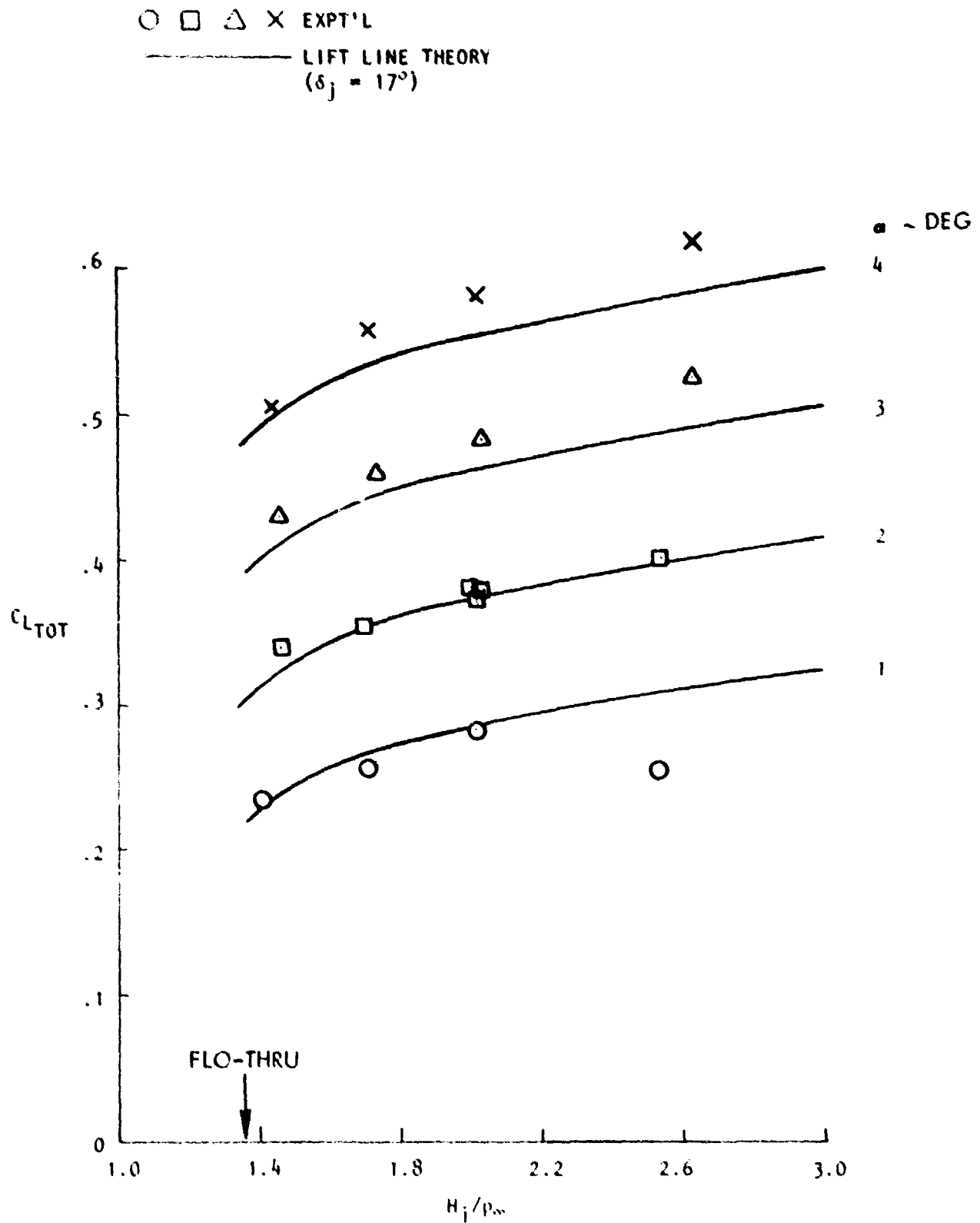


Figure 185. Comparison of USB test results with three-dimensional lifting-line theory, no  $N_5$ ,  $AR = 6$ ,  $M_\infty = 0.68$ .

equals the wing trailing-edge angle of 17 degrees (again, contrary to the static test results).

From the foregoing correlation studies, it appears that the present USB test configurations operate essentially as a limited-span jet flap, at least from the standpoints of lift and pitching-moment. Effects of compressibility on lift performance is adequately portrayed by jet flap theory up to the moderate drag-rise Mach numbers of the subject designs. Design for higher Mach numbers, or operation well into the drag-rise, may produce effects detrimental to the good correlation achieved in the present study. Additional experimental/analytical work in this area is needed.

## 5.0 CONCLUSIONS - TASK II

As a result of a detailed experimental/analytical program for the study of the upper-surface-blowing concept, a number of significant conclusions may be identified. Such conclusions, however, must reflect the "data-base" nature of the experimental work ... which relatively unrefined models and a broadly-spaced test matrix were necessary features. Within these constraints, it is believed that the aerodynamic and geometric trends developed have general applicability; this has been the major objective of Task II. With particular regard for the levels of cruise drag portrayed, ultimate levels of USB-cruise performance, obtained through more highly refined design processes, are not necessarily represented by the present data.

### 5.1 EXPERIMENTAL PROGRAM

1. In the unrefined state, the total drag penalty of typical USB-nacelle configurations, under transonic-cruise, powered conditions, can be exceptionally high by current standards.
2. The major drag producing phenomena in the general case, appears to be
  - o a jet-scrubbing effect on the aft-wing surface
  - o the conventional aerodynamic friction drag of the nacelle/nozzle and associated external hardware
  - o a pressure-drag component representing deflection of the jet over the aft-wing surface
  - o a drag-due-to-lift component inclusive of all lift-related transonic phenomena under powered model conditions



- o a potential drag penalty reflecting excessive nozzle boattail angles which promote local flow separation.

3. The major drag components are generally identifiable by force and surface-pressure measurements of powered models tested under both static and wind-on conditions.
4. Scrubbing losses tend to increase with nozzle two-dimensionality (i.e. with measuring aspect ratio) and nozzle pressure ratio.
5. Pressure drag, tending to increase with nozzle width, aft-wing camber, angle-of-attack, and nozzle pressure-ratio can be moderated by the jet shock formations at high nozzle pressure ratios.
6. Highly three-dimensional jets, such as a circular shape, show significant amounts of pressure drag at cruise conditions.
7. For moderate nozzle aspect ratios, jet deflection by the aft wing appears to be within several degrees less than that of the wing upper-surface at the trailing-edge.
8. Total lift performance at constant angle-of-attack is improved by increasing nozzle exit aspect ratio — typical values at a nozzle pressure ratio of 3.0 are  $\Delta C_L \approx .03$  for a circular nozzle and about  $\Delta C_L \approx 0.10$  for an aspect ratio 6.0 nozzle.
9. A semi-circular ("D-Duct") nozzle (AR = 2.5) represents a reasonable compromise between good cruise and potentially-favorable high-lift performance.

10. Nozzle boattail angles in excess of about 25 degrees may cause significant drag penalties due to local flow separation.

11. On a multi-jet configuration with nacelles spaced 1.6 D. apart, both lift and drag increments due to blowing were diminished by an apparent mutual interference between jets.

12. At a flow-through pressure ratio, and at sub-critical Mach numbers, a faired-over forebody nacelle showed essentially the same drag penalty as that of a flow-through type of forebody.

13. Cruise drag penalties associated with a pylon-mounted (OTW) nacelle positioned one-half nozzle diameter above the wing surface, compared favorable with a surface-integrated USB-type arrangement under similar test conditions.

14. A small streamlined USB-nacelle, integrated with a straight wing-body combination, showed favorable drag due-to-lift performance when compared to that of a symmetrical design; the effect of streamlining on the total cruise drag penalty showed only a modest benefit due, it is believed, to the straight-wing installation.

## 5.2 THEORETICAL PROGRAM

The USB wing/nacelle/propulsive interactions are complex not only in their viscous aspects, but also with regard to the viscous flows involved.

Theoretical studies have, therefore, been aimed at understanding the

potential flows with minimal representation of viscous effects. The overall philosophy has been to implement the simplest realistic method for simulating the nacelle environment and to embed in this a simplified model of the spreading jet plume.

#### 5.2.1 Vortex Lattice Studies

A major effort has been directed towards a vortex lattice representation of the wing/nacelle combination, with sufficient detail to permit comparisons with surface pressure measurements. A power effects package was developed, for use with the vortex lattice, which comprises vorticity panels which model the jet surface and simulate both its trajectory and its changing cross section. Compressibility effects for the complete model were simulated via geometric transformation according to Gothert's rule.

The vortex lattice study, which was restricted to the N<sub>3E</sub> 'D-duct' nacelle at  $M = 0.60$ , leads to the following conclusions:

1. Where experimental surface pressure measurements were available (i.e., in the scrubbed region, in the aft part of the boattail and on sections just inboard and just outboard of the nacelle), there was generally good correlation between vortex lattice predictions and measured surface pressure coefficients. The correlation was particularly good in the impingement and turning regions. Some differences were noted for supercritical pressure ratios (the theory was for  $M_{JET} < 1$ ) and in small regions inboard and outboard of the nacelle location where the theoretical jet spreading angle was too large towards the trailing edge.

2. Lift increments in the scrubbed region are small. Upload due to jet turning is almost entirely offset by download in the impingement region. However, there is an adverse effect on drag because of wing surface curvature. This causes the aft facing, suction area in the turning region to be several times greater than the aft facing area in the impingement region and significant net pressure drag results.

3. Drag increments occur as relatively small differences between opposing thrust and drag forces both along the nacelle and across the wing span. Large drag forces within the nacelle span are offset to a significant degree by thrust to each side. This redistribution effect is largely associated with upwash and downwash induced by a vortex pair which springs from the lifting region on the nacelle boattail.

4. Correlation between the theoretical drag predictions and experiment shows differences which are largely independent of  $\alpha$ , but which vary with pressure ratio. At flow-through, this difference agrees well with independent estimates of nacelle skin friction. Thereafter, the difference increases with  $H_j/p_\infty$  at a rate consistent with estimated jet scrubbing drag effects. At supercritical pressure ratios this trend reverses, possibly due to reduced aft-suction and reduced scrubbing when shocks in the jet reduce its ability to turn.

#### 5.2.2 Applications of Jet Flap Theory

The two-dimensional jet flap theory of Spence was empirically modified by McCormick for application to finite-span models in incompressible flows. In

the interest of providing quick, overall estimates of USB performance over a range of nacelle nozzle configurations at cruise, the Spence/McCormick method has been further modified, as described herein, to include compressibility corrections. For present purposes the resulting procedure has been designated "Simplified Jet-Flap Theory".

In a further approach, which also relies upon jet flap theory, Holmes et al use a three-dimensional, lifting line program in which the computation of finite span effects is less empirical. This existing program was also applied to selected USB configurations.

The conclusions of the above studies are as follows:

1. Both the simplified jet flap theory and the lifting line theory give good predictions of lift increments for nozzle configurations ranging from circular to aspect-ratio four. To achieve this correlation it was necessary to employ jet deflection angles, which approached the upper surface trailing edge angle, in conjunction with measured values of wing sectional lift curve slope.
2. The simplified jet flap theory also predicted pitching moment increments well for the cases tried, namely the D-duct and aspect-ratio four nozzles.
3. Neither method predicted drag increments which correlated consistently with experiment.

## 6.0 COMPATABILITY STUDIES — TASK III

Under the basic Program Plan (Reference 16), the sequence of detailed investigations of the USB-concept called for, first, an extensive experimental investigation employing geometric variations in the nacelle design. Secondly, a candidate nacelle would be selected from the experimental results around which more detailed, systems-oriented studies would be performed. Thirdly, a wind-tunnel test would investigate the low-speed, high-lift performance of the candidate nacelle as integrated with the aircraft high-lift system. The effort associated with steps 2 and 3 above are denoted as the Task III — Compatability Study. In this phase of the contractual effort, the aerodynamic studies are closely combined with the companion acoustics program (NAS1-13870, Noise Characteristics of Upper Surface Blown Configurations) for evaluating USB as applied to a commercial transport design. The Appendix of this document details the aerodynamic nacelle selection process, the aerodynamic/acoustics design compromises and the transport configuration evolving from these combined studies. Conclusions are drawn as appropriate. The second half of the aerodynamic Task III effort, an experimental study of the high-lift characteristics of the selected system, is contained in Volume II(D).

## 7.0 REFERENCES

1. Hackett, J. E.; Wilsden, D. J.: Determination of Low Speed Wake Blockage Corrections via Tunnel Wall Static Pressure Measurements. AGARD CP174, October 1975.
2. Roderick, W. E. B.: Use of the Coanda Effect for the Deflection of Jet Sheets Over Smoothly Curved Surfaces. Institute of Aerophysics, University of Toronto, September 1961.
3. Kettle, D. J.; Kurn, A. G.; and Bagley, J. A.: Exploratory Tests of a Forward-Mounted Over Wing Engine Installation. CP No. 1207, R.A.E., Farnborough, 1972.
4. Korbacher, G. K. and Sridhar, K.: A Review of the Jet Flap. University of Toronto, Review No. 14, May 1960.
5. Lan, C. E.: A Wing-Jet Interaction Theory for USB Configurations. *Journal of Aircraft*, September 1976, p. 718.
6. Reubush, D. E.: An Investigation of Induced Drag Reductions Through Over-the-Wing Blowing. Paper No. 77-884, AIAA/SAE 13<sup>th</sup> Propulsion Conf., Orlando, Fla., July 1977.
7. Braden, J. A.; Hancock, J. P.; and Hackett, J. E.: Transonic Experimental and Analytical Studies of USB Nozzle/Wing Installations. LG74ER0132, October 1974.
8. Perry, Boyd and Mendenhall, Michael R.: Measured and Calculated Steady Aerodynamic Loads on a Large-Scale USB Model. In "Powered Lift Aerodynamics and Acoustics", p. 415, NASA SP 406, May 1976.
9. Dillenius, M. F. E.; Mendenhall, M. R.; and Spangler, S. B.: Calculation of the Longitudinal Aerodynamic Characteristics of STOL Aircraft with Externally-Blown, Jet-Augmented Flaps. NASA CR2358, Feb. 1974.
10. Hackett, J. E. and Miller, H. R.: A theoretical Investigation of a Circular Lifting Jet in a Cross-Flowing Mainstream. AFFDL TR70-170, January 1971.
11. Spence, D. A.: The Lift Coefficient of a Thin Jet-Flapped Wing. Proc. Roy. Soc. Series A, Vol. 121, 1956.
12. McCormick, B. W.: *Aerodynamics of V/STOL Flight*. Chapter 7, Academic Press, New York, 1967.
13. Elzweig, S.: Subsonic Similarity Rule for Jet Flapped Airfoil. *Journal of Aircraft*, Vol. 8, No. 9, September 1971.

14. Woodland, H.: Subsonic and Transonic Similarity Rules for Jet Flapped Wings. AFFDL-TR-86, October 1976.
15. Holmes, A. E., Barnett, L.; and Jacobs, W.: Application of the Equivalent Mechanical Flap Concept to Jet-Flapped Wing-Body Combinations. Aerospace Research Laboratory Report No. ARL 74-0126, December 1973.
16. Exploratory Studies of the Cruise Performance of Upper-Surface Blown Configurations — Program Plan. Lockheed-Georgia Contractual Report, NASA Contract NAS1-13871, dated May 1, 1975.



## APPENDIX

### COMPATIBILITY STUDY

A. P. Pennock and J. P. Hancock

To investigate the compatibility of USB/OTW nacelle installations with advanced transport aircraft, a detailed design feasibility study was performed based on aircraft developed in the NASA short-haul studies of References A-1 through A-4. Accomplishment of the study required the following three steps:

- ° Selection of a suitable mission and definition of the associated baseline aircraft.
- ° Determination of the effects of perturbations from the baseline and selection of a final configuration.
- ° Establishment of the design feasibility of the final configuration.

Throughout the study the basic goals of (1) cruise drag competitive with that of conventional installations, (2) satisfactory short-field characteristics, and (3) a 90 EPNdB noise footprint area of  $2.59 \text{ km}^2$  ( $1 \text{ s.m.}^2$ ) were kept in mind.

#### 1.0 AIRCRAFT PERFORMANCE REQUIREMENTS

The principal operating requirements considered in this phase of the investigation were the stage length, field length, and cruise Mach number. The nacelle drag levels were high enough to indicate that the analysis should concentrate on short-range and medium-range missions. These were

selected to be 805 km (500 n.m.) and 2414 km (1500 n.m.) respectively. The design field lengths chosen were 610 m (2000 ft) for the short-haul aircraft and 1219 m (4000 ft) for the medium-haul aircraft. The design payload was set at 148 passengers, a break point above which more cabin attendants are required under FAA regulations.

## 2.0 CANDIDATE ENGINES AND AIRCRAFT

The engines used in the analysis were the Allison PD-287-11, with a design fan pressure ratio of 1.35, and the General Electric CFM56, with a design fan pressure ratio of 1.47. The PD-287-11 is a study engine developed in the program that led to the Quiet Clean STOL Experimental Engine (QCSEE). The CFM56 is a current engine now undergoing test. A lower fan pressure ratio results in a quieter, but sometimes heavier and more expensive, aircraft and vice versa. The tradeoff between noise and cost was determined at both stage lengths by designing aircraft around each of the two engines.

Drag considerations and preliminary sensitivity studies led to the choice of nacelle configurations. The two types considered were (1) USB integrated nacelles and (2) OTW pylon-mounted configurations.

For the USB integrated nacelles, a range of different nozzle types was examined. The sensitivity of a selected short-haul aircraft to the drag and weight characteristics of the different nozzle types was examined across a range of nozzle pressure ratios. Of the configurations examined, the D-duct nozzles resulted in the lowest ramp weight penalties, as shown in Figure A-1. It was also true that these minimum penalties were experienced at the lowest pressure ratios tested. Thus, among the integrated nacelles, the choice of the D-duct was clear cut.

Although the drag of the pylon-mounted configurations was not measured directly under power, it was measured for the flow-through case. A comparison of the integrated D-duct versus short and long pylon-mounted nacelle configurations is shown in Figure A-2 for the flow-through pressure ratio. Here the short pylon shows significantly lower drag, while the long pylon nacelle drag is slightly higher than for the integrated. The drag penalty due to power is expected to be lower for the pylon-mounted nacelles because there is no scrubbing. Based on these results, the short pylon-mounted nacelle was chosen for installation in the second study aircraft.

Since the best integrated nacelle had a higher drag level than the short pylon configuration, it was decided to employ the D-duct for the 805 km (500 n.m.) mission. It then followed that the short pylon nacelle would be used on the 2414 km (1500 n.m.) mission.

Aircraft weight and cost usually increase with cruise Mach number, but it was not clear how strong the effect of Mach number would be on these aircraft. The basic combinations - short range/1.35 fan pressure ratio/integrated nacelle and medium range/1.47 fan pressure ratio/pylon-mounted nacelle - were therefore run at 0.70, 0.75, and 0.80 cruise Mach numbers.

The matrix of eight aircraft that evolved from the factors just discussed and was used in the analyses is shown below:

Aircraft No.	1	2	3	4	5	6	7	8
No. of Passengers	148	—————→			—————→			
Stage Length, km (n.m.)	805(500)	—————→			2414(1500)	—————→		
Field Length, m (ft)	610(2000)	—————→			1214(4000)	—————→		
Fan Pressure Ratio	1.35	—————→		1.47	1.47	—————→		1.35
Nacelle Type	Integrated			—————→	Pylon-mounted —————→			
Cruise Mach No.	0.70	0.75	0.80	0.75	0.70	0.75	0.80	0.70

### 3.0 ANALYSIS

The analysis used computer programs, data bases, and experience developed during Lockheed's three-year study of short-haul transportation systems for NASA, reported in References A-1 through A-4. The sequence of operations was as follows:

1. An airport performance program was used to determine the wing loading and thrust loading needed to meet the takeoff and landing field length requirements. USB high-lift system characteristics developed in the short-haul work were used. These characteristics, drawn largely from tests conducted in the Questol program, which led to the Quiet STOL Research Aircraft (QSRA) competition, are based on the use of a large flap of moderate deflection with a final segment, blown at the knee, that can be further deflected as needed. The airport performance program also provided takeoff and landing flight paths and landing thrust settings and flap settings for use in calculating noise.
2. Aerodynamic parameters such as wing aspect ratio, sweep angle, taper ratio, thickness ratio, etc., were selected on the basis of optimization studies conducted under the short-haul transportation system contracts. Two-engine aircraft were chosen for the medium-range mission to reduce the takeoff noise footprint area. A two-engine aircraft requires more total thrust than a four-engine, but the steeper climbout angle more than compensates for the added thrust when footprint area is the criterion. A two-engine design may also be marginal at the short landing field length associated with the short-range mission. Highly deflected landing flaps are needed to get the aircraft into the short field, and their drag is such that the installed thrust required to

handle an engine-out go-around can become excessive. Four-engine aircraft were therefore used for the short-haul mission.

3. The aircraft thus defined were run through their missions in the general aircraft sizing program (GASP), with the performance curves of the selected engine, to determine the component sizes and weights needed to meet the requirements. GASP converges to the required combination of engine size, wing area, and mission fuel, calculating the drag, weight, and size of each major component and system of the aircraft as it does. It also calculates procurement and operating costs. The cost equations were not updated for the present analysis, but are indicative of relative magnitudes.

Nacelle drag coefficients were input to GASP as a function of aircraft lift coefficient and were based on the design nozzle pressure ratios of the study engines. Drag values used were actual test data from the USB cruise performance program reported in Reference A-5. They were modified for scale effect and corrected for the difference in wing aspect ratio between the test model and the full-scale study aircraft.

4. The noise levels and footprint areas of the resulting aircraft were calculated using the noise prediction program described in Section 6 of this volume.

#### 4.0 RESULTS

The salient characteristics of the eight aircraft analyzed in the baseline selection phase are listed in Table A-1. Cost, weight, and noise comparisons are presented in Figures A-3 through A-5. It can be seen in Figure A-3

that neither procurement cost nor direct operating cost (DOC) are strongly affected by the mission variables; a factor of 1.2 covers the spread between the highest and lowest values of both costs.

Ramp weight shows more overall variation, primarily because the medium-haul mission requires considerably more fuel, and thus a larger aircraft, than the short-haul mission. One interesting feature of the weight comparison is that aircraft 2, designed for Mach 0.75, is slightly lighter than aircraft 1, which is designed for Mach 0.70. There are two reasons for this. First, the field length requirement is so stringent that the engine size is set by takeoff requirements; as it turns out, the resulting engine size is better matched to Mach 0.75 than to Mach 0.70 cruise. Second, nacelle drag is very sensitive to lift coefficient at the lower wing loadings. Since the cruise lift coefficient for the Mach 0.75 airplane is slightly lower than for Mach 0.70, the drag coefficient is also lower. It is possible that further optimization of the wing would eliminate the weight minimum at 0.75 cruise Mach number.

Noise shows the largest variation among the parameters shown. Takeoff noise levels are dictated primarily by the choice of engine, as can be seen from the following table.

Fan Pressure Ratio	1.35	1.47
Aircraft Nos.	1-3,8	4-7
Range of Values -		
Takeoff Footprint, Km <sup>2</sup>	3-4	10-17
Takeoff Flyover, EPNdB	83-86	89-96
Takeoff Sideline, EPNdB	99-101	106-107

Landing noise is more a function of field length, The shorter field requires highly deflected flaps and substantial thrust settings (38-46%)

during approach, while the flap deflections are much lower and the thrust settings are only 12-24% with the longer field. Thus the 1.47 fan pressure ratio aircraft at the shorter field length (aircraft 4) has the highest approach flyover measurement point noise (99 EPNdB) and the only appreciable landing footprint. Otherwise the landing footprints are negligible and the approach flyover noise levels are all in the range of 91-95 EPNdB.

The effect of design cruise Mach number is fairly small at either stage length. Weight, cost and noise generally increase with Mach number along an accelerating curve, with little difference between 0.70 and 0.75 M and somewhat more increase at 0.80 M.

## 5.0 BASELINE AIRCRAFT SELECTION

The 1.47 fan pressure ratio aircraft (4-7) were ruled out as baselines because of their noise. It appears from Figure A-5 that a fan pressure ratio of about 1.35 is required to meet the 90 EPNdB total footprint area goal of  $2.59 \text{ km}^2$  (1 s.m.<sup>2</sup>).

The study showed that satisfactory aircraft could be designed with true USB nacelles (aircraft 1-3). It was therefore decided to eliminate aircraft 8 with its pylon-mounted nacelle. This left a choice to be made between the three cruise Mach numbers represented by aircraft 1-3. The differences between aircraft 2, at 0.75 M, and aircraft 1, at 0.70 M, are minor. Aircraft 3, at 0.80 M, is somewhat poorer than the other two on all counts, and the time saved by its extra speed is small at the 805 km (500 n.m.) range - four minutes, compared to the 0.75 M aircraft, if the full 805 km is covered at design cruise speed. Aircraft 2 was therefore selected as the baseline design.

## 6.0 PERTURBATION STUDIES

With a baseline design selected, the effects of perturbations of aircraft variables which affect performance and noise were investigated. The cruise performance parameters varied were nozzle boattail angle, aspect ratio, relative size, and discharge position. Parameters affecting noise that were varied were nozzle aspect ratio and impingement angle on the wing, flap extension, deflection, and radius of curvature, fan duct noise treatment, and total noise source strength. Each parameter was varied individually while holding the others constant. In addition, for the noise studies, the effects of a long-chord flap combined with changes in nozzle aspect ratio and fan duct noise treatment were determined. Only takeoff footprint area and takeoff measurement point flyover noise were considered in this study.

### 6.1 CRUISE PERFORMANCE

Using force test results, the effects of the various nozzle geometric parameters were examined across a wide range of thrust coefficients. Performance data for the straight and swept wings were evaluated at the appropriate drag divergence Mach numbers of 0.68 and 0.73 respectively. The criterion for evaluation was total nacelle interference drag,  $\Delta C_{D_{NIT}}$ , which is the sum of the nacelle aerodynamic drag, scrubbing drag, and vectoring, less nacelle skin friction drag.

Results from the evaluation of boattail angle effects are presented in Figure A-6(A) for thrust coefficients ( $C_T$ 's) ranging from 0.04 to 0.12. The approximate corresponding range of pressure ratio is 1.6 to 2.9. Two distinctly different trends are apparent. In the subcritical range of pressure



ratios considerably greater tolerance to boattail angle is evident. Here little or no drag penalty is experienced until the boattail angle reaches 25° or more. At supercritical pressure ratios, on the other hand, a neatly defined optimum occurs at around 15-18° and the drag increments rise sharply above those values. Since most transports cruise in the critical-to-supercritical range, good design practice will call for holding boattail angles to less than 20°.

Nacelle drag increments as a function of nozzle pressure ratio are shown in Figure A-6(B). Except for the lowest pressure ratio examined, a definite preference was indicated for the D-duct (AR = 2.5). At the pressure ratios of greatest interest, i.e. 1.9 to 2.6, a 22 to 30% drag reduction is shown relative to the circular nozzle. Next to the D-duct, the nozzle with AR = 6 appeared to have the lowest drag increment, although it is not clear why this is so. The advantage shown over an aspect ratio of 4 is relatively small.

To determine the effect of size, two nozzles which were identical except for size were selected from the cruise performance program matrix. These were nozzle N<sub>4</sub>, with  $c^2/A_N = 24$ , and nozzle N<sub>12</sub>, with  $c^2/A_N = 48$ , where  $c$  is the wing chord and  $A_N$  is the nozzle area. (These nozzles and others referred to below are defined in Reference A-5.) Evaluation of the drags of these nozzles at various pressure ratios resulted in the curves shown in Figure A-6(C). Surprisingly, the data show that as the nacelle gets smaller, the drag coefficient based on nacelle frontal area goes up. This is probably related to the effect of the nacelle on spanloading and thus on wing efficiency. Although the basic drag of the nacelle is a function of nacelle cross-sectional area, the span affected varies with nacelle

diameter. Thus the change in wing efficiency is really a function of the square root of the cross-sectional area.

The change in nacelle incremental drag with chordwise position is presented in Figure A-6(D). This was based on results obtained with circular nozzles (primarily nozzles  $N_{1E}$  and  $N_{2E}$ ) with discharges at different chordwise positions. Drag was shown to be consistently reduced by forward movement of the nacelles. This result is highly credible since it is the same trend as has been obtained before for conventional under-the-wing installations. The favorable trend is due to the improvement in nacelle-wing area distribution as the nacelle is moved forward.

As had been anticipated, the perturbation studies of the basic nozzle geometric variables did not result in any changes of these parameters from their baseline values. A boattail angle of  $16^\circ$ , previously selected for the baseline, is seen in Figure A-6(A) to be near optimum. The choice of a D-duct nozzle is unassailable from a performance standpoint, based on the nozzle aspect ratio effects of Figure A-6(B).

Figure A-6(C) indicates that larger nozzles result in lower drag penalties. This would mean that for the same installed thrust, two large engines would be better than four small ones. For an aircraft that must operate from a 2000-foot field, however, switching to a twin-engine design would result in a considerable increase in required installed thrust capability, more than negating the potential drag saving. The value of  $c^2/A_N$  employed on the baseline is approximately 14, which, as is seen in Figure A-6(C), results in a significantly lower drag coefficient than the reference (intermediate) nacelle test value of 24.

In the case of nozzle exit position, Figure A-6(D) shows that nacelle drag is reduced as the nacelle is moved forward right up to where  $x/c$  approaches zero. The tradeoff here is against weight and scrubbing drag, and the choice of  $x/c = 0.35$  was made based on extensive work performed for the QSRA effort, which indicated this was a near-optimum value.

## 6.2 NOISE

Noise effects were determined from the noise prediction program alone, without resizing the aircraft or recalculating its airport performance. For most variables this procedure is believed to yield results that are either approximately correct or conservative (higher than the true noise levels). Incorporating size and flight path effects would yield higher noise levels only in the case of the nozzle aspect ratio variation; the higher aspect ratios of the nozzle variants are associated with higher cruise drag and thus with less noise reduction when size and flight path effects are considered.

Size and flight path effects in the other cases are generally either favorable (especially with the long-chord flap) or small. Greater flap deflection could have either adverse or favorable indirect effects on noise, depending on what other changes were made in the high-lift system to hold the field length constant.

The results are shown in Figure B-7, in which takeoff footprint area at 90 EPNdB is plotted against takeoff flyover noise level at the 6.49 km (3.5 n.m.) measurement point. The baseline aircraft has a 90 EPNdB footprint area of  $3.03 \text{ km}^2$  ( $1.17 \text{ s.m.}^2$ ) and a flyover noise level of 83.4 EPNdB. The goal is a total footprint area of  $2.59 \text{ km}^2$  ( $1 \text{ s.m.}^2$ ); allowing  $0.11 \text{ km}^2$  for the landing footprint, the takeoff footprint goal becomes  $2.48 \text{ km}^2$ .

Changes in flap radius of curvature, flap deflection, nozzle impingement angle, and fan duct noise attenuation cause essentially no change in the baseline noise values. The points representing these variations are grouped near the baseline point. However, the other variables - nozzle aspect ratio increase, noise source strength reduction, and flap extension - are quite effective in reducing noise. Aircraft incorporating these modifications are indicated to be capable of beating the noise goal. These variables are discussed below.

Nozzle Aspect Ratio — Flat rectangular nozzles are shown to markedly reduce both footprint area and flyover noise. As is noted above, however, they have higher drags than the baseline semicircular D nozzle, and the effects of the drag increase on aircraft size and flight path are not included in the analysis. The favorable effects of increased nozzle aspect ratio on noise would be diminished if size and flight path effects were considered.

Since the noise goal is achievable with the D nozzle, nozzle aspect ratio variations were not pursued further. If the nozzle were to be changed, however, the aspect ratio 6 design would be preferred to the aspect ratio 4. Both configurations have more drag than the D nozzle, but aspect ratio 6 has slightly less drag than aspect ratio 4 and is considerably quieter.

High-Lift System Noise Reduction — The noise generated by a USB high-lift system can be reduced by modifying the flow conditions at the flap trailing edge. Although preliminary results by Hayden (Reference A-6) indicate reductions of up to 10 dB, attempts to repeat these results in the present program were unsuccessful; the OASPL reductions achieved were about 2 dB with passive treatment of the flap surface and about 5 dB with trailing edge blowing.

The effect of a 3 dB decrease is shown in Figure A-7. (For convenience in using the prediction program the decrease was applied to all sources but the effect is essentially the same as applying it to high-lift system noise alone, as high-lift system noise is the only significant contributor to the noise of the baseline aircraft.) The effect is to reduce the takeoff flyover measurement point noise by slightly more than 3 EPNdB and to cut the takeoff footprint area in half. The effects of flap treatment on aircraft size and performance and thus on noise should be considered in a more complete analysis but such effects are expected to be small. Surface treatments would affect only takeoff and landing, being covered when the flaps are retracted. Blowing would be off at cruise and is already included in the baseline flap system.

Flap Extension -- As is discussed in Sections 5 and 6 of this volume, extending the flap chord is the most effective way to reduce noise. The baseline flap, described earlier, deflects  $20^\circ$  over most of its chord, with a final blown segment that deflects further. There is no increase in chord when the flap is deployed. By changing to an unslotted Fowler flap, with the segments sliding back on tracks to extend the basic wing chord by 50%, high-lift system noise is reduced enough to lower the flyover noise from 83.4 EPNdB to 77.6 EPNdB and the takeoff footprint area from  $3.0 \text{ km}^2$  to  $1.2 \text{ km}^2$ . These reductions do not include the effects of the increased lifting area on the climbout angle, which would cause further decreases in both of the noise parameters.

In view of the large reductions achieved by extending the flap, this perturbation was combined with changes in fan duct noise treatment and in nozzle aspect ratio. The results, plotted as solid symbols at the left

in Figure A-7, are similar to those obtained with the baseline flap. Fan duct treatment has somewhat more effect because high-lift system noise is reduced, but fan noise is still unimportant. Increasing the nozzle aspect ratio is less beneficial than with the baseline flap because the noise levels are already low and further improvements yield diminishing returns.

### 6.3 FINAL DESIGN

The selected final design, shown in Figure A-8, is the same as the baseline, aircraft 2 of Table A-1, in most respects. It is a high-wing four-engine aircraft designed for a passenger capacity of 148, field length of 610 m (2000 ft), stage length of 927 km (500 n.m.), and cruise Mach number of 0.75. The ramp weight is 66,067 kg (145, 678 lb) and the wing area is  $170 \text{ m}^2$  ( $1828 \text{ ft}^2$ ), for a wing loading of  $387 \text{ kg/m}^2$  (79.2 psf). The engines are Allison PD-287-11's scaled to a takeoff rated thrust of 83,200 N (18,705 lb), giving an installed thrust-to-weight ratio of 0.48. Other features and characteristics are shown in Table A-1 and Figure A-8.

The initial cruise lift coefficient for the final design is 0.31, which reflects a relatively low wing loading. The associated drag coefficient is 0.0256, resulting in a cruise lift/drag ratio of 12.1. The total nacelle drag coefficient is 0.0096. The approach speed is 160 km/hr (86 kn) while climbout speed is 185 km/hr (100 kn).

In accordance with earlier discussion, the nacelle has a D nozzle located at 35% chord, with a boattail angle of  $16^\circ$ . Extended-chord flaps are used to get the noise benefit of the increased flow length from the nozzle to the flap trailing edge, and the flap internal blowing system is deleted. The aft fan duct noise treatment is deleted, leaving the fan duct untreated

forward and aft, although there is provision to incorporate treatment in both areas if it is found to be desirable.

## 7.0 NACELLE DESIGN

The propulsion and high-lift system installation for the outboard position is shown in Figure A-9. Installation design details are discussed in the following paragraphs.

### 7.1 INLET

The fan intake is a standard short-duct arrangement which extends roughly one-half nacelle diameter forward of the fan face. A generous lip thickness is employed to facilitate efficient inflow at high angles of attack. The cowl is circular with the exception of the lower lobe, which is slightly elliptical to provide space for the engine accessory package.

The inlet leading edge and the internal lip downstream to the throat are protected with an evaporative anti-icing system, which employs aluminum skins in conjunction with overheat detectors. Downstream of the throat, provision is made for acoustical treatment of the inlet duct to attenuate forward radiated flap noise.

The inlet-forebody assembly is supported by and attached to the front flange of the engine fan case. It is considered to be a component of the quick engine change unit (QECU), although its overhaul schedule is based on airframe time-between-overhauls (TBO) rather than engine TBO.

### 7.2 FAN CASE COWLING

The fan case cowling is divided into upper and lower segments. The lower

segment can be opened by unlatching the lower center seam and is hinged at or just below the engine horizontal centerline for quick access to the engine reduction gear case and accessories. The upper half is attached to the fan case flanges and is removable for engine access or removal.

### 7.3 FAN DUCT AND NACELLE STRUCTURE

The upper fan duct is integrated into the nacelle by two heavy main rings and carries the engine loads into the wing box skins with a pin attachment on the upper surface and by skate angles on the lower surface. A monocoque shell, which incorporates the front and rear engine mounts is thereby effected. This type of construction allows the engine to be changed in the conventional manner by lowering it onto a transportation trailer, either with AGE attached to the nacelle or with an elevator on the ground cart. The inner surface of the fan duct can be acoustically treated to minimize aft radiated fan noise.

### 7.4 THRUST REVERSER

The rear upper external contour of the nacelle is formed by the outer surface of the target thrust reverser door. The inner surface of this door is constructed of high-temperature material to maintain structural strength and rigidity during its short, but high-temperature, duty cycle. Extension or retraction of the door on its four-bar linkage is accomplished hydraulically with the movable hinge points describing the arcs illustrated in Figure A-9. The total jet, both primary and secondary, is deflected forward and upward, providing a reverse force plus a downward force on the aircraft, making its brakes more effective. As is also illustrated in the figure, there is an articulated eyebrow-shaped section on the aft lip of



thrust reverser which can be extended to exert a downward force on the discharging jet and thereby assure its attachment to the upper surface of the wing and flap. The deflector would be employed whenever high lift coefficients are required, as during takeoff and landing.

A pair of stangs extends aft of the nozzle from along the sides to provide fixed hinge points for the aft bars on the door linkage. The stangs are located several boundary layer heights above the wing surface and outside the jet efflux. Because of the venting thus provided, their interference with the local flow patterns is expected to be minimal.

## 7.5 NOZZLE

Separation of the fan and primary duct flow streams is maintained right up to the nozzle discharge in order to minimize flow suppression and other interaction effects. The primary nozzle is slightly S-shaped in the side view, but a circular cross-section is maintained throughout. It is constructed of steel honeycomb with the forward inner portion fabricated to include a perforated face sheet to attenuate turbine noise. The outer fan duct above the wing surface is conventional sheet metal/stiffener construction.

## 7.6 WING INSULATION

The upper surface of the wing box beam aft of the nozzle discharge is insulated with a fireproof coating. This protects the upper wing and flap structure from burning fuel which can result from a wet start and reduces the temperature variation in the wing structure to within acceptable limits.

## 7.7 FLAP SYSTEM

To obtain maximum acoustic attenuation for the upper surface jet flow, a long-chord high-extension flap system was selected. Directly behind the engine the flap surface is continuous, as is shown in Figure A-9. Away from the nacelles, however, slots are provided to assure attachment of the freestream. In case of engine failure, slots can be opened in the unslotted portion of the wing behind the dead engine.

The flap system shown indicates how chord extension can be obtained. The first flap segment slides back on a fixed track. The second segment is mounted to the first through another track which provides further extension. As shown, in a representative landing configuration, the extension, measured along the upper surface, is 36% of the wing chord.

At takeoff the extension with this track configuration would be about 25% of the wing chord. Interpolation on Figure A-7 indicates that a 25% chord extension is in itself sufficient to achieve the noise footprint area goal, even with the baseline takeoff performance. Baseline performance can be improved, however, in several ways. First, the 12% of fan airflow used by the baseline internal flap blowing system can be returned to the main nozzle for more efficient thrust production and the weight of the flap ducts can be saved. Second, the flap tracks can be designed so that the takeoff setting provides considerably more chord extension, with only the angular deflection required for takeoff, while the final extension to the landing setting serves primarily to increase deflection with little increase in chord. This arrangement is in use today. Chord extensions of 40% or more at take-off should be feasible.

## 8.0 NOISE CHARACTERISTICS

The noise characteristics of the final design were calculated based on the following -

- ° Aircraft size, weight, and performance as in baseline.
- ° 40% chord flap extension at both takeoff and landing.
- ° Flap deflections and landing thrust setting as in baseline.
- ° No internal flap blowing.
- ° No fan duct noise treatment.

The calculated values are -

Takeoff Footprint Area, 90 EPNdB -	1.76 km <sup>2</sup> (0.68 s.m. <sup>2</sup> )
Takeoff Flyover at 6.49 Km (3.5 n.m.) -	79.5 EPNdB
Takeoff, Maximum at 152.4 M (500 Ft) Sideline -	98.4 EPNdB
Landing Footprint Area, 90 EPNdB -	0.12 km <sup>2</sup> (0.05 s.m. <sup>2</sup> )
Landing Flyover at 1.86 Km (1 n.m.) -	86.8 EPNdB
Total Footprint Area, 90 EPNdB -	1.88 km <sup>2</sup> (0.73 s.m. <sup>2</sup> )

It can be seen that the calculated total footprint area of 1.88 km<sup>2</sup> (0.73 s.m.<sup>2</sup>) betters the 2.59 km<sup>2</sup> (1 s.m.<sup>2</sup>) goal by a considerable margin. The area would be further reduced if the overlap of the takeoff area and landing area were subtracted.

The flight path and footprint are shown in Figure A-10. The takeoff spectra of the various noise sources considered in the prediction program and of the complete aircraft are presented for the flyover location in Figure A-11. Even with no fan duct treatment, high-lift system noise is the strongest source, although fan noise exceeds it at the higher frequencies. The PNL directivity pattern at takeoff is shown in Figure A-12.

## REFERENCES

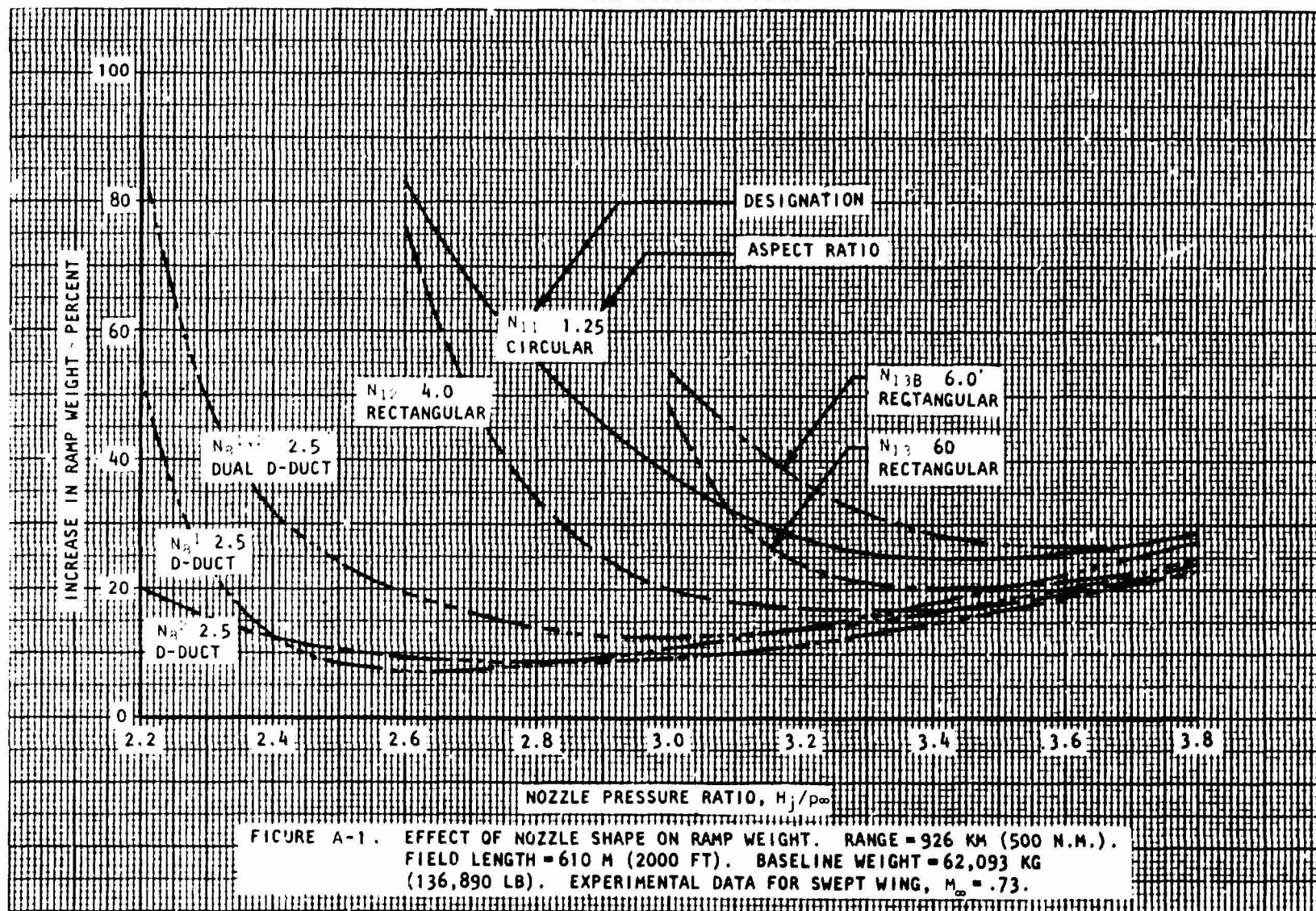
- A-1. NASA CR-114612 and 114613. Quiet Turbofan STOL Aircraft for Short-Haul Transportation. Lockheed Aircraft Corporation, June 14, 1973.
- A-2. Higgins, T. T.; Stout, E. G.; and Sweet, H. S.: Study of Quiet Turbofan STOL Aircraft for Short-Haul Transportation. NASA CR-2355, December 1973.
- A-3. NASA CR-137525 and 137526. Evaluation of Advanced Lift Concepts and Fuel-Conservative Short-Haul Aircraft. Lockheed Aircraft Corporation, June 1974.
- A-4. Sweet, H. S.; Renshaw, J. H.; and Bowden, M. K.: Evaluation of Advanced Lift Concepts and Potential Fuel Conservation for Short-Haul Aircraft. NASA CR-2502, September 1974.
- A-5. Final Report of USB Cruise Performance Program, NASA Contract NAS1-13871, in preparation.
- A-6. Hayden, R. E.; Beranek, Bolt; and Newman, Inc.: Reduction of Noise from Airfoils and Propulsive Lift Systems Using Variable Impedance Systems. AIAA Paper 76-500, July 1976.

# USB CRUISE PROGRAM

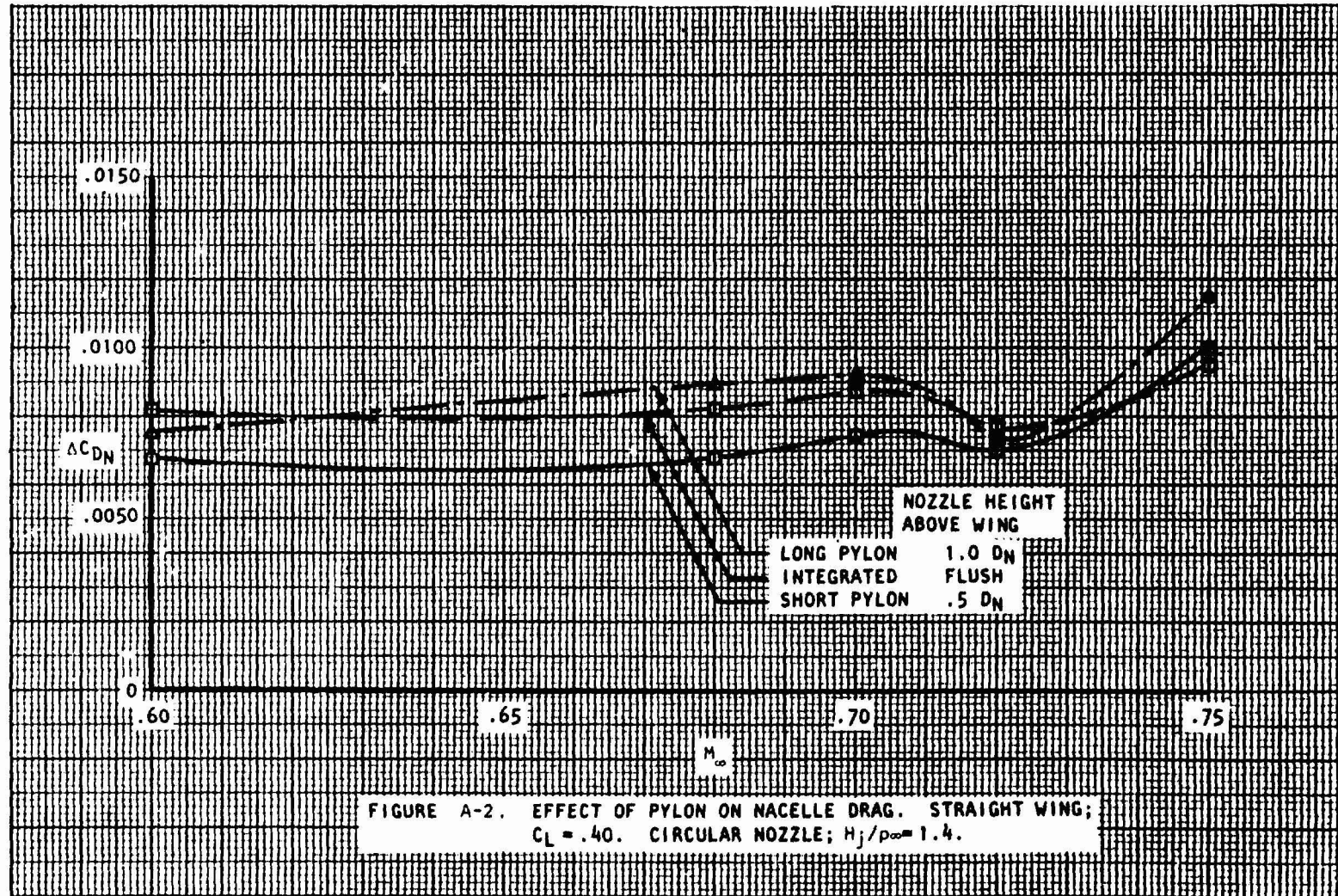
AIRCRAFT NO.	1	2	3	4	5	6	7	8
<b>MISSION</b>								
NO. OF PASSENGERS	148				2780 (1500)			
STAGE LENGTH, KM (N.M.)	127 (500)				1219 (6000)			
FIELD LENGTH, M (FT)	610 (2000)							
CRUISE MACH NO.	0.70	0.75	0.80	0.75	0.70	0.75	0.80	0.70
CRUISE ALTITUDE, M (FT)	9144 (30000)							
<b>PROPULSION SYSTEM</b>								
NOZZLE SHAPE	D (SEMICIRCULAR)				CIRCULAR			
NACELLE TYPE	BLENDED				PYLON-MOUNTED			
NO. OF ENGINES	4				2			
FAN PRESSURE RATIO	1.35			1.47	1.47			1.35
RATED THRUST, N (LB)	74993 (17984)	83201 (18705)	90753 (20403)	101307 (22711)	160978 (36191)	160946 (36184)	183395 (41231)	203447 (45739)
NACELLE DIAMETER, M (FT)	2.05 (6.72)	2.09 (6.85)	2.18 (7.15)	2.14 (7.02)	2.70 (8.85)	2.70 (8.85)	2.88 (9.45)	3.26 (10.71)
<b>AIRCRAFT</b>								
RAMP WEIGHT, KG (LB)	16266 (36116)	66067 (145678)	68765 (151626)	72563 (160001)	78893 (173959)	80728 (178806)	85544 (188625)	83511 (184141)
WING AREA, M <sup>2</sup> (FT <sup>2</sup> )	186.1 (2003)	169.8 (1828)	159.0 (1711)	199.9 (2152)	172.9 (1861)	182.3 (1995)	169.9 (1829)	204.1 (2197)
WING LOADING, KG/M <sup>2</sup> (LB/FT <sup>2</sup> )	354 (72.5)	387 (79.2)	430 (88.0)	359 (73.6)	453 (92.8)	443 (88.6)	499 (102.3)	407 (83.3)
THRUST-TO-WEIGHT RATIO	0.460	0.480	0.503	0.536	0.381	0.382	0.410	0.464
ASPECT RATIO	10.0				7.73			
SWEEP ANGLE, 0.25°, DEGREES	20							
TAPER RATIO	0.3							
THICKNESS RATIO, AVG.	0.141		0.123	0.141	0.141		0.123	0.141
<b>CRUISE DATA</b>								
F <sub>N</sub> /MAX CRUISE F <sub>N</sub>	1.000			0.600	0.890	0.975	1.000	1.000
CL	0.325	0.310	0.304	0.291	0.415	0.344	0.350	0.372
CD	0.0273	0.0256	0.0248	0.0204	0.0335	0.0284	0.0303	0.0317
LD	11.9	12.1	12.3	14.2	12.4	12.1	11.5	11.7
NACELLE C <sub>D</sub> , TOTAL	0.0104	0.0096	0.0096	0.0050	0.0116	0.0096	0.0120	0.0112
<b>TAKEOFF AND LANDING DATA</b>								
CLIMBOUT ANGLE	14.2	14.8	15.5	18.3	11.4	11.2	11.7	14.8
CLIMBOUT SPEED, KM/HR (KT)	184.7 (99.6)	184.7 (99.6)	185.4 (100.0)	187.6 (101.2)	250.8 (135.3)	250.5 (135.1)	252.0 (135.9)	228.0 (123.4)
APPROACH ANGLE, DEGREES	5.9	5.9	5.9	6.1	3.8	3.8	3.8	3.6
APPROACH SPEED, KM/HR (KT)	160.7 (86.7)	160.2 (86.4)	159.4 (86.0)	152.9 (83.0)	250.5 (135.1)	251.6 (135.7)	247.9 (133.7)	262.9 (141.8)
RATE OF SINK, M/S (FT/MIN)	4.57 (900)							
APPROACH F <sub>N</sub> /TAKEOFF F <sub>N</sub>	0.38	0.42	0.47	0.45	0.28	0.19	0.24	0.12
<b>COSTS (1972 \$)</b>								
ENGINES	\$3.59M	\$3.64M	\$3.75M	\$2.83M	\$2.08M	\$2.60M	\$2.18M	\$3.11M
COMPLETE AIRCRAFT	\$10.58M	\$10.92M	\$11.34M	\$10.36M	\$9.49M	\$9.68M	\$10.40M	\$11.15M
DOC, 2 x 1972 FUEL PRICE (234/GAL), \$/SEAT-S.M.	2.33	2.26	2.27	2.27	2.28	2.29	2.36	2.56
DOC, 4 x 1972 FUEL PRICE (466/GAL), \$/SEAT-S.M.	2.94	2.36	2.89	2.99	2.88	3.12	3.25	3.35
<b>NOISE</b>								
TAKEOFF FOOTPRINT, 90 EPNdB, KM <sup>2</sup> (S.M. <sup>2</sup> )	2.83 (1.09)	3.03 (1.17)	3.47 (1.30)	9.90 (3.82)	15.20 (5.87)	14.66 (5.66)	17.35 (6.70)	4.87 (1.87)
TAKEOFF FLYOVER AT 6.49 KM (3.5 N.M.), EPNdB	83.4	83.4	83.7	80.6	95.8	95.6	96.5	85.6
TAKEOFF, MAXIMUM AT 152.4 M (500 FT), SIDELINE, EPNdB	99.1	99.1	100.3	106.3	106.4	106.2	107.4	101.4
LANDING FOOTPRINT, 90 EPNdB, KM <sup>2</sup> (S.M. <sup>2</sup> )	0.11 (0.04)	0.18 (0.07)	0.36 (0.14)	1.14 (0.44)	0.11 (0.04)	0.11 (0.04)	0.16 (0.06)	0.11 (0.04)
LANDING FLYOVER AT 1.84 KM (1 N.M.), EPNdB	86.8	88.7	91.1	95.0	86.1	85.9	88.5	85.5
TOTAL FOOTPRINT, 90 EPNdB, KM <sup>2</sup> (S.M. <sup>2</sup> )	2.94 (1.13)	3.21 (1.24)	3.83 (1.48)	11.04 (4.26)	15.31 (5.91)	14.77 (5.70)	17.51 (6.76)	6.18 (2.37)

TABLE A-1 USB STUDY AIRCRAFT.

## USB CRUISE PROGRAM



# USB CRUISE PROGRAM



ORIGINAL PAGE IS  
 OF FIGURE A-23



# USB CRUISE PROGRAM

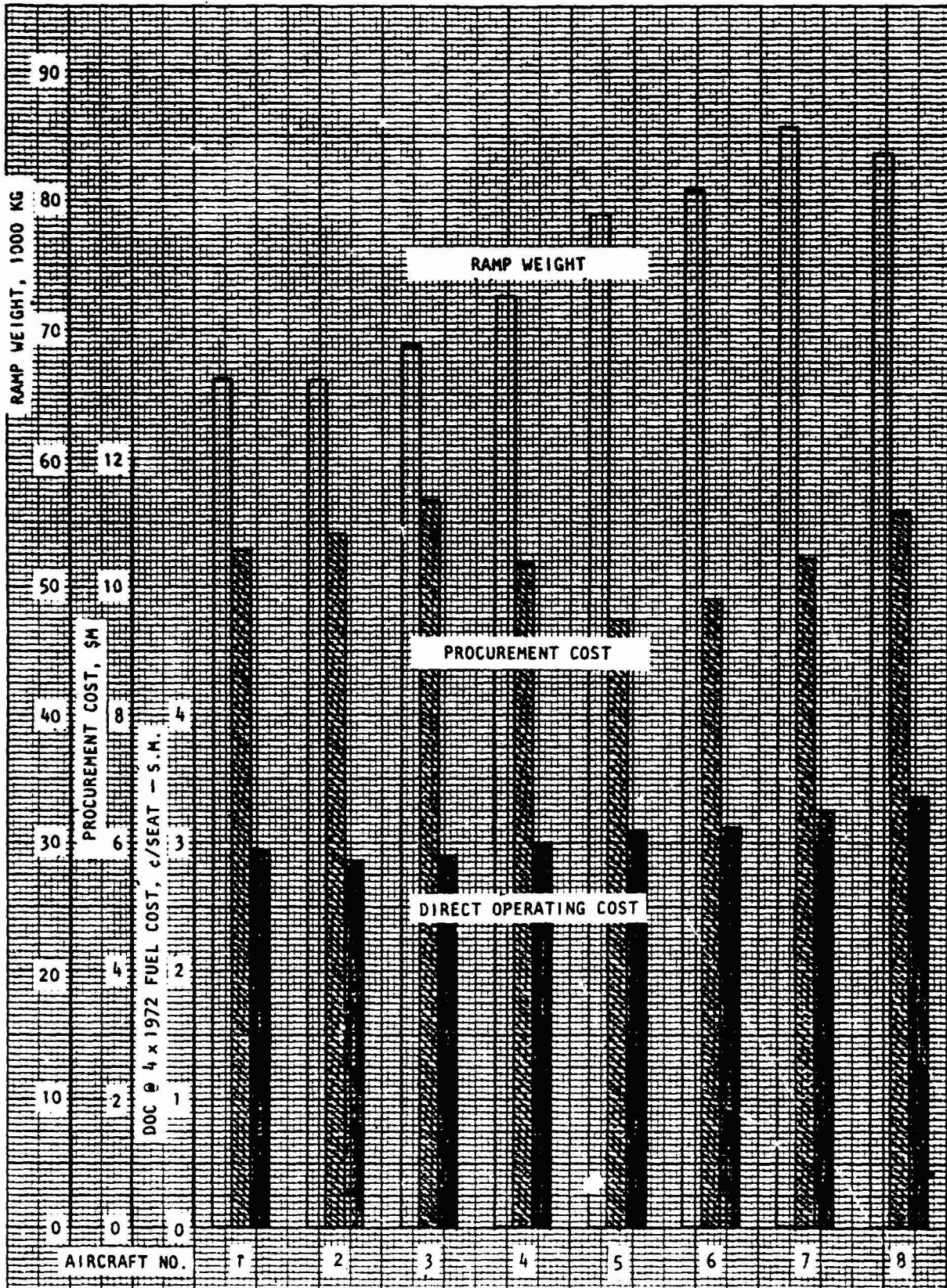
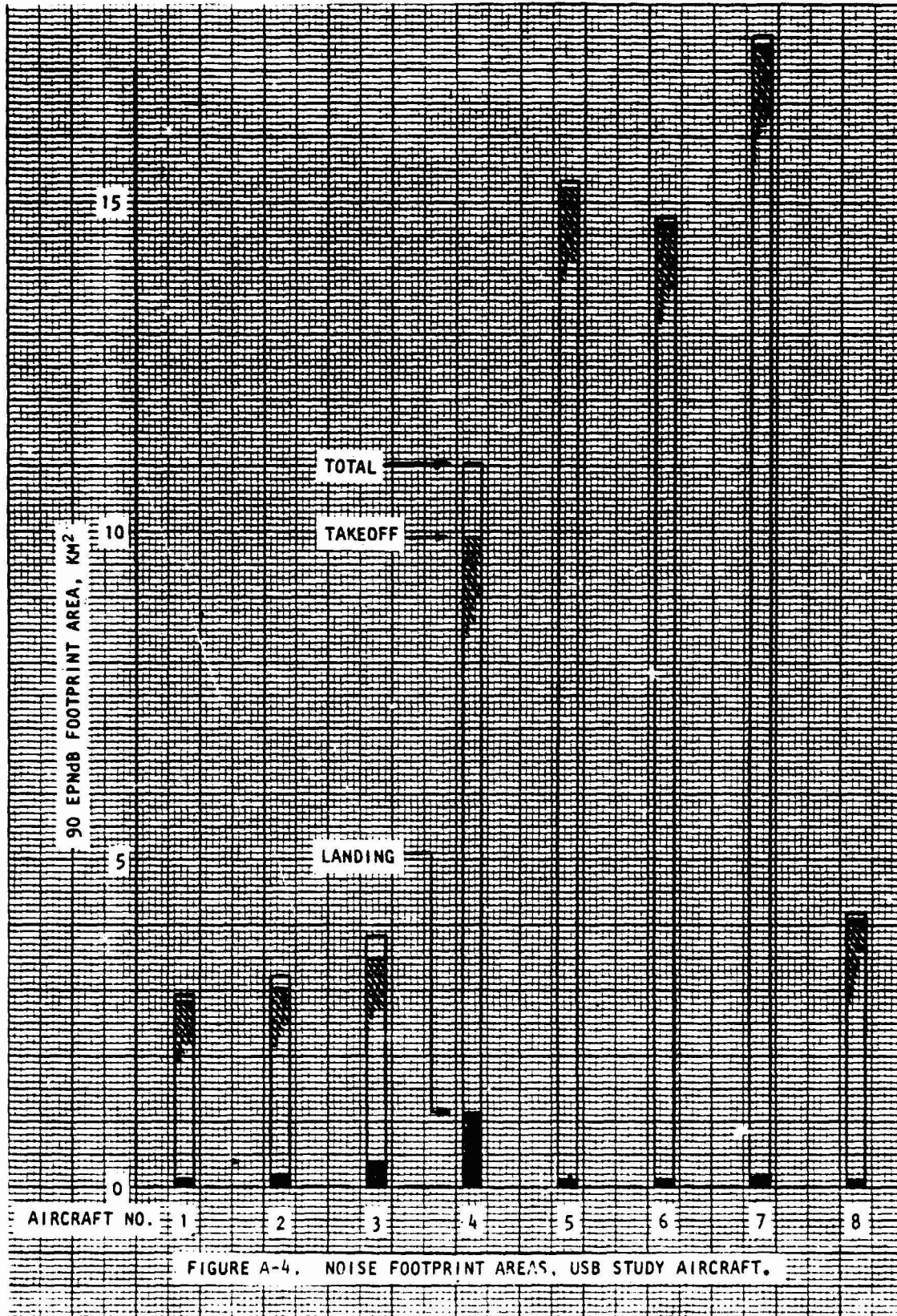


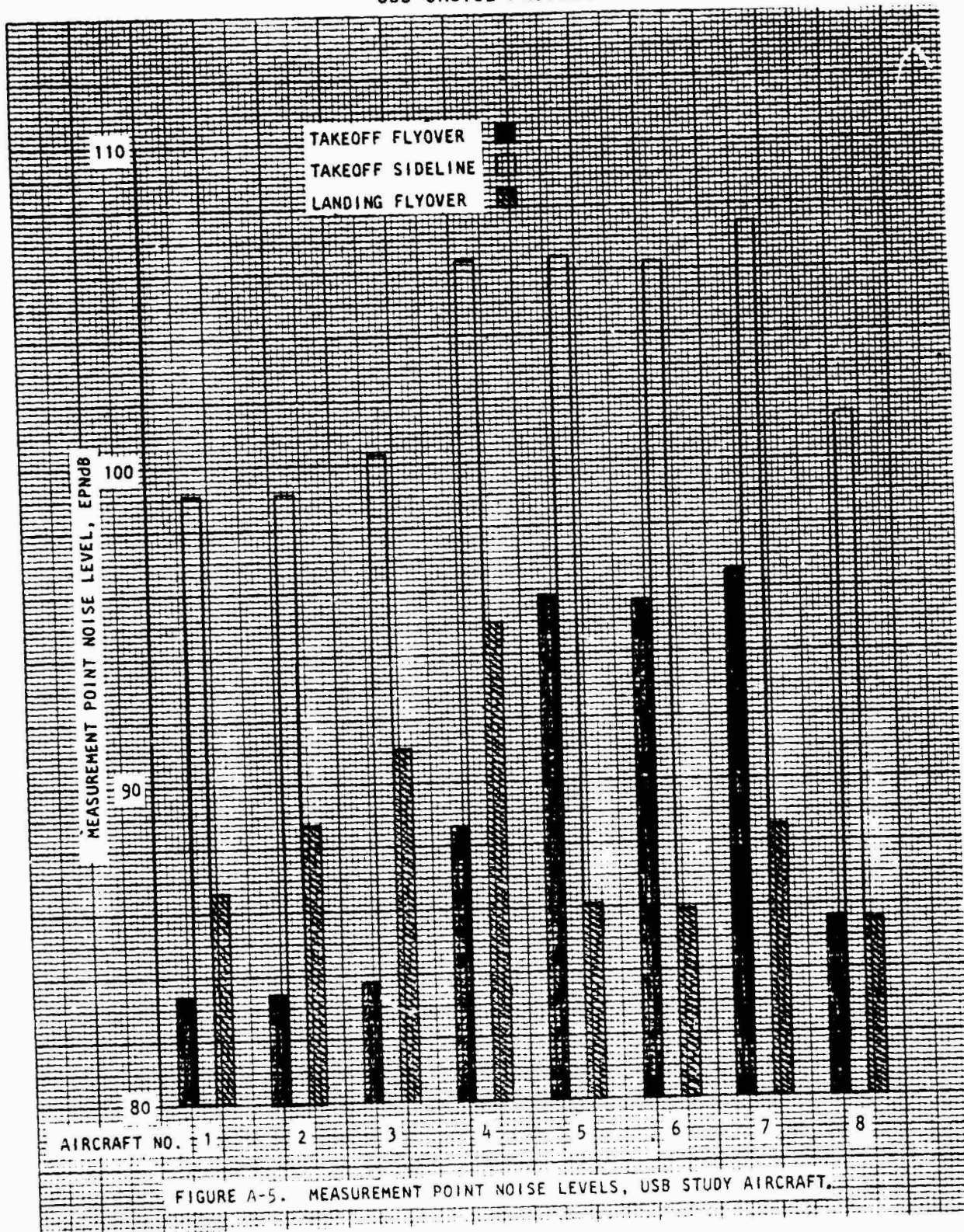
FIGURE A-3. WEIGHT AND COST - USB STUDY AIRCRAFT.



# USB CRUISE PROGRAM

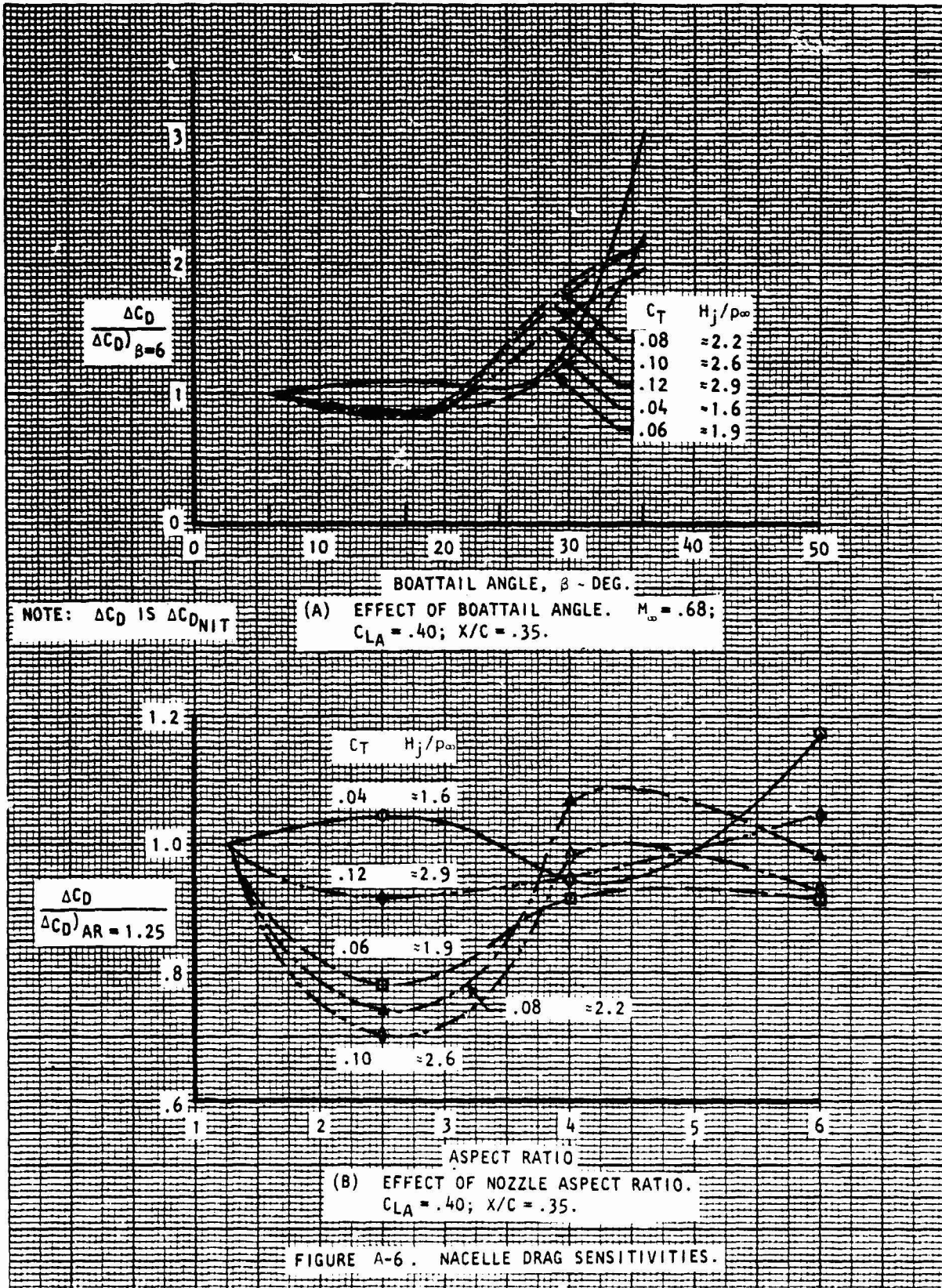


# USB CRUISE PROGRAM

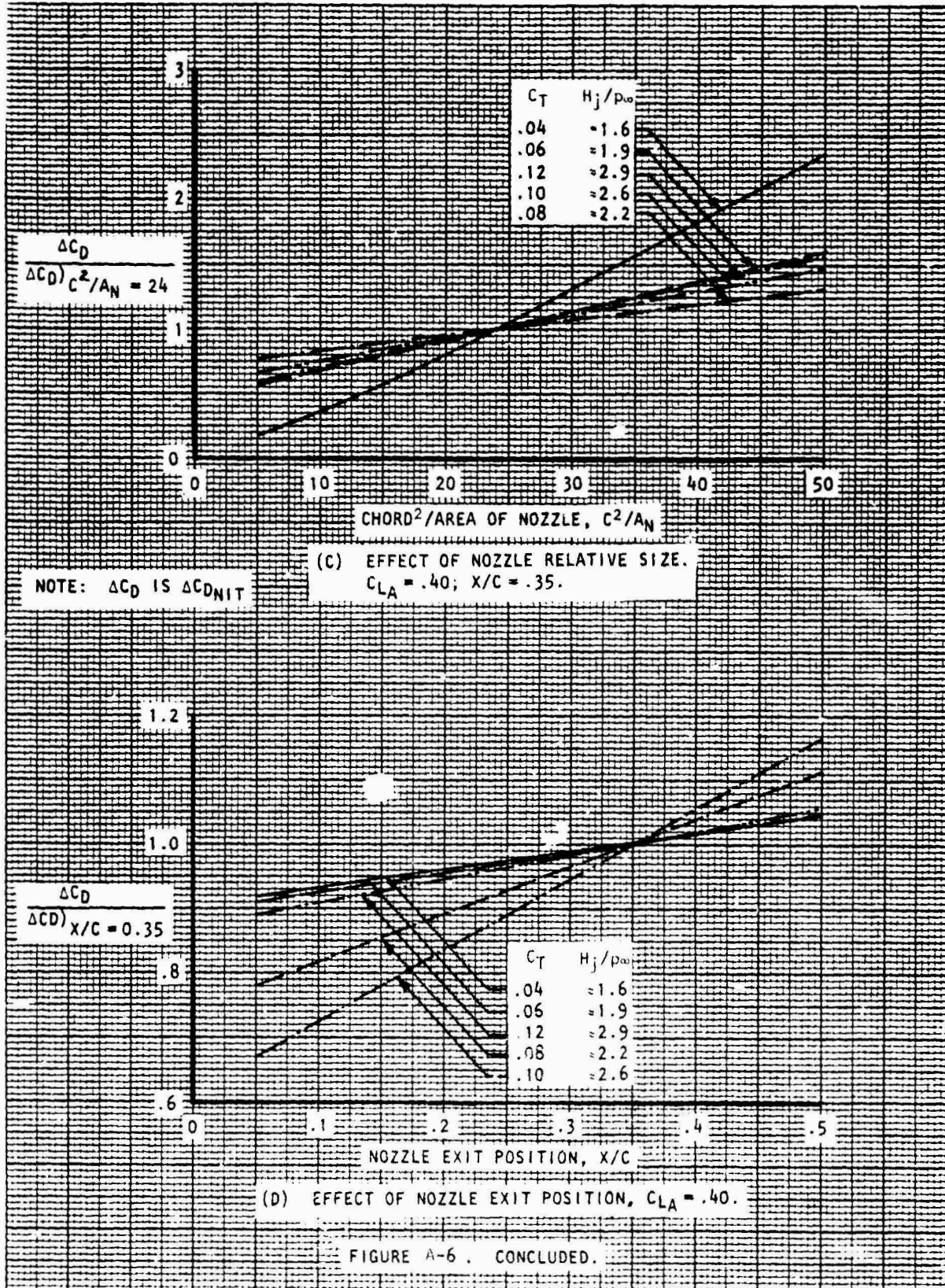




# USB CRUISE PROGRAM

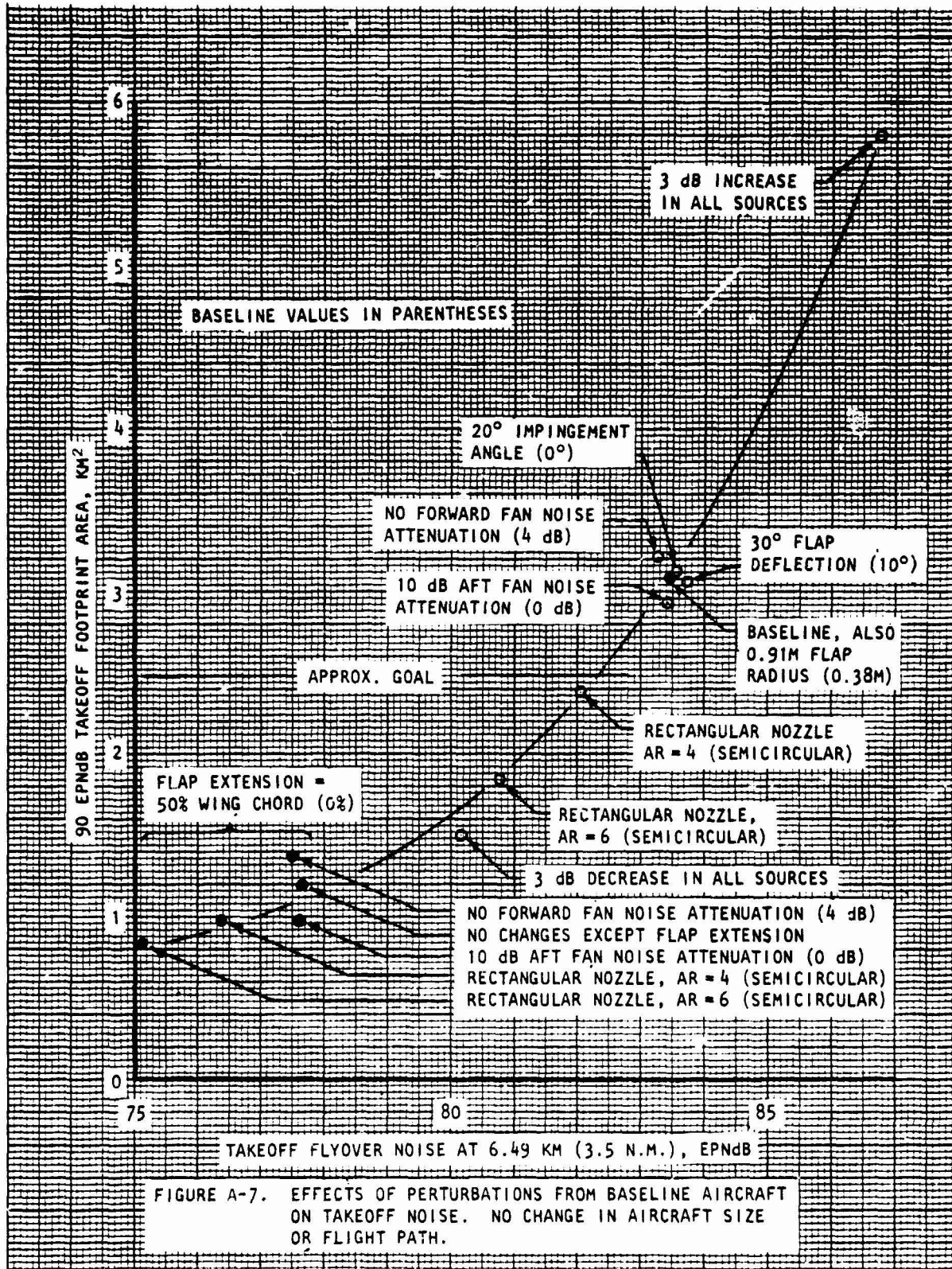


# USB CRUISE PROGRAM

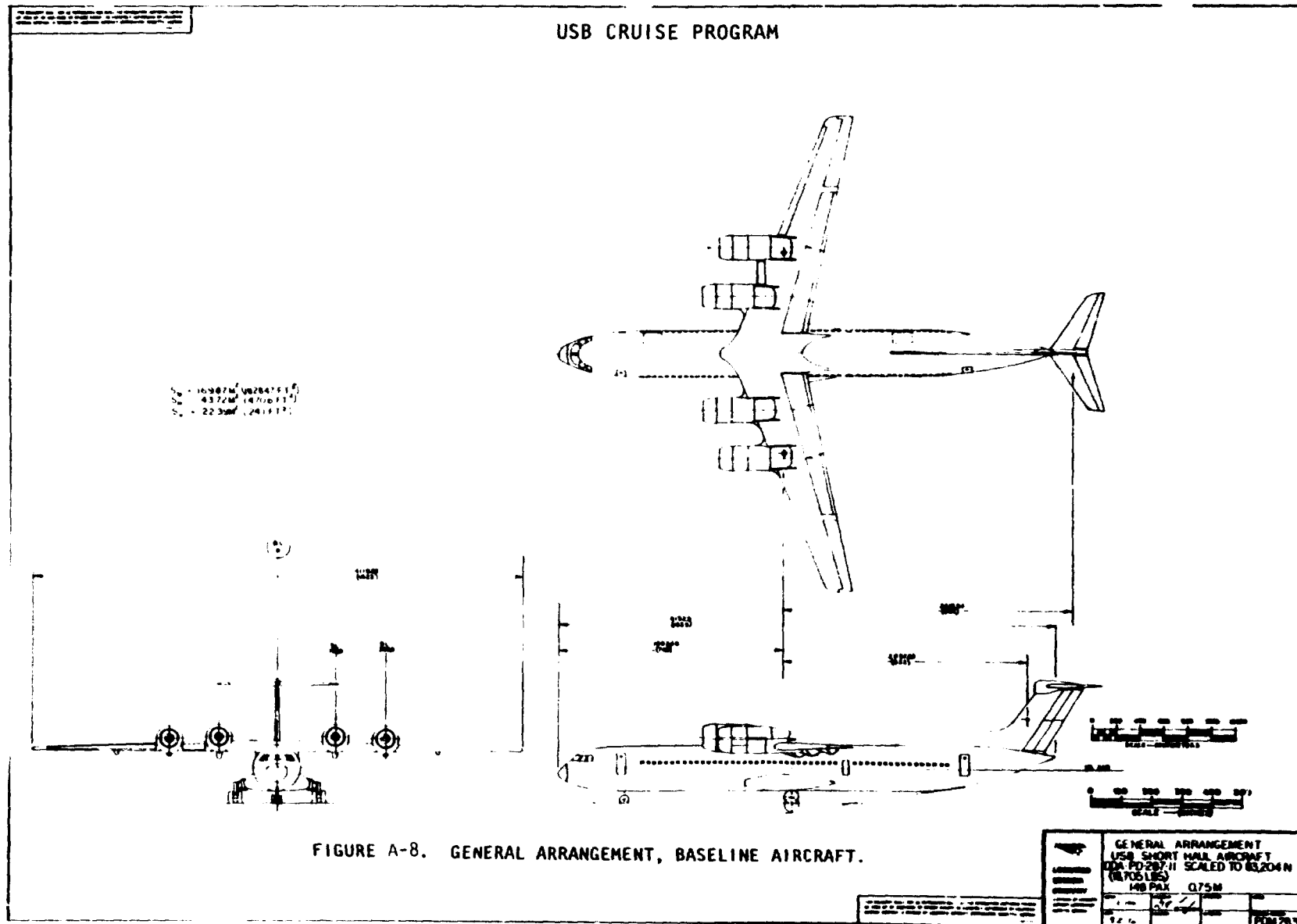




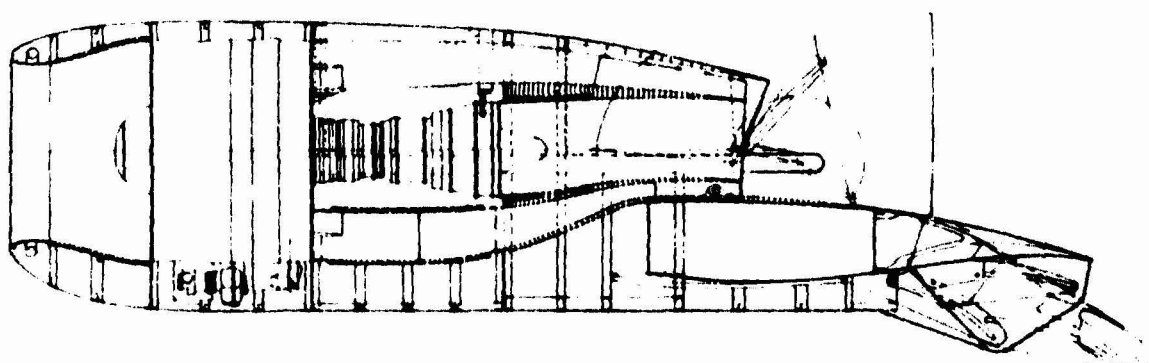
# USB CRUISE PROGRAM



## USB CRUISE PROGRAM



ORIGINAL PAGE IS  
OF POOR QUALITY

[illegible]

ORIGINAL PAGE IS  
OF POOR  
QUALITY

# USB CRUISE PROGRAM

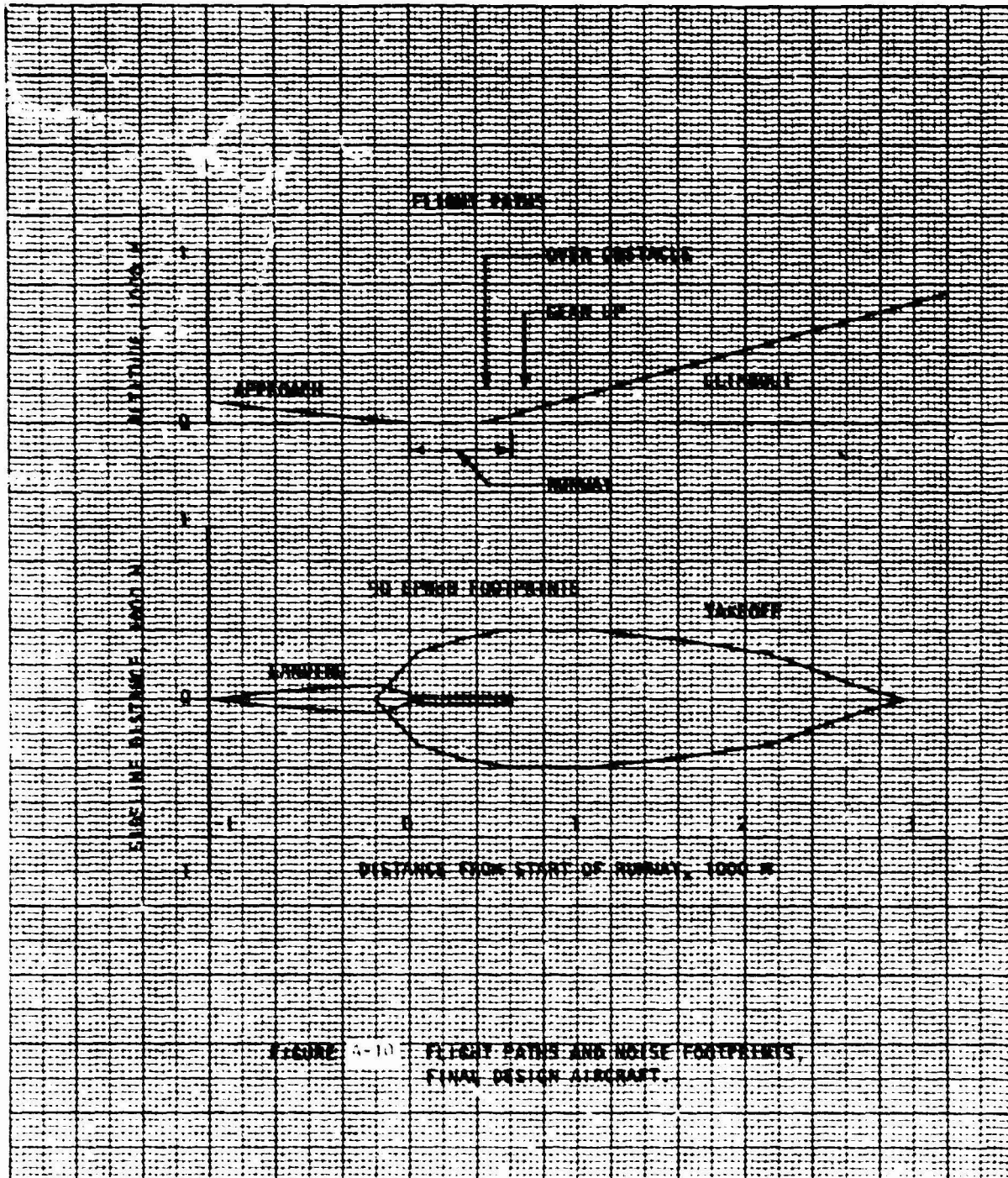
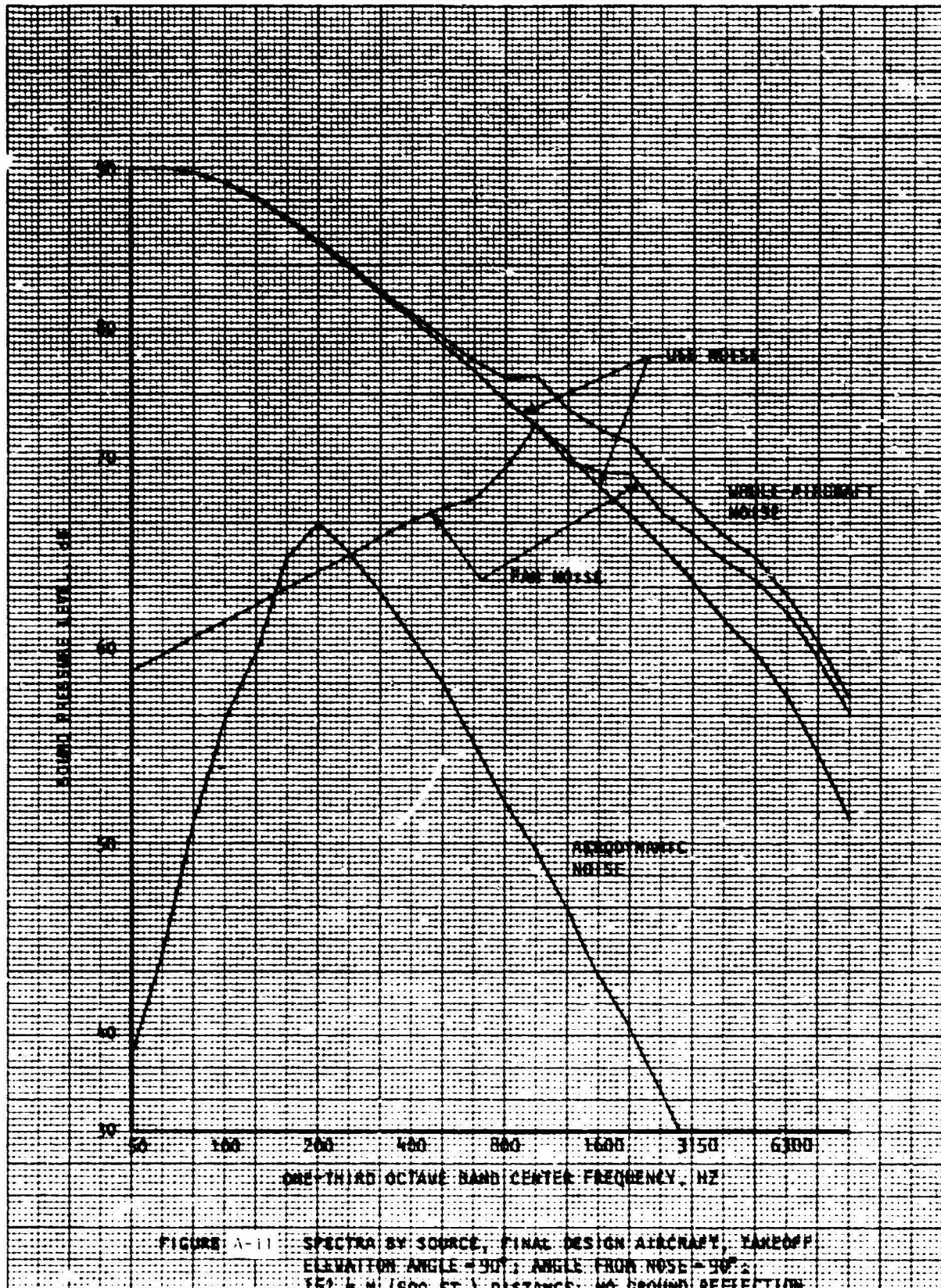


FIGURE 4-10 FLIGHT PATHS AND NOISE FOOTPRINTS, FINAL DESIGN AIRCRAFT.



# USB CRUISE PROGRAM



# USB CRUISE PROGRAM

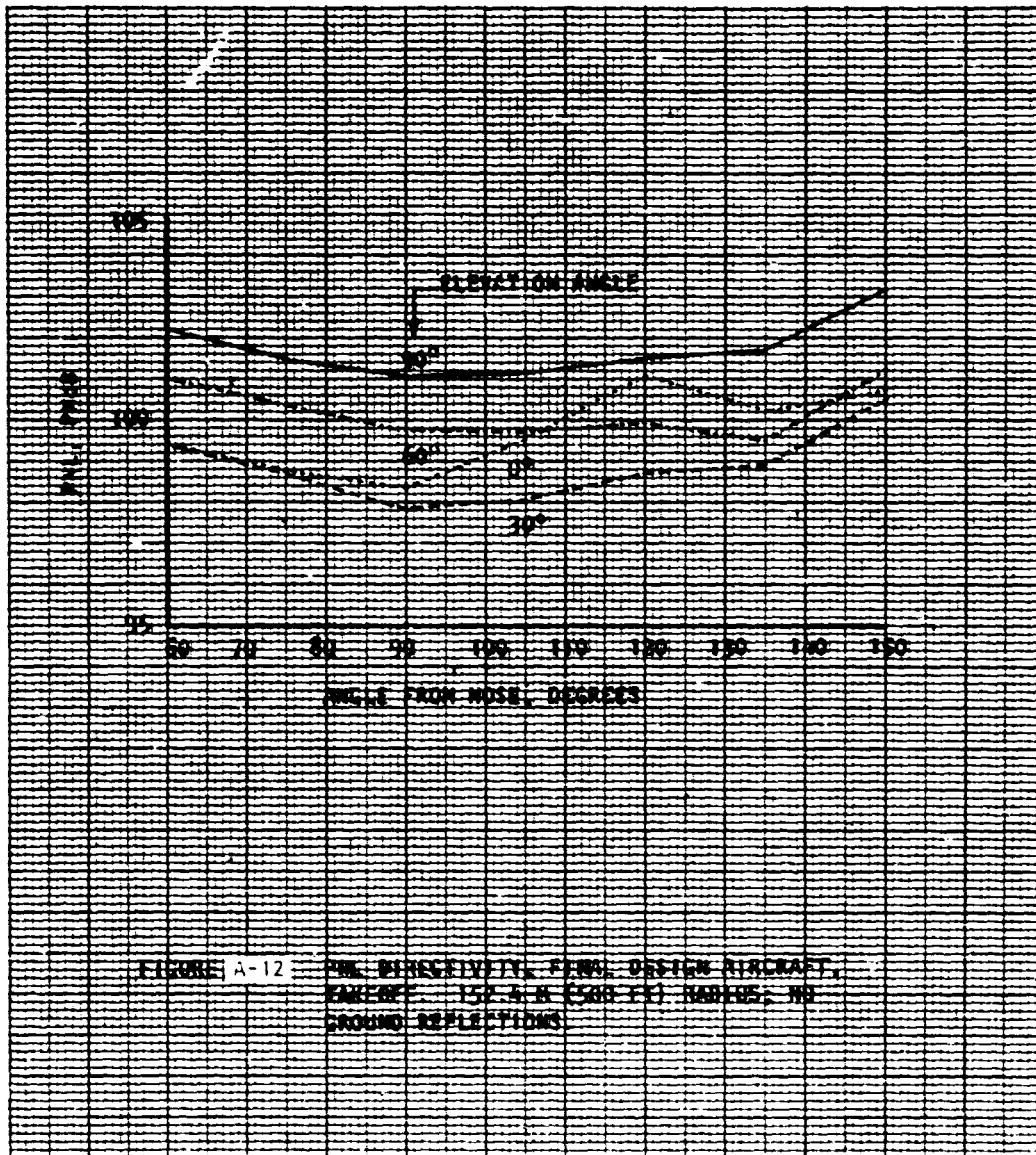


FIGURE A-12 F-105 DIRECTIVITY, F-105 DESIGN AIRCRAFT, EARLY-150 A.M. (500 FT) RADIUS, NO GROUND REFLECTIONS